Mathematical modeling and simulation of non-equilibrium plasmas : application to magnetic reconnection in the Sun atmosphere

Quentin Wargnier

université PARIS-SACLAY | École doctorale de mathématiques Hadamard (EDMH)

université PARIS-SACLAY

NNT : 2019SACLC066

CentraleSupélec

THÈSE DE DOCTORAT

de

L'UNIVERSITÉ PARIS-SACLAY

École doctorale de mathématiques Hadamard (EDMH, ED 574)

Établissement d'accueil : Ecole polytechnique

Laboratoire d'accueil : Centre de mathématiques appliquées de Polytechnique, UMR 7641 CNRS

Établissement d'inscription : Centrale-Supélec

Spécialité de doctorat : Mathématiques appliquées

Quentin WARGNIER

Mathematical modeling and simulation of non-equilibrium plasmas: application to magnetic reconnection in the Sun atmosphere

Date de soutenance : 15th November 2019

Jury de soutenance :

ELENA KHOMENKO	(Instituto de Astrofisica de Canarias) Examinateur
IRENE GAMBA	(Austin, University of Texas) Examinateur
CHRISTOPHE CHALONS	(Université Versailles) Examinateur et Président de jury
THIERRY MAGIN	(von Karman Institute) Examinateur
MARC MASSOT	(Ecole Polytechnique) Directeur de thèse
NAGI NICOLAS MANSOUR	(NASA Ames Research Center) Invité
STEFAAN POEDTS	(KU Leuven) Rapporteur
STÉPHANE BRULL	(Institut de Mathématiques de Bordeaux) Rapporteur

Fondation mathématique FMJH Jacques Hadamard

NASA

ÉCOLE POLYTECHNIQUE UNIVERSITÉ PARIS-SACLAY

CMAP

To Yvette, Sylvie, Bernard and Florian.

I pay no attention whatever to anybody's praise or blame.
I simply follow my own feelings.

Wolfgang Amadeus Mozart

ACKNOWLEDGMENTS

Lorsque j'écris ces lignes pour conclure la rédaction de cette thèse, je ne peux m'empêcher de penser à cet enfant curieux du fonctionnement de l'univers et admiratif devant la grandeur de ce dernier. Il y avait dans l'esprit de cet enfant une passion et une admiration pour les étoiles, un désir de comprendre et d'apprendre qui allait se muer en plaisir, puis virer en rêve qu'il souhaitait un jour toucher du bout du coeur. Ses pensées les plus folles, les plus impossibles, difficiles ou inaccessibles en apparence, se sont implantées si fortement dans son esprit qu'il a fini par les croire possibles voire réalisables. Cette pensée liée à un désir violent et passionné, s'est traduite naturellement comme quelque chose de nécessaire, fatale et prédestinée, comme un évènement qui devait se produire...

Thesis commitee First, I would like to thank the commitee members for not only travelling to Paris for my defense but for their honest and helpful feedback, their questions, which served to elevate the quality of this thesis beyond what I was capable on my own. I would like to thank you for your extremely detailed comments and insights.

In particular, Stefaan Poedts and Stephane Brull have my utmost gratitude for agreeing to review the manuscript. I would like to thank Irene Gamba for our interactions during the defense. Additionally, I have really appreciated my trip to Austin during the summer 2019, it was a very productive, satisfying and interesting collaboration. I hope that we will have the opportunity to collaborate and work again on topics of our interests. I want to thank Elena Khomenko for participating in my defense and agreeing to be part of the commitee members. It was a great opportunity for me to meet you, I really hope that we will have the opportunity to interact again. Finally, I would like to thank Christophe Chalons and Stéphane Brull for all the interactions we had during the past years, in particular during the CANUM 2018 or SMAI 2017. These interactions helped me a lot in the understanding of some mathematical aspects of this thesis.

Again, I would like to acknowledge the commitee members. I would like to point out that this thesis has shown that, without a multidisciplinary approach with many collaborations from several scientific fields, it would not have been possible to accomplish this work.

Encadrants et collaborateurs Tout d'abord, je tiens à remercier Pierre Kestener pour sa patience. J'ai particulièrement apprécié les interactions ainsi que le travail que nous avons réalisé en terme d'implémentation et développement de code. J'ai appris beaucoup de ces interactions et j'espère sincèrement avoir l'occasion de pouvoir à nouveau travailler avec lui sur ces questions.

Je tiens à remercier Thierry Magin. Je n'oublierai pas toutes ces interactions que nous avons pu avoir au VKI. En particulier, je le remercie pour sa patience, l'attention qu'il a portée à ce travail et sa disponibilité. Depuis la première fois où je l'ai rencontré en Avril 2015, il m'a toujours orienté et guidé pendant la thèse tout en me faisant confiance et en me laissant une grande liberté de travail. Grâce à lui, j'ai pu avoir des grandes opportunités et rencontrer beaucoup de personnes dans le domaine. Pour toutes ces raisons, et bien d'autres encore, je le remercie pour avoir fait de cette thèse un succès et un travail clairement accompli.

Je souhaiterais également de tout coeur exprimer ma gratitude à Nagi Mansour pour cette opportunité en or. Je le remercie pour ses conseils, ses encouragements, sa confiance en moi et surtout le soutien qu'il a pu me donner pendant toutes ces années. Ce qui a commencé comme un stage de fin d'études en 2015, s'est finalement avéré être une collaboration très productive et satisfaisante, tant sur le plan humain que scientifique, qui j'espère, continuera dans le futur. Il n'y aura pas de mots assez forts pour décrire ces premières expériences à NASA qui resteront à jamais gravées dans ma mémoire et qui ont eu un impact important dans ma vie. Et tout cela, grâce à lui.

Je ne pourrai jamais assez remercier Benjamin Graille. Sa confiance, sa rigueur, son excellente communication, sa méthodologie, sa connaissance et son expertise ont été clairement à l'origine de tout ce travail. J'ai pu apprendre énormément de choses dans le domaine des mathématiques appliquées grâce à lui. Par ailleurs, j'insisterais personnellement sur son aspect humain qui a permis de transformer l'homme impatient et peu rigoureux que j'étais. Je n'oublierai pas les échanges que nous avons pu avoir, je pense notamment au débat sur la notion de conscience (CANUM 2018) ou tout simplement l'aspect après thèse. Je tiens à noter également qu'il a aussi été très présent dans les moments difficiles que j'ai pu rencontrer au cours de cette thèse, et je l'en remercie.

Enfin, je remercie un grand monsieur: Marc Massot. Je pense que nous pourrions écrire un second manuscrit si nous avions à décrire tout le long chemin parcouru ces 5 dernières années. Bien que ce fut un plaisir d'écrire ces papiers scientifiques et de travailler avec lui, nous aurions pu aussi prendre le temps d'écrire une pièce de théâtre ou un roman sur tout le déroulement incroyable de cette thèse, qui aurait pu être digne d'un grand sketch comique ou bien d'une oeuvre tragédique à la Shakespeare. Merci pour tout. Il y a 5 ans, il m'a donné une opportunité de stage de fin d'études aux Etats-Unis, suivi d'une thèse qui changera ma vie pour toujours. Ce sont des mots qui peuvent paraître forts mais il s'agit de la vérité. Il m'a fait confiance à un moment inattendu, rendant un rêve d'enfant une réalité. Ce qui fut impossible pendant ces nombreuses années d'études, a été rendu possible grâce à lui. Il a eu la capacité et la patience de me donner les outils et la force pour repousser mes limites. Ainsi, je ne le remercierai jamais assez pour tout cela.

CMAP Ecole Polytechnique Pendant toutes ces années de thèse, j'ai eu la chance de pouvoir travailler avec Alejandro Alvarez Laguna, un encadrant de thèse et ami, qui m'a permis d'accomplir tout ce travail. Je garderai en mémoire cette session violon et piano sur le thème de Bohemian Rhapsody, ces interactions dans le fameux building 566, le beer meeting du VKI, plus générale-

ment tous nos séjours en Californie. Merci également d'avoir été présent, tant sur le plan humain que sur le plan scientifique, dans les moments difficiles de la thèse. Je le remercie pour sa relecture détaillée et son encadrement de manière générale. J'espère avoir la chance de pouvoir travailler avec lui à l'avenir.

Je remercie également Monsieur Scoggins. Il a été d'un grand soutien tout au long de cette thèse. Merci pour toutes ces interactions. J'espère que nous aurons la possibilité de nous revoir en France ou aux Etats-Unis.

Je remercie notre futur Elon Musk européen Ruben Di Battista. Merci pour son aide et je lui souhaite le meilleur pour la fin de sa thèse et son avenir professionnel dans le domaine de l'aérospatial. Une partie de ce travail a pu être réalisé grâce à lui.

Je remercie Teddy Pichard pour sa relecture détaillée de la thèse. Grâce à lui j'ai pu accomplir cette rédaction de thèse et ce travail. Je lui souhaite également le meilleur pour la suite de sa carrière académique.

Je ne pourrai imaginer ces années de thèse sans penser à mes camarades Marc Arthur N'Guessan et Pierre Cordesse. Je pense que nous sommes d'accord pour statuer que l'été 2018 restera à jamais gravé dans nos mémoires. On aura quand même bien rigolé pendant ces années. N'oublions pas qu'il "faut toujours rigoler".

Enfin, je remercie tout le bureau 2003 du CMAP, Léa, Thomas, Alejandro, Othmane. Je remercie également l'ensemble du secrétariat du CMAP.

von Karman Institute et Belgique Comment oublier ces périodes passées au VKI et en Belgique ? Ces beer-meeting ? Ces soirées au Centro Cabraliego ?

I would like to thank Fran for his support. I will never forget our times spent in Brussels as well as our summer program at NASA 2017 living in our mansion: the Pool-House ! I hope we will have the opportunity to meet again and spend some times at Centro Cabraliego or at the University of Louvain-la-neuve. I wish him the best for his future in terms of career and personal achievements.

I would like to thank Andrea Fagnani for his support as well. I will never forget the time we have spent in California, our surfing sessions in Santa Cruz during the week end, our party in San Francisco... Without him, California would have been a complete different story. Again, I wish him the best for his future in terms of career and personal achievements. I would add one last word: Psss sh.

Obviously, I would like to thank Thanos Margaritis for his support. Without him, California in 2018 would have been much more less funny and incredible.

Je souhaiterais également remercier Nicolas Gerbal et Edouard Bissen ainsi que tous les autres stagiaires VKI de 2016. Ces périodes de stage furent des moments incroyables que je ne suis pas prêt d'oublier.

NASA Ames Research Center et Etats-Unis Dans un premier temps, je tenais à remercier Jeremie Meurisse pour son soutien et son aide. Je le remercie de m'avoir accueilli en Californie plusieurs fois pendant toutes ces années. Il y aurait tellement de choses à dire sur toutes ces

périodes en Californie que nous aurions pu en faire une oeuvre cinématographique. Je pense en particulier au Bus Party, Las Vegas, notre trip Silicon Valley-San Francisco en vélo, nos week-ends à Los Angeles. Finalement, toutes ces périodes qui ont rendu mes séjours en Californie incroyables et inoubliables. Je le remercie également pour tout ce qu'il m'a appris cet été 2019 concernant l'implémentation du code sur la structure Pleiades.

Ensuite, je remercie également Patricia Ventura Diaz. Je lui souhaite également le meilleur sur le plan personnel et professionnel (en particulier à NASA).

Par ailleurs, je remercie l'ensemble de l'équipe de Nagi Mansour à NASA Ames Research Center. Je pense notamment à Seokkwan Yoon, Joseph Ferguson, Alexandre Quintart, Marcos, John.

Je tiens également à remercier Khalil Bensassi pour son encadrement. Il a également beaucoup contribué à mon stage de fin d'étude en 2015, et mes opportunités après thèse.

I would like to thank Alan Wray, David Hathaway and the whole Heliophysics team of NASA Ames Research Center. I would like to thank them for their honest and helpful feedback during all these years.

A quoi aurait pu ressembler le Summer program 2018 et 2019 sans Joffrey Coheur ? Merci à lui pour son soutien et d'avoir fait le déplacement depuis la Belgique pour assister à ma soutenance de thèse. J'espère que nous aurons l'occasion de refaire des sessions de Surf, de limousines et de musculation ainsi que des soirées. Bon courage à lui pour sa fin de thèse et j'espère que nous aurons l'occasion de nous revoir en Californie. Psss sh.

I would like to thank Karishma alias Karishmush for her support during all these years. Unfortunately, the time goes fast but in fact, we both know that "there is no space-time for friendships". Thank you so much for your encouragement before my PhD. Thank you for everything.

Merci à Olivier van Cutsem. Remerciements en quelques mots: Las Vegas, limousine, divans du monde, soirée anniversaire Patricia. Voilà.

Par ailleurs, je remercie Bérénice Charrez pour ses encouragements et son soutien, sans qui cette fin de thèse aurait été bien plus compliquée. Elle a été présente et m'a donné beaucoup de courage pour atteindre cet objectif et finaliser la rédaction de la thèse dans les meilleures conditions.

France Tout d'abord, je souhaiterais remercier Thomas Monnot alias Michel et Loïc Souffois. Sans eux, les années SUPMECA auraient été bien moins fun. Merci d'avoir fait le déplacement pour assister à ma soutenance de thèse, ce fut un moment surréaliste et incroyable. Il est temps de nous revoir en Californie.

Je ne remercierai jamais assez Gautier Billaux qui a été d'un soutien incroyable pendant ces longs mois de rédaction. Il a été très présent, il est celui qui a su me redonner la motivation, le courage et la force de terminer la thèse. Il ne put porter ce fardeau à ma place, mais il put me porter jusqu'en haut de la montagne du destin pour terminer ce périple. Un jour, alors que tout espoir de finir la rédaction semblait disparaître, que la fatigue prenait peu à peu le dessus, il s'adressa à moi en disant: "Je lis dans tes yeux cette même peur qui pourrait saisir mon coeur, un jour peut venir où ton courage faillira, où tu abandonneras ta thèse et tes amis et briseras tout lien, mais ce

jour n'est pas arrivé, aujourd'hui tu combattras". Et c'est ainsi que je pus entamer la conclusion de cette thèse.

Je remercie également Monsieur Hariel et l'ensemble de la meute. Ces liens d'amitié m'ont donné l'envie et le courage de démarrer cette thèse. Glatigny forever.

Je remercie Mathieu pour tout ce qu'il a fait pour moi. Sans lui, ces dernières années à Paris auraient été différentes. Je n'oublierai pas ce voyage en Chine, ces soirées sur Paris, le côté obscur de la force, Interstellar, ces débats sur les trous noirs en amphithéâtre qui ont réveillé en moi cette envie de travailler dans le domaine astrophysique. Je remercie également mes deux camarades Thomas Epalle et Jérôme Vacher. Grâce à ce quatuor, nous avons pu traverser l'espace et le temps à de nombreuses reprises.

Merci à Adeline. Un jour, alors que tout espoir semblait éteint, que l'obscurité semblait dominer la lumière, que la fin de thèse approchait, elle se tourna vers moi et s'écria :" En avant Quentin! Ne crains aucune obscurité! Debout! Debout cavalier de Cachan! Une journée de thèse, une journée de rédaction, une journée rouge avant que le soleil ne se lève! Au galop !".

Je pense également à Tibo et Oillic. Je n'oublierai jamais ces moments passées à Paris. Les sessions de Surf à Hossegor, week-end à Lille, notre soirée sur Castro Street ...

Pour la passion que nous partageons et pour son soutien, je remercie également Floriane.

Je remercie également mon très cher Ryan d'avoir fait tout ce chemin depuis Perpignan pour assister à ma soutenance de thèse et d'avoir rendu ce dernier week-end unique et inoubliable. Et pour que cette amitié perdure et continue de transcender l'espace et le temps, je ne dirai qu'une chose: Tepalal.

Je remercie ma colocataire de toujours Flora pour son incroyable soutien et ses conseils concernant mes choix de vie et de carrière. Merci également à Matthieu.

Merci à Julie, Noémie, Alexandre et Thomas d'être venus me soutenir. Vous avez toujours été d'un grand soutien pendant toutes ces années. Vous avez toujours cru en moi depuis les années lycée, depuis le début. Merci infiniment.

Par ailleurs, je pense également à Michel Laffilée, qui a joué un rôle déterminant concernant mon orientation post-baccalauréat et mes choix de carrière.

Pour son soutien, je remercie le député et ancien Maire de Dieppe Sébastien Jumel. Son aide a été déterminante et essentielle dans la réalisation de ce projet à NASA. Je remercie également Nicolas Langlois et l'ensemble de la mairie de Dieppe qui m'ont toujours soutenu et encouragé.

Famille Je remercie toute la famille qui a toujours cru en moi et m'a toujours fait confiance. Je remercie mes oncles, tantes, cousins et cousines.

Merci à Philippe, Dominique, Caroline et Damien. Merci d'avoir fait tout ce voyage depuis le sud de la France pour venir assister à cette fin de thèse. Cela m'a beaucoup touché et m'encourage à aller encore plus loin. J'espère vous revoir en Californie. Merci pour vos encouragements.

Merci à Magali pour son soutien et ses encouragements. Merci également d'avoir fait ce voyage depuis la Normandie pour venir assister à ma soutenance de thèse.

C'est avec beaucoup d'émotions que je remercie mon grand frère pour tout. Je ne le remercierai

jamais assez pour tout ce qu'il a fait pour moi, et qui, pendant toutes ces années de thèse a su me redonner confiance en moi et me remettre sur le droit chemin. Je suis fier de lui et je m'inspirerai toujours de son pragmatisme, sa détermination, son courage, sa sensibilité artistique, sa perspicacité hors norme, son ambition et sa ténacité qui ont permis de faire évoluer l'enfant que je fus en l'homme que je suis. Je remercie également Charlotte pour son soutien. Je sais qu'elle a toujours eu confiance en moi et cru en mes choix.

Je souhaiterais remercier mes parents. Ils ont été d'un grand soutien et une source constante d'amour et d'encouragement pendant toute ma vie. Sans eux, tout cela n'aurait pas pu être possible. Je leur dois tout. Je suis fier de ce qu'ils sont, de ce qu'ils représentent et de ce qu'ils sont devenus. Merci pour tout.

Enfin, je remercie ma grand-mère. Elle fut toujours à l'écoute et tenta en vain de répondre à mes innombrables questions scientifiques. Dorénavant, nous serons à jamais liés dans le temps, par cette promesse que je lui avais faite un soir de Printemps.

CONTENTS

LIST OF FIGURES

LIST OF TABLES

GENERAL INTRODUCTION

0.1 Context of the thesis

Partially ionized plasma in general, and, especially in the study of magnetic reconnections (MR), are characterized by a multi-scale nature involving multiple spatial and temporal scales. Depending on the application (for example, in Tokamak (Pamela et al. (2019)), astrophysical plasmas (Goedbloed & Poedts (2004)), space weather applications (Lapenta (2012))), partially ionized plasmas may be strongly or weakly magnetized, out of thermal and chemical equilibrium, in highly or weakly collisional regimes, thus, in many possible regimes and conditions. Therefore, the study of partially ionized plasma involved in MR presents a specific challenge. The physical understanding and study of this phenomenon give rise to a wide variety of models whose complexity is intrinsically related to the level of description of these scales. Several applications fall within this multiscale framework such as combustion (see Duarte (2011)) or plasma discharges (see Bourdon et al. (2016); Croes et al. (2018)). The rigorous development of mathematical models for partially ionized plasmas and their numerical simulation, constitutes an important step in the description and understanding of the MR process. However, this approach raises several difficulties in terms of modeling and numerical strategy. Considering the large range of temporal and spatial scales involved, an effort is essential to develop models with a rigorous mathematical structure combined with proper asymptotic limits. From the numerical point of view, a numerical strategy is required to tackle the problem of numerical stiffness induced by the multi-scale nature of these models.

Such plasmas are essential in various astrophysical environments such as the Sun, the heliosphere, magnetosphere of the Earth and planets, the interstellar medium. They involve a wide range of parameters and conditions. In particular, in the atmosphere of the Sun, several plasma regimes and conditions are to be found. At the photosphere, which is a 500 km thick layer that emits the visible light of the Sun, the temperature can vary from 4000 K to 6600 K and the pressure is around thousands of Pascals (Bellot Rubio & Orozco Suárez (2019); Vernazza et al. (1981); Carlsson & Stein (1995)). The magnitude of the magnetic field can be either large in active regions, *i.e.*, around thousands of Gauss in sunspots (Bhowmik & Nandy (2018); Fröhlich & Lean (2004);

Solanki (2003)), or weak, a few Gauss in orders of magnitude in quiet Sun regions (see Wiegelmann et al. (2014)). In general, the photosphere contains weakly ionized and highly collisional plasmas. Then, we have the chromosphere which is a 2000 km thick layer at the top of the photosphere, and, the transition region which is a 100 km thick layer at the top of the chromosphere. In these regions, the temperature can vary from 4000 K to 10^6 K and the pressure from thousands of Pascal to just a few Pascal. Eventually, at the top layer of the Sun atmosphere, we have the solar corona where the plasma is mainly fully ionized and weakly collisional with a high temperature (up to several million of Kelvin). Therefore, in the whole solar atmosphere, the plasma can be partially or fully ionized, weakly or strongly magnetized, weakly or strongly collisional, allowing for thermal nonequilibrium processes, depending on the region considered. The observations of the low Sun atmosphere provided by the Solar Optical Telescope (SOT) (see Kosugi et al. (2007)), and the Interface Region Imaging Spectrograph (IRIS) mission (see De Pontieu et al. (2014); Li et al. (2019); Kowalski et al. (2019)), have confirmed that the solar atmosphere is a complex and dynamic environment involving a wide unsteady processes occurring at different temporal and spatial scales. Some characteristic properties of the plasma such as the characteristic mean free path, hall parameter, collision times between the particles may vary by several orders of magnitude. Therefore, it is desirable and a challenge to develop a unified model that can be used under the large diversity of plasma parameters, unsteady processes occuring at different spatial and temporal scales, for conditions in the solar atmosphere.

Apart from the various conditions and regimes that are involved in the solar atmosphere, the spectacular rise of temperature in the transition region attracts the attention of the scientific community (see Vernazza et al. (1981); Amari et al. (2014); Amari et al. (2018)). In particular, several studies have been performed to explain the mechanisms responsible for the coronal heating. The process of coronal heating is one of the biggest enigmas in solar physics, (see De Pontieu et al. (2011); Klimchuk (2015)). Several models have been proposed to explain this phenomenon. The propagation of Alfvén waves (see Poedts et al. (1989); Goossens (1991); Vranjes et al. (2006); Mcintosh et al. (2011)) that dissipate energy either by phase mixing (see Heyvaerts & Priest (1982); Cargill et al. (2016)) or by resonant absorption (see Grossmann & Tataronis (1973)). Then, we have the model based on the propagation of drift waves (see Vranjes & Poedts (2009, 2010)). Finally, we have the magnetic reconnection process, where the reconnection itself is shown to be an efficient process for heating, as shown by N. Parker (1972); Priest et al. (2002); Shay et al. (2018). In addition, we also have the process of nanoflares which arises from a magnetic reconnection event, as shown by Parker (1988); Cargill (2013). More recent observations have shown that the heating is taking place at chromospheric height related to chromospheric phenomena, as shown by De Pontieu et al. (2009, 2014); Rogava et al. (2010). Thus, several approaches have been envisioned by the scientific community to explain the rise of temperature observed in the transition region.

The magnetic reconnection process is a relaxation of the topology of the magnetic field created by a local change of the connectivity of the magnetic field lines. This process is due to relevant dissipative effects taking place in a localized region, called current sheets, where the magnetic field lines are reconnecting. In this region, the resistivity is playing a major role. Several models have been developed to explain the process of magnetic reconnection. Parker (1957) has proposed a model of the current sheet, where the spatial scale of the transverse direction is proportional to the

square root of the resistivity. However, this model appears to be not appropriate to represent the framework of chromospheric phenomena. Indeed, the characteristic time of the mechanism (or the reconnection rate), predicted by the model, is too large to explain the chromospheric phenomena (even the magnetospheric phenomena). Alternatively, Petschek (1964) has introduced an alternative model where slow shocks are considered. In this model, a higher reconnection rate is obtained and a more realistic description of the energy release is given. In addition, the magnetic reconnection process may involve shock waves when the reconnection occurs. Unfortunately, it is still not evident which conditions make Petschek-type reconnection possible. Numerical simulations are not able to reproduce Petschek-type reconnection unless the resistivity is localized in a small region (see Scholer (1989); Biskamp (2000); Ugai (1999), more recently Baty et al. (2014)). Further investigations have been performed to study ambipolar diffusion, produced by the interactions between ions and neutrals. These interactions reduce the magnetic field profile and increase the reconnection rate, as shown by Brandenburg & Zweibel (1994); Heitsch & Zweibel (2003); Tsap & Stepanov (2011); Khomenko & Collados Vera (2012). Additionally, the recombination rate of the ions induces a loss of ions in the reconnection region which increases the reconnection rate too, as shown by Alvarez Laguna et al. (2016); Leake et al. (2012); Leake et al. (2013). In addition, in the diffusion region, small-scale structure such as tearing instabilities can be produced. These structures can increase the reconnection rate, as shown by Zweibel (1989); Papini et al. (2018); Tolman et al. (2018). In Lapenta (2008); Horiuchi (2018), the formation of magnetic islands in the reconnection region increases the reconnection rate. This reconnection rate appears to be higher than in the Sweet-Parker approach. This phenomenon has been observed in partially ionized plasma in Leake et al. (2012). In summary, since the dissipative effects are playing a major role in the magnetic reconnection process, we point out that an accurate description of these effects is the key to fully understand these phenomena in the chromosphere.

The understanding and study of the multiscale mechanism of magnetic reconnection in solar chromosphere conditions, is essentially based on two key ingredients which are strongly linked: a model and a robust numerical strategy. First, a model is proposed, thus, a numerical strategy can be developed to perform numerical simulations. Then, in order to guarantee that the proposed numerical scheme is sufficiently accurate, either we guarantee that all the scales associated with the model are captured, or, a strategy is established to guarantee that the asymptotic limits of the model are preserved. However, performing a numerical simulation with a multiscale model, where a large spectrum of temporal and spatial scales is involved, is difficult from the numerical point of view due to the high numerical stiffness. Therefore, reducing the complexity of the model to overcome these issues can be envisioned.

However, it is a challenge to guarantee a sufficient level of description of the main leading processes involved in magnetic reconnections, while reducing the level of complexity of the model. This step requires a mathematical study of the model where its asymptotic limits are clearly identified. The asymptotic limits allow to eliminate all the scales which are not relevant in the context of the considered application. For example, in the solar atmosphere, it appears natural to neglect the effects at Debye length scales, since the characteristic scales in the solar atmosphere are much larger. Or, the characteristic collision times between particles may be considered much smaller than the characteristic time of a particular region in the solar atmosphere (for example, in regions

where the plasma is highly collisional), thus, leading to a fluid level of modeling.

A large variety of numerical strategies has been devoted to the numerical simulation of magnetic reconnection under solar chromosphere conditions (see Leake et al. (2012); Alvarez Laguna et al. (2016)). Among all the possible numerical methods, we can identify some of the required conditions for effectiveness and performance, in the context of our application. Generally, the numerical method is shown to be effective by its capability in terms of accuracy and quality/high fidelity of the numerical solution. This property is directly related to the mathematical theoretical background upon which the numerical method is built. In the context of partially ionized plasmas, the numerical method has to guarantee that all the physical and temporal scales, relevant in MR process, are correctly captured. Therefore, a good quality of the solution has to be ensured, even in the presence of a high numerical stiffness. Then, one of the main issues encountered in this process, is the propagation of shock waves, discontinuities or sharp gradients appearing in localized regions. The chosen numerical method has to ensure that these waves are properly captured and guarantee a good quality of the numerical solution in these regions. Additionally, a high level of accuracy has to be guaranteed in the reconnection region, in order to describe all the dissipative processes occuring in this region.

One of the possibilities to tackle these issues, is to combine a numerical method with a High Performance Computing (HPC) and Adaptive Mesh Refinement (AMR) strategy. Therefore, a high level of mesh refinement is guaranteed in the regions of our interest and all the scales can be numerically resolved. This approach requires the development of techniques to take advantage of massively parallel architectures. Following this strategy, an effort is focused on the exploitation of the computational ressources to perform numerical simulations with a high degree of details. Here, a robust numerical method, simple from the algorithmic point of view, is adopted to overcome computing limitations and ease the numerical implementation. Thus, the numerical method has to be efficient in terms of practical implementation, degree of algorithmic complexity and computational requirements.

The purpose of thesis is to develop 1-a model for magnetized plasmas, with a detailed description of the dissipative effects, and 2- development of an efficient numerical strategy, guaranteeing robustness and high accuracy, for the purpose of simulating a magnetic reconnection process under solar chromosphere conditions. Therefore, our attention is focused on three main aspects :

1. **The development of a unified model** for plasmas valid in the whole solar chromosphere which inherits a rigorous mathematical structure combined with proper asymptotic limits. The model has to be sufficiently accurate and should involve all the required scales to fully describe the process of magnetic reconnection.

2. **Modeling of the dissipative processes** related to the proposed model. Therefore, the unsteady energy from magnetic energy to kinetic and thermal involved in the magnetic reconnection by dissipative process is properly described.

3. **The development of an efficient numerical strategy** coupled with modern computer architecture to perform numerical simulations with a high level of accuracy at an affordable time. A robust and accurate numerical scheme is developed to tackle the multiscale problem of

magnetic reconnection.

0.2 State-of-the-art

Strong efforts have been performed by the scientific community to develop models, for the purpose of representing partially ionized plasmas under solar chromosphere conditions, transport properties for multicomponent plasmas and numerical strategies for simulating astrophysical plasmas, and, more specifically, for solar physics plasmas. In order to identify the key issues, a state-of-the-art is established and built on these three main topics.

0.2.1 Modeling

The most accurate description of a plasma is based on kinetic models, where the distribution function in the phase space for each species is solved, as used by Dawson (1983); Markidis et al. (2010); Aunai et al. (2013). Mainly, this approach is used for plasmas in a fully-ionized low-collisional regime, thus, in space weather applications (see Lapenta (2012)). However, this approach appears to be computationally too costly for a full scale representation of highly collisional partially ionized plasmas, for example, in solar lower atmosphere conditions.

Therefore, fluid Magnetohydrodynamic (MHD) models have been introduced in order to reduce the computational cost. Here, the plasma is modeled as a conducting fluid in the presence of a magnetic field. In this category, two types of fluid models to study the solar lower atmosphere have been developed: the single-fluid MHD and multi-fluid MHD models.

In the single-fluid approach, the plasma is considered as a one fluid in thermal equilibrium conditions, where all the species are considered to be at the same temperature. Conservation equations for mass, momentum, and energy, coupled to the magnetic induction equation, are solved. This model is assumed to be valid in a sufficiently collisional framework. In solar physics, this approach allows to study the formation of magnetic field concentrations at the solar surface in sunspots, magnetic pores, and the large-scale flow patterns associated with them (see Hartlep et al. (2012)). It is also used for simulating the lower part of the atmosphere of the Sun, *e.g.*, incorporating subgrid-scale turbulence models for the transport of heat and electrical resistivity (see Kitiashvili et al. (2015)). This approach has been widely used for astrophysical and nuclear confinement plasmas (see Goedbloed et al. (2010)). However, this approach only deals with thermal equilibrium plasmas. Therefore, this approach does not describe all the regimes involved with partially-ionized plasma in the solar lower atmosphere. In this context, modifications of the single-fluid MHD equation have been proposed to take into account the effect of the collisions between ions and neutrals. These interactions are relevant for describing the magnetic reconnection process since it reduces the magnetic field profile and increases the reconnection rate. This effect could be taken into account by including ambipolar diffusion (Pedersen dissipation) in the magnetic induction equation (Khomenko & Collados Vera (2012); Martínez-Sykora et al. (2015)). In Carlsson et al. (2016); Gudiksen et al. (2011), a simulation is performed with a 3D radiation magnetohydrodynamic code

Bifrost, where ambipolar diffusion is considered.

However, the single-fluid approach does not represent all the spectrum of temporal and spatial scales which are relevant to fully describe the process of magnetic reconnection. The dynamics of each species considered in a partially ionized plasma can not be captured with the single-fluid approach. In addition, this approach does not represent all the regimes and conditions to be found in the solar atmosphere. Therefore, other approaches have to be envisioned.

As an alternative to single-fluid and kinetic approaches, the multi-fluid MHD models have been introduced and used more recently to represent the non-equilibrium conditions of the chromosphere, based on continuity, momentum, and energy conservation equations for each species considered in the mixture (see Leake et al. (2012); Alvarez Laguna et al. (2016, 2018); Ni et al. (2018)). Here, the species are treated as separate fluids that can interact among each other through collisions and reactions, while the charged species interact with the electromagnetic field. Leake et al. (2012) performed a multi-fluid simulation of magnetic reconnection for a weakly ionized reacting plasma, with a particular focus on the solar chromosphere, by considering collisional transport, chemical reactions between species, as well as radiative losses. Khomenko et al. (2014) proposed a model for the description of a multi-component partially ionized solar plasma. Similarly, Wójcik et al. (2019) has proposed a novel multifluid model for partially ionized plasma to study the propagation of magnetoacoustic-gravity waves, which are generated by solar granulation. As performed by Braginskii (1965), the multi-fluid equations can be obtained by taking moments of the Boltzmann equation for each species. In this approach, a multi-fluid model for fully ionized plasmas including a complete description of the transport properties at the kinetic level, has been derived. Small-scale phenomena related to the decoupling between particles are captured while representing the full-scale dynamics. Therefore, deriving a model from kinetic theory appears to be the most rigorous and accurate way to derive macroscopic equations for plasmas.

Although the multi-fluid approach allows to describe partially ionized plasmas in many collisional regimes, no rigorous development from the kinetic theory based on correct physical hypotheses has been performed. Indeed, as shown by S. Benilov (1997), the multi-fluid equations can be obtained by means of the Chapman-Enskog method, assuming that the Knudsen numbers characterizing collisions of particles of any species between themselves are smaller than Knudsen numbers characterizing collisions of particles of different species. The multifluid approach is valid in conditions where collisions of particles of each species between themselves are more frequent compared with collisions of particles involving different species. Therefore, the multifluid model is showing several relaxation terms which make the system stiff, in particular, when a highly-collisional regime is considered, as shown by Alvarez Laguna et al. (2016) and Alonso Asensio et al. (2019). The scales associated with the stiffness of the multifluid system have not been considered and correctly eliminated in the development from kinetic theory.

Generally, the models used to describe partially ionized plasmas, such as multifluid models, consider thermal nonequilibrium processes between particles. Mostly, these models are found to be nonconservative, in particular, the equations of thermal energies. However, solving nonconservative hyperbolic systems is a delicate problem because of the definition of weak admissible solutions. If no dissipative effects are considered in the system, the nonconservative formulation is not suitable for the definition of discontinous solutions. In this framework, several studies have

been performed to properly define nonconservative products when discontinuous solutions are involved.

In the community of mathematics, only studies focusing on the convective part of such systems have been performed. Dal Maso et al. (1995) have proposed a new theory to define nonconservative products based on the introduction of paths, that generalizes in the sense of distributions the notion of weak solution for conservative systems. From the theoretical point of view, even if progress has been made in the field, the understanding of nonconservative systems of equations when shock solutions or discontinuities are involved is still an open question.

In the community of physics, several fields have encountered this problem, and several alternatives have been found. Mostly, the dissipative effects are considered in the system. In the field of plasma physics, Coquel & Marmignon (1995) have replaced the equation of thermal energy of electrons by an equation of conservation of entropy for a model applicable to weakly ionized hypersonic flows in thermal non-equilibrium. Candler & Maccormack (1991) have considered the nonconservative product in the equation of thermal energy for electrons as a source term for a model applicable to weakly ionized flows. These methods lead to conservative system of equations where the structure of discontinuous solution is identified, however, the link with the original nonconservative system of equations is still incomplete. In the work performed by Shafranov (1957), Zel'dovich & Raizer (1967), and Mihalas & Mihalas (1984), the structure of the shock wave has been obtained for a thermal nonequilibrium fully ionized plasma in the context of a two-fluid model without nonconservative terms. It is shown that the dissipative effects are playing a relevant role in the structure of discontinuous solution or shock waves, depending on both gradients of macroscopic quantities and transport coefficients. However, this study has been performed on a two-fluid conservative system of equations and has not been generalize to nonconservative systems.

Therefore, in both communities, no satisfactory solution has been obtained to tackle theoretically the problem of discontinuous solutions for nonconservative system of equations.

0.2.2 Dissipative effects

For a given model used for partially or fully ionized plasmas, several methods have been introduced in the literature to derive the transport properties. In the classical multi-fluid approaches (see Leake et al. (2012); Khomenko et al. (2014); Alvarez Laguna et al. (2016)), a simplification of the transport coefficients is considered. Indeed, constant cross sections between particles are assumed. Thus, solid sphere elastic collisions are assumed. However, theoretically, without considering any simplifications, the cross-sections depend on the deflection angle and impact parameter describing binary collisions (see Woods (1995)). More specifically, the cross sections depend on the interaction potentials of the particles considered in the collision. It strongly depends on the species considered in the multicomponent plasma. Therefore, the most accurate way to obtain the expression of the transport properties, is to derive them at the kinetic level, starting from the Boltzmann equation.

A first method to derive the transport properties at the kinetic level is to follow the path of Grad (see Haines (1990); Woods (1995); Zhdanov (2002)). In the Grad's method, irreducible tensorial

Hermite polynomials are used. The accuracy of the transport coefficients depend on the number of Hermite polynomials considered. In general, three main approximations are used: the 13M, 21M and 29 M-moment approximations (see Zhdanov (2002)).

Then, we have the spectral Galerkin method based on Laguerre-Sonine polynomials approximation. This method is described by C. H. Kruger & Mitchner (1967); C. Kruger et al. (1968); Daybelge (1970) for computing transport coefficients for ionized gases in thermal equilibrium in the presence of a magnetic field. This method is also presented by Ferziger & Kaper (1973) for multicomponent plasmas in thermal equilibrium. In Ferziger & Kaper (1973), the transport properties are computed by solving integro-differential systems. The method requires only few Laguerre-Sonine polynomials to converge. The transport properties are depending on collision integrals which link the macroscopic transport fluxes to the kinetic level, and depend on the interaction potentials which govern the collisions taking place in the multicomponent plasma.

However, even if these methods allow to compute the transport properties with a high level of accuracy, taking into account the type of interactions in a multicomponent mixture, no transfer of energy in the electron-heavy collisions is considered. Therefore, this approach is valid only in thermal equilibrium regimes. No decoupling between the thermal bath of the electron and heavy-particles temperature is considered, thus, no relaxation state between the two temperatures is taken into account.

0.2.3 Numerical strategy

Several efficient numerical strategies have been developed to perform numerical simulations, which can be used for solar physics applications. Mainly, these numerical strategies have been developed for the set of multi- or single-fluid MHD equations.

Generally, the numerical methods fall into four main categories: finite elements, finite volumes, finite differences and discontinuous Galerkin methods. In each category, robust and stable numerical strategies have been developed to tackle astrophysical problems or magnetic reconnection problems with a high level of accuracy. For example, Baty (2019) has studied the magnetic reconnection process and plasmoid chains formation using finite elements methods with an adaptive mesh, based on a single-fluid MHD approach. In addition, in the category of finite differences schemes, WENO schemes have been developed and have been formulated in the context of MHD (see Guang-Shan & Cheng-Chin (1999); Balsara & Shu (2000)). In Wray et al. (2015), a fourth-order Padé spatial differentiation scheme combined with a fourth order Runge-Kutta scheme for the time discretization has been used to discretize a single-fluid MHD model for solar applications. Discontinuous Galerkin methods have been developed for astrophysical plasma applications in Bauer & Springel (2012); Sijacki, Hernquist, Vogelsberger, Genel, et al. (2013); Zhu et al. (2013). Alternatively, in the category of finite volume methods, the MUSCL-Hancock scheme developed by Van Leer (1997) and the Piece-Wise Linear method developed by Colella (1985) have been widely used to perform MHD simulations. However, most of these numerical strategies have been developed mainly for single-fluid MHD models. There is a need to go further in developing a numerical strategy to specifically address a multi-scale problem for partially ionized plasmas

involved in the magnetic reconnections.

Additionally, one of the main problems encountered is the solenoidal condition on the magnetic field. Indeed, this constraint is creating errors which are accumulating during a simulation and may develop instabilities. Several approaches have been developed to tackle this issue. As an example, the constrained transport methods may be used, which is a divergence-preserving update procedure for the magnetic field components which are collated on a staggered grid centered on volume interfaces, as used by Brecht et al. (1981); DeVore (1991). The projection method is another alternative to tackle the divergence free constraint. This method uses the space of divergence-free vector fields (see Balsara (1998a,b); Tóth (2000); Munz et al. (2000)). Additionally, Dedner et al. (2002) has developed the hyperbolic divergence cleaning method based on a Generalized Lagrange Multiplier (GLM) approach. In summary, several methods have been developed in the literature to enforce the solenoïdal condition, adapted for a large variety of numerical methods.

In order to simulate the multiscale problem of magnetic reconnection with partially ionized plasmas, modeled by a time dependent system of equations (such as multi-fluid MHD models), a key aspect is given by the definition of the numerical schemes that will be used to describe the evolution in time of the system of equations. As briefly shown above, several numerical strategies have been introduced by the scientific community. Generally, this numerical strategy is based on a numerical time integration of the equations for a given spatial discretization of the problem. If the spatial discretization is sufficiently fine to represent all the space multi-scale aspects of the phenomenon, an effort has to be performed on the numerical method to properly handle the large spectrum of time scales associated with multicomponent plasmas. Several phenomena with different time scales, such as convection, dissipative effects, reactions and other processes, have to be considered in the MR process. Therefore, the numerical description of the time multi-scale features of the problem may consider the two following configurations:

- An implicit time discretization to deal with the numerical stiffness associated with the system of equations,
- An explicit time discretization of the equations, implying relevant numerical stability restrictions and very long computations due to the small time steps, restricted by the fastest physical timescale in the magnetic reconnection configuration.

The first approach has been followed by Alvarez Laguna et al. (2016), where a numerical strategy based on an implicit integration to deal with the numerical stiffness of the multi-fluid MHD equations. This numerical strategy allows to properly handle the entire spectrum of time scales and ensure accurate numerical approximations in terms of stability. However, implicit approaches require large memory resources (more specifically in 3D) and very costful linear algebra tools.

On the other hand, explicit schemes are simple to implement. However, this approach appears to be inefficient when we consider a time integration of stiff equations, such as multi-fluid MHD model for example. One way to reduce the long computation requirements induced by small time steps is to consider Adaptive Mesh Refinement (AMR) representations, as performed by Drui (2017) and Essadki (2018). In this framework, the mesh is refined only in regions of interest. Therefore, the computation is performed on some regions of fine spatial representation within the

entire computational domain. This approach is appropriate for the magnetic reconnection process, since the region of interest is located only in the diffusion region, where the magnetic field lines are reconnecting. By doing so, computational memory is saved and large computational domains can be considered with reduced computational ressources. However, additional challenges are represented by the development of efficient computational implementations, which are more complex compared to the standard meshing techniques. In addition, the compressed spatial representations used in AMR introduce some approximation errors. Therefore, it is necessary to find the appropriate criterion for local refinement/coarsening in order to guarantee a good quality of the numerical solution. Finally, the AMR approach can be coupled with standard explicit time integration, even if very fine discretization involve high stability constraints. But, special techniques have been developed to overcome this restriction based on a local time stepping approach, taking into account the local grid size, and coupled with time operator splitting (see Strang (1968); Duarte et al. (2012)).

Finally, the development of numerical methods dedicated to nonconservative systems which take into account thermal nonequilibrium process may encounter some difficulties. Such difficulties are to be found in several fields which concern two-phase flows (Pelanti & Shyue (2014); Raviart & Sainsaulieu (1995)) or plasma physics (Coquel & Marmignon (1995); Candler & Maccormack (1991)). In particular, the discretization of the nonconservative terms may lead to numerical difficulties, such as the propagation of nonphysical shocks, due to the numerical dissipation. In this context, following the theory developed by Dal Maso et al. (1995), Pares (2006) have developed path-conservative schemes for nonconservative hyperbolic systems. Nevertheless, as shown by Abgrall & Karni (2010), these numerical schemes fail to converge to the right solutions. In fact, for a given correct path, the numerical solution can be far from the expected solution because of the numerical dissipation of the scheme. More recently, Chalons & Coquel (2017) have proposed a different strategy for nonconservative hyperbolic systems by introducing Roe-type conservative schemes. Aregba-Driollet & Breil (2017) and Brull et al. (2018) have proposed several numerical schemes for the approximation of a nonconservative compressible Euler system applied to the modeling of fully ionized plasmas in thermal non-equilibrium, even if the question of how to evaluate the proper physical jump conditions is not solved. However, no solution has been achieved to handle both the nonconservative terms from the modeling and numerical point of view. This still remains an open problem.

0.3 Main contributions

The contributions of this thesis in the modeling and development of a numerical strategy, for the purpose of representing partially ionized plasmas in magnetic reconnections under Sun chromosphere conditions, cover several fields: mathematical modeling, transport properties, numerical methods and high performance computing. In the following, these contributions are detailed in four parts.

0.3.1 Mathematical modeling

In this thesis, we focus on the model theoretically derived from kinetic theory by Graille et al. (2009). This model is derived from a generalized Chapman-Enskog expansion of the Boltzmann equations, where a multi-scale perturbation method based on a dimensional analysis has been performed. This analysis is focused on non-dimensional parameters such as the square root of the mass ratio between electrons and heavy particles and the Knudsen number. These parameters are considered as small, at the same order of magnitude, and allows thermal nonequilibrium between the electrons and heavy-particles. We extend this approach by coupling the Boltzmann equation with the set of Maxwell equations, introducing a scaling consistent with the one introduced by Graille et al. (2009). In this framework, additional scales such as Debye length are taken into account in the multiscale analysis. Then, the macroscopic equations are obtained through a Chapman-Enskog expansion. The multiscale expansion leads to several processes occuring at different timescales. At the last order investigated in the expansion, the Navier-Stokes equations for heavy-particle and second-order drift diffusion equations for electrons coupled to the set of Maxwell's equations are obtained. The proposed model has an extended range of validity for partially and fully ionized, non and weakly multicomponent magnetized plasmas, valid in the weakly and highly collisional regime, including thermal nonequilibrium processes between electrons and heavy-particles. The model is valid at the Debye length scales, where the electroneutrality is not necessarly assumed. We thus obtain a model where all the scales, from the Debye length to the macroscopic length scale, including the electrons and heavy-particle kinetic time and spatial scales, are taken into account. Eventually, the proposed model inherits a rigorous mathematical structure combined with proper asymptotic limits.

Following this rigorous approach where the asymptotic limits and scales have been clearly identified, we thus consider that the Debye length scales are negligible compared to the characteristic length scales of the solar chromosphere. Therefore, the general model is simplified to a so-called multicomponent model, in the small Debye length limit, valid in the whole solar chromosphere. In this approach, one hydrodynamic velocity is considered and all the species are assumed to diffuse in the same reference frame, which is the hydrodynamic reference frame of heavy-particles. In the multicomponent model, the dynamics of each particles is captured by the dissipative aspects. Therefore, the diffusive velocities of each particles is assumed to be small compared with the hydrodynamic velocity of heavy-particles. Only one momentum equation for heavy-particles is obtained. The electrons are participating to the momentum balance only through the total pressure and the Lorentz force. The model is assuming the same temperature for all the heavy-particles, and a different temperature for the electrons.

Besides, the coupling of the multicomponent model with the set of Maxwell equations allows to derive a new generalized Ohm's law. A new definition of the resistivity is provided, which takes into account all the possible interactions involved in a multicomponent plasma.

0.3.2 Transport properties

The transport properties of the multicomponent model are derived from the kinetic theory. The closure of the proposed model is at a microscopic level, determined from experimental measurements. In this thesis, the transport properties are shown to depend on both the electron and heavy-particle temperature. Unlike Braginskii (1965), the electron transport properties are shown to be anisotropic, whereas, the heavy-particle transport properties are isotropic.

Following the path of Kolesnikov (2003); Ferziger & Kaper (1973), the expressions of the transport properties are computed using a spectral Galerkin method based on a third order Laguerre-Sonine polynomial approximation. This method is shown to converge quickly and guarantees a sufficient level of accuracy. Therefore, the cross-sections are not considered as constant, but depend on the mixture considered, the thermodynamic properties and the magnitude of the magnetic field.

The computation of the transport properties through a spectral Galerkin method requires the computation of the so-called collision integrals, which link the macroscopic tranport fluxes to the kinetic level. These collision integrals depend on interaction potentials which govern the collisions considered among the multicomponent plasma particles. In the literature, several experimental measurements have been performed to compute the interaction potentials. In this thesis, we focus on a Helium-Hydrogen mixture, to be representative of the composition of the solar atmosphere. The collision integrals data of this mixture are taken from Bruno et al. (2011). These datas are approximated by considering a curve-fit up to third order exponential polynomials function.

Considering the high number of species to be considered in the Helium-Hydrogen mixture, algorithms have to be developed for computing the heavy-particle transport properties. Indeed, the transport coefficients are expressed as solution of linear systems where the size is proportional to the number of heavy species. In this context, we follow the path of Magin & Degrez (2004); Ern & Giovangigli (2010, 1995) where "low-cost" accurate algorithms are developed for computing these coefficients.

The proposed method used for computing the transport coefficients are verified and compared with the approach of Braginskii (1965) in a fully ionized plasma. The transport properties for the Helium-Hydrogen mixture are computed in more general conditions representative of the solar lower atmosphere. Finally, the transport properties are assessed in a 3D radiative MHD simulation of a pore, performed by Kitiashvili et al. (2010). We also assess the transport properties in the 3D MHD dynamic code Bifrost, where the conditions encompassing the upper part of the convection zone, the photosphere, chromosphere, transition region and corona are considered (see Carlsson et al. (2016); Gudiksen et al. (2011)).

0.3.3 Numerical strategy

The contributions in the field of numerical methods is splitted into two parts: 1- the development of a numerical strategy for the purpose of implementing the multicomponent model, and 2- the numerical study of the nonconservative terms involved in the multicomponent model.

Numerical methods

Based on advances described in the literature, a numerical strategy is established. The numerical strategy is developed in order to 1- capture the large spectrum of scales associated with the multicomponent model, 2- ensure robustness and stability while guaranteeing a sufficient level of accuracy, 3- be coupled with modern computer architecture to achieve highly accurate simulation, for the purpose of representing the magnetic reconnection process under solar chromosphere conditions.

In this thesis, we focus on a finite volume approach. Based on advances described in the literature, the multicomponent model is discretized following a Kurganov & Tadmor (2000) (KT) scheme for the spatial discretization, with a second-order Runge Kutta method for the time discretization, combined with a Generalized Lagrange Multiplier (GLM) mixed parabolic-hyperbolic correction for the solenoïdal constraint on the magnetic field, described by Dedner et al. (2002). The chosen numerical method is adapted for AMR and implemented into the massively parallel cell-based AMR code called `CanoP` (see Drui (2017); Essadki (2018)).

The numerical scheme is assumed to be second order in space and time. The KT scheme combined with an AMR strategy, guarantees that all the scales associated with the multicomponent model are captured, thus, is adapted for representing the multiscale process of magnetic reconnection. It is showing relevant properties in terms of quality of the numerical solution. Indeed, even if small timesteps are involved in the simulation (for example, due to Fourier constraints limited by the dissipative effects of the multicomponent model), a good approximation of the solution is still ensured. Therefore, the numerical strategy is able to tackle the numerical stiffness of the multicomponent approach.

The choice of such a scheme guarantees good behavior close to discontinuities, that is a good approximation of the numerical solution when shock waves or sharp gradients are present in the simulation. Additionally, it is shown to be robust and stable and does not require the use of Riemann solvers. Therefore, it is efficient from an algorithmic point of view, which allow to be easily coupled with modern computer architecture.

The coupling with an AMR strategy allows to provide a high level of accuracy in the regions of our interest, such as the reconnection region. A high level of accuracy is guaranteed in the reconnection region, thus, all the dissipative processes are correctly captured.

Study of nonconservative terms in the multicomponent model

The development of the multicomponent model based on a generalized multiscale Chapman-Enskog expansion, yields a hyperbolic system of equations with a parabolic regularization of the electron variables due to dissipative effects. Both the electron and heavy-particle internal energy equations exhibit nonconservative terms leading to some numerical difficulties when weak solutions are involved, that have been reviewed previously. However, unlike the classical nonconservative hyperbolic system (see Chalons & Coquel (2017)), the natural regularization of the electron variables in our model allows to tackle the numerical issues involved by nonconservative terms.

In a simplified framework where no electromagnetic fields is considered, we focus on a spe-

cific class of regular solutions written as travelling waves, where the nonconservative terms are well defined. The regularity of the electronic variables is ensured since dissipative effects, such as thermal conductivity and electron diffusion coefficient, are present in the equation of internal energy and density of electrons. This simplified approach allows a complete analytical solution of the travelling wave, as well as an explicit expression of the missing jump relation for the thermal energy of electrons, where nonconservative terms are to be found.

Assuming a standard discretization of the nonconservative product, the required characteristic scales to be numerically resolved is identified. These scales are associated with compatibility equations, which have to be numerically verified to properly resolve the travelling wave. If these scales are not numerically resolved, nonphysical shocks are appearing in the numerical solution, as shown by Abgrall & Karni (2010).

A new scheme based on a specific treatment of the nonconservative product is developed to verify the compatibility equations in a discretized sense. This approach allows to capture the travelling wave, even if the required characteristic scales are not numerically resolved, for any discretization. It guarantees that no nonphysical shocks or numerical issues are involved. The proposed strategy can be generalized to a multidimensional framework, many finite volume methods and combined with Strang operator splitting techniques (see Strang (1968)) to avoid of the small timesteps limited by the Fourier stability.

More generally, this numerical strategy can be extended to the multicomponent model, including the electromagnetic field. The general case has not been investigated in this thesis.

0.3.4 High performance computing and numerical simulations with AMR

Following this numerical strategy, in this thesis, the multicomponent approach is implemented in a massively parallel code `CanoP`, which is an application layer built at the top of the `p4est` library (see Drui (2017)).

The `p4est` library is a cell-based parallel AMR library which is managing the mesh in parallel computations. It is providing a high compression ratio of the data, is scalable on highly parallel architecture. It has been implemented such as the management of the mesh remains independent of the application and the numerical methods considered. On the other hand, the model and the numerical strategy are implemented into the `CanoP` code. This code, written in C++, is mainly used as an application layer of `p4est`, where several type of applications and numerical schemes are integrated. Mainly, second order finite volume approaches have been implemented in this code. In this thesis, numerical simulations with finite volume schemes on two and three dimensional AMR non uniform cartesian grids are performed.

After implementing the multicomponent model into `CanoP`, we couple the code with the "MUlticomponent Thermodynamic And Transport Properties for IONized gases, in C++" (MUTATION++) library developed by Scoggins et al. (2016). The library is used to compute thermodynamic and transport properties, and can be coupled to CFD codes such as `CanoP`.

First, the transport coefficients of the multicomponent model are implemented in the library. Then, we interface this library to `CanoP` to be able to compute the transport coefficients with a high level of accuracy, during a simulation.

The robustness, stability and accuracy of the numerical strategy are assessed. The AMR capability of `p4est` is verified through several test cases. In summary, in both two and three dimentional configurations, we have verified

- the accuracy of the numerical scheme,
- the ability of the numerical strategy to enforce the solenoidal condition on the magnetic field,
- the refinement criterions used for our application,
- the robustness at handling the formation of MHD shocks and shock-shock interaction,
- the performance of the code (weak and strong capability of `CanoP`).

In a two and three dimensional AMR framework, we perform numerical simulations of magnetic reconnections under solar atmosphere conditions, with the multicomponent model, for fully and partially ionized plasmas. In order to assess the impact of the modeling on the magnetic reconnection, the results obtained with the multicomponent approach are compared with a classical single fluid MHD model, which is implemented into `CanoP` , following a similar numerical strategy.

0.4 Manuscript organization

The thesis is divided into a total of nine chapters

Chapter 1 presents the atmosphere of the Sun and the magnetic reconnection process.

Chapter 2 presents the extension of the derivation of the general model performed by Graille et al. (2009) from a generalized Chapman-Enskog expansion, based on a multiscale analysis, coupled to the set of Maxwell's equations. The assumptions, nondimensional parameters and transport fluxes are given.

Chapter 3 presents the multicomponent model, which is a simplified case of the general model. The asymptotic limit of the general approach is considered by assuming that Debye length scales are negligible compared to the characteristic scales involved in our application. In this Chapter, a generalized Ohm's law and a new definition of the resistivity are defined. Additionally, the multicomponent model is compared with classical approaches developed in the literature.

Chapter 4 presents the spectral Galerkin method based on Laguerre-Sonine polynomials approximation for computing the transport properties. Then, the transport systems for general multicomponent mixtures are presented. Based on a Helium-Hydrogen mixture, the collision integrals data as well as the corresponding potential of interactions used for computing the transport coefficients are exhibited, based on the work performed by Bruno et al. (2011). Based on advances described in the literature (see Magin & Degrez (2004); Ern & Giovangigli (2010), transport algorithms used for the heavy-particle transport systems are presented.

Chapter 5 details the computation of the transport properties in conditions representative of the solar atmosphere. First, the method on a fully-ionized plasma is verified by comparing the results with those obtained with the theory of Braginskii (1965). Then, all the transport properties for the Helium-Hydrogen mixture are computed. Finally, the transport coefficients and the components of the generalized Ohm's law are computed for 3D radiative MHD simulations of 1- a pore in the solar lower atmosphere (see Kitiashvili et al. (2010)), and 2- in the whole atmosphere of the Sun, from the convection zone to the solar corona (see Carlsson et al. (2016); Gudiksen et al. (2011)).

Chapter 6 presents the numerical strategy of the thesis, based on advances described in the literature. The choice of the numerical method is justified. The discretization on monodimensional uniform grid is extended to AMR non-uniform cartesian grids.

Chapter 7 is focused on the study of the nonconservative terms involved in the multicomponent model, in a simplified framework where no electromagnetic fields are considered. A decoupling of the system of equations is proposed. A complete analytical study combined with an expression of the missing jump condition associated with the internal energy of electrons is obtained by looking for piecewise smooth travelling wave solutions. Based on a monodimensional finite volume Godunov scheme with a standard discretization of the nonconservative term, the relevant scales to be numerically resolved for capturing the travelling wave are identified. Finally, a new scheme based on a specific treatment of the nonconservative product has been proposed to catch the travelling wave and avoid the propagation of non physical shocks.

Chapter 8 presents the structure of the code and detail the implementation of the numerical strategy into the massively parallel code `CanoP`. The structure of the `p4est` and `MUTATION++` library is detailed. The coupling between `MUTATION++` library and `CanoP` is presented. Several refinement criterions are defined.

Chapter 9 presents the verification and assessment of the numerical strategy as well as the results obtained. The accuracy and robustness of the numerical strategy and AMR capability of `p4est` is assessed. Numerical simulations of magnetic reconnection under Sun atmosphere conditions in a two and three dimensional configuration are performed.

The present PhD Thesis has been officially co-advised by Benjamin Graille and Marc Massot, but has benefited from a strong help from Alejandro Alvarez-Laguna (CMAP and LPP) and from

the fruitful collaboration with Thierry Magin (VKI) and Nagi Mansour (NASA). The support of James B. Scoggins (VKI and then CMAP) and Pierre Kestener (MdlS) and the discussions with Frédéric Coquel have also been really helpful.

The research is funded by an Idex Paris-Saclay interdisciplinary IDI PhD grant, and relies on the the support of NASA Ames Research Center (ARC), Advanced Supercomputing Division, von Karman Institute for Fluid Dynamics, CMAP - Initiative HPC@Maths from Ecole Polytechnique and of Ecole doctorale de Mathématiques Hadamard. Part of this work was conducted during the 2016, 2017, 2018 and 2019 NASA Summer Program at ARC.

List of publications

These contributions resulted in publications in international journals :

1. Wargnier, Q. Alvarez-Laguna, A. Kestener, P. Graille, B. Mansour, N.N. Massot & M. Magin, T. Multicomponent fluid model for two-temperature plasmas derived from kinetic theory : application to magnetic reconnection, (2018) *JPCS - Proceedings of the Joint Varenna - Lausanne International Workshop on Theory of Fusion Plasma*, Vol. 1125 012021 - 1-16

2. Wargnier, Q., Alvarez-Laguna, A., Scoggins, J. B., Mansour, N. N., Massot, M., & Magin, T. (2019), Consistent transport properties in a two temperature multicomponent plasma model: Application to the magnetized Sun chromosphere. *In revision for Astronomy & Astrophysics.* 1-14, https://hal.archives-ouvertes.fr/hal-01898695

3. Wargnier, Q., Faure, S., Graille, B., Magin, T., & Massot, M. (2019). Numerical treatment of the nonconservative product in a multiscale fluid model for plasmas in thermal nonequilibrium: application to solar physics. *In revision for SIAM SISC* (2018) 1-27, https://hal.archives-ouvertes.fr/hal-01811837

4. Wargnier, Q., Kestener, P., Alvarez-Laguna, A., Mansour, N. N., & Massot, M. (2019). Mathematical modeling and high fidelity adaptive simulations of partially ionized plasmas with accurate multicomponent transport: application to magnetic reconnection in solar physics. *In preparation for Journal of Computational Physics*

Book chapter

1. Wargnier, Q., Graille, B., Magin, T., & Massot, M. (2017). Numerical treatment of the nonconservative product in a multiscale fluid model for plasmas in thermal nonequilibrium: application to solar physics , *Review of the VKI Doctoral Research 2017-2018*, SintGenesius Rode, Belgium.

2. Wargnier, Q., Alvarez-Laguna, A., Kestener, P., Graille, B., Mansour, N. N., Massot, M., & Magin, T. (2018). Mathematical modeling and high fidelity adaptive simulations of astrophysical plasmas with accurate transport: application in solar physics. In *Nasa Technical Memorandum, proveedings of the 2018 summer program* (p. 1-16).

3. Wargnier, Q., Alvarez-Laguna, A., Scoggins, J. B., Mansour, N. N., Massot, M., & Magin, T. (2018), Transport Properties in Multicomponent Two-Temperature Magnetized Plasmas: Application to the Sun Atmosphere. *Review of the VKI Doctoral Research 2018-2019*, Sint-Genesius Rode, Belgium.

List of conferences and seminars

These contributions resulted in conferences and seminars in international institutions:

Conferences

1. **Partially Ionised Plasmas in Astrophysics (PIPA)**, La Laguna, Tenerife, Spain (August 2016): *Transport properties for magnetized sun chromosphere based on the Chapman-Enskog expansion*,

2. **European Geosciences Union, Theory and Simulation of Solar system plasmas**, Austria (April 2017): *Transport properties for multicomponent plasma based on the Chapman-Enskog expansion*

3. **Congrès SMAI,** 8^{e} **Biennale Française des Mathématiques Appliquées et Industrielles**, France (June 2017): *Godunov method for Riemann problem with nonconservative product*

4. **Conference CEA/SMAI-GAMNI of numerical fluid mechanics**, Institut Henri Poincaré France (February 2018): *Multiscale modeling from kinetic theory and numerical treatment of the nonconservative product for multicomponent plasma in thermal nonequilibrium*, invited talk

5. **PhD Symposium at the von Karman Institute for Fluid dynamics**, Belgium (2017, 2018 and 2019)

6. **44e Congrès National d'Analyse Numérique**, France (June 2018): *Numerical treatment of the nonconservative product in a multiscale fluid model for plasma in thermal nonequilibrium : Application in solar physics*

7. **Joint Varenna-Lausanne International Workshop on the Theory of Fusion Plasmas 2018**, organized by the Swiss Plasma Center from Ecole Polytechnique Fédérale de Lausanne, Italy (August 2018): *Multicomponent fluid model for two-temperature plasmas derived from kinetic theory: Application to magnetic reconnection in the Sun chromosphere,*

8. **Numerical simulation of plasma flows**, workshop at Ecole polytechnique, France (December 2018)

9. **Partially Ionised Plasmas in Astrophysics (PIPA)**, Palma de Mallorca, Spain (June 2019): *Consistent transport properties in multicomponent two-temperature magnetized plasmas*, invited conference for Alejandro Alvarez Laguna and Quentin Wargnier

Seminars

1. **The Centre for mathematical Plasma-Astrophysics, K.U. Leuven** (February 2017): *Transport properties for multicomponent plasma based on the Chapman Enskog expansion*, invited by Stefaan Poedts and Alejandro Alvarez Laguna,

2. **Institut de mathématiques de Bordeaux, France** (October 2017): *Simulation of multicomponent plasma in thermal nonequilibrium with application to magnetic reconnection: Numerical treatment of the nonconservative product*, at the "Modeling and Numerical Methods for Hot Plasmas III" workshop invited by Stéphane Brull,

3. **Oxford University at Rudolf Peierls Centre for Theoretical Physics** (March 2019): *Mathematical modeling and high fidelity adaptive simulations of partially ionized plasmas with accurate multicomponent transport: application to magnetic reconnection in solar physics,* invited by Michael Barnes and Alexandre A. Schekochihin,

4. **Lockheed Martin Solar and Astrophysics Laboratory** (August 2019): *Mathematical modeling and AMR of astrophysical plasmas: application to magnetic reconnection in solar physics,* invited by Juan Martinez Sykora,

5. **Department of Mathematics, University of Texas at Austin** (August 2019): *Mathematical modeling and AMR of astrophysical plasmas: application to magnetic reconnection in solar physics,* invited by Irene Gamba.

6. **NASA Ames Research Center, NASA Supercomputing division** (August 2019): *AMR simulations of astrophysical plasmas with a massively parallel code* `CanoP`*: application to magnetic reconnection in solar physics,* invited by Nagi Mansour.

CHAPTER 1

THE SUN ATMOSPHERE AND MAGNETIC RECONNECTION

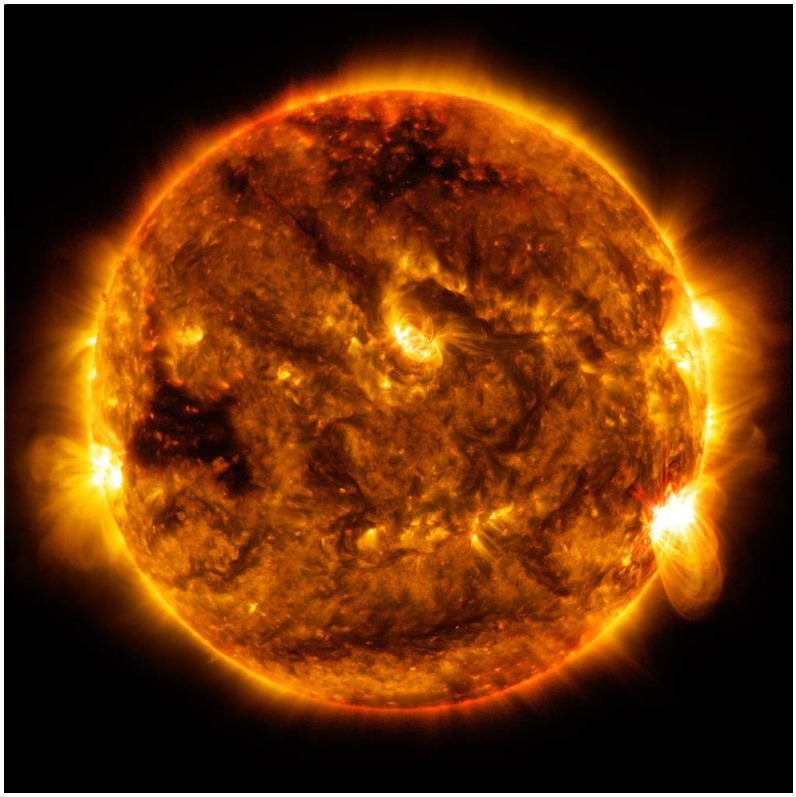

Figure 1-1: The Sun. Source: NASA/Solar Dynamics Observatory (SDO) on Oct. 1, 2015.

1.1 The solar surface and atmosphere

Like the other stars, the Sun (see Figure 1-1) is a ball of gas mainly made of 91% of Hydrogen and 8.9% of Helium, in terms of molar composition. In terms of mass, it corresponds to about 70.6% and 27.4% for Hydrogen and Helium respectively[1]. In addition, other heavy species such as O, C, Fe, Ne, N, Si, Mg and S can be found. The Sun is maintained by gravitational attraction, producing immense pressure and temperature at its center.

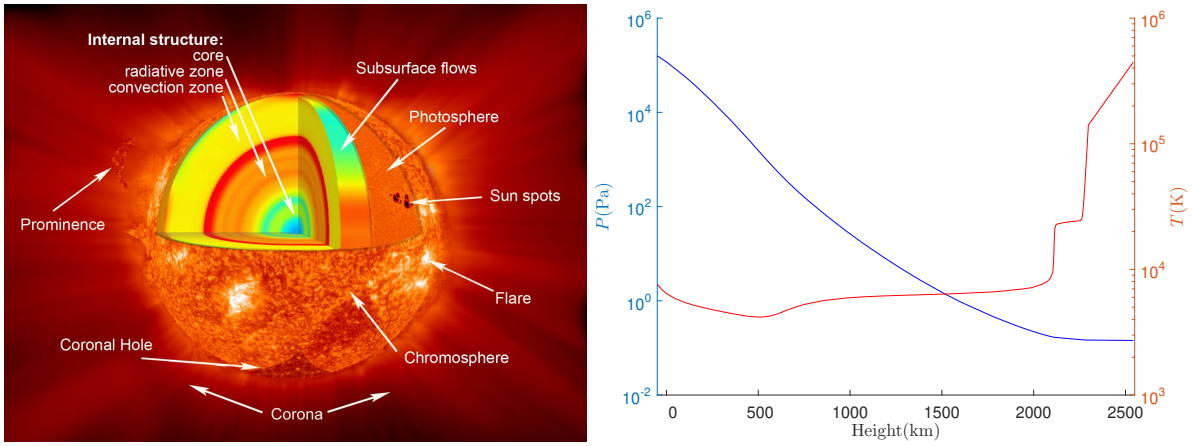

Figure 1-2: Left: Structure of the Sun[2]. Right: Distribution of temperature and pressure as function of the height in the Sun atmosphere, (Model C from Vernazza et al. (1981)). The altitude 0 km corresponds to the photosphere.

As presented in Figure 1-2, the Sun contains several layers: the internal structure (composed of the core, radiative zone and convective zone), the photosphere and atmosphere (chromosphere, transition region and corona).

The core is a region where the temperature is about 15×10^6 degrees Celsius, and nuclear fusion occurs to fuse Hydrogen into Helium. Then, we have the radiative zone. In this region, the energy transfer occurs by means of radiation, due to photons rather than by convection. Finally, in the internal structure of the Sun, we have the convective zone. In this region, the internal heat is evacuated towards the outlayer thanks to convection movements due to the difference of temperature between the internal structure and the outside layer of the Sun. It creates at the surface a super granulation dividing the photosphere in cells and creating spicules at the chromosphere.

As described in the general introduction, the surface and atmosphere of the Sun is usually splitted into several layers, where several regimes and conditions are to be found. In Figure 1-2, the distribution of temperature and pressure from the bottom of the photosphere (0 km) up to the bottom of the solar corona (2500 km) is represented, according to the model C of Vernazza et al. (1981). As shown in Figure 1-2, from 0 km to 2000 km the temperature lies between 5000 and 10 000 K. This region contains the photosphere and chromosphere. Then, from 2000 km to

[1]URL Source: https://solarsystem.nasa.gov/solar-system/sun/in-depth/
[2]URL Source: https://www.nasa.gov/mission_pages/sunearth/science/Sunlayers.html

2500 km (and more), a spectacular rise of temperature from 10^4 K to 10^6 K is observed from the transition region to the bottom of the solar corona. This rise of temperature attracts the attention of the scientific community (see Vernazza et al. (1981); Amari et al. (2014); Amari et al. (2018)) and several studies have tried to explain the mechanisms responsible for the coronal heating. In the following, a description of the solar surface and atmosphere is given.

1.1.1 The photosphere

The photosphere is the visible surface of the sun and the uppermost opaque level in the Sun. The photosphere is tens to hundreds of kilometers thick. It is the transitional region between deeper opaque regions of the internal structure of the Sun and the atmosphere. This leads to the relevant features of the photosphere; in the photosphere, the opacity drops from high to low, and the temperatures fall with increasing height. This region is mainly composed of Hydrogen and Helium. In average, the temperature is about 5800 K. At the photosphere, the plasma is partially ionized, pressure dominated and highly collisional.

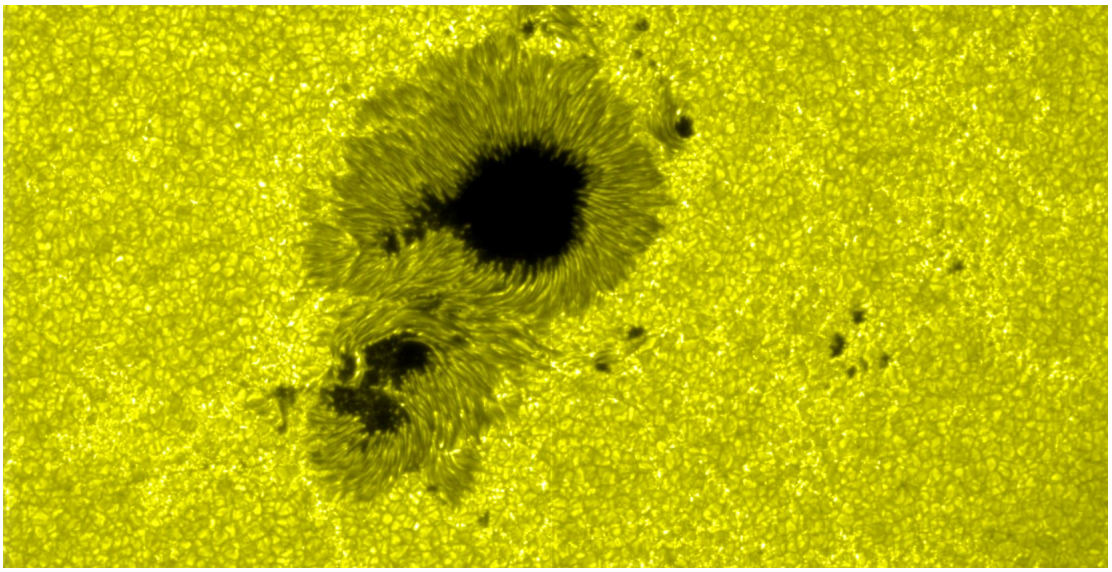

Figure 1-3: Zoom-in from a full view of the Hinode Solar Optical Telescope (SOT), a Sunspot is observed at the middle of the picture.[3]

In this region, several characteristic phenomena such as sunspots or granules can be observed. Figure 1-3 is a picture of the SDO telescope showing a sunspot and granules. The granulation are due to the formation of small scale pattern of convective cells. It results from temperature gradients close to the solar surface. The typical scales of these patterns are about 1000 ~ 2000 km and last approximately 8 or 10 minutes. Then, the sunspots are dark areas in the photosphere. They are formed by the concentration of large magnetic field (around thousands of Gauss according to

[3]URL Source: https://nasaviz.gsfc.nasa.gov/3412

Fröhlich & Lean (2004); Solanki (2003)). These phenomena appear dark because they are cooler (around 4300 K). In these regions of the photosphere, the plasma is magnetic-pressure dominated. In Section 5.4, a pore, which is a transitional sunspot at the photosphere, is studied.

1.1.2 The chromosphere

Above the photosphere is a layer of less dense but higher temperature gases called the chromosphere. This region can be observed at the edge of the Moon during solar eclipses. As shown in Figure 1-2, the temperature increases gradually with altitude from a photospheric temperature up to around 10000 K to 20000 K. Additionally, the ionization level is increasing gradually, and Helium becomes partially ionized. In the height range encompassing the photosphere up to the chromosphere, the plasma is essentially partially ionized with an ionization degree of about $10^{-4}-10^{-1}$ (see Vernazza et al. (1981)). This region attracts the attention of the scientific community since some recent observations have shown that the heating of the transition region is taking place at chromospheric height related to chromospheric phenomena, as shown by De Pontieu et al. (2009, 2014). Therefore, several processes considered in solar chromosphere conditions have been envisioned by the scientific community to explain the observations. In the chromosphere, the magnetic-pressure is increasing with the altitude, thus, the plasma beta parameter is decreasing. In this region of the atmosphere, several phenomena can be observed such as spicules, plages, filaments or prominences.

Spicules are dynamic jets of about 500 km diameter in the chromosphere of the Sun. It moves upwards at about 20 km.s^{-1} from the photosphere. It last for about 15 minutes. Figure 1-4 is a picture which represent the solar flux tubes (spicules). Then, we have the plages, composed of hot plasmas, which are bright regions in the chromosphere located near sunspots. Additionally, as shown in Figure 1-4, the prominences or filaments are cool volume of gas suspended above the chromosphere by the magnetic fields. It can extend outwards into the solar corona. Since the corona consist of extremely hot gases which do not emit in the visible light, the prominences can be observed since they contain cooler plasma. The typical timescale of the formation of a prominence is about a day up to several weeks or months. These phenomena can lead to coronal mass ejections. Currently, the scientific community is trying to explain the formation of prominences.

1.1.3 The transition region and solar corona

Above the chromosphere, we have the transition region. It is a thin 200 km region where the temperature rise from 10000 K up to 10^6 K. Above the transition region, we have the solar corona. This region can extends millions of kilometers into outer space. The average temperature of the corona is much hotter than the surface and is about 10^6 or 2.10^6 K. Today, no complete theory exists to explain the increase of the temperature in the solar corona. However, recent studies have shown that the heat may come from the magnetic reconnection process.

[5]URL Source: https://apod.nasa.gov/apod/ap081102.html
[5]URL Source: https://www.nasa.gov/mission_pages/sunearth/news/News090412-filament.html

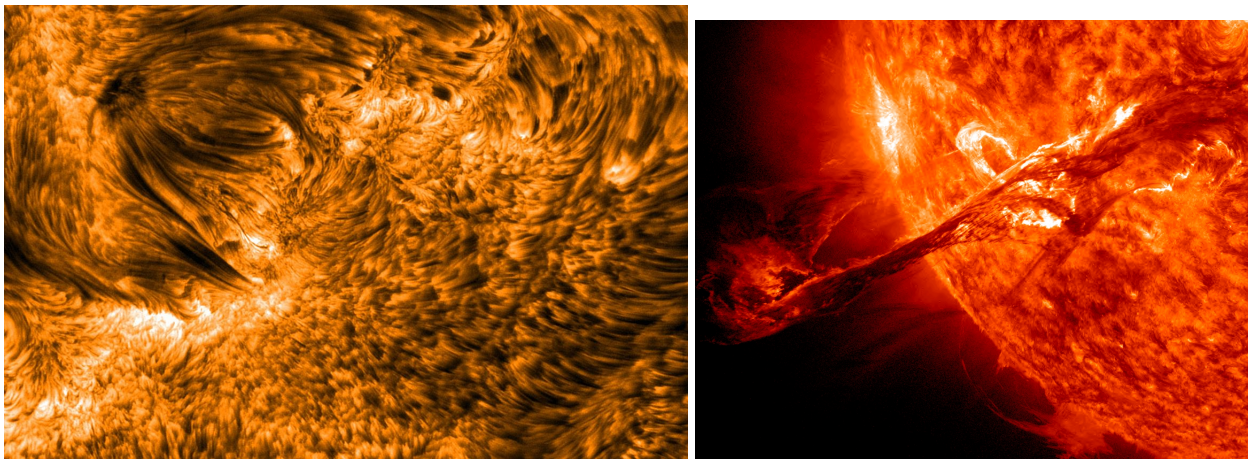

Figure 1-4: Left: Spicules, visible as dark tubes. Solar active region 10380, June 2004.[4]Right: A long filament erupted on the sun on August 31, 2012, captured by NASA's Solar Dynamics Observatory (SDO).[5]

In the solar corona, the density of the plasma is very low (of the order of 10^{15} particles.m^{-3}), about 10^{-12} times as dense as the photosphere. The plasma is fully ionized and magnetic-pressure dominated. Thus, the dynamics of the solar corona is dominated by the solar magnetic field. Generally, the structure of the solar corona is quite varied and complex. Generally, several regions are distinguished by the astronomers.

In the solar corona, we have active regions. They are ensembles of loop structures, such as coronal loops, which connect points of opposite magnetic polarity in the photosphere, as shown in Figure 1-5. The loops are the basic structure of the magnetic solar corona. In these structures, the plasma is heated from 6000 K to 10^6 K from the photosphere through the corona region. The lifetime of these structures is ranging from the order of seconds to days. Additionally, we can observe interconnection of active regions, called Helmet streamers, which are arcs connecting active regions of opposite magnetic field. These structures are sources of slow solar wind. The solar wind is a stream of charged particles released from the upper atmosphere of the Sun. Usually, the slow solar wind have a velocity of 300−500 km.s^{-1}, with a temperature of 10^6 K with a composition similar to the solar corona.

Additionally, using an X-ray telescope, we can observe coronal holes, as shown in Figure 1-5. These structures look dark since they do not emit radiation. The structure of the magnetic field is unipolar and opened to the interplanetary space allowing for high speed solar wind to emerge. The high solar wind have a velocity of 750 km.s^{-1}, with a temperature of 8.10^5 K with a composition similar to the photosphere. Finally, the solar regions which are not part of active regions and coronal holes are called the quiet Sun region.

The study of these events is part of the space weather (see Lapenta et al. (2013)). It is a field which encompasses solar conditions and its interaction with the Earth's space environment that

[7]URL Source: https://sdo.gsfc.nasa.gov/gallery/main/item/567
[7]URL Source: https://www.nasa.gov/multimedia/imagegallery/image_feature_2268.html

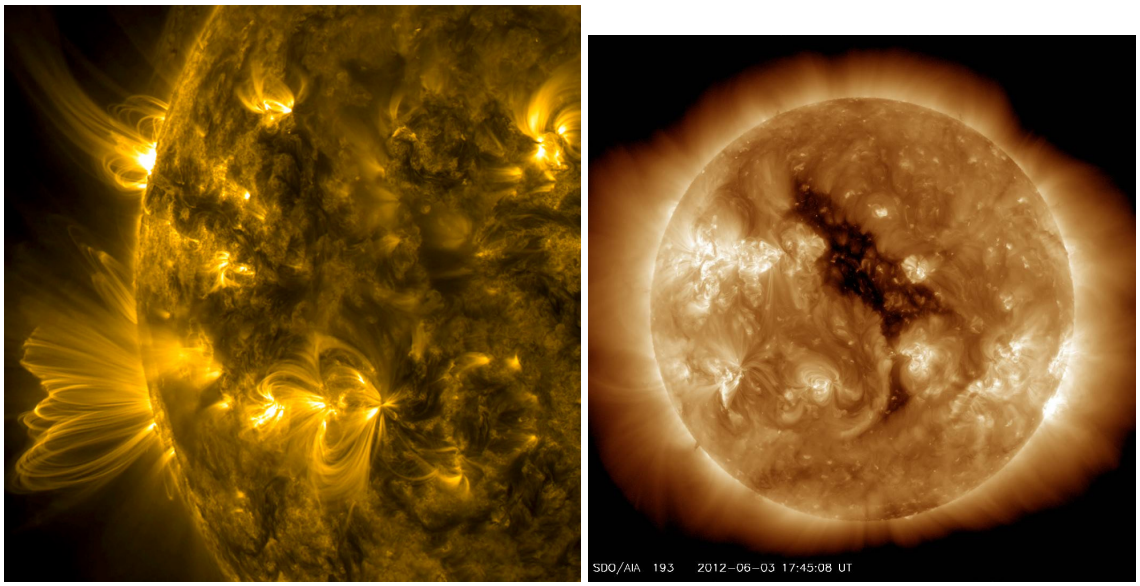

Figure 1-5: Left: Coronal loops seen in profile at the edge of the Sun (2014).[6]Right: Coronal holes are regions where the sun's corona is dark. This picture has been taken with an X-ray telescope. The high-speed solar wind is known to originate in coronal holes. [7]

can influence performance, reliability of technologies such as telecommunications satellites, or, impact the human being. Our modern society based on new technologies is very vulnerable to space weather. Therefore, we can expect to have more and more safety problems related to solar activity (see Siscoe (2000)), thus, it is necessary to predict all the physical processes involved in these events, such as magnetic reconnections.

1.2 The magnetic reconnection process

The magnetic reconnection process is based on a new connection of the magnetic field lines. This process requires a violation of Ohm's law in a very small region, called diffusion region (current sheet). Figure 1-6 represents the geometry of the reconnection and how the magnetic field lines are reconnecting. The magnetic field lines that cross in the center are called separatrices, and the point where they cross is the X-point (or X line in a three dimensional configuration). The yellow arrows show qualitatively the plasma flow. Generally, outside the reconnection region, the plasma is assumed to be in the frozen-in condition (Alfvén's theorem). The plasma is a perfectly conducting fluid, thus, the magnetic field is frozen into the fluid and has to move along with it.

In Figure 1-6, one can notice that the key property of the magnetic reconnection, is the transport of plasma from one side of the reconnection geometry (inflow region), across the separatrix towards the out flow regions. This transport process implies a violation of the frozen-in condition since plasma elements which were connected by a field line, are later found on a different magnetic field line.

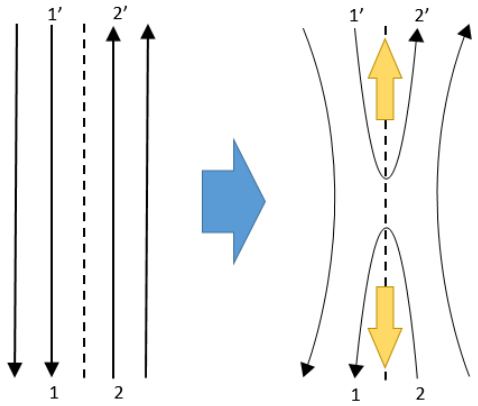

Figure 1-6: Geometry of the magnetic reconnection.

Since magnetic reconnection is a general process which can develop in many regions of the Sun atmosphere, a general criterion for reconnection should be defined. Generally, the dynamics of a plasma and the magnetic field are coupled through a so-called Ohm's law which reads

$$\boldsymbol{E} + \boldsymbol{v} \wedge \boldsymbol{B} = \boldsymbol{D} \tag{1.2.1}$$

where $\boldsymbol{E}$ is the electric field, $\boldsymbol{v}$ is the macroscopic velocity of the plasma, $\boldsymbol{B}$ is the magnetic field, and $\boldsymbol{D}$ represents the electric field generated by non-ideal processes. This term include the resistive term, the terms associated with the decoupling between species or associated with thermodynamic forces, turbulent transport, *etc*.

A general criterion which allows for magnetic reconnections, has been provided by Schindler et al. (1988). This criterion reads

$$\boldsymbol{B} \wedge \left(\boldsymbol{\partial_x} \wedge \boldsymbol{D}^{\parallel} \right) \neq 0, \tag{1.2.2}$$

where $\boldsymbol{D}^{\parallel}$ is the parallel component of the electric field generated by the non-ideal processes. Therefore, according to (1.2.2), all the processes which produce electric field that are parallel to the magnetic field result in reconnection, if their curl is non zero.

1.2.1 Magnetic reconnection in the sun atmosphere

The magnetic reconnection plays a major role in the solar corona. It is a key process in eruptions (flares, filaments, coronal mass ejections (CME)), jets, *etc*. This process is also relevant in the lower solar atmosphere, playing a major role in many solar activities such as microflares (see Gontikakis, C. et al. (2013)) or chromospheric jets (see Bharti et al. (2013)). Additionally, as explained above, the magnetic reconnection probably plays an important role in the heating of the chromosphere and corona (see Klimchuk (2015)).

In the solar atmosphere, the main mechanism responsible of the magnetic reconnection process is the resistivity due to collisions between particles. In order to compare the timescales of (1.2.1),

we define S the Lundquist number as

$$S = \frac{L^0 v^0}{\eta}, \tag{1.2.3}$$

where L^0 is the characteristic length scale, v^0 is the Alfvén velocity of the plasma and η is the magnetic diffusivity (resistivity). This ratio compares the timescale of an Alfvén wave crossing to the timescale of the resistive diffusion. If the ratio is high, the plasma can be considered highly conductive. On the other hand, if the ratio is low, the plasma is highly resistive.

We choose some values of temperature, pressure and magnitude of magnetic field in order to compute the mean free path l^0 and hall parameter β_e^0 at the photosphere, lower and middle chromosphere, and coronal loop regions of the sun atmosphere, for the purpose of characterizing the Sun atmosphere. The thermodynamic properties have been chosen from Vernazza et al. (1981). They have been computed using a spectral Galerkin method with Laguerre-Sonine polynomial approximation for a Helium-Hydrogen mixture composed of 91.2% of Hydrogen and 8.8% of Helium by volume. A deeper description of the method and the way of computing such properties are described in Chapter 4. Results are presented in Table 1.1.

Table 1.1: Reference quantities in the sun atmosphere from Vernazza et al. (1981)

	T[K]	P[Pa]	B[T]	$l^0[m]$	β_e^0
Photosphere	5000	3000	6.10^{-3}	$2.2\ 10^{-4}$	0.343
Low chromosphere	5200	80	3.10^{-3}	$8.77\ 10^{-3}$	0.671
Mid chromosphere	6000	0.08	1.10^{-3}	0.63	150
Coronal loop	10^6	0.13	3.10^{-2}	25497	$4.7\ 10^6$

These preliminary results show that the mean free path l^0 varies by several orders of magnitude in the solar atmosphere. Additionally, the Hall parameter for electrons is showing that the magnetic field has a large impact on the dynamics of the electrons. The Hall parameter is small at the photosphere but higher in the mid chromosphere. Therefore, the electrons can be weakly or strongly magnetized. In summary, the characteristic scales are varying by several orders of magnitude and the plasma can be weakly or strongly magnetized, in the Sun atmosphere.

Additionally, from the upper photosphere to the middle chromosphere, for a length scale $L^0 = 10^6$ m and Alfven velocity $v^0 = 10 - 100\ km.s^{-1}$, the Lundquist number is of order $S = 10^6 - 10^8$, as shown by Ni et al. (2018, 2015). In the solar corona, for scales of order 10^4 km, the Lundquist number is around $S = 10^{12}$. Finally, solar physics plasmas are mainly highly conductive. However, when magnetic reconnection event occurs, the length scale associated with the current sheet (or reconnection region) is much smaller than the characteristic length scale. In Leake et al. (2013), the characteristic length of the current sheet is assumed to be around 120 m, computed from the Sweet-Parker model Parker (1957). Therefore, the Lundquist number is much smaller in the reconnection regions of the Sun atmosphere.

Part I

Modeling from kinetic theory

CHAPTER 2

MODELING OF THERMAL NONEQUILIBRIUM MULTICOMPONENT PLASMAS BASED ON A MULTISCALE ANALYSIS

Introduction

The lower atmosphere of the Sun is a complex and dynamic layer where the plasma is found in a wide range of different regimes – from weakly-ionized and non-magnetized at the bottom of the photosphere to fully ionized and magnetized at the top of the transition region. In the solar chromosphere, the pressure varies from a thousand Pascals just above the photosphere to a few pascals in the high chromosphere, as described by Vernazza et al. (1981). Similarly, the magnitude of the magnetic field is large in active regions, around thousands of Gauss in sunspots, whereas it is just a few Gauss in quiet-Sun regions, as shown by Wiegelmann et al. (2014). It is still nowadays a great challenge to develop a unified model that can be used for both partially- and fully-ionized regimes under the large disparity of plasma parameters in the lower atmosphere.

In the literature, two types of fluid models to study the solar lower atmosphere can be found. First, the single-fluid MHD description considers the plasma as a conducting fluid in the presence of a magnetic field. It has the main drawback of assuming thermal equilibrium conditions, where all the species are considered to be at the same temperature. This model is assumed to be valid in a highly collisional framework, allowing us to study the formation of magnetic field concentrations at the solar surface in sunspots, magnetic pores, and the large-scale flow patterns associated with them (see Hartlep et al. (2012)). It is also used for simulating the lower part of the atmosphere of the Sun, *e.g.*, incorporating subgrid-scale turbulence models for the transport of heat and electrical resistivity (see Kitiashvili et al. (2015)). The full MHD equations are solved by Martínez-Sykora et al. (2015) accounting for non-grey radiative transfer and thermal conduction outside local thermodynamic equilibrium, in order to study the effects of the partial ionization of

the solar chromosphere.

Multi-fluid MHD models have been used more recently to represent the non-equilibrium conditions of the chromosphere, based on continuity, momentum, and energy conservation equations for each species considered in the mixture (see Leake et al. (2012); Alvarez-Laguna et al. (2018); Ni et al. (2018)). Leake et al. (2012) performed a multi-fluid simulation of magnetic reconnection for a weakly ionized reacting plasma, with a particular focus on the solar chromosphere, by considering collisional transport, chemical reactions between species, as well as radiative losses. Khomenko et al. (2014) proposed a model for the description of a multi-component partially ionized solar plasma. Braginskii (1965) has derived rigorous thermal nonequilibrium multi-fluid model for fully ionized plasmas including expressions for the transport properties starting from the Boltzmann equation. Deriving rigorous multi-fluid model is complex, and so far, the theory has not yet been developed to the same level of accuracy as Braginskii's. Thus, deriving a fluid model from kinetic theory, starting from the Boltzmann equations appear to be the most rigorous way to derive macroscopic equations for partially ionized plasmas. Therefore, we have focused on this approach to derive macroscopic equations.

Several studies have been carried out to study partially ionized/multicomponent plasmas based on a kinetic approach. Chapman & T.G. (1939, second edition, 1960) have used the Chapman-Enskog theory for ionized mixtures in the case of monoatomic binary mixtures. Then, Kaneko (1960) has extended this work for neutral binary mixtures under a uniform magnetic field, in a simplified kinetic framework. R. S. Devoto (1966) has studied multicomponent gas mixtures using a Chapman-Enskog-Burnett method, based on the kinetic theory. In addition, Ferziger & Kaper (1973) have focused on the study of multicomponent plasma in thermal equilibrium. This study has been used to develop transport properties for multicomponent plasmas in thermal equilibrium, using a spectral Galerkin method. However, in the presented approaches, thermal nonequilibrium process are not taken into account. The first model derived from kinetic theory which allows for thermal nonequilibrium process, in the presence of magnetic field, with self-consistent transport properties is the one developed by Kolesnikov (2003). This model is derived from a Chapman-Enskog expansion method based on the Boltzmann equation for electrons and heavy-particles. In this framework, the distribution function is assumed to be a small perturbation of the Maxwellian distribution function. However, according to Magin (2004), some steps and approximations in the development of the model of Kolesnikov (2003) remain debatable, in particular, the scaling used in the Boltzmann equation for electrons and heavy-particles.

Petit & Darrozes (1975) have shown that the Chapman-Enskog perturbative method has to be reviewed. In particular, a dimensional analysis of the Boltzmann equation shows that electrons and heavy particles have different relaxation times. They exhibit different kinetic timescales and can show several temperatures. These differences are due to the large mass disparity between electrons and heavy-particles. At the hydrodynamic time scale, the energy exchanged between electrons and heavy particles tends to equalize both temperatures. In this context, Degond & B. (1996) have followed the work of Petit & Darrozes (1975) by considering a specific dimensional analysis which takes into account the different kinetic scales, and temperatures which are involved in a multicomponent plasma. Finally, deriving a model for partially ionized plasmas based on a Chapman-Enskog method requires a proper scaling of the Boltzmann equations with a consistent

dimensional analysis to be able to capture all the scales for electrons and heavy-particles.

We have focused on the model derived by Graille et al. (2009). It is a multi-component drift-diffusion model for two-temperature magnetized plasmas. It was derived from a generalized Chapman-Enskog expansion to the Boltzmann equation, based on a multiscale analysis. This analysis is based on non-dimensional parameters, combining the usual Knudsen number and the square root of the electron-to-heavy-particle mass ratio, defined as Kn and ε respectively. Note that, the model assumes the Knudsen number to be small and of order ε. The parameter ε drives thermal nonequilibrium between the electron and heavy-particle baths. In addition, the magnitude of the magnetic field is taken into account in the proposed scaling, through the Hall parameter. Therefore, the strongly-,weakly- magnetized cases have been investigated. Non-dimensional Boltzmann equations for electrons and heavy species are involved and the order of magnitude of the terms are studied through chosen reference quantities. The model has been derived in the hydrodynamic reference frame of heavy-particles, where all the particules are assumed to diffuse in this reference frame. In the development, the electrons and heavy-particles are shown to thermalize at different temperature $T_{\mathfrak{e}}$ and $T_{\mathfrak{h}}$, occurring at the kinetic timescale for electrons and heavy-particles respectively. At the last order investigated, the Navier-Stokes equations for heavy particles and first-order drift diffusion equations for electrons are obtained. In this thesis, we couple this model to the set of Maxwell equations and introduce additional quantities such as the Debye length. We introduce a non-dimensional parameter ε_{λ_D} equal to square of the Debye-to-macroscopic length ratio. These quantities are carefully chosen to be consistent with the scaling introduced by Graille et al. (2009) based on the ε parameter. Therefore, a general approach, where Debye length scales are taken into account, is considered. For the sake of clarity, considering the large disparity between the characteristic length scales related to the solar atmosphere and the Debye length scale, this quantity will be assumed to be small. Thus, we consider the electroneutrality assumption.

These developments lead to a model with an extended range of validity for partially and fully ionized plasma, for non and weakly magnetized plasmas and general multicomponent mixtures, that allows for charge separation effects. In addition, an entropy inequality has been obtained as well as Onsager reciprocity relations for the transport properties. The model is valid in solar atmosphere conditions and this approach is able to capture most of the multi-fluid phenomena, *i.e.*, different velocities between species, collisional exchange of mass momentum and energy, chemical reactions, thermal non-equilibrium, and magnetized transport. The transport properties are retrieved through a generalized Chapman-Enskog solution to the Boltzmann equation using a multiscale perturbation method.

The Chapter is organized as follows: in Section 2.1, the assumptions, nondimensional parameters and the classical dimensional Boltzmann equation coupled to the set of Maxwell equations are introduced. In this section, we provide some classical concepts such as the particle distribution functions and the macroscopic properties at the kinetic level. We introduce the concepts of collisional invariants and Maxwell-Boltzmann distribution function in the case where no dimensional analysis is performed. In Section 2.2, a dimensional analysis is performed on both Boltzmann and Maxwell equations. We extend the dimensional analysis of Graille et al. (2009) by considering the Debye length scale. We exhibit the nondimensional Boltzmann and set of Maxwell equations. In Section 2.3, a generalized Chapman-Enskog expansion is performed on the nondimensional Boltz-

mann equations for electrons and heavy-particles. A comparison with the approach of Braginskii (1965) is performed. We exhibit the impact of the proposed scaling on the derivation of the model. Finally, in Section 2.4, the transport fluxes are presented.

2.1 Assumptions and dimensional Boltzmann equation coupled to Maxwell equations

In this section, we focus on the assumptions used to derive a model from kinetic theory by Graille et al. (2009). We present the classical Boltzmann equations and concepts related to the particle distribution functions. In addition, we extend the work performed by Graille et al. (2009), by coupling the dimensional Boltzmann equations with the set of Maxwell equations. We exhibit these notions in a dimensional context.

We will present the hypotheses, parameters and some notations relevant for the derivation of the model. Then, we will focus on some basic concepts such as the distribution functions as well as the classical Boltzmann equation coupled to the set of Maxwell equations for multicomponent plasmas, in a dimensional context. Finally, we exhibit the impact of the multiscale analysis on the notion of thermal equilibrium in a multi-temperature plasma.

2.1.1 Assumptions and nondimensional parameters

The plasma consists of a set of a large numbers of microscopic particles that are moving freely and independently in a region of physical space which is available to them. The multicomponent plasma is a gas mixture mainly composed of electrons, denoted by the index $\mathfrak{e}$, and heavy particles, denoted by H. The heavy particles are composed of ions and neutrals denoted by I and N respectively. Therefore, the plasma is composed of n_S species referred to the set of indices $S = \{1, ..., n_S\} = H \cup \{\mathfrak{e}\}$. The set of heavy particles can be written as $H = I \cup N$.

The plasma is described by the kinetic theory of gases based on classical mechanics. Indeed, quantum mechanical effects on transport phenomena in a gas are caused by their statistic behaviors. Diffraction effects become important if the de Broglie wavelength is as large as the dimension of molecules, whereas symmetry effects depend on the gas density and appear when the de Broglie wavelength is of the order of magnitude of the average distance between the gas molecules. In all the considered physical applications, we consider scales which are much larger than the characteristic scales of de Broglie. However, these quantum effects are correctly described by classical expressions of the transport properties, since the corresponding transport collision integrals are computed from a quantum mechanic description, as explained by Hirschfelder et al. (1964).

In the following, we perform a dimensional analysis based on nondimensional parameters. Thus, we present the nondimensional parameters to be used in this work. The parameters are based on reference quantities which are presented in this section. For the sake of clarity, the index 0 denotes for reference quantities. In this framework, the mean distance between the gas particles

is larger than the thermal de Broglie wavelength l_{th} , and the square of the ratio of the electron thermal speed $V_{\mathfrak{e}}^0$ to the speed of light c is small, *i.e.*,

$$\frac{1}{(n^0)^{\frac{1}{3}}} \gg l_{th}, \quad \text{and} \quad \sqrt{\frac{V_{\mathfrak{e}}^0}{c}} \ll 1, \tag{2.1.1}$$

where n^0 is a reference number density of the plasma. Besides, the reactive collisions and particle internal energy are not accounted for, as assumed by Magin (2004). The particle interactions are modeled as binary encounters by means of a Boltzmann collision operator, provided that

1. The gas is sufficiently dilute, *i.e.*, the mean distance between the gas particles is much larger than the particle interaction distance $\sqrt{\sigma^0}$, which leads to $1/(n^0)^{1/3} \gg \sqrt{\sigma^0}$, where σ^0 is a reference differential cross-section common to all species,

2. The plasma parameter, quantity proportional to the number of electrons in a sphere of radius equal to the Debye length λ_D, is supposed to be large. Consequently, multiple charged particle interactions are treated as equivalent binary collisions by means of a Coulomb potential screened at the Debye length, as described by S. R. Devoto (1969); Haines (1990).

The ratio of the electron mass $m_{\mathfrak{e}}^0$ to a characteristic heavy-particle mass $m_{\mathfrak{h}}^0$ is such that the nondimensional number reads

$$\varepsilon = \sqrt{\frac{m_{\mathfrak{e}}^0}{m_{\mathfrak{h}}^0}} \ll 1, \tag{2.1.2}$$

thus, we assume that the nondimensional number ε is small. In the next sections, this parameter will appear to be a scaling factor at different orders in the generalized Chapman-Enskog expansion, as shown by Graille et al. (2009). Due to the assumption of small electron heavy-particle mass-ratio, the electron temperature may depart from the heavy particle temperature. We envisage the case of thermal nonequilibrium.

We define the pseudo-Mach number $M_{\mathfrak{h}}$, which is a ratio of a reference hydrodynamic velocity v^0 divided by the heavy-particle thermal speed $V_{\mathfrak{h}}^0$:

$$M_{\mathfrak{h}} = \frac{v^0}{V_{\mathfrak{h}}^0}. \tag{2.1.3}$$

In the presented model, we suppose that $M_{\mathfrak{h}}$ is of order one. Thus, the model obtained will be established in the heavy particle reference frame. In Graille et al. (2009), it is proved to be the natural and optimal reference frame in which the heavy particles thermalize in the context of the proposed multiscale analysis. The macroscopic timescale t^0 is assumed to be

$$t^0 = \frac{t_{\mathfrak{h}}^0}{\varepsilon}, \tag{2.1.4}$$

where $t_{\mathfrak{h}}^0$ is the heavy particle kinetic timescale. The macroscopic length scale is based on a refer-

ence convective length L^0 such as

$$L^0 = v^0 t^0. \tag{2.1.5}$$

The reference electrical and thermal energies of the system are of the same order of magnitude. The mean free path l^0 and macroscopic length scale L^0 allow for the Knudsen number to be defined as

$$Kn = \frac{l^0}{L^0}. \tag{2.1.6}$$

In the following, this quantity is assumed to be small, which guarantees a continuum description of the plasma.

Finally, we introduce the following ratio

$$\varepsilon_{\lambda_D} = \left(\frac{\lambda_D}{L^0}\right)^2. \tag{2.1.7}$$

This parameter allows a coupling of the set of Maxwell's equations with the Boltzmann equations, while being consistent with the scaling proposed by Graille et al. (2009). If ε_{λ_D} is considered to be small, the electroneutrality assumption is considered. In the following, for the considered applications, we will assume that the characteristic scales are much larger than the Debye length, thus, ε_{λ_D} is considered to be small.

2.1.2 Particle velocity distribution functions and macroscopic properties

In kinetic theory, a fundamental concept which is introduced is the particle velocity distribution function, f_i^*. It is defined in a six-dimensional phase-space, including physical and velocity space. The plasmas particles of species $i \in \mathrm{S}$, are described by $f_i^* = f_i^*\left(\boldsymbol{x}^*, \boldsymbol{c}_i^*, t^*\right)$, where $\boldsymbol{x}^*$ stands for space, t^* for time and $\boldsymbol{c}_i^*$ the velocity of the particle i in the inertial reference frame. This function gives the probability of finding one particle of species i at position $\boldsymbol{x}^*$ and time t^* with a velocity $\boldsymbol{c}_i^*$. For the sake of clarity, here the index $*$ denotes for dimensional quantities.

We consider an infinitesimal 6-D volume such as $d\boldsymbol{x}^* d\boldsymbol{c}_i^*$, centred at the point $(\boldsymbol{x}^*, \boldsymbol{c}_i^*, t^*)$, which contains sufficient number of particles i. The velocity distribution function f_i^* is defined in such a way that the product $f_i^* d\boldsymbol{x}^* d\boldsymbol{c}_i^*$ is the expected number of particle i in the volume element $d\boldsymbol{x}^*$ located at $\boldsymbol{x}^*$, where the velocities lie in the velocity element $d\boldsymbol{c}_i^*$ at time t^*. From these definitions, some macroscopic properties for electrons and heavy particles such as mass and number densities, mean velocities and internal energies can be defined. First, we have the mass densities

$$\rho_{\mathfrak{e}}^* = m_{\mathfrak{e}}^* n_{\mathfrak{e}}{}^* = \int f_{\mathfrak{e}}^* m_{\mathfrak{e}}^* d\boldsymbol{c}_{\mathfrak{e}}^*, \quad \text{and} \quad \rho_{\mathfrak{h}}^* = \sum_{i \in \mathrm{H}} m_i^* n_i{}^* = \sum_{i \in \mathrm{H}} \rho_i^* = \sum_{i \in \mathrm{H}} \int f_i^* m_i^* d\boldsymbol{c}_i^*, \tag{2.1.8}$$

where $\rho_{\mathfrak{e}}^*$ and $\rho_{\mathfrak{h}}^*$ are the mass density of electrons and heavy particles, $n_{\mathfrak{e}}{}^*$ and $n_{\mathfrak{h}}^* = \sum_{i \in \mathrm{H}} n_i{}^*$ are the number densities of electrons and heavy particles. We remind that the integration is performed

over the entire velocity space of each particle $i \in \mathrm{S}$,

$$\int (\cdot)\, d\boldsymbol{c}_i^* = \int_{-\infty}^{+\infty} \int_{-\infty}^{+\infty} \int_{-\infty}^{+\infty} (\cdot)\, dc_{i,x}^* dc_{i,y}^* dc_{i,z}^*, \tag{2.1.9}$$

where x, y and z denote for the first, second and third direction respectively. In addition, one can also define a mixture mass and number density as

$$\rho^* = \sum_{i \in \mathrm{S}} \rho_i^* = \rho_{\mathfrak{e}}^* + \rho_{\mathfrak{h}}^*, \quad \text{and} \quad n^* = n_{\mathfrak{e}}{}^* + n_{\mathfrak{h}}^*. \tag{2.1.10}$$

Then, the mean velocities are defined as :

$$\rho_{\mathfrak{e}}^* \boldsymbol{v}_{\mathfrak{e}}^* = \int m_{\mathfrak{e}}^* f_{\mathfrak{e}}^* \boldsymbol{c}_{\mathfrak{e}}^* d\boldsymbol{c}_{\mathfrak{e}}^*, \quad \text{and} \quad \rho_{\mathfrak{h}}^* \boldsymbol{v}_{\mathfrak{h}}^* = \sum_{i \in \mathrm{H}} \int m_i^* f_i^* \boldsymbol{c}_i^* d\boldsymbol{c}_i^*, \tag{2.1.11}$$

where $\boldsymbol{v}_{\mathfrak{e}}^*$ and $\boldsymbol{v}_{\mathfrak{h}}^*$ are the hydrodynamic velocities of electrons and heavy particles respectively. Finally, the internal energies of electrons $E_{\mathfrak{e}}^* = \rho_{\mathfrak{e}}^* e_{\mathfrak{e}}^*$ and heavy particles $E_{\mathfrak{h}}^* = \rho_{\mathfrak{h}}^* e_{\mathfrak{h}}^*$ can be defined as:

$$E_{\mathfrak{e}}^* = \rho_{\mathfrak{e}}^* e_{\mathfrak{e}}^* = \int \frac{1}{2} m_{\mathfrak{e}}^* f_{\mathfrak{e}}^* \boldsymbol{c}_{\mathfrak{e}}^* \cdot \boldsymbol{c}_{\mathfrak{e}}^* d\boldsymbol{c}_{\mathfrak{e}}^*, \quad \text{and} \quad E_{\mathfrak{h}}^* = \rho_{\mathfrak{h}}^* e_{\mathfrak{h}}^* = \sum_{i \in \mathrm{H}} \int \frac{1}{2} m_i^* f_i^* \boldsymbol{c}_i^* \cdot \boldsymbol{c}_i^* d\boldsymbol{c}_i^*, \tag{2.1.12}$$

where $e_{\mathfrak{e}}^*$ and $e_{\mathfrak{h}}^*$ stand for the electron and heavy-particle thermal energy per unit mass respectively.

2.1.3 Boltzmann and Maxwell equations

As described by Ferziger & Kaper (1973), the temporal evolution of the velocity distribution function is governed by the following Boltzmann equation

$$\mathcal{D}_i^*(f_i^*) = \sum_{j \in S} \mathcal{J}_{ij}^*(f_i^*, f_j^*), \quad i \in \mathrm{S}, \tag{2.1.13}$$

where the streaming operator $\mathcal{D}_i^*$ reads

$$\mathcal{D}_i^*(f_i^*) = \partial_{t^*} f_i^* + \boldsymbol{c}_i^* \cdot \boldsymbol{\partial}_{\boldsymbol{x}^*} f_i^* + \frac{q_i^*}{m_i^*} (\boldsymbol{E}^* + \boldsymbol{c}_i^* \wedge \boldsymbol{B}^*) \cdot \boldsymbol{\partial}_{\boldsymbol{c}_i^*} f_i^*, \quad i \in \mathrm{S}, \tag{2.1.14}$$

where $\boldsymbol{E}^*$ is the electric field, $\boldsymbol{B}^*$ the magnetic field and q_i^* the charge of particle i with mass m_i^*. Note that, the first terms of the streaming operator (2.1.14), can be seen as a temporal derivative of the distribution function f_i^* in the phase space, *i.e.*,

$$\frac{df_i^*}{dt^*} = \partial_{t^*} f_i^* + \boldsymbol{c}_i^* \cdot \boldsymbol{\partial}_{\boldsymbol{x}^*} f_i^* + \frac{d\boldsymbol{c}_i^*}{dt^*} \cdot \boldsymbol{\partial}_{\boldsymbol{c}_i^*} f_i^*, \quad i \in \mathrm{S} \tag{2.1.15}$$

which accounts for the acceleration $d\boldsymbol{c}_i^*/dt^*$ of the particle i due to the Lorentz force per unit mass acting on the charged particles. On the right hand side of (2.1.13), we have the collision operator, which describes the changes of the distribution function due to collisions with all the particles of the mixture. The partial collision operator between particle i and j reads

$$\mathcal{J}_{ij}^*(f_i^*, f_j^*) = \int \left(f_i^{*\prime} f_j^{*\prime} - f_i^* f_j^*\right) \sigma_{ij}^* d\boldsymbol{\omega}' d\boldsymbol{c}_j^*, \quad i, j \in \mathrm{S}^2 \tag{2.1.16}$$

where $'$ denotes for quantities after collision, $\boldsymbol{\omega}' = (\boldsymbol{c}_i^{*\prime} - \boldsymbol{c}_j^{*\prime})/|\boldsymbol{c}_i^{*\prime} - \boldsymbol{c}_j^{*\prime}|$ is the direction of relative velocity after collision and $f^{*\prime}$ represents the distribution function after collisions. The collision operator include a gain and a loss term.

The loss term is proportionnal to the number of particles j with velocity $\boldsymbol{c}_j^*$, which collide with particles i with velocity $\boldsymbol{c}_i^*$. Consequently, this term is proportional to the product $f_i^* f_j^*$. Then, the differential cross-section σ_{ij}^* is defined such as the probable number of collisions per unit volume and time with direction $\boldsymbol{\omega}'$, reads $f_i^* f_j^* \sigma_{ij}^* d\boldsymbol{\omega}' d\boldsymbol{c}_j^* d\boldsymbol{c}_i^*$. The differential cross-section σ_{ij}^* depends on the relative kinetic energy between the colliding particles and the deflection angle χ between the unit vectors of relative velocities $\boldsymbol{\omega}'$ and $\boldsymbol{\omega} = (\boldsymbol{c}_i^* - \boldsymbol{c}_j^*)/|\boldsymbol{c}_i^* - \boldsymbol{c}_j^*|$, which is represented in Figure 2-1. We notice that the differential cross sections σ_{ij}^* are symmetric, *i.e.*, $\sigma_{ij}^* = \sigma_{ji}^*$, $i, j \in \mathrm{S}^2$.

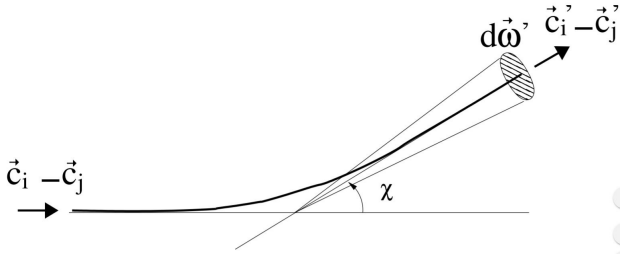

Figure 2-1: Description of a binary collision involving all the parameters of (2.1.16)

On the other hand, the expression of the gain term in (2.1.16), is obtained by means of the inverse collision, described in Figure 2-2, which is defined as a collision between particles i and j with velocity $\boldsymbol{c}_i^{*\prime}$ and $\boldsymbol{c}_j^{*\prime}$ after an impact with velocities $\boldsymbol{c}_i^*$ and $\boldsymbol{c}_j^*$ respectively. In the inverse collision, the same differential cross-section is used as for binary collision, because their relative kinetic energy and deflection angle χ are identical. Similarly to the loss term, the gain term is proportional to $f_i^{*\prime} f_j^{*\prime}$. Finally, the partial collision operator of particle j impacting particle i is obtained by integrating over all the velocities $\boldsymbol{c}_j^*$ of particle j and all the directions $\boldsymbol{\omega}'$.

We underline that these operators are written in an inertial reference frame. Alternatively, as performed by Graille et al. (2009), Sutton & Sherman (1965), or Chapman & T.G. (1939, second edition, 1960), we can rewrite the Boltzmann equation of (2.1.13) in a reference frame linked with the heavy particles. We define the peculiar velocity in the heavy particle reference frame such as

$$\boldsymbol{C}_i^* = \boldsymbol{c}_i^* - \boldsymbol{v}_{\mathfrak{h}}^*, \quad i \in \mathrm{S}. \tag{2.1.17}$$

Finally, the Boltzmann equation in (2.1.13) can be expressed in this reference frame, which leads

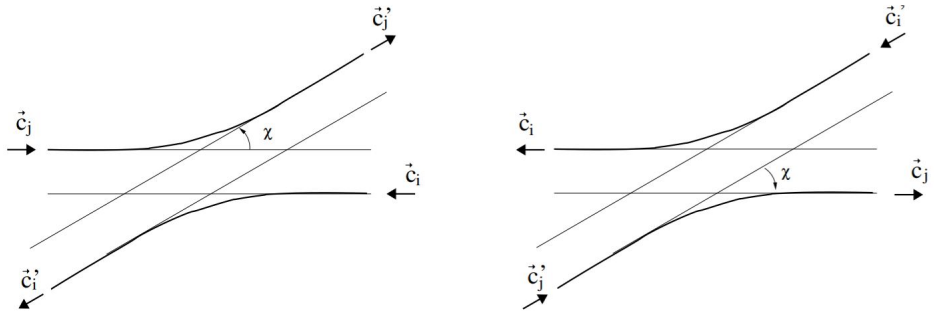

Figure 2-2: Left: Description of a binary collision. Right: Description of an inverse collision.

to a new expression of the streaming operator, as follows:

$$\mathcal{D}_i^*(f_i^*) = \partial_{t^*} f_i^* + \left(\boldsymbol{C}_i^* + \boldsymbol{v}_\mathfrak{h}^*\right)\cdot\boldsymbol{\partial}_{\boldsymbol{x}^*} f_i^* + \frac{q_i^*}{m_i^*}\left[\boldsymbol{E}^* + \left(\boldsymbol{C}_i^* + \boldsymbol{v}_\mathfrak{h}^*\right)\wedge\boldsymbol{B}^*\right]\cdot\boldsymbol{\partial}_{\boldsymbol{C}_i^*} f_i^* - \frac{D\boldsymbol{v}_\mathfrak{h}^*}{Dt^*}\cdot\boldsymbol{\partial}_{\boldsymbol{C}_i^*} f_i^* - \left(\boldsymbol{\partial}_{\boldsymbol{C}_i^*} f_i^* \otimes \boldsymbol{C}_i^*\right) : \boldsymbol{\partial}_{\boldsymbol{x}^*}\boldsymbol{v}_\mathfrak{h}^*, \quad i \in \mathrm{S}, \quad (2.1.18)$$

where $D/Dt^* = \partial_{t^*} + \boldsymbol{v}_\mathfrak{h}^*\cdot\boldsymbol{\partial}_{\boldsymbol{x}^*}$. In addition, we can rewrite (2.1.16) in terms of peculiar velocities, which leads to

$$\mathcal{J}_{ij}^*(f_i^*, f_j^*) = \int \left(f_i^{*\prime} f_j^{*\prime} - f_i^* f_j^*\right)|\boldsymbol{C}_i^* - \boldsymbol{C}_j^*|\sigma_{ij}^* d\boldsymbol{\omega}' d\boldsymbol{C}_j^*, \quad i, j \in \mathrm{S}^2. \quad (2.1.19)$$

In this reference frame, all the quantities such as the distribution functions, the differential cross-sections and the unit vectors depend on the peculiar velocities.

In this thesis, the dynamic of the electric and magnetic fields for a given charge and current distribution, is determined from Maxwell's equations and coupled to the presented Boltzmann equations in (2.1.13), as follows

$$\boldsymbol{\partial}_{\boldsymbol{x}^*}\cdot\boldsymbol{E}^* = \frac{n^* q^*}{\varepsilon_0}, \quad \boldsymbol{\partial}_{\boldsymbol{x}^*}\cdot\boldsymbol{B}^* = 0, \quad \partial_{t^*}\boldsymbol{B}^* = -\boldsymbol{\partial}_{\boldsymbol{x}^*}\wedge\boldsymbol{E}^*, \quad \boldsymbol{\partial}_{\boldsymbol{x}^*}\wedge\boldsymbol{B}^* = \mu_0\mathbf{I}^* + \mu_0\varepsilon_0\partial_{t^*}\boldsymbol{E}^* \quad (\mathrm{Mx}^*)$$

where ε_0 is the vacuum permittivity, μ_0 is the vacuum permeability, $\mathbf{I}^*$ is the total current density and $n^* q^*$ is the global charge defined as

$$n^* q^* = \sum_{i\in\mathrm{S}} n_i^* q_i^*. \quad (2.1.20)$$

2.1.4 Collisional invariants and Maxwell-Boltzmann distribution

In order to define the notions of equilibrium state and collisional invariants, we want to make use of the well known H-theorem from Boltzmann (see Cercignani (1987)). Boltzmann showed that the distribution introduced by Maxwell is the unique steady solution of his equation.

From (2.1.13), we consider a simplified case where the gas is spacially uniform, i.e. $\partial_{x^*} = 0$, in the absence of electromagnetic forces. We define the following quantity

$$\mathcal{H} = \sum_{i \in \mathrm{S}} \int f_i^* \ln f_i^* d\boldsymbol{c}_i^*. \tag{2.1.21}$$

Then, we take the time derivative of (2.1.21) and use (2.1.13) in the inertial reference frame, in order to obtain :

$$\frac{d\mathcal{H}}{dt^*} = -\frac{1}{4} \sum_{i,j \in \mathrm{S}} \int \left(f_i^{*\prime} f_j^{*\prime} - f_i^* f_j^*\right) \left[\ln\left(f_i^{*\prime} f_j^{*\prime}\right) - \ln\left(f_i^* f_j^*\right)\right] |\boldsymbol{c}_i^* - \boldsymbol{c}_j^*| \sigma_{ij}^* d\omega' d\boldsymbol{c}_i^* d\boldsymbol{c}_j^*. \tag{2.1.22}$$

Boltzmann has shown that $d\mathcal{H}/dt^* < 0$, and $\mathcal{H}$ is bounded as $t \to \infty$, corresponding to the equilibrium state where $d\mathcal{H}/dt^* = 0$. Finally, at equilibrium we have $f_i^{*\prime} f_j^{*\prime} = f_i^* f_j^*$, which leads to

$$\ln(f_i^*) + \ln(f_j^*) = \ln(f_i^{*\prime}) + \ln(f_j^{*\prime}), \quad i, j \in \mathrm{S}^2 \tag{2.1.23}$$

From this classical result, we extract a property which is typical of a collisional invariant, which is a microscopic quantity conserved during a collision between two particles. Using the definitions from (2.1.8), (2.1.11) and (2.1.12), we obtain :

$$\begin{aligned} & m_i^* = m_i^{*\prime}, \quad m_j^* = m_j^{*\prime} \\ & m_i^* \boldsymbol{c}_i^* + m_j^* \boldsymbol{c}_j^* = m_i^{*\prime} \boldsymbol{c}_i^{*\prime} + m_j^{*\prime} \boldsymbol{c}_j^{*\prime}, \qquad i, j \in \mathrm{S}^2 \\ & \frac{1}{2} m_i^* \boldsymbol{c}_i^* \cdot \boldsymbol{c}_i^* + \frac{1}{2} m_j^* \boldsymbol{c}_j^* \cdot \boldsymbol{c}_j^* = \frac{1}{2} m_i^{*\prime} \boldsymbol{c}_i^{*\prime} \cdot \boldsymbol{c}_i^{*\prime} + \frac{1}{2} m_j^{*\prime} \boldsymbol{c}_j^{*\prime} \cdot \boldsymbol{c}_j^{*\prime}, \end{aligned} \tag{2.1.24}$$

which corresponds to the conservation of mass, momentum and energy when a collision occurs between particle i and j. We introduce the space of vectors known as the space of the collisional invariants

$$\mathcal{I}^* = \begin{cases} \psi_i^{*,l} = \left(m_i^* \delta_{il}\right)_{i \in \mathrm{S}}, & l \in \mathrm{S} \\ \psi_i^{*,n^{\mathrm{S}}+\nu} = \left(m_i^* c_{i,\nu}^*\right)_{i \in \mathrm{S}}, & \nu \in \{x, y, z\}, \\ \psi_i^{*,n^{\mathrm{S}}+4} = \left(\frac{1}{2} m_i^* \boldsymbol{c}_i^* \cdot \boldsymbol{c}_i^*\right)_{i \in \mathrm{S}}, \end{cases} \tag{2.1.25}$$

where δ_{il} is the Kroenecker symbol and n^{S} is the cardinality of the set of species S. We point out that (2.1.24) and (2.1.25) can be also written in the heavy reference frame by simply replacing the velocities by their corresponding peculiar velocities $\boldsymbol{C}_i^*$.

Finally, (2.1.24) can be written in a more compact way as

$$\psi_i^{*,l} + \psi_j^{*,l} = \psi_i^{*,l'} + \psi_j^{*,l'}, \quad i, j \in \mathrm{S}, \quad l \in n^{\mathrm{S}} + 4. \tag{2.1.26}$$

Since $\ln(f_i^*)$ is in the space of collisional invariants, it can be expressed as a linear combination of the vectors $\psi_i^{*,l}$. As shown by Ferziger & Kaper (1973), we obtain the Maxwell-Boltzmann distribution function for each heavy particles and electrons

$$f_i^{*,M} = {n_i}^* \left(\frac{m_i^*}{2\pi k_B T^*}\right)^{\frac{3}{2}} \exp\left(\frac{-m_i^* \boldsymbol{C}_i^{*2}}{2k_B T^*}\right), \quad i \in \mathrm{H}, \quad f_{\mathfrak{e}}^{*,M} = {n_{\mathfrak{e}}}^* \left(\frac{m_{\mathfrak{e}}^*}{2\pi k_B T^*}\right)^{\frac{3}{2}} \exp\left(\frac{-m_{\mathfrak{e}}^* \boldsymbol{C}_{\mathfrak{e}}^{*2}}{2k_B T^*}\right), \tag{2.1.27}$$

where k_B is the Boltzmann constant. Such distribution in (2.1.27) corresponds to the velocity distribution for a gas in equilibrium state where the electrons and heavy particles are in thermal equilibrium, *i.e.*, $T_{\mathfrak{e}}^* = T_{\mathfrak{h}}^* = T^*$, where $T_{\mathfrak{e}}^*$ and $T_{\mathfrak{h}}^*$ correspond to the temperature of electrons and heavy-particle respectively. Note that, in the case where we consider the multiscale analysis based on the mass ratio parameter ε, two Maxwell-Boltzmann distribution function for heavy particles and electrons at different temperature $T_{\mathfrak{e}}^*$ and $T_{\mathfrak{h}}^*$ are obtained.

Additionally, as performed by Ferziger & Kaper (1973), we also introduce a scalar product involving dimensional quantities in the heavy reference frame such as

$$\langle\!\langle \xi^*, \zeta^* \rangle\!\rangle = \sum_{j \in \mathrm{S}} \int \xi_j^* \odot \bar{\zeta}_j^* d\boldsymbol{C}_j^*, \tag{2.1.28}$$

for families $\xi^* = (\xi_i^*)_{i \in \mathrm{S}}$ and $\zeta^* = (\zeta_i^*)_{i \in \mathrm{S}}$. The symbol $\odot$ stands for the fully contracted product in space, and $\bar{}$ stands for the conjugate transpose operation. One of the most relevant properties of this scalar product is that the collision operator defined is orthogonal to the space of collisional invariants $\mathcal{I}^*$. The collisional invariants will be used to derive macroscopic equations.

2.2 Multi-scale analysis of the Boltzmann and Maxwell equations

Thereafter, we present the dimensional and multiscale analysis of the concepts introduced in the previous section. The multiscale analysis is performed on the set of Maxwell's equations coupled to the presented Boltzmann equations. With this analys we aim at the following goal. We will perform a generalized Chapman-Enskog expansion on dimensionless Boltzmann equations, in order to deduce macroscopic equations. Such expansion is performed through the mass ratio parameter ε, considered as small.

First, we will present the dimensional analysis, *i.e.*, all reference quantities used in this thesis. This analysis is performed in a thermal nonequilibrium framework, considering several kinetic timescales, for electrons and heavy particles. In addition, we will introduce the Debye length scale and non-dimensional parameter, such as ε_{λ_D}, to investigate the case of the electroneutrality

assumption. These quantities are chosen to be consistent with the assumptions presented in the previous section. Then, we will present the nondimensional Boltzmann and Maxwell equations, collisional invariants and collision operators. Finally, we will highlight the impact of the scaling introduced on these concepts.

2.2.1 Dimensional analysis

The dimensional analysis of the Boltzmann equation of (2.1.13) is inspired by the work of Petit & Darrozes (1975). We present the reference quantities common to all species, for electrons and heavy particles in Table 2.1 and in Table 2.2.

Table 2.1: Reference quantities common to all species

Quantity	Notation
Temperature	T^0
Number density	n^0
Differential cross-section	σ^0
Mean free path	l^0
Macroscopic timescale	t^0
Hydrodynamic velocity	v^0
Macroscopic length	L^0
Electric field	E^0
Magnetic field	B^0
Debye length	λ_D
Speed of light	c

Table 2.2: Reference quantities for electrons and heavy particles

	Electrons	Heavy particles
Mass	m_e^0	m_h^0
Thermal speed	V_e^0	V_h^0
Kinetic timescale	t_e^0	t_h^0

In Section 2.1.1, we have assumed that the mass ratio ε is small. Therefore, electrons show a larger thermal speed than the one of the heavy particles

$$V_e^0 = \sqrt{\frac{k_B T^0}{m_e^0}}, \quad V_h^0 = \sqrt{\frac{k_B T^0}{m_h^0}} = \varepsilon V_e^0. \tag{2.2.1}$$

The differential cross-sections σ^0 are of the same order of magnitude for all the species, thus, the characteristic mean free path l^0 is identical for all species. Thus, the presented kinetic timescale for electrons is lower than for heavy particles which leads to

$$t_e^0 = \frac{l^0}{V_e^0}, \quad t_h^0 = \frac{l^0}{V_h^0}, \quad \text{and} \quad t^0 = \frac{t_h^0}{\varepsilon}. \tag{2.2.2}$$

Physically, the kinetic timescales t_h^0 and t_e^0 correspond to the relaxation time of a distribution function towards its respective quasi-equilibrium state. The macroscopic timescale t^0 correspond to the average time during which electrons and heavy particles exchange their energy through encounters.

According to (2.1.3), the pseudo-Mach number is considered to be of order one, therefore, the Knudsen number can be rewritten as

$$Kn = \frac{l^0}{L^0} = \frac{\varepsilon}{M_h}, \tag{2.2.3}$$

thus, the Knudsen number is of order ε, due to our choice of macroscopic and temporal scales leading to a continuum description of the gas. Then, the reference electric field and thermal energies are linked by the following relation

$$q^0 E^0 L^0 = k_B T^0, \tag{2.2.4}$$

where E^0 and q^0 are the reference electric field and charge respectively. According to (2.2.4), the assumption ensures that the space gradient and velocity gradient terms of the streaming operator in (2.1.14) are of the same order of magnitude, as shown by Degond & Lucquin-Desreux (1996b).

Finally, in order to take into account the intensity of the magnetic field, we introduce the Hall numbers for electrons and heavy particles

$$\beta_e^0 = \frac{q^0 B^0}{m_e^0} t_e^0 = \varepsilon^{1-b}, \quad \text{and} \quad \beta_h^0 = \frac{q^0 B^0}{m_h^0} t_h^0 = \varepsilon \beta_e^0, \tag{2.2.5}$$

where $q^0 B^0 / m_e^0$ and $q^0 B^0 / m_h^0$ are the Larmor frequencies for electrons and heavy particle respectively. The magnitude of the magnetic field is assumed to be related to a power of ε by means of an integer $b \leq 1$. The integer is defined in such a way that $b < 0$ corresponds to unmagnetized plasma, $b = 0$ weakly magnetized plasma, and $b = 1$ strongly magnetized plasma.

Finally, we have the Debye length defined as

$$\lambda_D = \sqrt{\frac{\varepsilon_0 k_B T^0}{n_e^0 q^{0^2}}}, \tag{2.2.6}$$

and the parameter ε_{λ_D} is chosen as

$$\varepsilon_{\lambda_D} \ll 1. \tag{2.2.7}$$

In summary, from (2.2.3) we have introduced 1- two spatial scales, one microscopic scale,

corresponding to the mean free path l^0, one macroscopic scale, corresponding to L^0, and 2- three temporal scales, two kinetic timescale $t_{\mathfrak{e}}^0$ and $t_{\mathfrak{h}}^0$ for electrons and heavy particles, and one macroscopic timescale corresponding to t^0.

We choose reference quantities coherent with the assumptions provided in Section 2.1.1. In the next section, we justify the assumption given in (2.2.7).

2.2.2 Nondimensional macroscopic properties and Boltzmann equations

Using the reference quantities introduced in Section 2.2.1, we express the variables and the Boltzmann equations, introduced in Section 2.1.2, in a nondimensional form. The following nondimensional variables will be denoted by dropping the superscript $*$.

Macroscopic variables

The particles velocities read

$$\boldsymbol{c}_{\mathfrak{e}}^* = V_{\mathfrak{e}}^0 \boldsymbol{c}_{\mathfrak{e}}, \quad \boldsymbol{c}_i^* = V_{\mathfrak{h}}^0 \boldsymbol{c}_i, \quad i \in \mathrm{H}. \tag{2.2.8}$$

Thus, the nondimensional form of the velocities shows that the velocity of the electrons is $1/\varepsilon$ faster than the velocity of heavy particles. Then, one can rewrite (2.1.11) in a nondimensional form as:

$$\rho_{\mathfrak{e}} M_{\mathfrak{h}} \boldsymbol{v}_{\mathfrak{e}} = \frac{1}{\varepsilon} \int f_{\mathfrak{e}} \boldsymbol{c}_{\mathfrak{e}} d\boldsymbol{c}_{\mathfrak{e}}, \quad \rho_{\mathfrak{h}} M_{\mathfrak{h}} \boldsymbol{v}_{\mathfrak{h}} = \sum_{i \in \mathrm{H}} \int m_i f_i \boldsymbol{c}_i d\boldsymbol{c}_i. \tag{2.2.9}$$

Similarly, the peculiar velocity in the heavy particle reference frame, defined in (2.1.17), can be written in a nondimensional form as:

$$\boldsymbol{C}_{\mathfrak{e}} = \boldsymbol{c}_{\mathfrak{e}} - \varepsilon M_{\mathfrak{h}} \boldsymbol{v}_{\mathfrak{h}}, \quad \boldsymbol{C}_i = \boldsymbol{c}_i - M_{\mathfrak{h}} \boldsymbol{v}_{\mathfrak{h}}. \tag{2.2.10}$$

From the definition (2.2.10), we find the following property

$$\sum_{i \in \mathrm{H}} \int m_i f_i \boldsymbol{C}_i d\boldsymbol{C}_i = 0, \tag{2.2.11}$$

thus, the heavy-particle diffusion flux is vanishing.

Similarly, one can rewrite the equation of internal energies (2.1.12) in a nondimensional form, as follows

$$\rho_{\mathfrak{e}} e_{\mathfrak{e}} = \int \frac{1}{2} f_{\mathfrak{e}} \boldsymbol{c}_{\mathfrak{e}} \cdot \boldsymbol{c}_{\mathfrak{e}} d\boldsymbol{c}_{\mathfrak{e}}, \quad \rho_{\mathfrak{h}} e_{\mathfrak{h}} = \sum_{i \in \mathrm{H}} \int \frac{1}{2} m_i f_i \boldsymbol{c}_i \cdot \boldsymbol{c}_i d\boldsymbol{c}_i. \tag{2.2.12}$$

Finally, the mass densities read

$$\rho_{\mathfrak{e}} = \int f_{\mathfrak{e}} d\boldsymbol{c}_{\mathfrak{e}}, \quad \rho_{\mathfrak{h}} = \sum_{i\in \mathrm{H}} \rho_i = \sum_{i\in \mathrm{H}} \int f_i m_i d\boldsymbol{c}_i. \tag{2.2.13}$$

Boltzmann equations

We investigate the Boltzmann equations at time t^0 and length L^0. In this framework, we rewrite (2.1.13) in a nondimensional form, for electrons and heavy particles respectively, as follows

$$\partial_t f_{\mathfrak{e}} + \frac{1}{\varepsilon} \boldsymbol{c}_{\mathfrak{e}} \cdot \boldsymbol{\partial}_{\boldsymbol{x}} f_{\mathfrak{e}} + \frac{M_{\mathfrak{h}} \beta_{\mathfrak{e}}^0}{\varepsilon^2} q_{\mathfrak{e}} \boldsymbol{c}_{\mathfrak{e}} \wedge \boldsymbol{B} \cdot \boldsymbol{\partial}_{\boldsymbol{c}_{\mathfrak{e}}} f_{\mathfrak{e}} + \frac{1}{\varepsilon} q_{\mathfrak{e}} \boldsymbol{E} \cdot \boldsymbol{\partial}_{\boldsymbol{c}_{\mathfrak{e}}} f_{\mathfrak{e}} = \frac{M_{\mathfrak{h}}}{\varepsilon^2} \mathcal{J}_{\mathfrak{e}} \tag{2.2.14}$$

$$\partial_t f_i + \boldsymbol{c}_i \cdot \boldsymbol{\partial}_{\boldsymbol{x}} f_i + M_{\mathfrak{h}} \beta_{\mathfrak{e}}^0 \left(\frac{q_i}{m_i} \right) \boldsymbol{c}_{\mathfrak{e}} \wedge \boldsymbol{B} \cdot \boldsymbol{\partial}_{\boldsymbol{c}_i} f_i + \left(\frac{q_i}{m_i} \right) \boldsymbol{E} \cdot \boldsymbol{\partial}_{\boldsymbol{c}_i} f_i = \frac{M_{\mathfrak{h}}}{\varepsilon} \mathcal{J}_i, \quad i \in \mathrm{H} \tag{2.2.15}$$

where the collision operators read

$$\mathcal{J}_{\mathfrak{e}} = \mathcal{J}_{\mathfrak{e}\mathfrak{e}} (f_{\mathfrak{e}}, f_{\mathfrak{e}}) + \sum_{j\in \mathrm{H}} \mathcal{J}_{\mathfrak{e}j} \left(f_{\mathfrak{e}}, f_j \right) \tag{2.2.16}$$

$$\mathcal{J}_i = \frac{1}{\varepsilon} \mathcal{J}_{i\mathfrak{e}} (f_i, f_{\mathfrak{e}}) + \sum_{j\in \mathrm{H}} \mathcal{J}_{ij} \left(f_i, f_j \right), \quad i \in \mathrm{H}. \tag{2.2.17}$$

The nondimensional Boltzmann equations (2.2.14) and (2.2.15) can be rewritten in the heavy-particle reference frame, in terms of peculiar velocities, as follows

$$\begin{aligned} \partial_t f_{\mathfrak{e}} + \frac{1}{\varepsilon M_{\mathfrak{h}}} (\boldsymbol{C}_{\mathfrak{e}} + \varepsilon M_{\mathfrak{h}} \boldsymbol{v}_{\mathfrak{h}}) \cdot \boldsymbol{\partial}_{\boldsymbol{x}} f_{\mathfrak{e}} + \varepsilon^{-(1+b)} q_{\mathfrak{e}} \Big[(\boldsymbol{C}_{\mathfrak{e}} + \varepsilon M_{\mathfrak{h}} \boldsymbol{v}_{\mathfrak{h}}) \wedge \boldsymbol{B} \Big] \cdot \partial_{\boldsymbol{C}_{\mathfrak{e}}} f_{\mathfrak{e}} \\ + \left(\frac{1}{\varepsilon M_{\mathfrak{h}}} q_{\mathfrak{e}} \boldsymbol{E} - \varepsilon M_{\mathfrak{h}} \frac{D\boldsymbol{v}_{\mathfrak{h}}}{Dt} \right) \cdot \partial_{\boldsymbol{C}_{\mathfrak{e}}} f_{\mathfrak{e}} - (\partial_{\boldsymbol{C}_{\mathfrak{e}}} f_{\mathfrak{e}} \otimes \boldsymbol{C}_{\mathfrak{e}}) : \boldsymbol{\partial}_{\boldsymbol{x}} \boldsymbol{v}_{\mathfrak{h}} = \frac{1}{\varepsilon^2} \mathcal{J}_{\mathfrak{e}}. \end{aligned} \tag{$\mathrm{B}_{\mathfrak{e}}$}$$

$$\begin{aligned} \partial_t f_i + \frac{1}{M_{\mathfrak{h}}} (\boldsymbol{C}_i + M_{\mathfrak{h}} \boldsymbol{v}_{\mathfrak{h}}) \cdot \boldsymbol{\partial}_{\boldsymbol{x}} f_i + \varepsilon^{1-b} q_i \Big[(\boldsymbol{C}_i + M_{\mathfrak{h}} \boldsymbol{v}_{\mathfrak{h}}) \wedge \boldsymbol{B} \Big] \cdot \partial_{\boldsymbol{C}_i} f_i \\ + \left(\frac{1}{M_{\mathfrak{h}}} \frac{q_i}{m_i} \boldsymbol{E} - M_{\mathfrak{h}} \frac{D\boldsymbol{v}_{\mathfrak{h}}}{Dt} \right) \cdot \partial_{\boldsymbol{C}_i} f_i - (\partial_{\boldsymbol{C}_i} f_i \otimes \boldsymbol{C}_i) : \boldsymbol{\partial}_{\boldsymbol{x}} \boldsymbol{v}_{\mathfrak{h}} = \frac{1}{\varepsilon} \mathcal{J}_i, \quad i \in \mathrm{H}. \end{aligned} \tag{$\mathrm{B}_{i\in \mathrm{H}}$}$$

We point out that in (2.2.14) or ($\mathrm{B}_{\mathfrak{e}}$), Boltzmann's equation for electrons is showing an original scaling. Indeed, if we remove the terms related to the electromagnetic forces, the electrons are showing a scaling similar to a kinetic equation for neutral gases in the low Mach number regime, which leads to a parabolic system of equations. On the contrary, in (2.2.15) or ($\mathrm{B}_{i\in \mathrm{H}}$), if we remove the terms related to the electro-magnetic forces, each heavy particles are showing a scaling similar to a classical kinetic equation for neutral gases in the compressible regime, as shown by Bardos et al. (1991), which leads to a hyperbolic macroscopic equation.

As proposed by Braginskii (1965), no dimensional analysis is performed on the Boltzmann equations for electrons and heavy particles respectively. Therefore, Boltzmann equations are showing identical scaling. In the work performed by S. Benilov (1997, 1996), the multi-fluid equations are derived from the kinetic theory. No dimensional analysis are performed in the Boltzmann equations for each particles, and, the distribution functions are expanded in terms of Knudsen numbers, considered as small. This approach is assumed to be valid in situations where the collisions between particles are frequent but the coupling between the different species is weak.

In such context, it is necessary to identify the resulting system of macroscopic equations related to our proposed parabolic-hyperbolic scaling.

2.2.3 Nondimensional Maxwell equations

Similarly as Section 2.2.2, we use the reference quantities introduced in the previous sections, and express the Maxwell equations (Mx*) in a nondimensional form. The system reads

$$\boldsymbol{\partial_x}\cdot\boldsymbol{E} = \varepsilon_{\lambda_D} nq, \tag{2.2.18}$$

$$\boldsymbol{\partial_x}\cdot\boldsymbol{B} = 0, \tag{2.2.19}$$

$$\partial_t \boldsymbol{B} = -\left[\frac{1}{M_{\mathfrak{h}}^2\beta_{\mathfrak{e}}^0}\right]\boldsymbol{\partial_x}\wedge\boldsymbol{E}, \tag{2.2.20}$$

$$\left[\left(\frac{v^0}{c}\right)^2\frac{1}{M_{\mathfrak{h}}^2\beta_{\mathfrak{e}}^0}\right]\partial_t\boldsymbol{E} - \boldsymbol{\partial_x}\wedge\boldsymbol{B} + \left[\left(\frac{v^0}{c}\right)^2\frac{1}{M_{\mathfrak{h}}^2\beta_{\mathfrak{e}}^0}\frac{4\pi}{\varepsilon_{\lambda_D}}\right]\mathbf{I} = 0, \tag{2.2.21}$$

where nq denotes for the nondimensional global charge. Considering a strongly magnetized case, we have $b = 1$, thus, $\beta_{\mathfrak{e}}^0 = 1$, and the product $M_{\mathfrak{h}}^2\beta_{\mathfrak{e}}^0$ is of order 1. In (2.2.21), several parameters are introduced such as the ratio v^0/c and $1/\varepsilon_{\lambda_D}$. These parameters have to be consistent with the scaling introduced in the previous sections, *i.e.*, with the ε parameter.

In the context of solar physics application, we assume that characteristic scales are much larger than the Debye length, therefore, ε_{λ_D} has to be a small parameter. In addition, the second and third term of (2.2.21) has to be in the same order of magnitude to allow phenomena such as reconnection events.

Therefore, considering the Gauss law in (2.2.18) and Ampere's law in (2.2.21), the only scaling which allow both a non null total current and electroneutrality is to choose a scaling such as

$$\varepsilon_{\lambda_D} = O(\varepsilon), \quad \text{and} \quad \left(\frac{v^0}{c}\right)^2 = O(\varepsilon)$$

In this context, at order ε, the set of Maxwell's equations read

$$\boldsymbol{\partial_x}\cdot\boldsymbol{E} = \varepsilon nq, \quad \boldsymbol{\partial_x}\cdot\boldsymbol{B} = 0, \quad \partial_t\boldsymbol{B} = -\frac{1}{M_{\mathfrak{h}}^2\beta_{\mathfrak{e}}^0}\boldsymbol{\partial_x}\wedge\boldsymbol{E}, \quad \varepsilon\frac{1}{M_{\mathfrak{h}}^2\beta_{\mathfrak{e}}^0}\partial_t\boldsymbol{E} - \boldsymbol{\partial_x}\wedge\boldsymbol{B} + \frac{1}{M_{\mathfrak{h}}^2\beta_{\mathfrak{e}}^0}4\pi\mathbf{I} = 0. \quad (Mx^{\varepsilon})$$

With the proposed scaling, the total current is non null and the electroneutrality is obtained at the order ε^0, in the strongly magnetized case. Finally, at order ε^0, the set of Maxwell's equations can be written as

$$\boldsymbol{\partial_x}\cdot\boldsymbol{E} = 0, \quad \boldsymbol{\partial_x}\cdot\boldsymbol{B} = 0, \quad \partial_t\boldsymbol{B} = -\frac{1}{M_{\mathfrak{h}}^2\beta_{\mathfrak{e}}^0}\boldsymbol{\partial_x}\wedge\boldsymbol{E}, \quad \boldsymbol{\partial_x}\wedge\boldsymbol{B} = \frac{4\pi}{M_{\mathfrak{h}}^2\beta_{\mathfrak{e}}^0}\mathbf{I}. \qquad (Mx^{\varepsilon=0})$$

2.2.4 Nondimensional collisional invariants and crossed collision operators

As shown previously, the proposed scaling has consequences on the electron heavy-particle collision dynamics, leading to a dependence of the peculiar velocities on the ε parameter. The crossed collision-operator $\mathcal{J}_{i\mathfrak{e}}(f_i, f_{\mathfrak{e}})$ and $\mathcal{J}_{\mathfrak{e}i}(f_{\mathfrak{e}}, f_i)$ can be expanded in terms of the ε parameter, as follows,

$$\mathcal{J}_{i\mathfrak{e}}(f_i, f_{\mathfrak{e}}) = \varepsilon\mathcal{J}_{i\mathfrak{e}}^1(f_i, f_{\mathfrak{e}}) + \varepsilon^2\mathcal{J}_{i\mathfrak{e}}^2(f_i, f_{\mathfrak{e}}) + \varepsilon^3\mathcal{J}_{i\mathfrak{e}}^3(f_i, f_{\mathfrak{e}}) + O\left(\varepsilon^4\right), \qquad i \in \mathrm{H}, \quad (2.2.22)$$

$$\mathcal{J}_{\mathfrak{e}i}(f_{\mathfrak{e}}, f_i) = \mathcal{J}_{\mathfrak{e}i}^0(f_{\mathfrak{e}}, f_i) + \varepsilon\mathcal{J}_{\mathfrak{e}i}^1(f_{\mathfrak{e}}, f_i) + \varepsilon^2\mathcal{J}_{\mathfrak{e}i}^2(f_{\mathfrak{e}}, f_i) + \varepsilon^3\mathcal{J}_{\mathfrak{e}i}^3(f_{\mathfrak{e}}, f_i) + O\left(\varepsilon^4\right), \qquad i \in \mathrm{H}. \quad (2.2.23)$$

For our understanding, we do not provide the definition of each terms from (2.2.22) and (2.2.23), they can be found in the work of Graille et al. (2009).

Similarly as in Section 2.1.4, we define two spaces of collisional invariants associated to our scaling. First, we have the electron collisional invariants space $\mathcal{I}_{\mathfrak{e}}$ which reads

$$\mathcal{I}_{\mathfrak{e}} = \begin{cases} \psi_{\mathfrak{e}}^1 = 1 \\ \psi_{\mathfrak{e}}^2 = \dfrac{1}{2}\boldsymbol{C}_{\mathfrak{e}}\cdot\boldsymbol{C}_{\mathfrak{e}}. \end{cases} \qquad (2.2.24)$$

Then, we have the heavy-particle collisional invariants space $\mathcal{I}_{\mathfrak{h}}$ defined as

$$\mathcal{I}_{\mathfrak{h}} = \begin{cases} \psi_{\mathfrak{h}}^l = (m_i\delta_{il})_{i\in\mathrm{H}}, \quad l \in \mathrm{H} \\ \psi_{\mathfrak{h}}^{n^{\mathrm{H}}+\nu} = (m_i C_{i,\nu})_{i\in\mathrm{S}}, \quad \nu \in \{x, y, z\}, \\ \psi_{\mathfrak{h}}^{n^{\mathrm{H}}+4} = \left(\dfrac{1}{2}m_i\boldsymbol{C}_i\cdot\boldsymbol{C}_i\right)_{i\in\mathrm{H}}, \end{cases} \qquad (2.2.25)$$

where n^{H} denotes for the cardinality of the set of heavy particles H. As presented in Section 2.1.4, we rewrite the scalar product considering two families in a nondimensional form $\xi = (\xi_i)_{i\in\mathrm{S}}$ and $\zeta = (\zeta_i)_{i\in\mathrm{S}}$. In the following, two separate contributions for each families are considered: $\xi_{\mathfrak{e}}$ for the electrons, and $\xi_{\mathfrak{h}} = (\xi_i)_{i\in\mathrm{H}}$ for the heavy particles. Therefore, the scalar product defined in (2.1.28) is decomposed into a sum of partial scalar products involving several scales, as follows

$$\langle\!\langle \xi, \zeta \rangle\!\rangle = \langle\!\langle \xi_{\mathfrak{e}}, \zeta_{\mathfrak{e}} \rangle\!\rangle_{\mathfrak{e}} + \varepsilon^3\langle\!\langle \xi_{\mathfrak{h}}, \zeta_{\mathfrak{h}} \rangle\!\rangle_{\mathfrak{h}}, \qquad \xi = (\xi_{\mathfrak{e}}, \xi_{\mathfrak{h}}), \ \zeta = (\zeta_{\mathfrak{e}}, \zeta_{\mathfrak{h}}) \qquad (2.2.26)$$

where

$$\langle\!\langle \xi_e, \zeta_e \rangle\!\rangle_e = \int \xi_e \odot \bar{\zeta}_e d\boldsymbol{C}_e, \quad \langle\!\langle \xi_h, \zeta_h \rangle\!\rangle_h = \sum_{j \in \mathrm{H}} \int \xi_j \odot \bar{\zeta}_j d\boldsymbol{C}_j. \tag{2.2.27}$$

We point out the novelty of the nature of electron collisional invariant space $\mathcal{I}_e$ in (2.2.24). Indeed, the vector $\boldsymbol{C}_e$ does not belong to $\mathcal{I}_e$. Graille et al. (2009) has shown that the partial collision operators $\mathcal{J}^0_{ei}(f_e, f_i)$ from (2.2.23) are not orthogonal to the space spanned by the electron momentum $\boldsymbol{C}_e$, *i.e.*,

$$\langle\!\langle \mathcal{J}^0_{ei}(f_e, f_i), \boldsymbol{C}_e \rangle\!\rangle_e \neq 0, \quad i \in \mathrm{H} \tag{2.2.28}$$

thus, $\boldsymbol{C}_e$ is not in the electron collisional invariant space. This property is due to the scaling used in the framework of the multiscale approach.

On the contrary, in Braginskii (1965), the velocity of electrons belong to the electron collisional invariant, since no multiscale analysis has been performed. The structure of the collisional invariants are identical between electrons and ions. In addition, the partial collision operator called "C_{ei}" is expanded in terms of ratio m_e/m_i and all the terms beyond the first term of the expansion are eliminated. This simplification allows to obtain separate transport equations for the electron and ions with temperatures T_e and T_h, and a decoupling between the electron and ion kinetic equations.

In summary, the proposed multiscale analysis is performed at three levels:

1. **In the kinetic equations** ($\mathrm{B}_{i\in\mathrm{H}}$) and ($\mathrm{B}_e$), where a different scaling is used for electrons and heavy particles.

2. **In the collision invariants** (2.2.25) and (2.2.24). The space spanned by the electron momentum appears not to be in the space of collisional invariants of the electrons $\mathcal{I}_e$. Since the collisional invariants allow to obtain macroscopic equation, this property impacts the structure of the momentum equation for electrons.

3. **In the crossed collision operators** $\mathcal{J}_{ei}(f_e, f_i)$ and $\mathcal{J}_{ie}(f_i, f_e)$ in (2.2.23) and (2.2.22), where the latter can be expanded in terms of the ε parameter.

In addition, the scaling used for the set of Maxwell equations is consistent with the scaling used by Graille et al. (2009), based on the ε parameter. In the next section, we perform a Chapman-Enskog expansion on the nondimensional Boltzmann equations ($\mathrm{B}_{i\in\mathrm{H}}$) and ($\mathrm{B}_e$). We want to make use of the proposed scaling to derive the corresponding set of macroscopic equations.

2.3 Chapman-Enskog expansion on nondimensional Boltzmann equations

In this section, a generalized Chapman-Enskog method is performed. The distribution functions are assumed to be perturbed Maxwellians, at different temperatures T_e and T_h for electrons and heavy particles, and the perturbations are expanded in successive orders of ε. The macroscopic

equations are retrieved by taking moments of the nondimensional Boltzmann equations presented in the previous section. We will see that the asymptotic analysis of the normalized Boltzmann equations exhibits several processes occurring at different time-scales. We also provide a comparison between this approach, and the one provided by Braginskii (1965) at the kinetic level. In the classical approach of Braginskii (1965), no multiscale analysis is performed, and the scaling used for the electrons is identical to the one used for heavy-particles. Therefore, the comparison between our approach and the classical approach of Braginskii (1965) will exhibit the impact of the multiscale analysis on the set of governing equations obtained.

2.3.1 Chapman-Enskog method

An Enskog expansion is used in order to obtain an approximate solution to the nondimensional Boltzmann equations in ($\mathrm{B}_{i\in\mathrm{H}}$) and ($\mathrm{B}_{\mathfrak{e}}$). The solutions of each equations, which represent the dynamics of the electrons and heavy particles respectively, are assumed to be perturbations of their corresponding equilibrium state defined as $f_{\mathfrak{e}}^0$ and f_i^0, $i \in \mathrm{H}$. Therefore, we assume that the macroscopic properties defined in (2.2.12), (2.2.9) and (2.2.13) are based on the zero-order distribution functions only $f_{\mathfrak{e}}^0$ and f_i^0, *i.e.*,

$$\langle\!\langle f_{\mathfrak{e}}, \psi_{\mathfrak{e}}^l \rangle\!\rangle_{\mathfrak{e}} = \langle\!\langle f_{\mathfrak{e}}^0, \psi_{\mathfrak{e}}^l \rangle\!\rangle_{\mathfrak{e}}, \quad l \in \{1, 2\} \tag{2.3.1}$$

$$\langle\!\langle f_i, \psi_{\mathfrak{h}}^l \rangle\!\rangle_{\mathfrak{h}} = \langle\!\langle f_i^0, \psi_{\mathfrak{h}}^l \rangle\!\rangle_{\mathfrak{h}}, \quad l \in \{1, n^{\mathrm{H}} + 4\} \tag{2.3.2}$$

because the gas state is considered to be not too far from equilibrium state. We expand the distribution functions $f_{\mathfrak{e}}$ and f_i in terms of ε:

$$f_{\mathfrak{e}} = f_{\mathfrak{e}}^0 \left(1 + \varepsilon\phi_{\mathfrak{e}} + \varepsilon^2\phi_{\mathfrak{e}}^2 + \varepsilon^3\phi_{\mathfrak{e}}^3\right) + O\left(\varepsilon^4\right) \tag{2.3.3}$$

$$f_i = f_i^0 \left(1 + \varepsilon\phi_i + \varepsilon^2\phi_i^2\right) + O\left(\varepsilon^3\right), \quad i \in \mathrm{H} \tag{2.3.4}$$

First, we inject the expression of (2.3.3) into the nondimensional Boltzmann equations for the electrons ($\mathrm{B}_{\mathfrak{e}}$). This leads to a new expression of the Boltzmann equation for electrons expanded in terms of ε parameter:

$$\varepsilon^{-2}\mathcal{D}_{\mathfrak{e}}^{-2}\left(f_{\mathfrak{e}}^0\right) + \varepsilon^{-1}\mathcal{D}_{\mathfrak{e}}^{-1}\left(f_{\mathfrak{e}}^0, \phi_{\mathfrak{e}}\right) + \mathcal{D}_{\mathfrak{e}}^{0}\left(f_{\mathfrak{e}}^0, \phi_{\mathfrak{e}}, \phi_{\mathfrak{e}}^2\right) + \varepsilon\mathcal{D}_{\mathfrak{e}}^{1}\left(f_{\mathfrak{e}}^0, \phi_{\mathfrak{e}}, \phi_{\mathfrak{e}}^2, \phi_{\mathfrak{e}}^3\right) = \mathcal{J}_{\mathfrak{e}}^{-2} + \mathcal{J}_{\mathfrak{e}}^{-1} + \mathcal{J}_{\mathfrak{e}}^{0} + \varepsilon\mathcal{J}_{\mathfrak{e}}^{1} + O\left(\varepsilon^2\right), \quad (\mathrm{B}_{\mathfrak{e}}^{\varepsilon})$$

where the electron streaming and collision operators at successive orders are defined in Appendix A.

Then, similarly, we inject (2.3.3) into the nondimensional Boltzmann equations for the heavy-particles ($\mathrm{B}_{i\in\mathrm{H}}$). After some algebra, we obtain

$$\mathcal{D}_i^0\left(f_i^0\right) + \varepsilon\mathcal{D}_i^1\left(f_{\mathfrak{e}}^0, \phi_i\right) = \varepsilon^{-1}\mathcal{J}_i^{-1} + \mathcal{J}_i^0 + \varepsilon\mathcal{J}_i^1 + O\left(\varepsilon^2\right), \quad i \in \mathrm{H} \tag{$\mathrm{B}_{i\in\mathrm{H}}^{\varepsilon}$}$$

where the heavy-particle streaming and collision operators at successive orders are defined in Ap-

pendix A.

By taking moments of (B^{ε}_{e}) and ($B^{\varepsilon}_{i\in H}$), the macroscopic equations are obtained. The asymptotic analysis leads to a hierarchy of time scales showing several processes that are presented in Table 2.3. At each order investigated, an equation of the perturbative functions ϕ_e and ϕ_i, $i \in H$ is obtained, which gives the closure of the transport fluxes for electrons and heavy particles at the corresponding next order. They are presented in Table 4.1.

Table 2.3: Macroscopic equations and related hierarchy of time scales from Graille et al. (2009)

Order	**Time**	**Heavy particles**	**Electrons**
ε^{-2}	t^0_e		Thermalization T_e
ε^{-1}	t^0_h	Thermalization T_h	
ε^{0}	t^0	Euler Eqs.: ($M^{\varepsilon=0}_h$)	0^{th}-order drift-diffusion Eqs.: ($M^{\varepsilon=0}_e$)
ε	t^0/ε	Navier-Stokes Eqs.: ($M^{\varepsilon=1}_h$)	1^{st}-order drift-diffusion Eqs.: ($M^{\varepsilon=1}_e$)

Table 2.4: Transport fluxes and related equations of perturbative functions

Order	**Heavy particles**	**Electrons**
ε^{-2}		Expression of f^0_e
ε^{-1}	Expression of f^0_i, $i \in H$	Equation for ϕ_e $\rightarrow$ Electron transport fluxes at order ε^0
ε^{0}	Equation for ϕ_i, $i \in H$ $\rightarrow$ HP transport fluxes at order ε	Equation for ϕ^2_e $\rightarrow$ Electron transport fluxes at order ε

Firstly, at the time scale t^0_e, the electron population thermalizes at the temperature T_e. We will see that the electron distribution function is a Maxwellian, *i.e.*, $f^0_e = f^M_e$. It is obtained by solving the electron Boltzmann's equation at the order ε^{-2}. Similarly, at order ε^{-1}, which corresponds to the time scale t^0_h, the heavy particle population thermalizes at the temperature T_h, *i.e.*, $f^0_i = f^M_i, i \in H$. At the zeroth order ε^0, which corresponds to the convective time scale, Euler's equations for heavy particle and first-order drift diffusion for electrons are obtained. Finally, at the last order ε investigated, corresponding to the diffusive time scale, we obtain the Navier-Stokes equations for heavy particle and second-order drift diffusion equations for electrons.

In the derivation of Braginskii (1965), the expansion of the distribution functions for electrons and heavy-particles are performed up to the first order only. Then, by taking moments of the Boltzmann equations for electrons and heavy-particles, the macroscopic equations obtained differ from those obtained with our approach. Indeed, at the last order investigated, the Navier-Stokes equations both for electrons and heavy particles are obtained.

2.3.2 Order ε^{-2} at time $t_{\mathfrak{e}}^0$

Here, we investigate the Boltzmann equation of electrons in ($\mathrm{B}_{\mathfrak{e}}^{\varepsilon}$) and ($\mathrm{B}_{i\in\mathrm{H}}^{\varepsilon}$), at order ε^{-2}, corresponding to the kinetic timescale $t_{\mathfrak{e}}^0$. For further details concerning the resolution of this equation, we refer to the proposition 4.1. of Graille et al. (2009).

Heavy-particle

At order ε^{-2}, the heavy-particles do not show any properties. They are in a kinetic regime.

Electrons: Maxwell-Boltzmann distribution function at temperature $T_{\mathfrak{e}}$

At this order, ($\mathrm{B}_{\mathfrak{e}}^{\varepsilon}$) reads

$$\mathcal{D}_{\mathfrak{e}}^{-2}\left(f_{\mathfrak{e}}^0\right) = \mathcal{J}_{\mathfrak{e}}^{-2} = \mathcal{J}_{\mathfrak{e}\mathfrak{e}}\left(f_{\mathfrak{e}}^0, f_{\mathfrak{e}}^0\right) + \sum_{j\in\mathrm{H}} \mathcal{J}_{\mathfrak{e}j}^0\left(f_{\mathfrak{e}}^0, f_j^{\,0}\right) = 0. \tag{2.3.5}$$

As presented in Section 2.1.4, a H-theorem can be established in the heavy particle reference frame for the zeroth-order distribution function for electrons. The entropy production rate is defined in the proof of proposition 4.1. of Graille et al. (2009). At this order, it is found that the electrons are shown to thermalize in the heavy-particle reference frame to an equilibrium state describe by a Maxwell-Boltzmann distribution function at temperature $T_{\mathfrak{e}}$, *i.e.*,

$$f_{\mathfrak{e}}^0 = f_{\mathfrak{e}}^M = n_{\mathfrak{e}}\left(\frac{1}{2\pi T_{\mathfrak{e}}}\right)^{\frac{3}{2}} \exp\left(-\frac{1}{2T_{\mathfrak{e}}}\boldsymbol{C}_{\mathfrak{e}}\cdot\boldsymbol{C}_{\mathfrak{e}}\right). \tag{2.3.6}$$

2.3.3 Order ε^{-1} at time $t_{\mathfrak{h}}^0$

We focus on ($\mathrm{B}_{i\in\mathrm{H}}^{\varepsilon}$) and ($\mathrm{B}_{\mathfrak{e}}^{\varepsilon}$), at order ε^{-1}, corresponding to the kinetic timescale $t_{\mathfrak{h}}^0$. We obtain the Maxwell-Boltzmann distribution function at temperature $T_{\mathfrak{h}}$ for the heavy-particles and an equation for $\phi_{\mathfrak{e}}$. For further details, we refer to the proposition 4.2. and definition 4.1. of Graille et al. (2009).

Heavy-particle: Maxwell-Boltzmann distribution function at temperature $T_{\mathfrak{h}}$

At this order, ($\mathrm{B}_{i\in\mathrm{H}}^{\varepsilon}$) reads

$$\mathcal{J}_i^{-1} = 0, \quad i \in \mathrm{H}. \tag{2.3.7}$$

Using the heavy-particle entropy production rate defined in the proof of proposition 4.2. of Graille et al. (2009), a H-theorem can be established in the heavy-particle reference frame for the zero-order distribution function for heavy particles. Thus, the heavy-particles are shown to thermalize

towards an equilibrium state described by a Maxwell-Boltzmann distribution function at temperature $T_\mathfrak{h}$, which reads

$$f_i^0 = f_i^M = n_i \left(\frac{m_i}{2\pi T_\mathfrak{h}} \right)^{\frac{3}{2}} \exp\left(-\frac{m_i}{2T_\mathfrak{h}} \boldsymbol{C}_i \cdot \boldsymbol{C}_i \right), \quad i \in \mathrm{H}. \tag{2.3.8}$$

Electrons: equation for $\phi_\mathfrak{e}$

At order ε^{-1}, ($\mathrm{B}_\mathfrak{e}^\varepsilon$) reads

$$f_\mathfrak{e}^0 \mathcal{F}_\mathfrak{e}(\phi_\mathfrak{e}) + \delta_{b1} q_\mathfrak{e} \boldsymbol{\partial}_{\boldsymbol{C}_\mathfrak{e}} \left(f_\mathfrak{e}^0 \phi_\mathfrak{e} \right) \cdot \boldsymbol{C}_\mathfrak{e} \wedge \boldsymbol{B} = -\mathcal{D}_\mathfrak{e}^{-1} \left(f_\mathfrak{e}^0 \right). \tag{2.3.9}$$

where the linearized collision operator for electrons $\mathcal{F}_\mathfrak{e} = \mathcal{F}_\mathfrak{e}(\phi_\mathfrak{e})$ is defined as

$$\mathcal{F}_\mathfrak{e}(\phi_\mathfrak{e}) = -\frac{1}{f_\mathfrak{e}^0} \left[\mathcal{J}_{\mathfrak{e}\mathfrak{e}} \left(f_\mathfrak{e}^0 \phi_\mathfrak{e}, f_\mathfrak{e}^0 \right) + \mathcal{J}_{\mathfrak{e}\mathfrak{e}} \left(f_\mathfrak{e}^0, f_\mathfrak{e}^0 \phi_\mathfrak{e} \right) + \sum_{j \in \mathrm{H}} \mathcal{J}_{\mathfrak{e}j} \left(f_\mathfrak{e}^0 \phi_\mathfrak{e}, f_j^0 \right) \right], \tag{2.3.10}$$

where $f_\mathfrak{e}^0$ is the Maxwell-Boltzmann distribution function defined in (2.3.6). Such operator is introduced, since it shows relevant properties for deriving macroscopic equations for electrons. Indeed, in Graille et al. (2009), it is proved that the image of the operator $\mathcal{F}_\mathfrak{e}$ is in the space of the scalar electron collisional invariants $\mathcal{I}_\mathfrak{e}$ for the scalar product $\langle\!\langle \cdot, \cdot \rangle\!\rangle_\mathfrak{e}$, *i.e.*,

$$\langle\!\langle f_\mathfrak{e}^0 \mathcal{F}_\mathfrak{e}(\phi_\mathfrak{e}), \psi_\mathfrak{e}^l \rangle\!\rangle_\mathfrak{e} = 0, \quad l \in \{1, 2\}. \tag{2.3.11}$$

We underline that Graille et al. (2009) has shown that the terms $\boldsymbol{\partial}_{\boldsymbol{C}_\mathfrak{e}} \left(f_\mathfrak{e}^0 \phi_\mathfrak{e} \right) \cdot \boldsymbol{C}_\mathfrak{e} \wedge \boldsymbol{B}$ and $\mathcal{D}_\mathfrak{e}^{-1} \left(f_\mathfrak{e}^0 \right)$ of (2.3.9) are orthogonal to the kernel of $\mathcal{F}_\mathfrak{e}$, for the scalar product $\langle\!\langle \cdot, \cdot \rangle\!\rangle_\mathfrak{e}$. Thus, at order ε^{-1}, no macroscopic equations are obtained for the electrons.

Finally, an original property of the expansion, associated with the absence of a momentum constraint in (2.3.1), can be obtained. This property will lead to an electron momentum relation, that will be described with further details in Section 2.3.6.

2.3.4 Order ε^0 at time t^0

We investigate ($\mathrm{B}_{i\in\mathrm{H}}^\varepsilon$) and ($\mathrm{B}_\mathfrak{e}^\varepsilon$) at order ε^0 corresponding to the macroscopic time scale t^0, which leads to a Euler system of equations for heavy-particles and zeroth-order drift diffusion equations for electrons respectively. The set of equations obtained for the heavy particles and electrons are shown to be identical to the set obtained by Lucquin-Desreux (1998). For more details about the derivation of the equations, we refer the reader to the proposition 4.4. and proposition 4.5. of Graille et al. (2009).

Heavy-particle: equation for $\phi_{\mathfrak{h}}$ and heavy-particle Euler equations

At order ε^0, ($\mathrm{B}^{\varepsilon}_{i\in\mathrm{H}}$) reads

$$f_i^0 \mathcal{F}_i(\phi_{\mathfrak{h}}) = -\mathcal{D}_i^0\left(f_i^0\right) + \mathcal{J}_{i\mathfrak{e}}^1\left(f_i^0, f_{\mathfrak{e}}^0\phi_{\mathfrak{e}}\right) + \mathcal{J}_{i\mathfrak{e}}^2\left(f_i^0, f_{\mathfrak{e}}^0\right), \quad i \in \mathrm{H}. \tag{2.3.12}$$

where f_i^0, $i \in \mathrm{H}$ is given by the expression of the Maxwellian distribution in (2.3.8) and the linearized collision operator for heavy particles $\mathcal{F}_i$ is defined as

$$\mathcal{F}_i(\phi_{\mathfrak{h}}) = -\frac{1}{f_i^0}\sum_{j\in\mathrm{H}}\left[\mathcal{J}_{ij}\left(f_i^0\phi_i, f_j^0\right) + \mathcal{J}_{ij}\left(f_i^0, f_j^0\phi_j\right)\right], \quad i \in \mathrm{H}, \tag{2.3.13}$$

Such operator is introduced, since it shows relevant properties for deriving macroscopic equations for heavy-particles. The image of the operator $\mathcal{F}_{\mathfrak{h}} = (\mathcal{F}_i)_{i\in\mathrm{H}}$ is shown to be in the space of the scalar collisional invariants $\mathcal{I}_{\mathfrak{h}}$ for the scalar product $\langle\!\langle\cdot,\cdot\rangle\!\rangle_{\mathfrak{h}}$, *i.e.*,

$$\langle\!\langle f_i^0 \mathcal{F}_i(\phi_{\mathfrak{h}}), \psi_{\mathfrak{h}}^l\rangle\!\rangle_{\mathfrak{h}} = 0, \quad i \in \mathrm{H}, \quad l \in \{1, ..., n^{\mathrm{H}} + 4\}. \tag{2.3.14}$$

Governing equations: We project (2.3.12) onto the collisional invariants of heavy particles $\psi_{\mathfrak{h}}^l$, $l \in \{1, ..., n^{\mathrm{H}} + 4\}$. After some algebra, we obtain the zeroth-order conservation equations of heavy-particle mass, momentum and internal energy

$$\begin{cases} \partial_t \rho_i + \boldsymbol{\partial_x}\cdot(\rho_i \boldsymbol{v}_{\mathfrak{h}}) = 0, \quad i \in \mathrm{H}, \\ \partial_t(\rho_{\mathfrak{h}}\boldsymbol{v}_{\mathfrak{h}}) + \boldsymbol{\partial_x}\cdot\left(\rho_{\mathfrak{h}}\boldsymbol{v}_{\mathfrak{h}}\otimes\boldsymbol{v}_{\mathfrak{h}} + \dfrac{1}{M_{\mathfrak{h}}^2}p\mathbb{I}\right) = \dfrac{1}{M_{\mathfrak{h}}^2}nq\boldsymbol{E} + \delta_{b1}\mathbf{I}_0\wedge\boldsymbol{B}, \\ \partial_t(\rho_{\mathfrak{h}}e_{\mathfrak{h}}) + \boldsymbol{\partial_x}\cdot(\rho_{\mathfrak{h}}e_{\mathfrak{h}}\boldsymbol{v}_{\mathfrak{h}}) = -p_{\mathfrak{h}}\boldsymbol{\partial_x}\cdot\boldsymbol{v}_{\mathfrak{h}} + \Delta E_{\mathfrak{h}}^{(0)}, \end{cases} \tag{$M_{\mathfrak{h}}^{\varepsilon=0}$}$$

where $p = p_{\mathfrak{e}} + \sum_{i\in\mathrm{H}} p_i = p_{\mathfrak{e}} + p_{\mathfrak{h}}$ is the total pressure, $p_{\mathfrak{e}}$,p_i and $p_{\mathfrak{h}}$ are the pressure of electrons, the partial pressure of each heavy particle i and the total pressure of heavy particle respectively, nq is the global charge, δ_{b1} is the Kronecker symbol related to the parameter b, $\mathbf{I}_0$ is the total current density at order ε^0, and $\Delta E_{\mathfrak{h}}^{(0)}$ is the energy transferred from heavy particles to electrons at order ε^0.

Transport fluxes: The pressure $p_{\mathfrak{e}}$, $p_{\mathfrak{h}}$ and p_i, $i \in \mathrm{H}$ are defined from the nondimensional thermodynamic law as

$$p_{\mathfrak{e}} = n_{\mathfrak{e}}T_{\mathfrak{e}}, \quad p_{\mathfrak{h}} = n_{\mathfrak{h}}T_{\mathfrak{h}}, \quad p_i = n_i T_{\mathfrak{h}}, \quad i \in \mathrm{H}. \tag{2.3.15}$$

Then, the global charge is defined as

$$nq = n_{\mathfrak{e}}q_{\mathfrak{e}} + \sum_{i\in\mathrm{H}} n_i q_i = n_{\mathfrak{e}}q_{\mathfrak{e}} + n_{\mathfrak{h}}q_{\mathfrak{h}} \tag{2.3.16}$$

Then, the total current density $\mathbf{I}_0$ at order ε^0 is defined as

$$\mathbf{I}_0 = nq\boldsymbol{v}_\mathfrak{h} + \frac{1}{M_\mathfrak{h}} n_\mathfrak{e} q_\mathfrak{e} \boldsymbol{V}_\mathfrak{e} = nq\boldsymbol{v}_\mathfrak{h} + \frac{1}{M_\mathfrak{h}} \boldsymbol{J}_\mathfrak{e}, \tag{2.3.17}$$

where $\boldsymbol{J}_\mathfrak{e} = n_\mathfrak{e} q_\mathfrak{e} \boldsymbol{V}_\mathfrak{e}$ is conduction current density of the electron in the heavy particle reference frame, and $\boldsymbol{V}_\mathfrak{e}$ is the electron diffusion velocity at order ε^0 in the heavy particle reference frame. The electron diffusion velocity is defined as

$$\boldsymbol{V}_\mathfrak{e} = \frac{1}{n_\mathfrak{e}} \int \boldsymbol{C}_\mathfrak{e} f_\mathfrak{e}^0 \phi_\mathfrak{e} d\boldsymbol{C}_\mathfrak{e}. \tag{2.3.18}$$

Finally, the energy transferred from heavy particles to electrons from elastic collisions at order ε^0 reads

$$\Delta E_\mathfrak{h}^{(0)} = \frac{\frac{3}{2} n_\mathfrak{e} \left(T_\mathfrak{e} - T_\mathfrak{h}\right)}{\tau_{\mathfrak{h}\mathfrak{e}}}, \quad \frac{1}{\tau_{\mathfrak{h}\mathfrak{e}}} = \nu_{\mathfrak{h}\mathfrak{e}} = \sum_{j \in \mathrm{H}} \frac{2n_j}{3n_\mathfrak{e} m_j} \nu_{j\mathfrak{e}} \tag{2.3.19}$$

where $\tau_{\mathfrak{h}\mathfrak{e}}$ and $\nu_{\mathfrak{h}\mathfrak{e}}$ are the average collision time and frequency between electron and heavy particles, and $\nu_{j\mathfrak{e}}$ is the collision frequency between particle j and electron.

Electrons: equation for $\phi_\mathfrak{e}^2$ and zeroth-order electron drift diffusion equations

At order ε^0, ($\mathrm{B}_\mathfrak{e}^\varepsilon$) reads

$$\begin{aligned} f_\mathfrak{e}^0 \mathcal{F}_\mathfrak{e}\left(\phi_\mathfrak{e}^2\right) + \delta_{b1} q_\mathfrak{e} \boldsymbol{\partial}_{\boldsymbol{C}_\mathfrak{e}} \left(f_\mathfrak{e}^0 \phi_\mathfrak{e}^2\right) \cdot \boldsymbol{C}_\mathfrak{e} \wedge \boldsymbol{B} = & -\mathcal{D}_\mathfrak{e}^0\left(f_\mathfrak{e}^0, \phi_\mathfrak{e}\right) + \mathcal{J}_{\mathfrak{e}\mathfrak{e}}\left(f_\mathfrak{e}^0 \phi_\mathfrak{e}, f_\mathfrak{e}^0 \phi_\mathfrak{e}\right) \\ & + \sum_{j \in \mathrm{H}} \left[\mathcal{J}_{\mathfrak{e}j}^0\left(f_\mathfrak{e}^0 \phi_\mathfrak{e}, {f_j}^0 \phi_j\right) + \mathcal{J}_{\mathfrak{e}j}^1\left(f_\mathfrak{e}^0, {f_j}^0 \phi_j\right) + \mathcal{J}_{\mathfrak{e}j}^2\left(f_\mathfrak{e}^0, {f_j}^0\right)\right]. \end{aligned} \tag{2.3.20}$$

Governing equations: We project (2.3.20) onto the collisional invariants of electrons $\psi_\mathfrak{e}^l$, $l \in \{1, 2\}$. After some algebra, we obtain the zeroth-order conservation equations of electron mass and internal energy:

$$\begin{cases} \partial_t \rho_\mathfrak{e} + \boldsymbol{\partial}_{\boldsymbol{x}} \cdot \left[\rho_\mathfrak{e} \left(\boldsymbol{v}_\mathfrak{h} + \frac{1}{M_\mathfrak{h}} \boldsymbol{V}_\mathfrak{e}\right)\right] = 0, \\ \partial_t \left(\rho_\mathfrak{e} e_\mathfrak{e}\right) + \boldsymbol{\partial}_{\boldsymbol{x}} \cdot \left(\rho_\mathfrak{e} e_\mathfrak{e} \boldsymbol{v}_\mathfrak{h}\right) = -p_\mathfrak{e} \boldsymbol{\partial}_{\boldsymbol{x}} \cdot \boldsymbol{v}_\mathfrak{h} - \frac{1}{M_\mathfrak{h}} \boldsymbol{\partial}_{\boldsymbol{x}} \cdot \boldsymbol{q}_\mathfrak{e} + \frac{1}{M_\mathfrak{h}} \boldsymbol{J}_\mathfrak{e} \cdot \boldsymbol{E}' + \Delta E_\mathfrak{e}^{(0)}, \end{cases} \tag{$M_\mathfrak{e}^{\varepsilon=0}$}$$

where $\boldsymbol{q}_\mathfrak{e}$ is the electron heat flux, and $\Delta E_\mathfrak{e}^{(0)}$ is the energy transferred from electrons to heavy particles at order ε^0, $\boldsymbol{E}' = \boldsymbol{E} + \boldsymbol{v}_\mathfrak{h} \wedge \boldsymbol{B}$.

Transport fluxes: The electron heat flux is defined as

$$\boldsymbol{q}_{\mathfrak{e}} = \int \frac{1}{2}\boldsymbol{C}_{\mathfrak{e}}\cdot\boldsymbol{C}_{\mathfrak{e}}\boldsymbol{C}_{\mathfrak{e}} f_{\mathfrak{e}}\phi_{\mathfrak{e}} d\boldsymbol{C}_{\mathfrak{e}}, \tag{2.3.21}$$

and the energy transferred from electrons to heavy particles reads

$$\Delta E_{\mathfrak{e}}^{(0)} + \Delta E_{\mathfrak{h}}^{(0)} = 0. \tag{2.3.22}$$

Note that, no conservation equation for the momentum of electrons can be derived at this order because $\boldsymbol{C}_{\mathfrak{e}}$ does not belong to the space of electron collisional invariants $\mathcal{I}_{\mathfrak{e}}$. However, an equation of momentum transferred from electrons to heavy particles can be obtained and is investigated in Section 2.3.6.

Unlike the system associated with heavy particles ($M_{\mathfrak{h}}^{\varepsilon=0}$), the electronic variables have a parabolic regularization due to the electron diffusion velocity $\boldsymbol{V}_{\mathfrak{e}}$ and heat flux $\boldsymbol{q}_{\mathfrak{e}}$. Note that, the associated equation system remains consistent with the scaling that was introduced in this chapter. Indeed, the electrons are assumed to diffuse in the heavy reference frame, at timescale t^0.

2.3.5 Order ε at time t^0/ε

We investigate the Boltzmann equations ($\mathrm{B}_{\mathfrak{e}}^{\varepsilon}$) and ($\mathrm{B}_{i\in\mathrm{H}}^{\varepsilon}$), at order ε, corresponding to the macroscopic timescale t^0/ε. We obtain the heavy-particle Navier-Stokes equations and a first-order electron drift-diffusion equations. For more details about the derivation, we refer to proposition 4.7. and 4.8. of Graille et al. (2009).

Heavy-particle: equation for $\phi_{\mathfrak{h}}^2$ and heavy-particle Navier-Stokes equations

Similarly as the previous sections, ($\mathrm{B}_{i\in\mathrm{H}}^{\varepsilon}$) at order ε, reads

$$\begin{aligned} f_i^0\mathcal{F}_i\left(\phi_{\mathfrak{h}}^2\right) = &-\mathcal{D}_i^1\left(f_i^0,\phi_i\right) + \sum_{j\in\mathrm{H}}\mathcal{J}_{ij}\left(f_i^0\phi_i, f_j{}^0\phi_j\right) \\ &+ \mathcal{J}_{i\mathfrak{e}}^1\left(f_i^0\phi_i, f_{\mathfrak{e}}^0\phi_{\mathfrak{e}}\right) + \mathcal{J}_{i\mathfrak{e}}^1\left(f_i^0, f_{\mathfrak{e}}^0\phi_{\mathfrak{e}}^2\right) + \mathcal{J}_{i\mathfrak{e}}^2\left(f_i^0\phi_i, f_{\mathfrak{e}}^0\right) + \mathcal{J}_{i\mathfrak{e}}^2\left(f_i^0, f_{\mathfrak{e}}^0\phi_{\mathfrak{e}}\right),\ i\in\mathrm{H} \end{aligned} \tag{2.3.23}$$

Governing equations: By projecting (2.3.23) onto the collisional invariants of heavy particles $\psi_{\mathfrak{h}}^l$, $l\in\{1,...,n^{\mathrm{H}}+4\}$, we obtain the first-order conservation equations of heavy-particle mass,

momentum and internal energy:

$$\begin{cases} \partial_t \rho_i + \boldsymbol{\partial_x}\cdot\left[\rho_i\left(\boldsymbol{v}_\mathfrak{h} + \dfrac{\varepsilon}{M_\mathfrak{h}}\boldsymbol{V}_i\right)\right] = 0, \quad i \in \mathrm{H}, \\ \partial_t\left(\rho_\mathfrak{h}\boldsymbol{v}_\mathfrak{h}\right) + \boldsymbol{\partial_x}\cdot\left(\rho_\mathfrak{h}\boldsymbol{v}_\mathfrak{h}\otimes\boldsymbol{v}_\mathfrak{h} + \dfrac{1}{M_\mathfrak{h}^2}p\mathbb{I}\right) = -\dfrac{\varepsilon}{M_\mathfrak{h}^2}\boldsymbol{\partial_x}\cdot\left(\boldsymbol{\Pi}_\mathfrak{h} + \boldsymbol{\Pi}_\mathfrak{e}\right) + \dfrac{1}{M_\mathfrak{h}^2}nq\boldsymbol{E} + \left[\delta_{b0}\mathbf{I}_0 + \delta_{b1}\mathbf{I}\right]\wedge\boldsymbol{B}, \\ \partial_t\left(\rho_\mathfrak{h}e_\mathfrak{h}\right) + \boldsymbol{\partial_x}\cdot\left(\rho_\mathfrak{h}e_\mathfrak{h}\boldsymbol{v}_\mathfrak{h}\right) = -\left(p_\mathfrak{h}\mathbb{I} + \varepsilon\boldsymbol{\Pi}_\mathfrak{h}\right)\otimes\boldsymbol{\partial_x}\boldsymbol{v}_\mathfrak{h} - \dfrac{\varepsilon}{M_\mathfrak{h}}\boldsymbol{\partial_x}\cdot\boldsymbol{q}_\mathfrak{h} + \dfrac{\varepsilon}{M_\mathfrak{h}}\boldsymbol{J}_\mathfrak{h}\cdot\boldsymbol{E}' + \Delta E_\mathfrak{h}^{(0)} + \varepsilon\Delta E_\mathfrak{h}^{(1)}, \end{cases} \tag{$M_\mathfrak{h}^{\varepsilon=1}$}$$

where $\boldsymbol{V}_i$ is the heavy particle diffusion velocity, $\boldsymbol{\Pi}_\mathfrak{h}$ and $\boldsymbol{\Pi}_\mathfrak{e}$ are the heavy particle and electron viscous tensor, $\mathbf{I}$ is the total current density at order ε, $\boldsymbol{J}_\mathfrak{h}$ is the current density of heavy particles in the heavy particle reference frame and $\Delta E_\mathfrak{h}^{(1)}$ is the energy transferred from heavy particles to electrons at order ε.

Transport fluxes: The heavy particle diffusion velocity is defined as

$$\boldsymbol{V}_i = \frac{1}{n_i}\int \boldsymbol{C}_i f_i^0 \phi_i d\boldsymbol{C}_i, \quad i \in \mathrm{H}. \tag{2.3.24}$$

The viscous tensor for electrons and heavy-particles read

$$\boldsymbol{\Pi}_\mathfrak{h} = \sum_{i\in\mathrm{H}}\int m_i\boldsymbol{C}_i\otimes\boldsymbol{C}_i f_i^0\phi_i d\boldsymbol{C}_i, \quad \boldsymbol{\Pi}_\mathfrak{e} = \int m_i\boldsymbol{C}_\mathfrak{e}\otimes\boldsymbol{C}_\mathfrak{e} f_\mathfrak{e}^0\phi_\mathfrak{e} d\boldsymbol{C}_\mathfrak{e}. \tag{2.3.25}$$

Then, the total current density at order ε is defined as

$$\mathbf{I} = \mathbf{I}_0 + \frac{\varepsilon}{M_\mathfrak{h}}\sum_{j\in\mathrm{H}} n_j q_j \boldsymbol{V}_j + \frac{\varepsilon}{M_\mathfrak{h}} n_\mathfrak{e} q_\mathfrak{e} \boldsymbol{V}_\mathfrak{e}^{(1)} = \mathbf{I}_0 + \frac{\varepsilon}{M_\mathfrak{h}}\left[\boldsymbol{J}_\mathfrak{h} + \boldsymbol{J}_\mathfrak{e}^{(1)}\right] \tag{2.3.26}$$

where $\boldsymbol{V}_\mathfrak{e}^{(1)}$ and $\boldsymbol{J}_\mathfrak{e}^{(1)}$ are the electron diffusion velocity and current density, at order ε. The latter is defined as:

$$\boldsymbol{V}_\mathfrak{e}^{(1)} = \frac{1}{n_\mathfrak{e}}\int \boldsymbol{C}_\mathfrak{e} f_\mathfrak{e}^0 \phi_\mathfrak{e}^2 d\boldsymbol{C}_\mathfrak{e}. \tag{2.3.27}$$

Then, the heavy particle heat flux is defined as

$$\boldsymbol{q}_\mathfrak{h} = \sum_{j\in\mathrm{H}}\int \frac{1}{2} m_i \boldsymbol{C}_i\cdot\boldsymbol{C}_i\boldsymbol{C}_i f_i^0\phi_i d\boldsymbol{C}_i, \tag{2.3.28}$$

Finally, the energy transferred from heavy particles to electrons at order ε is defined as

$$\Delta E_\mathfrak{h}^{(1)} = \sum_{j\in\mathrm{H}} n_j \boldsymbol{V}_j\cdot\boldsymbol{F}_{je} \tag{2.3.29}$$

where $\boldsymbol{F}_{je}$ is the average force of an electron acting on a heavy particle j. It will contribute to the heavy-particle diffusion driving forces, and yield anisotropic diffusion velocities for heavy particles in the $b = 1$ case. It allows for a coupling between heavy particles and electrons. In the next section, we will see that this term is considered also in the thermal nonequilibrium model derived by Kolesnikov (2003).

Note that, when we consider only one single type of heavy particles or a fully ionized plasma, the first-order energy transfer term $\Delta E_{\mathfrak{h}}^{(1)}$, heavy-particle diffusion velocities, and conduction current degenerate, $\Delta E_{\mathfrak{h}}^{(1)} = 0$, $\boldsymbol{V}_i = 0$, $i \in \mathrm{H}$, and $\boldsymbol{J}_{\mathfrak{h}} = 0$, which leads to a total current density $\mathbf{I} = nq\boldsymbol{v}_{\mathfrak{h}} + n_{\mathfrak{e}}q_{\mathfrak{e}}\boldsymbol{V}_{\mathfrak{e}}/M_{\mathfrak{h}}$. Therefore, we get the same formalism as Degond & Lucquin-Desreux (1996b). In this context, the Navier-Stokes system ($M_{\mathfrak{h}}^{\varepsilon=1}$) can be coupled to the system of drift-diffusion equations for the electrons obtained at order ε^0: ($M_{\mathfrak{e}}^{\varepsilon=0}$). Since no energy transfer occurs at this order, there is no need to solve the electrons at order ε to obtain a conservative model. However, for a multicomponent mixture, it is necessary to extend one order further the model obtained for the electrons, as done in the next subsection.

Electrons: equation for $\phi_{\mathfrak{e}}^3$ and first-order electron drift diffusion equations

At order ε, ($\mathrm{B}_{\mathfrak{e}}^{\varepsilon}$) reads

$$
\begin{aligned}
f_{\mathfrak{e}}^0\mathcal{F}_{\mathfrak{e}}\left(\phi_{\mathfrak{e}}^3\right) + \delta_{b1}q_{\mathfrak{e}}\boldsymbol{\partial}_{\boldsymbol{C}_{\mathfrak{e}}}\left(f_{\mathfrak{e}}^0\phi_{\mathfrak{e}}^3\right)\cdot\boldsymbol{C}_{\mathfrak{e}}\wedge\boldsymbol{B} = -\mathcal{D}_{\mathfrak{e}}^1\left(f_{\mathfrak{e}}^0, \phi_{\mathfrak{e}}, \phi_{\mathfrak{e}}^2\right) + \mathcal{J}_{\mathfrak{e}\mathfrak{e}}\left(f_{\mathfrak{e}}^0\phi_{\mathfrak{e}}^2, f_{\mathfrak{e}}^0\phi_{\mathfrak{e}}\right) + \mathcal{J}_{\mathfrak{e}\mathfrak{e}}\left(f_{\mathfrak{e}}^0\phi_{\mathfrak{e}}, f_{\mathfrak{e}}^0\phi_{\mathfrak{e}}^2\right) \\
+ \sum_{j\in\mathrm{H}}\left[\mathcal{J}_{\mathfrak{e}j}^0\left(f_{\mathfrak{e}}^0\phi_{\mathfrak{e}}^2, f_j{}^0\phi_j\right) + \mathcal{J}_{\mathfrak{e}j}^0\left(f_{\mathfrak{e}}^0\phi_{\mathfrak{e}}, f_j{}^0\phi_j^2\right) + \mathcal{J}_{\mathfrak{e}j}^1\left(f_{\mathfrak{e}}^0\phi_{\mathfrak{e}}, f_j{}^0\phi_j\right)\right] \\
+ \sum_{j\in\mathrm{H}}\left[\mathcal{J}_{\mathfrak{e}j}^1\left(f_{\mathfrak{e}}^0, f_j{}^0\phi_j^2\right) + \mathcal{J}_{\mathfrak{e}j}^2\left(f_{\mathfrak{e}}^0\phi_{\mathfrak{e}}, f_j{}^0\right) + \mathcal{J}_{\mathfrak{e}j}^2\left(f_{\mathfrak{e}}^0, f_j{}^0\phi_j\right) + \mathcal{J}_{\mathfrak{e}j}^3\left(f_{\mathfrak{e}}^0, f_j{}^0\right)\right].
\end{aligned}
\tag{2.3.30}
$$

Governing equations: We project (2.3.30) onto the collisional invariants of electrons $\psi_{\mathfrak{e}}^l$, $l \in \{1, 2\}$, which leads to the first-order conservation equations of electron mass and internal energy

$$
\begin{cases}
\partial_t\rho_{\mathfrak{e}} + \boldsymbol{\partial}_{\boldsymbol{x}}\cdot\left[\rho_{\mathfrak{e}}\left(\boldsymbol{v}_{\mathfrak{h}} + \dfrac{1}{M_{\mathfrak{h}}}(\boldsymbol{V}_{\mathfrak{e}} + \varepsilon\boldsymbol{V}_{\mathfrak{e}}^{(1)})\right)\right] = 0, \\
\partial_t\left(\rho_{\mathfrak{e}}e_{\mathfrak{e}}\right) + \boldsymbol{\partial}_{\boldsymbol{x}}\cdot\left(\rho_{\mathfrak{e}}e_{\mathfrak{e}}\boldsymbol{v}_{\mathfrak{h}}\right) = -p_{\mathfrak{e}}\boldsymbol{\partial}_{\boldsymbol{x}}\cdot\boldsymbol{v}_{\mathfrak{h}} - \dfrac{1}{M_{\mathfrak{h}}}\boldsymbol{\partial}_{\boldsymbol{x}}\cdot\left(\boldsymbol{q}_{\mathfrak{e}} + \varepsilon\boldsymbol{q}_{\mathfrak{e}}^{(1)}\right) + \dfrac{1}{M_{\mathfrak{h}}}\left(\boldsymbol{J}_{\mathfrak{e}} + \varepsilon\boldsymbol{J}_{\mathfrak{e}}^{(1)}\right)\cdot\boldsymbol{E}' \\
\qquad\qquad + \delta_{b0}\varepsilon M_{\mathfrak{h}}\boldsymbol{J}_{\mathfrak{e}}\cdot\boldsymbol{v}_{\mathfrak{h}}\wedge\boldsymbol{B} + \Delta E_{\mathfrak{e}}^{(0)} + \varepsilon\Delta E_{\mathfrak{e}}^{(1)},
\end{cases}
\qquad (M_{\mathfrak{e}}^{\varepsilon=1})
$$

where $\boldsymbol{q}_{\mathfrak{e}}^{(1)}$ is the electron heat flux at order ε and $\Delta E_{\mathfrak{e}}^{(1)}$ is the energy transferred from electrons to heavy particles at order ε.

Transport fluxes: The electron heat flux at order ε is defined as

$$\boldsymbol{q}_{\mathfrak{e}}^{(1)} = \int \frac{1}{2} \boldsymbol{C}_{\mathfrak{e}} \cdot \boldsymbol{C}_{\mathfrak{e}} \boldsymbol{C}_{\mathfrak{e}} f_{\mathfrak{e}}^{0} \phi_{\mathfrak{e}}^{2} d\boldsymbol{C}_{\mathfrak{e}}. \tag{2.3.31}$$

The energy transferred from electrons to heavy particles at order ε reads

$$\Delta E_{\mathfrak{e}}^{(1)} + \Delta E_{\mathfrak{h}}^{(1)} = 0. \tag{2.3.32}$$

In this subsection, the conservation equations for electrons at order ε have been obtained. The system is showing new terms of diffusion and relaxation types at a higher order. Also, electrons/heavy-particles coupling terms, known as the Kolesnikov (2003) effect, are considered at this order.

2.3.6 About the electron momentum relation at order ε^{-1} and ε^{0}

In this subsection, we focus on the relation of the electron momentum and consider the electron Boltzmann equation ($\mathrm{B}_{\mathfrak{e}}^{\varepsilon}$) at order ε^{-1} and ε^{0}, *i.e.*, (2.3.9) and (2.3.20) respectively.

First, an electron momentum relation at order ε^{-1} can be obtained by projecting (2.3.9) onto the space spanned by $\boldsymbol{C}_{\mathfrak{e}}$. A relation on the zeroth-order momentum transferred from electrons to heavy particles is obtained, as follows

$$\sum_{j \in \mathrm{H}} \langle\!\langle \mathcal{J}_{\mathfrak{e}j}^{0}\left(f_{\mathfrak{e}}^{0}\phi_{\mathfrak{e}}, f_{j}^{0}\right), \boldsymbol{C}_{\mathfrak{e}} \rangle\!\rangle_{\mathfrak{e}} = \frac{1}{M_{\mathfrak{h}}} \boldsymbol{\partial}_{x} p_{\mathfrak{e}} - \frac{n_{\mathfrak{e}} q_{\mathfrak{e}}}{M_{\mathfrak{h}}} \boldsymbol{E} - \delta_{b1} n_{\mathfrak{e}} q_{\mathfrak{e}} \left(\boldsymbol{v}_{\mathfrak{h}} + \frac{1}{M_{\mathfrak{h}}} \boldsymbol{V}_{\mathfrak{e}} \right) \wedge \boldsymbol{B}. \tag{2.3.33}$$

Note that, this relation is expressed in terms of the electron pressure and electric force. However, this relation is not an equation of conservation of momentum.

At order ε^{0} another electron momentum relation can be obtained by projecting the Boltzmann equation for electrons (2.3.20) onto $\boldsymbol{C}_{\mathfrak{e}}$, as follows

$$\begin{aligned} \sum_{j \in \mathrm{H}} \langle\!\langle \left[\mathcal{J}_{\mathfrak{e}j}^{0}\left(f_{\mathfrak{e}}^{0}\phi_{\mathfrak{e}}^{2}, f_{j}^{0}\right) + \mathcal{J}_{\mathfrak{e}j}^{0}\left(f_{\mathfrak{e}}^{0}\phi_{\mathfrak{e}}, f_{j}^{0}\phi_{j}\right) + \mathcal{J}_{\mathfrak{e}j}^{1}\left(f_{\mathfrak{e}}^{0}, f_{j}^{0}\phi_{j}\right) + \mathcal{J}_{\mathfrak{e}j}^{2}\left(f_{\mathfrak{e}}^{0}, f_{j}^{0}\right) \right], \boldsymbol{C}_{\mathfrak{e}} \rangle\!\rangle_{\mathfrak{e}} = \\ \frac{1}{M_{\mathfrak{h}}} \boldsymbol{\partial}_{\boldsymbol{x}} \cdot \boldsymbol{\Pi}_{\mathfrak{e}} - \delta_{b1} n_{\mathfrak{e}} q_{\mathfrak{e}} \left(\boldsymbol{v}_{\mathfrak{h}} + \frac{1}{M_{\mathfrak{h}}} \boldsymbol{V}_{\mathfrak{e}} + \delta_{b1} \boldsymbol{V}_{\mathfrak{e}}^{(1)} \right) \wedge \boldsymbol{B}. \end{aligned} \tag{2.3.34}$$

Thus, the first-order momentum relation transferred from electrons to heavy particles obtained in (2.3.34) is expressed in terms of the electron viscous tensor and electric force. Finally, it should be mentionned that, the momentum of electrons can be computed in terms of the electron pressure and electric force at order ε^{-1}, or, in terms of electron viscous tensor and electric force at order ε^{0}.

This result is unusual compared with the usual multi-fluid MHD model (see Khomenko (2017); Alvarez Laguna et al. (2016, 2018); Leake et al. (2012)), or the one developped by Braginskii (1965). In the multi-fluid approach, a conservation equation of the momentum for electrons is

obtained because no dimensional analysis is performed on the Boltzmann equations. The scaling used for the electrons and heavy-particles is identical. Therefore, the collisional invariants is identical for both electrons and heavy-particles, and, in particular, the space spanned by the velocity of electrons belongs to the space of the electron collisional invariants.

2.3.7 A comment about the heavy particle reference frame

As mentioned by Graille et al. (2009), the hydrodynamic reference frame of heavy particles is not commonly used in the literature to perform a Chapman-Enskog expansion. One choice could be to follow the approach of Degond & Lucquin-Desreux (1996a,c) and work in the inertial reference frame, but a different path has been followed by Graille et al. (2009). Indeed, the choice of the heavy particle reference frame is justified as the overall hydrodynamic velocity depends on the parameter ε. In this configuration, the hydrodynamic velocity of the mixture can be expanded with the ε parameter and has several contributions at different orders ε. Consequently, the hydrodynamic velocity of the mixture appears not to be the appropriate reference frame, to obtain a rigorous and simplified algebra in the Chapman-Enskog expansion framework, through the parameter ε.

Indeed, as shown by Graille et al. (2009), the expansion of the collision operators in terms of ε depends on the choice of the reference frame. The hydrodynamic reference frame of heavy-particles allows some simplification, *i.e.*, some terms to vanish in the Chapman-Enskog expansion. In particular, the crossed collision operator $\mathcal{J}^1_{\mathfrak{e}j}\left(f^0_{\mathfrak{e}}, f_j{}^0\phi^2_j\right)$ vanishes.

Finally, at order ε, it is shown that the choice of the reference frame has an impact on the structure of the equation for $\phi^2_{\mathfrak{e}}$. Therefore, a different reference frame from the hydrodynamic reference frame of heavy-particles makes the equation on $\phi^2_{\mathfrak{e}}$ difficult to solve. These difficulties, found in the Boltzmann equation for the electrons, have not been encountered in the Boltzmann equation for the heavy-particles.

2.3.8 Summary of the derivation and comparison with Braginskii's approach

The derivation has been performed up to the order ε, corresponding to a second and third order perturbation of the distribution functions for heavy particles and electrons, respectively. A comparison with Braginskii (1965) at the kinetic level has been investigated. In summary,

- **At orders ε^{-2} and ε^{-1}**, the Maxwellian distributions functions for electrons and heavy-particle have been obtained in (2.3.6) and (2.3.8), occuring at time $t^0_{\mathfrak{e}}$ and $t^0_{\mathfrak{h}}$ respectively. In the derivation of Braginskii (1965), the Maxwellian distribution functions for electrons and heavy-particles, at temperature $T_{\mathfrak{e}}$ and $T_{\mathfrak{h}}$ are obtained at the same order of the expansion, *i.e.*, at the same timescale.

- **At order ε^{-1}**, an equation for $\phi_{\mathfrak{e}}$ is obtained in (2.3.9). Because of the structure of the streaming operator, no macroscopic equation for electrons are obtained. On the contrary, in

Braginskii (1965), the structure of this operator allows to derive macroscopic equations for the electrons at the first order of the expansion.

- **At order ε^0**, the Euler equations for heavy particles ($M_{\mathfrak{h}}^{\varepsilon=0}$), and a zeroth-order drift diffusion equations for electrons ($M_{\mathfrak{e}}^{\varepsilon=0}$) have been obtained. At this order, we have an equation on $\phi_{\mathfrak{h}}$ in (2.3.12), and $\phi_{\mathfrak{e}}^2$ in (2.3.20).

  - **Equation on $\phi_{\mathfrak{h}}$:** The equation on $\phi_{\mathfrak{h}}$ in (2.3.12) is identical to the one obtained by Braginskii (1965), except that 1-some crossed collision operators terms are absent, and 2- an additional term related to the anisotropy of the the heavy-particle transport fluxes is considered. In particular, in Braginskii (1965), the crossed collision operators $\mathcal{J}_{i\mathfrak{e}}^1$ and $\mathcal{J}_{i\mathfrak{e}}^2$ are neglected since the terms $\mathcal{J}_{ij}$ are considered as higher order due to the large mass disparity between electrons and heavy particles. In Braginskii (1965), the transport fluxes of heavy-particles are anisotropic, whereas in the multiscale approach, they are isotropic.
  - **Equation on $\phi_{\mathfrak{e}}^2$:** The resulting system obtained for the electrons ($M_{\mathfrak{e}}^{\varepsilon=0}$) is similar to the one obtained by Braginskii (1965) at the first order of the expansion, except that 1- a hydrodynamic velocity for electrons is considered and 2- a momentum equation for the electrons is obtained, since the velocity of electrons belongs to the electron collisional invariants.

- **At order ε**, the Navier-Stokes equations for heavy particles ($M_{\mathfrak{h}}^{\varepsilon=1}$) and a first-order drift diffusion equations for electrons ($M_{\mathfrak{e}}^{\varepsilon=1}$) have been obtained. At this order, we have an equation on $\phi_{\mathfrak{h}}^2$ in (2.3.23) and $\phi_{\mathfrak{e}}^3$ in (2.3.30). This order has not been investigated by Braginskii (1965).

The structure of the governing equations has been identified at the several orders investigated in the Chapman-Enskog expansion. However, it is still necessary to define the transport fluxes.

2.4 Transport fluxes

In order to obtain an expression of the transport fluxes presented in the previous section, we solve for the equations of $\phi_{\mathfrak{e}}$, $\phi_{\mathfrak{h}}$ and $\phi_{\mathfrak{e}}^2$ presented in (2.3.9), (2.3.12), and (2.3.20) respectively. We focus on the general case where the plasma is strongly magnetized, *i.e.*, $b = 1$, which leads to anisotropic electron transport coefficients. In this subsection, the cases of weakly and unmagnetized plasmas, *i.e.*, $b = 0$ and $b < 0$ are not fully investigated. These cases are not relevant for our application and can be deduced easily from the strongly magnetized case.

First, some notations are introduced for the anisotropic electron transport properties. Then, we present the electron transport fluxes at order ε^0, *i.e.*, $\boldsymbol{V}_{\mathfrak{e}}$, $\boldsymbol{q}_{\mathfrak{e}}$ and $\boldsymbol{\Pi}_{\mathfrak{e}}$. In addition, we derive the expression of the heavy-particle transport fluxes at order ε, *i.e.*, $\boldsymbol{V}_i$, $\boldsymbol{\Pi}_{\mathfrak{h}}$ and $\boldsymbol{q}_{\mathfrak{h}}$. Then, we give the expression of the electron transport fluxes at order ε, such as $\boldsymbol{V}_{\mathfrak{e}}^{(1)}$, $\boldsymbol{q}_{\mathfrak{e}}^{(1)}$ and $\boldsymbol{F}_{ie}$. In addition, a

comparison with the transport fluxes from the model of Braginskii (1965) and Kolesnikov (2003) is provided. Finally, we briefly present the weakly-magnetized case where $b = 0$.

2.4.1 Extra-notation for anisotropy

We introduce some extra notations in order to express the anisotropic transport properties in the presence of a magnetic field. First, a unit vector for the magnetic field $\mathcal{B} = \boldsymbol{B}/|\boldsymbol{B}|$ is defined and also three direction matrices

$$\boldsymbol{M}^{\parallel} = \mathcal{B}\otimes\mathcal{B}, \quad \boldsymbol{M}^{\perp} = \mathbb{I} - \mathcal{B}\otimes\mathcal{B}, \quad \boldsymbol{M}^{\odot} = \begin{pmatrix} 0 & -\mathcal{B}_3 & \mathcal{B}_2 \\ \mathcal{B}_3 & 0 & -\mathcal{B}_1 \\ -\mathcal{B}_2 & \mathcal{B}_1 & 0 \end{pmatrix}$$

so that we have for any vector $\boldsymbol{x}$ in three dimensions

$$\boldsymbol{x}^{\parallel} = \boldsymbol{M}^{\parallel}\boldsymbol{x} = \boldsymbol{x}\cdot\mathcal{B}\ \mathcal{B}, \qquad \boldsymbol{x}^{\perp} = \boldsymbol{M}^{\perp}\boldsymbol{x} = \boldsymbol{x} - \boldsymbol{x}\cdot\mathcal{B}\ \mathcal{B},$$

$$\boldsymbol{x}^{\odot} = \boldsymbol{M}^{\odot}\boldsymbol{x} = \mathcal{B}\wedge\boldsymbol{x}.$$

In the $(\boldsymbol{x}, \mathcal{B})$ plane, the vector $\boldsymbol{x}^{\parallel}$ is the component of $\boldsymbol{x}$ that is parallel to the magnetic field and $\boldsymbol{x}^{\perp}$ is the perpendicular component. Therefore, we have $\boldsymbol{x} = \boldsymbol{x}^{\parallel} + \boldsymbol{x}^{\perp}$. The vector $\boldsymbol{x}^{\odot}$ lies in the direction transverse to the $(\boldsymbol{x}, \mathcal{B})$ plane. The three vectors $\boldsymbol{x}^{\parallel}$, $\boldsymbol{x}^{\perp}$, and $\boldsymbol{x}^{\odot}$ are then mutually orthogonal. The anisotropic transport coefficients are expressed by means of the matrix notation

$$\bar{\bar{\mu}} = \mu^{\parallel}\boldsymbol{M}^{\parallel} + \mu^{\perp}\boldsymbol{M}^{\perp} + \mu^{\odot}\boldsymbol{M}^{\odot}$$

If the transport coefficients are identical in the parallel and perpendicular directions, $\mu^{\parallel} = \mu^{\perp}$, and vanish in the transverse direction, $\mu^{\odot} = 0$ an isotropic system is obtained.

Then, the direction matrices satisfy the following two properties. The matrices $\boldsymbol{M}^{\parallel}$, $\boldsymbol{M}^{\perp}$ and $\boldsymbol{M}^{\odot}$ are linearly independent, that is

$$\bar{\bar{\mu}} = 0 \Rightarrow \mu^{\parallel} = \mu^{\perp} = \mu^{\odot} = 0$$

Moreover, the space spanned by the matrices $\boldsymbol{M}^{\parallel}$, $\boldsymbol{M}^{\perp}$ and $\boldsymbol{M}^{\odot}$ is stable under their multiplication, since we have the following relations

$$\begin{aligned}
&\boldsymbol{M}^{\parallel}\boldsymbol{M}^{\parallel} = \boldsymbol{M}^{\parallel}, \quad &&\boldsymbol{M}^{\parallel}\boldsymbol{M}^{\perp} = 0, \quad &&\boldsymbol{M}^{\parallel}\boldsymbol{M}^{\odot} = 0 \\
&\boldsymbol{M}^{\perp}\boldsymbol{M}^{\parallel} = 0, \quad &&\boldsymbol{M}^{\perp}\boldsymbol{M}^{\perp} = 0, \quad &&\boldsymbol{M}^{\perp}\boldsymbol{M}^{\odot} = \boldsymbol{M}^{\odot} \\
&\boldsymbol{M}^{\odot}\boldsymbol{M}^{\parallel} = 0, \quad &&\boldsymbol{M}^{\odot}\boldsymbol{M}^{\perp} = \boldsymbol{M}^{\odot}, \quad &&\boldsymbol{M}^{\odot}\boldsymbol{M}^{\odot} = -\boldsymbol{M}^{\perp}
\end{aligned}$$

One can find a representation of the anisotropic transport flux in Figure 2-3.

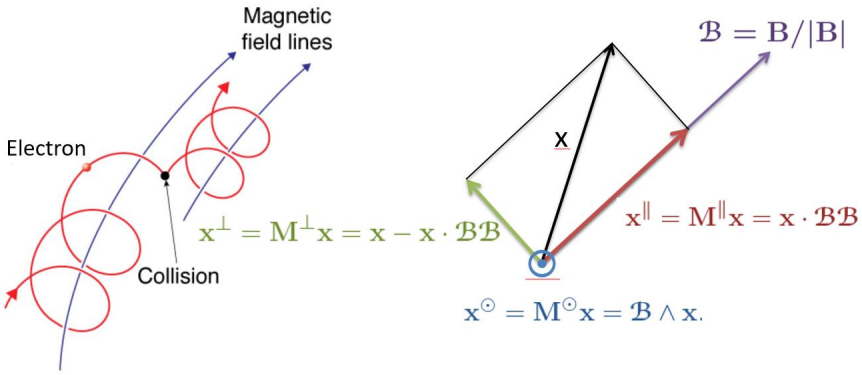

Figure 2-3: Representation of the parallel, perpendicular and transverse component of a transport flux in the $(\boldsymbol{x}, \mathcal{B})$ plane

2.4.2 Electron transport fluxes at order ε^0: $\boldsymbol{V}_e$, $\boldsymbol{q}_e$ and $\boldsymbol{\Pi}_e$

In order to obtain the expression of the electron transport fluxes at order ε^0, it is necessary to solve the equation of the first-order perturbation function ϕ_e in (2.3.9). We rewrite (2.3.33) as follows

$$\mathcal{F}_e(\phi_e) + \delta_{b1} q_e \boldsymbol{\partial}_{\boldsymbol{C}_e}\left(f_e^0 \phi_e\right)\cdot\boldsymbol{C}_e\wedge\boldsymbol{B} = \Psi_e, \tag{2.4.1}$$

where $\Psi_e = -\mathcal{D}_e^{-1}\left(f_e^0\right)/f_e^0$. After some algebra based on the expression of f_e^0, an expression of Ψ_e can be obtained

$$\Psi_e = -p_e \boldsymbol{\Psi}_e^{D_e}\cdot\boldsymbol{d}_e - \boldsymbol{\Psi}_e^{\lambda_e'}\cdot\boldsymbol{\partial}_{\boldsymbol{x}}\left(\frac{1}{T_e}\right), \tag{2.4.2}$$

where the electron diffusion driving force $\boldsymbol{d}_e$ is defined as

$$\boldsymbol{d}_e = \frac{1}{p_e}\boldsymbol{\partial}_{\boldsymbol{x}} p_e - \frac{n_e q_e}{p_e}\boldsymbol{E}', \tag{2.4.3}$$

with

$$\boldsymbol{\Psi}_e^{D_e} = \frac{1}{M_\mathfrak{h} p_e}\boldsymbol{C}_e, \quad \boldsymbol{\Psi}_e^{\lambda_e'} = \frac{1}{M_\mathfrak{h}}\left(\frac{5}{2}T_e - \frac{1}{2}\boldsymbol{C}_e\cdot\boldsymbol{C}_e\right)\boldsymbol{C}_e. \tag{2.4.4}$$

Note that, in Braginskii (1965), the expression of Ψ_e is identical except that an additional term related to the rate-of-strain tensor is considered. It leads to an expression of the electron viscous stress tensor. In the multiscale approach, unlike the model of Braginskii (1965), the electron viscous stress tensor is vanishing.

In addition, in (2.4.1), the right hand-side is not depending on the heavy-particle driving forces, which leads to a first-order electron perturbation function decoupled from heavy-particles.

Resolution of (2.4.1): expression of $\phi_\mathfrak{e}$

For the complete resolution of (2.4.1), we refer to the proof of the proposition 5.1. of Graille et al. (2009). The solution $\phi_\mathfrak{e}$ in (2.4.1) is given by

$$\phi_\mathfrak{e} = -p_\mathfrak{e}\Re\left[\boldsymbol{M}^{\parallel}\boldsymbol{\varphi}_\mathfrak{e}^{D_\mathfrak{e}(1)} + (\boldsymbol{M}^{\perp} + \mathtt{i}\boldsymbol{M}^{\odot})\,\boldsymbol{\varphi}_\mathfrak{e}^{D_\mathfrak{e}(2)}\right]\cdot\boldsymbol{d}_\mathfrak{e} - \Re\left[\boldsymbol{M}^{\parallel}\boldsymbol{\varphi}_\mathfrak{e}^{\lambda'_\mathfrak{e}(1)} + (\boldsymbol{M}^{\perp} + \mathtt{i}\boldsymbol{M}^{\odot})\,\boldsymbol{\varphi}_\mathfrak{e}^{\lambda'_\mathfrak{e}(2)}\right]\cdot\boldsymbol{\partial}_x\left(\frac{1}{T_\mathfrak{e}}\right) \tag{2.4.5}$$

where $\mathtt{i}$ is the imaginary unit defined as $\mathtt{i}^2 = -1$. The vectorial functions $\boldsymbol{\varphi}_\mathfrak{e}^{D_\mathfrak{e}(1)}$, $\boldsymbol{\varphi}_\mathfrak{e}^{D_\mathfrak{e}(2)}$, $\boldsymbol{\varphi}_\mathfrak{e}^{\lambda'_\mathfrak{e}(1)}$ and $\boldsymbol{\varphi}_\mathfrak{e}^{\lambda'_\mathfrak{e}(2)}$ are solutions to the following equations

$$\mathcal{F}_\mathfrak{e}\left(\boldsymbol{\varphi}_\mathfrak{e}^{\mu(1)}\right) = \boldsymbol{\Psi}_\mathfrak{e}{}^{\mu}, \tag{2.4.6a}$$

$$\left(\mathcal{F}_\mathfrak{e} + \mathtt{i}\,|\boldsymbol{B}|\,\mathcal{F}_\mathfrak{e}^{q_\mathfrak{e}}\right)\left(\boldsymbol{\varphi}_\mathfrak{e}^{\mu(2)}\right) = \boldsymbol{\Psi}_\mathfrak{e}{}^{\mu}, \tag{2.4.6b}$$

under the constraints

$$\langle\!\langle f_\mathfrak{e}^0\boldsymbol{\varphi}_\mathfrak{e}^{\mu(1)}, \psi_\mathfrak{e}^l\rangle\!\rangle_\mathfrak{e} = 0, \quad l \in \{1,2\}, \tag{2.4.7a}$$

$$\langle\!\langle f_\mathfrak{e}^0\boldsymbol{\varphi}_\mathfrak{e}^{\mu(2)}, \psi_\mathfrak{e}^l\rangle\!\rangle_\mathfrak{e} = 0, \quad l \in \{1,2\}, \tag{2.4.7b}$$

with $\mu \in \{D_\mathfrak{e}, \lambda'_\mathfrak{e}\}$ and $\mathcal{F}_\mathfrak{e}^{q_\mathfrak{e}}(\boldsymbol{u}) = q_\mathfrak{e}\boldsymbol{u}$.

Electron diffusion velocity $\boldsymbol{V}_\mathfrak{e}$

We introduce the electron bracket operators $[\![\cdot,\cdot]\!]_\mathfrak{e}$ and $((\cdot,\cdot))_\mathfrak{e}$. For any family $\xi_\mathfrak{e}$ and $\zeta_\mathfrak{e}$, the electron bracket operators are defined as

$$[\![\xi_\mathfrak{e}, \zeta_\mathfrak{e}]\!]_\mathfrak{e} = \langle\!\langle f_\mathfrak{e}^0\xi_\mathfrak{e}, \mathcal{F}_\mathfrak{e}(\zeta_\mathfrak{e})\rangle\!\rangle_\mathfrak{e}, \quad ((\xi_\mathfrak{e}, \zeta_\mathfrak{e}))_\mathfrak{e} = |\boldsymbol{B}|\,\langle\!\langle f_\mathfrak{e}^0\xi_\mathfrak{e}, \mathcal{F}_\mathfrak{e}^{q_\mathfrak{e}}(\zeta_\mathfrak{e})\rangle\!\rangle_\mathfrak{e}. \tag{2.4.8}$$

The bracket operator $[\![\cdot,\cdot]\!]_\mathfrak{e}$ is symmetric, $[\![\xi_\mathfrak{e}, \zeta_\mathfrak{e}]\!]_\mathfrak{e} = [\![\zeta_\mathfrak{e}, \xi_\mathfrak{e}]\!]_\mathfrak{e}$, and positive semi-definite $[\![\xi_\mathfrak{e}, \xi_\mathfrak{e}]\!]_\mathfrak{e} \geq 0$. Additionally, the bracket operator $((\cdot,\cdot))_\mathfrak{e}$ is symmetric $((\xi_\mathfrak{e}, \zeta_\mathfrak{e}))_\mathfrak{e} = ((\zeta_\mathfrak{e}, \xi_\mathfrak{e}))_\mathfrak{e}$ and negative definite $((\xi_\mathfrak{e}, \xi_\mathfrak{e}))_\mathfrak{e} < 0$.

In order to obtain the electron diffusion velocity $\boldsymbol{V}_\mathfrak{e}$, we inject (2.4.5) into (2.3.18). Then, we obtain

$$\boldsymbol{V}_\mathfrak{e} = -\bar{\bar{D}}_\mathfrak{e}\boldsymbol{d}_\mathfrak{e} - \frac{1}{T_\mathfrak{e}}\bar{\bar{\theta}}_\mathfrak{e}\boldsymbol{\partial}_x T_\mathfrak{e} \tag{2.4.9}$$

where the components of the tensor of the electron diffusion and thermal diffusion coefficient are defined as

$$\begin{aligned}
D_\mathfrak{e}^{\parallel} &= \frac{1}{3}p_\mathfrak{e}T_\mathfrak{e}\,M_\mathfrak{h}\left[\!\left[\boldsymbol{\varphi}_\mathfrak{e}^{D_\mathfrak{e}(1)}, \boldsymbol{\varphi}_\mathfrak{e}^{D_\mathfrak{e}(1)}\right]\!\right]_\mathfrak{e}, & \theta_\mathfrak{e}^{\parallel} &= \frac{1}{3}M_\mathfrak{h}\left[\!\left[\boldsymbol{\varphi}_\mathfrak{e}^{D_\mathfrak{e}(1)}, \boldsymbol{\varphi}_\mathfrak{e}^{\lambda'_\mathfrak{e}(1)}\right]\!\right]_\mathfrak{e}, \\
D_\mathfrak{e}^{\perp} &= \frac{1}{3}p_\mathfrak{e}T_\mathfrak{e}\,M_\mathfrak{h}\left[\!\left[\boldsymbol{\varphi}_\mathfrak{e}^{D_\mathfrak{e}(2)}, \boldsymbol{\varphi}_\mathfrak{e}^{D_\mathfrak{e}(2)}\right]\!\right]_\mathfrak{e}, & \theta_\mathfrak{e}^{\perp} &= \frac{1}{3}M_\mathfrak{h}\left[\!\left[\boldsymbol{\varphi}_\mathfrak{e}^{D_\mathfrak{e}(2)}, \boldsymbol{\varphi}_\mathfrak{e}^{\lambda'_\mathfrak{e}(2)}\right]\!\right]_\mathfrak{e}, \\
D_\mathfrak{e}^{\odot} &= -\frac{1}{3}p_\mathfrak{e}T_\mathfrak{e}\,M_\mathfrak{h}\left(\left(\boldsymbol{\varphi}_\mathfrak{e}^{D_\mathfrak{e}(2)}, \boldsymbol{\varphi}_\mathfrak{e}^{D_\mathfrak{e}(2)}\right)\right)_\mathfrak{e}, & \theta_\mathfrak{e}^{\odot} &= \frac{1}{3}M_\mathfrak{h}\left(\left(\boldsymbol{\varphi}_\mathfrak{e}^{D_\mathfrak{e}(2)}, \boldsymbol{\varphi}_\mathfrak{e}^{\lambda'_\mathfrak{e}(2)}\right)\right)_\mathfrak{e},
\end{aligned} \tag{2.4.10}$$

Note that, in (2.4.10), a simplification of these bracket operators will be performed in Chapter 4, using a spectral Galerkin method based on Laguerre-Sonine polynomials approximation. An alternative expression of the diffusion velocity can be obtained by factorizing (2.4.9) with the electron diffusion coefficient tensor $\bar{\bar{D}}_{\mathfrak{e}}$ as follows

$$\boldsymbol{V}_{\mathfrak{e}} = -\bar{\bar{D}}_{\mathfrak{e}}\left(\boldsymbol{d}_{\mathfrak{e}} + \frac{1}{T_{\mathfrak{e}}}\bar{\bar{\chi}}_{\mathfrak{e}}\boldsymbol{\partial}_x T_{\mathfrak{e}}\right) \tag{2.4.11}$$

where $\bar{\bar{\chi}}_{\mathfrak{e}}$ is the electron thermal diffusion ratio tensor. The latter is defined as

$$\bar{\bar{\theta}}_{\mathfrak{e}} = \bar{\bar{D}}_{\mathfrak{e}}\bar{\bar{\chi}}_{\mathfrak{e}}, \tag{2.4.12}$$

or, equivalently,

$$\theta_{\mathfrak{e}}^{\parallel} = D_{\mathfrak{e}}^{\parallel}\chi_{\mathfrak{e}}^{\parallel}, \quad \theta_{\mathfrak{e}}^{\perp} + \mathtt{i}\theta_{\mathfrak{e}}^{\odot} = (D_{\mathfrak{e}}^{\perp} + \mathtt{i}D_{\mathfrak{e}}^{\odot})(\chi_{\mathfrak{e}}^{\perp} + \mathtt{i}\chi_{\mathfrak{e}}^{\odot}) \tag{2.4.13}$$

Physically, the first term of the electron diffusion velocity in (2.4.11) yields the diffusion effects due to the pressure gradients and electromagnetic forces acting on the electrons, whereas the second term represents diffusion due to the electron temperature gradient known as the Soret effect, as described by Magin & Degrez (2004).

Electron viscous stress tensor $\boldsymbol{\Pi}_{\mathfrak{e}}$

Similarly, in order to get the electron viscous stress tensor, we inject (2.4.5) into (2.3.25). Thus, we obtain that the electron viscous stress tensor is vanishing, *i.e.*,

$$\boldsymbol{\Pi}_{\mathfrak{e}} = 0. \tag{2.4.14}$$

Note that, in the model of Braginskii (1965), this term is not vanishing, since 1- the velocity of electrons is a collisional invariant, and, 2- $\Psi_{\mathfrak{e}}$ has a component in the space spanned by the electron viscous stress tensor.

Electron heat flux $\boldsymbol{q}_{\mathfrak{e}}$

Finally, the electron heat flux at order ε^0 is obtained by injecting (2.4.5) into (2.3.21). Thus, we obtain

$$\boldsymbol{q}_{\mathfrak{e}} = -\bar{\bar{\lambda}}'_{\mathfrak{e}}\boldsymbol{\partial}_x T_{\mathfrak{e}} - p_{\mathfrak{e}}\bar{\bar{\theta}}_{\mathfrak{e}}\boldsymbol{d}_{\mathfrak{e}} + \rho_{\mathfrak{e}}h_{\mathfrak{e}}\boldsymbol{V}_{\mathfrak{e}}, \tag{2.4.15}$$

where the components of the partial electron thermal conductivity tensor are given by

$$\begin{aligned}
\lambda'^{\parallel}_{\mathfrak{e}} &= \frac{1}{3T_{\mathfrak{e}}^2} M_{\mathfrak{h}} \left[\!\!\left[\boldsymbol{\varphi}_{\mathfrak{e}}^{\lambda'_{\mathfrak{e}}(1)}, \boldsymbol{\varphi}_{\mathfrak{e}}^{\lambda'_{\mathfrak{e}}(1)} \right]\!\!\right]_{\mathfrak{e}}, \\
\lambda'^{\perp}_{\mathfrak{e}} &= \frac{1}{3T_{\mathfrak{e}}^2} M_{\mathfrak{h}} \left[\!\!\left[\boldsymbol{\varphi}_{\mathfrak{e}}^{\lambda'_{\mathfrak{e}}(1)}, \boldsymbol{\varphi}_{\mathfrak{e}}^{\lambda'_{\mathfrak{e}}(1)} \right]\!\!\right]_{\mathfrak{e}}, \\
\lambda'^{\odot}_{\mathfrak{e}} &= -\frac{1}{3T_{\mathfrak{e}}^2} M_{\mathfrak{h}} \left(\left(\boldsymbol{\varphi}_{\mathfrak{e}}^{\lambda'_{\mathfrak{e}}(2)}, \boldsymbol{\varphi}_{\mathfrak{e}}^{\lambda'_{\mathfrak{e}}(2)} \right) \right)_{\mathfrak{e}},
\end{aligned} \tag{2.4.16}$$

Using the definition previously introduced in (2.4.12), the electron heat flux $\boldsymbol{q}_{\mathfrak{e}}$ can be rewritten as

$$\boldsymbol{q}_{\mathfrak{e}} = -\bar{\bar{\lambda}}_{\mathfrak{e}} \boldsymbol{\partial}_{\boldsymbol{x}} T_{\mathfrak{e}} + p_{\mathfrak{e}} \bar{\bar{\chi}}_{\mathfrak{e}} \boldsymbol{V}_{\mathfrak{e}} + \rho_{\mathfrak{e}} h_{\mathfrak{e}} \boldsymbol{V}_{\mathfrak{e}} \tag{2.4.17}$$

where the electron thermal conductivity tensor is defined as

$$\bar{\bar{\lambda}}_{\mathfrak{e}} = \bar{\bar{\lambda}}'_{\mathfrak{e}} - n_{\mathfrak{e}} \bar{\bar{\chi}}_{\mathfrak{e}} \bar{\bar{\theta}}_{\mathfrak{e}}. \tag{2.4.18}$$

Physically, the first term of the electron heat flux in (2.4.15) represents the Fourier's classical law. The second term is the heat diffusion due to 1-the gradient of the electron partial pressure (known as the Soret effect) and 2-the electro magnetic-force. The third term corresponds to the transfer of electron energy by diffusion of the enthalpy of the electrons.

2.4.3 Heavy-particle transport fluxes at order ε: $\boldsymbol{V}_i$, $\boldsymbol{\Pi}_{\mathfrak{h}}$ and $\boldsymbol{q}_{\mathfrak{h}}$

In this subsection, we derive the heavy particle transport fluxes at order ε of the Chapman-Enskog expansion. At this order, the expressions of $\boldsymbol{q}_{\mathfrak{h}}$, $\boldsymbol{\Pi}_{\mathfrak{h}}$ and $\boldsymbol{V}_i$ are obtained. In order to obtain the heavy transport fluxes, it is necessary to obtain the expression of the first-order heavy-particle perturbation function $\phi_{\mathfrak{h}}$.

We rewrite (2.3.12) as follows

$$\mathcal{F}_i(\phi_{\mathfrak{h}}) = \Psi_i + \frac{1}{f_i^0} \left[\mathcal{J}_{i\mathfrak{e}}^1 \left(f_i^0, f_{\mathfrak{e}}^0 \phi_{\mathfrak{e}} \right) + \mathcal{J}_{i\mathfrak{e}}^2 \left(f_i^0, f_{\mathfrak{e}}^0 \right) \right], \quad i \in \mathrm{H}. \tag{2.4.19}$$

where $\Psi_i = -\mathcal{D}_i^0 \left(f_i^0 \right) / f_i^0$, $i \in \mathrm{H}$. Similarly as the previous section, after some algebra based on the expression of f_i^0, we obtain

$$\mathcal{F}_i(\phi_{\mathfrak{h}}) = -\boldsymbol{\Psi}_i^{\nu_{\mathfrak{h}}} : \boldsymbol{\partial}_{\boldsymbol{x}} \boldsymbol{v}_{\mathfrak{h}} - p_{\mathfrak{h}} \sum_{j \in \mathrm{H}} \boldsymbol{\Psi}_i^{D_j} \cdot \boldsymbol{d}_j - \boldsymbol{\Psi}_i^{\lambda'_{\mathfrak{h}}} \cdot \boldsymbol{\partial}_{\boldsymbol{x}} \left(\frac{1}{T_{\mathfrak{h}}} \right) - \Psi_i^{\Theta} \left(T_{\mathfrak{e}} - T_{\mathfrak{h}} \right), \tag{2.4.20}$$

where

$$\begin{cases} \boldsymbol{\Psi}_i^{\nu_\mathfrak{h}} = \dfrac{m_i}{T_\mathfrak{h}}\left(\boldsymbol{C}_i{\otimes}\boldsymbol{C}_i - \dfrac{1}{3}\boldsymbol{C}_i{\cdot}\boldsymbol{C}_i\mathbb{I}\right), & i \in \mathrm{H} \\ \boldsymbol{\Psi}_i^{D_j} = \dfrac{1}{M_\mathfrak{h} p_i}\left(\delta_{ij} - \dfrac{\rho_i}{\rho_\mathfrak{h}}\right)\boldsymbol{C}_i, & i,j \in \mathrm{H} \\ \boldsymbol{\Psi}_i^{\lambda'_\mathfrak{h}} = \dfrac{1}{M_\mathfrak{h}}\left(\dfrac{5}{2}T_\mathfrak{h} - \dfrac{1}{2}m_i\boldsymbol{C}_i{\cdot}\boldsymbol{C}_i\right)\boldsymbol{C}_i, & i \in \mathrm{H} \\ \Psi_i^{\Theta} = \dfrac{2}{T_\mathfrak{h}^2}\left(\dfrac{\nu_{i\mathfrak{e}}}{3m_i} - \displaystyle\sum_{j\in\mathrm{H}}\dfrac{n_j\nu_{j\mathfrak{e}}}{n_\mathfrak{h} m_j}\right)\left(\dfrac{3}{2}T_\mathfrak{h} - \dfrac{1}{2}m_i\boldsymbol{C}_i{\cdot}\boldsymbol{C}_i\right), & i \in \mathrm{H} \end{cases} \tag{2.4.21}$$

and the family of diffusion driving forces is defined as

$$\boldsymbol{d}_i = \frac{1}{p_\mathfrak{h}}\boldsymbol{\partial}_{\boldsymbol{x}} p_i - \frac{n_i q_i}{p_\mathfrak{h}}\boldsymbol{E}' - \frac{n_i M_\mathfrak{h}}{p_\mathfrak{h}}\boldsymbol{F}_{ie}, \quad i \in \mathrm{H}. \tag{2.4.22}$$

Note that, in Braginskii (1965), the equation on $\phi_\mathfrak{h}$ which gives the expression of the transport fluxes for heavy particles is similar to (2.4.20) except that, 1- $\boldsymbol{\varphi}_\mathfrak{h}^{D_j}$ and $\varphi_\mathfrak{h}^{\Theta}$ are not considered and 2- an additional term on the left-hand side is considered, which gives the anisotropic property of the heavy-particle transport coefficients.

Resolution of (2.4.19): expression of $\phi_\mathfrak{h}$

For the complete resolution of (2.4.19), we refer to the proof of the proposition 5.5. of Graille et al. (2009). The solution $\phi_\mathfrak{h} = \left(\phi_i\right)_{i\in\mathrm{H}}$ of (2.4.19) is given by

$$\phi_i = -\boldsymbol{\varphi}_i^{\nu_\mathfrak{h}} : \boldsymbol{\partial}_{\boldsymbol{x}}\boldsymbol{v}_\mathfrak{h} - p_\mathfrak{h}\sum_{j\in\mathrm{H}}\boldsymbol{\varphi}_i^{D_j}\cdot\boldsymbol{d}_j - \boldsymbol{\varphi}_i^{\lambda'_\mathfrak{h}}\cdot\boldsymbol{\partial}_{\boldsymbol{x}}\left(\frac{1}{T_\mathfrak{h}}\right) - \varphi_i^{\Theta}\left(T_\mathfrak{e} - T_\mathfrak{h}\right), \quad i \in \mathrm{H} \tag{2.4.23}$$

where the family of tensorial functions $\boldsymbol{\varphi}_\mathfrak{h}^{\nu_\mathfrak{h}} = \left(\boldsymbol{\varphi}_i^{\nu_\mathfrak{h}}\right)_{i\in\mathrm{H}}$, the families of vectorial functions $\boldsymbol{\varphi}_\mathfrak{h}^{D_j} = \left(\boldsymbol{\varphi}_i^{D_j}\right)_{i\in\mathrm{H}}$, $j \in \mathrm{H}$ and $\boldsymbol{\varphi}_\mathfrak{h}^{\lambda'_\mathfrak{h}} = \left(\boldsymbol{\varphi}_i^{\lambda'_\mathfrak{h}}\right)_{i\in\mathrm{H}}$, and the family of scalar function $\varphi_\mathfrak{h}^{\Theta} = \left(\varphi_i^{\Theta}\right)_{i\in\mathrm{H}}$ are solutions to

$$\mathcal{F}_i\left(\boldsymbol{\varphi}_\mathfrak{h}^{\mu}\right) = \boldsymbol{\Psi}_i^{\mu}, \quad i \in \mathrm{H}, \tag{2.4.24}$$

under the scalar constraints

$$\langle\!\langle f_\mathfrak{h}^0\boldsymbol{\varphi}_\mathfrak{h}^{\mu}, \psi_\mathfrak{h}^l\rangle\!\rangle_\mathfrak{h} = 0, \quad l \in \{1, ..., n^{\mathrm{H}} + 4\} \tag{2.4.25}$$

with $\mu \in \{\nu_\mathfrak{h}, \left(D_j\right)_{j\in\mathrm{H}}, \lambda'_\mathfrak{h}, \Theta\}$.

Heavy-particle diffusion velocity $\boldsymbol{V}_i$

Similarly as the previous section, in order to properly define the heavy-particle transport coefficient, we introduce a heavy-particle bracket operator $[\![\cdot,\cdot]\!]_{\mathfrak{h}}$. For any $\xi_{\mathfrak{h}}$ and $\zeta_{\mathfrak{h}}$, we define

$$[\![\xi_{\mathfrak{h}},\zeta_{\mathfrak{h}}]\!]_{\mathfrak{h}} = \langle\!\langle f_{\mathfrak{h}}^{0}\xi_{\mathfrak{h}}, \mathcal{F}_{\mathfrak{h}}(\zeta_{\mathfrak{h}})\rangle\!\rangle_{\mathfrak{h}} \tag{2.4.26}$$

The bracket operator $[\![\cdot,\cdot]\!]_{\mathfrak{h}}$ is symmetric, i.e., $[\![\xi_{\mathfrak{h}},\zeta_{\mathfrak{h}}]\!]_{\mathfrak{h}} = [\![\zeta_{\mathfrak{h}},\xi_{\mathfrak{h}}]\!]_{\mathfrak{h}}$, positive semi-definite, $[\![\xi_{\mathfrak{h}},\xi_{\mathfrak{h}}]\!]_{\mathfrak{h}} \geq 0$.

In order to obtain an expression of the diffusion velocity of the heavy-particle, we inject the solution of the perturbation function of the heavy-particle in (2.4.23) into (2.3.24). We obtain the following expression

$$\boldsymbol{V}_i = -\sum_{j\in\mathrm{H}} D_{ij}\boldsymbol{d}_j - \frac{\theta_i^{\mathfrak{h}}}{T_{\mathfrak{h}}}\boldsymbol{\partial}_{\boldsymbol{x}}T_{\mathfrak{h}}, \quad i\in\mathrm{H}, \tag{2.4.27}$$

where the heavy-particle diffusion and thermal diffusion coefficients are given by

$$D_{ij} = \frac{1}{3}p_{\mathfrak{h}}T_{\mathfrak{h}}M_{\mathfrak{h}}\left[\!\!\left[\boldsymbol{\varphi}_{\mathfrak{h}}^{D_i},\boldsymbol{\varphi}_{\mathfrak{h}}^{D_j}\right]\!\!\right]_{\mathfrak{h}}, \quad i,j\in\mathrm{H} \tag{2.4.28}$$

$$\theta_i^{\mathfrak{h}} = -\frac{1}{3}M_{\mathfrak{h}}\left[\!\!\left[\boldsymbol{\varphi}_{\mathfrak{h}}^{D_i},\boldsymbol{\varphi}_{\mathfrak{h}}^{\lambda'_{\mathfrak{h}}}\right]\!\!\right]_{\mathfrak{h}}, \quad i\in\mathrm{H} \tag{2.4.29}$$

Similarly as the previous section, an alternative expression of the heavy particle diffusion velocity can be obtained by factorizing (2.4.27) with the heavy particle diffusion coefficient D_{ij}, as follows

$$\boldsymbol{V}_i = -\sum_{j\in\mathrm{H}} D_{ij}\left(\boldsymbol{d}_j + \frac{\chi_{\mathfrak{h},j}}{T_{\mathfrak{h}}}\boldsymbol{\partial}_{\boldsymbol{x}}T_{\mathfrak{h}}\right), \quad i\in\mathrm{H}. \tag{2.4.30}$$

We point out that the heavy-particle thermal diffusion ratios, diffusion and thermal diffusion coefficients are linked with the following relations

$$\begin{cases} \displaystyle\sum_{j\in\mathrm{H}} D_{ij}\chi_{\mathfrak{h},j} = \theta_i^{\mathfrak{h}}, \\ \displaystyle\sum_{j\in\mathrm{H}} \chi_{\mathfrak{h},j} = 0. \end{cases} \tag{2.4.31}$$

Physically, the first term of (2.4.30) is related to the diffusion effects due to the pressure gradients and electromagnetic forces acting on each heavy particle $i\in\mathrm{H}$. The second term is related to the gradient of the temperature of the heavy-particles $T_{\mathfrak{h}}$, which is known as the Soret effect, as described by Magin & Degrez (2004). The heavy-particle diffusion velocities are thus proportional to the electron driving force and electron temperature gradient through the contribution of $\boldsymbol{F}_{ie}$ in the diffusion driving force $\boldsymbol{d}_i$ acting on the ith particle. Kolesnikov (2003) has already introduced electron heavy-particle diffusion coefficients and thermal diffusion coefficients to couple the heavy-particle diffusion velocities to the electron forces. In the following, such terms will be refered as the Kolesnikov effect for heavy particles.

Heavy particle viscous tensor $\boldsymbol{\Pi}_{\mathfrak{h}}$

By injecting the solution of the perturbation function of the heavy-particle (2.4.23) into (2.4.32), the heavy-particle viscous tensor is derived, as follows

$$\boldsymbol{\Pi}_{\mathfrak{h}} = -\nu_{\mathfrak{h}} \mathbf{S} \tag{2.4.32}$$

where

$$\mathbf{S} = \left(\boldsymbol{\partial}_{\boldsymbol{x}} \boldsymbol{v}_{\mathfrak{h}} + (\boldsymbol{\partial}_{\boldsymbol{x}} \boldsymbol{v}_{\mathfrak{h}})^{\top} - \tfrac{2}{3}(\boldsymbol{\partial}_{\boldsymbol{x}} \cdot \boldsymbol{v}_{\mathfrak{h}})\mathbb{I}\right), \tag{2.4.33}$$

and the heavy-particle viscosity is defined as

$$\nu_{\mathfrak{h}} = \frac{T_{\mathfrak{h}}}{10} \left[\!\!\left[\boldsymbol{\varphi}_{\mathfrak{h}}^{\nu_{\mathfrak{h}}}, \boldsymbol{\varphi}_{\mathfrak{h}}^{\nu_{\mathfrak{h}}} \right]\!\!\right]_{\mathfrak{h}}. \tag{2.4.34}$$

Heavy particle heat flux $\boldsymbol{q}_{\mathfrak{h}}$

Similarly, we inject $\phi_{\mathfrak{h}}$ of (2.4.23) into (2.3.28). We obtain the expression for the heavy-particle heat flux

$$\boldsymbol{q}_{\mathfrak{h}} = -\lambda'_{\mathfrak{h}} \boldsymbol{\partial}_{\boldsymbol{x}} T_{\mathfrak{h}} - p_{\mathfrak{h}} \sum_{j \in \mathrm{H}} \theta_j^{\mathfrak{h}} \boldsymbol{d}_j + \sum_{j \in \mathrm{H}} \rho_j h_j \boldsymbol{V}_j \tag{2.4.35}$$

where the heavy-particle partial thermal conductivity is given by

$$\lambda'_{\mathfrak{h}} = \frac{1}{3T_{\mathfrak{h}}^2} M_{\mathfrak{h}} \left[\!\!\left[\boldsymbol{\varphi}_{\mathfrak{h}}^{\lambda'_{\mathfrak{h}}}, \boldsymbol{\varphi}_{\mathfrak{h}}^{\lambda'_{\mathfrak{h}}} \right]\!\!\right]_{\mathfrak{h}}. \tag{2.4.36}$$

Similarly as the electron heat flux, the heavy-particle heat flux can be rewritten as

$$\boldsymbol{q}_{\mathfrak{h}} = -\lambda_{\mathfrak{h}} \boldsymbol{\partial}_{\boldsymbol{x}} T_{\mathfrak{h}} + p_{\mathfrak{h}} \sum_{j \in \mathrm{H}} \chi_{\mathfrak{h},j} \boldsymbol{V}_j + \sum_{j \in \mathrm{H}} \rho_j h_j \boldsymbol{V}_j \tag{2.4.37}$$

where the heavy-particle thermal conductivity is given by

$$\lambda_{\mathfrak{h}} = \lambda'_{\mathfrak{h}} - n_{\mathfrak{h}} \sum_{j \in \mathrm{H}} \chi_{\mathfrak{h},j} \theta_j^{\mathfrak{h}} \tag{2.4.38}$$

2.4.4 Electron transport fluxes at order ε: $\boldsymbol{V}_{\mathfrak{e}}^{(1)}$, $\boldsymbol{q}_{\mathfrak{e}}^{(1)}$ and $\boldsymbol{F}_{ie}$

In this section, we focus on the electron transport fluxes, at the order ε. At this order, the expressions of $\boldsymbol{V}_{\mathfrak{e}}^{(1)}$, $\boldsymbol{q}_{\mathfrak{e}}^{(1)}$ and $\boldsymbol{F}_{ie}$ are obtained. Having an expression of these transport fluxes required an expression of the second order perturbative function for electrons $\phi_{\mathfrak{e}}^2$ by solving (2.3.20). We rewrite (2.3.20) as follows

$$\mathcal{F}_{\mathfrak{e}}\left(\phi_{\mathfrak{e}}^2\right) + \delta_{b1} q_{\mathfrak{e}} \boldsymbol{\partial}_{\boldsymbol{C}_{\mathfrak{e}}} \left(f_{\mathfrak{e}}^0 \phi_{\mathfrak{e}}^2\right) \cdot \boldsymbol{C}_{\mathfrak{e}} \wedge \boldsymbol{B} = \Psi_{\mathfrak{e}}^2 \tag{2.4.39}$$

where

$$\Psi_{\mathfrak{e}}^2 = \frac{1}{f_{\mathfrak{e}}^0}\Bigg(- \mathcal{D}_{\mathfrak{e}}^0\left(f_{\mathfrak{e}}^0, \phi_{\mathfrak{e}}\right) + \mathcal{J}_{\mathfrak{e}\mathfrak{e}}\left(f_{\mathfrak{e}}^0\phi_{\mathfrak{e}}, f_{\mathfrak{e}}^0\phi_{\mathfrak{e}}\right) + \sum_{j\in \mathrm{H}}\left[\mathcal{J}_{\mathfrak{e}j}^0\left(f_{\mathfrak{e}}^0\phi_{\mathfrak{e}}, {f_j}^0\phi_j\right) + \mathcal{J}_{\mathfrak{e}j}^1\left(f_{\mathfrak{e}}^0, {f_j}^0\phi_j\right) + \mathcal{J}_{\mathfrak{e}j}^2\left(f_{\mathfrak{e}}^0, {f_j}^0\right)\right]\Bigg). \tag{2.4.40}$$

After some algebra based on the expression of $f_{\mathfrak{e}}^0$, an expression of $\Psi_{\mathfrak{e}}^2$ is obtained, as follows

$$\Psi_{\mathfrak{e}}^2 = -{\boldsymbol{\Psi}_{\mathfrak{e}}}^{\eta_{\mathfrak{e}}} \otimes \boldsymbol{\partial}_{\boldsymbol{x}} \boldsymbol{v}_{\mathfrak{h}} + p_{\mathfrak{e}} \sum_{j\in \mathrm{H}} {\boldsymbol{\Psi}_{\mathfrak{e}}}^{D_j} \cdot \boldsymbol{V}_j - \widetilde{\Psi_{\mathfrak{e}}^2} \tag{2.4.41}$$

where $\widetilde{\Psi_{\mathfrak{e}}^2}$ is a scalar function of $\boldsymbol{C}_{\mathfrak{e}}\cdot\boldsymbol{C}_{\mathfrak{e}}$, and

$$\begin{cases} {\boldsymbol{\Psi}_{\mathfrak{e}}}^{\eta_{\mathfrak{e}}} = \dfrac{1}{T_{\mathfrak{e}}}\left(\boldsymbol{C}_{\mathfrak{e}}\otimes\boldsymbol{C}_{\mathfrak{e}} - \dfrac{1}{3}\boldsymbol{C}_{\mathfrak{e}}\cdot\boldsymbol{C}_{\mathfrak{e}}\mathbb{I}\right), \\ {\boldsymbol{\Psi}_{\mathfrak{e}}}^{D_i} = \dfrac{n_i}{p_{\mathfrak{e}}T_{\mathfrak{e}}} Q_{ei}^{(1,1)}\left(|\boldsymbol{C}_{\mathfrak{e}}|^2\right)|\boldsymbol{C}_{\mathfrak{e}}|\boldsymbol{C}_{\mathfrak{e}}, \quad i \in \mathrm{H} \end{cases} \tag{2.4.42}$$

where $Q_{ei}^{(1,1)}$ is the nondimensional momentum cross-section as a function of $|\boldsymbol{C}_{\mathfrak{e}}|^2$ which will be discussed and described with further details in the Chapter 4.

Resolution of (2.4.39): expression of $\phi_{\mathfrak{e}}^2$

For further details about the resolution of (2.4.39), we refer to the proof of the proposition 5.9. of Graille et al. (2009). Note that, the complete solution of (2.4.39) is not necessary since only the expression of $\boldsymbol{V}_{\mathfrak{e}}^{(1)}$ and $\boldsymbol{q}_{\mathfrak{e}}^{(1)}$ is required in terms of bracket operators. Only the contribution of ${\boldsymbol{\Psi}_{\mathfrak{e}}}^{D_i}$ and ${\boldsymbol{\Psi}_{\mathfrak{e}}}^{D_{\mathfrak{e}}}$ will be investigated.

After some calculations performed by Graille et al. (2009), the scalar function $\phi_{\mathfrak{e}}^2$ is found to be

$$\phi_{\mathfrak{e}}^2 = -\boldsymbol{\varphi}_{\mathfrak{e}}^{\eta_{\mathfrak{e}}} : \boldsymbol{\partial}_{\boldsymbol{x}} \boldsymbol{v}_{\mathfrak{h}} + p_{\mathfrak{e}} \sum_{j\in \mathrm{H}} \Re\left[\boldsymbol{M}^{\parallel} {\boldsymbol{\varphi}_{\mathfrak{e}}}^{D_j(1)} + \left(\boldsymbol{M}^{\perp} + \mathtt{i}\boldsymbol{M}^{\circlearrowright}\right){\boldsymbol{\varphi}_{\mathfrak{e}}}^{D_j(2)}\right]\cdot\boldsymbol{V}_j - \widetilde{\varphi_{\mathfrak{e}}^2} \tag{2.4.43}$$

where the vectorial functions ${\boldsymbol{\varphi}_{\mathfrak{e}}}^{D_j(2)}$ and ${\boldsymbol{\varphi}_{\mathfrak{e}}}^{D_j(1)}$ are solutions to the equations

$$\mathcal{F}_{\mathfrak{e}}({\boldsymbol{\varphi}_{\mathfrak{e}}}^{D_i(1)}) = {\boldsymbol{\Psi}_{\mathfrak{e}}}^{D_i}, \tag{2.4.44a}$$

$$\left(\mathcal{F}_{\mathfrak{e}} + \mathtt{i}|\boldsymbol{B}|\mathcal{F}_{\mathfrak{e}}^{q_{\mathfrak{e}}}\right)({\boldsymbol{\varphi}_{\mathfrak{e}}}^{D_i(2)}) = {\boldsymbol{\Psi}_{\mathfrak{e}}}^{D_i}, \tag{2.4.44b}$$

under the constraints

$$\langle\!\langle f_{\mathfrak{e}}^0 {\boldsymbol{\varphi}_{\mathfrak{e}}}^{D_i(1)}, \psi_{\mathfrak{e}}^l\rangle\!\rangle_{\mathfrak{e}} = 0, \quad l \in \{1,2\} \tag{2.4.45a}$$

$$\langle\!\langle f_{\mathfrak{e}}^0 {\boldsymbol{\varphi}_{\mathfrak{e}}}^{D_i(2)}, \psi_{\mathfrak{e}}^l\rangle\!\rangle_{\mathfrak{e}} = 0, \quad l \in \{1,2\}. \tag{2.4.45b}$$

Note that, the tensorial function $\boldsymbol{\varphi}_{\mathfrak{e}}^{\eta_{\mathfrak{e}}}$ is also satisfying an equation that is not shown here. We also find that $\widetilde{\varphi_{\mathfrak{e}}^2}$ is a scalar function of $\boldsymbol{C}_{\mathfrak{e}}\cdot\boldsymbol{C}_{\mathfrak{e}}$ and $(\boldsymbol{C}_{\mathfrak{e}}\cdot\boldsymbol{B})^2$.

Second-order electron diffusion velocity $\boldsymbol{V}_{\mathfrak{e}}^{(1)}$

By injecting (2.4.43) into (2.3.27), we obtain the second-order electron diffusion velocity $\boldsymbol{V}_{\mathfrak{e}}^{(1)}$, as follows

$$\boldsymbol{V}_{\mathfrak{e}}^{(1)} = \sum_{j\in \mathrm{H}} \bar{\bar{\alpha}}_{\mathfrak{e}j}\boldsymbol{V}_j, \tag{2.4.46}$$

where the components of the tensor coupling term $\bar{\bar{\alpha}}_{\mathfrak{e}j}$ are defined as

$$\begin{aligned}
\alpha_{\mathfrak{e}i}^{\parallel} &= \frac{1}{3}p_{\mathfrak{e}}T_{\mathfrak{e}}\,M_{\mathfrak{h}}\left[\!\left[\boldsymbol{\varphi}_{\mathfrak{e}}^{D_{\mathfrak{e}}(1)},\boldsymbol{\varphi}_{\mathfrak{e}}^{D_i(1)}\right]\!\right]_{\mathfrak{e}}, \quad i\in \mathrm{H},\\
\alpha_{\mathfrak{e}i}^{\perp} &= \frac{1}{3}p_{\mathfrak{e}}T_{\mathfrak{e}}\,M_{\mathfrak{h}}\left[\!\left[\boldsymbol{\varphi}_{\mathfrak{e}}^{D_{\mathfrak{e}}(2)},\boldsymbol{\varphi}_{\mathfrak{e}}^{D_i(2)}\right]\!\right]_{\mathfrak{e}}, \quad i\in \mathrm{H},\\
\alpha_{\mathfrak{e}i}^{\odot} &= -\frac{1}{3}p_{\mathfrak{e}}T_{\mathfrak{e}}\,M_{\mathfrak{h}}\left(\left(\boldsymbol{\varphi}_{\mathfrak{e}}^{D_{\mathfrak{e}}(2)},\boldsymbol{\varphi}_{\mathfrak{e}}^{D_i(2)}\right)\right)_{\mathfrak{e}}, \quad i\in \mathrm{H}.
\end{aligned} \tag{2.4.47}$$

In this framework, the second-order electron diffusion velocity is proportional to the heavy-particle diffusion velocity; known as the Kolesnikov effect for the electrons, as described by Kolesnikov (2003).

Second-order electron heat flux $\boldsymbol{q}_{\mathfrak{e}}^{(1)}$

The second-order electron heat flux is obtained by injecting (2.4.43) into (2.4.48). Thus, we obtain

$$\boldsymbol{q}_{\mathfrak{e}}^{(1)} = p_{\mathfrak{e}}\sum_{i\in \mathrm{H}}\bar{\bar{\chi}}_{\mathfrak{e}i}\boldsymbol{V}_i + \rho_{\mathfrak{e}}h_{\mathfrak{e}}\boldsymbol{V}_{\mathfrak{e}}^{(1)} \tag{2.4.48}$$

where the second-order electron thermal diffusion ratios reads

$$\begin{aligned}
\chi_{\mathfrak{e}i}^{\parallel} &= -\frac{1}{3}M_{\mathfrak{h}}\left[\!\left[\boldsymbol{\varphi}_{\mathfrak{e}}^{D_i(1)},\boldsymbol{\varphi}_{\mathfrak{e}}^{\lambda'_{\mathfrak{e}}(1)}\right]\!\right]_{\mathfrak{e}}, \quad i\in \mathrm{H},\\
\chi_{\mathfrak{e}i}^{\perp} &= -\frac{1}{3}M_{\mathfrak{h}}\left[\!\left[\boldsymbol{\varphi}_{\mathfrak{e}}^{D_i(2)},\boldsymbol{\varphi}_{\mathfrak{e}}^{\lambda'_{\mathfrak{e}}(2)}\right]\!\right]_{\mathfrak{e}}, \quad i\in \mathrm{H},\\
\chi_{\mathfrak{e}i}^{\odot} &= \frac{1}{3}M_{\mathfrak{h}}\left(\left(\boldsymbol{\varphi}_{\mathfrak{e}}^{D_i(2)},\boldsymbol{\varphi}_{\mathfrak{e}}^{\lambda'_{\mathfrak{e}}(2)}\right)\right)_{\mathfrak{e}}, \quad i\in \mathrm{H}.
\end{aligned} \tag{2.4.49}$$

Note that, the second order thermal diffusion ratios satisfies the following relation

$$\sum_{i\in \mathrm{H}}\chi_{\mathfrak{e}i}^{\parallel} = 0 \quad \text{and} \quad \sum_{i\in \mathrm{H}}\left(\chi_{\mathfrak{e}i}^{\perp} + \mathtt{i}\chi_{\mathfrak{e}i}^{\odot}\right) = 0. \tag{2.4.50}$$

Average electron heavy particle force $\boldsymbol{F}_{ie}$

Finally, as done previously, the average electron force acting on i heavy-particles $\boldsymbol{F}_{ie}$ is defined as

$$\boldsymbol{F}_{ie} = -\frac{p_e}{n_i M_h}\bar{\bar{\alpha}}_{ei}\boldsymbol{d}_e - \frac{p_e}{n_i M_h}\frac{\bar{\bar{\chi}}_{ei}}{T_e}\boldsymbol{\partial}_x T_e \tag{2.4.51}$$

where the tensors of coupling terms $\bar{\bar{\alpha}}_{ei}$ and $\bar{\bar{\chi}}_{ei}$ are defined in terms of bracket operators in (2.4.47) and (2.4.49) respectively.

2.4.5 Weakly magnetized plasma, case $b = 0$

In this subsection, we show a summary of the derivation of the transport fluxes obtained by Graille et al. (2009) in the case of weakly magnetized plasmas, *i.e.*, $b = 0$. The full derivation is not shown here. The unmagnetized plasma case is not investigated here. This case is not relevant for our applications.

Mostly, in the case of weakly and unmagnetized plasmas, the transport fluxes for heavy particles are identical as those found in the strongly magnetized case, in the previous section. Indeed, according to the scaling introduced, the transport fluxes for heavy particles do not depend on the magnitude of the magnetic field.

However, in the case of the electron transport fluxes, the electron and electron-heavy particle transport coefficients tensors are isotropic in the case of weakly magnetized plasma ($b = 0$). In this framework, using the notation introduced in Section 2.4.1, we simply obtain that

$$\bar{\bar{\mu}} = \mu^{\parallel}\mathbb{I}, \quad \mu \in \{\bar{\bar{D}}_e, \bar{\bar{\theta}}_e, \bar{\bar{\chi}}_e, \bar{\bar{\alpha}}_{ei}, \bar{\bar{\chi}}_{ei}\}, \quad i \in \mathrm{H}. \tag{2.4.52}$$

Only the parallel component of each tensor is considered. Consequently, the expressions of the electron transport fluxes, presented in the previous section, are simplified.

Conclusion

In this Chapter, we have focused on the model derived by Graille et al. (2009). A dimensional analysis has been performed by introducing nondimensional parameters and reference quantities that are presented in Table 2.1 and Table 2.2. This analysis is based on the parameters ε and Kn, which are assumed to be small. Additionally, the Debye length scale and the nondimensional parameter ε_{λ_D} in the analysis have been introduced.

The nondimensional Boltzmann equations (B_e) and ($\mathrm{B}_{i\in\mathrm{H}}$), have been obtained, for the electrons and heavy-particles respectively. Due to the dimensional analysis performed through the ε parameter, the Boltzmann equation for electrons is showing a parabolic scaling whereas the Boltzmann equations for heavy-particles is showing an hyperbolic scaling. Then, the nondimensional Maxwell's equations have been coupled to the Boltzmann equations, by choosing a scaling consis-

tent with the one proposed by Graille et al. (2009). Finally, we have highlighted that the proposed scaling is performed at three levels: in the kinetic equations, in the crossed collision operators and in the collision invariants. In particular, the space spanned by the electron momentum is not in the space of collision invariants, therefore, no equation of conservation of the electron momentum has been obtained in the derivation of the fluid model. However, as shown in Section 2.3.6, an electron momentum relations can be obtained.

Then, a Chapman-Enskog expansion has been performed on the nondimensional Boltzmann equations to derive the macroscopic equations, as presented in Table 2.3. The model has been established in the heavy-particle reference frame, where all the species of the multicomponent plasma diffuse in this reference frame. The proposed model is valid in the solar atmosphere conditions, including conditions where the electroneutrality is not assumed. The proposed model has an extended range of validity for partially and fully ionized plasma, for non and weakly magnetized plasmas and general multicomponent mixtures, including thermal nonequilibrium processes between electrons and heavy-particles. A comparison with the approach of Braginskii (1965) has been performed. Unlike Braginskii (1965), the asymptotic analysis of the normalized Boltzmann equations shows several processes occurring at different time-scales. In the derivation of Braginskii (1965), no multiscale analysis has been performed on the Boltzmann equations and the expansion of the distribution functions for electrons and heavy-particles are performed up to the first order. The Navier-Stokes equations for both electrons and heavy-particles have been obtained in the approach of Braginskii (1965). In the multiscale approach, the Navier-Stokes equations for heavy-particles ($M_{\mathfrak{h}}^{\varepsilon=1}$) and first order drift diffusion equations for electrons ($M_{\mathfrak{e}}^{\varepsilon=1}$), have been derived. In addition, since the scaling between the two approaches are different, differences have been obtained in the equation of the perturbative functions. Therefore, the structure of the transport properties in the two models are different. In particular, the transport properties for electrons and heavy particles are both anisotropic in Braginskii (1965), whereas, only the electrons are magnetized in the case of Graille et al. (2009). Further details on the comparison between the two approaches are given in Chapter 5.

Finally, the transport fluxes of the model have been presented. In particular, the electron transport fluxes at order ε^0 and ε, and the heavy-particle transport fluxes have been exhibited. The transport coefficients have been expressed in terms of bracket integrals. The electron viscous stress tensor is shown to vanish due to our multiscale analysis, and some new terms such as Soret/dufour effect or Kolesnikov effect have been obtained in the transport fluxes of the model. Further details on the transport properties of the model will be given in Chapter 4.

CHAPTER 3

MULTICOMPONENT PLASMA EQUATIONS UNDER THE ELECTRONEUTRALITY ASSUMPTION

Introduction

In the previous Chapter, the model derived by Graille et al. (2009) coupled to the set of Maxwell equations has been presented. The model has been obtained from a multiscale analysis of the Boltzmann equations based on the nondimensional parameters ε and Kn. A dimensional analysis has been performed on the Maxwell equations to be consistent with the scaling introduced by Graille et al. (2009). Then, a generalized Chapman-Enskog expansion has been performed. At the last order investigated ε, the Navier-Stokes equations and first-order drift diffusion equations have been obtained for the heavy-particles and electrons respectively. The obtained model has an extended range of validity for partially and fully ionized plasma, for non- and weakly- magnetized plasma and general multicomponent mixtures, including thermal nonequilibrium processes between electrons and heavy-particles.

Considering the level of complexity of the general model developed in the previous Chapter, we simplify it in the framework of our application. Indeed, in the solar atmosphere, the characteristic macroscopic scales are much larger than the Debye length scale. Therefore, the electroneutrality is assumed.

In this Chapter, we have focused on the coupling between the general model and the set of Maxwell equations at order ε^0. At this order of the expansion, the electroneutrality is assumed since the global charge nq is assumed to be small, at order ε in the law of Gauss. This coupling allows a simplification of the general model which leads to the multicomponent model.

As performed by Torrilhon (2003), the eigenstructure of the multicomponent model is studied. The system is composed of convective, diffusive and source terms. The source terms are composed of two terms: relaxation and nonconservative terms. The relaxation terms are due to the relaxation of the temperature of electrons towards the temperature of heavy-particles. The non-

conservative terms are considered in the equation of internal energy of electrons, due to the term $p_e \partial_x \cdot v_h$ and the Joule effect. The impact of these nonconservative terms on the eigenstructure of the multicomponent model is highlighted.

In this Chapter, we have focused on the strongly magnetized case, where $b = 1$. In Section 3.1, we present the general governing equations at order ε coupled to the set of Maxwell equations (Mx^{ε}). Then, we derive a generalized Ohm's law, to obtain an expression of the total current and electric field as function of the transport fluxes. We provide a new definition of the resistivity, which appears to be general, taking into account all the possible interactions in the mixture considered. Then, in Section 3.2, we derive the simplified multicomponent model for our solar physics application, by coupling the general model to the set of Maxwell's equations ($Mx^{\varepsilon=0}$), where the electroneutrality is assumed at order ε^0. We provide a conservative form of the system of equations and a simplification of the generalized Ohm's law. A comparison with the multi-fluid approach is provided. Then, in Section 3.3, we investigate the simplified case where the plasma is fully ionized. The model is simplified and some classical terms can be identified. Finally, in Section 3.4, we study the eigenstructure of the multicomponent model.

3.1 General governing equations coupled to Maxwell's equations (Mx^{ε})

In this section, we present the set of general governing equations at order ε, corresponding to ($M_h^{\varepsilon=1}$) for the heavy particles and ($M_e^{\varepsilon=1}$) for the electrons coupled to the set of Maxwell's equations at order ε defined in (Mx^{ε}). We present the system in the strongly-magnetized case, where $b = 1$. Then, a generalized Ohm's law is derived. This derivation is based on the coupling between the electric field $\boldsymbol{E}$ and the transport fluxes defined in Section 2.4. The goal of this section is to show the general set of equations at order ε which will be simplified in the next section under the electroneutrality assumption.

First, the general set of macroscopic equations coupled to the set of Maxwell equations (Mx^{ε}) is presented. Then, the generalized Ohm's law is derived.

3.1.1 Set of macroscopic equations at order ε

In this section, we focus on the heavy-particle Navier-Stokes equations ($M_h^{\varepsilon=1}$) and electron drift diffusion equations ($M_e^{\varepsilon=1}$). A total energy, mass and internal energy conservation equation are also derived from these equations. The set of equations is coupled to the set of Maxwell equations defined in (Mx^{ε}).

Mass conservation

At order ε, the species mass conservations read

$$\partial_t \rho_i + \boldsymbol{\partial_x}\cdot\left[\rho_i\left(\boldsymbol{v}_\mathfrak{h} + \frac{\varepsilon}{M_\mathfrak{h}}\boldsymbol{V}_i\right)\right] = 0, \quad i \in \mathrm{H}, \tag{3.1.1}$$

$$\partial_t \rho_\mathfrak{e} + \boldsymbol{\partial_x}\cdot\left[\rho_\mathfrak{e}\left(\boldsymbol{v}_\mathfrak{h} + \frac{1}{M_\mathfrak{h}}(\boldsymbol{V}_\mathfrak{e} + \varepsilon\boldsymbol{V}_\mathfrak{e}^{(1)})\right)\right] = 0. \tag{3.1.2}$$

Note that, by suming (3.1.1) over all the heavy particles, we obtain the heavy-particle mass conservation equation, as follows

$$\partial_t \rho_\mathfrak{h} + \boldsymbol{\partial_x}\cdot(\rho_\mathfrak{h}\boldsymbol{v}_\mathfrak{h}) = 0. \tag{3.1.3}$$

Using (3.1.3), we found that the hydrodynamic velocity frame of the mixture is defined as

$$\rho\boldsymbol{v} = \rho_\mathfrak{h}\boldsymbol{v}_\mathfrak{h} + \varepsilon^2\rho_\mathfrak{e}\left(\boldsymbol{v}_\mathfrak{h} + \frac{1}{M_\mathfrak{h}}\left(\boldsymbol{V}_\mathfrak{e} + \boldsymbol{V}_\mathfrak{e}^{(1)}\right)\right), \tag{3.1.4}$$

where the total density is $\rho = \rho_\mathfrak{h} + \varepsilon^2\rho_\mathfrak{e}$ and a conservation equation of global mass is obtained in the hydrodynamic velocity frame, *i.e.*,

$$\partial_t \rho + \boldsymbol{\partial_x}\cdot(\rho\boldsymbol{v}) = 0. \tag{3.1.5}$$

Momentum equation for heavy-particles

At order ε, the momentum equation for heavy-particles reads

$$\partial_t\left(\rho_\mathfrak{h}\boldsymbol{v}_\mathfrak{h}\right) + \boldsymbol{\partial_x}\cdot\left(\rho_\mathfrak{h}\boldsymbol{v}_\mathfrak{h}\otimes\boldsymbol{v}_\mathfrak{h} + \frac{1}{M_\mathfrak{h}^2}p\mathbb{I}\right) = -\frac{\varepsilon}{M_\mathfrak{h}^2}\boldsymbol{\partial_x}\cdot(\boldsymbol{\Pi}_\mathfrak{h}) + \frac{1}{M_\mathfrak{h}^2}nq\boldsymbol{E} + [\delta_{b0}\mathbf{I}_0 + \delta_{b1}\mathbf{I}]\wedge\boldsymbol{B}, \tag{3.1.6}$$

We recall that, since the electron viscous stress tensor is vanishing, the electrons participate in the momentum balance through the total pressure gradient p and the Lorentz force $1/M_\mathfrak{h}^2 nq\boldsymbol{E} + [\delta_{b0}\mathbf{I}_0 + \delta_{b1}\mathbf{I}]\wedge\boldsymbol{B}$.

In addition, we remind that no momentum equation for electrons has been obtained in the derivation due to the multiscale approach performed in the previous Chapter.

Energy equations

By multiplying (3.1.6) by the mean heavy-particle velocity, we obtain an equation on the kinetic energy

$$\partial_t\left(\frac{1}{2}\rho_{\mathfrak{h}}|\boldsymbol{v}_{\mathfrak{h}}|^2\right)+\boldsymbol{\partial_x}\cdot\left[\boldsymbol{v}_{\mathfrak{h}}\left(\frac{1}{2}\rho_{\mathfrak{h}}|\boldsymbol{v}_{\mathfrak{h}}|^2+\frac{1}{M_{\mathfrak{h}}^2}p\right)\right]$$
$$=\frac{1}{M_{\mathfrak{h}}^2}p\boldsymbol{\partial_x}\cdot\boldsymbol{v}_{\mathfrak{h}}-\frac{\varepsilon}{M_{\mathfrak{h}}^2}\boldsymbol{v}_{\mathfrak{h}}\cdot\boldsymbol{\partial_x}\cdot\boldsymbol{\Pi}_{\mathfrak{h}}+\frac{1}{M_{\mathfrak{h}}^2}nq\boldsymbol{E}\cdot\boldsymbol{v}_{\mathfrak{h}}+\boldsymbol{v}_{\mathfrak{h}}\cdot(\delta_{b0}\mathbf{I}_0+\delta_{b1}\mathbf{I})\wedge\boldsymbol{B}. \quad (3.1.7)$$

Then, from ($M_{\mathfrak{h}}^{\varepsilon=1}$) and ($M_{\mathfrak{e}}^{\varepsilon=1}$), we have the equation of internal energy of electrons and heavy particles

$$\partial_t(\rho_{\mathfrak{e}}e_{\mathfrak{e}})+\boldsymbol{\partial_x}\cdot(\rho_{\mathfrak{e}}e_{\mathfrak{e}}\boldsymbol{v}_{\mathfrak{h}})=-p_{\mathfrak{e}}\boldsymbol{\partial_x}\cdot\boldsymbol{v}_{\mathfrak{h}}-\frac{1}{M_{\mathfrak{h}}}\boldsymbol{\partial_x}\cdot\left(\boldsymbol{q}_{\mathfrak{e}}+\varepsilon\boldsymbol{q}_{\mathfrak{e}}^{(1)}\right)+\frac{1}{M_{\mathfrak{h}}}\left(\boldsymbol{J}_{\mathfrak{e}}+\varepsilon\boldsymbol{J}_{\mathfrak{e}}^{(1)}\right)\cdot\boldsymbol{E}'$$
$$+\delta_{b0}\varepsilon M_{\mathfrak{h}}\boldsymbol{J}_{\mathfrak{e}}\cdot\boldsymbol{v}_{\mathfrak{h}}\wedge\boldsymbol{B}+\Delta E_{\mathfrak{e}}^{(0)}+\varepsilon\Delta E_{\mathfrak{e}}^{(1)}, \quad (3.1.8)$$

$$\partial_t(\rho_{\mathfrak{h}}e_{\mathfrak{h}})+\boldsymbol{\partial_x}\cdot(\rho_{\mathfrak{h}}e_{\mathfrak{h}}\boldsymbol{v}_{\mathfrak{h}})=-(p_{\mathfrak{h}}\mathbb{I}+\varepsilon\boldsymbol{\Pi}_{\mathfrak{h}})\otimes\boldsymbol{\partial_x}\boldsymbol{v}_{\mathfrak{h}}-\frac{\varepsilon}{M_{\mathfrak{h}}}\boldsymbol{\partial_x}\cdot\boldsymbol{q}_{\mathfrak{h}}+\frac{\varepsilon}{M_{\mathfrak{h}}}\boldsymbol{J}_{\mathfrak{h}}\cdot\boldsymbol{E}'+\Delta E_{\mathfrak{h}}^{(0)}+\varepsilon\Delta E_{\mathfrak{h}}^{(1)} \quad (3.1.9)$$

Finally, a total energy can be derived by suming the equation of the total internal and kinetic energy. Thus, we obtain

$$\partial_t(\mathcal{E})+\boldsymbol{\partial_x}\cdot(\mathcal{H}\boldsymbol{v}_{\mathfrak{h}})=-\varepsilon\boldsymbol{\partial_x}\cdot(\boldsymbol{\Pi}_{\mathfrak{h}}\cdot\boldsymbol{v}_{\mathfrak{h}})-\frac{1}{M_{\mathfrak{h}}}\boldsymbol{\partial_x}\cdot\boldsymbol{Q}+\mathbf{I}\cdot\boldsymbol{E}, \quad (3.1.10)$$

where the total energy is $\mathcal{E}=\rho e+1/2\rho_{\mathfrak{h}}|\boldsymbol{v}_{\mathfrak{h}}|^2$, $\mathcal{H}=\mathcal{E}+p$ is the total enthalpy, the total heat flux is $\boldsymbol{Q}=\boldsymbol{q}_{\mathfrak{e}}+\varepsilon\boldsymbol{q}_{\mathfrak{e}}^{(1)}+\varepsilon\boldsymbol{q}_{\mathfrak{h}}$ and the total internal energy is $\rho e=\rho_{\mathfrak{h}}e_{\mathfrak{h}}+\rho_{\mathfrak{e}}e_{\mathfrak{e}}$. Note that the term $\mathbf{I}\cdot\boldsymbol{E}$ on the right hand-side of (3.1.10) represents the power developped by the electromagnetic field, where the form is prescribed by Poyntingś theorem.

In summary, from ($M_{\mathfrak{h}}^{\varepsilon=1}$) and ($M_{\mathfrak{e}}^{\varepsilon=1}$), we have reviewed the general governing equations and deduce a conservation equation of total mass and energy. In order to take into account the dynamic of the electromagnetic field, we have coupled these governing equations with the set of Maxwell equations, presented in (Mx^{ε}). This coupling allows to obtain an expression of the electric field as function of the transport fluxes.

3.1.2 Derivation of a generalized Ohm's law

Here, we derive a generalized Ohm's law, *i.e.*, we couple the electric field to the transport fluxes introduced in the previous Chapter.

First, we recall that the total current density $\mathbf{I}$ is written as

$$\mathbf{I}=\mathbf{I}_0+\frac{\varepsilon}{M_{\mathfrak{h}}}\left[\boldsymbol{J}_{\mathfrak{h}}+\boldsymbol{J}_{\mathfrak{e}}^{(1)}\right]=nq\boldsymbol{v}_{\mathfrak{h}}+\frac{1}{M_{\mathfrak{h}}}\boldsymbol{J}_{\mathfrak{e}}+\frac{\varepsilon}{M_{\mathfrak{h}}}\left[\boldsymbol{J}_{\mathfrak{h}}+\boldsymbol{J}_{\mathfrak{e}}^{(1)}\right],$$

where the current densities $\boldsymbol{J}_{\mathfrak{e}}$, $\boldsymbol{J}_{\mathfrak{h}}$ and $\boldsymbol{J}_{\mathfrak{e}}^{(1)}$ are defined in (2.3.17) and (2.3.26) respectively. As seen in Chapter 2, these current densities depend on the diffusion velocities. These velocities depend on the following transport coefficients

$$\bar{\bar{D}}_{\mathfrak{e}},\ \bar{\bar{\chi}}_{\mathfrak{e}},\ \bar{\bar{\alpha}}_{\mathfrak{e}i},\ D_{ij},\ \chi_{\mathfrak{h},j},\ \bar{\bar{\chi}}_{\mathfrak{e}i},\quad i,j \in \mathrm{H}$$

and driving forces

$$\boldsymbol{\partial}_{\boldsymbol{x}} p_{\mathfrak{e}},\ \frac{\boldsymbol{\partial}_{\boldsymbol{x}} T_{\mathfrak{e}}}{T_{\mathfrak{e}}},\ \boldsymbol{E}',\ \boldsymbol{\partial}_{\boldsymbol{x}} p_i,\ \frac{\boldsymbol{\partial}_{\boldsymbol{x}} T_{\mathfrak{h}}}{T_{\mathfrak{h}}}.$$

In addition, for the sake of simplicity, we define the tensor

$$\bar{\bar{\xi}}_{\mathfrak{e}i} = \frac{n_i q_i}{n_{\mathfrak{e}} q_{\mathfrak{e}}} \mathbb{I} + \bar{\bar{\alpha}}_{\mathfrak{e}i},\quad i \in \mathrm{H}. \tag{3.1.11}$$

In the following, we rewrite the expression of the electric current grouping the terms in each driving force. This step allows to obtain an expression of the electric field $\boldsymbol{E}$, as function of the transport coefficents and the driving forces.

Expression of the total current

Using (2.3.17) and (2.3.26), the first order conduction current reads

$$\boldsymbol{J}_{\mathfrak{h}} + \boldsymbol{J}_{\mathfrak{e}}^{(1)} = n_{\mathfrak{e}} q_{\mathfrak{e}} \sum_{j \in \mathrm{H}} \bar{\bar{\xi}}_{\mathfrak{e}j} \boldsymbol{V}_j. \tag{3.1.12}$$

Using the definition of the driving forces, the diffusion velocity of electron and heavy-particle can be written in terms of driving forces, as follows

$$\boldsymbol{V}_{\mathfrak{e}} = -\bar{\bar{D}}_{\mathfrak{e}} \left(\frac{\boldsymbol{\partial}_{\boldsymbol{x}} p_{\mathfrak{e}}}{p_{\mathfrak{e}}} - \frac{n_{\mathfrak{e}} q_{\mathfrak{e}}}{p_{\mathfrak{e}}} \boldsymbol{E}' \right) - \frac{1}{T_{\mathfrak{e}}} \bar{\bar{\theta}}_{\mathfrak{e}} \boldsymbol{\partial}_{\boldsymbol{x}} T_{\mathfrak{e}} \tag{3.1.13}$$

$$\boldsymbol{V}_i = -\sum_{j \in \mathrm{H}} D_{ij} \Bigg[\frac{\boldsymbol{\partial}_{\boldsymbol{x}} p_j}{p_{\mathfrak{h}}} - \frac{n_j q_j}{p_{\mathfrak{h}}} \boldsymbol{E}' + \frac{n_j}{p_{\mathfrak{h}}} \left(\frac{p_{\mathfrak{e}}}{n_j} \bar{\bar{\alpha}}_{\mathfrak{e}j} \left(\frac{\boldsymbol{\partial}_{\boldsymbol{x}} p_{\mathfrak{e}}}{p_{\mathfrak{e}}} - \frac{n_{\mathfrak{e}} q_{\mathfrak{e}}}{p_{\mathfrak{e}}} \boldsymbol{E}' \right) + \frac{p_{\mathfrak{e}}}{n_j} \frac{\bar{\bar{\chi}}_{\mathfrak{e}j}}{T_{\mathfrak{e}}} \boldsymbol{\partial}_{\boldsymbol{x}} T_{\mathfrak{e}} \right) \Bigg] - \frac{\theta_i^{\mathfrak{h}}}{T_{\mathfrak{h}}} \boldsymbol{\partial}_{\boldsymbol{x}} T_{\mathfrak{h}}. \tag{3.1.14}$$

We inject (3.1.13) and (3.1.14) into the definition of the total current density in (2.3.26). Finally, we express the total current in terms of transport coefficients and driving forces, as follows,

$$\mathbf{I} = nq\boldsymbol{v}_{\mathfrak{h}} + \frac{(n_{\mathfrak{e}}q_{\mathfrak{e}})^2}{p_{\mathfrak{e}}}\bar{\bar{\mathcal{M}}}_{\boldsymbol{E}'}\boldsymbol{E}' - n_{\mathfrak{e}}q_{\mathfrak{e}}\Bigg[\bar{\bar{\mathcal{M}}}_{p_{\mathfrak{e}}}\frac{\partial_{\boldsymbol{x}}p_{\mathfrak{e}}}{p_{\mathfrak{e}}} + \sum_{j\in\mathrm{H}}\bar{\bar{\mathcal{M}}}_{p_j}\frac{\partial_{\boldsymbol{x}}p_j}{p_{\mathfrak{h}}} + \bar{\bar{\mathcal{M}}}_{T_{\mathfrak{e}}}\frac{\partial_{\boldsymbol{x}}T_{\mathfrak{e}}}{T_{\mathfrak{e}}} + \bar{\bar{\mathcal{M}}}_{T_{\mathfrak{h}}}\frac{\partial_{\boldsymbol{x}}T_{\mathfrak{h}}}{T_{\mathfrak{h}}}\Bigg] \tag{3.1.15}$$

where the multicomponent electromagnetic matrices $\bar{\bar{\mathcal{M}}}$ are defined as

$$\bar{\bar{\mathcal{M}}}_{\boldsymbol{E}'} = \left(\frac{\varepsilon}{M_{\mathfrak{h}}}\right)\frac{p_{\mathfrak{e}}}{p_{\mathfrak{h}}}\left[\sum_{i\in\mathfrak{h}}\bar{\bar{\xi}}_{\mathfrak{e}i}\left(\sum_{j\in\mathfrak{h}}D_{ij}\bar{\bar{\xi}}_{\mathfrak{e}j}\right) + \frac{1}{\varepsilon}\bar{\bar{D}}_{\mathfrak{e}}\right] = \frac{1}{M_{\mathfrak{h}}}\left(\varepsilon\bar{\bar{\mathcal{M}}}^{(1)}_{\boldsymbol{E}'} + \bar{\bar{\mathcal{M}}}^{0}_{\boldsymbol{E}'}\right), \tag{3.1.16}$$

$$\bar{\bar{\mathcal{M}}}_{p_{\mathfrak{e}}} = \left(\frac{\varepsilon}{M_{\mathfrak{h}}}\right)\frac{p_{\mathfrak{e}}}{p_{\mathfrak{h}}}\left[\sum_{i\in\mathfrak{h}}\bar{\bar{\xi}}_{\mathfrak{e}i}\left(\sum_{j\in\mathfrak{h}}D_{ij}\bar{\bar{\alpha}}_{\mathfrak{e}j}\right) + \frac{1}{\varepsilon}\bar{\bar{D}}_{\mathfrak{e}}\right] = \frac{1}{M_{\mathfrak{h}}}\left(\varepsilon\bar{\bar{\mathcal{M}}}^{(1)}_{p_{\mathfrak{e}}} + \bar{\bar{\mathcal{M}}}^{0}_{p_{\mathfrak{e}}}\right), \tag{3.1.17}$$

$$\bar{\bar{\mathcal{M}}}_{p_j} = \left(\frac{\varepsilon}{M_{\mathfrak{h}}}\right)\sum_{i\in\mathfrak{h}}\bar{\bar{\xi}}_{\mathfrak{e}i}D_{ij}, \quad j\in\mathrm{H}, \tag{3.1.18}$$

$$\bar{\bar{\mathcal{M}}}_{T_{\mathfrak{e}}} = \left(\frac{\varepsilon}{M_{\mathfrak{h}}}\right)\frac{p_{\mathfrak{e}}}{p_{\mathfrak{h}}}\left[\sum_{i\in\mathfrak{h}}\bar{\bar{\xi}}_{\mathfrak{e}i}\left(\sum_{j\in\mathfrak{h}}D_{ij}\bar{\bar{\chi}}_{\mathfrak{e}j}\right) + \frac{1}{\varepsilon}\bar{\bar{D}}_{\mathfrak{e}}\bar{\bar{\chi}}_{\mathfrak{e}}\right] = \frac{1}{M_{\mathfrak{h}}}\left(\varepsilon\bar{\bar{\mathcal{M}}}^{(1)}_{T_{\mathfrak{e}}} + \bar{\bar{\mathcal{M}}}^{0}_{T_{\mathfrak{e}}}\right), \tag{3.1.19}$$

$$\bar{\bar{\mathcal{M}}}_{T_{\mathfrak{h}}} = \left(\frac{\varepsilon}{M_{\mathfrak{h}}}\right)\left[\sum_{i\in\mathfrak{h}}\bar{\bar{\xi}}_{\mathfrak{e}i}\left(\sum_{j\in\mathfrak{h}}D_{ij}\chi_{\mathfrak{h},j}\right)\right]. \tag{3.1.20}$$

Expression of the electric field

The general expression of the electric field is obtained from (3.1.15), as follows,

$$\boldsymbol{E}' = \bar{\bar{\mathcal{M}}}^{-1}_{\boldsymbol{E}'}\Bigg[\frac{p_{\mathfrak{e}}}{(n_{\mathfrak{e}}q_{\mathfrak{e}})^2}\left(\boldsymbol{J}_{\mathfrak{e}} + \boldsymbol{J}_{\mathfrak{h}} + \boldsymbol{J}^{(1)}_{\mathfrak{e}}\right) + \frac{p_{\mathfrak{e}}}{n_{\mathfrak{e}}q_{\mathfrak{e}}}\Big(\bar{\bar{\mathcal{M}}}_{p_{\mathfrak{e}}}\frac{\partial_{\boldsymbol{x}}p_{\mathfrak{e}}}{p_{\mathfrak{e}}} + \sum_{j\in\mathrm{H}}\bar{\bar{\mathcal{M}}}_{p_j}\frac{\partial_{\boldsymbol{x}}p_j}{p_{\mathfrak{h}}} + \bar{\bar{\mathcal{M}}}_{T_{\mathfrak{e}}}\frac{\partial_{\boldsymbol{x}}T_{\mathfrak{e}}}{T_{\mathfrak{e}}} + \bar{\bar{\mathcal{M}}}_{T_{\mathfrak{h}}}\frac{\partial_{\boldsymbol{x}}T_{\mathfrak{h}}}{T_{\mathfrak{h}}}\Big)\Bigg] \tag{E}$$

The expression of the multicomponent electromagnetic matrices $\bar{\bar{\mathcal{M}}}_{\boldsymbol{E}'}, \bar{\bar{\mathcal{M}}}_{p_{\mathfrak{e}}}, \bar{\bar{\mathcal{M}}}_{T_{\mathfrak{e}}}$, can be subdivided into two terms

- **The terms $\bar{\bar{\mathcal{M}}}^{(1)}_{\boldsymbol{E}'}$, $\bar{\bar{\mathcal{M}}}^{(1)}_{p_{\mathfrak{e}}}$ and $\bar{\bar{\mathcal{M}}}^{(1)}_{T_{\mathfrak{e}}}$** are tensors that depend on the coupled heavy particle-electron transport properties, such as $\bar{\bar{\alpha}}_{\mathfrak{e}j}, \bar{\bar{\chi}}_{\mathfrak{e}j}, D_{ij}$ and $\chi_{\mathfrak{h},j}$. In other words, such terms take into account interactions, such as electron/heavy particles and heavy-particle/heavy-particle interactions. These terms scale at the dissipative timescale at order ε.

- **The terms $\bar{\bar{\mathcal{M}}}^{0}_{E'}$, $\bar{\bar{\mathcal{M}}}^{0}_{p_\mathfrak{e}}$ and $\bar{\bar{\mathcal{M}}}^{0}_{T_\mathfrak{e}}$** are tensors that depend on the electron transport properties $\bar{\bar{D}}_\mathfrak{e}$ and $\bar{\bar{\chi}}_\mathfrak{e}$. Such terms take into account only collisions between electrons. These terms scale at the convective timescale for the heavy particles at order ε^0.

The matrices $\bar{\bar{\mathcal{M}}}_{p_j}$ and $\bar{\bar{\mathcal{M}}}_{T_\mathfrak{h}}$ depend only on transport properties related to the interactions heavy-particle/electron and heavy-particle/heavy-particle. These terms scale at the dissipative timescale at order ε, which is consistent with the proposed scaling.

For the sake of clarity, some usual terms can be identified in (E). First, the first term of (E) is a general multicomponent resistive term, where the expression of the resistivity tensor is defined as

$$\bar{\bar{\eta}} = \frac{p_\mathfrak{e}}{(n_\mathfrak{e} q_\mathfrak{e})^2} \bar{\bar{\mathcal{M}}}^{-1}_{E'} = M_\mathfrak{h} \frac{p_\mathfrak{e}}{(n_\mathfrak{e} q_\mathfrak{e})^2} \left(\varepsilon \bar{\bar{\mathcal{M}}}^{(1)}_{E'} + \bar{\bar{\mathcal{M}}}^{0}_{E'} \right)^{-1}. \tag{3.1.21}$$

The resistivity, defined in (3.1.21), takes into account all the possible interactions in a multicomponent plasma composed of heavy particles and electrons.

Then, the second term and third term of (E), can be identified as a general expression of the battery term for a multicomponent plasma due to the pressure gradients of electrons and heavy particles. The fourth and last term of (E) are additional terms due to the presence of Soret/Dufour terms in the equations of the diffusion velocities. In summary, the last four terms of (E) are related to the thermodynamic forces acting on each particles of the multicomponent plasma.

In Section 3.3 a simplified fully ionized plasma case is considered. In this context, a simplified expression of the electric field has been obtained. The multicomponent electromagnetic matrices can be simplified, and a classical expression of the electric field for fully ionized plasma is obtained.

3.2 Multicomponent model coupled to the set of Maxwell equations ($Mx^{\varepsilon=0}$)

In the previous section, we have focused on the general model coupled with the Maxwell's equations at order ε. At this order, the global charge of the plasma in the law of Gauss is assumed to be at order ε, thus, the electroneutrality is not assumed.

In this thesis, we underline that we are interested in applications, such as solar physics, for which the characteristic macroscopic scales are larger than the Debye length scale. Thus, the electroneutrality assumption can be considered. Therefore, we have considered the set of Maxwell's equations ($Mx^{\varepsilon=0}$) at order ε^0. In this case, the electroneutrality is assumed and the total current density $\mathbf{I}$ is non null. The goal of this section is to exhibit the multicomponent model. It is a simplified case of the general model for which the electroneutrality is assumed.

First, we exhibit the multicomponent model. We rewrite the set of equations in a conservative form. Then, we show the generalized Ohm's law simplified under the electroneutrality assumption.

Finally, the resulting multicomponent model is compared with multi-fluid MHD models.

3.2.1 Electroneutrality and electron diffusion velocity

In order to derive a set of governing equations under the electroneutrality assumption, we couple the set of general governing equation introduced in the previous section, with the set of Maxwell equations ($Mx^{\varepsilon=0}$), at order ε^0. Here, the electroneutrality is assumed. At order ε^0, we have

$$\boldsymbol{\partial_x}\cdot\boldsymbol{E} = nq = n_{\mathfrak{e}}q_{\mathfrak{e}} + \sum_{i\in\mathrm{I}} n_i q_i = 0.$$

Then, if the ions and electrons are opposite charges, we obtain

$$n_{\mathfrak{e}} = n_{\mathrm{I}} \Leftrightarrow \rho_{\mathfrak{e}} = \frac{m_{\mathfrak{e}}}{m_{\mathrm{I}}}\rho_{\mathrm{I}}, \tag{3.2.1}$$

Then, using (3.1.1) and (3.1.2), we rewrite the mass conservation laws for ions and electrons at order ε^0, as follows

$$\partial_t\rho_{\mathrm{I}} + \boldsymbol{\partial_x}\cdot\left[\rho_{\mathrm{I}}\boldsymbol{v}_{\mathfrak{h}}\right] = 0, \tag{3.2.2a}$$

$$\partial_t\rho_{\mathfrak{e}} + \boldsymbol{\partial_x}\cdot\left[\rho_{\mathfrak{e}}\left(\boldsymbol{v}_{\mathfrak{h}} + \frac{1}{M_{\mathfrak{h}}}\boldsymbol{V}_{\mathfrak{e}}\right)\right] = 0, \tag{3.2.2b}$$

Finally, using (3.2.1) at order ε^0, allow us to combine (3.2.2a) and (3.2.2b), which leads to

$$\boldsymbol{V}_{\mathfrak{e}} = 0. \tag{3.2.3}$$

This result shows that assuming electroneutrality at order ε^0 leads to a case where the electrons do not diffuse in the heavy-particle reference frame. The electrons have the same dynamics as the ions. Therefore, the total curent density reads

$$\mathbf{I} = n_{\mathfrak{e}}q_{\mathfrak{e}}\boldsymbol{V}_{\mathfrak{e}}^{(1)} + \sum_{i\in\mathrm{I}} n_i q_i \boldsymbol{V}_i. \tag{3.2.4}$$

Finally, the coupling with the set of Maxwell's equations ($Mx^{\varepsilon=0}$) at order ε^0 allows to simplify the transport fluxes, the general governing equations introduced in the previous section and the generalized Ohm's law, since the electron diffusion velocity is vanishing, *i.e.*, $\boldsymbol{V}_{\mathfrak{e}} = 0$.

3.2.2 Governing equations

We focus on the strongly magnetized case where $b = 1$. We provide a conservative form of the governing equations. For the sake of clarity, we have also removed the scaling parameters by considering $\varepsilon = M_{\mathfrak{h}} = 1$.

First, we present the conservative form of the momentum and total energy. Then, we introduce

the governing equations of the multicomponent model coupled with the set of Maxwell's equations ($Mx^{\varepsilon=0}$), and its simplified transport fluxes.

Conservative form of the momentum equation

First, in the momentum equation (3.1.6), the Lorentz force $\mathbf{I}\wedge\boldsymbol{B}$ can be rewritten as a flux using Faraday's law from ($Mx^{\varepsilon=0}$), as follows

$$\mathbf{I}\wedge\boldsymbol{B} = \frac{1}{4\pi}\left(\boldsymbol{\partial}_{\boldsymbol{x}}\wedge\boldsymbol{B}\right)\wedge\boldsymbol{B} = \frac{1}{4\pi}\left(\boldsymbol{\partial}_{\boldsymbol{x}}\cdot\left(\boldsymbol{B}\otimes\boldsymbol{B}\right) - \left(\boldsymbol{\partial}_{\boldsymbol{x}}\boldsymbol{B}\right)\cdot\boldsymbol{B}\right)$$

Using the identity $\boldsymbol{\partial}_{\boldsymbol{x}}\left(\boldsymbol{B}\cdot\boldsymbol{B}\right) = 2\boldsymbol{\partial}_{\boldsymbol{x}}\boldsymbol{B}\cdot\boldsymbol{B}$, we have

$$\boldsymbol{\partial}_{\boldsymbol{x}}\boldsymbol{B}\cdot\boldsymbol{B} = \frac{1}{2}\boldsymbol{\partial}_{\boldsymbol{x}}\left(\boldsymbol{B}\cdot\boldsymbol{B}\right) = \boldsymbol{\partial}_{\boldsymbol{x}}\cdot\left(\frac{1}{2}|\boldsymbol{B}|^2\mathbb{I}\right), \tag{3.2.5}$$

Therefore, the Lorentz force can be rewritten as

$$\mathbf{I}\wedge\boldsymbol{B} = \boldsymbol{\partial}_{\boldsymbol{x}}\cdot\left(\frac{\boldsymbol{B}\otimes\boldsymbol{B}}{4\pi} - \frac{|\boldsymbol{B}|^2}{8\pi}\mathbb{I}\right).$$

Consequently, under the electroneutrality assumption, a conservative form of the momentum equation is obtained as follows

$$\partial_t\left(\rho_{\mathfrak{h}}\boldsymbol{v}_{\mathfrak{h}}\right) + \boldsymbol{\partial}_{\boldsymbol{x}}\cdot\left[\rho_{\mathfrak{h}}\boldsymbol{v}_{\mathfrak{h}}\otimes\boldsymbol{v}_{\mathfrak{h}} + \left(p + \frac{|\boldsymbol{B}|^2}{8\pi}\right)\mathbb{I} - \frac{\boldsymbol{B}\otimes\boldsymbol{B}}{4\pi}\right] + \boldsymbol{\partial}_{\boldsymbol{x}}\cdot\left(\boldsymbol{\Pi}_{\mathfrak{h}}\right) = 0. \tag{3.2.6}$$

Conservative form of the total energy

Using Poynting's theorem , we can write the electromagnetic energy, as follows

$$\partial_t\left(\frac{|\boldsymbol{B}|^2}{8\pi}\right) + \boldsymbol{\partial}_{\boldsymbol{x}}\cdot\left(\frac{\boldsymbol{E}\wedge\boldsymbol{B}}{4\pi}\right) = -\mathbf{I}\cdot\boldsymbol{E}. \tag{3.2.7}$$

If we sum (3.2.7) to (3.1.10), we obtain a conservation form for the total energy, including the electromagnetic energy, as follows,

$$\partial_t\mathcal{E}_{\text{tot}} + \boldsymbol{\partial}_{\boldsymbol{x}}\cdot\left(\mathcal{H}\boldsymbol{v}_{\mathfrak{h}} + \frac{1}{4\pi}\boldsymbol{E}\wedge\boldsymbol{B}\right) + \boldsymbol{\partial}_{\boldsymbol{x}}\cdot\left(\boldsymbol{\Pi}_{\mathfrak{h}}\cdot\boldsymbol{v}_{\mathfrak{h}}\right) + \boldsymbol{\partial}_{\boldsymbol{x}}\cdot\boldsymbol{Q} = 0, \tag{3.2.8}$$

where $\mathcal{E}_{\text{tot}} = \mathcal{E} + |\boldsymbol{B}|^2/8\pi$.

Note that, in (3.2.7), the displacement current term has been neglected since it is not considered at the order ε^0 in ($Mx^{\varepsilon=0}$).

Governing equations of the multicomponent model

Finally, by considering the conservative form of the equations (3.2.8) and (3.2.6), the multicomponent model coupled with ($Mx^{\varepsilon=0}$) is obtained, as follows

$$\begin{cases} \partial_t \rho_i + \boldsymbol{\partial_x}\cdot(\rho_i\,(\boldsymbol{v}_\mathfrak{h} + \boldsymbol{V}_i)) = 0, \quad i \in \mathrm{H} \\ \partial_t(\rho_\mathfrak{h}\boldsymbol{v}_\mathfrak{h}) + \boldsymbol{\partial_x}\cdot\Big(\rho_\mathfrak{h}\boldsymbol{v}_\mathfrak{h}\otimes\boldsymbol{v}_\mathfrak{h} + (p + \frac{1}{8\pi}|\boldsymbol{B}|^2)\mathbb{I} - \frac{1}{4\pi}\boldsymbol{B}\otimes\boldsymbol{B}\Big) + \boldsymbol{\partial_x}\cdot\boldsymbol{\Pi}_\mathfrak{h} = 0, \\ \partial_t\mathcal{E}_{\mathrm{tot}} + \boldsymbol{\partial_x}\cdot\Big(\mathcal{H}\boldsymbol{v}_\mathfrak{h} + \frac{1}{4\pi}\boldsymbol{E}\wedge\boldsymbol{B}\Big) + \boldsymbol{\partial_x}\cdot(\boldsymbol{\Pi}_\mathfrak{h}\cdot\boldsymbol{v}_\mathfrak{h}) + \boldsymbol{\partial_x}\cdot\boldsymbol{Q} = 0, \\ \partial_t(\rho_\mathfrak{e} e_\mathfrak{e}) + \boldsymbol{\partial_x}\cdot(\rho_\mathfrak{e} e_\mathfrak{e}\boldsymbol{v}_\mathfrak{h}) + p_\mathfrak{e}\boldsymbol{\partial_x}\cdot\boldsymbol{v}_\mathfrak{h} + \boldsymbol{\partial_x}\cdot\Big(\boldsymbol{q}_\mathfrak{e} + \boldsymbol{q}_\mathfrak{e}^{(1)}\Big) = \boldsymbol{J}_\mathfrak{e}^{(1)}\cdot\boldsymbol{E}' + \Delta E_\mathfrak{e}^{(0)} + \Delta E_\mathfrak{e}^{(1)}, \end{cases} \tag{Mc}$$

where $\boldsymbol{q}_\mathfrak{h}$, $\boldsymbol{\Pi}_\mathfrak{h}$, $\boldsymbol{q}_\mathfrak{e}^{(1)}$, $\boldsymbol{V}_\mathfrak{e}^{(1)}$, $\Delta E_\mathfrak{e}^{(0)}$ and $\Delta E_\mathfrak{e}^{(1)}$ are defined in (2.4.37), (2.4.32), (2.4.48), (2.4.46), (2.3.19) and (2.3.32) respectively. Additionally, we recall the thermodynamic laws defined by

$$p_\mathfrak{e} = n_\mathfrak{e} T_\mathfrak{e}\,, \quad p_i = n_i T_\mathfrak{h}, \quad p = p_\mathfrak{e} + \sum_{k\in\mathrm{H}} p_k, \quad \text{where } i \in \mathrm{H}. \tag{3.2.9}$$

Since the electron diffusion velocity is vanishing, the transport fluxes are simplified. The electron heat flux is simplified as follows

$$\boldsymbol{q}_\mathfrak{e} = -\bar{\bar{\lambda}}_\mathfrak{e}\boldsymbol{\partial_x} T_\mathfrak{e} \tag{3.2.10}$$

Then, the expression of the diffusion velocities of heavy particles is identical except that the driving and average force for electrons $\boldsymbol{d}_\mathfrak{e}$ and $\boldsymbol{F}_{ie}$ read

$$\begin{aligned} \boldsymbol{d}_\mathfrak{e} &= -\frac{\bar{\bar{\chi}}_\mathfrak{e}}{T_\mathfrak{e}}\boldsymbol{\partial_x} T_\mathfrak{e}\,, \\ \boldsymbol{F}_{ie} &= \frac{p_\mathfrak{e}}{n_j}\frac{\boldsymbol{\partial_x} T_\mathfrak{e}}{T_\mathfrak{e}}\left[\bar{\bar{\alpha}}_{\mathfrak{e}i}\bar{\bar{\chi}}_\mathfrak{e} - \bar{\bar{\chi}}_{\mathfrak{e}i}\right], \quad i \in \mathrm{H} \end{aligned} \tag{3.2.11}$$

The presented model (Mc) is a thermal non-equilibrium model. Source terms are involved in the equation of internal energy of electrons that can be decomposed as nonconservative and relaxation terms.

The nonconservative terms such as $p_\mathfrak{e}\boldsymbol{\partial_x}\cdot\boldsymbol{v}_\mathfrak{h}$ or the power developed by the electromagnetic field $\boldsymbol{J}_\mathfrak{e}\cdot\boldsymbol{E}'$, are part of the thermal non-equilibrium process which tends to change the electronic temperature with respect to the temperature of the heavy particles.

In the presented model, the source term $\Delta E_\mathfrak{e}^{(0)}$, present in the equation of internal energy of electron, tends to relax the system towards a state of thermal equilibrium between the electrons and the heavy particles. This relaxation is related to the parameter τ, which is the characteristic time of collision between electrons and heavy particles. Physically, if this characteristic collision time is small enough compared to the characteristic reference time, we have a thermal equilibrium state. If not, the power generated by the electromagnetic field $\boldsymbol{J}_\mathfrak{e}\cdot\boldsymbol{E}'$ dominates the dynamic of the internal energy of electron, the electronic temperature becomes different from the temperature of the heavy ones, we get a thermal non-equilibrium state.

The set of governing equations (*Mc*) coupled with Maxwell's equations ($Mx^{\varepsilon=0}$) have been identified. Under this assumption, the generalized Ohm's law is also simplified. An expression of the electric as function of the transport fluxes can be determined.

3.2.3 Simplified Ohm's law for the multicomponent model

If the electroneutrality is assumed at order ε^0, the total current density in (3.1.15) and the related multicomponent matrices defined in (3.1.16)-(3.1.20), do not depend on the zeroth-order transport coefficients, *i.e.*, $\bar{\bar{D}}_{\mathfrak{e}}$ and $\bar{\bar{\chi}}_{\mathfrak{e}}$. Therefore, the multicomponent matrices do not depend on the interations electrons/electrons anymore.

The expression of the electric field defined in (*E*) is identical, except that the following multicomponent matrices $\bar{\bar{\mathcal{M}}}_{\boldsymbol{E}'}$, $\bar{\bar{\mathcal{M}}}_{p_{\mathfrak{e}}}$ and $\bar{\bar{\mathcal{M}}}_{T_{\mathfrak{e}}}$ read

$$\bar{\bar{\mathcal{M}}}_{\boldsymbol{E}'} = \frac{p_{\mathfrak{e}}}{p_{\mathfrak{h}}} \sum_{i\in\mathfrak{h}} \bar{\bar{\xi}}_{\mathfrak{e}i} \left(\sum_{j\in\mathfrak{h}} D_{ij} \bar{\bar{\xi}}_{\mathfrak{e}j} \right) = \bar{\bar{\mathcal{M}}}^{(1)}_{\boldsymbol{E}'}, \tag{3.2.12}$$

$$\bar{\bar{\mathcal{M}}}_{p_{\mathfrak{e}}} = \frac{p_{\mathfrak{e}}}{p_{\mathfrak{h}}} \sum_{i\in\mathfrak{h}} \bar{\bar{\xi}}_{\mathfrak{e}i} \left(\sum_{j\in\mathfrak{h}} D_{ij} \bar{\bar{\alpha}}_{\mathfrak{e}j} \right) = \bar{\bar{\mathcal{M}}}^{(1)}_{p_{\mathfrak{e}}}, \tag{3.2.13}$$

$$\bar{\bar{\mathcal{M}}}_{T_{\mathfrak{e}}} = \frac{p_{\mathfrak{e}}}{p_{\mathfrak{h}}} \sum_{i\in\mathfrak{h}} \bar{\bar{\xi}}_{\mathfrak{e}i} \left(\sum_{j\in\mathfrak{h}} D_{ij} \bar{\bar{\chi}}_{\mathfrak{e}j} \right) = \bar{\bar{\mathcal{M}}}^{(1)}_{T_{\mathfrak{e}}}, \tag{3.2.14}$$

Note that, the general resistivity defined in (3.1.21) is simplified to

$$\bar{\bar{\eta}} = \frac{p_{\mathfrak{e}}}{(n_{\mathfrak{e}} q_{\mathfrak{e}})^2} \left(\bar{\bar{\mathcal{M}}}^{(1)}_{\boldsymbol{E}'} \right)^{-1}. \tag{3.2.15}$$

3.2.4 Comparison with multi-fluid approach used for solar physics application

Multi-fluid MHD models have been used more recently to represent the non-equilibrium conditions of the chromosphere, based on continuity, momentum, and energy conservation equations for each species considered in the mixture (see Leake et al. (2012); Khomenko et al. (2014); Shelyag et al. (2016); Khomenko (2017); Alvarez Laguna et al. (2016); Ni et al. (2018)). Indeed in the multicomponent model, only one hydrodynamic velocity in the heavy-particle reference frame is considered. All the species are diffusing in the same reference frame, whereas in the standard multi-fluid MHD equations one hydrodynamic velocity per species is considered. In the multicomponent approach (*Mc*), the electrons participate in the momentum balance through the total pressure gradient and Lorentz force. Therefore, the electrons do not participate in the stress tensor. Generally, in multi-fluid models, for instance in the model of Braginskii (1965), or Alvarez-Laguna et al. (2018), a viscous stress tensor for electrons is considered.

In addition, new effects appear in the multicomponent model that are absent in the multi-fluid MHD model. These effects, called Soret/Dufour effects (see Kolesnikov (2003)), play a role both in the diffusion velocities and in the dynamics of the electric field through the multicomponent matrices. Thus, in the multicomponent model, two types of forces are considered: 1-the electromagnetic forces, and 2- the thermodynamic forces related to the pressure and temperature (Soret effects). If the plasma is weakly ionized and thermal pressure dominated, these new terms such as the Soret / Dufour effects (related to the temperature or pressure gradients) are dominating the dynamics of the plasma. In such conditions, these new terms allow magnetic reconnection process to occur. Indeed, according to (E), the parallel component of these terms may produce an electric field parallel to the magnetic field which may result in reconnection. These terms do not appear in the classical multi-fluid approach, since only a resistive term is generally considered, which allows magnetic reconnection to occur only in the magnetic pressure dominated plasma regime.

Then, a new resistivity (3.2.15) has been defined. This term depends on the multicomponent transport coefficients by taking into account all possible interactions in the mixture. This new term, relevant in solar physics, appears to be a much more general term than the standard resistivity such as ambipolar resistivity (see Khomenko & Collados Vera (2012); Khomenko (2017); Khomenko et al. (2014)) or Spitzer resistivity (see Spitzer (1963)). The resistivity is studied in Chapter 5.

The multi-fluid approach allows to describe partially ionized plasmas in many collisional regimes. However, no rigorous development from the kinetic theory based on correct physical hypotheses has been performed. Indeed, as shown by S. Benilov (1997), the multifluid approach is valid only in conditions where collisions of particles of each species between themselves are more frequent compared with collisions of particles involving different species. Additionally, the multi-fluid model is showing several relaxation terms which make the system stiff, in particular, when a highly-collisional regime is considered, as shown by Alvarez Laguna et al. (2016) and Alonso Asensio et al. (2019). They exhibit characteristic times that range from the convective and diffusive times of each fluid down to the collisional and chemical kinetics time scales. The scales associated with the stiffness of the system have not been considered and correctly eliminated in the development from kinetic theory. However, in the multicomponent approach, a consistent scaling combined with proper asymptotic limits at the kinetic level allows to reduce the stiffness of the resulting system. Therefore, in the multi-fluid approach, several source terms and coupling terms in the momentum equations and energy equations of each particles are considered, which is not the case in the multicomponent approach. The dynamics of each particles is captured by the dissipative effects (diffusion velocities). No source terms are present in the system except in the equation of internal energy of electrons, to take into account the thermal nonequilibrium processes.

In summary, even though the multicomponent and multifluid model are capturing the same physics, the differences between the multicomponent (Mc) and multi-fluid model (see Alvarez Laguna et al. (2016)) operate at three levels:

1. **In the hydrodynamic system of equations:** several hydrodynamic velocities are considered in the multi-fluid model, whereas one heavy-particle hydrodynamic velocity with several diffusion velocities are considered in the multicomponent model. The decoupling of the particles are captured by the dissipative effects. Besides, coupling source terms in the equation of momentum are considered, whereas the latter do not appear in the multicomponent

case. Only relaxation terms related to the thermal nonequilibrium process, appearing in the equation of internal energy, are present in both models.

2. **In the transport fluxes:** new effects appear such as the Soret/Dufour effect in the multicomponent model. Such new terms impact the law of the electric field (E). A new definition of the resistivity which take into account all the possible interactions between species, has been considered.

3.3 Fully ionized plasma case

In this section, we study the particular case of a fully ionized plasma composed only of electrons and ions, $S = \{\mathfrak{e}, \mathrm{I}\}$ under the hypothesis of electroneutrality out of thermal equilibrium. The goal is to show the general model in a simplified framework. The resulting model, being close to the single-fluid approach, will be compared with single-fluid MHD models.

As performed in the previous sections, we will exhibit the system of equation. Then, we will derive a simplified Ohm's law. In doing so, it allows the reader to understand the new expression of the electric field that was introduced in previous sections, in a simplified framework. Finally, we will compare this approach with single-fluid models used for solar physics applications, and highlight the advantages of this approach.

3.3.1 Governing equations

We focus on a fully ionized plasma composed of $S = \{\mathfrak{e}, \mathrm{I}\}$, considering scales which are much larger than the Debye length. Under these assumptions, the heavy diffusion velocity of ions is null $\boldsymbol{V}_i = 0, i \in \mathrm{I}$, and the global charge is nul $nq = 0$, so the total current density is equal to the zeroth-order electron current density, *i.e.*, $\mathbf{I} = \boldsymbol{J}_\mathfrak{e}$. Then, the governing equations coupled to the set of Maxwell's equations ($Mx^{\varepsilon=0}$) reads

$$
\begin{cases}
\partial_t \rho_\alpha + \boldsymbol{\partial_x}\cdot(\rho_\alpha \boldsymbol{v}_\mathfrak{h}) = 0, \quad \alpha \in \{\mathfrak{e}, \mathrm{I}\} \\
\partial_t(\rho_\mathfrak{h}\boldsymbol{v}_\mathfrak{h}) + \boldsymbol{\partial_x}\cdot\Big(\rho_\mathfrak{h}\boldsymbol{v}_\mathfrak{h}\otimes\boldsymbol{v}_\mathfrak{h} + (p + \frac{1}{8\pi}|\boldsymbol{B}|^2)\mathbb{I} - \frac{1}{4\pi}\boldsymbol{B}\otimes\boldsymbol{B}\Big) + \boldsymbol{\partial_x}\cdot\boldsymbol{\Pi}_\mathfrak{h} = 0, \\
\partial_t \mathcal{E}_{\mathrm{tot}} + \boldsymbol{\partial_x}\cdot\Big(\mathcal{H}\boldsymbol{v}_\mathfrak{h} + \frac{1}{4\pi}\boldsymbol{E}\wedge\boldsymbol{B}\Big) + \boldsymbol{\partial_x}\cdot(\boldsymbol{\Pi}_\mathfrak{h}\cdot\boldsymbol{v}_\mathfrak{h}) + \boldsymbol{\partial_x}\cdot(\boldsymbol{q}_\mathfrak{e} + \boldsymbol{q}_\mathfrak{h}) = 0, \\
\partial_t(\rho_\mathfrak{e} e_\mathfrak{e}) + \boldsymbol{\partial_x}\cdot(\rho_\mathfrak{e} e_\mathfrak{e}\boldsymbol{v}_\mathfrak{h}) + p_\mathfrak{e}\boldsymbol{\partial_x}\cdot\boldsymbol{v}_\mathfrak{h} + \boldsymbol{\partial_x}\cdot\boldsymbol{q}_\mathfrak{e} = \boldsymbol{J}_\mathfrak{e}\cdot\boldsymbol{E}' + \Delta E^{(0)}_\mathfrak{e},
\end{cases}
\tag{Mf}
$$

Additionally, we have the thermodynamic laws defined as

$$
p_\mathfrak{e} = n_\mathfrak{e} T_\mathfrak{e}, \quad p_i = n_i T_\mathfrak{h}, \quad p = p_\mathfrak{e} + \sum_{k\in\mathrm{I}} p_k, \quad i \in \mathrm{I}. \tag{3.3.1}
$$

Then, the transport fluxes read

$$\boldsymbol{q}_{\mathfrak{e}} = -\bar{\bar{\lambda}}_{\mathfrak{e}}\partial_{\boldsymbol{x}}T_{\mathfrak{e}} + (p_{\mathfrak{e}}\bar{\bar{\chi}}_{\mathfrak{e}} + \rho_{\mathfrak{e}}h_{\mathfrak{e}})\boldsymbol{V}_{\mathfrak{e}}, \quad \boldsymbol{q}_{\mathfrak{h}} = -\lambda_{\mathfrak{h}}\partial_{\boldsymbol{x}}T_{\mathfrak{h}}, \quad \boldsymbol{V}_{\mathfrak{e}} = \frac{1}{n_{\mathfrak{e}}q_{\mathfrak{e}}}\frac{\partial_{\boldsymbol{x}}\wedge\boldsymbol{B}}{4\pi}, \tag{3.3.2}$$

Similarly as the previous section, the simplified model for fully ionized plasma (Mf) is coupled to Maxwell's equations ($Mx^{\varepsilon=0}$). Thus, a generalized Ohm's law can be derived.

3.3.2 Ohm's law for a fully ionized plasma

Similarly as in Section 3.2.3, we focus on the generalized Ohm's law (E) coupled to the model for fully ionized plasma (Mf). In this context, unlike the multicomponent case, the related multicomponent matrices are simplified, and depend only on the zeroth-order transport coefficients, *i.e.*, $\bar{\bar{D}}_{\mathfrak{e}}$ and $\bar{\bar{\chi}}_{\mathfrak{e}}$. Then, the multicomponent matrices depend only on the interactions electrons/electrons and electrons/ions. Finally, the expression of the multicomponent matrices read

$$\bar{\bar{\mathcal{M}}}_{\boldsymbol{E}'} = \bar{\bar{D}}_{\mathfrak{e}}, \tag{3.3.3}$$
$$\bar{\bar{\mathcal{M}}}_{p_{\mathfrak{e}}} = \bar{\bar{D}}_{\mathfrak{e}}, \tag{3.3.4}$$
$$\bar{\bar{\mathcal{M}}}_{p_j} = 0, \tag{3.3.5}$$
$$\bar{\bar{\mathcal{M}}}_{T_{\mathfrak{e}}} = \bar{\bar{D}}_{\mathfrak{e}}\bar{\bar{\chi}}_{\mathfrak{e}}, \tag{3.3.6}$$
$$\bar{\bar{\mathcal{M}}}_{T_{\mathfrak{h}}} = 0, \tag{3.3.7}$$

where the general expression of the electric field reads

$$\boldsymbol{E}' = \bar{\bar{\eta}}\boldsymbol{J}_{\mathfrak{e}} + \frac{\partial_{\boldsymbol{x}}p_{\mathfrak{e}}}{n_{\mathfrak{e}}q_{\mathfrak{e}}} + \frac{p_{\mathfrak{e}}}{n_{\mathfrak{e}}q_{\mathfrak{e}}}\frac{\bar{\bar{\chi}}_{\mathfrak{e}}}{T_{\mathfrak{e}}}\partial_{\boldsymbol{x}}T_{\mathfrak{e}}, \tag{Ef}$$

and the resistivity is defined as

$$\bar{\bar{\eta}} = \frac{p_{\mathfrak{e}}}{(n_{\mathfrak{e}}q_{\mathfrak{e}})^2}\bar{\bar{D}}_{\mathfrak{e}}^{\,-1}. \tag{3.3.8}$$

In (Ef), the Ohm's law for fully ionized plasma is shown. The first term corresponds to the classical resistive term, the second term is the battery term for electrons and the last additional term correspond to the Soret/Dufour effect. In addition, we can notice that the resistivity in (5.2.8), is depending only on the tensor $\bar{\bar{D}}_{\mathfrak{e}}$, thus, on the electrons/electrons or electrons/ions interactions. The expression obtained for the electric field is similar to the one obtained in the usual single-fluid approach.

The presented model for fully ionized plasma (Mf) is coupled with the set of Maxwell's equations ($Mx^{\varepsilon=0}$) and an Ohm's law (Ef) has been derived. In the next section, we compare this model with another approach mainly used for solar physic application, *i.e.*, the single fluid MHD model.

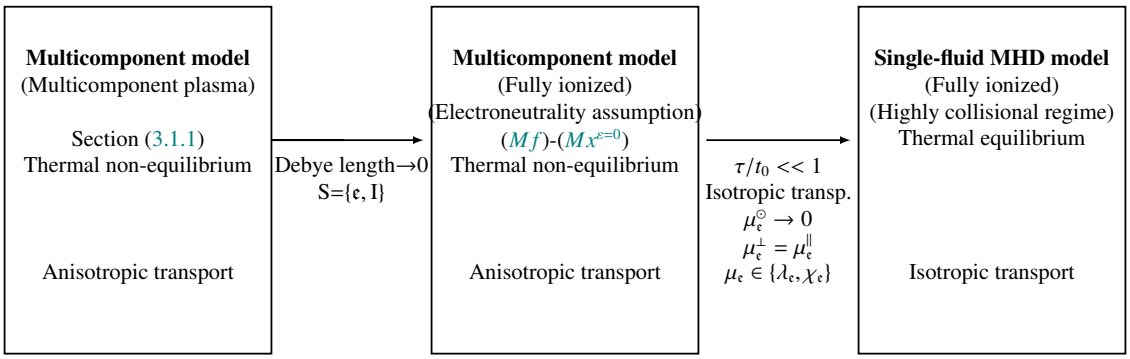

Figure 3-1: Link between the presented general multicomponent model from 3.1.1, the simplified model from (Mf)-$(Mx^{\varepsilon=0})$ and the single-fluid MHD model, assuming that the structure of the transport system and the method used for computing the transport coefficients is the same between the two models.

3.3.3 Comparison with single-fluid model

The single-fluid MHD approach is a model in thermal equilibrium between heavy particles and electrons. The system is conservative, without source terms, in which the structure of the diffusive terms, *i.e.*, heat fluxes and viscous stress tensor, is in general isotropic. For example, the classical single-fluid MHD system considered by Wray et al. (2015) does not depend on the characteristic collision time and does not represent regimes where there is thermal non-equilibrium. More generally, Figure 3-1 represents the link between the presented general multicomponent model defined in the section Section 3.1.1, the simplified model given by (Mf)-$(Mx^{\varepsilon=0})$ and the single-fluid MHD model, if the structure of the transport systems as well as the method used for computing the transport coefficients are identical between the three models.

The proposed model allows for describing all collisional regimes, for fully ionized plasma, in equilibrium or thermal non-equilibrium, through source terms of relaxation type. On the other hand, we have a conservative model valid only in thermal equilibrium cases, *i.e.*, in highly collisional regimes. The possibility of being able to represent all these regimes is particularly important in the solar atmosphere, since we can find highly or weakly collisional regimes in different parts of the solar atmosphere.

Finally, in the classical single fluid approach for fully ionized plasma, the Spitzer resistivity is mainly used for taking into account the interaction between ions and electrons (see Braginskii (1965); Spitzer (1963)). In our case, the latter is computed through the electron diffusion coefficients tensor $\bar{\bar{D}}_e$.

3.4 Eigenstructure of the multicomponent models (Mc) and (Mf)

This section is devoted to the study of the eigenstructure of the purely hyperbolic multicomponent model (Mc). The eigenstructure of the simplified model (Mf) can be easily deduced from the general multicomponent case. In this thesis, a study has been performed on the hyperbolic part of (Mc) by not considering the electromagnetic field, as shown in Chapter 7 and in Appendix E. We have been able to study the eigenstructure of the hyperbolic system and highlight the impact of the nonconservative terms on this eigenstructure. For the purpose of the work, we introduce $\boldsymbol{n}$ as a unit vector.

The considered general system of equations can be written as follows,

$$\partial_t \mathcal{U} + \boldsymbol{\partial_x} \cdot \mathcal{F}(\mathcal{U}) + \boldsymbol{\partial_x} \cdot \mathcal{G}(\mathcal{U}, \boldsymbol{\partial_x} \mathcal{U}) = \mathcal{S}(\mathcal{U}, \boldsymbol{\partial_x} \mathcal{U}), \tag{3.4.1}$$

where $\mathcal{U} \in \mathbb{R}^{8+n^{\mathrm{H}}}$, $\mathcal{F}(\mathcal{U}) \in \mathbb{R}^{3\times(8+n^{\mathrm{H}})}$, $\mathcal{G}(\mathcal{U}, \boldsymbol{\partial_x}\mathcal{U}) \in \mathbb{R}^{3\times(8+n^{\mathrm{H}})}$ and $\mathcal{S}(\mathcal{U}, \boldsymbol{\partial_x}\mathcal{U}) \in \mathbb{R}^{3\times(8+n^{\mathrm{H}})}$. These terms are defined by

$$\begin{aligned}
\mathcal{U} &= \Big((\rho_i)_{i\in \mathrm{H}},\ \rho_{\mathfrak{h}} \boldsymbol{v}_{\mathfrak{h}}^T,\ \mathcal{E},\ \rho_{\mathfrak{e}} e_{\mathfrak{e}},\ \boldsymbol{B}^T \Big)^T, \\
\mathcal{F}(\mathcal{U}) &= \Big((\rho_i)_{i\in \mathrm{H}} \boldsymbol{v}_{\mathfrak{h}},\ \rho_{\mathfrak{h}} \boldsymbol{v}_{\mathfrak{h}} \otimes \boldsymbol{v}_{\mathfrak{h}} + \Big(p_{\mathfrak{e}} + p_{\mathfrak{h}} + \tfrac{1}{8\pi} |\boldsymbol{B}|^2 \Big) \mathbb{I} - \tfrac{1}{4\pi} \boldsymbol{B} \otimes \boldsymbol{B}, \\
&\qquad (\mathcal{E} + p_{\mathfrak{e}} + p_{\mathfrak{h}}) \boldsymbol{v}_{\mathfrak{h}} + \tfrac{1}{4\pi} \boldsymbol{E} \wedge \boldsymbol{B},\ \rho_{\mathfrak{e}} e_{\mathfrak{e}} \boldsymbol{v}_{\mathfrak{h}},\ \mathbb{I}_{\wedge} (\boldsymbol{v}_{\mathfrak{h}} \wedge \boldsymbol{B}) \Big)^T, \\
\mathcal{G}(\mathcal{U}, \boldsymbol{\partial_x}\mathcal{U}) &= \Big((\boldsymbol{V}_i)_{i\in \mathrm{H}},\ \boldsymbol{\Pi}_{\mathfrak{h}}^T,\ \boldsymbol{\Pi}_{\mathfrak{h}} \cdot \boldsymbol{v}_{\mathfrak{h}} + \boldsymbol{q}_{\mathfrak{e}} + \boldsymbol{q}_{\mathfrak{h}},\ \boldsymbol{q}_{\mathfrak{e}},\ -\mathbb{I}_{\wedge} (\boldsymbol{E}')^T \Big)^T, \\
\mathcal{S}(\mathcal{U}, \boldsymbol{\partial_x}\mathcal{U}) &= \Big(0_{n^{\mathrm{H}}}^T,\ 0_3^T,\ 0,\ -p_{\mathfrak{e}} \boldsymbol{\partial_x} \cdot \boldsymbol{v}_{\mathfrak{h}} + \boldsymbol{J}_{\mathfrak{e}} \cdot \boldsymbol{E}' + \Delta E_{\mathfrak{e}}^{(0)} + \Delta E_{\mathfrak{e}}^{(1)},\ 0_3^T \Big)^T,
\end{aligned} \tag{3.4.2}$$

where $\boldsymbol{v}_{\mathfrak{h}} = (u_{\mathfrak{h}},\ v_{\mathfrak{h}},\ w_{\mathfrak{h}})^T$, $\boldsymbol{B} = \big(B_x,\ B_y,\ B_z\big)^T$ and $\mathbb{I}$ is the identity matrix. We recall that the source terms $\mathcal{S}$ are composed of two terms, relaxation terms and nonconservative terms as follows

$$\mathcal{S}(\mathcal{U}, \boldsymbol{\partial_x}\mathcal{U}) = N(\mathcal{U}, \boldsymbol{\partial_x}\mathcal{U}) + \mathcal{S}^{\mathrm{relax}}(\mathcal{U}) \tag{3.4.3}$$

The relaxation terms $\mathcal{S}^{\mathrm{relax}}$ depend only on $\mathcal{U}$, whereas the nonconservative terms N depend on both $\mathcal{U}$ and its gradient $\boldsymbol{\partial_x}\mathcal{U}$. These terms are defined as

$$N(\mathcal{U}, \boldsymbol{\partial_x}\mathcal{U}) = \Big(0_{n^{\mathrm{H}}}^T,\ 0_3^T,\ 0,\ -p_{\mathfrak{e}} \boldsymbol{\partial_x} \cdot \boldsymbol{v}_{\mathfrak{h}} + \boldsymbol{J}_{\mathfrak{e}} \cdot \boldsymbol{E}',\ 0_3^T \Big)^T, \tag{3.4.4}$$

$$\mathcal{S}^{\mathrm{relax}}(\mathcal{U}) = \Big(0_{n^{\mathrm{H}}}^T,\ 0_3^T,\ 0,\ \Delta E_{\mathfrak{e}}^{(0)} + \Delta E_{\mathfrak{e}}^{(1)},\ 0_3^T \Big)^T, \tag{3.4.5}$$

As performed in Appendix E, in order to study the hyperbolicity of (3.4.1), it is necessary to

rewrite the hyperbolic part of the conservation laws in a quasi-linear form, as follows

$$\partial_t \mathcal{U} + \mathcal{A}(U)\partial_x \mathcal{U} = 0, \tag{3.4.6}$$

where $\mathcal{A}(U) = \partial \mathcal{F}/\partial \mathcal{U}$ is the Jacobian matrix. Then, we show that $\mathcal{A}$ is diagonalizable with real eigenvalues. Since the hyperbolic system is similar to the usual single-fluid ideal MHD system, it is trivial to show the hyperbolicity and find the eigenvalues of $\mathcal{A}$, as described by Torrilhon (2003). Thus, the set of eigenvalues of $\boldsymbol{n}\cdot\mathcal{A}$ reads

$$\lambda_1^i = \boldsymbol{v}_\mathfrak{h}\cdot\boldsymbol{n}, \quad i \in \mathrm{H}, \tag{3.4.7}$$

$$\lambda_2 = \lambda_3 = \boldsymbol{v}_\mathfrak{h}\cdot\boldsymbol{n}, \tag{3.4.8}$$

then, the Alfven waves have been obtained:

$$\lambda_4 = \boldsymbol{v}_\mathfrak{h}\cdot\boldsymbol{n} - \frac{\boldsymbol{B}\cdot\boldsymbol{n}}{\sqrt{4\pi\rho_\mathfrak{h}}} = \boldsymbol{v}_\mathfrak{h}\cdot\boldsymbol{n} - \boldsymbol{c_a}\cdot\boldsymbol{n}, \tag{3.4.9}$$

$$\lambda_5 = \boldsymbol{v}_\mathfrak{h}\cdot\boldsymbol{n} + \frac{\boldsymbol{B}\cdot\boldsymbol{n}}{\sqrt{4\pi\rho_\mathfrak{h}}} = \boldsymbol{v}_\mathfrak{h}\cdot\boldsymbol{n} + \boldsymbol{c_a}\cdot\boldsymbol{n}, \tag{3.4.10}$$

where $\boldsymbol{c_a} = \boldsymbol{B}/\sqrt{4\pi\rho_\mathfrak{h}}$. The slow magnetosonic waves have been obtained:

$$\lambda_6 = \boldsymbol{v}_\mathfrak{h}\cdot\boldsymbol{n} - \sqrt{\frac{1}{2}\left[c^2 + \boldsymbol{c_a}^2 - \sqrt{(c^2+\boldsymbol{c_a}^2)^2 - 4c^2(\boldsymbol{c_a}\cdot\boldsymbol{n})^2}\right]}, \tag{3.4.11}$$

$$\lambda_7 = \boldsymbol{v}_\mathfrak{h}\cdot\boldsymbol{n} + \sqrt{\frac{1}{2}\left[c^2 + \boldsymbol{c_a}^2 - \sqrt{(c^2+\boldsymbol{c_a}^2)^2 - 4c^2(\boldsymbol{c_a}\cdot\boldsymbol{n})^2}\right]}, \tag{3.4.12}$$

where $c = \sqrt{\gamma p/\rho_\mathfrak{h}}$ is the speed of sound. Finally, we have the fast magnetosonic waves defined by

$$\lambda_8 = \boldsymbol{v}_\mathfrak{h}\cdot\boldsymbol{n} - \sqrt{\frac{1}{2}\left[c^2 + \boldsymbol{c_a}^2 + \sqrt{(c^2+\boldsymbol{c_a}^2)^2 - 4c^2(\boldsymbol{c_a}\cdot\boldsymbol{n})^2}\right]}, \tag{3.4.13}$$

$$\lambda_9 = \boldsymbol{v}_\mathfrak{h}\cdot\boldsymbol{n} + \sqrt{\frac{1}{2}\left[c^2 + \boldsymbol{c_a}^2 + \sqrt{(c^2+\boldsymbol{c_a}^2)^2 - 4c^2(\boldsymbol{c_a}\cdot\boldsymbol{n})^2}\right]}, \tag{3.4.14}$$

Physically, the Alfven wave corresponds to a wave in which ions are oscillating in response to a restoring force due to a tension on the magnetic field lines. The magnetosonic wave are longitudinal wave of charges particles propagating perpendicular to the magnetic field.

Note that, the eigenstructure of the Jacobian matrix of the hyperbolic problem in the fully ionized case (Mf) is identical to (3.4.6) by simply replacing the set of heavy particles H by the set of ions I.

In (3.4.1), in the study of the hyperbolic problem, the nonconservative terms in the equation of internal energy of electrons, have been considered as source terms. Another possibility would be to consider these terms as part of the hyperbolic problem. In this framework, the eigenvalues

of the two systems would be identical but the corresponding eigenvectors may differ, as shown in Appendix E with a simplified system where no electromagnetic field has been considered. Considering the nonconservative terms as a source term or as part of the hyperbolic system, does not change the jump conditions of rarefaction and shock waves for all the conservative variables, except the jump conditions associated with the internal energy of electrons (in the case where the adiabatic constants for electrons and heavy-particles are equal $\gamma = \gamma_e = \gamma_h$). Therefore, it is necessary to consider the nonconservative terms as part of the hyperbolic problem if the exact solution of the corresponding Riemann problem is investigated. This study has been performed by Wargnier, Faure, et al. (2018) in the case where no electromagnetic field has been considered. An extension of this study, considering the electromagnetic field, is required. Further details and discussions are provided in Chapter 7 and in Appendix E.

Conclusion

The general macroscopic model ($M_h^{\varepsilon=1}$) and ($M_e^{\varepsilon=1}$) coupled with the set of Maxwell's equations (Mx^{ε}) has been identified. The total current and electric field have been expressed in terms of transport fluxes, and a new generalized Ohm's law has been derived. The electric field has been expressed in terms of multicomponent electromagnetic matrices. These matrices depend on the interactions and the order of ε considered. Indeed, the multicomponent matrices which take into account the heavy-particle/heavy-particle or heavy-particle/electrons interactions scale at order ε, whereas those which take into account the electrons/electrons interactions scale at order ε^0. In addition, a general expression of the resistivity has been defined. This term takes into account all the possible interactions in the multicomponent plasma. The expression of the electric field (E) can be divided into three categories: 1-a resistive term, which takes into account the definition of the general resistivity and the current densities, 2- a term related to the thermodynamic forces of electrons, which takes into account the gradient of pressure and temperature of electrons and 3- a term related to the thermodynamic forces of heavy-particles, which takes into account the gradient of pressure and temperature of heavy-particles.

Then, we have simplified the general set of governing equations at order ε by coupling with the set of Maxwell's equations ($Mx^{\varepsilon=0}$). This coupling ensures the electroneutrality assumption at order ε^0. In this framework, we have obtained a vanishing electron diffusion velocity $\boldsymbol{V}_e = 0$. This leads to simplified expression of the general governing equations and transport fluxes. Therefore, the multicomponent model (Mc) has been obtained. A generalized Ohm's law has been derived. In this framework, the multicomponent matrices related to the interactions electrons/electrons, at order ε^0 are vanishing. Then, we have compared this simplified multicomponent model (Mc) with the classical multi-fluid models used for solar physics applications. In the multicomponent approach, only one hydrodynamic velocity for each species is considered. All the species are assumed to diffuse in this reference frame. Only one momentum equation is considered, and the electrons do not participate in the stress tensor, but participate in the momentum balance through the total pressure and Lorentz force. In the multicomponent approach, the dynamics of each particles are captured by the dissipative effects. In addition, new effects appear in the multicomponent model

that are absent in the classical multi-fluid MHD model, such as Soret/Dufour effects, described by Kolesnikov (2003). These terms play a role in the diffusion velocities and in the dynamics of the electric field through the multicomponent matrices.

We have investigated the fully ionized plasma case. We have obtained the simplified system (Mf) and the Ohm's law (Ef). We have compared this approach with the classical single-fluid approach. The classical single-fluid approach is a model in thermal equilibrium between heavy particles and electrons. However, in the fully ionized model (Mf), all collisional regimes are described, and thermal nonequilibrium processes between ions and electrons are allowed. The possibility of being able to represent all of these regimes is relevant in the solar atmosphere, since the plasma can be either highly collisional and multicomponent (such as the bottom of the chromosphere, or the photosphere) or fully ionized and weakly collisional (such as the top of the chromosphere, solar corona), as shown in Chapter 1.

Finally, we have studied the eigenstructure of the multicomponent models (Mc) and (Mf). The eigenvalues of this model are identical to the classical single-fluid ideal MHD model. Since thermal nonequilibrium processes are considered, the multicomponent system is showing nonconservative terms in the equation of internal energy of electrons. In the following, according to the numerical strategy established in Chapter 6, we have considered these terms as source terms and not as part of the hyperbolic problem. The hyperbolic problem associated with the multicomponent system has not been fully investigated in this thesis. Only a simplified case, where no electromagnetic field has been considered, has been studied in Chapter 7.

However, we underline that considering nonconservative terms as a source term or as part of the hyperbolic problem does not change the eigenstructure, but the eigenvectors may differ, as shown in Appendix E. In this context, the jump conditions associated with all the fields are identical in both cases, except the jump condition for the internal energy of electrons (in the case). Therefore, it is necessary to consider these terms in the study of the hyperbolic problem.

Part II

Transport properties

CHAPTER 4

TRANSPORT PROPERTIES FOR MULTICOMPONENT PLASMAS

Introduction

In the previous Chapters, the multicomponent models have been derived from the kinetic theory through a nondimensional asymptotic analysis performed on a generalized Chapman-Enskog expansion. The transport properties are retrieved through a generalized Chapman-Enskog solution to the Boltzmann equation using a multiscale perturbation method. The model includes thermal nonequilibrium between electrons and heavy particles, thus, the transport properties are depending on two temperatures T_e and T_h. As in Braginskii's theory, our model includes anisotropy in the transport properties of electrons, that is created by the magnetic field. However, the transport properties for heavy particle are isotropic at the last order investigated in the expansion. As shown in the previous Chapters, the developpement of the transport fluxes are similar to the Braginskii (1965) and Kolesnikov (2003) approach, where their derivations are based on a Chapman-Enskog expansion. However, at this step, all the transport coefficients are written in terms of bracket integrals. Therefore, it is necessary to solve these integrals to obtain an expression of the transport coefficients.

Several methods have been developed to obtain expressions of the transport coefficients for partially or fully ionized plasma. Generally, the development of the transport coefficients strongly depends on the method used to derive the governing equations; in particular, for models derived from the kinetic theory such as the multicomponent model. As an alternative example of the Chapman-Enskog method, Grad's method (see Haines (1990); Woods (1995); Zhdanov (2002)) can be also used to obtain an expression of the transport coefficients using irreducible tensorial Hermite polynomials. The accuracy of the transport coefficients depend on the number of Hermite polynomials taken for the closure. The convergence of the solution depends on the type of collisions considered. In the literature, three main approximations are generally used: the 13M,

21M and 29M-moment approximations. In fully ionized plasma, an accuracy higher than the 13M-moment approximation is required when only charged interactions between species are considered. The approximation is shown to be not accurate when the electrons are highly magnetized but the ions are weakly magnetized (see Haines (1990); Zhdanov (2002)). However, the difference between the 21M and 29-moment approximation is small. Alternatively, other studies have been performed on the development of transport properties for partially ionized plasmas.

In C. H. Kruger & Mitchner (1967); C. Kruger et al. (1968); Daybelge (1970), a spectral Galerkin method based on Laguerre-Sonine polynomials approximation is used to compute the transport coefficients for ionized gases in thermal equilibrium in the presence of a magnetic field. In Chmieleski & Ferziger (1967), the authors have presented an elegant formalism to derive the transport properties of ionized gases assuming that heavy particles have an infinite mass in collisions with electron partners. In Ferziger & Kaper (1973), this method is used to develop transport properties for a multicomponent plasma in thermal equilibrium. However, in these approaches, no transfer of energy in the electron-heavy collisions is considered. This assumption is necessary to decouple the thermal bath of heavy particles from the one of the electrons. Thus, no relaxation state of the system, where the electron temperature T_e differs from the heavy particles temperature T_h, is considered. In this context, Kolesnikov (2003) has developped transport systems for two-temperature plasmas in the presence of magnetic field, based on kinetic theory, where the transfer of energy between electrons and heavy-particles is considered.

In this thesis, the path of Kolesnikov (2003); Ferziger & Kaper (1973) has been followed by developing transport systems in thermal nonequilibrium, accounting for the influence of the magnetic field, using a spectral Galerkin method based on a third order Laguerre-Sonine polynomial approximation. This approach has been studied in depth for various applications (see S. R. Devoto (1969); Ferziger & Kaper (1973); Woods (1995); Zhdanov (2002); Magin & Degrez (2004); Bruno et al. (2011); Capitelli et al. (2013)). The transport properties are computed by solving for the integro-differential systems presented in Section 2.4. In Magin & Degrez (2004); Tirsky (1993), this method is shown to converge quickly, *i.e.*, only few Laguerre-Sonine polynomials are required to obtain the convergence. The transport properties are depending on the so called collision integrals which link the macroscopic transport fluxes to the kinetic level. The collision integrals depend on interaction potentials which govern the collisions taking place among the multicomponent plasma particles. Thus, the closure of the model is realized at a microscopic level since the interaction potentials are determined from experimental measurements.

For the purpose of this work, a Helium-Hydrogen mixture, composed of 92% Hydrogen and 8% of Helium in mole fraction, which is typical in the solar atmosphere (see Asplund et al. (2009)), is considered. The set of species considered in this mixture is denoted as

$$S_1 = \{\mathrm{He},\ \mathrm{He}^+,\ \mathrm{H},\ \mathrm{H}_2,\ \mathrm{He}^{++},\ \mathrm{H}^+,\ e-\}. \tag{4.0.1}$$

The heavy species such as carbon, oxygen or metals are not considered. We assume that they do not impact the transport properties as they are trace elements, *i.e.*, their mole fractions are small. However, the calculation of the collision integrals require the determination of the interaction potentials to be used for this mixture. Therefore, it is necessary to find the appropriate kinetic data

to compute them. For example, collision integrals data are provided for air mixture, as done by Capitelli et al. (2000); Abeele (2000). Riabov (1996) has computed transport properties in the Mars atmosphere conditions, including kinetic data for carbon dioxide mixtures. This data has been used to model high enthalpy plasmas flows for Mars atmospheric entries. Additionally, Park et al. (2001) have published a review of collision integrals for a pyrolysis gas of carbonous ablative material subjected to Earth entry. In this thesis, the collision integrals have been taken from Bruno et al. (2011) where collision integrals data for Helium-Hydrogen, or Hydrogen mixtures are provided. In order to be used in any conditions for our application, these data have been approximated by considering a curve-fit up to third order exponential polynomials function.

In this thesis, the heavy-particle transport coefficients are expressed as solution of linear systems whose size is proportional to the number of heavy species in the mixture. Consequently, the evaluation of these coefficients by direct inversion of linear systems can be computationally expensive if the number of species is too large, such as in the Helium-Hydrogen mixture. The computational effort for solving these systems may be excessive for multicomponent plasma simulations. Therefore, approximate mixture rules can be used to compute the multicomponent transport coefficients, as done by Wilke (1950); Gupta et al. (1990). However, these methods are known to be inaccurate in the dissociation and ionization ranges. In this thesis, the method proposed by Magin & Degrez (2004) has been followed, where low-cost accurate algorithms have been developed for partially ionized and unmagnetized plasmas. These algorithms rely either on convergent iterative Krylov projection methods, such as the conjugate gradient.They have been used for solving the heavy-particle transport systems.

In Section 4.1, for the purpose of assisting the reader, we provide a reminder of the transport fluxes and their corresponding transport coefficients. The transport coefficients are expressed in terms of bracket integrals. In Section 4.2, the spectral Galerkin method based on the Laguerre-Sonine polynomial approximation is described. The anisotropic electron transport systems and the isotropic heavy-particle transport systems are presented for a third order of Laguerre-Sonine polynomials approximation. In addition, the collision integrals required to solve the transport systems are provided. In Section 4.3, the collision integrals data used for the Helium-Hydrogen mixture, as well as the corresponding potential interactions are given. Finally, in Section 4.4, the transport algorithms used for the heavy-particle transport systems are presented.

4.1 List of the transport fluxes and coefficients of the multicomponent models

For the purpose of assisting the reader, we provide a reminder of the transport fluxes and coefficients presented in Chapter 2.

In Table 4.1, a list of all the transport fluxes of the model is provided, with the corresponding order of the Chapman-Enskog expansion, the equation and their transport coefficients. In Table 4.2 a list of these transport coefficients is provided in terms of bracket integrals. These coefficients are written in terms of components of perturbation functions which have been introduced in Chapter

Table 4.1: List of the transport fluxes

Order	Transport fluxes	Equation	Corresponding transport coefficient
ε^0	$\boldsymbol{V}_\mathfrak{e}$	(2.4.9)	$\bar{\bar{D}}_\mathfrak{e}$, $\bar{\bar{\chi}}_\mathfrak{e}$
	$\boldsymbol{q}_\mathfrak{e}$	(2.4.17)	$\bar{\bar{\lambda}}_\mathfrak{e}$ and those from $\boldsymbol{V}_\mathfrak{e}$
ε	$\boldsymbol{V}_i$	(2.4.30)	D_{ij}, $\chi_{\mathfrak{h},j}$
	$\boldsymbol{q}_\mathfrak{h}$	(2.4.37)	$\lambda_\mathfrak{h}$ and those from $\boldsymbol{V}_i$
	$\boldsymbol{\Pi}_\mathfrak{h}$	(2.4.32)	$\nu_\mathfrak{h}$
	$\boldsymbol{V}_\mathfrak{e}^{(1)}$	(2.4.46)	$\bar{\bar{\alpha}}_{\mathfrak{e}i}$ and those from $\boldsymbol{V}_i$
	$\boldsymbol{q}_\mathfrak{e}^{(1)}$	(2.4.48)	$\bar{\bar{\chi}}_{\mathfrak{e}i}$ and those from $\boldsymbol{V}_\mathfrak{e}^{(1)}$
	$\boldsymbol{F}_{ie}$	(2.4.51)	$\bar{\bar{\alpha}}_{\mathfrak{e}i}$ and $\bar{\bar{\chi}}_{\mathfrak{e}i}$

Table 4.2: List of the transport coefficients

Order	Interactions	Transport coefficient	Bracket integrals	Pert. functions
ε^0	Elec. - Elec.	$\bar{\bar{D}}_\mathfrak{e}$	(2.4.10)	$\boldsymbol{\varphi}_\mathfrak{e}^{D_\mathfrak{e}(l)}$, $l \in \{1,2\}$
		$\bar{\bar{\chi}}_\mathfrak{e}$	(2.4.12)	$\boldsymbol{\varphi}_\mathfrak{e}^{D_\mathfrak{e}(l)}, \boldsymbol{\varphi}_\mathfrak{e}^{\lambda'_\mathfrak{e}(l)}$ $l \in \{1,2\}$
		$\bar{\bar{\lambda}}_\mathfrak{e}$	(2.4.16)	$\boldsymbol{\varphi}_\mathfrak{e}^{\lambda'_\mathfrak{e}(l)}$ $l \in \{1,2\}$
ε	Elec. - HP	$\bar{\bar{\alpha}}_{\mathfrak{e}i}$, $i \in \mathrm{H}$	(2.4.47)	$\boldsymbol{\varphi}_\mathfrak{e}^{D_\mathfrak{e}(l)}, \boldsymbol{\varphi}_\mathfrak{e}^{D_i(l)}$ $l \in \{1,2\}$
		$\bar{\bar{\chi}}_{\mathfrak{e}i}$, $i \in \mathrm{H}$	(2.4.49)	$\boldsymbol{\varphi}_\mathfrak{e}^{\lambda'_\mathfrak{e}(l)}, \boldsymbol{\varphi}_\mathfrak{e}^{D_i(l)}$ $l \in \{1,2\}$
	HP - HP	D_{ij}, $i,j \in \mathrm{H}$	(2.4.28)	$\boldsymbol{\varphi}_\mathfrak{h}^{D_i}$
		$\chi_{\mathfrak{h},j}$, $j \in \mathrm{H}$	(2.4.31)	$\boldsymbol{\varphi}_\mathfrak{h}^{D_i}, \boldsymbol{\varphi}_\mathfrak{h}^{\lambda'_\mathfrak{h}}$
		$\nu_\mathfrak{h}$	(2.4.34)	$\boldsymbol{\varphi}_\mathfrak{h}^{\nu_\mathfrak{h}}$
		$\lambda_\mathfrak{h}$	(2.4.38)	$\boldsymbol{\varphi}_\mathfrak{h}^{\lambda'_\mathfrak{h}}$

2.

In Table 4.2, we underline that the transport coefficients are written in terms of bracket integrals. Therefore, it is still necessary to reduce these integrals and find the expression of all the perturbation functions. This step allows to obtain an expression of each transport coefficients. The solution of these integro-differential equations proceeds by expanding the perturbation functions into series of orthogonal polynomials and cutting the expansion to the desired order of approximation. The equations are thus reduced to sets of algebraic linear equations. The coefficients of these linear systems are functions of the macroscopic parameters and of the so-called collision integrals. They can be computed by standard methods once the cross-sections for collisions between the species of the mixture are known.

4.2 Transport systems

In this thesis, these integral equations (see Table 4.2) are solved by using a spectral Galerkin method based on the Laguerre-Sonine polynomial approximation. This method is widely stud-

ied in depth for various applications (see Scoggins et al. (2016); Bruno et al. (2011); Ferziger & Kaper (1973); Woods (1995); Magin & Degrez (2004); Zhdanov (2002); Magin & Degrez (2004); Capitelli et al. (2013)), and yields asymptotic solutions of the transport coefficients in terms of solutions to complex linear transport system. Note that these transport coefficients are expressed as generalized out of thermal equilibrium, where $T_{\mathfrak{e}} \neq T_{\mathfrak{h}}$.

First, the method used for the reduction of such systems, is presented. Among the various possibilities to compute the bracket integrals, we justify the choice of the method used for computing the transport coefficients. Then, we will show the thermal nonequilibrium transport systems for heavy particles and electrons. The transport systems obtained are written for any order of Laguerre Sonine polynomials.

4.2.1 Spectral Galerkin method based on Laguerre-Sonine polynomials approximation

An efficient method of reducing the integral equations of Table 4.2 is by using an approximation method based on a series expansion method. One possibility would be to follow the method of Grad (1949, 1963) to use a series expansion in Hermite polynomials. In this thesis, we follow an other path by expressing them in terms of Sonine polynomials. This method has been first introduced into kinetic theory by Burnett (1935). The two methods have shown to be equivalent in Jancel & Kahan (1966). But a discussion on the two methods is performed by Kumar (1966), showing that the method used with Sonine polynomials in Burnett (1935), is the most economial form in terms of algebra involved. In addition, in the work performed by Magin & Degrez (2004), this method is shown to converge quickly, *i.e.*, only few Laguerre-Sonine polynomials are required to obtain a sufficient level of accuracy. Indeed, Magin & Degrez (2004) have shown that a second or third order, for the heavy-particles and electrons respectively, is sufficient for the transport properties computation.

The Sonine polynomial of order integer n and index m is defined by

$$\mathcal{S}_m^{(n)}(x) = \sum_{p=0}^{n} \frac{\Gamma(m+n+1)}{(n-p)!p!\Gamma(m+p)} (-x)^p \,. \tag{4.2.1}$$

where Γ is the Gamma function. From (4.2.1), we note the particular values

$$\mathcal{S}_m^{(0)}(x) = 1, \quad \mathcal{S}_m^{(1)}(x) = m + 1 - x. \tag{4.2.2}$$

These polynomials are the coefficients of the following generating function

$$(1-s)^{-m-1} \exp\left(-\frac{xs}{1-s}\right) = \sum_{n=0}^{\infty} \mathcal{S}_m^{(n)}(x) s^n. \tag{4.2.3}$$

Then, we can verify that $\mathcal{S}_m^{(n)}(x)$ satisfy the following orthogonality relation

$$\int_0^\infty \exp(-x)\mathcal{S}_m^{(p)}(x)\mathcal{S}_m^{(q)}(x)x^m dx = \left.\begin{array}{ll} 0, & p \neq q \\ \Gamma(m+p+1)/p!, & p = q \end{array}\right\} \tag{4.2.4}$$

Finally, as developed by Ferziger & Kaper (1973); Zhdanov (2002); Magin & Degrez (2004), the perturbation functions related to the transport coefficients (see Table 4.2) are assumed to be expanded in a convergent series of Laguerre Sonine polynomials. Using the definition of the Sonine polynomials in (4.2.1) and the relation obtained in (4.2.4), the transport systems can be deduced. Solving such systems allow to obtain an expression of the transport coefficients.

In the following, the development of the perturbation functions in Laguerre-Sonine polynomials is shown for any order of approximation. Then, we show both electron and heavy-particle transport systems to be solved for having an expression of the transport coefficients. The systems are shown to be functions of collision integrals.

4.2.2 Electron transport systems

In this subsection, we focus on the development of the electron and electron/heavy particle transport systems. The systems allow for computing the anisotropic electron transport coefficients such as $\bar{\bar{D}}_e$, $\bar{\bar{\chi}}_e$ and $\bar{\bar{\lambda}}_e$ and the electron/heavy particle transport coefficients such as $\bar{\bar{\alpha}}_{ei}$ and $\bar{\bar{\chi}}_{ei}$.

To obtain these systems, the electron perturbation functions (see Table 4.2) are assumed to be expanded in terms of Laguerre Sonine polynomials. For example, as shown by Scoggins et al. (2016), we have

$$\boldsymbol{\varphi}_e^{D_e(l)} = \frac{1}{p_e}\sqrt{\frac{2m_e}{k_B T_e}}\sum_{q\in P_\xi} \alpha_e^{qD_e(l)} \mathcal{S}_{3/2}^{(q)}\left(\frac{2|\boldsymbol{C}_e|^2}{k_B T_e}\right)\sqrt{\frac{2\boldsymbol{C}_e}{k_B T_e}} \quad , \; l \in \{1,2\} \tag{4.2.5}$$

where $P_\xi = \{0, ..., \xi - 1\}$ is the order of Sonine polynomials and $\xi \geq 1$. The other perturbation functions such as $\boldsymbol{\varphi}_e^{\lambda'_e(l)}, \boldsymbol{\varphi}_e^{D_i(l)}$, $l \in \{1,2\}$ are expanded in a similar way. Then, by injecting (4.2.5) into (2.4.6a) , using the definition of (4.2.1) and the orthogonality relation (4.2.4), the following system is obtained:

$$\begin{aligned} &\sum_{q\in P_\xi} L_{ee}^{pq}\alpha_e^{qD_e(1)}(\xi) = \beta_e^{pD_e}, \quad p \in P_\xi, \\ &\sum_{q\in P_\xi} (L_{ee}^{pq} + \mathtt{i}L_{ee}^{Bpq})\alpha_e^{qD_e(2)}(\xi) = \beta_e^{pD_e}, \quad p \in P_\xi, \end{aligned} \tag{4.2.6}$$

where the expression of the coefficients $L_{ee}^{pq}, L_{ee}^{Bpq}$ and $\beta_e^{pD_e}$ are given in Appendix B.1, up to $\xi = 3$. Similarly, by following a similar pattern as $\boldsymbol{\varphi}_e^{D_e(l)}$, a transport system for the coefficients $\alpha_e^{qD_i(1)}$ and $\alpha_e^{qD_i(2)}$ related to $\boldsymbol{\varphi}_e^{D_i(l)}$, $l \in \{1,2\}$ can be obtained by simply replacing D_e by D_i in (4.2.6).

Then, in a similar pattern, we 1- expand $\boldsymbol{\varphi}_e^{\lambda'_e(l)}$, $l \in 1,2$ as (4.2.5), 2- inject the expression of $\boldsymbol{\varphi}_e^{\lambda'_e(l)}$ into (2.4.6a) and 3- use the definition of (4.2.1) and the orthogonality relation (4.2.4) to obtain

the following system

$$\begin{aligned}
&\sum_{q\in P_{\xi 1}} L_{\mathfrak{e}\mathfrak{e}}^{pq}\alpha_{\mathfrak{e}}^{q\lambda'_{\mathfrak{e}}(1)}(\xi) = \beta_{\mathfrak{e}}^{p\lambda'_{\mathfrak{e}}}, \quad p\in P_{\xi 1},\\
&\sum_{q\in P_{\xi 1}} (L_{\mathfrak{e}\mathfrak{e}}^{pq} + \mathtt{i}L_{\mathfrak{e}\mathfrak{e}}^{Bpq})\alpha_{\mathfrak{e}}^{q\lambda'_{\mathfrak{e}}(2)}(\xi) = \beta_{\mathfrak{e}}^{p\lambda'_{\mathfrak{e}}}, \quad p\in P_{\xi 1},
\end{aligned} \tag{4.2.7}$$

where $P_{\xi 1} = \{1,\dots,\xi-1\}$ for $\xi \geq 2$.

Note that, the presented systems are depending on the coefficients $L_{\mathfrak{e}\mathfrak{e}}^{pq}, L_{\mathfrak{e}\mathfrak{e}}^{Bpq}$. These coefficients are expressed in terms of reduced binary collision integrals, which take into account the interaction between particles at the kinetic level. They are functions of the collision cross-sections between each particles.

Finally, three systems have been obtained. They allow to obtain expressions of the coefficients $\alpha_{\mathfrak{e}}^{qD_{\mathfrak{e}}(l)}$, $\alpha_{\mathfrak{e}}^{qD_i(l)}$ and $\alpha_{\mathfrak{e}}^{q\lambda'_{\mathfrak{e}}(l)}$ of their respective perturbative functions $\boldsymbol{\varphi}_{\mathfrak{e}}^{D_{\mathfrak{e}}(l)}, \boldsymbol{\varphi}_{\mathfrak{e}}^{D_i(l)}$ and $\boldsymbol{\varphi}_{\mathfrak{e}}^{\lambda'_{\mathfrak{e}}(l)}$. The next step is to express the electron and electron/heavy particle transport coefficients as function of these coefficients.

Electron diffusion coefficient $\bar{\bar{D}}_{\mathfrak{e}}$

According to Table 4.2, the expression of the electron diffusion coefficient $\bar{\bar{D}}_{\mathfrak{e}}$ can be obtained by injecting the expression of $\boldsymbol{\varphi}_{\mathfrak{e}}^{D_{\mathfrak{e}}(l)}$, in terms of Laguerre-Sonine polynomials defined in (4.2.5), into (2.4.10). Finally, we obtain the transport coefficients as function of the coefficients of the Laguerre-Sonine polynomials approximation:

$$D_{\mathfrak{e}}^{\parallel}(\xi) = \alpha_{\mathfrak{e}}^{0D_{\mathfrak{e}}(1)}(\xi), \quad \text{and} \quad (D_{\mathfrak{e}}^{\perp} + \mathtt{i}D_{\mathfrak{e}}^{\odot})(\xi) = \alpha_{\mathfrak{e}}^{0D_{\mathfrak{e}}(2)}(\xi). \tag{4.2.8}$$

where $\alpha_{\mathfrak{e}}^{0D_{\mathfrak{e}}(1)}$ and $\alpha_{\mathfrak{e}}^{0D_{\mathfrak{e}}(2)}$ are computed from the system (4.2.6). The electron diffusion coefficient $\bar{\bar{D}}_{\mathfrak{e}}$ is expressed in terms of collision integrals.

Electron thermal conductivity $\bar{\bar{\lambda}}_{\mathfrak{e}}$ and $\bar{\bar{\lambda}}'_{\mathfrak{e}}$

Similarly, according to Table 4.2, the expression of $\bar{\bar{\lambda}}'_{\mathfrak{e}}$ can be determined by injecting the expression of $\boldsymbol{\varphi}_{\mathfrak{e}}^{\lambda'_{\mathfrak{e}}(l)}$ in terms of Laguerre-Sonine polynomials, into (2.4.16). Then, we obtain the following expressions:

$$\lambda'^{\parallel}_{\mathfrak{e}}(\xi) = \frac{5}{2}n_{\mathfrak{e}}k_B\alpha_{\mathfrak{e}}^{1\lambda'_{\mathfrak{e}}(1)}(\xi), \quad \text{and} \quad (\lambda'^{\perp}_{\mathfrak{e}} + \mathtt{i}\lambda'^{\odot}_{\mathfrak{e}})(\xi) = \frac{5}{2}n_{\mathfrak{e}}k_B\alpha_{\mathfrak{e}}^{1\lambda'_{\mathfrak{e}}(2)}(\xi). \tag{4.2.9}$$

where $\alpha_{\mathfrak{e}}^{1\lambda'_{\mathfrak{e}}(1)}$ and $\alpha_{\mathfrak{e}}^{1\lambda'_{\mathfrak{e}}(2)}$ can be computed from the system (4.2.7). Then, the component of the electron thermal conductivity $\bar{\bar{\lambda}}_{\mathfrak{e}}$ are determined from the relation (2.4.18). The electron thermal conductivity $\bar{\bar{\lambda}}_{\mathfrak{e}}$ is expressed in terms of collision integrals.

Electron thermal diffusion coefficients $\bar{\bar{\chi}}_{\mathfrak{e}}$ and $\bar{\bar{\theta}}_{\mathfrak{e}}$

Similarly, based on Table 4.2, the expressions of the transport coefficients $\bar{\bar{\chi}}_{\mathfrak{e}}$ and $\bar{\bar{\theta}}_{\mathfrak{e}}$ are determined from the expression of $\boldsymbol{\varphi}_{\mathfrak{e}}^{\lambda'_{\mathfrak{e}}(l)}$ and $\boldsymbol{\varphi}_{\mathfrak{e}}^{D_{\mathfrak{e}}(l)}$, defined in terms of Laguerre-Sonine polynomials, injected into (2.4.10). Thus, the components of the electron thermal diffusion ratio are defined as

$$\chi_{\mathfrak{e}}^{\parallel}(\xi) = \sum_{q\in P_{\xi 1}} L_{\mathfrak{e}\mathfrak{e}}^{0q}\alpha_{\mathfrak{e}}^{q\lambda'_{\mathfrak{e}}(1)}(\xi), \quad \text{and} \quad (\chi_{\mathfrak{e}}^{\perp} + \mathtt{i}\chi_{\mathfrak{e}}^{\odot})(\xi) = \sum_{q\in P_{\xi 1}} L_{\mathfrak{e}\mathfrak{e}}^{0q}\alpha_{\mathfrak{e}}^{q\lambda'_{\mathfrak{e}}(2)}(\xi), \tag{4.2.10}$$

where $L_{\mathfrak{e}\mathfrak{e}}^{0q}$ are defined in Appendix B, and, $\alpha_{\mathfrak{e}}^{q\lambda'_{\mathfrak{e}}(1)}$ and $\alpha_{\mathfrak{e}}^{q\lambda'_{\mathfrak{e}}(2)}$ are determined from the system (4.2.7). Then, the components of $\bar{\bar{\theta}}_{\mathfrak{e}}$ are determined from the relation (2.4.12). Finally, the electron thermal diffusion ratio is also expressed in terms of collision integrals

Electron/Heavy-particle transport coefficient $\bar{\bar{\alpha}}_{\mathfrak{e}i}$

As shown in Table 4.2, the expression of $\bar{\bar{\alpha}}_{\mathfrak{e}i}$ is obtained by using the perturbative functions $\boldsymbol{\varphi}_{\mathfrak{e}}^{D_{\mathfrak{e}}(l)}$ and $\boldsymbol{\varphi}_{\mathfrak{e}}^{D_i(l)}$ expanded in terms of Laguerre-Sonine polynomials, injected into (2.4.47). Then, the components of the transport coefficients $\bar{\bar{\alpha}}_{\mathfrak{e}i}$ are defined as

$$\alpha_{\mathfrak{e}i}^{\parallel}(\xi) = \sum_{q\in P_{\xi 1}} \alpha_{\mathfrak{e}}^{qD_{\mathfrak{e}}(1)}(\xi)\beta_{\mathfrak{e}}^{qD_i}, \quad \text{and} \quad (\alpha_{\mathfrak{e}i}^{\perp} + \mathtt{i}\alpha_{\mathfrak{e}i}^{\odot})(\xi) = \sum_{q\in P_{\xi 1}} \alpha_{\mathfrak{e}}^{qD_{\mathfrak{e}}(2)}(\xi)\beta_{\mathfrak{e}}^{qD_i}. \tag{4.2.11}$$

where $\beta_{\mathfrak{e}}^{qD_i}$ is defined in Appendix B, and, the coefficients $\alpha_{\mathfrak{e}}^{qD_{\mathfrak{e}}(1)}$ and $\alpha_{\mathfrak{e}}^{qD_{\mathfrak{e}}(2)}$ are computed from the system (4.2.6). Finally, the components of $\bar{\bar{\alpha}}_{\mathfrak{e}i}$ are expressed as function of collision integrals.

Electron/Heavy-particle transport coefficient $\bar{\bar{\chi}}_{\mathfrak{e}i}$

The anisotropic transport coefficient $\bar{\bar{\chi}}_{\mathfrak{e}i}$ is obtained by using the perturbative functions $\boldsymbol{\varphi}_{\mathfrak{e}}^{\lambda'_{\mathfrak{e}}(l)}$ and $\boldsymbol{\varphi}_{\mathfrak{e}}^{D_i(l)}$ expanded in terms of Laguerre-Sonine polynomials, injected into (2.4.49). Then, we obtain

$$\chi_{\mathfrak{e}i}^{\parallel}(\xi) = -\frac{5}{2}\alpha_{\mathfrak{e}}^{1D_i(1)}(\xi), \quad \text{and} \quad (\chi_{\mathfrak{e}i}^{\perp} + \mathtt{i}\chi_{\mathfrak{e}i}^{\odot})(\xi) = -\frac{5}{2}\alpha_{\mathfrak{e}}^{1D_i(2)}(\xi). \tag{4.2.12}$$

where the coefficients $\alpha_{\mathfrak{e}}^{1D_i(1)}$ and $\alpha_{\mathfrak{e}}^{1D_i(2)}$ are determined from (4.2.6) by replacing $D_{\mathfrak{e}}$ by D_i.

Finally all the electron and electron/heavy-particle transport properties have been determined and expressed as function of the coefficients of the Laguerre-Sonine expansion. They are computed by solving a system, where the coefficients are depending on the collision integrals.

4.2.3 Heavy-particle transport systems

Similarly as the previous Section 4.2.2, we expand the perturbation functions $\boldsymbol{\varphi}_{\mathfrak{h}}^{D_i}, \boldsymbol{\varphi}_{\mathfrak{h}}^{\nu_{\mathfrak{h}}}, \boldsymbol{\varphi}_{\mathfrak{h}}^{\lambda'_{\mathfrak{h}}}$ in terms of Sonine polynomials. These functions are injected into (2.4.24), which lead to heavy particle transport systems, which are not exhibit here. These systems allow us to obtain the heavy-particle transport coefficients D_{ij}, $\chi_{\mathfrak{h},j}$, $i, j \in \mathrm{H}$, $\lambda_{\mathfrak{h}}$ and $\nu_{\mathfrak{h}}$, as presented in the previous section for the electron transport systems.

Multicomponent diffusion coefficient D_{ij}

First order heavy-particle multicomponent diffusion coefficients are found to be the solution of n^{H} linear systems of the form

$$D_{ij} = d_i^j, \tag{4.2.13}$$

$$\sum_{j\in\mathrm{H}} \Lambda_{ij}^{00} d_j^k = \delta_{ki} - \hat{y}_i, \quad k, i \in \mathrm{H}, \tag{4.2.14}$$

where Λ_{ij}^{00} is defined in terms of reduced collision integral in Appendix B, $\hat{y}_i$ is the mass fraction of specie i, where the hat denotes that it is only over heavy species, ie: $\hat{y}_i = y_i/(1 - y_{\mathrm{e}})$ for $i \in \mathrm{H}$. Note that, the coefficients D_{ij} are related to the solutions d_i^j of the linear system (4.2.14). This relation is simply written as (4.2.13).

Usually diffusion matrices may be singular, *i.e.* non invertible, because of the total mass conservation constraints. A consequence is that when all mass fractions are treated as independent unknowns, a widely used approach in complex chemistry reacting flow solvers-artificial singularities may appear in the governing equations. It becomes necessary to modify the usual diffusion algorithms in order to eliminate singularities without changing the actual values of the diffusion velocities. One alternative would be to follow the work performed by Magin & Degrez (2004); Magin (2004); Bruno et al. (2011). In addition, iterative methods proposed by Giovangigli (1990); Ern & Giovangigli (1994), is also an alternative to eliminate these singularities. Such alternatives will be presented in the final section of this chapter.

Heavy thermal conductivity $\lambda_{\mathfrak{h}}$

Similarly, the heavy-particle thermal conductivity $\lambda_{\mathfrak{h}}$ is found to be the solution of a linear system of the form

$$\lambda_{\mathfrak{h}} = \sum_{i\in\mathrm{H}} \alpha_i^{\lambda_{\mathfrak{h}}} \hat{x}_i, \tag{4.2.15}$$

$$\sum_{j\in\mathrm{H}} G_{ij}^{\lambda_{\mathfrak{h}}} \alpha_j^{\lambda_{\mathfrak{h}}} = \hat{x}_i, \quad i \in \mathrm{H}, \tag{4.2.16}$$

where the hat on mole denotes that they are only over heavy species, i.e., $\hat{x}_i = x_i/(1 - x_e)$ for $i \in \mathrm{H}$, the matrix $G_{ij}^{\lambda_h}$ is defined in terms of collision integrals in Appendix B.

Heavy-particle viscosity ν_h

The heavy-particle viscosity ν_h is the solution of the following linear transport system

$$\nu_h = \sum_{i \in \mathrm{H}} \alpha_i^{\nu_h} \hat{x}_i, \tag{4.2.17}$$

$$\sum_{j \in \mathrm{H}} G_{ij}^{\nu_h} \alpha_j^{\nu_h} = \hat{x}_i, \quad i \in \mathrm{H}, \tag{4.2.18}$$

where the matrix $G_{ij}^{\nu_h}$ is defined in terms of collision integrals in Appendix B.

Heavy-particle thermal diffusion ratio $\chi_{h,j}$

The heavy-particle thermal diffusion ratio $\chi_{h,j}$, $j \in \mathrm{H}$ is the solution of the following linear transport system

$$\chi_{h,j} = \frac{5}{2} \sum_{k \in \mathrm{H}} \Lambda_{jk}^{01} \alpha_k^{\lambda_h}, \quad j \in \mathrm{H}, \tag{4.2.19}$$

where $\alpha_k^{\lambda_h}$ is determined from the system (4.2.15) and (4.2.16), and Λ_{jk}^{01} is defined in Appendix B.

In summary, we have determined an expression of each transport coefficient of Table 4.2, in thermal nonequilibrium for a multicomponent plasma. We have expanded the components of each perturbation functions in terms of Laguerre Sonine polynomials up to the third order. The transport systems have been obtained for both electrons and heavy particles. These systems allow to obtain expressions for each transport coefficient as a function of collision integrals. A list of the collision integrals related to each transport coefficient can be found in Table 4.3. Note that, the total number of collision integrals required to compute all of the transport coefficients scales with the number of species squared, since all collision pairs must be taken into account.

Although the transport coefficients have been expressed in terms of collision integrals, they remain to be determined. The collision integrals depend on the potential of interactions and cross sections of the species involved.

Table 4.3: Required collision integrals for each transport coefficients at the third order of Laguerre-Sonine polynomials and number of unique reduced collision integrals which must be evaluated. Some reduced collision integrals are required by several coefficients.

Property	**Collision integrals**	**Number**
$\bar{\bar{D}}_{\mathfrak{e}}$	$\bar{Q}_{\mathfrak{e}j}^{(1,k)}$ and $\bar{Q}_{\mathfrak{e}j}^{(2,2)}$, $j \in \mathrm{H}$, $k \in \{1,3\}$	$(3n^{\mathrm{H}}+1)$
$\bar{\bar{\lambda}}_{\mathfrak{e}}$	$\bar{Q}_{\mathfrak{e}j}^{(1,k)}$, $\bar{Q}_{\mathfrak{e}j}^{(2,l)}$, $j \in \mathrm{H}$, $k \in \{1,3\}$ and $l \in \{2,4\}$	$(5n^{\mathrm{H}}+3)$
$\bar{\bar{\chi}}_{\mathfrak{e}}$	$\bar{Q}_{\mathfrak{e}j}^{(1,k)}$, $\bar{Q}_{\mathfrak{e}j}^{(2,l)}$, $j \in \mathrm{H}$, $k \in \{1,3\}$ and $l \in \{2,4\}$	$(5n^{\mathrm{H}}+3)$
$\bar{\bar{\alpha}}_{\mathfrak{e}i}$	$\bar{Q}_{\mathfrak{e}j}^{(1,k)}$, $\bar{Q}_{\mathfrak{e}j}^{(2,l)}$, $j \in \mathrm{H}$, $k \in \{1,3\}$ and $l \in \{2,4\}$	$(5n^{\mathrm{H}}+3)$
$\bar{\bar{\chi}}_{\mathfrak{e}i}$	$\bar{Q}_{\mathfrak{e}j}^{(1,k)}$, $\bar{Q}_{\mathfrak{e}j}^{(2,l)}$, $j \in \mathrm{H}$, $k \in \{1,3\}$ and $l \in \{2,4\}$	$(5n^{\mathrm{H}}+3)$
D_{ij}	$\bar{Q}_{ij}^{(1,1)}$, $i,j \in \mathrm{H}$	$n^{\mathrm{H}}(n^{\mathrm{H}}+1)/2$
$\lambda_{\mathfrak{h}}$	$\bar{Q}_{ij}^{(1,k)}$ and $\bar{Q}_{ij}^{(2,2)}$, $i,j \in \mathrm{H}$, $k \in \{1,3\}$	$2n^{\mathrm{H}}(n^{\mathrm{H}}+1)$
$\nu_{\mathfrak{h}}$	$\bar{Q}_{ij}^{(1,1)}$ and $\bar{Q}_{ij}^{(2,2)}$, $i,j \in \mathrm{H}$	$n^{\mathrm{H}}(n^{\mathrm{H}}+1)$
$\chi_{\mathfrak{h},j}$	$\bar{Q}_{ij}^{(1,k)}$, $i,j \in \mathrm{H}$, $k \in \{1,2\}$	$n^{\mathrm{H}}(n^{\mathrm{H}}+1)$

4.3 Transport collision integrals

The collision integrals are denoted by $\bar{Q}_{ij}^{(l,s)}$, associated with the (i, j) interaction pair and characterized by the order (l, s). These terms are relevant since they link the macroscopic transport fluxes to microscopic dynamics of binary particles encountered. The calculation of the collision integrals is performed in the frame of the classical mechanics of elastic collisions. We point out the effects of chemistry and internal energy on the transport systems are neglected. The collision integrals are computed by specifying a potential of interaction ϕ_{ij} between the two particles which are colliding. In this thesis, we have focused on mixtures such as the Helium-Hydrogen mixture defined in (4.0.1) in order to be representative of the solar atmosphere and consistent with our applications.

In the first subsection, the general collision integrals are defined. Then, the corresponding potential of interactions are introduced for simplifying the collision integrals, depending on the type of interactions considered. A complete description of the collision integrals data associated with the Helium-Hydrogen and Hydrogen mixture is provided. Such data are provided by Bruno et al. (2011).

4.3.1 Collision integrals

Following Magin & Degrez (2004); Magin (2004); Bruno et al. (2011); Capitelli et al. (2013), the classical reduced collision integrals associated to the (i, j) interaction pair, characterized by the order (l, s) are defined as

$$\bar{Q}_{ij}^{(l,s)} = \frac{4(l+1)}{(s+1)!\,[2l+1-(-1)^l]} \int_0^\infty \exp(-\mathfrak{g}_{ij}^2)\mathfrak{g}_{ij}^{2s+3} Q_{ij}^{(l)} d\mathfrak{g}_{ij}, \quad i,j \in \mathrm{S} \tag{4.3.1}$$

where

$$\mathfrak{g}_{ij} = \begin{cases} \{m_i m_j / \left[(m_i + m_j) 2k_B T_{\mathfrak{h}}\right]\}^{1/2} \boldsymbol{g}_{ij}, & i, j \in \mathrm{H} \\ \{m_{\mathfrak{e}} / 2k_B T_{\mathfrak{e}}\}^{1/2} \boldsymbol{g}_{ij}, & i = \mathfrak{e} \quad \text{and} \quad j \in \mathrm{H} \\ \{m_{\mathfrak{e}} / 4k_B T_{\mathfrak{e}}\}^{1/2} \boldsymbol{g}_{ij}, & i = j = \mathfrak{e} \end{cases} \tag{4.3.2}$$

and $\boldsymbol{g}_{ij} = \boldsymbol{c}_i - \boldsymbol{c}_j = \boldsymbol{\omega}|\boldsymbol{c}_i - \boldsymbol{c}_j|$ is the relative velocity between particle i and j and $Q_{ij}^{(l)}$ is the transport cross-section. Alternatively, the reduced collision integrals in (4.3.1) can be seen as a deviation from the rigid sphere model (see S. R. Devoto (1969); Hirschfelder et al. (1964)), as follow

$$\bar{Q}_{ij}^{(l,s)} = \pi \sigma_{HS}^2 \, \Omega_{(i,j)}^{(l,s)}, \quad i, j \in \mathrm{S} \tag{4.3.3}$$

where $\Omega_{(i,j)}^{(l,s)}$ are the standard reduced collision integrals normalized by the corresponding hard-sphere values (see Hirschfelder et al. (1964)), and $\pi\sigma_{HS}^2$ is the hard-sphere cross-section.

It should be mentionned that charged interactions excluded, the reduced collision integrals depend only on temperature. In addition, if the particles are assumed to interact as rigid hard spheres, they are independent on temperature and equal to the interaction cross-section σ_{HS}^2. Such approximation are usually considered in the closure of multi-fluid models applied to the modeling of the solar atmosphere as done by Ni et al. (2018); Leake et al. (2013); Leake et al. (2012); Martínez-Sykora et al. (2015). However, we will see that such approximation may have a strong impact on the accuracy of the transport coefficients.

In this thesis,more general interactions between particles have been considered. The generalized cross-section given in classical mechanics is defined by

$$Q_{ij}^{(l)} = 2\pi \int_0^\infty \left(1 - \cos^l \hat{\chi}_{ij}\right) b db. \tag{4.3.4}$$

where $\hat{\chi}$ and b are the deflection angle and impact parameter describing a binary collision (see Ferziger & Kaper (1973)). Figure 4-1 represent a scheme involving these parameters. Then, the deflection angle is given from classical mechanics as

$$\hat{\chi}_{ij} = \pi - 2b \int_{r_m}^\infty \frac{1/r^2}{\sqrt{1 - b^2/r^2 - \phi_{ij}(r) / \left(\frac{1}{2}\left[\frac{m_i m_j}{m_i + m_j}\right] \boldsymbol{g}_{ij}^2\right)}} dr, \quad i, j \in \mathrm{H} \tag{4.3.5}$$

where r_m is the distance of closest approach (or the location of the potential wall), and $\phi_{ij}(r)$ is the spherical interaction potential.

Generally, the collision integrals defined in (4.3.1) are computed by numerically integrating them from accurate *ab initio* potential energy surfaces, from experimental measurements. For example, recent reviews of collision integrals data for neutral-neutral interactions are provided by Wright et al. (2005, 2007) for air, Mars, and Venus mixtures. The collision integrals have been tabulated from a temperature up to 20000 K. Additionally, we have the review of Bruno et al. (2011) where collision integrals data are provided as accurate curve-fits for Helium-Hydrogen Jupiter mixtures, up to 50000 K.

Most of the collision integrals data considered for the Helium-Hydrogen and Hydrogen mixture

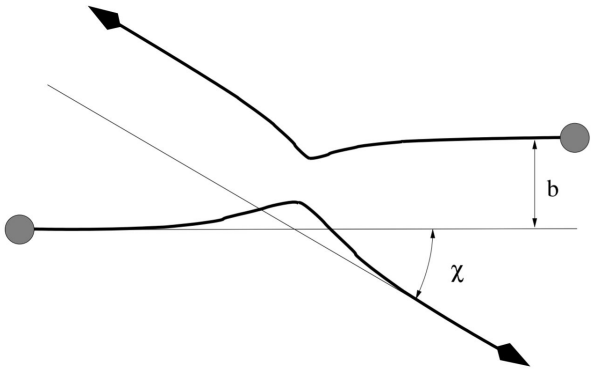

Figure 4-1: Elastic binary collision involving parameters $\hat{\chi}$ and b

have been taken from the work of Bruno et al. (2011). For these data, a curve-fit up to third order exponential polynomials is proposed, as follows

$$\Omega^{(l,s)}_{(i,j)}(T) = \exp\left[A\ln(T)^3 + B\ln(T)^2 + C\ln(T) + D\right]. \tag{4.3.6}$$

where the coefficients of these fits are given Appendix C. These data have been computed using several type of potential interactions ϕ which are provided with further details in the next subsection. The potential of interactions depend on the type of interactions considered such as: neutral-neutral, neutral-ions, electron-neutral or charged interactions.

When such collision integrals data are not available, it is necessary to integrate the collision integrals from model interaction potentials, depending on the interaction considered. For example, in the Helium-Hydrogen mixture, the collision integrals data for the charged interactions are computed following the potential interaction of Coulomb.

In the next subsection, we exhibit the data sources that have been used by Bruno et al. (2011) to compute the collision integrals of the Helium-Hydrogen mixture.

4.3.2 Potential of interactions

The computation of collision integrals is fundamentally connected to the interaction potential ϕ which governs the interaction between the species of the mixture considered. These potentials have been invented in order to reproduce the general features of electronic states, bound states charaterized by a potential with a short-range repulsive region or purely repulsive states, and increasing as the internuclear coordinate tends to zero. Such functions ensure the correct behavior in the asymptotic regions and allow to integrate them in a wide energy range.

Neutral interactions

In the case of the Helium-Hydrogen mixture, the potential interactions used depend on the species considered. Indeed, for the $H/H, H/H_2$ and H_2/H_2 interactions, accurate collision integrals com-

putation have been performed by R. Stallcop et al. (1998); Chhabra et al. (1996), based on *ab initio* potential energy surfaces. For H/H_2 and H_2/H_2 interactions, the data are provided up to $T = 20000$ K, which is enough for our application. Concerning the He/H and He/H_2 interactions, the Hulburt-Hirschfelder potentials (see Hirschfelder et al. (1964)), which include short-range repulsive and long-range weakly attractive *ab initio* results have been used by Meyer & Frommhold (1994); Olson & Liu (1980); Y. Li & Lin (1999). Finally, for the He/He interaction, data are provided by Tang et al. (1995); Tang & Toennies (2003).

The data are provided by Bruno et al. (2011). As presented in (4.3.6), these data have been fitted with a third order exponential function, where the coefficients are given in Appendix C.

Ion-Neutral interactions

Concerning the H/He^+ interaction, the collision integrals data are provided by Aubreton et al. (2004). The data are based on a Hulburt-Hirschfelder fitting from accurate *ab initio* potential. Similarly, the He/He^+ interaction, data are given by Aubreton et al. (2003), where a Hulburt-Hirschfelder combined to a modified repulsive potential has been used. Then, for the H/H^+ interaction, the data are provided by Sharp (1970); Sourd et al. (2006), where a Hulburt-Hirschfelder and a modified Morse potential have been used. In addition, the data for H^+/H_2 and H^+/He interactions have been highly investigated by Krstic (2002); Krstic & Schultz (2003, 1999), where a Hulburt-Hirschfelder and a polarisation model, have been used. The collision integrals data for the interaction He/He^{++} can be found in the work of Schmidt (1989). Finally, for the other ion-neutral interactions such as H/He^{++}, H_2/He^+ and H_2/He^{++} the collision integrals data have been obtained using the repulsive/attractive polarization potential (see Kihara et al. (1960); Woods (1995)), where the polarisability values can be found in Bruno et al. (2011).

Note that, a fit of these data have been provided in this work using an exponential approach in (4.3.6), where the coefficients of these fits are also given in Appendix C.

Electron-neutral interactions

Considering the complexity of the interaction, it is difficult to find an approximation of the collision integrals. The usual method for computing the collision integrals is based on numerical integration of the differential elastic cross section. The cross section is integrated over all scatering angles to provide integral cross section versus energy. Then, a Boltzmann energy distribution is assumed to obtain the collisions integrals as functions of the temperature. This method has been highly used in Wright et al. (2005, 2007) for application to air, Mars and Venus atmosphere. Further details are given by Scoggins (2017).

This method has also been used for the Helium-Hydrogen mixture. The e/H interaction has been studied by Gupta & Mathur (1978); Bray et al. (1991) and find good agreement with experiments performed by Williams (1975b,a). Then, the e/H_2 interaction has been studied by Brunger & Buckman (2002); Shyn & Grafe (1992). Finally, the cross-section functions for the e/He interaction can be found online in Biagi (2012).

Similarly as the previous interactions considered in the Helium-Hydrogen mixture, the electron-neutral interactions have been fitted also with an exponential approach.

Charged interactions

In order to model charged interactions, we have used the screened Coulomb potential from Capitelli et al. (2013); Bruno et al. (2011). It is shielded by the Debye length, and has the form

$$\phi_{ij}(r) = \frac{z_i z_j q_e^2}{4\pi\varepsilon_0 r} \exp\left(\frac{-r}{\lambda_D}\right), \tag{4.3.7}$$

with z_i and z_j are the charges of particles i and j and λ_D is the Debye length. It is a characteristic length over which the charged particles in a plasma can be considered shielded from other charged particles. The Debye length in thermal nonequilibrium, including both electrons and ions densities, is defined as

$$\lambda_D = \sqrt{\frac{\varepsilon_0 k_B / q_e^2}{n_e/T_e + \sum_{j\in \mathrm{H}} z_j^2 n_j / T_h}}. \tag{4.3.8}$$

Such definition of the Debye length (4.3.8), is inspired from Andre et al. (2007), where the Debye length account for the screening effects of ions. Usually, an alternative is proposed in the literature (see S. R. Devoto (1969)) where only the screening due to electrons is considered. Note that, for neutral plasmas with $T_e = T_h = T$, the usual Debye length accounting only for the screening due to electrons is retrieved :

$$\lambda_D = \sqrt{\frac{\varepsilon_0 k_B T}{2 q_e^2 n_e}}. \tag{4.3.9}$$

In order to model the charged interactions, as a first approximation, one possibility would be to use the closed form of the collision integrals obtained by R. S. Devoto (1967); Capitelli et al. (2013) from the interaction potential (4.3.8), as follows

$$\begin{aligned}
\bar{Q}_{ij}^{(1,s)} &= \pi \left[\frac{4}{s(s+1)}\right] b_0^2 \left[\ln \frac{2\lambda_D}{b_0} - \frac{1}{2} - 2\bar{\gamma} + \bar{\psi}(s)\right], \\
\bar{Q}_{ij}^{(2,s)} &= \pi \left[\frac{12}{s(s+1)}\right] b_0^2 \left[\ln \frac{2\lambda_D}{b_0} - 1 - 2\bar{\gamma} + \bar{\psi}(s)\right], \\
\bar{Q}_{ij}^{(3,s)} &= \pi \left[\frac{12}{s(s+1)}\right] b_0^2 \left[\ln \frac{2\lambda_D}{b_0} - \frac{7}{6} - 2\bar{\gamma} + \bar{\psi}(s)\right], \\
\bar{Q}_{ij}^{(4,s)} &= \pi \left[\frac{16}{s(s+1)}\right] b_0^2 \left[\ln \frac{2\lambda_D}{b_0} - \frac{4}{3} - 2\bar{\gamma} + \bar{\psi}(s)\right],
\end{aligned} \tag{4.3.10}$$

where $b_0 = z_i z_j q_e^2 / 2k_B T$, $\bar{\gamma}$ is the Euler constant and $\bar{\psi}(s) = \sum_1^{s-1}(1/n)$, $\bar{\psi}(1) = 0$.

In addition, Mason et al. (1967) have provided collision integrals data as a function of a reduced temperature $T^* = (\lambda_D k_B T_e)/\left[q_e^2/(4\pi\varepsilon_0)\right]$. Then, R. S. Devoto (1973) has extended this work in

Table 4.4: Collision integrals data for the Helium-Hydrogen mixture provided by Bruno et al. (2011)

Type	Interactions	Collision integrals data
Neutral	$H/H, H/H_2, H_2/H_2$ $He/H, He/H_2$ He/He	R. Stallcop et al. (1998); Chhabra et al. (1996) Meyer & Frommhold (1994); Y. Li & Lin (1999) Tang et al. (1995); Tang & Toennies (2003)
Ion-neutral	H/He^+ He/He^+ H/H^+ $H^+/H_2, H^+/He$ He/He^{++} $H/He^{++}, H_2/He^+$	Aubreton et al. (2004) Aubreton et al. (2003) Sharp (1970); Sourd et al. (2006) Krstic (2002); Krstic & Schultz (2003, 1999) Schmidt (1989) Polarization potential Kihara et al. (1960)
Electron-neutral	e/H e/H_2 e/He	Gupta & Mathur (1978); Bray et al. (1991) Brunger & Buckman (2002); Shyn & Grafe (1992) Biagi (2012)
Charged interactions		Mason et al. (1967); R. S. Devoto (1973)

order to take into account the collision integrals $\bar{Q}_{ij}^{(1,4)}$, $\bar{Q}_{ij}^{(1,5)}$ and $\bar{Q}_{ij}^{(2,4)}$. These integrals are essential to compute the third-order electron transport properties from Table 4.3.

These data, provided by R. S. Devoto (1973), are valid for reduced temperatures $T^* \in [0.1, 10000]$, which is sufficient to describe conditions related from the photosphere up to the upper part of the chromosphere.

Finally, the collision integrals defined in Table 4.3 can be computed, depending on the type of interactions considered. The collision integrals data are used from the work Bruno et al. (2011), fitted by an exponential approach proposed in (4.3.6). For each of these interactions, a reminder of these data are provided in Table 4.4.

4.3.3 Results for equilibrium Helium-Hydrogen mixture

The required collision integrals data for the Helium-Hydrogen mixture have been presented in Table 4.4. The data have been taken from Bruno et al. (2011) and fitted by an exponential approach. However, it is still necessary to verify 1-the computation of the transport coefficients, 2- the accuracy of the proposed fit, and, 3- verify the convergence in term of Laguerre-Sonine polynomials.

Consequently, we focus on preliminary and verification results based on the Helium-Hydrogen mixture. First, we verify that the proposed fit is consistent with the data provided by Bruno et al. (2011). Then, a convergence result in terms of Laguerre-Sonine polynomials is presented. Finally, results of several collision integrals as function of the temperature, which are consistent with the literature, are presented.

Verification of the curve-fit

We verify the exponential fitting approach proposed in (4.3.6) related to the results obtained by Bruno et al. (2011). Such verification is performed on three several mixtures: a pure Hydrogen mixture composed of $\{H, H^+, H_2, {H_2}^+, e\}$, a pure Helium mixture composed of $\{He, He^+, He^{++}, e\}$, and the Helium-Hydrogen mixture. The Helium-Hydrogen mixture is composed of 92% Hydrogen and 8% of Helium in mole fraction. Several mixtures have been considered to verify that the collision integrals are correctly fitted for all the possible interactions in the Helium-Hydrogen mixture.

For each mixtures, we compute the viscosity $\nu_\mathfrak{h}$ at the third-order of Laguerre Sonine polynomials approximation, as function of the temperature, in equilibrium, at $p = 1$ atm, and compared with the results obtained by Bruno et al. (2011).

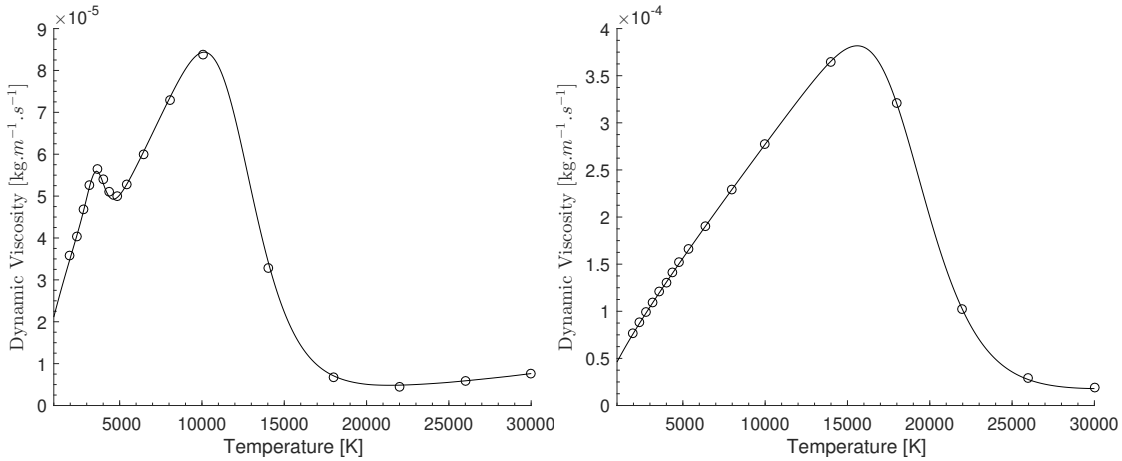

Figure 4-2: Dynamic viscosity $\nu_\mathfrak{h}$ as function of the temperature, in equilibrium at $p = 1$ atm. Left and right: Pure Hydrogen and Helium mixtures respectively. Full line: Exponential fit obtained with (4.3.6). ◯: Results from Bruno et al. (2011)

The dynamic viscosity of the Helium-Hydrogen, pure Hydrogen and Helium mixture Figure 4-3 and Figure 4-2 are showing good agreement with Bruno et al. (2011). Thus, the proposed fit is verified and can be used to compute the transport coefficients of our model.

Convergence results in terms of Laguerre-Sonine polynomials

Then, a convergence result in terms of Laguerre-Sonine polynomials is presented. In order to perform this analysis, we have focused on the transport system related to the electron diffusion coefficient $\bar{\bar{D}}_e$ in (4.2.8), and investigated several orders: $\xi = 0,\ 1$ and 2, for the Helium-Hydrogen mixture, in equilibrium, at $p = 1$ atm, as function of the temperature. The result is presented in Figure 4-4.

The result clearly show that the convergence in terms of Laguerre-Sonine polynomials approximation is reached from $\xi = 1$ and small differences are obtained between the case $\xi = 1$ and $\xi = 2$.

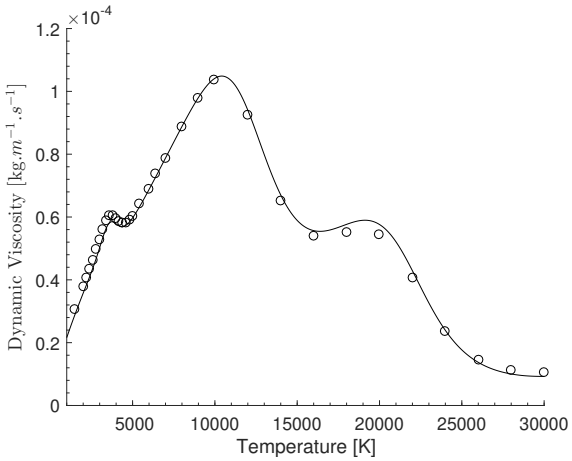

Figure 4-3: Dynamic viscosity $\nu_{\mathfrak{h}}$ as function of the temperature, in equilibrium at $p = 1$ atm for the Helium-Hydrogen mixture. Full line: Exponential fit obtained with (4.3.6). ◯: Results from Bruno et al. (2011)

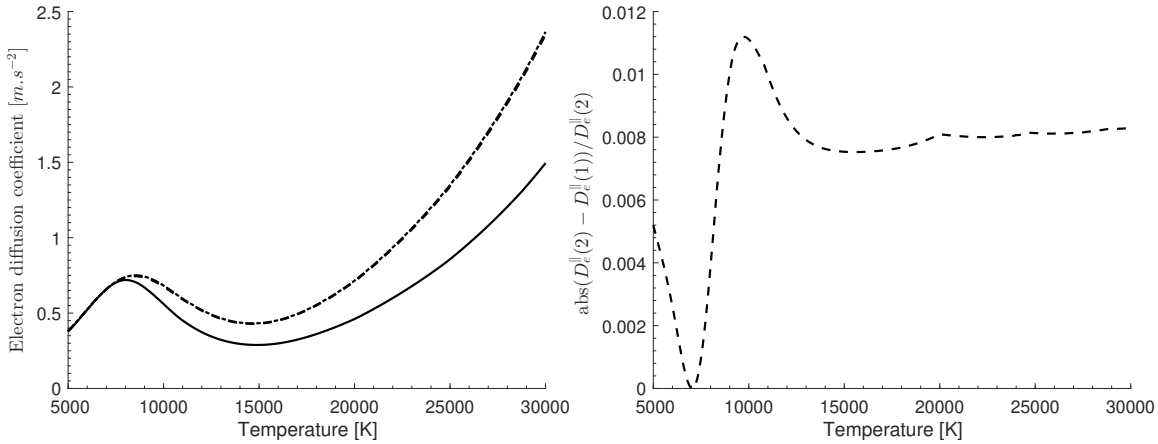

Figure 4-4: Left: Parallel component of the electron diffusion coefficient $D_e^{\parallel}$ as function of the temperature, at $p = 1$ atm, in equilibrium for the Helium-Hydrogen mixture. Full black line: order $\xi = 0$, black dashed line: order $\xi = 1$, and black semi-dashed line: order $\xi = 2$.
Right: difference $(D_e^{\parallel}(2) - D_e^{\parallel}(1))/(D_e^{\parallel}(2))$ between the order $\xi = 1$ and $\xi = 2$.

Note that, small differences (less than 1%) are obtained between the last two orders investigated.

Similar results have been obtained with the other transport properties, showing that convergence is reached from the second non-vanishing order of Laguerre Sonine polynomials. Such results are in good agreement with the results obtained in Magin & Degrez (2004); Scoggins et al. (2016), for an air mixture in equilibrium.

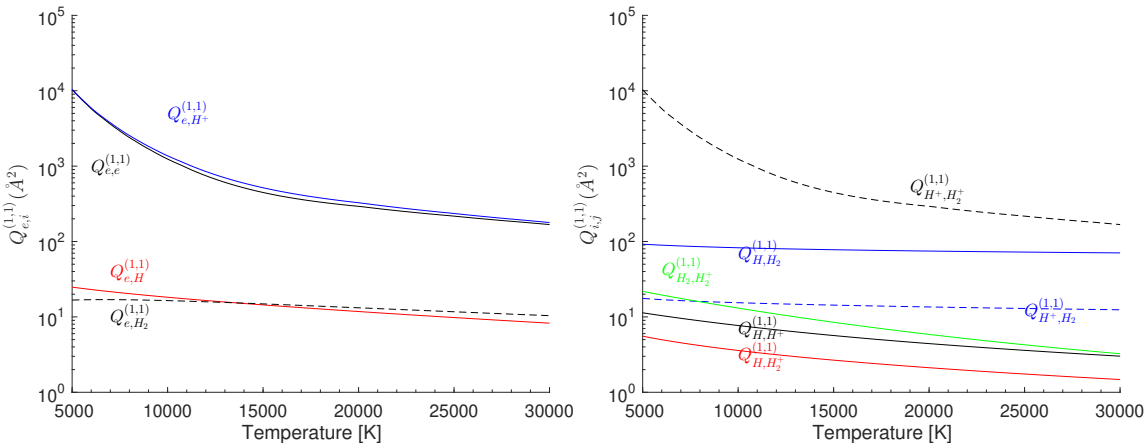

Figure 4-5: Selected reduced collision integrals $\bar{Q}_{ij}^{(1,1)}$, as function of the temperature, at $p = 1$ atm, for various type of interactions. Left: Electron-heavy particles interactions, right: heavy-heavy interactions

Results for collision integrals

Preliminary results for collision integrals are presented here. They have been computed in equilibrium, at $p = 1$ atm, as a function of the temperature. A selection of the collision integrals is presented in Figure 4-5.

Figure 4-5 show that the Coulomb collision integrals such as $\bar{Q}_{eH^+}^{(1,1)}$, $\bar{Q}_{ee}^{(1,1)}$ and $\bar{Q}_{H^+H_2^+}^{(1,1)}$ are orders of magnitude larger compared to neutral interactions. These differences are due to the Coulomb forces acting on charged particles (electrons or ions) which are much stronger than the forces acting on neutrals. These results are consistent with those obtained by Scoggins et al. (2016); Magin & Degrez (2004), for an equilibrium air mixture.

4.4 Transport algorithms for heavy-particle transport systems

In this section, we focus on transport systems associated with heavy particles presented in Section 4.2.3. When the number of heavy species becomes important in the mixture considered, it is necessary to find methods / algorithms to solve them. Transport systems associated with electrons do not present difficulties in terms of computational cost and algorithms.

On the one hand, as described in the previous section, the multicomponent diffusion matrix D_{ij}, $i, j \in$ H defined in (4.2.14) is singular due to the total mass constraint. Thus, without changing the structure of the diffusion velocities, some specific algorithms are needed, as shown by Giovangigli (1990); Ern & Giovangigli (1994); Magin & Degrez (2004). On the other hand, if the number of species becomes relevant, the inversion of linear systems can be computationally expensive (see Magin & Degrez (2004); Magin (2004)). One alternative based on approximate

mixture rules, can be used to evaluate multicomponent transport coefficients, as used by Gupta et al. (1990); Wilke (1950). Then, Ern and Giovangigli Ern & Giovangigli (1995) have developped algorithms in order to obtain multicomponent transport properties including neutrals.

A review of the transport algorithms for the heavy-particle transport subsystem presented in Section 4.2.3 is presented.

Method for heavy particle tranport subsystem

Here, we focus on the transport algorithms used for solving the transport systems (4.2.17)-(4.2.18) and (4.2.15)-(4.2.16) which leads to the heavy-particle thermal conductivity, viscosity and, also, the thermal diffusion ratios $\chi_{\mathfrak{h},j}$.

Such systems can be simply solved using a determinant method (see Hirschfelder et al. (1964)) using

$$\alpha = -\frac{\begin{vmatrix} G^{\alpha} & x \\ x^{T} & 0 \end{vmatrix}}{|G^{\alpha}|}, \quad \alpha \in \{\nu_{\mathfrak{h}}, \lambda_{\mathfrak{h}}\}, \tag{4.4.1}$$

or using simplified mixture rules, described by Wilke (1950); Gupta et al. (1990). An alternative is proposed by Ern & Giovangigli (2010, 1995); Giovangigli (1990). It consists in writting the heavy-particle transport systems as symmetric positive definite systems, and solving them by using a direct method such as LDL^{T} decomposition (see Magin & Degrez (2004)) or with iterative methods using Conjugate-Gradient (CG) method. According to Magin & Degrez (2004), the main differences between the two methods is that solution based on LDL^{T} would require a computational cost which scales with $O((n^{\mathrm{H}})^{3}/6)$, whereas the Conjugate-Gradient method is $O(m(n^{\mathrm{H}})^{2})$, where m is the number of iterations required. Therefore, the CG method has been used for the Helium-Hydrogen mixture, since six heavy species are considered.

The performance of these methods has been investigated by Magin & Degrez (2004) for an equilibrium air mixture. This study has shown that the mixture rules from Wilke (1950) and Gupta et al. (1990) are less accurate and computationally more expensive than the CG method. Therefore, these mixture rules are abandoned in favor of the CG method.

Multicomponent diffusion coefficient

Here, we focus on the algorithms used for obtaining the multicomponent diffusion coefficient D_{ij} through the transport linear system obtained in (4.2.14) and (4.2.13). Obtaining the multicomponent diffusion matrix from the presented transport system is not trivial since the matrix is singular due to the total mass constraint. Therefore, several methods have been developed to tackle this issue.

In this thesis, we have followed the path of Giovangigli (1990), and Magin & Degrez (2004). They have investigated multicomponent diffusion algorithms, and show several singularities due to mass conservation constraints. A modification of the usual algorithms have been proposed to 1-get rid of the singularities appearing in the transport systems and 2- be consistent with the usual Stefan-

Maxwell equations (see Magin & Degrez (2004)) and with the Hirschfelder-Curtiss expressions with mass corrections (see Hirschfelder et al. (1964)). In order to get rid of the singularities, a mass balance relation is considered in the algorithm. This relation make the diffusion matrix nonsingular. Then, a LDL^T method is used to obtain the multicomponent diffusion matrix D_{ij}, as presented by Magin & Degrez (2004).

Another alternative would be to follow the work performed by Giovangigli (1997). He has developed iterative methods to compute the multicomponent diffusion matrix, and is shown to be competitive with direct methods. Such methods have been extended by Giovangigli & Graille (2009) to multicomponent magnetized transport system.

In addition, one possibility would be to rewrite the transport fluxes related to the diffusion velocities $\boldsymbol{V}_i$ as a Stefan-Maxwell (SM) system, as done by Magin & Degrez (2004); Kolesnikov (1974). In this framework, the diffusion velocities are computed from solving the SM system. However, in this thesis, the multicomponent diffusion matrix D_{ij} is required for computing the electric field of the generalized Ohm's law defined in (E) and its multicomponent electromagnetic matrices. Therefore, this alternative has not been studied.

Conclusion

The transport properties of the multicomponent model have been summarized in Table 4.1 and in Table 4.2. The transport coefficients have been derived from the kinetic theory and written in terms of bracket integrals. These integrals have been reduced by assuming that the perturbative functions are expanding in Laguerre-Sonine polynomials. The transport systems for electrons and heavy-particles have been obtained and expressed up to the third order in Laguerre-Sonine polynomials approximation. The obtained transport coefficients are depending on the collision integrals, as presented in Table 4.3. They depend on interaction potentials which govern the collisions taking place among the multicomponent plasma particles.

In this thesis, we have focused on a Helium-Hydrogen mixture in order to be representative of the solar atmosphere without considering heavy species such as carbon, oxygen or metals. The kinetic data, which allow to compute the collision integrals data, have been taken from Bruno et al. (2011). In order to use the data for our simulation, a curve-fit up to third order exponential polynomials function has been used in (4.3.6) where the coefficients can be found in Appendix C. These data, provided by Bruno et al. (2011), have been summarized in Table 4.4. Then, the curve-fit has been verified and a study of the convergence of the transport coefficients as function of the order of Laguerre-Sonine polynomials has been given. Results show good agreement with the work of Magin & Degrez (2004), for an equilibrium air mixture.

Finally, to solve the heavy-particle transport systems, transport algorithms have been developed in the literature to reduce the computational cost required. In order to compute the heavy-particle viscosity $\nu_\mathfrak{h}$ and thermal conductivity $\lambda_\mathfrak{h}$, a CG method has been used, as described by Magin & Degrez (2004). This approach is shown to be the most efficient algorithm for the Helium-Hydrogen mixture, where six heavy species are considered. The multicomponent diffusion matrix D_{ij} has been computed by following the path of Magin & Degrez (2004). A mass balance relation

is considered in the algorithm in order to make the diffusion matrix nonsingular. Then, a LDL^T method has been used on the modified system to obtain the multicomponent diffusion matrix.

CHAPTER 5

APPLICATION AND VALIDATION OF THE TRANSPORT PROPERTIES FOR A HELIUM-HYDROGEN MIXTURE UNDER SUN ATMOSPHERE CONDITION

Introduction

In the previous Chapter, the transport properties of the multicomponent models have been computed for a Helium Hydrogen mixture S_1 defined in (4.0.1). The properties have been computed using a spectral Galerkin method based on a third order of Laguerre-Sonine polynomials approximation. The collision integrals data required to compute the transport properties have been based on the work of Bruno et al. (2011). In this work, the transport systems have been implemented in the `MUTATION++` library that compiles state-of-the-art transport collision integral data for the different pairs of species in the mixture (see Scoggins & Magin (2014)). Further details of the library are given in Section 8.4.

In a simplified framework where the plasma is fully ionized, we compare the transport properties for the solar lower atmosphere to the conventional expressions for magnetized plasmas due to Braginskii (1965). For more general partially ionized conditions representative of the solar lower atmosphere, we compute the multicomponent transport properties corresponding to the species diffusion velocities, heavy-particle and electron heat fluxes, and viscous stress tensor, for the Helium-Hydrogen mixture in local thermodynamic equilibrium. Finally, the model is assessed for the 3D radiative magnetohydrodynamic simulation of a pore, in the highly turbulent upper layer of the solar convective zone, performed by Kitiashvili et al. (2010). In addition, we compute the transport properties by postprocessing results from a simulation of a 3D radiation magnetohydrodynamic code Bifrost, described by Carlsson et al. (2016); Gudiksen et al. (2011). The simulation

encompass the upper part of the convection zone, the photosphere, chromosphere, transition region and corona. We compute the thermal conductivity, electrical conductivity, species diffusion coefficients, and components of the generalized Ohm's law. We conclude on the importance of the contribution of its components, in particular, of the resistive and thermodynamic terms.

The structure of the Chapter is as follows. In Section 5.1, we describe the mixture considered and the conditions representative of the solar lower atmosphere. In section Section 5.2, we verify the model proposed on a fully-ionized case by comparing the results with those obtained by means of Braginskii's theory. Then, in section Section 5.3, we discuss all the transport properties for a partially ionized case. Additionally, in Section 5.4, we compute the transport properties and the components of the generalized Ohm's law for 3D radiative MHD simulations of a pore in the solar lower atmosphere. Finally, in Section 5.5, the transport properties are computed for a general Helium-Hydrogen plasma in the solar atmosphere based on the simulation performed by Carlsson et al. (2016); Gudiksen et al. (2011).

5.1 Methodology

For the purpose of this work, we have focused on a Helium-Hydrogen mixture S_1 defined in (4.0.1).

We study the transport coefficients for the Helium-Hydrogen mixture within a range of temperature, pressure, and magnetic field that are largely representative of the solar lower atmosphere (see Vernazza et al. (1981); Carlsson & Stein (1995)): the temperature varies from 1000 K to 30000 K, the pressure from 1 Pa to 10^4 Pa, and the magnetic field from a few Gauss to thousands of Gauss (see Wiegelmann et al. (2014)). In the following, the plasma beta parameter is defined as $\beta_p = 2\mu_0 p/|\boldsymbol{B}|^2$, where p is the total pressure of the plasma in Pascal and $|\boldsymbol{B}|$ is the magnetic field in Tesla.

Consequently, for a range of temperature between 1000 K and 30000 K, two cases have been considered. The **case A**, where the total pressure is $p = 10^4$ Pa, and $\beta_p = 10$. The **case B**, where the total pressure is $p = 1$ Pa, and $\beta_p = 0.1$. Finally, the case A is chosen as a thermally pressure dominated case whereas, the case B is a magnetically pressure dominated case. In this framework, in the case A, the transport coefficients are shown to be isotropic and in the case B the latter are shown to be anisotropic. The latter example may include conditions that we can find in a cool sunspot (where the average temperature is generally around 4000K and the magnitude of magnetic field is about 1000G as shown by Fröhlich & Lean (2004); Solanki (2003)), in the quiet Sun photosphere, in the lower and upper part of the chromosphere, where the temperature is varying from 5000K to 10000K, and the pressure from 10^4 Pa to 0.1 Pa, as shown by Vernazza et al. (1981); Russell (1929); Asplund et al. (2009) (in orders of magnitude).

Based on the chosen conditions, we compute the thermochemical equilibrium composition. The mole fraction and the ionization degree of the Helium-Hydrogen mixture S_1 for the **case A** and **case B** are shown in Figure 5-1a, Figure 5-1b and Figure 5-2, respectively. These results are obtained with a method that is based on the minimization of the Gibbs free energy with suitable mass balance constraints, used by Scoggins & Magin (2015) in thermal equilibrium between electrons and heavy-particles. The compositions that are shown in Figure 5-1a and Figure 5-1b will be

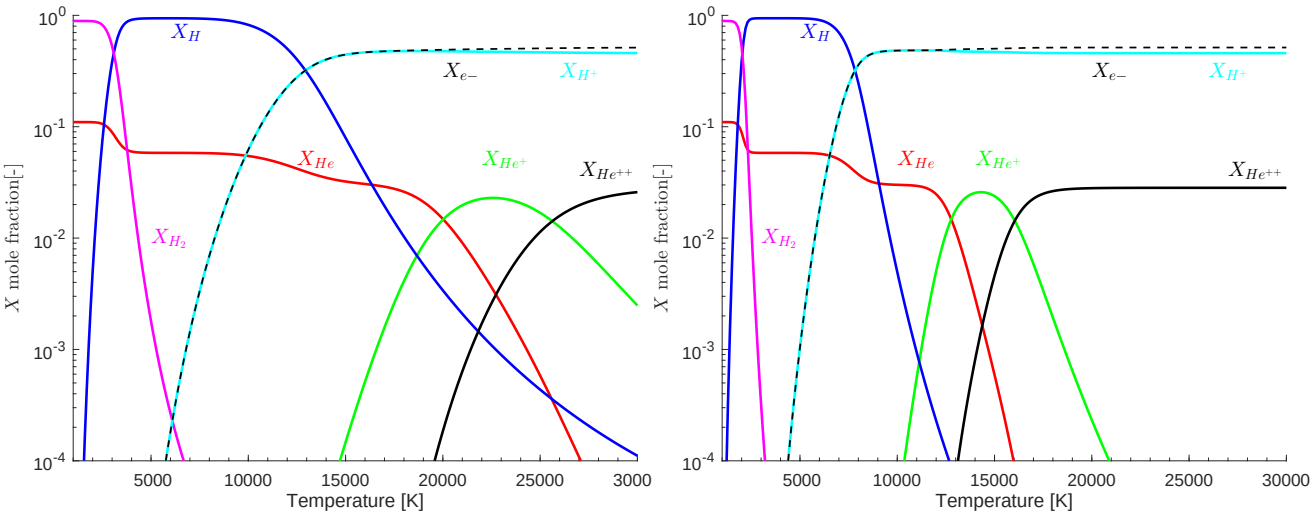

(a) $P = 10^4$ Pa (**case A**) (b) $P = 1$ Pa (**case B**)

Figure 5-1: Mole fraction of the Helium-Hydrogen mixture S_1 as function of the temperature

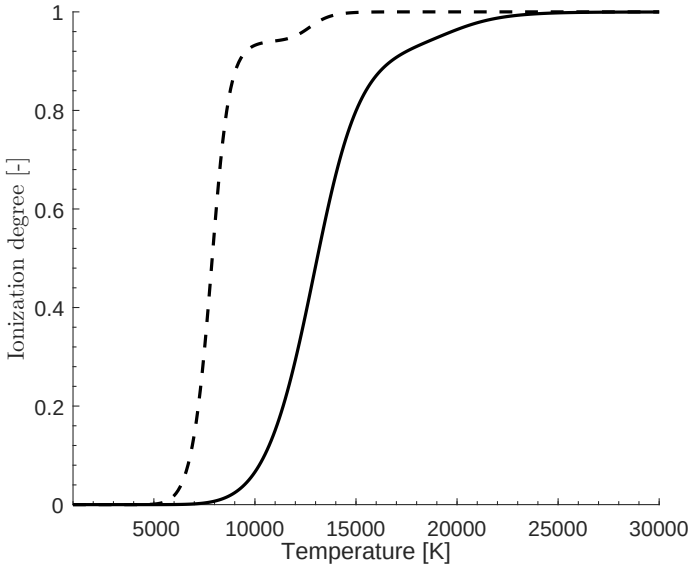

Figure 5-2: Ionization degree of S_1, for **case A** and **case B** as function of the temperature. **Case A** in full line, **case B** in dashed line

used to study the transport properties in the following sections.

As described by Scoggins et al. (2016); Magin & Degrez (2004), the calculation of the transport coefficients is based on the solution of integro-differential equations where a spectral Galerkin method based on a third order Laguerre-Sonine polynomials approximation, is applied. The method used and the transport systems related to the presented multicomponent model from Graille et al. (2009) have been highly described in the previous Chapter 4, and thus, are not presented here.

5.2 Verification with Braginskii approach for a fully ionized plasma

In order to verify the presented method in Chapter Chapter 4, we perform a comparison with Braginskii's transport properties. In the method of Braginskii (1965), the computation of the transport properties as well as the derivation of the governing equations are used only for fully ionized plasmas. As it can be seen in Figure 5-2, the Helium-Hydrogen mixture S_1 can be considered to be fully-ionized, mainly composed of $S_2 = \{H^+, e^-\}$, when the temperature is higher than 15000 K. Thus, the comparison will be performed in conditions where the mixture is S_2 in a range of temperatures from $T = 15000$ K to $T = 30000$ K for the **case A** and **case B**.

5.2.1 Comparison with Braginskii approach

On the one hand, in the work of Braginskii (1965), the derivation of the governing equations can be summarized in three main steps: 1- A fully ionized ion-electron plasma is considered in a constant magnetic field, 2- The Landau collision operators are used, simplified by the Lorentz process, and 3- an adapted Chapman-Enskog method is used based on the square root of the mass ratio between electron and ions (see Haines (1990)). On the other hand, we remind that in the model of Graille et al. (2009), a general multicomponent plasma that can be partially or fully ionized is considered in a constant magnetic field, the Chapman and Cowling collision operators highly studied by Ferziger & Kaper (1973); Woods (1995) are used and the Chapman-Enskog expansion is performed after a dimensional analysis of the Boltzmann equation. Finally, the two methods lead to distinct governing equations. Note that, a deeper comparison on the kinetic theory point of view has been investigated in Chapter 2.

Although the governing equations between the two models are different, the integro-differential systems for computing the transport properties are similar or even identical in the case of a fully ionized plasma. In both models, the anisotropic electron transport properties have the same integro-differential systems. However, only the systems related to the parallel component of the heavy particle transport properties are identical to those from the model derived by Graille et al. (2009). Consequently, only the parallel component of the heavy particle transport properties can be compared with those from the model of Graille et al. (2009). This is due to the fact that both models are based on the Chapman-Enskog expansion. However, the differences result from the scale analysis from the Boltzmann equation that is carried out by Graille et al. (2009) before applying the expansion. Note that, a comparison in terms of transport fluxes has been highly investigated in the Chapter 2.

In both models, the transport coefficients are expanded in a series of orthogonal Laguerre-Sonine polynomials. As described in the previous Chapter 4, the latter are written as linear combinations of collision integrals that are simplified by potential interactions, based on the usual Coulomb interaction screened by the Debye length. This approximation assumes collisions with large impact parameters and small scattering angles. However, in Braginskii (1965), the series are

truncated at the second order approximation whereas a third order approximation has been performed in our case. The expression of the transport coefficients depends on the mean collision times $\bar{\tau}_e$ and $\bar{\tau}_h$ defined as

$$\bar{\tau}_e = \frac{3{m_e}^2{\varepsilon_0}^2}{n_h q_e^4 \log(\Lambda)} \left(\frac{2\pi k_B T_e}{q_e^2 n_e}\right)^{\frac{3}{2}}, \quad \bar{\tau}_h = \sqrt{\frac{2m_h}{m_e}} \left(\frac{T_h}{T_e}\right)^{\frac{3}{2}} Z^{-2}\bar{\tau}_e, \tag{5.2.1}$$

where $\log(\Lambda)$ is the Coulomb logarithm defined by Spitzer (1963), and Z is the charge number. The mean collision times as defined in (5.2.1), can be seen as a first order Chapman Cowling approximation of the collision time for electron/ion and ion/ion collisions (see Woods (1995)). Correction terms depending on Z are used for the computation of the transport coefficients. This method leads to simplified expressions of the transport coefficients that depend only on the mean collision times and the charge number of the fully ionized plasma considered, as shown by Haines (1990); Woods (1995).

5.2.2 Electron transport properties

In Braginskii (1965) (see Eq. 4.37), the parallel, perpendicular and transverse components of the electron thermal conductivity tensor are defined as

$$\lambda_e^{\parallel} \underset{\mathbf{Br}}{:=} \frac{n_e k_B^2 T_e}{m_e} \bar{\tau}_e \, [3.16], \tag{5.2.2}$$

$$\lambda_e^{\perp} \underset{\mathbf{Br}}{:=} \frac{n_e k_B^2 T_e}{m_e} \bar{\tau}_e \left[\frac{4.664x^2 + 11.92}{x^4 + 14.79x^2 + 3.77}\right], \tag{5.2.3}$$

$$\lambda_e^{\odot} \underset{\mathbf{Br}}{:=} \frac{n_e k_B^2 T_e}{m_e} \bar{\tau}_e \left[x\frac{2.5x^2 + 21.67}{x^4 + 14.79x^2 + 3.77}\right] \tag{5.2.4}$$

where **Br** denotes the computation of the transport coefficient as derived by Braginskii (1965). $x = \omega_e \bar{\tau}_e$ and $\omega_e = q_e \boldsymbol{B}/m_e^0$ and the values in brackets correspond to Braginskii's coefficients for a charge number $Z = 1$.

Figure 5-3a, Figure 5-3b and Figure 5-3c show the parallel, perpendicular and transverse component of the electron thermal conductivity tensor $\bar{\bar{\lambda}}_e$, as function of the temperature, for the **case A** and the **case B**, for the fully ionized plasma S_2. Here, we compare the expressions from Braginskii (5.2.2), (5.2.3) and (5.2.4) with those that are given in (4.2.9) that are based on a third order Laguerre-Sonine polynomials approximation. Strong similarities are obtained in all the considered cases. In Braginskii (1965), the components of the electron thermal conductivity tensor are underestimated leading to differences that are less than 20%. These differences are increasing at high temperatures.

The components of the electron thermal diffusion ratio $\bar{\bar{\chi}}_e$ from (4.2.10) have been compared with those from the corresponding "friction coefficient" in Braginskii (1965), (Eq. 4.35). In the model of Braginskii (1965), the component of the friction coefficients or electron thermal diffusion

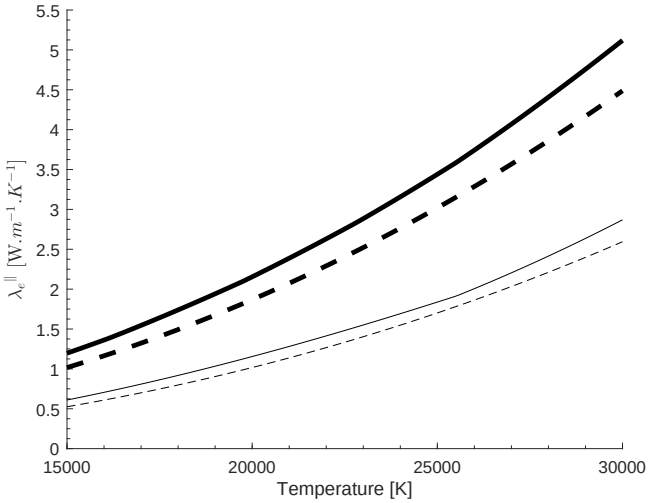

(a) Parallel component $\lambda_e^{\parallel}$

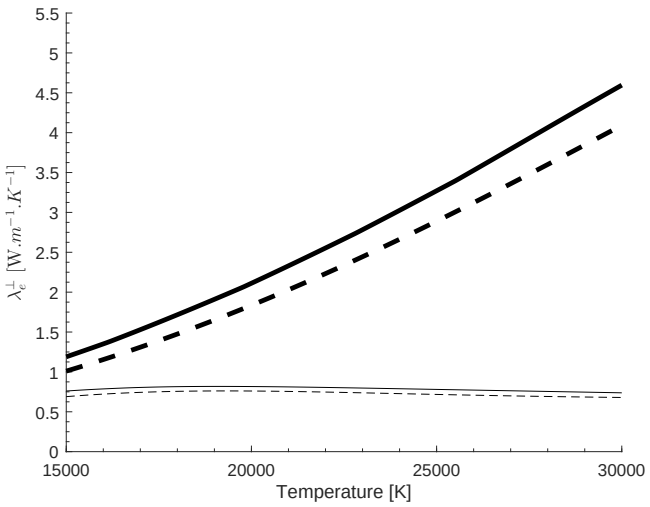

(b) Perpendicular component $\lambda_e^{\perp}$

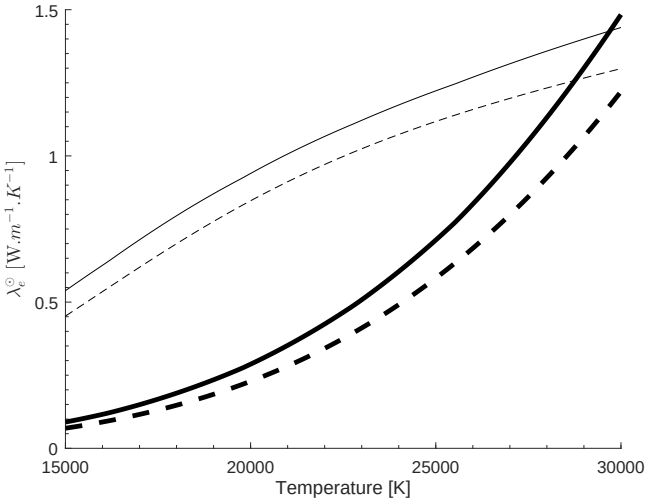

(c) Transverse component $\lambda_e^{\odot}$

Figure 5-3: Component of the electron thermal conductivity tensor $\bar{\bar{\lambda}}_e$ for a fully ionized plasma S_2, as function of temperature: Dashed lines and full lines correspond to the transport coefficient from the model of Braginskii (1965), and from Graille et al. (2009) respectively. Bold lines correspond to the **case A**, the other lines correspond to the **case B**

ratios read:

$$\chi_{\mathfrak{e}}^{\parallel} \underset{\textbf{Br}}{:=} [0.711] \tag{5.2.5}$$

$$\chi_{\mathfrak{e}}^{\perp} \underset{\textbf{Br}}{:=} \left[\frac{5.101x^2 + 2.681}{x^4 + 14.79x^2 + 3.77}\right] \tag{5.2.6}$$

$$\chi_{\mathfrak{e}}^{\odot} \underset{\textbf{Br}}{:=} x\left[\frac{1.5x^2 + 3.053}{x^4 + 14.79x^2 + 3.77}\right] \tag{5.2.7}$$

where the values in bracket are the Braginskii coefficient for a charge number $Z = 1$. Figure 5-4a, Figure 5-4b and Figure 5-4c show the parallel, perpendicular and transverse component of the electron thermal diffusion ratio $\bar{\bar{\chi}}_{\mathfrak{e}}$, as function of the temperature, for the **case A** and the **case B**, for the fully ionized plasma S_2. Here, we compare the expressions from Braginskii (5.2.5), (5.2.6) and (5.2.7) with those that are given in (4.2.10). Similarly as the component of the electron thermal conductivity, strong similarities have been obtained with the two approaches.

Finally, the parallel component of the resistivity $\eta^{\parallel}$ from (5.2.8) in the fully ionized plasma case has been compared with the one obtained by Braginskii (1965), (Eq. 2.8). Note that, the latter required to compute the electron diffusion coefficients $\bar{\bar{D}}_{\mathfrak{e}}$ defined in the Chapter Chapter 4 by (4.2.8). In Braginskii (1965), the parallel component of the resistivity is defined by

$$\eta^{\parallel} \underset{\textbf{Br}}{:=} [0.51]\frac{m_{\mathfrak{e}}}{n_{\mathfrak{e}}q_{\mathfrak{e}}\bar{\tau}_{\mathfrak{e}}} \tag{5.2.8}$$

Figure 5-5 shows the parallel component of the resistivity $\eta^{\parallel}$, as function of the temperature, for the **case A** and the **case B**, for the fully ionized plasma S_2. Similarly as the components of the electron thermal conductivity and thermal diffusion ratios, strong similarities have been obtained with the two approaches.

5.2.3 Heavy-particle transport properties

Similarly, the parallel component of the heavy thermal conductivity and heavy particle viscosity of the model of Braginskii (1965) (see Eq. 4.44), have been compared with the expression obtained by solving the transport linear systems (4.2.15)-(4.2.16) and (4.2.17)-(4.2.18). In Braginskii (1965), the heavy-particle thermal conductivity and heavy-particle viscosity are defined as

$$\lambda_{\mathfrak{h}}^{\parallel} \underset{\textbf{Br}}{:=} n_{\mathfrak{h}}k_B^2 T_{\mathfrak{h}}\bar{\tau}_{\mathfrak{h}}\,[3.91]\,, \tag{5.2.9}$$

$$\nu_{\mathfrak{h}}^{\parallel} \underset{\textbf{Br}}{:=} n_{\mathfrak{h}}k_B T_{\mathfrak{h}}\bar{\tau}_{\mathfrak{h}}\,[0.96]\,. \tag{5.2.10}$$

Figure 5-6a and Figure 5-6b show the heavy thermal conductivity $\lambda_{\mathfrak{h}}$ and the heavy particle viscosity $\nu_{\mathfrak{h}}$ respectively, in the same conditions as in Figure 5-3a and Figure 5-3b. As before, strong similarities have been obtained in all the considered cases for the chosen conditions, which leads to differences that are smaller than 20%. In addition, it can be shown that the heavy transport properties from Braginskii (1965) are isotropic at the chosen conditions.

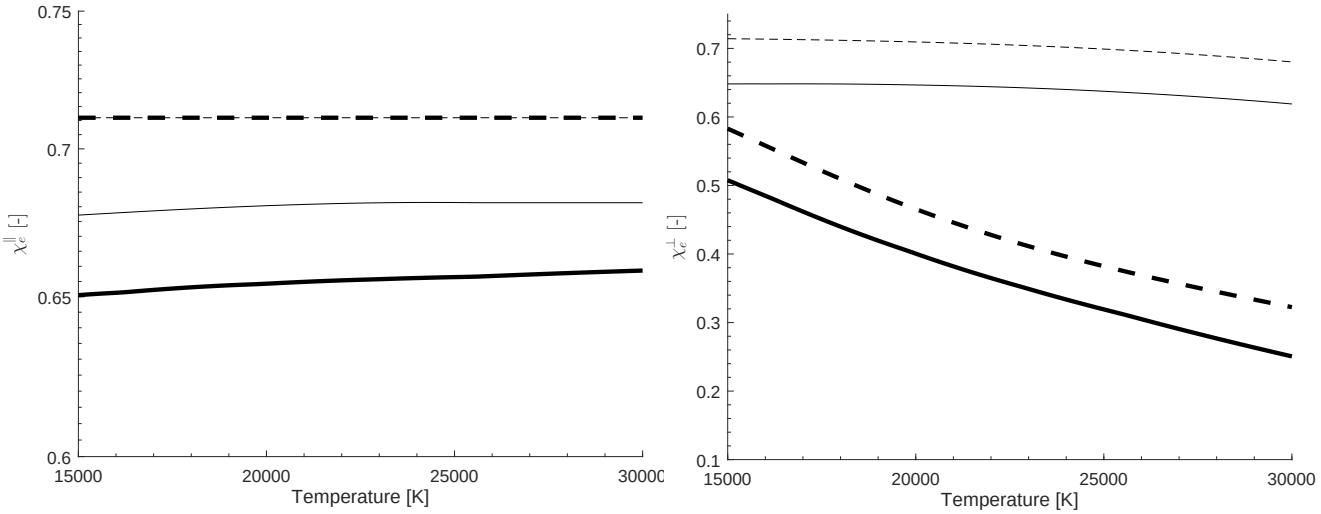

(a) Parallel component $\chi_{\mathfrak{e}}^{\parallel}$

(b) Perpendicular component $\chi_{\mathfrak{e}}^{\perp}$

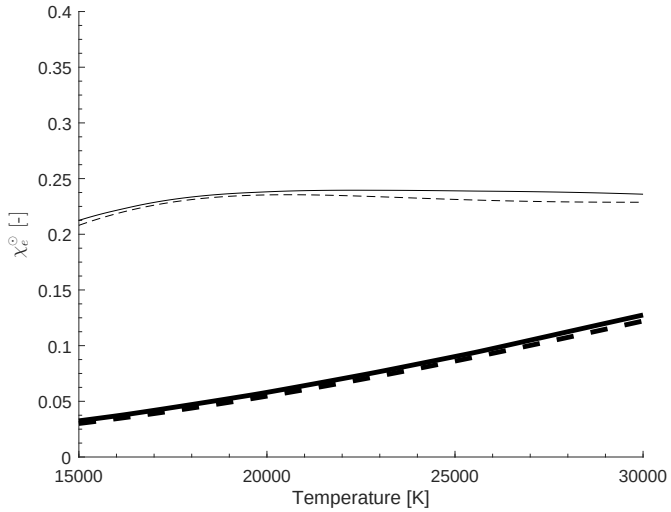

(c) Transverse component $\chi_{\mathfrak{e}}^{\odot}$

Figure 5-4: Component of the electron thermal diffusion ratio tensor $\bar{\bar{\chi}}_{\mathfrak{e}}$ for a fully ionized plasma S_2, as function of temperature: Dashed lines and full lines correspond to the transport coefficient from the model of Braginskii (1965), and from Graille et al. (2009) respectively. Bold lines correspond to the **case A**, the other lines correspond to the **case B**

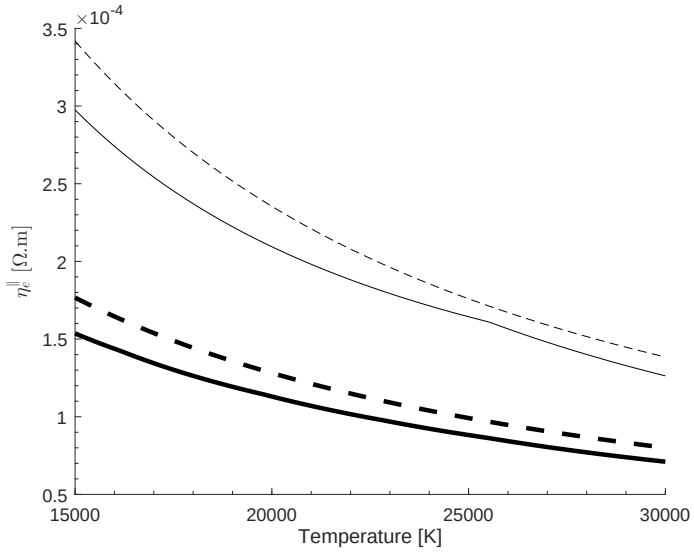

Figure 5-5: Parallel component of the resistivity $\eta^{\parallel}$ for a fully ionized plasma S_2, as function of temperature: Dashed lines and full lines correspond to the transport coefficient from the model of Braginskii (1965), and from Graille et al. (2009) respectively. Bold lines correspond to the **case A**, the other lines correspond to the **case B**

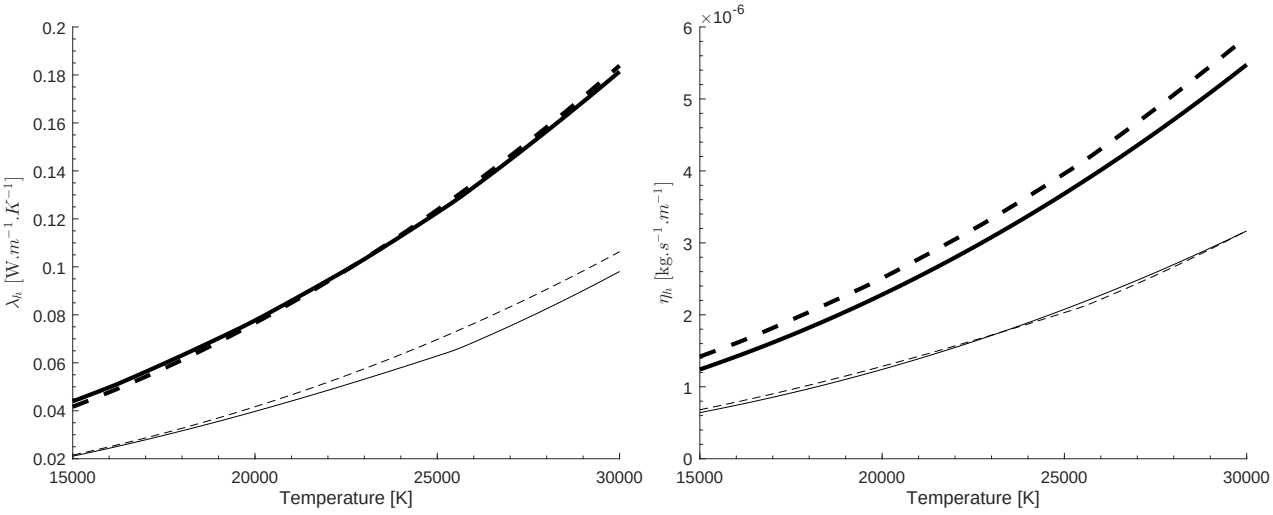

(a) Heavy thermal conductivity $\lambda_{\mathfrak{h}}$

(b) Heavy particle viscosity $\nu_{\mathfrak{h}}$

Figure 5-6: Heavy particle transport properties for a fully ionized plasma S_2, as function of temperature: Dashed lines and full lines correspond to the transport coefficient from the model of Braginskii (1965), and from Graille et al. (2009) respectively. Bold lines correspond to the **case A**, the other lines correspond to the **case B**

In summary, we can conclude that the proposed method is verified for the fully ionized case. The main differences that are obtained between the two models are due to 1-the order of Laguerre Sonine polynomials that was used, *i.e.*, second order in Braginskii's model and third order in the proposed method, and 2- the nature of the collision operators used, Landau collision operators in the model of Braginskii and Chapman and Cowling collision operators in the model of Graille et al. (2009). Additionally, the formulation of the transport properties that are considered in this work are generalized for any type of partially ionized mixture.

5.3 Application to a Helium-Hydrogen partially ionized plasma

5.3.1 Transport fluxes in thermochemical equilibrium

We have studied thermochemical conditions for a Helium-Hydrogen mixture to assess the importance of transport phenomena based on a simplified test case. The model developped for transport should remain valid for nonequilibrium conditions provided that suitable chemical production terms are considered. Thus, we consider thermochemical equilibrium $T_e = T_h = T$, isobaric mixtures at rest. As shown by Scoggins et al. (2016), the total heat flux is entirely a function of the temperature gradient and magnetic field and may be written as

$$\boldsymbol{q}_h + \boldsymbol{q}_e = -\left(\lambda_h + \bar{\bar{\lambda}}_e + \bar{\bar{\lambda}}_S + \bar{\bar{\lambda}}_R\right) \boldsymbol{\partial}_x T, \tag{5.3.1}$$

where the Soret and reactive thermal conductivities may be written as

$$\bar{\bar{\lambda}}_S = -p_e \bar{\bar{\chi}}_e \mathcal{V}_e - \sum_{j \in \mathrm{H}} \left[p_h \chi_{h,j} + p_e \bar{\bar{\chi}}_e \right] \mathcal{V}_i, \tag{5.3.2}$$

$$\bar{\bar{\lambda}}_R = -\rho_e h_e \mathcal{V}_e - \sum_{j \in \mathrm{H}} \left[\rho_j h_j + \rho_e h_e \bar{\bar{\alpha}}_{ej} \right] \mathcal{V}_j. \tag{5.3.3}$$

where $\mathcal{V}_e$ and $\mathcal{V}_i,\ i \in \mathrm{H}$ are defined as

$$\mathcal{V}_e = -\bar{\bar{D}}_e \left[\frac{1}{x_e} \frac{\partial x_e}{\partial T} + \frac{\bar{\bar{\chi}}_e}{T} \right], \tag{5.3.4}$$

$$\mathcal{V}_i = \sum_{j \in \mathrm{H}} D_{ij} \left[\frac{1}{1 - x_e} \left(\frac{\partial x_i}{\partial T} + \frac{\partial x_e}{\partial T} \bar{\bar{\alpha}}_{ej} \right) + \frac{\chi_{h,j}}{T} + \frac{p_e}{p_h} \frac{\bar{\bar{\chi}}_{ej}}{T} \right], i \in \mathrm{H}. \tag{5.3.5}$$

Here, $\mathcal{V}_e$ and $\mathcal{V}_i,\ i \in \mathrm{H}$ correspond to diffusion velocities for a temperature gradient of 1, i.e, $\boldsymbol{V}_e = \mathcal{V}_e \boldsymbol{\partial}_x T$ and $\boldsymbol{V}_i = \mathcal{V}_i \boldsymbol{\partial}_x T$. Finally, we compute all the transport properties for the Helium-Hydrogen mixture S_1 for **case A** and **case B**.

5.3.2 Results in solar atmosphere condition

This section is devoted to the results obtained for the transport coefficients of the Helium-Hydrogen mixture under thermochemical equilibrium conditions. Figure 5-7a and Figure 5-7b present the parallel, perpendicular and transverse components of the electron thermal conductivity tensor $\bar{\bar{\lambda}}_e$ as a function of the temperature, for both cases.

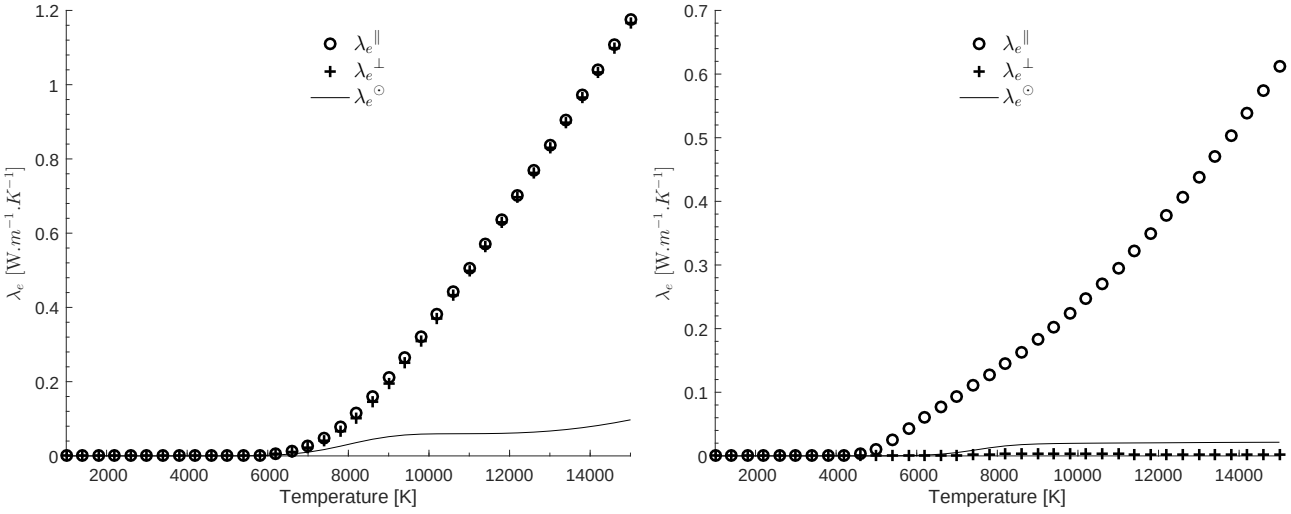

(a) **Case A** (b) **Case B**

Figure 5-7: Components of the electron thermal conductivity tensor $\bar{\bar{\lambda}}_e$, at the third order Laguerre Sonine polynomials, for the Helium-Hydrogen mixture S_1 as a function of temperature

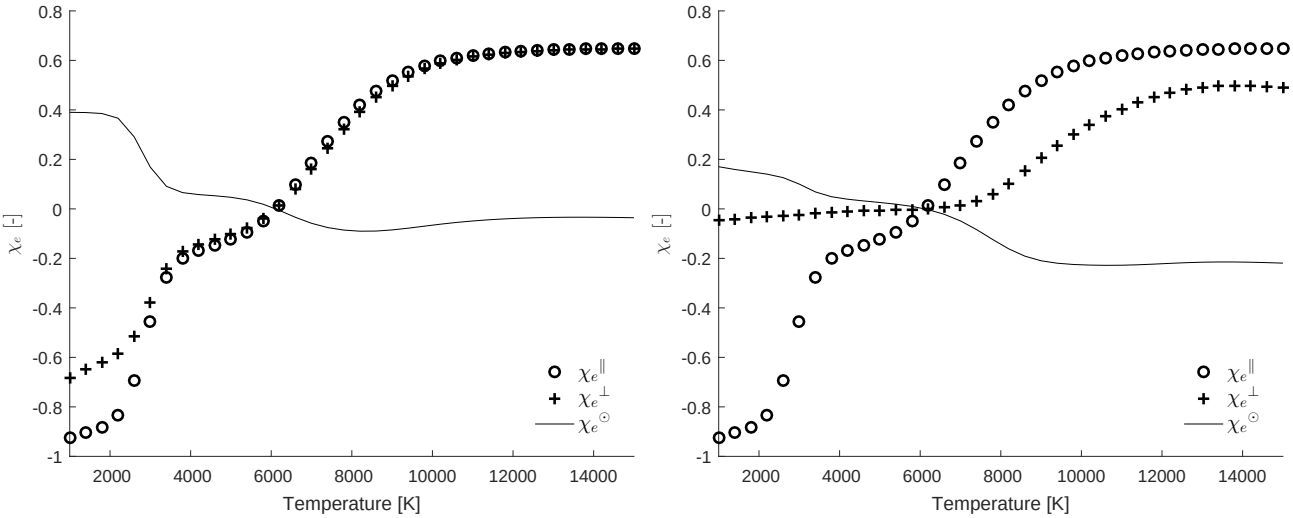

(a) **Case A** (b) **Case B**

Figure 5-8: Components of the electron thermal diffusion ratio tensor $\bar{\bar{\chi}}_e$, at the third order Laguerre Sonine polynomials, for the Helium-Hydrogen mixture S_1 as a function of temperature

According to Figure 5-7a (**case A**), the perpendicular component is equal to the parallel component for the entire range of temperatures, *i.e*, the electron thermal conductivity is isotropic. Indeed, the pressure forces are dominating the magnetic pressure forces, so the plasma is almost considered as unmagnetized. On the other hand, in Figure 5-7b (**case B**), for temperatures higher than $T = 5000$ K, the electron thermal conductivity $\bar{\bar{\lambda}}_e$ is anisotropic since the magnitude of magnetic field is higher. These results show that the transverse component is higher than the perpendicular component of $\bar{\bar{\lambda}}_e$. Similar results have been obtained for the other anisotropic electron transport properties such as $\bar{\bar{\chi}}_e$, as presented in Figure 5-8.

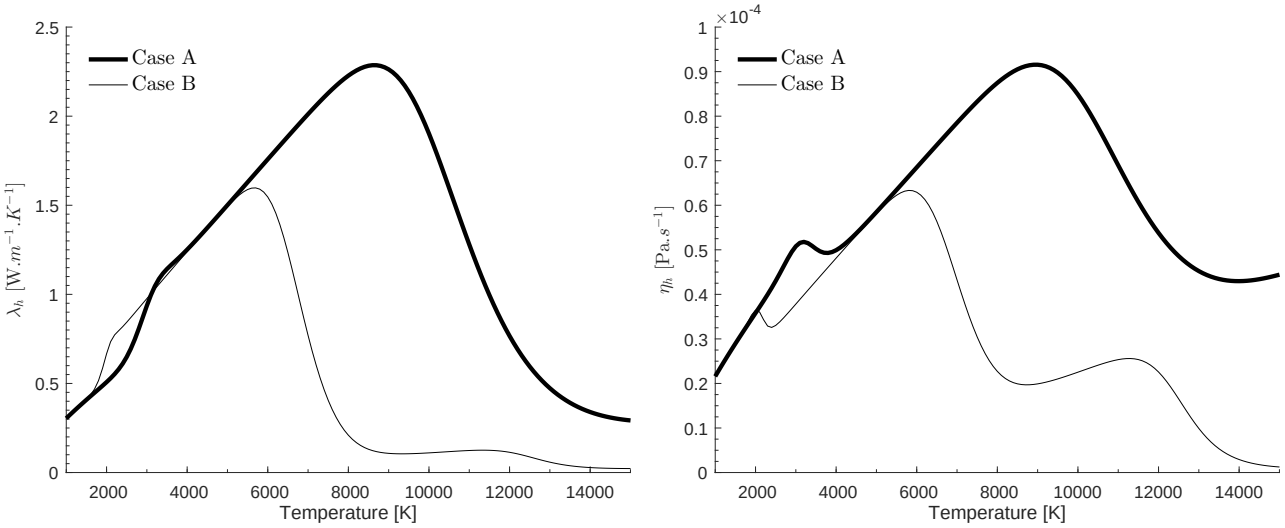

(a) Heavy thermal conductivity λ_h

(b) Heavy particle viscosity ν_h

Figure 5-9: Heavy particle transport coefficients at the third order Laguerre Sonine polynomials, for **case A** and **case B**, for the Helium-Hydrogen mixture S_1 as a function of temperature

In Figure 5-9a, strong differences between the two cases for a temperature higher than 6000 K can be seen. In the **case A**, λ_h increases from 1000 K to 9000 K, which is expected since λ_h is an increasing function of the temperature. However, in the **case A** after 9000 K, λ_h decreases. This decrease is due to the ionization of H. Indeed, the heavy particle thermal conductivity is related to a combination of the cross sections variations of all the heavy species in the mixture, which are proportional to the mole fractions of each heavy particles. This result is coherent with Figure 5-1a, which shows that the mole fraction of H is decreasing after 9000 K. Similar behavior as the **case A** have been observed for the **case B**, except that the ionization of H starts at 6000 K for this pressure. In Figure 5-9a, the second modulation observed around 12000 K is due to the ionization of He as shown in Figure 5-1b. Similar behavior have been obtained with the heavy-particle viscosity in Figure 5-9b.

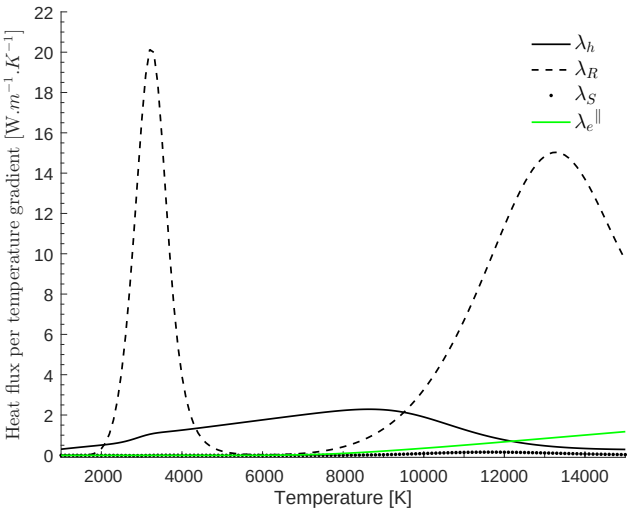

(a) **Case A**, full scale range

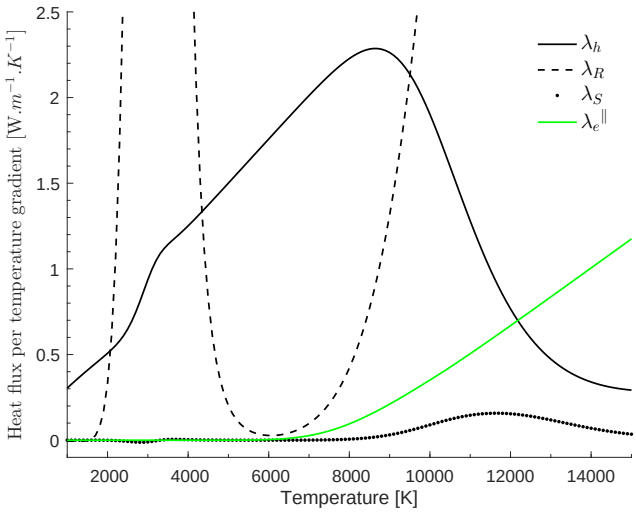

(b) **Case A**, heat flux in $[0, 2.5]$ $W.m^{-}1.K^{-1}$

Figure 5-10: Component of the total heat flux (5.3.1) as a function of the temperature for the **case A** for the Helium-Hydrogen mixture S_1

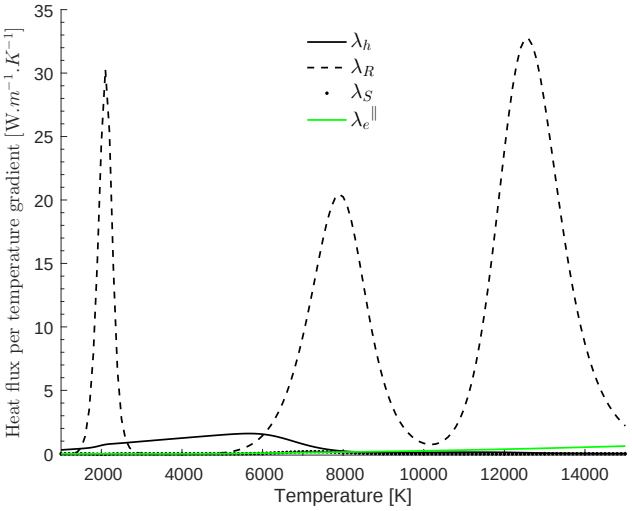

(a) **Case B**, full scale range

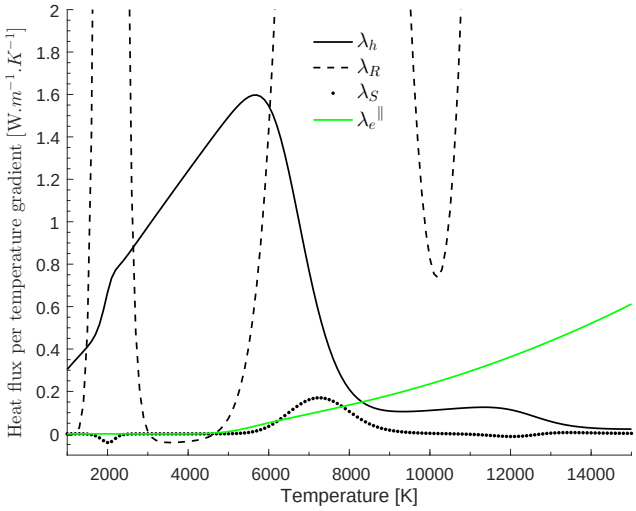

(b) **Case B**, heat flux in $[0, 2]$ $W.m^{-}1.K^{-1}$

Figure 5-11: Component of the total heat flux (5.3.1) as a function of the temperature for the **case B** for the Helium-Hydrogen mixture S_1

Figure 5-10 and Figure 5-11 show the components of the total heat flux of (5.3.1) as a function of the temperature, for the **case A** and **case B**. In the **case A**, it is clear that the reactive thermal conductivity $\lambda_R^{\parallel}$ is higher than the other components for certain ranges of temperature between 2200 K and 4300 K and for temperature higher than 10000 K. The heavy thermal conductivity $\lambda_{\mathfrak{h}}$ is the second term which dominates the total heat flux, and is higher than $\lambda_R^{\parallel}$ for a range of temperature

between 4200 K and 10000 K. Similarly, in the **case B**, the reactive thermal conductivity is also higher than the other components for ranges between 1800 K and 3000 K and for temperature higher than 6000 K. Then, the heavy thermal conductivity is also the second term which dominates the total heat flux, and is higher than $\lambda_R^{\parallel}$ for a range of temperature between 3000 K and 6000 K. The results here obtained are consistent with those of Scoggins et al. (2016) for an equilibrium air mixture.

Figure 5-12a and Figure 5-12b show the parallel component of each term of the electron-heavy particle transport coefficients $\alpha_{\mathfrak{e}i}^{\parallel}$, as a function of the temperature, for the **case A** and **case B**. As expected, each term of the electron-heavy particle transport tensor $\alpha_{\mathfrak{e}i}^{\parallel}$, is proportional to the mole fraction.

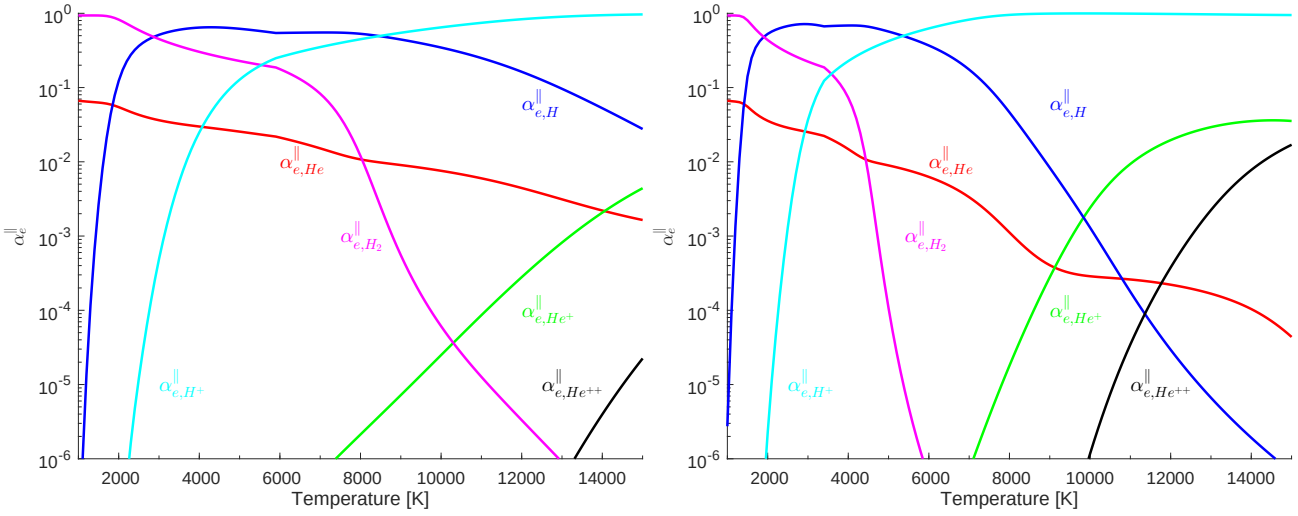

(a) **Case A** (b) **Case B**

Figure 5-12: Parallel component of the electron-heavy particle transport coefficient $\alpha_{\mathfrak{e}i}^{\parallel}$, $i \in \{\mathrm{He}, \mathrm{He}^+, \mathrm{H}, \mathrm{H}_2, \mathrm{He}^{++}, \mathrm{H}^+\}$, for the Helium-Hydrogen mixture S_1

Figure 5-13a and Figure 5-13b represent the second order electron thermal diffusion ratio $\chi_{\mathfrak{e}i}^{\parallel}$, $i \in \{\mathrm{He}, \mathrm{He}^+, \mathrm{H}, \mathrm{H}_2, \mathrm{He}^{++}, \mathrm{H}^+\}$ as a function of the temperature, for the **case A** and **case B** respectively. Here again, similarly as the results obtained with the heavy-particle transport properties, the each heavy thermal diffusion ratio terms $\chi_{\mathfrak{e}i}^{\parallel}$ is related to the mole fractions of each heavy particles. For example, in Figure 5-13a, the maximum and minimum obtained for $\chi_{\mathfrak{e},H}$ and $\chi_{\mathfrak{e},H^+}$ respectively, around 8000 K is due to the dissociation of H into H^+ (see Figure 5-1a). The same maximum is obtained in Figure 5-13a around 8000 K. Similarly, the maximum and minimum obtained for $\chi_{\mathfrak{e},H_2}$ and $chi_{\mathfrak{e},H}$ around 3000 K is due to the dissociation H_2 into H. Similar results have been obtained for $\chi_{\mathfrak{h},j}$, $j \in \mathrm{H}$. In addition, the results show that the constraint $\sum_{j\in\mathrm{H}} \chi_{\mathfrak{e}i}^{\parallel} = 0$, from (2.4.50), has been verified.

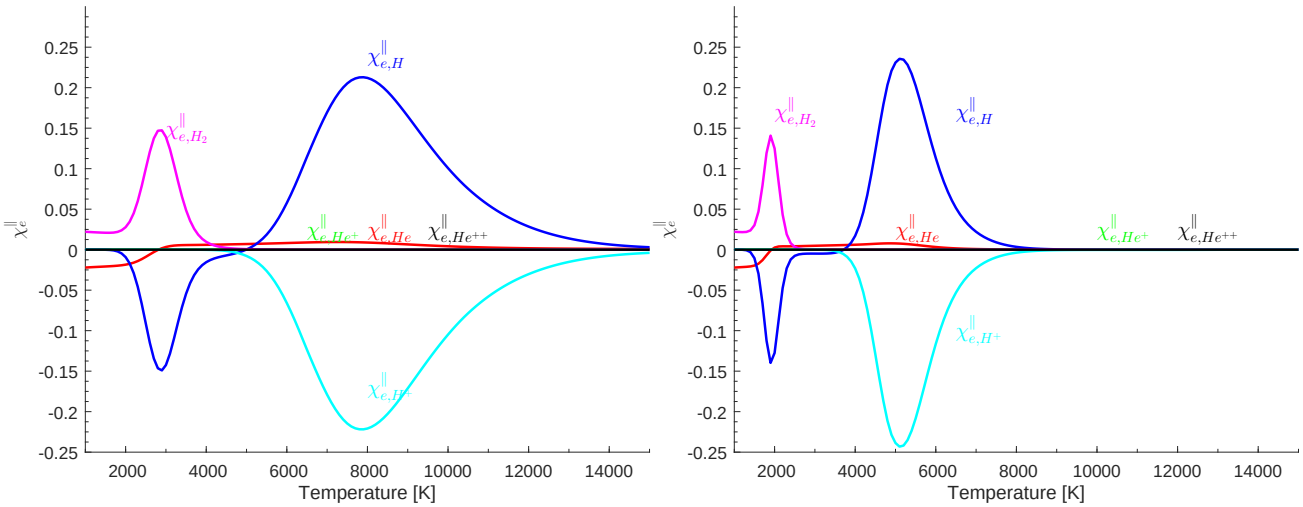

(a) **Case A** (b) **Case B**

Figure 5-13: Parallel component of the electron-heavy particle transport coefficient $\chi^{\parallel}_{ei}$, $i \in \{\mathrm{He}, \mathrm{He}^{+}, \mathrm{H}, \mathrm{H}_2, \mathrm{He}^{++}, \mathrm{H}^{+}\}$, for the Helium-Hydrogen mixture S_1

5.4 Application to a pore at the photosphere

As done in the previous section, the transport coefficients of the previous Helium-Hydrogen mixture are computed for the conditions found in the upper layer of the solar convective zone from the radiative 3D MHD simulations of a pore by Kitiashvili et al. (2010). The simulation results are obtained for the computational domain of $6.4 \times 6.4 \times 5.5$ Mm with the grid sizes: $50 \times 50 \times 43$ km, $25 \times 25 \times 21.7$ km and $12.5 \times 12.5 \times 11$ km ($128^2 \times 127$, $256^2 \times 253$ and $512^2 \times 505$ mesh points). The domain includes a top, 5 Mm-deep, layer of the convective zone and the chromosphere. In this section, the results and quantities are obtained from simulations in Kitiashvili et al. (2010) via a single-fluid MHD model. This is a postprocessed calculation for quantities that belong to the multicomponent model presented. Assuming that the electron-heavy particle collision frequency is high in the conditions chosen, a thermal equilibrium case $T_{\mathfrak{e}} = T_{\mathfrak{h}}$ has been considered for the computation of the transport coefficients. For the sake of clarity, only results from a slice at a constant geometrical height $z = -0.5Mm$, in the lower photosphere has been presented.

Figure 5-14c, Figure 5-14a, Figure 5-14b and Figure 5-14d show snapshots of the distribution of the plasma beta parameter β_p, temperature T, total mass density ρ and orthogonal velocity v_z respectively. As it can be seen, the temperature is varying from 4000 K to 6500 K, the plasma beta parameter is varying on a large range of magnitude, from weakly- to strongly-magnetized. In the snapshot of the simulation, a characteristic granulation pattern with the relatively hot ($T > 5500$ K) and less dense upflowing weakly-magnetized plasma in the middle of the granular cells can be observed. In addition, the lower temperature ($T < 4500$ K) and higher density downflowing strongly-magnetized plasma at the intergranulation boundaries can be perceived (red lines of granulation). A strongly-magnetized cold plasma can be seen in the middle of the snapshot.

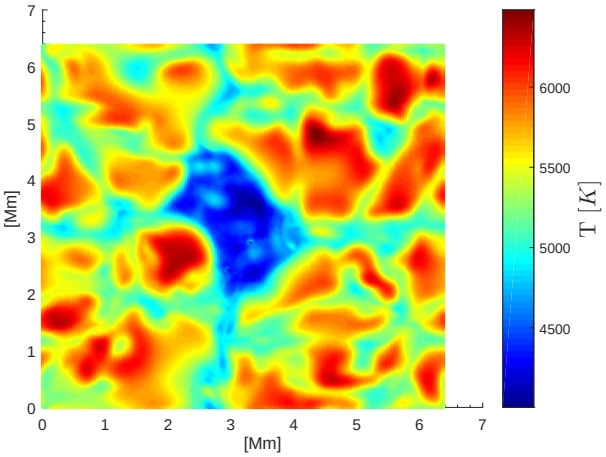

(a) Distribution of the temperature (K)

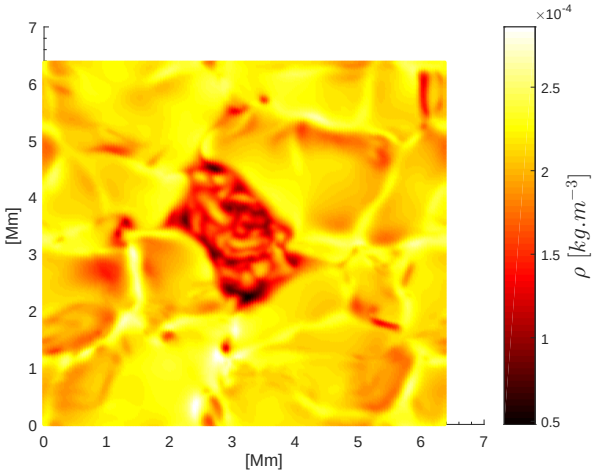

(b) Distribution of the total density ($kg.m^{-3}$)

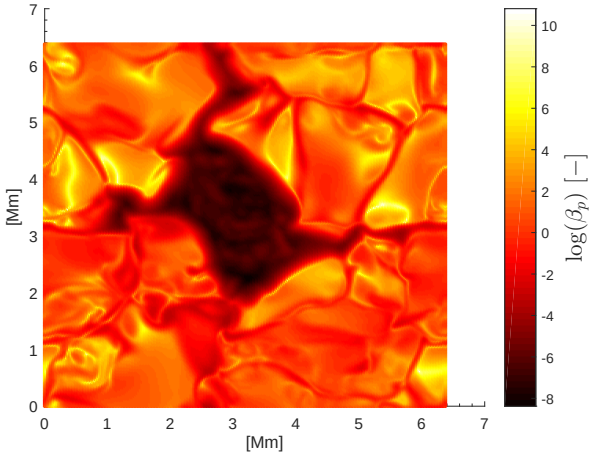

(c) Distribution of the plasma beta coefficient β_p

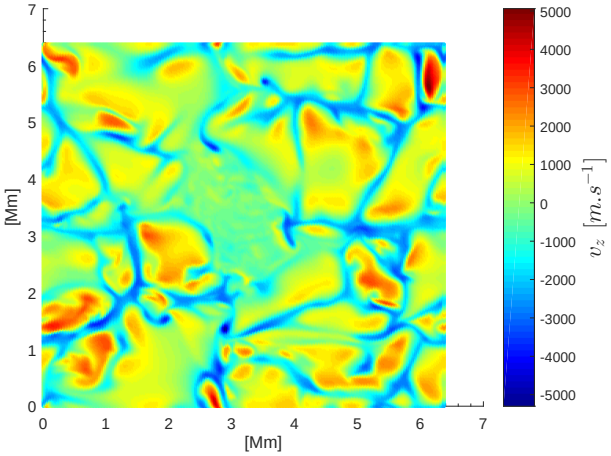

(d) Distribution of the orthogonal velocity v_z

Figure 5-14: Data from the radiative 3D MHD simulations of a pore by Kitiashvili et al. (2010)

From these datas, some properties can be computed for a Helium-Hydrogen mixture. First, some results related of the transport coefficients are shown. Then, the several terms of the generalized Ohm's law for multicomponent plasma, defined in (*E*), is investigated.

5.4.1 Results for the transport properties

In this subsection, some transport properties are computed for a Helium-Hydrogen mixture in thermochemical equilibrium. Figure 5-15a and Figure 5-15f present the distribution of the heavy particle heat flux $\lambda_\mathfrak{h}|\partial_x T|$, the ratio $\lambda_\mathfrak{e}^{\parallel}/\lambda_\mathfrak{e}^{\perp}$, $\lambda_R^{\parallel}/\lambda_\mathfrak{h}$, $\lambda_\mathfrak{e}^{\parallel}/\lambda_\mathfrak{h}$, $\nu_\mathfrak{h}$ and $D_{H,H}$ respectively. Figure 5-15b shows that the electron thermal conductivity tensor $\bar{\bar{\lambda}}_\mathfrak{e}$ is almost isotropic everywhere, except in the middle of the snapshot where $\lambda_\mathfrak{e}^{\parallel}/\lambda_\mathfrak{e}^{\perp} = 1.08$. Figure 5-15d shows that the electron thermal conductivity is small compared to the heavy thermal conductivity. These results are coherent with the calculation from Figure 5-1a and Figure 5-1b, where the mole fraction of electrons is shown to be small compared to the mole fraction of heavy particles in a range of temperature between 4000 K to 6500 K. In addition, Figure 5-15e shows that the distribution of the heavy-particle viscosity $\nu_\mathfrak{h}$ is similar to the distribution of the temperature shown in Figure 5-14a. Such result is expected since the heavy-particle viscosity is proportional to the temperature in these conditions, as shown in the Figure 5-9a for a temperature range between 4000 K and 6500 K. Finally, the distribution of the component $D_{H,H}$ of the multicomponent diffusion matrix, show that the diffusion process of hydrogen particles is more relevant in the middle of the pore than out.

5.4.2 Analysis of the generalized Ohm's law

As in Section 5.4, we compute the components of the generalized Ohm's law from (*E*) using a Helium-Hydrogen mixture, from the simulation performed by Kitiashvili et al. (2010). According to the result found in Figure 5-15b, we assume an isotropic distribution of the transport properties. Figure 5-16a and Figure 5-16e show the distribution of the resistive term, the electron battery term, the heavy particle battery term and the Soret terms for electron and heavy particle respectively.

Under this condition, the dynamics of the electric field are dominated by the resistive term at the middle of the pore. The battery term for heavy particles appears to be higher at the middle of the pore and at some intergranulation boundaries. Finally, the Soret and battery terms for electrons have higher magnitude at the intergranulation boundaries. They are negligible compared to the other terms of the generalized Ohm's law. Indeed, this is due to the mole fraction of electrons which is small compared to heavy particles under these conditions. These results are coherent with the mole fraction distribution presented in Figure 5-1a, Figure 5-1b and Figure 5-2. Note that these results are also consistent with the properties of the electric field (*E*). We recall that the terms present in (*E*) are related to two types of forces: 1- electromagnetic forces, through the resistive term, and 2- thermodynamic forces, related to temperature and pressure gradients (Soret/Dufour terms). According to the results, at the middle of the pore where the magnetic field is intense, the resistive term is higher than in the quiet Sun photosphere where the plasma is weakly magnetized.

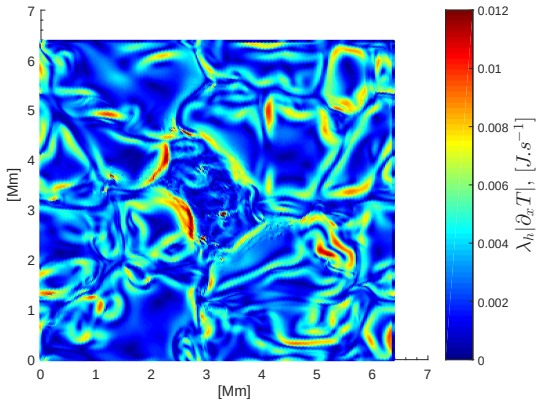

(a) Heavy particle heat flux $\lambda_{\mathfrak{h}}|\partial_{\boldsymbol{x}} T|$

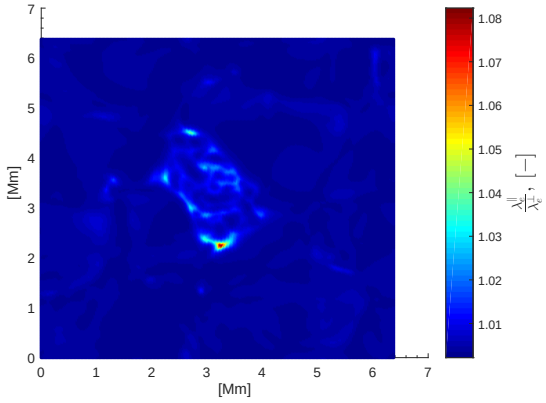

(b) Ratio $\lambda_{\mathfrak{e}}^{\parallel}/\lambda_{\mathfrak{e}}^{\perp}$

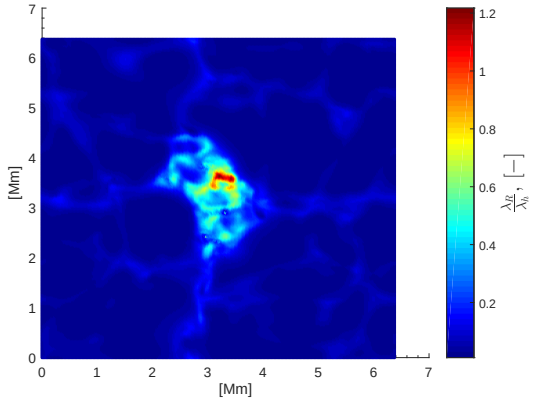

(c) Ratio $\lambda_R^{\parallel}/\lambda_{\mathfrak{h}}$

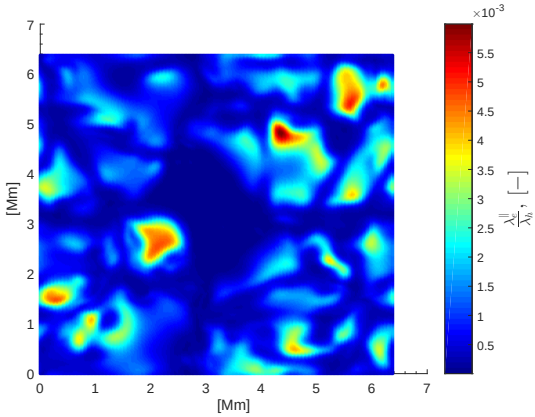

(d) Ratio $\lambda_{\mathfrak{e}}^{\parallel}/\lambda_{\mathfrak{h}}$

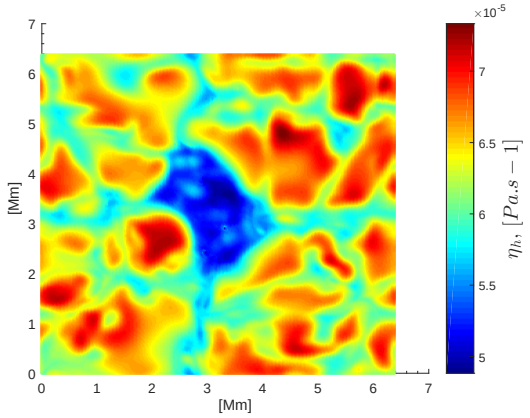

(e) Heavy-particle viscosity $\nu_{\mathfrak{h}}$

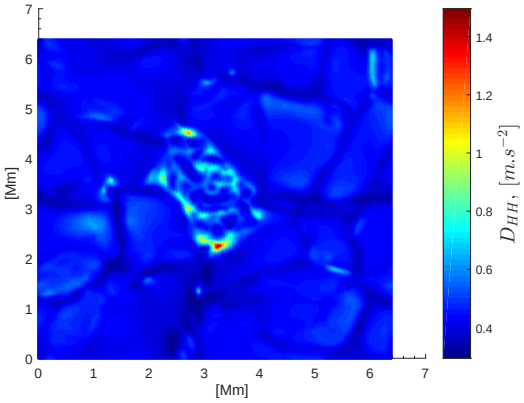

(f) Diffusion coefficient $D_{H,H}$

Figure 5-15: Distribution of transport coefficients. Postprocessed calculation based on a the third order of the Laguerre-Sonine polynomials approximation, for the Helium-Hydrogen mixture S_2 based on the results of the radiative 3D MHD simulations of a pore by Kitiashvili et al. (2010)

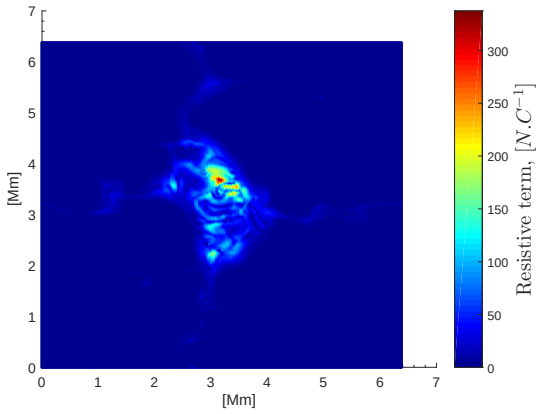

(a) Resistive term (first term of (E))

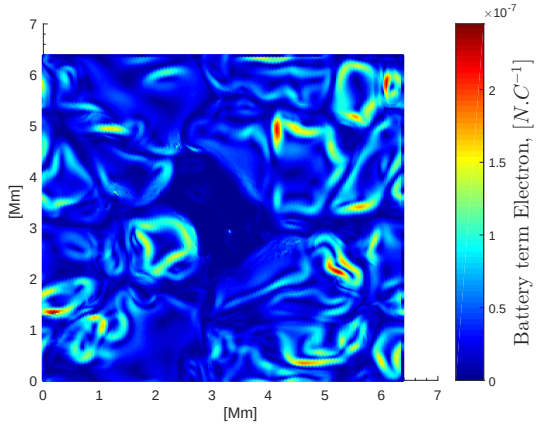

(b) Electron battery term (second term of (E))

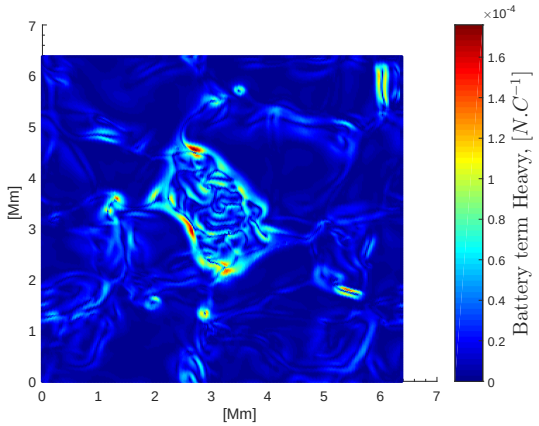

(c) Heavy battery term (third term of (E))

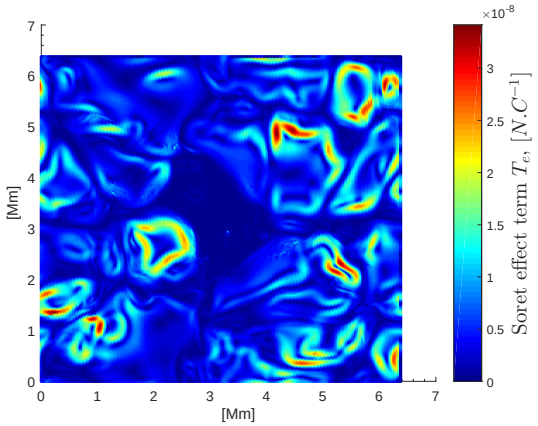

(d) Soret/Dufour term (fourth term of (E))

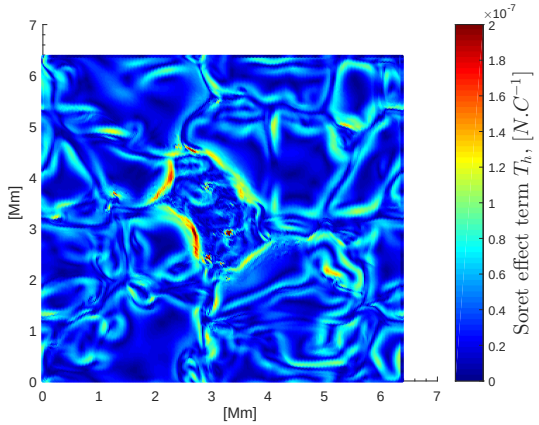

(e) Soret/Dufour term (last term of (E))

Figure 5-16: Distribution of the components of the generalized Ohm's law. Postprocessed calculation based on a the third order of the Laguerre-Sonine polynomials approximation, for the Helium-Hydrogen mixture S_2 based on the results of the radiative 3D MHD simulations of a pore by Kitiashvili et al. (2010)

5.5 Results from Bifrost simulation

5.5.1 Description of the simulation

As done in Section 5.4, we study the dynamics of a general Helium-Hydrogen multicomponent plasma in solar atmosphere conditions based on another simulation. By doing so, we have computed the transport properties of a general Helium-Hydrogen mixture in thermochemical equilibrium, by postprocessing the results of a simulation performed with a 3D radiation magnetohydrodynamic code Bifrost, described by Carlsson et al. (2016); Gudiksen et al. (2011). The simulation has been performed in a 24 by 24 Mm^2 periodic box horizontally with periodic boundary conditions, and extends 2.4 Mm below the visible surface and 14.4 Mm above encompassing the upper part of the convection zone, the photosphere, chromosphere, transition region and corona. $768 \times 768 \times 768$ grid points have been used for the simulation. In this simulation, a magnetic field configuration characterized as "coronal hole" has been used. In this configuration, an average unsigned magnetic field strength in the photosphere about 40 G with no large scale magnetic field, and, an average signed magnetic field strength about 5 G mimicking a coronal hole, have been used. A classical single-fluid MHD model including radiative transfer was used. The full simulation cubes with all variables as function of grid position are available from the Hinode Science Data Centre Europe [1]. In this work, the snapshot at time $t = 2490$ s and at $y = 12Mm$ has been used. Such large scale simulations is relevant since it gather all the conditions found in the solar atmosphere: from the photosphere to the corona.

Figure 5-17a, Figure 5-17b, Figure 5-17c and Figure 5-17d represent the distribution of the common logarithm of temperature, total density, plasma beta coefficient and magnitude of magnetic field respectively. Similarly, as Section 5.1, we compute the distribution of the mole fraction of all the species. Figure 5-18 represents the mole fractions of selected species. From these results, we distinguish four domains:

1. From $z = 0$ Mm to $z = 3.8$ Mm, we have a weakly magnetized dense plasma with a total density ranging from $\rho = 10^6\ kg.m^{-3}$ to $\rho = 10^4\ kg.m^{-3}$, with a temperature varying from $T = 10^{4.4}$ K to $T = 10^{4.1}$ K, with a high plasma beta between $\beta_p = 10^{1.2}$ and $10^{1.5}$, composed essentially of He, H_2 and H.

2. From $z = 3.8$ Mm to $z = 5$ Mm, the plasma is less dense $\rho = 10^4\ kg.m^{-3}$ to $\rho = 10^2\ kg.m - 3$, with a temperature from $T = 10^{3.4}$ K to $T = 10^4$ K, with a lower plasma beta between $\beta_p = 10^1$ and $\beta_p = 10^{1.2}$, composed of He, H_2 with a decrease in H, and a weak ionization level.

3. From $z = 5$ Mm to $z = 10$ Mm (the limit corresponding to the height of the spicules), the plasma is weakly dense and magnetized from $\rho = 10^2\ kg.m^{-3}$ to $\rho = 10^{-3}\ kg.m^{-3}$, with a temperature increasing from $T = 10^{3.4}$ K to $T = 10^{4.8}$ K, with a weak plasma beta less than

[1] In this work, results from the *ch*024031_*by*200*bz*005 configuration have been used. The full simulation cubes are available here : http://www.sdc.uio.no/search/simulations

$\beta_p = 10^{0.9}$, composed of H and He, with an ionization level that increases from 10^{-6} to 10^{-1}. In this zone the H_2 dissociates in H. At the boundary of this zone, He dissociates into He^+ and H into H^+.

4. From $z = 10$ Mm to $z = 17$ Mm, the plasma is weakly dense $\rho = 10^{-3}\ kg.m^{-3}$, with a high temperature higher than $T = 10^5$ K, with a plasma beta approximately $\beta_p = 10^1$, fully ionized, composed essentially of H^+, He^{++} and electrons.

5.5.2 Results for the transport properties

As done in Section 5.4, some transport properties have been computed. Figure 5-19a, Figure 5-19b, Figure 5-19c, Figure 5-19d, Figure 5-19e and Figure 5-19f represent the distribution of the common logarithm of the heavy particle heat flux, ratio $\lambda_{\mathfrak{e}}^{\parallel}/\lambda_{\mathfrak{e}}^{\perp}$, $\lambda_R^{\parallel}/\lambda_{\mathfrak{h}}$, $\lambda_{\mathfrak{e}}^{\parallel}/\lambda_{\mathfrak{h}}$, $\nu_{\mathfrak{h}}$ and $D_{\mathfrak{e}}^{\parallel}$ respectively. Figure 5-19b shows that the electron thermal conductivity is isotropic everywhere except for $z > 10$ Mm. Similar results have been obtained for the electron thermal diffusion ratio $\bar{\bar{\chi}}_{\mathfrak{e}}$ and the electron diffusion coefficient $\bar{\bar{D}}_{\mathfrak{e}}$. Then, Figure 5-19d shows that the electron thermal conductivity is lower than the heavy-particle thermal conductivity, except for $z > 10$ Mm. This result is strongly related to the ionization level in Figure 5-18f, and coherent with the results obtained in the previous Section 5.4, where a similar behavior has been obtained for the ratio $\lambda_{\mathfrak{e}}^{\parallel}/\lambda_{\mathfrak{h}}$. Figure 5-19f shows that the increasing of $D_{\mathfrak{e}}^{\parallel}$ as a function of height, is related to the increasing of the mole fraction of electrons in the solar atmosphere. Such result is expected since $D_{\mathfrak{e}}^{\parallel}$ is proportional to the mole fraction of electrons. Figure 5-19e shows that the heavy-particle viscosity $\nu_{\mathfrak{h}}$ is decreasing from $z = 0$ to $z = 10$ Mm and then increasing from $z = 10$ to $z = 17$ Mm. The decrease of $\nu_{\mathfrak{h}}$ is due to the decrease of the mole fractions of all the heavy particles. Then, the increase is due to the high rise of temperature from $z = 10$ to $z = 17$ Mm. Finally, the distribution obtained in Figure 5-19c, shows that the reactive thermal conductivity $\lambda_R^{\parallel}$ is clearly not negligible from $z = 0$ to $z = 10$ Mm.

5.5.3 Generalized Ohm's law in the solar atmosphere

As done in Section 5.4.2, we have computed the components of the generalized Ohm's law (E), using a Helium-Hydrogen mixture, from the the conditions obtained in Figure 5-17. According to the result obtained in Figure 5-19b, we assume an isotropic distribution of the transport properties. Figure 5-20a, Figure 5-20b, and Figure 5-20c show the distribution of the resistive term, the electron and heavy-particle thermal force terms respectively. The thermal force terms are the sum of the battery term and the Soret effect terms.

In Figure 5-20a, we see that the distribution of the resistive term follows the distribution of the magnetic field in Figure 5-17d. We see that this term is clearly dominating in the convection-photosphere-chromosphere region, from $z = 0$ to $z = 6$ Mm, with a magnitude varying from 10^{-2} to $10^5\ N.C^{-1}$. In this region, the electron thermal forces term are clearly negligible, since the ionization level is weak. However, since the plasma is mainly composed of heavy particles, the heavy particle thermal force terms have a higher magnitude between $10^{-5}N.C^{-1}$ and $10^{-3}N.C^{-1}$.

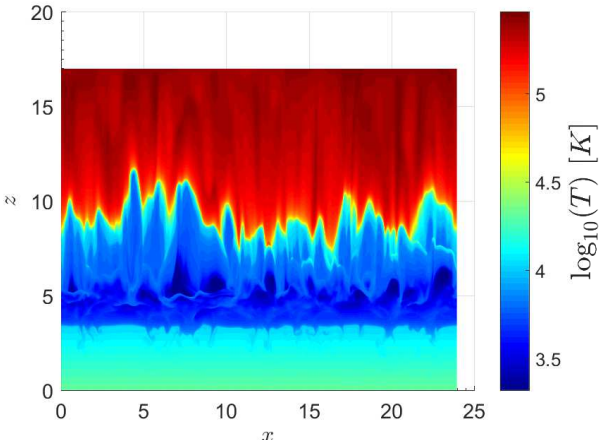

(a) Logarithm of temperature (K)

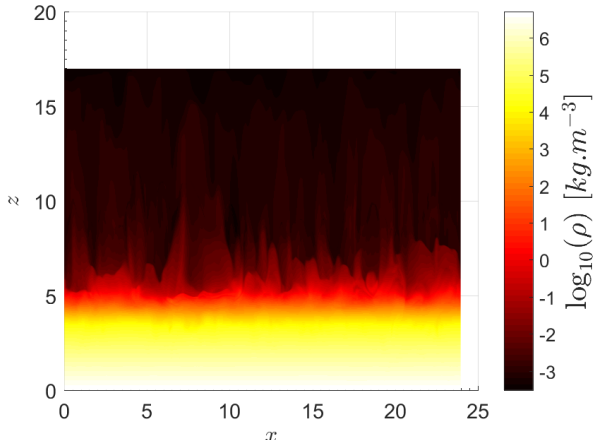

(b) Logarithm of total density ($kg.m^{-3}$)

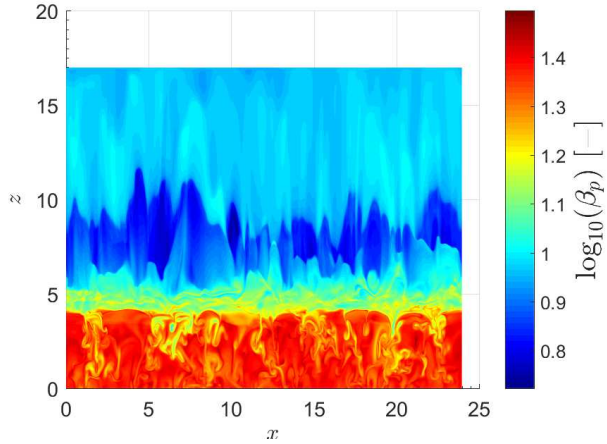

(c) Logarithm of plasma beta coefficient β_p

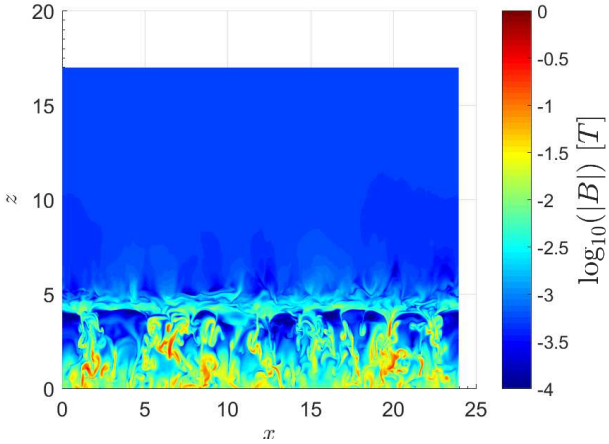

(d) Logarithm of the magnetic field $|\boldsymbol{B}|$

Figure 5-17: Data from the radiative 3D MHD simulations Bifrost performed by Carlsson et al. (2016); Gudiksen et al. (2011) of the solar atmosphere

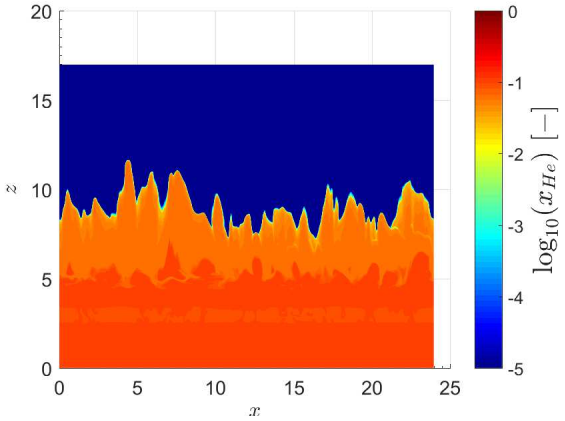

(a) Distribution of He

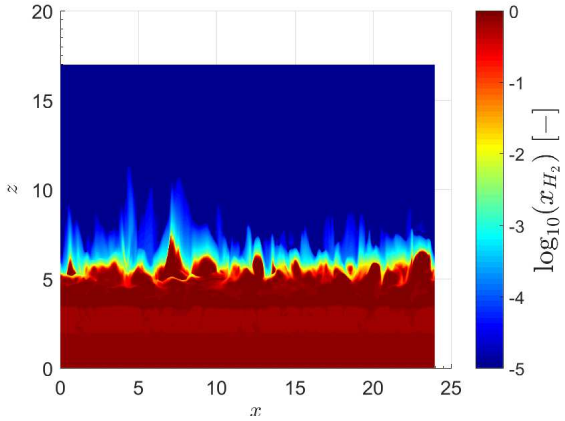

(b) Distribution of H_2

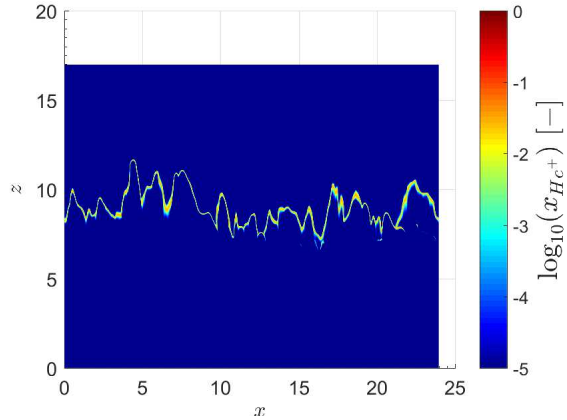

(c) Distribution of He^+

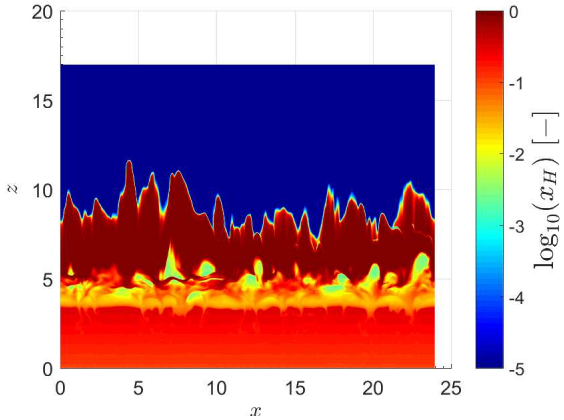

(d) Distribution of H

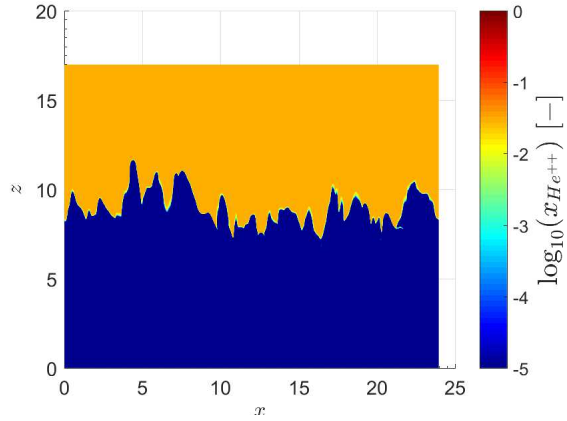

(e) Distribution of He^{++}

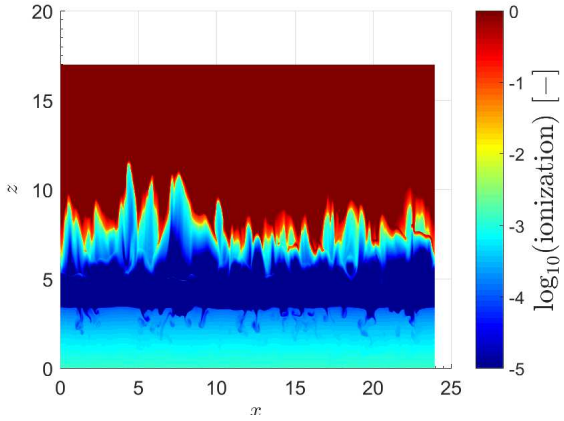

(f) Distribution of ionization degree

Figure 5-18: Distribution of the mole fractions of selected species for a Helium-Hydrogen mixture, in thermochemical equilibrium. Conditions have been chosen from Figure 5-17

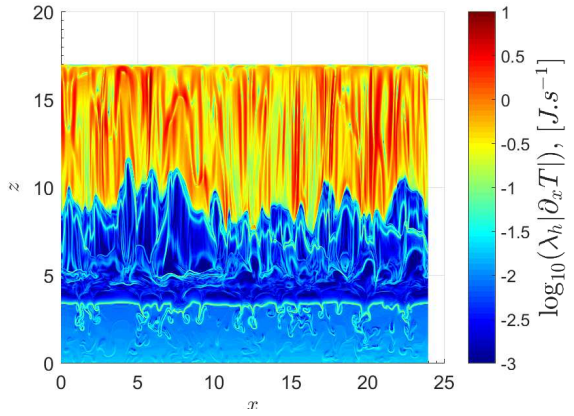

(a) Heavy particle heat flux $\lambda_\mathfrak{h}|\partial_x T|$

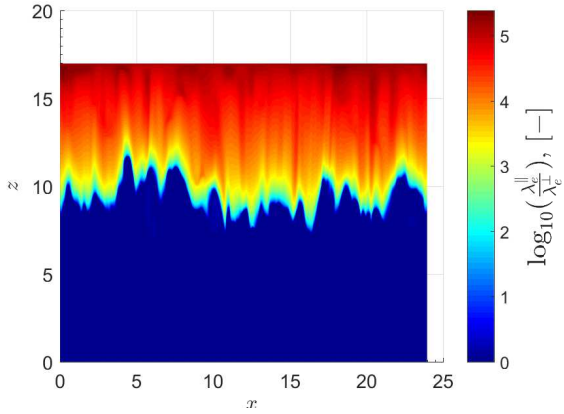

(b) Ratio $\lambda_\mathfrak{e}^{\parallel}/\lambda_\mathfrak{e}^{\perp}$

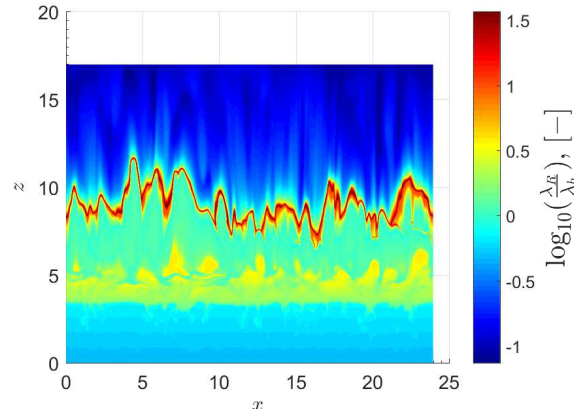

(c) Ratio $\lambda_R^{\parallel}/\lambda_\mathfrak{h}$

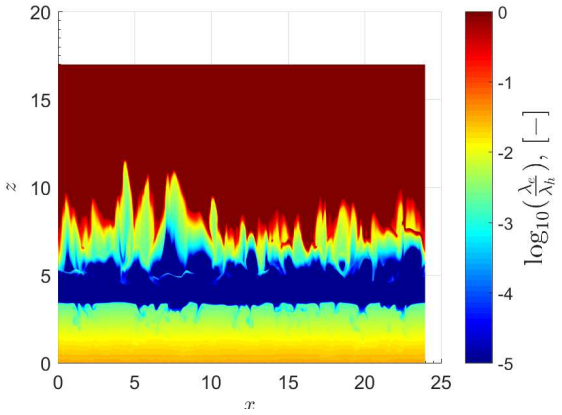

(d) Ratio $\lambda_\mathfrak{e}^{\parallel}/\lambda_\mathfrak{h}$

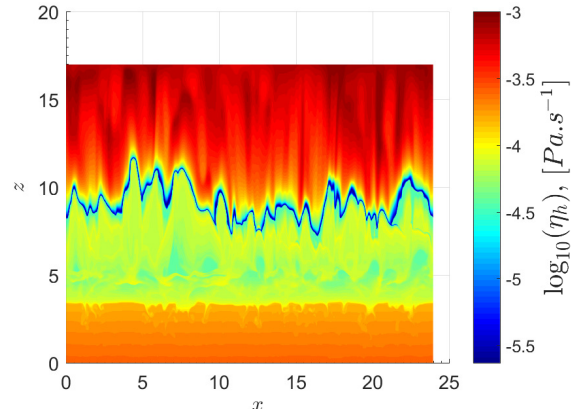

(e) Heavy-particle viscosity $\nu_\mathfrak{h}$

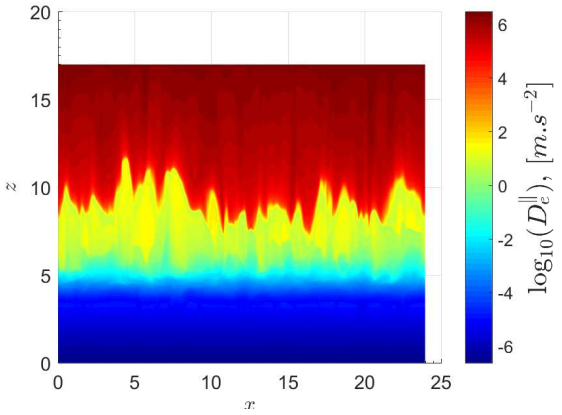

(f) Diffusion coefficient $D_\mathfrak{e}^{\parallel}$

Figure 5-19: Postprocessed calculation based on a the third order of the Laguerre-Sonine polynomials approximation, for the Helium-Hydrogen mixture S_2 based on the results of the radiative 3D MHD simulations Bifrost of the solar atmosphere performed by Carlsson et al. (2016); Gudiksen et al. (2011)

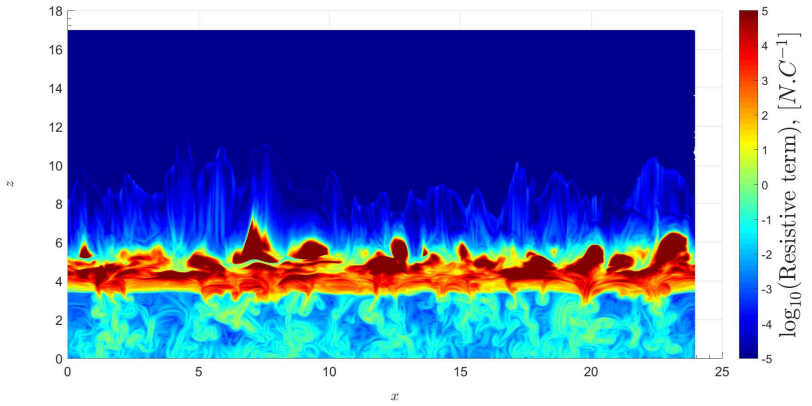

(a) Distribution of the logarithm of the resistive term

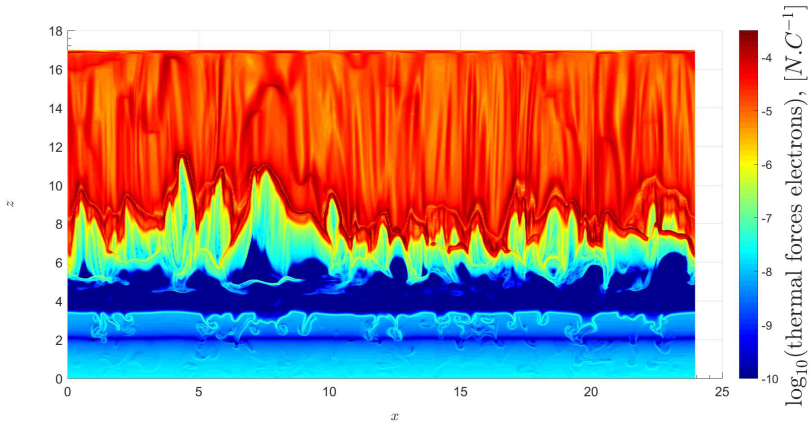

(b) Distribution of the logarithm of the electron thermal forces term

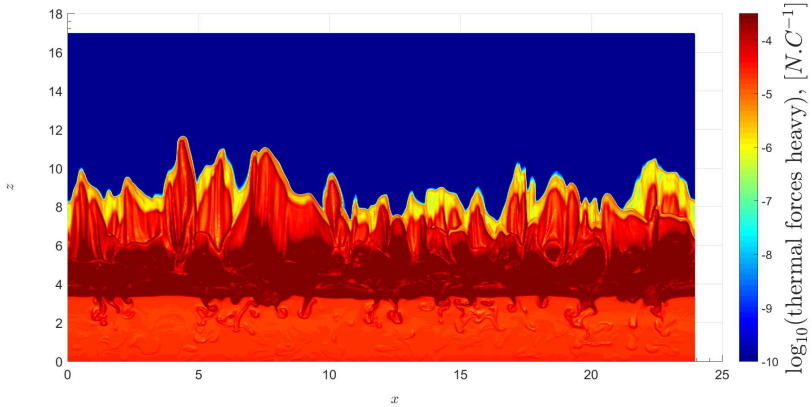

(c) Distribution of the logarithm of the heavy-particle thermal forces term

Figure 5-20: Distribution of the terms of the generalized Ohm's law (E). Postprocessed calculation based on the results of the radiative 3D MHD simulations Bifrost of the solar atmosphere performed by Carlsson et al. (2016); Gudiksen et al. (2011)

Then, from $z = 6$ to $z = 10$ Mm, the resistive term is decreasing up to 10^{-3}-$10^{-4} N.C^{-1}$, and the heavy-particle thermal force terms up to $10^{-5} N.C^{-1}$. However, since the ionization is increasing, the electron thermal force terms are increasing up to $10^{-5} N.C^{-1}$. Finally, for $z > 10$ Mm, since the plasma is fully ionized mainly composed of electrons, H^+ and He^{++}, the heavy-particle thermal force terms are negligible whereas the electron thermal force and resistive terms are dominating the dynamics of the plasma.

In these results, conditions of thermochemical equilibrium with a Helium-Hydrogen mixture have been considered. We have a tool that allow us to compute the transport properties of the multicomponent model for a multicomponent mixture, with a high level of precision, in the whole solar atmosphere.

Conclusion

General conditions largely representative of the solar lower atmosphere have been chosen in order to compute all the transport properties for a Helium-Hydrogen mixture S_1. They are obtained by solving transport systems which are presented in the previous chapter. A spectral Galerkin method based on a third-order Laguerre-Sonine polynomials approximation has been used. For convenience, we have implemented the transport model described in the paper in `MUTATION++`, an open-source library presented in Section 8.4. In order to validate our model, a comparison with the model of Braginskii (1965) has been performed in the case of a fully ionized plasma S_2. Both models are derived from the kinetic theory based on a Chapman-Enskog method. While the heavy transport properties are anisotropic in the work of Braginskii (1965), in our model, they remain isotropic. Nevertheless, under the chosen range of conditions, both behave as isotropic. In the work of Braginskii (1965), the corresponding series of Laguerre-Sonine polynomials are truncated at the second order, whereas a third-order accuracy is reached in our model. Good agreement has been obtained for the considered fully ionized S_2 mixture, in the chosen conditions.

Finally, the proposed method allows us to compute all the transport properties for a partially ionized plasma for a given mixture. The obtained results strongly depend on the mole fractions of the species involved in the mixture. We have been able to identify the behavior of the transport coefficients related to the chemistry of the species in the partially ionized mixture S_1. Considering the complexity of the multicomponent model and the new terms that appear, postprocessing calculations were performed based on the results of a pore simulation with a Helium Hydrogen mixture S_1 in thermochemical equilibrium in the highly turbulent upper layer of the solar convective zone (see Kitiashvili et al. (2010)). In addition, the transport properties have been computed in the whole solar atmosphere by postprocessing a simulation performed by Carlsson et al. (2016); Gudiksen et al. (2011). These results allow us to both understand the effect and magnitude of these terms under the conditions we chose, especially the terms of the generalized Ohm's law. Generally, the plasma being weakly ionized under these conditions, all the transport fluxes related to the electrons are negligible compared to those from heavy particles. Especially, we show a new formulation of the resistivity which depends on the multicomponent transport coefficients taking into account all possible interactions in the mixture. It appears to be much more general than standard resistivity

such as ambipolar resistivity, Spitzer resistivity and Ohmic resistivity. Under conditions where the plasma is dominated by electromagnetic forces, which is the case at the center of the pore in Section 5.4 or in the upper chromosphere in Section 5.5, we find qualitatively that the resistive term is dominating the dynamics of the weakly ionized Helium-Hydrogen plasma. On the other hand, at the interboundary granulations (or more generally in the case of quiet Sun photosphere conditions), where the plasma is weakly ionized and thermal pressure dominated, the new terms such as the Soret / Dufour effects (associated with the temperature gradients) are dominating the plasma dynamics. t role in the dynamics of the plasma.

Part III

Numerical methods

CHAPTER 6

DISCRETIZATION STRATEGY - NUMERICAL METHODS

Introduction

In Chapter 3, the governing equations (Mc) and (Mf) combined with Maxwell equations ($Mx^{\varepsilon=0}$) have been identified. These systems of equation describe configurations where we have thermal nonequilibrium between electrons and heavy-particles. Therefore, a nonconservative internal energy equation of electrons naturally appears.

As shown in Chapter 7, solving hyperbolic nonconservative system is a major problem from both a theoretical and numerical point of view, because of the definition of weak admissible solution. An effort is required to study these systems when sharp gradients or discontinuities are involved. In particular, if these terms are not properly discretized, non-physical shocks may appear at discontinuites due to the numerical dissipation induced by the discretization, and shock waves may be not correctly captured by the numerical scheme. It is necessary to define a numerical strategy to avoid these non-physical shocks and guarantee that discontinuities are numerically captured. In order to tackle this issue, it is required first to perform a deeper study of the multicomponent system when discontinuities are involved. As presented in Wargnier, Faure, et al. (2018), this study allows to identify the characteristic scales of the system which have to be numerically resolved to capture the discontinuities/shock waves. Then, based on this study, two paths are proposed for discretizing the nonconservative terms:

1. developing a specific numerical treatment of the nonconservative terms to properly capture shock waves/discontinuities. This development is essentially based on the study of the system when discontinuities are involved and the identification the scales to be numerically resolved. Then, the specific treatment of the nonconservative terms allows to correctly capture discontinuities and avoid the propagation of nonphysical shocks for any discretization

considered.

2. using a standard or consistent discretization of the nonconservative terms. However, following this path, we have to guarantee that a sufficient number of cells or nodes is considered in the discretization, to numerically resolve the characteristic scales.

The first path is investigated in the next Chapter, but on a simplified case where no electromagnetic fields are considered. A specific numerical treatment of the nonconservative terms is provided. This study should be extended to the general case (see Wargnier, Faure, et al. (2018)). In the following, the numerical strategy is focused on the second path. In our simulation, we guarantee that the physical dissipation is dominating the numerical dissipation and a sufficient number of cells is considered in the discretization. Therefore, we avoid the propagation of non-physical shocks appearing at discontinuities.

This Chapter is devoted to the description of the numerical strategy involved in this thesis. The choice of this numerical strategy is based on advances described in the literature. Then, the contributions of this thesis are 1- the implementation this strategy into the massively parallel code `CanoP` which allow for cell-based AMR (Adaptive Mesh Refinement) simulations, presented in Chapter 8, and 2- the definition of a numerical strategy to discretize the nonconservative terms, presented in Chapter 7.

The development of numerical methods for hyperbolic-parabolic systems combined with Maxwell equations, has been widely studied in the literature. One of the major problems encountered with such systems, is the constraint $\boldsymbol{\partial_x \cdot B} = 0$, which is difficult to satisfy at the numerical level. Indeed, a naive discretization of such a term creates errors that accumulate during the simulation and develop numerical instabilities. Directly applying well-studied shock-capturing scheme could cause instability and leads to nonphysical results, due to accumulation of errors from violating the divergence-free constraint. Therefore, enforcing $\boldsymbol{\partial_x \cdot B} = 0$ as part of global conservation condition is crucial to achieve accurate solutions in MHD systems, especially where discontinuities exist. This effect has been widely studied by Brackbill & Barnes (1980), Brackbill (1985), and Balsara & Spicer (1999). In this context, several methods have been developed in the literature. For example, we have the constrained transport methods (Brecht et al. (1981); DeVore (1991); Evans & Hawley (1988); K. S. Yee (1966)) that enforce $\boldsymbol{\partial_x \cdot B} = 0$ using a so-called staggered-mesh approach. An alternative is to use a projection method using the space of divergence-free vector fields, called "Hodge projection" developed by Balsara (1998a,b), in order to enforce the divergence-free constraint. Such method has been used also by Tóth (2000). Then, we have the diffusive method where a modification of the induction equation is proposed by adding a diffusive term, as performed by van der Holst & Keppens (2007). Finally, we have the hyperbolic divergence cleaning method used by Dedner et al. (2002) where a Generalized Lagrange Multiplier (GLM) is considered. Considering the large set of methods developed in the literature, it is still necessary to choose the most appropriate one.

In the literature, there is a large range of possible numerical methods to discretize the presented multicomponent models (Mc) and (Mf). From the numerical point of view, the presence of diffusive terms in the multicomponent systems may involve small timesteps limited by Fourier-type conditions. Generally, for our solar physics application, this timestep is much smaller than

the convective timestep which is limited by a classical Courant-Friedrichs-Lewy (CFL) condition (see, for example Section 7.4). Therefore, the proposed numerical method has to provide the possibility of having small timesteps constrained by Fourier conditions due to diffusive terms, while guaranteeing a good approximation of the numerical solution.

Generally, four main strategies of discretization have been developed, in the literature: 1-finite difference, 2-finite element, 3-discontinuous Galerkin and 4-finite volume methods. In this thesis, we have chosen to focus on a finite volume framework in order to be able to perform cell-based Adaptive Mesh Refinement (AMR) simulations (Almgren et al. (2013); Drui, Fikl, et al. (2016); Drui (2017); Essadki (2018)). The advantage of this approach is to be able to capture all the spectrum of scales associated with the multicomponent models, and, in particular, those involved in magnetic reconnection processes (Smith & Sakai (2008); Leake et al. (2012)). In order to reach a high level of stability and robustness, we have focused on second order finite volume schemes. Thus, combined with an AMR approach, a high level of accuracy is reached at the same time. Due to their simplicity, robustness and accuracy to capture all the discontinuities, we turn to Riemann solver-free schemes developed by Kurganov & Tadmor (2000); Nessyahu & Tadmor (1990); Kurganov & Petrova (2000); Kurganov et al. (2007); Kurganov & Lin (2007). These schemes are second-order and are shown to avoid numerical oscillations during the presence of shocks or discontinuities.

In this context, we have chosen to discretize the systems of equations with a Kurganov & Tadmor (2000) (KT) scheme, with a second-order Runge Kutta method for the time discretization (Dormand & Prince (1980)), combined with a GLM mixed parabolic-hyperbolic correction method for the $\boldsymbol{\partial_x \cdot B} = 0$ constraint from Dedner et al. (2002), and implemented in a massively parallel cell-based AMR code called `CanoP` (described in the next Chapter 8). Indeed, the choice of the GLM method is justified by its adaptability with finite volume schemes such as KT. Therefore, a slight modification of the multicomponent systems is required: a transport-like equation is considered and an additional source term is integrated. These modifications do not require any difficulties in terms of implementation. In addition, this method has been widely used in an AMR framework and has given satisfactory results (see Gomes et al. (2015b)).

The KT scheme is a second order finite volume scheme which can be adapted to an AMR cell-based strategy. In addition, unlike the classical Nessyahu & Tadmor (1990) (NT) scheme, this scheme is showing interesting properties in terms of numerical approximation of the solution when the timesteps tend to be small. It can be rewritten in a semi-discrete form, which allows the possibility of numerically integrating the system with accurate time integration methods such as Rock4 (see Abdulle (2001)) or operators splitting techniques (see Strang (1968); Duarte et al. (2012); Descombes et al. (2014a); Duarte (2011)). This property is relevant in our application, where small timesteps are involved, as explained above. The proposed scheme is robust and stable with second-order accuracy and does not require any Riemann solver. It only needs local magnetosonic speed of propagation.

Finally, the choice of a finite volume type scheme is justified by legacy of the presented `CanoP` code (see Chapter 8), used for our simulation. It is a massively parallel code for AMR cell-based implementations. In this code, essentially finite volume type schemes with a second order stencil can be found. Thus, the scheme of KT appears to be appropriate for being implemented in such a

code.

In Section 6.1, an overview of the main methods used for the incompressibility constraint $\partial_x \cdot \boldsymbol{B} = 0$ is presented. Then, we present the classical GLM mixed parabolic-hyperbolic correction method by Dedner et al. (2002) which is used in this work. Additionally, we exhibit the influence of this method on the eigenstructure of the multicomponent systems. Then, in Section 6.2, a general overview of finite volume numerical methods possible to discretize the multicomponent systems is presented. Thus, we provide some level of justification as well as a presentation of the KT scheme. In Section 6.3, we present the scheme in a uniform monodimensional grid framework. We also exhibit the discretization of the diffusive and source terms. Finally, in Section 6.5, we generalize this discretization to the case for AMR cell-based framework on multidimensional grids.

6.1 Incompressibility condition on the magnetic field

In the multicomponent system (Mc) and (Mf) combined with Maxwell equations, a special attention has to be paid to the incompressibility constraint, because, as shown in practice, uncontrolled divergence errors can modify the underlying physics (Brackbill & Barnes (1980); Brackbill (1985)). In this context, several methods have been developed in order to enforce this incompressibility constraint, and, without being exhaustive, can be classified as follows

- **The constrained transport methods**, which is a multidimensional, divergence-preserving update procedure for the magnetic field components which are collated on a staggered grid centered on the computational volume interfaces (see Brecht et al. (1981); DeVore (1991); Evans & Hawley (1988); K. S. Yee (1966)).

- **The projection method** which is using the space of divergence-free vector fields (see Balsara (1998a,b); Tóth (2000); Munz et al. (2000)). In this approach, a Poisson equation is solved to eliminate the divergences errors at each timestep.

- **The eight-wave formulation approach** explored by Powell et al. (1999) to give alternative formulations of the MHD equations to prevent the local magnetic divergence error by advecting monopoles to regions of the grid where they are of less consequence to the dynamics of the flow.

- **The GLM approach** defined by Dedner et al. (2002), who introduce a Generalized Lagrange Multiplier (GLM). In this framework, a new variable ψ is introduced to the system to play the role of convecting local divergence error out of the domain(see Dedner et al. (2003); Mignone & Tzeferacos (2010); Mignone et al. (2010); Susanto et al. (2013)). In this category, we have the GLM mixed hyperbolic-parabolic correction, where the local divergence error are convected out of the domain and damped by dissipation. Such methods have been used for solar physics application Alvarez Laguna et al. (2016, 2018). Alternatively, we have the GLM parabolic correction which is a modification of the induction equation by adding a diffusive term (see van der Holst & Keppens (2007)).

We thus focus on a GLM mixed parabolic-hyperbolic correction method. Indeed, this method avoids the computational cost associated with an elliptic cleaning step used by projection methods, and the scrupulous treatment of staggered fields demanded by constrained transport algorithms. Furthermore, in Mignone & Tzeferacos (2010) it is shown that, through several numerical tests based on second-order accurate schemes, the GLM approach is robust and can achieve accuracy comparable to the constrained transport methods. In addition, the resulting system is shown to be still in conservation form. Here, the method is presented in a cell-center framework. Therefore, the method is 1- not showing any difficulties in terms of implementation, thus, can be implemented into an AMR cell-based strategy such as `CanoP` (see Chapter 8), and 2- well adapted to the KT scheme.

In this section, we present the GLM mixed parabolic-hyperbolic corrections. This method is obtained from a constrained formulation described by Dedner et al. (2002). The constrained formulation is obtained by focusing on the hyperbolic part of the multicomponent systems (Mc) and (Mf). First, the classical constrained formulation is shown. Then, the GLM mixed parabolic-hyperbolic correction is presented. Finally, we detail the impact of the GLM method on the eigenstructure of the multicomponent model considered.

6.1.1 Constrained formulation

For the sake of clarity we rewrite the magnetic induction equation as follows,

$$\partial_t \boldsymbol{B} - \boldsymbol{\partial_x}\wedge(\boldsymbol{v}_\mathfrak{h}\wedge\boldsymbol{B}) + \boldsymbol{\partial_x}\wedge\boldsymbol{E}' = 0, \tag{6.1.1}$$

where the general expression of $\boldsymbol{E}'$ is defined in (E) at the page 78. Expressing the induction equation as presented in (6.1.1), allow us to distinguish the hyperbolic and parabolic terms. Indeed, the first two terms of (6.1.1) correspond to the usual hyperbolic part of the magnetic induction equation, as in the common ideal MHD systems. The last term $\boldsymbol{\partial_x}\wedge\boldsymbol{E}'$ is the sum of diffusive terms, depending on gradients of partial pressures, temperatures and magnetic field. In this section, we focus on the hyperbolic part of the governing equations in order to introduce the classical GLM method.

Following Dedner et al. (2002), we introduce a new scalar function ψ. The latter is used for coupling the divergence free constraint $\boldsymbol{\partial_x}\cdot\boldsymbol{B} = 0$ with the induction equation. We couple the divergence constraint with the hyperbolic evolution equations of the multicomponent model and inviscid magnetic induction equation, through a linear differential operator. Thus, the equation describing the evolution of the magnetic field without diffusive terms, is replaced by the following equations

$$\partial_t \boldsymbol{B} - \boldsymbol{\partial_x}\wedge(\boldsymbol{v}_\mathfrak{h}\wedge\boldsymbol{B}) + \boldsymbol{\partial_x}\psi = 0, \tag{6.1.2}$$

$$\mathcal{P}(\psi) + \boldsymbol{\partial_x}\cdot\boldsymbol{B} = 0, \tag{6.1.3}$$

where $\mathcal{P}$ is a linear differential operator. Then, we choose $\mathcal{P}$, the initial and boundary conditions for ψ , in such a way that the numerical approximation presented in (6.1.2) and (6.1.3), are a good approximation to the original system. In the next subsection, we present several choices for the

operator $\mathcal{P}$ according to the suggestions introduced by Dedner et al. (2002). In addition, combining (6.1.2) and (6.1.3), for smooth solutions we have

$$\begin{aligned}
&\partial_t\left(\boldsymbol{\partial_x}\cdot\boldsymbol{B}\right)+\boldsymbol{\partial_x}\cdot\left(\boldsymbol{\partial_x}\psi\right)=0,\\
&\partial_t\mathcal{P}\left(\boldsymbol{\partial_x}\cdot\boldsymbol{B}\right)+\boldsymbol{\partial_x}\cdot\boldsymbol{\partial_x}\left[\mathcal{P}(\psi)\right]=0,\\
&\partial_t\mathcal{P}(\psi)+\partial_t\left(\boldsymbol{\partial_x}\cdot\boldsymbol{B}\right)=0,\\
&\boldsymbol{\partial_x}\cdot\boldsymbol{\partial_x}\left[\mathcal{P}(\psi)\right]+\boldsymbol{\partial_x}\cdot\left[\boldsymbol{\partial_x}\left(\boldsymbol{\partial_x}\cdot\boldsymbol{B}\right)\right]=0.
\end{aligned}\tag{6.1.4}$$

Thus, from (6.1.4), we obtain

$$\partial_t\mathcal{P}\left(\boldsymbol{\partial_x}\cdot\boldsymbol{B}\right)-\boldsymbol{\partial_x}\cdot\left[\boldsymbol{\partial_x}\left(\boldsymbol{\partial_x}\cdot\boldsymbol{B}\right)\right]=0,\tag{6.1.5}$$

$$\partial_t\mathcal{P}\left(\psi\right)-\boldsymbol{\partial_x}\cdot\left[\boldsymbol{\partial_x}\left(\psi\right)\right]=0.\tag{6.1.6}$$

Thus, (6.1.6) and (6.1.5) show that $\boldsymbol{\partial_x}\cdot\boldsymbol{B}$ and ψ are verifying the same equation for any choice of linear differential operator $\mathcal{P}$ according to the coupling introduced in (6.1.3) and (6.1.2). However, it is still necessary to choose an appropriate linear differential operator to enforce the divergence cleaning constraint on the magnetic field.

6.1.2 GLM mixed hyperbolic-parabolic correction

In the mixed hyperbolic-parabolic correction introduced by Dedner et al. (2002), we consider

$$\mathcal{P}\left(\psi\right)=\frac{1}{c_h^2}\partial_t\psi+\frac{1}{c_p^2}\psi\quad\text{with}\quad c_p,c_h\in(0,\infty)\,.\tag{6.1.7}$$

By injecting (6.1.7) into (6.1.6), we obtain the telegraph equation which involve dissipation and propagation of divergence errors

$$\partial_{tt}^2\psi+\frac{c_h^2}{c_p^2}\partial_t\psi-c_h^2\boldsymbol{\partial_x}\cdot(\boldsymbol{\partial_x}\psi)=0.\tag{6.1.8}$$

Then, using (6.1.3) we obtain

$$\partial_t\psi+c_h^2\boldsymbol{\partial_x}\cdot\boldsymbol{B}=-\frac{c_h^2}{c_p^2}\psi.\tag{6.1.9}$$

In this context, the damping of the local divergence error is performed by a source term. This method ensures that the local divergence errors induced by $\boldsymbol{\partial_x}\cdot\boldsymbol{B}$ are convected out of the domain with a speed c_h and damped by the dissipation coefficient c_p. Thus, this method offers both propagation and dissipation of the errors. Such methods appear to be efficient for damping the local divergence error, and has been used in multi-fluid models for solar physics application (see Alvarez Laguna et al. (2016, 2018)). However, this approach is modifying the eigenstructure of the model. Further details concerning the values of the coefficients c_h and c_p will be given in the next subsection.

As shown by Dedner et al. (2002) with the ideal MHD system, the system composed of the hyperbolic part of the multicomponent or fully ionized plasma model, *i.e.*, (Mc) and (Mf), combined with (6.1.2) and (6.1.9), is hyperbolic and is called the GLM formulation of the multicomponent approach. In this approach, a conservation equation on ψ has to be solved and a source term has to be integrated. Therefore, this method does not show any difficulties in terms of implementation and can be adapted to a wide variety of numerical schemes. As an example, it can be adapted to an AMR cell-based framework where a KT scheme is used.

6.1.3 Eigenstructure of the GLM formulation and modification of the multicomponent systems

In the mixed parabolic-hyperbolic GLM approach, the eigenvalues of the system are modified. Two additional velocities $\pm c_h$ are considered, due to the additional equation on ψ. Here, the study of the eigenstructure is mainly focus on the model described by (Mc). The study of the eigenstructure of the fully ionized model (Mf) can be easily determined from the study with (Mc).

The general system of equations is similar to the one described in Section 3.4. Here, the quantities are $\mathcal{U} \in \mathbb{R}^{9+n^{\mathrm{H}}}$, $\mathcal{F}(\mathcal{U}) \in \mathbb{R}^{3\times(9+n^{\mathrm{H}})}$, $\mathcal{G}(\mathcal{U}, \partial_x \mathcal{U}) \in \mathbb{R}^{3\times(9+n^{\mathrm{H}})}$ and $\mathcal{S}(\mathcal{U}, \partial_x \mathcal{U}) \in \mathbb{R}^{3\times(9+n^{\mathrm{H}})}$ and are defined by

$$
\begin{aligned}
\mathcal{U} &= \Big((\rho_i)_{i\in\mathrm{H}},\, \rho_{\mathfrak{h}}\boldsymbol{v}_{\mathfrak{h}}^T,\, \mathcal{E},\, \rho_{\mathfrak{e}}e_{\mathfrak{e}},\, \boldsymbol{B}^T,\, \psi\Big)^T,\\
\mathcal{F}(\mathcal{U}) &= \Big((\rho_i)_{i\in\mathrm{H}}\boldsymbol{v}_{\mathfrak{h}},\, \rho_{\mathfrak{h}}\boldsymbol{v}_{\mathfrak{h}}\otimes\boldsymbol{v}_{\mathfrak{h}} + \Big(p_{\mathfrak{e}} + p_{\mathfrak{h}} + \tfrac{1}{8\pi}|\boldsymbol{B}|^2\Big)\mathbb{I} - \tfrac{1}{8\pi}\boldsymbol{B}\otimes\boldsymbol{B},\\
&\qquad (\mathcal{E} + p_{\mathfrak{e}} + p_{\mathfrak{h}})\boldsymbol{v}_{\mathfrak{h}} + \tfrac{1}{4\pi}\boldsymbol{E}\wedge\boldsymbol{B},\, \rho_{\mathfrak{e}}e_{\mathfrak{e}}\boldsymbol{v}_{\mathfrak{h}},\, \mathbb{I}_\wedge(\boldsymbol{v}_{\mathfrak{h}}\wedge\boldsymbol{B}) + \psi\mathbb{I},\, c_h^2\boldsymbol{B}\Big)^T, \qquad (Mc^{\mathrm{GLM}})\\
\mathcal{G}(\mathcal{U}, \partial_x\mathcal{U}) &= \Big((\boldsymbol{V}_i)_{i\in\mathrm{H}},\, \boldsymbol{\Pi}_{\mathfrak{h}}^T,\, \boldsymbol{\Pi}_{\mathfrak{h}}\cdot\boldsymbol{v}_{\mathfrak{h}} + \boldsymbol{q}_{\mathfrak{e}} + \boldsymbol{q}_{\mathfrak{h}},\, \boldsymbol{q}_{\mathfrak{e}},\, -\mathbb{I}_\wedge(\boldsymbol{E}')^T,\, 0_3\Big)^T,\\
\mathcal{S}(\mathcal{U}, \partial_x\mathcal{U}) &= \Big(0_{n^{\mathrm{H}}}^T,\, 0_3^T,\, 0,\, -p_{\mathfrak{e}}\partial_{\boldsymbol{x}}\cdot\boldsymbol{v}_{\mathfrak{h}} + \boldsymbol{J}_{\mathfrak{e}}\cdot\boldsymbol{E}' + \Delta E_{\mathfrak{e}}^{(0)} + \Delta E_{\mathfrak{e}}^{(1)},\, 0_3^T,\, -\frac{c_h^2}{c_p^2}\psi\Big)^T,
\end{aligned}
$$

where the source terms $\mathcal{S}$ are composed of two terms, relaxation terms and nonconservative terms as follows

$$
\mathcal{S}(\mathcal{U}, \partial_x\mathcal{U}) = N(\mathcal{U}, \partial_x\mathcal{U}) + \mathcal{S}^{\mathrm{relax}}(\mathcal{U}). \tag{6.1.10}
$$

The relaxation terms and the nonconservative terms are defined as

$$
N(\mathcal{U}, \partial_x\mathcal{U}) = \Big(0_{n^{\mathrm{H}}}^T,\, 0_3^T,\, 0,\, -p_{\mathfrak{e}}\partial_{\boldsymbol{x}}\cdot\boldsymbol{v}_{\mathfrak{h}} + \boldsymbol{J}_{\mathfrak{e}}\cdot\boldsymbol{E}',\, 0_3^T,\, 0\Big)^T, \tag{6.1.11}
$$

$$
\mathcal{S}^{\mathrm{relax}}(\mathcal{U}) = \Big(0_{n^{\mathrm{H}}}^T,\, 0_3^T,\, 0,\, \Delta E_{\mathfrak{e}}^{(0)} + \Delta E_{\mathfrak{e}}^{(1)},\, 0_3^T,\, -\frac{c_h^2}{c_p^2}\psi\Big)^T, \tag{6.1.12}
$$

Without considering the diffusive and source terms $\mathcal{G}$ and $\mathcal{S}$, the system (Mc^{GLM}) is hyperbolic

with eigenvalues identical to the original system, presented in Section 3.4, with the additional eigenvalues $\pm c_h$. Note that, the nonconservative terms are considered as a source term

As presented in Dedner et al. (2002), the coefficient c_h is taken as the maximum signal speed compatible with the timestep, *i.e.*, the fastest magnetosonic speed taken in all the direction, defined in (3.4.13) and (3.4.14). Then, the coefficient c_p is computed as

$$c_p = \sqrt{-\Delta t \frac{c_h^2}{\ln(c_d)}}, \quad c_d \in (0,1)\,, \tag{6.1.13}$$

where Δt is the timestep of the simulation.

In summary, the GLM mixed parabolic-hyperbolic correction has been chosen tor enforce the divergence constraint of the magnetic field and the resulting system (Mc^{GLM}) to be implemented has been identified. In the next section, we focus on the numerical method to be used for discretizing (Mc^{GLM}).

6.2 Choice of the numerical method

This section is devoted to an overview of the numerical methods to be used for system (Mc^{GLM}) and the justification of the choice of the numerical scheme in a finite volume framework.

System (Mc^{GLM}) is an hyperbolic-parabolic system of equations with source terms, for which a numerical strategy has to established in order to discretize in space and time this system. The numerical strategy has to take into account the numerical stiffness induced by the source terms present in the equation of internal energy of electrons. The large spectrum of scales considered in our approach presents a challenge to the numerical modeling. Such a system includes a large range of time and space scales such as the electromagnetic, convective, diffusive and collisional scales of each fluid.

In particular, the presence and structure of diffusive terms in the multicomponent systems implies that the timestep is limited by a Fourier-type condition. Generally, for our solar physics application, this timestep is much smaller than the convective timestep, which is limited by a Courant-Friedrichs-Lewy (CFL) condition. The chosen numerical method has to give the possibility of having small timesteps while guaranteeing a good approximation of the numerical solution.

Additionally, the numerical scheme has to not introduce some spurious oscillations where discontinuities or shocks arise. Indeed, in a magnetic reconnection configuration, shocks may appear. The numerical strategy has to ensure a maximum of robustness and stability while guaranteeing a high level of accuracy and offering a simple extension to AMR formalism.

In the literature, four main possibilities of discretization for the system (Mc^{GLM}) can be found: 1- **Finite Difference** (FD), 2-**Finite elements** (FE) 3-**Discontinous Galerkin** (DG) and 4-**Finite Volume** (FV) methods.

6.2.1 FD methods

In the category of FD methods, one possibility to discretize in space and time the system (Mc^{GLM}) would be to use a traditional second-order scheme developed by Artebrant & Torrilhon (2008); Balsara (2004); Londrillo & del Zanna (2004); Crockett et al. (2005). These second-order schemes are based on the Total Variation Diminishing property and use slope-limited reconstructions. In spite of the excellent results produced in proximity of discontinuous waves where sharp non-oscillatory transitions can be obtained, TVD schemes still suffer from excessive unwanted numerical dissipation in regions of smooth flow.

In this context, piecewise parabolic method (PPM) have been developed and extend to MHD systems (see Dai & Woodward (1994, 1997)). Then, we have the Weighted Essentally Non-Oscillatory (WENO) schemes, originally developed by Shu (1998). The latter provide highly accurate solutions in regions of smooth flow and non-oscillatory transitions in presence of discontinuous waves by combining several interpolation stencils of order r into a weighted average of order $2r-1$. The nonlinear weights are adjusted by the local smoothness of the solution. In summary, zero weights are given to non-smooth stencils whereas specific weights are prescribed in smooth regions. WENO scheme have been also formulated in the context of MHD (see Guang-Shan & Cheng-Chin (1999); Balsara & Shu (2000)). However, it has been shown that these schemes are very accurate in smooth regions, capture very well the shock-waves but show a too diffusive behavior in the vicinity of contact discontinuities.

Several studies have been performed to get better prediction for WENO-based schemes (see Adams & Shariff (1996); Hill & Pullin (2004); Qiu & Shu (2004)). Additionally, in Wray et al. (2015), a fourth-order Padé spatial differentiation scheme combined to a fourth order Runge-Kutta scheme for the time discretization has been used to discretized a single-fluid MHD model for solar atmosphere application. All of these schemes are separate time-space methods, where the time integration is generally based on high-order multi-stage Runge-Kutta (RK) methods Shu & Osher (1988).

Then, we have the category of coupled space-time methods. The latter are generally based on are a Lax-Wendroff approach developed by Lax & Wendroff (1960). In this category, we have the One Step (OS) schemes which have a minimal stencil, and optimal non-oscillatory conditions based on Monotonicity-Preserving constraints (see Daru & Tenaud (2000, 2004)). In addition, we have the Monotonicity Preserving (MP) family of schemes developed by Suresh & Huynh (1997). In this scheme, the reconstruction step is performed by 1-calculating an interface value, and 2-imposing monotonicity and accuracy preserving constraints to limit the original value.

Finally, semi-implicit scheme may be used to discretize the multicomponent system (Mc^{GLM}). As an example, in Baboolal (2001) a Lax-Wendroff type semi-implicit scheme has been used for integrating an unmagnetized plasma inviscid multi-fluid system of equations.

6.2.2 FE methods

The finite element methods are defined through the weak formulation of the problem. Various finite element methods for discretizing linear and non-linear MHD systems can be found in the literature. In Baty (2019), a study of magnetic reconnection process and plasmoid chains formation has been performed using FE methods with adaptive mesh. In this context, the two dimensional dissipative MHD equations have been implemented. Similarly, in Strauss & Longcope (1998), a finite element discretization for two dimensional MHD has been developed, where the considered elements are triangles with piecewise linear basis functions. In Lankalapalli et al. (2007), the incompressible MHD equations are solved using a stabilitzed finite element formulation, where the mesh is adapted on a posteriori spatial error estimates of te magnetic field. In this work, the current sheets and tilt instability problem have been studied. Then, several finite element codes for the simulation of MHD instabilities on the edge of tokamak plasma have been developed such as `NIMROD` (see Sovinec et al. (2004)), `M3D-C1` (see Ferraro & Jardin (2009)), or `JOREK` (see Pamela et al. (2019)).

6.2.3 DG methods

In this configuration, a continuous high order solution inside each elements composing a cell is considered (see Raviart & Thomas (1977); Hesthaven & Warburton (2007)). The DG methods are offering a lot of advantages compared to the finite difference or finite volume approach as shown in Luo et al. (2008). Such methods can be extended to arbitrary mesh (moving meshes or AMR) and the method is compact since each cell are treated independently and the elements are communicating only through neighbor elements which have common face, independently of the considered order of accuracy. A lot of research activities have been focusing on this approach (Balsara & Käppeli (2017); F. Li & Shu (2005); Hesthaven & Warburton (2007)). Further details of the method are given by Cockburn et al. (2000). Since DG methods operate any spatial order, the numerical dissipation is controllable and can be reduced. Thus, this approach has been highly investigated for astrophysical plasmas application (Bauer & Springel (2012); Sijacki, Hernquist, Vogelsberger, Genel, et al. (2013); Zhu et al. (2013)). In addition, recent studies have shown that the DG methods may reach a high-level of accuracy, by reducing the advection errors and total time-to-solution for a given problem, as shown in Sijacki, Hernquist, Vogelsberger, Pakmor, & Mocz (2013); Bauer et al. (2015). In the chosen examples, most of these schemes are separate time-space methods. Indeed, in Sijacki, Hernquist, Vogelsberger, Pakmor, & Mocz (2013), a second-order time-stepping scheme has been used. In Bauer et al. (2015), a Runge-Kutta scheme has been used for the time integration. Finally, in Zhu et al. (2013), a third-order low storage Runge-Kutta method has been used for the time integration.

6.2.4 FV methods

Here, we solve (Mc^{GLM}) under an integrated form which leads to a property of conservation of the governing equations (see Toro (2009)). A great advantage of such approach is the possibility to generalize to multidimensional framework and complex geometry. It can be naturally implemented in an AMR cell-based framework.

In the finite volume approach, one possibility would be to follow the path of Godunov (1959, 1999), who has introduced the resolution of Riemann problems at each interfaces of cells. In this context, one can develop an exact Riemann solver for (Mc^{GLM}) as performed by Takahashi et al. (2014); Torrilhon (2003); Mignone (2007) with the MHD equations. However, an exact Riemann solver requires a high computational cost since it is generally combined with an iterative solver. Consequently, approximate Riemann solver are generally preferred to decrease the computational cost (see Toro (2009)). Therefore, we have the category of the Harten, Lax can Leer (HLL) schemes (Harten et al. (1983); Toro (2009); Davis (1988)), where intercell fluxes from approximated solutions of the Riemann problems are computed, assuming the existence of a uniform state bounded by only two velocities. In addition, we have the HLL-Contact (HLLC) schemes (Toro (2009); Toro et al. (1994)). These schemes extend the ideas of the HLL schemes, except two constant states separated by a contact discontinuity bounded by two velocities, are considered. In Amano (2015), a two-fluid ion-electron system of equations is solved with a HLL approximate Riemann solver combined with an upwind constraint transport scheme has been used. In Balsara et al. (2016), a two relativistic plasma is solved with a multidimensional Riemann solver. A Riemann solver is also used for a two-fluid plasma model in Shumlak & Loverich (2003). However, exact or approximate Riemann solvers are still computational costly and may be complex to implement in an AMR cell-based on non uniform grids.

Like the finite difference schemes introduced in the previous subsection, Monotonic Upwind-Centred Scheme for Conservation Laws (MUSCL) schemes can be used for constructing highly accurate numerical solutions for the multicomponent model (Mc^{GLM}). They have been first introduced by van Leer (1997) in a series of contributions, and by Boris & Book (1973) with the Flux-Corrected Transport (FCT). In these schemes, a high-order of accuracy is obtained by reconstructing piecewise linear function from the piecewise constant average values of each cells. Spurious oscillations are eliminated and high-order accuracy in smooth regions are performed. In this category, we have the MUSCL-Hancock scheme developed by Van Leer (1997) and the Piece-Wise Linear method developed by Colella (1985). However, although these methods are accurate in space and easy to implement, they are showing high numerical viscosity for small timesteps.

Finally, we have the semi-discrete central-upwind schemes as proposed by Kurganov & Tadmor (2000) (KT). Such scheme are showing interesting properties in terms of numerical approximation of the solution when the timesteps become small due to the Fourier condition imposed by the diffusive terms. Such scheme can be rewritten in a semi-discrete form which allows the possibility of numerically integrating the system with time integration methods such as using splitting operators techniques (see Strang (1968); Duarte et al. (2012); Descombes et al. (2014a); Duarte (2011)) or high order Runge-Kutta methods. Then, in Kurganov & Petrova (2000), new family of second-order central schemes are introduced for one-dimensional systems of conservation laws

where the construction is based on the maximal one-sided local speeds of propagation aim to simplify the implementation. In Kurganov et al. (2007), a new version of the central-upwind schemes combined to second-order limiters are applied near shock waves, and a fifth-order reconstruction is used in the rest of the domain. In order to decrease the numerical viscosity, a modification of one-dimensional semi-discrete central-upwind schemes have been developed by Kurganov & Lin (2007). Considering the simplicity and robustness of these central-upwind schemes, several studies have been performed and extended to the MHD equations for one, two and three dimensions, satisfying the divergence cleaning constraint (see Balbás & Tadmor (2006); Arminjon & Touma (2008)). Finally, in Greenshields et al. (2010), these schemes are implemented and shown to be competitive and well suited in a finite volume approach.

6.2.5 Choice of the method

In the state-of-the-art, we note that several numerical schemes are possible to discretize the multicomponent system (Mc^{GLM}) as part of our application. We aim at implementing this scheme into a massively parallel cell-based AMR code such as `CanoP` (described in Section 8.3), where essentially finite volume schemes have been developed (see Drui (2017); Essadki (2018)). Thus, by legacy of the code, a finite volume approach appears to be the most suitable path to follow.

Several choices are available for discretizing our multicomponent systems in a finite volume approach. In this thesis, we have focused on the numerical scheme developed by Kurganov & Tadmor (2000); Kurganov et al. (2007). The numerical scheme is combined to a second order Runge-Kutta method for the time integration.

The scheme is based on volumetric fluxes combined with local magnetosonic speed of propagation. The semi-discrete central scheme allows to extend to multidimensional problem with diffusive terms, and, be combined with splitting operator techniques to integrate diffusive, convective and source terms separately. In addition, we recall that this scheme is nonoscillatory, thus, is guaranteeing a good behavior of the solution near shock or discontinuities, and does not require any Riemann solver. The chosen scheme is second order of accuracy in space and time. Therefore, this numerical strategy combined with AMR allows to both reach a maximum level of robustness, stability and accuracy.

The proposed scheme can be adapted to non uniform grids (and even non conformal grids), and may be used in an AMR cell based framework such as `CanoP`.

6.3 Discretization of the multicomponent system in a monodimensional uniform grid

In this section, we focus on a 1D case, on a uniform cartesian grid. We introduce the notation used in this work, the second-order KT scheme, the discretization of the diffusive and source terms. We discretize in space and time the multicomponent system (Mc^{GLM}). A second order Runge-Kutta scheme is used for the time integration.

6.3.1 Discretization and notation

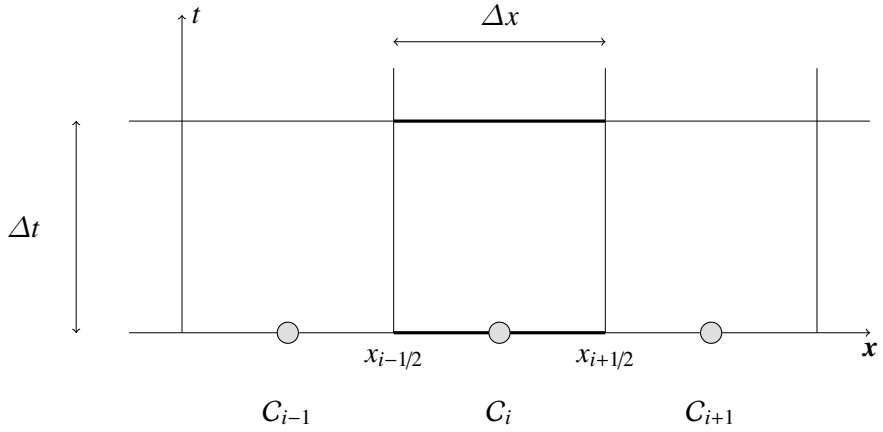

Figure 6-1: Notations for finite volume approaches.

We consider a uniform discretization $(x_i)_{i=1,\dots N_x}$ of a 1D compact domain $[x_{min}, x_{max}]$. The position of each cell C_i, is defined by

$$C_i = [x_{min} + (i-1)\Delta x,\ x_{min} + i\Delta x]\,, \quad \frac{x_{max} - x_{min}}{N_x} = \Delta x, \quad i \in [\![1, N_x]\!] \tag{6.3.1}$$

Then, the position of the center of the cell C_i is defined by x_i. In addition, we denote by $x_{i+1/2} = x_i + \Delta x/2$ (respectively $x_{i-1/2} = x_i - \Delta x/2$) the right (respectively the left) face of cell C_i. In the finite volume representations, we look for an approximation of the solution $\mathcal{U}$ at a discrete time t_n

$$\mathcal{U}_i^n \simeq \frac{1}{\Delta x}\int_{x_{i-1/2}}^{x_{i+1/2}} \mathcal{U}(t_n, x)\, dx, \quad i \in [\![1, N_x]\!], \quad n \in [\![1, n_f]\!]. \tag{6.3.2}$$

where $t_n = \sum_{j=1}^{n} \Delta t_j$ (with $t_0 = 0$) and $\Delta t_j = t_j - t_{j-1}$ is the timestep. We define t_{n_f} as the final time.

By integrating the system over time $[t_n, t_{n+1}]$ and space $[x_{i-1/2}, x_{i+1/2}]$, and, if the Euler method is used to approximate all time integrals, the finite volume numerical scheme reads

$$\mathcal{U}_i^{n+1} = \mathcal{U}_i^n - \frac{\Delta t_n}{\Delta x}\left(\mathcal{F}_{i+1/2}^n - \mathcal{F}_{i-1/2}^n\right) - \frac{\Delta t_n}{\Delta x}\left(\mathcal{G}_{i+1/2}^n - \mathcal{G}_{i-1/2}^n\right) + \Delta t_n \mathcal{S}_i^n, \quad i \in [\![1, N_x]\!], \quad n \in [\![1, n_f]\!]. \tag{6.3.3}$$

where $\mathcal{F}_{i\pm1/2}^n$ are the convective fluxes, $\mathcal{G}_{i\pm1/2}^n$ are the diffusive fluxes and $\mathcal{S}_i^n$ the source term, at time t_n. The convective and diffusive fluxes $\mathcal{F}_{i\pm1/2}^n$ and $\mathcal{G}_{i\pm1/2}^n$ evaluated at the faces are approximations of the exact mean-time fluxes:

$$\mathcal{F}_{i\pm1/2}^n \simeq \frac{1}{\Delta t_n}\int_{t_n}^{t_{n+1}} \mathcal{F}(t, x_{i\pm1/2})\, dt, \quad \mathcal{G}_{i\pm1/2}^n \simeq \frac{1}{\Delta t_n}\int_{t_n}^{t_{n+1}} \mathcal{G}(t, x_{i\pm1/2})\, dt, \quad i \in [\![1, N_x]\!], \quad n \in [\![1, n_f]\!]. \tag{6.3.4}$$

As written here, no choice has been made on the definition of the convective and diffusive fluxes.

Additionally, no discretization has been defined for the source term of (6.3.3). However, note that the source term can be decomposed into nonconservative terms and relaxation terms, which do not require the same numerical integration. Thus, we rewrite the source term as

$$\mathcal{S}_i^n = N_i^n + \mathcal{S}_i^{\text{relax},n}, \quad i \in [\![1, N_x]\!], \quad n \in [\![1, n_f]\!]. \tag{6.3.5}$$

where N_i^n and $\mathcal{S}_i^{\text{relax},n}$ are the nonconservative and relaxation source terms integrated over time $[t_n, t_{n+1}]$ and space $[x_{i-1/2}, x_{i+1/2}]$, defined by

$$N_i^n \simeq \frac{1}{\Delta t_n} \int_{t_n}^{t_{n+1}} \int_{x_{i-1/2}}^{x_{i+1/2}} \left(0,\, 0,\, 0,\, 0,\, -p_{\mathfrak{e}} \boldsymbol{\partial_x} \cdot \boldsymbol{v}_{\mathfrak{h}} + \boldsymbol{J}_{\mathfrak{e}} \cdot \boldsymbol{E}',\, 0,\, 0\right)^T dt dx, \tag{6.3.6}$$

$$\mathcal{S}_i^{\text{relax},n} \simeq \frac{1}{\Delta t_n} \int_{t_n}^{t_{n+1}} \int_{x_{i-1/2}}^{x_{i+1/2}} \left(0,\, 0,\, 0,\, 0,\, \Delta E_{\mathfrak{e}}^{(0)} + \Delta E_{\mathfrak{e}}^{(1)},\, 0,\, -\frac{c_h^2}{c_p^2}\psi\right)^T dt dx, \quad i \in [\![1, N_x]\!], \quad n \in [\![1, n_f]\!]. \tag{6.3.7}$$

6.3.2 Convective and diffusive fluxes

In this section, we focus on the definition of the convective and diffusive fluxes $\mathcal{F}_{i\pm1/2}^n$ and $\mathcal{G}_{i\pm1/2}^n$ using a KT approach. This second-order scheme is based on reconstructed values at interfaces. In this work, the convective flux at interface $x_{i+1/2}$ are defined as

$$\mathcal{F}_{i+1/2}^n = \frac{1}{2}\left[\mathcal{F}(\mathcal{U}_i^{L,n}) + \mathcal{F}(\mathcal{U}_{i+1}^{R,n}) - a_{i,i+1}\left(\mathcal{U}_i^{L,n} - \mathcal{U}_{i+1}^{R,n}\right)\right], \quad i \in [\![1, N_x]\!], \quad n \in [\![1, n_f]\!]. \tag{6.3.8}$$

where $\mathcal{U}_i^{L,n}$ and $\mathcal{U}_{i+1}^{R,n}$ denote for the reconstructed values of $\mathcal{U}_i$ and $\mathcal{U}_{i+1}$, at the left and right of the interface $i + 1/2$, respectively, $a_{i,i+1}^n$ is defined as the local maximum speed based on the spectral radius r of the Jacobian of $\mathcal{F}$

$$a_{i,i+1}^n = \max_{\mathcal{U} \in \{\mathcal{U}_i^{L,n}, \mathcal{U}_{i+1}^{R,n}\}} \left(\frac{\partial \mathcal{F}}{\partial \mathcal{U}}(\mathcal{U})\right). \tag{6.3.9}$$

As seen in Section 3.4, the spectral radius of $a_{i,i+1}^n$ is equal to the maximum speed of the fast magnetosonic wave from the reconstructed values $\mathcal{U}_i^{L,n}$ and $\mathcal{U}_{i+1}^{R,n}$. The flux $\mathcal{F}_{i-/2}^n$ is similar to (6.3.8) except that the reconstructed values are computed according to the interface $i - 1/2$.

The computation of the reconstructed values is based on the use of limiters. For example, the linear reconstruction of $\mathcal{U}_i^{L,n}$ is defined as

$$\mathcal{U}_i^{L,n} = \mathcal{U}_i^n + \frac{\mathcal{U}_{i+1}^n - \mathcal{U}_i^n}{2} h(\boldsymbol{r_i^n}), \tag{6.3.10}$$

where h is a limiter involving cells C_{i-1}, C_i and C_{i+1}, and r_i^n is a ratio of successive gradient defined as

$$\boldsymbol{r_i^n} = \frac{\mathcal{U}_i^n - \mathcal{U}_{i-1}^n}{|x_i - x_{i-1}|} \frac{|x_i - x_{i+1}|}{\mathcal{U}_{i+1}^n - \mathcal{U}_i^n}, \tag{6.3.11}$$

where $|x_i - x_{i-1}| = \Delta x$ is the distance between the middle of the cell C_i and C_{i-1}, and $|x_i - x_{i+1}| = \Delta x$ is the distance between the middle of the cell C_i and C_{i+1}. The limiter function h is constrained to be greater than or equal to zero. Therefore, if the limiter is equal to zero (sharp gradient, opposite slopes or zero gradient), the flux is represented by a low resolution scheme. If the limiter is equal to 1 (smooth solution), it is represented by a high resolution scheme. The various limiters have differing switching characteristics and are selected according to the particular problem and solution scheme. No particular limiter has been found to work well for all problems, and a particular choice is usually made on a trial and error basis. In this thesis, several limiters have been implemented:

- The MINMOD limiter (Roe (2003))

$$h_{MM}(r) = \max\left[0, \min(1, r)\right] \tag{6.3.12}$$

- The OSPRE limiter (Waterson & Deconinck (2007))

$$h_{OP}(r) = \frac{1.5(r^2 + r)}{r^2 + r + 1} \tag{6.3.13}$$

- The van Albada 2 limiter, which is not second order TVD but is mainly used on high spatial order schemes (Hassanzadeh et al. (2009))

$$h_{va2}(r) = \frac{2r}{r^2 + 1}. \tag{6.3.14}$$

In addition, we can also list the monotonized central (van Leer (1997)), the Osher (Chakravarthy & Osher (1983)), the CHARM limiter (Zhou (1885)), the superbee (Roe (2003)), the van Albada 1 (van Albada et al. (1997)), and van Leer limiter (van Leer (1997)).

In the implemented limiter, the OSPRE and MINMOD limiter are shown to be symmetric, which guarantees that the backward and forward gradients are operating in the same way. In addition, they are shown to be second order TVD. Thus, they pass through a TVD region which guarantee the stability of the scheme. This region is shown in the Sweby Diagram opposite (see Sweby (1984)) where plots are showing the admissible limiter region for second-order TVD scheme.

Thus, the integration of the convective scheme can be summarized as follows

1. we reconstruct the data at cells interface from left and right data $\mathcal{U}_i^{L,n}$, $\mathcal{U}_{i+1}^{R,n}$, $\mathcal{U}_i^{R,n}$ and $\mathcal{U}_{i-1}^{L,n}$,
2. the physical fluxes of the reconstructed values $\mathcal{F}(\mathcal{U}_i^{L,n})$ and $\mathcal{F}(\mathcal{U}_{i+1}^{R,n})$ are computed,
3. the maximum wave speed $a_{i,i+1}^n$ from (6.3.9) is computed,
4. the mix convective flux $\mathcal{F}_{i+1/2}^n$ is computed according to (6.3.8),
5. we sum over each convective flux $\mathcal{F}_{i+1/2}^n - \mathcal{F}_{i-1/2}^n$.

Then, the diffusive fluxes $\mathcal{G}$ are discretized as a simple central difference approximation, as prescribed by Kurganov & Tadmor (2000) (Section 4.2). The fluxes are written as

$$\mathcal{G}^n_{i+1/2} = \frac{1}{2}\left[\mathcal{G}\left(\mathcal{U}^n_i, \frac{\mathcal{U}^n_{i+1} - \mathcal{U}^n_i}{x_{i+1} - x_i}\right) + \mathcal{G}\left(\mathcal{U}^n_{i+1}, \frac{\mathcal{U}^n_{i+1} - \mathcal{U}^n_i}{x_{i+1} - x_i}\right)\right], \quad i \in [\![1, N_x]\!], \quad n \in [\![1, n_f]\!], \tag{6.3.15a}$$

$$\mathcal{G}^n_{i-1/2} = \frac{1}{2}\left[\mathcal{G}\left(\mathcal{U}^n_i, \frac{\mathcal{U}^n_i - \mathcal{U}^n_{i-1}}{x_i - x_{i-1}}\right) + \mathcal{G}\left(\mathcal{U}^n_{i-1}, \frac{\mathcal{U}^n_i - \mathcal{U}^n_{i-1}}{x_i - x_{i-1}}\right)\right], \quad i \in [\![1, N_x]\!], \quad n \in [\![1, n_f]\!]. \tag{6.3.15b}$$

6.3.3 Source terms

Two type of source terms have to be discretized: the nonconservative and the relaxation terms.

Nonconservative terms

Solving nonconservative systems is a major problem from the numerical point of view. As described in the introduction of this Chapter, when sharp gradients, discontinuities or shock waves are involved, nonphysical shocks may appear. To tackle this issue, there are two possibilities of discretization

1. a specific numerical discretization of the nonconservative terms can be developed to properly capture shock waves and discontinuities, for any discretization. As performed in Chapter 7, with a simplified system where no electromagnetic fields are considered, this treatment requires a study of travelling wave solutions of the multicomponent system. This study allows to identify the scales to be numerically resolved and derive compatibility equations at discontinuities, and, thus, define the nonconservative terms when discontinuities are involved. Further details are given in Chapter 7. This study should be extended to the magnetized case before reaching the general framework of the present strategy.

2. a standard discretization of the nonconservative terms may be considered. In this case, we guarantee that a sufficient number of cells or nodes is considered in the discretization, to numerically resolve the characteristic scales and avoid the propagation of artificial or numerical shocks. We guarantee that the physical diffusion dominates the numerical diffusion.

In this thesis, the nonconservative terms are given by (6.3.6). These terms are standardly discretized according to the value of the current cell $\mathcal{U}^n_i$ and a second order centered discretization of the gradients, as follows,

$$N^n_i = N\left(\mathcal{U}^n_i, \frac{\mathcal{U}^n_{i+1} - \mathcal{U}^n_{i-1}}{x_{i+1} - x_{i-1}}\right), \quad i \in [\![1, N_x]\!], \quad n \in [\![1, n_f]\!]. \tag{6.3.16}$$

Relaxation terms

We focus on the integration of the relaxation terms defined in (6.3.7). In many applications, it is convenient to apply a time-operator splitting approach to numerically decouple the relaxation source terms $\mathcal{S}_i^{\text{relax},n}$ from the convective-diffusive system. This decoupling is based on a Strang splitting operator technique (see Strang (1968); Duarte et al. (2012); Descombes et al. (2014a)). The operators are splitted: one operator $\mathcal{H}$ corresponds to convective, diffusive and nonconservative terms defined in (6.3.8), (6.3.15a) and (6.3.16) respectively, where the timestep $\Delta t_{n,s}$ is computed from Fourier conditions; an other operator $\mathcal{S}^{\text{relax}}$ corresponds to relaxation terms defined in (6.3.7), where they are integrated based on a classical second order implicit scheme. Therefore, the convective, diffusive and nonconservative terms combined to relaxation terms are integrated on a Strang splitting operator technique, as follows

$$\mathcal{U}^{n+1} = \mathcal{H}^{\Delta t_{n,s}/2}\mathcal{S}^{\text{relax},\Delta t_{n,s}}\mathcal{H}^{\Delta t_{n,s}/2}(\mathcal{U}^n), \quad n \in [\![1, n_f]\!]. \tag{6.3.17}$$

where $\mathcal{U}^n = (\mathcal{U}_i^n)_{i\in[1,\dots,N_x]}$.

In summary, the scheme is constructed as follows: 1-the convective, diffusive and nonconservative terms are integrated over a half timestep $\Delta t_{n,s}/2$, then, 2- the relaxation terms are integrated over $\Delta t_{n,s}$, finally, 3- the convective, diffusive and relaxation terms are integrated again over a half timestep $\Delta t_{n,s}/2$.

6.4 Time integration and global scheme in a monodimensional uniform grid

The KT scheme, may be rewritten in a semi-discrete form allowing us to use a high order scheme for the time integration. In this thesis, we have focused on a second order Runge-Kutta scheme for the time integration of the convective-diffusive system. In this case, the timestep is limited by a classical Fourier condition which consider the maximum value of all the transport coefficients of the multicomponent system (Mc^{GLM}). If no diffusive terms are considered, a classical CFL condition is used for computing the convective time step.

The global scheme used for the multicomponent system (Mc^{GLM}) may be summarized as follows

1. **The convective flux** $\mathcal{F}_{i+1/2}^n$, $i \in [\![1, N_x]\!]$, $n \in [\![1, n_f]\!]$ is discretized using a KT scheme based on (6.3.8). It is a second-order discretization based on a reconstructed values at interfaces.

2. **The diffusive flux** $\mathcal{G}_{i+1/2}^n$, $i \in [\![1, N_x]\!]$, $n \in [\![1, n_f]\!]$ is discretized to be compatible with the KT scheme, based on (6.3.15a) and (6.3.15b). The scheme is based on a classical second-order centered discretization.

3. **The nonconservative terms** N_i^n, $i \in [\![1, N_x]\!]$, $n \in [\![1, n_f]\!]$ are computed based on standard discretization defined in (6.3.16). These terms are computed as products of 1-the value $\mathcal{U}_i^n$

of the current cell C_i by 2- a second-order centered gradient $(\mathcal{U}_{i+1}^n - \mathcal{U}_{i-1}^n)/(x_{i+1} - x_{i-1})$ between the cell C_{i-1} and C_{i+1}. Thus, we have a standard second-order discretization of the nonconservative terms.

4. **The relaxation terms** $\mathcal{S}_i^{\text{relax},n},\ i \in [\![1, N_x]\!],\ n \in [\![1, n_f]\!]$ are computed in a time-operator splitting framework, to be numerically decoupled from the convective-diffusive-nonconservative system (6.3.17). The relavation terms are integrated with a second-order implicit scheme combined to a Strang operator splitting technique.

The proposed scheme is second order of accuracy in space and time. For further details, a verification of the order of the scheme is provided in Section 9.1.1. In Chapter 9, the proposed numerical scheme is shown to be stable and robust. The numerical strategy is able to tackle classical MHD problems involving shock waves and shock-shock interactions such as the Orszag-Tang test case or Kelvin-Helmoltz instabilities.

The global scheme has been identified. The next step is to extend this scheme to a multidimensional AMR approach.

6.5 Generalization to a multidimensional AMR framework

In order to capture the large spectrum of scales associated with the multicomponent models for the purpose of representing the multiscale process of magnetic reconnection, we extend the numerical strategy to a multidimensional AMR cell-based framework. The main goal is to implement the system into a massively parallel AMR code, such as `CanoP`. It is built at the top of the `p4est` library which constructs AMR cell-based methods in a 2:1 balance context, *i.e.*, the size ratio between two neighboring cells does not exceed two. Further details on `CanoP` are given in Chapter 8. We focus on cartesian grids.

In Section 6.5.1, some notations for describing AMR cartesian non uniform grids in 2D/3D are provided. Then, in Section 6.5.2, we describe the computation of the fluxes. In Section 6.5.3, we discretize the convective and diffusive fluxes. In Section 6.5.4, a discretization of the source terms is provided. Finally in Section 6.6, the global scheme is described.

6.5.1 Discretization

We adopt the following notations for describing AMR non uniform cartesian grids in 2D/3D: the cell i is noted C_i and its interface is Γ_{ij}, whose volume (area in 2D) is $|C_i|$, while $|\Gamma_{ij}|$ and $\boldsymbol{n}_{ij}$ are respectively the surface and the unit normal of the interface between two neighboring cells i and j. In addition, ∂C_i denotes for the border of the cell i. The vector $\boldsymbol{n}_{ij}$ is oriented from cell i to cell j. We have

$$|C_i| = \Delta x_i \Delta y_i \Delta z_i = \Delta x_i^3, \quad \Delta x_i \in [\Delta x_{\min}, \Delta x_{\max}] \tag{6.5.1}$$

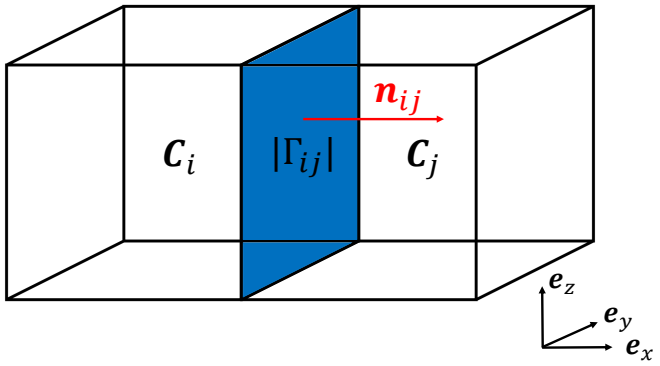

Figure 6-2: Notations for finite volume schemes in multidimensional framework

where Δx_i corresponds to the size of the cell C_i, $\Delta x_{\min}$ and $\Delta x_{\max}$ are the size of cells at the minimum and maximum level of refinement, respectively. Since a 2:1 balance has been considered in this work, the size of cells at the minimum and maximum level of refinement are defined by the following relation

$$\Delta x_{\max} = 2^d \Delta x_{\min}, \quad \text{for a given } d \in \mathbb{N}. \tag{6.5.2}$$

In addition, we note by $\mathcal{N}_q(i)$ and $\boldsymbol{e}_q$, the set of neighboring cells of the current cell i and the component of the canonical base of $\mathbb{R}^3$, in the direction $q = x, y, z$, respectively. Figure 6-2 represents the notations used.

As shown in Section 6.3.1, we consider a discretization $(\boldsymbol{x}_i)_{i=1,\dots N} = \left(x_j, y_k, z_l\right)$ (respectively $\left(x_j, y_k\right)$ in 2D) where $j \in [\![1, \dots, N_x]\!]$, $k \in [\![1, \dots, N_y]\!]$ and $l \in [\![1, \dots, N_z]\!]$ of a 3D compact domain $[x_1, x_{N_x}] \times [y_1, y_{N_y}] \times [z_1, z_{N_z}]$ (respectively $[x_1, x_{N_x}] \times [y_1, y_{N_y}]$ in 2D), where $N = N_x * N_y * N_z$ (respectively $N = N_x * N_y$ in 2D). The position of each cell C_i, $1 \leq i \leq N$ is defined by its center $(\boldsymbol{x}_i)_{i=1,\dots N}$. In addition, the position of the vertices of the cell i is defined by $(x_{i\pm1/2}, y_{i\pm1/2}, z_{i\pm1/2})$ (respectively $(x_{i\pm1/2}, y_{i\pm1/2})$ in 2D) where

$$\nu_{i+\pm1/2} = \nu_i \pm \Delta x_i/2, \quad \nu \in [x, y, z] \tag{6.5.3}$$

In the finite volume representations, we look for an approximation of the solution $\mathcal{U}$, at a discrete time t_n, with position $\boldsymbol{x}_i$, *i.e.*,

$$\mathcal{U}_i^n \simeq \frac{1}{\Delta x_i^3} \int_{x_{i-1/2}}^{x_{i+1/2}} \int_{y_{i-1/2}}^{y_{i+1/2}} \int_{z_{i-1/2}}^{z_{i+1/2}} \mathcal{U}(t_n, x, y, z)\, dxdydz = \frac{1}{\Delta x_i^3} \int_{C_i} \mathcal{U}(t_n, x, y, z)\, dV,$$
$$i \in [\![1, N]\!], \quad n \in [\![1, n_f]\!], \tag{6.5.4}$$

where $t_n = \sum_{j=1}^{n} \Delta t_j$ (with $t_0 = 0$) , $\Delta t_j = t_j - t_{j-1}$ is the timestep and $t = t_{n_f}$ is the final time. We integrate the multicomponent system over time $[t_n, t_{n+1}]$ and space $[x_{i-1/2}, x_{i+1/2}] \times [y_{i-1/2}, y_{i+1/2}] \times [z_{i-1/2}, z_{i+1/2}]$. If the Euler method is used to approximate all time integrals, the finite volume

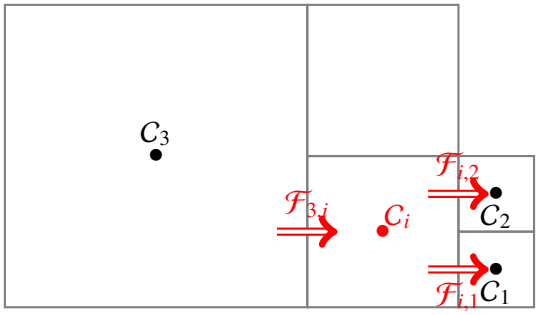

Figure 6-3: Representation of an AMR cartesian non uniform grid for a cell C_i with three neighbors $C_j,\ j \in [1,3]$ from two levels of refinement.

numerical scheme reads

$$\mathcal{U}_i^{n+1} = \mathcal{U}_i^n - \frac{\Delta t_n}{|C_i|} \sum_{q\in\{x,y,z\}, j\in\mathcal{N}_q(i)} |\Gamma_{ij}| \left(\boldsymbol{e}_q^T \boldsymbol{n}_{ij}\right) \left[\mathcal{F}_{i,j}^n + \mathcal{G}_{i,j}^n\right] + \Delta t_n \mathcal{S}_i^n, \quad i \in [\![1, N]\!], \quad n \in [\![1, n_f]\!], \tag{6.5.5}$$

where $\mathcal{F}_{i,j}^n$ and $\mathcal{G}_{i,j}^n$ denote for the convective and diffusive flux, at time t_n, from the current cell to the neighboring cell $C_i,\ i \in \mathcal{N}_q(i)$, and $\mathcal{S}_i^n$ are the source terms. The convective and diffusive fluxes are defined by

$$\sum_{j\in\mathcal{N}_q(i)} |\Gamma_{ij}| \left[\mathcal{F}_{i,j} + \mathcal{G}_{i,j}\right] \simeq \int_{\partial C_i} \left[\mathcal{F}(\mathcal{U}) + \mathcal{G}(\mathcal{U})\right] \cdot \boldsymbol{n}_i \, d\Sigma, \tag{6.5.6}$$

where $\boldsymbol{n}_i$ is a unit vector perpendicular to the surface ∂C_i. The source term is defined as

$$\mathcal{S}_i^n = \int_{C_i} \mathcal{S}(\mathcal{U}, \partial_x \mathcal{U}) \, dV. \tag{6.5.7}$$

As shown in the previous section, the source term (6.5.7) is divided into two terms: nonconservative (6.3.6) and relaxation terms (6.3.7). These terms are integrated over the volume of the current cell C_i.

6.5.2 Fluxes in the case of AMR cartesian grids in a 2:1 balance framework

If AMR cartesian grids in a 2:1 balance framework are considered, the interface $|\Gamma_{ij}|$ between the current cell C_i and its neighbors $C_j,\ j \in \mathcal{N}_q(i)$ can be simply computed:

- If the direct neighboring $C_j,\ j \in \mathcal{N}_q(i)$ is smaller than the current cell C_i, we have $|\Gamma_{ij}| = (\Delta x_i/2)^2$,
- If the direct neighboring $C_j,\ j \in \mathcal{N}_q(i)$ is larger than (or has the same size) the current cell

C_i, we have $|\Gamma_{ij}| = (\Delta x_i)^2$,

The interfaces between cells being defined, it is necessary to compute the fluxes at all interfaces to update the current cell. For the purpose of assisting the reader, Figure 6-3 represents the current cell C_i with three neighbors: C_3 on the left, and, C_1 and C_2 on the right, with two levels of refinement respectively. To update the cell C_i, it is necessary to compute three fluxes: an inflow flux $\mathcal{F}_{3,i}$ from C_3 to C_i, and, two outflow fluxes $\mathcal{F}_{i,2}$ and $\mathcal{F}_{i,1}$ from cell C_i to C_2 and C_1, respectively.

In order to compute these fluxes, three situations may happen, depending on the size of the neighboring cells:

1. **If the neighboring cell is smaller than the current cell** (such as $\mathcal{F}_{i,2}$ and $\mathcal{F}_{i,1}$ in Figure 6-3), a uniform value in the whole current cell is assumed, and, a uniform flux at the corresponding interface with the neighboring cell is computed,

2. **If the neighboring cell is larger than the current cell** (such as $\mathcal{F}_{3,i}$ in Figure 6-3), a uniform value in the whole neighboring cell is assumed, and, a uniform flux at the interface with the current cell is computed,

3. **If the neighboring cell has the same size** as the current cell, it is identical to uniform grids cases.

Note that, in the case where the neighboring cell is larger than the current cell (or in the case where the current cell is larger than the neighboring cell), we assume a uniform value in the cell to compute the flux at interfaces. This approach is cheaper in terms of computational cost, because it does not require any additional degrees of freedom in the larger cell. However, this assumption can introduce numerical dissipation. Therefore, one possibility would be to add degrees of freedom and re-compute a value at the corresponding interface by considering additional neighboring cells. This would reduce the numerical diffusion and increase the level of accuracy of the computation of the fluxes.

The global scheme has been defined in (6.5.5) for a multidimensional AMR cartesian grids in a 2:1 balance framework. In the next subsection, we focus on the computation of the convective and diffusive fluxes $\mathcal{F}^n_{i,j} + \mathcal{G}^n_{i,j}$, and source terms $\mathcal{S}^n_i$.

6.5.3 Convective and diffusive fluxes

As presented in Section 6.3.2, the convective flux defined between the current cell C_i and the neighboring cell C_j reads

$$\mathcal{F}^n_{i,j} = \frac{1}{2}\left[\mathcal{F}(\mathcal{U}^{*,n}_i) + \mathcal{F}(\mathcal{U}^{*,n}_j) - a^{*,n}_{i,j}(\mathcal{U}^{*,n}_i - \mathcal{U}^{*,n}_j)\right], \quad i \in [\![1, N]\!], \quad j \in \mathcal{N}_q(i), \quad q \in (x, y, z), \quad n \in [\![1, n_f]\!]. \tag{6.5.8}$$

where $\mathcal{U}^{*,n}_i$ and $\mathcal{U}^{*,n}_j$ are the reconstructed values on each side of the corresponding interface Γ_{ij} respectively, and $a^{*,n}_{i,j}$ is defined as the local maximum speed based on the spectral radius r of the

Jacobian of $\mathcal{F}$

$$a_{i,j}^{*,n} = \max_{\mathcal{U}\in\{\mathcal{U}_i^{*,n},\mathcal{U}_j^{*,n}\}} \left(\frac{\partial \mathcal{F}}{\partial \mathcal{U}}(\mathcal{U}) \right). \tag{6.5.9}$$

Here, the local maximum speed is defined as the fastest magnetosonic wave.

The linear reconstruction of $\mathcal{U}_i^{*,n}$ at the interface Γ_{ij} with neighboring cell C_j is based on the use of limiters. As described by P. T. Groth & Northrup (2005); Deiterding, Ralf (2011), the reconstructed values are determined via a classical piece-wise limited linear reconstruction procedure using limiter functions, developed in the AMR framework. The reconstructed value $\mathcal{U}_i^{*,n}$, is defined as

$$\mathcal{U}_i^{*,n} = \mathcal{U}_i^n + \frac{\mathcal{U}_j^n - \mathcal{U}_i^n}{2} h(r_i^n), \quad i \in [\![1, N]\!], \quad j \in \mathcal{N}_q(i), \quad q \in (x, y, z), \quad n \in [\![1, n_f]\!]. \tag{6.5.10}$$

where h is a limiter function, which has been defined in Section 6.3.2.

As presented in the previous section, the computation of the reconstructed values involve three cells in addition to the cell i and neighboring cell $j \in \mathcal{N}_q(i)$, involving the interface Γ_{ij}. Considering a cell i with a neighboring cell $j \in \mathcal{N}_q(i)$, we define cells $C_{k,j}$ such as

$$(k, j) \in \mathcal{N}_q^2(i) \quad \text{such as} \quad \boldsymbol{e}_q \cdot \boldsymbol{n}_{ik} \neq \boldsymbol{e}_q \cdot \boldsymbol{n}_{ij}. \tag{6.5.11}$$

Therefore, cells $C_{k,j}$ are the opposite neighboring cells of C_j with respect to cell C_i in the direction q. The ratio of successive gradients is defined as

$$r_i^n = \frac{\mathcal{U}_i^n - \sum_{k=1,\dots,\mathcal{N}_k} \left(\mathcal{U}_{k,j}^n / \mathcal{N}_k \right)}{(\Delta x_{k,j} + \Delta x_i)/2} \frac{(\Delta x_j + \Delta x_i)/2}{\mathcal{U}_j^n - \mathcal{U}_i^n}, \quad i \in [\![1, N]\!], \quad j \in \mathcal{N}_q(i),$$
$$q \in (x, y, z), \quad n \in [\![1, n_f]\!]. \tag{6.5.12}$$

where $\Delta x_{k,j}$ is the size of the cells $C_{k,j}$ and $\mathcal{N}_k$ is the number of neighboring cells $C_{k,j}$.

Then, as presented in the previous section, the diffusive fluxes $\mathcal{G}$ are discretized as a simple central difference approximation, as follows

$$\mathcal{G}_{i,j}^n = \frac{1}{2} \left[\mathcal{G}\left(\mathcal{U}_i^n, \frac{\mathcal{U}_j^n - \mathcal{U}_i^n}{(\Delta x_j + \Delta x_i)/2} \right) + \mathcal{G}\left(\mathcal{U}_j^n, \frac{\mathcal{U}_j^n - \mathcal{U}_i^n}{(\Delta x_j + \Delta x_i)/2} \right) \right], \quad i \in [\![1, N]\!], \quad j \in \mathcal{N}_q(i),$$
$$q \in (x, y, z), \quad n \in [\![1, n_f]\!]. \tag{6.5.13}$$

6.5.4 Source terms

The computation of the source terms is inspired from Section 6.3.3. Here, we integrate the source terms over the volume C_i.

The discretization of the nonconservative terms, introduced in the previous section, is extended to the AMR case. We have chosen to simply discretize the nonconservative terms with the value

of the current cell $\mathcal{U}_i^n$ and a second order centered discretization of the gradients, as follows

$$N_i^n = N\left(\mathcal{U}_i^n, \frac{\sum_{j=1,\dots,\mathcal{N}_j}\left(\mathcal{U}_j^n/\mathcal{N}_j\right) - \sum_{k=1,\dots,\mathcal{N}_k}\left(\mathcal{U}_{k,j}^n/\mathcal{N}_k\right)}{(\Delta x_j + \Delta x_{k,j})/2}\right), \quad i \in [\![1, N]\!], \quad (k, j) \in \mathcal{N}_q^2(i),$$
$$q \in (x, y, z), \quad \boldsymbol{e}_q \cdot \boldsymbol{n}_{ik} \neq \boldsymbol{e}_q \cdot \boldsymbol{n}_{ij}, \quad n \in [\![1, n_f]\!], \quad (6.5.14)$$

where $\mathcal{N}_j$ is the number of neighboring cell C_j.

Then, the relaxation terms are computed with a second-order implicit scheme combined with a Strang splitting approximation as presented in the monodimensional case (Strang (1968); Duarte et al. (2012); Descombes et al. (2014b)).

6.6 Time integration and global scheme in the multidimensional nonuniform AMR cartesian grid case

As presented in (6.5.5), a classical Euler method has been used for the time integration. However, the KT scheme may be written in a semi-discrete form. Therefore, a second order Runge-Kutta scheme has been used for the time integration of the convective-diffusive system. The timestep is limited by Fourier conditions, as described in the monodimensional case.

The proposed scheme used for discretizing the multicomponent model (Mc^{GLM}) in a multidimensional AMR framework can be summarized as follow

1. **The convective flux** $\mathcal{F}_{i,j}^n$, $i \in [\![1, N]\!]$, $j \in \mathcal{N}_q(i)$, $q \in (x, y, z)$, $n \in [\![1, n_f]\!]$ is discretized using a KT scheme adapted for AMR nonuniform grids based on (6.5.8),

2. **The diffusive flux** $\mathcal{G}_{i,j}^n$, $i \in [\![1, N]\!]$, $j \in \mathcal{N}_q(i)$, $q \in (x, y, z)$, $n \in [\![1, n_f]\!]$ is computed with a second order centered scheme, as shown in (6.5.13),

3. **The nonconservative terms** $\mathcal{N}_i^n$, $i \in [\![1, N_x]\!]$, $n \in [\![1, n_f]\!]$, are computed with a second order centered discretization of the gradients, as presented in (6.5.14),

4. **The relaxation terms** $\mathcal{S}_i^{\mathrm{relax},n}$, $i \in [\![1, N_x]\!]$, $n \in [\![1, n_f]\!]$, are integrated with a second order implicit scheme combined with a Strang splitting operator techniques, to be numerically decoupled the convective-diffusive-nonconservative systems, as presented in the monodimensional case.

The numerical scheme presented in the monodimensional case has been extended to the multidimensional AMR framework for nonuniform cartesian grids. The proposed numerical scheme, is second order in space and time. The accuracy, stability and robustness of the scheme have been studied and verified in Chapter 9.

Conclusion

A numerical strategy has been defined for the multicomponent models. In order to guarantee that all the scales of the multicomponent systems are captured, the numerical strategy is combined with a cell-based AMR approach for nonuniform cartesian grids. This strategy has been implemented into the massively parallel code `CanoP` (described in Section 8.3). In this code, essentially finite volume schemes have been developed for several applications (Drui, Fikl, et al. (2016); Essadki (2018); Drui (2017)). In this chapter, we focus on the development of a numerical scheme with second order of accuracy, to ensure a high level of robustness and stability. This approach combined with an AMR strategy allows to reach a sufficient level of accuracy required for our application.

From the numerical point of view, one of the main difficulties encountered with the multicomponent systems are the presence of diffusive and source terms. Indeed, in the context of our application, the timesteps are limited by Fourier conditions type, which are much smaller than the convective timesteps limited by a classical CFL condition. Therefore, the proposed numerical strategy has to guarantee that a good approximation of the numerical solution is provided, even though small timesteps constrained by Fourier conditions are involved.

After investigating a large state-of-the-art of all the possible numerical methods, the Riemann-solver free of Kurganov & Tadmor (2000) (KT) scheme appears to be the most appropriate choice. This approach allows to be extended to multidimensional problem and be combined with splitting operator techniques to integrate diffusive, convective and source terms separately, or high order scheme such as Runge-Kutta. Therefore, by using these techniques, the problems encountered with small timesteps is tackled. In addition, the numerical scheme is guaranteeing a good behavior of the numerical solution near shocks or discontinuities. This approach is second order of accuracy in space and time, as shown in Chapter 9.

Starting from a monodimensional case on uniform grids, we have extended the KT numerical scheme to AMR nonuniform cartesian grids in a 2:1 balance framework, in multidimensional cases. We have presented the discretization of the convective and diffusive fluxes, and integrated the source terms over the volume of each cells. The nonconservative terms have been standardly discretized by taking the value of the current cell and a second order centered gradient. The relaxation terms have been 1- decoupled from the convective-diffusive system using a Strang operator splitting approach, and 2- integrated in time with a second order implicit scheme. Further details on the verification of the implementation have been performed in Chapter 9. Concerning the incompressibility constraint of the magnetic field, a GLM mixed parabolic-hyperbolic correction method from Dedner et al. (2002) has been used. This method appears to be both 1- performant for reducing the divergence errors and 2- adapted to the proposed numerical scheme.

However, in the chosen approach, some weaknesses have been identified and require some improvements:

- In this approach, the numerical scheme is "only" second order in space and time. As a good perspective, a discontinuous Galerkin method may be used to increase the level of accuracy of the proposed strategy. This requires an extension of the work performed by Essadki (2018) and an implementation into the `CanoP` code.

- In this study, the nonconservative terms have been standardly discretized. However, when sharp gradients, discontinuities or shock waves are involved, nonphysical shocks may appear if the numerical diffusion, induced by the discretization of the nonconservative terms, is relevant. A better way to discretize these terms would be to extend the work performed in the next Chapter, where a specific numerical discretization of the nonconservative terms is provided. In this framework, shock waves and discontinuities are correctly captured, even in weakly discretized cases. The scales of the multicomponent systems, which have to be numerically resolved, have been identified. The specific treatment of the nonconservative terms allows to capture the discontinuities and avoid artificial or numerical shocks for any discretization. However, this study has been performed on a simplified case where no electromagnetic fields are considered. The general approach is currently under study.

CHAPTER 7

STUDY OF NONCONSERVATIVE PRODUCT FOR PLASMAS IN THERMAL NONEQUILIBRIUM: APPLICATION IN SOLAR PHYSICS

Introduction

As seen in the Chapter 2, at the zeroth order of the expansion, the development yields a hyperbolic system of equations with a parabolic regularization of the electron variables due to dissipative terms such as the electron diffusion velocity and heat flux. When weak solutions (shocks) are considered, the total energy equation is used regarding its conservative form suitable for the development of a numerical scheme. Both the electron and heavy-particle energy equations exhibit non conservative terms leading to some numerical difficulties that will be reviewed in the next paragraph. In this work, the electron energy equation is selected to close the system, allowing us to benefit from the regularization of the electron variables. Although our model directly inspired from Graille et al. (2009) is well identified and applicable to the solar chromosphere conditions, it is still necessary to understand how to treat the nonconservative term present in the hyperbolic convection part of the system.

Indeed, solving nonconservative hyperbolic systems is a delicate problem because of the definition of weak admissible solutions. First, from a theoretical point of view, Dal Maso et al. (1995) have proposed a new theory to define nonconservative products based on the intoduction of paths, that generalizes in the sense of distributions the notion of weak solution for conservative systems. In this context, Pares (2006) have developed path-conservative schemes for nonconservative hyperbolic systems. However, it has been proved by Abgrall & Karni (2010) that these numerical schemes fail to converge to the right solutions. In fact, even if the correct path is known, the numerical solution obtained can be far from the expected solution, depending mainly on the numerical dissipation of the scheme. Chalons & Coquel (2017) have proposed a different strategy

for nonconservative hyperbolic systems using Roe-type conservative schemes. They changed the common path-conservative schemes by introducing modified cells in order to compute correctly the solution. Even if progress has been made in the field, the design of accurate and efficient schemes for shock solutions to nonconservative systems of equations and their numerical analysis still lacks completeness. Second, from an application point of view, several fields have encountered this difficulty. For example, in the community of two-phase flows, Pelanti & Shyue (2014) have proposed an alternative strategy: a Roe solver is used in order to simulate liquid-gas flows with cavitation, neglecting the nonconservative part of the system. Raviart & Sainsaulieu (1995) have succeeded in evaluating jump conditions relying on the fact that, in two-phase flows, the nonconservative product acts on linearly degenerate fields. More specifically, in the field of plasma physics, the problem has already been investigated. Coquel & Marmignon (1995) have replaced the equation of thermal energy of electrons by an equation of conservation of entropy for a model applicable to weakly ionized hypersonic flows in thermal non-equilibrium. Candler & Maccormack (1991) have considered the nonconservative product in the equation of thermal energy for electrons as a source term for a model applicable to weakly ionized flows. These methods lead to conservative system of equations where the structure of the shock waves is identified, but the link with the original system of equations is still incomplete. More recently, Aregba-Driollet & Breil (2017); Brull et al. (2018) have proposed several numerical schemes for the approximation of a nonconservative compressible Euler system applied to the modeling of fully ionized plasmas in thermal non-equilibrium, even if the question of how to evaluate the proper physical jump conditions is not solved. Lowrie & Rauenzahn (2007) and Lowrie & Edwards (2008) have defined semi-analytic solutions for planar radiative shock waves, which can be used for verifying codes for thermal equilibrium diffusion-radiation models. These ideas are also used by Masser et al. (2011) to analyze the structure of shock waves in a two-temperature model for fully ionized plasmas. The corresponding ordinary differential equations are integrated and the missing jump relation is obtained by replacing the equation of thermal energy of electrons by a conservative equation of entropy as done by Coquel & Marmignon (1995), thus avoiding the proper definition and evaluation of a jump condition in the presence of a nonconservative term. This is more difficult in this case, since the nonconservative product acts directly on the genuinely nonlinear waves. Besides, in the work performed by Shafranov (1957), Zel'dovich & Raizer (1967), and Mihalas & Mihalas (1984), the shock wave structure has been identified for a nonequilibrium fully ionized plasma in the context of a two-fluid model without nonconservative product. Relying on the high thermal conductivity of the electrons compared to the one of the ions, the structure of the wave is studied and the temperature of the electrons is shown to be smooth whereas the temperature of the ions exhibits a discontinuity. Zel'dovich & Raizer (1967) has shown that the dissipative processes play a major role in the jump conditions for the shock wave: it depends on both the gradients of macroscopic quantities and the transport coefficients. Even if we know what to expect in terms of physics, such waves structure and jump conditions have not been obtained in the framework of a one-fluid model exhibiting a nonconservative product. In summary, no fully satisfactory solution has yet been achieved to handle both theoretically and numerically the nonconservative product appearing in a one-fluid model and it remains an open problem.

In this contribution, we focus on a specific class of solutions written as travelling waves. These

solutions are regular enough to ensure that all the terms appearing in the systems are well defined (in particular the nonconservative product). Obviously, the gain of regularity is allowed thanks to the diffusion terms on the electronic fields. The main goal of this contribution is to build a numerical scheme able to capture first the regular solutions of the system and second these particular travelling waves. This is a first step towards capturing the solution of the Riemann problems corresponding to an intermediate scale where the electronic diffusion terms remain. The question of the existence of weak solutions (with or without the diffusion terms) is not the subject of this work. Moreover, we do not deal with the interesting question of the limit of these travelling waves when the diffusion terms fully vanish: the formal limit of the solution is not clearly a weak solution of the hyperbolic system without diffusion terms because of the nonconservative product.

We focus on the model derived by Graille et al. (2009) at the zeroth order of the Chapman-Enskog expansion. First, we identify a simplified model, which inherits the same difficulty of dealing with nonconservative products and proper shock numerical solution as the original system, but which is tractable mathematically. A decoupling of the governing equations is proposed and we look for piecewise smooth traveling wave solutions to the decoupled problem, as it is coherent with Zel'dovich & Raizer (1967); Shafranov (1957). This analysis leads to a complete analytical solution, as well as an explicit expression of the missing jump relation for the thermal energy of electrons, where the nonconservative term is to be found. The ability of conducting the full analysis strongly relies on the proper form of the system and on the presence of a regularizing effect in the electron variables at this order of the expansion. For the numerical solution, we first use a standard finite volume Godunov scheme based on a consistent discretization of the nonconservative product, in order to resolve the traveling wave. When the level of resolution is too coarse, some artificial and non-physical additional shock appears in the solution, whereas for fine resolution, the proper and expected travelling wave solution is reproduced. We thus identify the characteristic scales associated with the compatibility conditions related to the analytic solution for the travelling wave in order to define the limit between the coarse and fine resolutions. Surprisingly enough, it is proved that the smallest diffusion scales associated with the electron mass diffusion have to be properly resolved for the travelling wave to be correctly captured by the numerical scheme. A new scheme based on a specific treatment of the nonconservative product is developed to verify the compatibility equations in a discretized sense. It is able to capture the proper travelling wave even in weakly-resolved cases without generating unexpected additional and artificial numerical shocks. Although we focused on a finite volume Godunov method, the numerical treatment of the nonconservative term and the proposed numerical scheme can be generalized to many finite volume methods: numerical experiments with a Lax-Friedrichs scheme and an upwind scheme are in good agreements. The proposed numerical strategy is assessed for a travelling wave test case based on the solar chromosphere conditions, for which the characteristic scales are identified and for which the resolution of the finest diffusion scales is out of reach. Using the new scheme combined to a Strang operator splitting technique, we obtain an accurate resolution of the test case with two main advantages: we do not have to resolve the smallest diffusion spatial scales in order to capture the proper travelling wave, as expected, and the timestep is not limited by the Fourier stability condition based on the largest diffusion coefficient. We eventually investigate the structure of the travelling wave for the original coupled system of equations and prove that: 1- the structure is

similar to the one of the decoupled problem, which allow us to have a precious insight on the wave structure and jump conditions; even if we have to resort to a numerical resolution of the missing jump condition by solving a system of ordinary differential equations using a Dormand-Prince (DOPRI853) method with dense output (see Dormand & Prince (1980); Hairer et al. (1993)), we can obtain the missing jump conditions for any Mach numbers in the general case, 2- in a regime of Mach numbers close to one, the missing jump condition for the decoupled and coupled problems are very close to one another, thus fully justifying our strategy to focus on a simplified problem.

In Section 7.1, a simplified model from the general one derived by Graille et al. (2009) is introduced. Then, the decoupling of the governing equations is discussed. In Section 7.2, piecewise smooth travelling wave solutions to the decoupled problem are derived, as well as the missing jump condition associated with the equation of thermal energy of electrons. The analytical solution calculated is then compared to the ones obtained by solving various models found in the literature. In Section 7.3, a 1D finite volume Godunov scheme with a standard discretization of the nonconservative product is developed, as well as a new scheme based on a specific treatment of the nonconservative product. In Section 7.4, a test case based on the solar chromosphere conditions is fully investigated and our numerical strategy assessed. Finally, in Section 7.5, we show how the ideas developed in the decoupled system case can be extended to the general case and highlight the validity of the decoupled approach in a reasonable Mach number range close to one. In addition, in Section 7.6, we also investigate the decoupled problem including the electric field.

7.1 Simplified model and decoupling of the governing equations

In this section, we identify a simplified system of equations, which reproduces the difficulty due to the nonconservative product encountered in the general model derived in the Chapter 2. An approximation of this system will allow us to conduct analytical studies in Section 7.2 and also to highlight the proper paths in the theoretical approach.

7.1.1 Simplified model for solar physics application

Considering the level of complexity of the general model shown in the Chapter 2 that we propose to use for solar physics applications, some simplified model is now introduced. We consider the system of equations associated to the zeroth-order of the Chapman-Enskog expansion. At this order, only the electrons have dissipative effects. For simplicity reason, neither Soret-Dufour effects nor electromagnetic forces have been considered. Thermal energy relaxation and chemical processes are assumed to be negligible. Both heavy particles (multiple species can be considered) and electrons have a common adiabatic coefficient $\gamma = 5/3$, since the internal energy modes are neglected. While diffusion can be anisotropic in the strongly magnetized case, we assume isotropic diffusion since no magnetic field is present. The diffusion structure is still nonlinear even if the electron diffusion coefficient and thermal conductivity are assumed to be constant. Under these

assumptions, the simplified system of equations is made up of the conservation equations for the heavy-particle mass, mixture momentum and total energy, and the electron mass and thermal energy. In nondimensional form (assuming a unit reference Mach number, see Graille et al. (2009)), this system reads:

$$\begin{cases} \partial_t \rho_\mathfrak{h} + \boldsymbol{\partial_x}\cdot(\rho_\mathfrak{h}\boldsymbol{v}_\mathfrak{h}) = 0, \\ \partial_t(\rho_\mathfrak{h}\boldsymbol{v}_\mathfrak{h}) + \boldsymbol{\partial_x}\cdot(\rho_\mathfrak{h}\boldsymbol{v}_\mathfrak{h}\otimes\boldsymbol{v}_\mathfrak{h} + p\mathbb{I}) = 0, \\ \partial_t \mathcal{E} + \boldsymbol{\partial_x}\cdot(\mathcal{E}\boldsymbol{v}_\mathfrak{h} + p\boldsymbol{v}_\mathfrak{h}) = \boldsymbol{\partial_x}\cdot(\lambda\boldsymbol{\partial_x} T_\mathfrak{e} + \frac{\gamma}{\gamma-1} D\boldsymbol{\partial_x} p_\mathfrak{e}), \\ \partial_t \rho_\mathfrak{e} + \boldsymbol{\partial_x}\cdot(\rho_\mathfrak{e}\boldsymbol{v}_\mathfrak{h}) = \boldsymbol{\partial_x}\cdot(D\frac{1}{T_\mathfrak{e}}\boldsymbol{\partial_x} p_\mathfrak{e}), \\ \partial_t(\rho_\mathfrak{e} e_\mathfrak{e}) + \boldsymbol{\partial_x}\cdot(\rho_\mathfrak{e} e_\mathfrak{e}\boldsymbol{v}_\mathfrak{h}) = -p_\mathfrak{e}\boldsymbol{\partial_x}\cdot\boldsymbol{v}_\mathfrak{h} + \boldsymbol{\partial_x}\cdot(\lambda\boldsymbol{\partial_x} T_\mathfrak{e} + \frac{\gamma}{\gamma-1} D\boldsymbol{\partial_x} p_\mathfrak{e}), \end{cases} \tag{M_S}$$

where λ is the isotropic electron thermal conductivity, D the isotropic electron diffusion coefficient. We remind that the mixture pressure is composed of both the electron and heavy-particle partial pressures $p = p_\mathfrak{e} + p_\mathfrak{h}$, obeying the perfect gas law $p_\mathfrak{e} = (\gamma-1)\rho_\mathfrak{e} e_\mathfrak{e}$, $p_\mathfrak{h} = (\gamma-1)\rho_\mathfrak{h} e_\mathfrak{h}$, where $\rho_\mathfrak{h} e_\mathfrak{h}$ is the heavy-particle thermal energy. The mixture total energy $\mathcal{E}$ is defined as $\mathcal{E} = \rho_\mathfrak{h}|\boldsymbol{v}_\mathfrak{h}|^2/2 + p/(\gamma-1)$. The term $-p_\mathfrak{e}\boldsymbol{\partial_x}\cdot\boldsymbol{v}_\mathfrak{h}$ in the electron energy equation is a nonconservative product examined in great details in this paper. The simplified model (M_S) inherits the difficulty of dealing with nonconservative products and proper shock numerical solution from the original system, but it remains mathematically tractable.

7.1.2 Structure of the system

System (M_S) is hyperbolic in the open set of admissible states $\Omega = \{\rho_\mathfrak{h} > 0, \quad \rho_\mathfrak{e} > 0, \quad \boldsymbol{v}_\mathfrak{h} \in \mathbb{R}^3, \quad p > 0, \quad p_\mathfrak{e} > 0\}$ with a parabolic regularization on the electron variables. For any direction defined by the unit vector $\boldsymbol{n}$, the matrix $\boldsymbol{n}\cdot\mathcal{A}$, where $\mathcal{A}$ is the Jacobian matrix of the hyperbolic part (removing the second order diffusion terms) is shown to be diagonalizable with real eigenvalues and a complete set of eigenvectors. The eigenvalue $\boldsymbol{v}_\mathfrak{h}\cdot\boldsymbol{n}$ is linearly degenerate of multiplicity $d+2$, where d is the space dimension, and the eigenvalues $\boldsymbol{v}_\mathfrak{h}\cdot\boldsymbol{n} \pm c$ are genuinely nonlinear, where c is the sound speed defined by $c = \sqrt{\gamma p/\rho_\mathfrak{h}}$. Electrons participate in the momentum balance through the pressure gradient. As a result, the sound speed includes as well the electron contribution to the pressure. Further details about the structure of the system can be found in Appendix E.

We recall that the equation of electron thermal energy is nonconservative in system (M_S). This leads to the difficulties mentioned in the introduction when looking for discontinuous solutions to the hyperbolic part of the problem. For shock wave solutions, one possibility would be to transform the system M_S into a conservative system. For instance, the equation of electronic thermal energy can be exchanged with a conservative equation for the electron entropy, as considered by Coquel & Marmignon (1995). This method works only for smooth solutions when there is no dissipation in the electron energy equation. Another possibility would be to consider the nonconservative product as a source term, as considered by Candler & Maccormack (1991). However, this strategy modifies the eigenstructure of the system and, as a consequence, the electronic temperature remains constant through a shock wave. Our approach is different: we want to make use of the sound structure

of system (M_S) in order to derive general jump conditions involving neither simplifications nor modifications of the system.

7.1.3 Approximate decoupled problem

This section is devoted to an approximate decoupled system obtained by removing the electronic diffusion in the conservation equation for the total energy. This modified system is so-called decoupled since the first three conservation equations constitute the Euler system and the electronic equations are then solved, once the heavy part velocity $\boldsymbol{v}_\mathfrak{h}$ is known. This simplification has no physical justification since the structure of the diffusion is modified. Nevertheless the decoupled system allows us to derive analytical expressions for travelling wave solutions. The wave structure of the decoupled problem obtained will be shown to be very close to the fully coupled problem of system (M_S) in a Mach number regime close to 1, shedding some light on the structure of travelling wave solutions for the fully coupled system. Moreover, this approach allows us to build a numerical scheme which is able to capture the associated travelling wave solutions.

The approximate decoupled system splits then into the Euler system

$$\begin{cases} \partial_t(\bar{\rho}_\mathfrak{h}) + \boldsymbol{\partial_x}\cdot(\bar{\rho}_\mathfrak{h}\bar{\boldsymbol{v}}_\mathfrak{h}) = 0, \\ \partial_t(\bar{\rho}_\mathfrak{h}\bar{\boldsymbol{v}}_\mathfrak{h}) + \boldsymbol{\partial_x}\cdot(\bar{\rho}_\mathfrak{h}\bar{\boldsymbol{v}}_\mathfrak{h}\otimes\bar{\boldsymbol{v}}_\mathfrak{h} + \bar{p}\mathbb{I}) = 0, \\ \partial_t\overline{\mathcal{E}} + \boldsymbol{\partial_x}\cdot(\overline{\mathcal{E}}\bar{\boldsymbol{v}}_\mathfrak{h} + \bar{p}\bar{\boldsymbol{v}}_\mathfrak{h}) = 0, \end{cases} \tag{$M_{\bar{S}_1}$}$$

and a nonconservative drift-diffusion system

$$\begin{cases} \partial_t\bar{\rho}_\mathfrak{e} + \boldsymbol{\partial_x}\cdot(\bar{\rho}_\mathfrak{e}\bar{\boldsymbol{v}}_\mathfrak{h}) = \boldsymbol{\partial_x}\cdot(\frac{1}{\overline{T}_\mathfrak{e}}D\boldsymbol{\partial_x}\bar{p}_\mathfrak{e}), \\ \partial_t(\bar{\rho}_\mathfrak{e}\bar{e}_\mathfrak{e}) + \boldsymbol{\partial_x}\cdot(\bar{\rho}_\mathfrak{e}\bar{e}_\mathfrak{e}\bar{\boldsymbol{v}}_\mathfrak{h}) = -\bar{p}_\mathfrak{e}\boldsymbol{\partial_x}\cdot\bar{\boldsymbol{v}}_\mathfrak{h} + \boldsymbol{\partial_x}\cdot(\lambda\boldsymbol{\partial_x}\overline{T}_\mathfrak{e} + \frac{\gamma}{\gamma-1}D\boldsymbol{\partial_x}\bar{p}_\mathfrak{e}). \end{cases} \tag{$M_{\bar{S}_2}$}$$

The mixture pressure is introduced as before, $\bar{p} = \bar{p}_\mathfrak{e} + \bar{p}_\mathfrak{h}$, with the partial pressures $\bar{p}_\mathfrak{e} = (\gamma-1)\bar{\rho}_\mathfrak{e}\bar{e}_\mathfrak{e}$, $\bar{p}_\mathfrak{h} = (\gamma-1)\bar{\rho}_\mathfrak{h}\bar{e}_\mathfrak{h}$. We also have $\bar{p}_\mathfrak{e} = \bar{\rho}_\mathfrak{e}\overline{T}_\mathfrak{e}$. The mixture total energy is given by $\overline{\mathcal{E}} = \bar{\rho}_\mathfrak{h}|\bar{\boldsymbol{v}}_\mathfrak{h}|^2/2 + \bar{p}/(\gamma-1)$. One can find a global solution to this decoupled problem. The first part ($M_{\bar{S}_1}$) admits discontinous solutions for which the discontinuity is propagating with the velocity prescribed by the usual Rankine-Hugoniot jump relations and Lax's condition. One can then calculate a solution to the sub-system of electron ($M_{\bar{S}_2}$) as one piecewise smooth travelling wave, and determine the missing jump condition, with a heavy-particle velocity field previously solved from system ($M_{\bar{S}_1}$).

7.2 Jump relations and travelling waves for the decoupled problem

In this section, we determine travelling wave solutions for the system ($M_{\bar{S}_2}$), being given the velocity $\bar{\boldsymbol{v}}_\mathfrak{h}$ as a piecewise constant function. The variables $(\bar{\rho}_\mathfrak{h}, \bar{\rho}_\mathfrak{h}\bar{\boldsymbol{v}}_\mathfrak{h}, \overline{\mathcal{E}})$ are assumed to be a shock

wave solution to the Euler System ($M_{\bar{S}_1}$) with velocity σ, which satisfies the Rankine-Hugoniot jump relations and the Lax entropy condition. We are subsequently looking for a piecewise smooth travelling wave solution in the variables $(\bar{\rho}_{\mathfrak{e}}, \bar{e}_{\mathfrak{e}})$, moving with the same velocity σ, solution to the system $M_{\bar{S}_2}$. Since the electron variables experience nonlinear heat and mass diffusion, their profile is expected to exhibit only weak discontinuities, that is discontinuities in their gradients. We derive boundary conditions at left and right infinities and show that they do not depend on the (constant) diffusion coefficients λ and D, hence they can be used as jump conditions associated with the electronic variables $\bar{\rho}_{\mathfrak{e}}$ and $\bar{\rho}_{\mathfrak{e}}\bar{e}_{\mathfrak{e}}$. It is consistent with the work of Zel'dovich & Raizer (1967). These jump conditions are then compared with literature results. A onedimensional case (d=1) is considered.

7.2.1 Structure of the travelling wave

We consider that the heavy-particle variables read as piecewise constant functions depending only on $\xi = \boldsymbol{x}\cdot\boldsymbol{n} - \sigma t$ where $\sigma > 0$ is the velocity of the travelling wave prescribed by the Rankine-Hugoniot jump conditions on the heavy-particle variables, and $\boldsymbol{n}$, a unit vector in the first direction, such that $\boldsymbol{x}\cdot\boldsymbol{n} = x$. The same notation is used for functions depending on time and space and for functions depending on ξ as there is no ambiguity. Superscript R denotes the right state and L denotes the left state. We have

$$\bar{\rho}_{\mathfrak{h}}(\xi) = \begin{cases} \bar{\rho}_{\mathfrak{h}}^{L} & \text{if } \xi < 0, \\ \bar{\rho}_{\mathfrak{h}}^{R} & \text{if } \xi > 0, \end{cases} \quad \bar{\boldsymbol{v}}_{\mathfrak{h}}(\xi) = \begin{cases} \bar{\boldsymbol{v}}_{\mathfrak{h}}^{L} & \text{if } \xi < 0, \\ \bar{\boldsymbol{v}}_{\mathfrak{h}}^{R} & \text{if } \xi > 0, \end{cases} \quad \bar{p}(\xi) = \begin{cases} \bar{p}^{L} & \text{if } \xi < 0, \\ \bar{p}^{R} & \text{if } \xi > 0. \end{cases} \tag{7.2.1}$$

We consider a 3-shock wave that propagates at velocity $\sigma > 0$. The case of a 1-shock wave is symmetric to the 3-shock case and can be solved in a similar way.

Based on the sub-system of electrons ($M_{\bar{S}_2}$), we look for piecewise smooth travelling wave for the electron variables that propagate at the velocity σ. More precisely, the functions $\bar{\rho}_{\mathfrak{e}}$ and $\bar{p}_{\mathfrak{e}}$ solutions to ($M_{\bar{S}_2}$) are assumed to satisfy

- $\bar{\rho}_{\mathfrak{e}} : \xi \mapsto \bar{\rho}_{\mathfrak{e}}(\xi) \in C^0(\mathbb{R})$, $\bar{p}_{\mathfrak{e}} : \xi \mapsto \bar{p}_{\mathfrak{e}}(\xi) \in C^0(\mathbb{R})$,
- $\bar{\rho}_{\mathfrak{e}}$ and $\bar{p}_{\mathfrak{e}}$ are C^∞ on $(-\infty, 0)$ and $(0, +\infty)$,
- $\bar{\rho}_{\mathfrak{e}}$ and $\bar{p}_{\mathfrak{e}}$ admit limits in $\pm\infty$ denoted by

$$\lim_{\xi\to-\infty} \bar{\rho}_{\mathfrak{e}}(\xi) = \bar{\rho}_{\mathfrak{e}}^{L}, \qquad \lim_{\xi\to+\infty} \bar{\rho}_{\mathfrak{e}}(\xi) = \bar{\rho}_{\mathfrak{e}}^{R}, \qquad \lim_{\xi\to\pm\infty} \bar{\rho}_{\mathfrak{e}}{}'(\xi) = 0,$$
$$\lim_{\xi\to-\infty} \bar{p}_{\mathfrak{e}}(\xi) = \bar{p}_{\mathfrak{e}}^{L}, \qquad \lim_{\xi\to+\infty} \bar{p}_{\mathfrak{e}}(\xi) = \bar{p}_{\mathfrak{e}}^{R}, \qquad \lim_{\xi\to\pm\infty} \bar{p}_{\mathfrak{e}}'(\xi) = 0.$$

The goal of this section is to exhibit the structure of these solutions in order to understand the relations between the left and right states according to the travelling wave velocity σ and structure of the diffusion (in particular the value of the coefficients D and λ). We assume that the right state R is known, and we look for state L connected to the state R.

System ($M_{\bar{S}_2}$) of partial differential equations becomes a system of ordinary differential equations:

$$\begin{cases} -\sigma\bar{\rho}_\mathfrak{e}' + (\bar{\rho}_\mathfrak{e}\bar{v}_\mathfrak{h})' = D(\frac{1}{\bar{T}_\mathfrak{e}}\bar{p}_\mathfrak{e}')', \\ -\frac{1}{\gamma-1}\sigma\,\bar{p}_\mathfrak{e}' + \frac{1}{\gamma-1}(\bar{p}_\mathfrak{e}\bar{v}_\mathfrak{h})' = -\bar{p}_\mathfrak{e}\bar{v}_\mathfrak{h}' + \lambda\,\bar{T}_\mathfrak{e}'' + \frac{\gamma}{\gamma-1}D\,\bar{p}_\mathfrak{e}'', \end{cases} \tag{7.2.2}$$

where $\bar{v}_\mathfrak{h}$ is a piecewise constant function given in (7.2.1). The Mach number M_R at state R is introduced as $M_R = (\sigma - \bar{v}_\mathfrak{h}^R)/c^R$, where c^R is the speed of sound at the right state defined by $c^R = \sqrt{\gamma\bar{p}^R/\bar{\rho}_\mathfrak{h}^R}$, and is written in such a way that $M_R > 1$ from the Lax conditions. The system (7.2.2) can be solved by considering the two domains $\xi > 0$ and $\xi < 0$ and their interface $\xi = 0$. For $\xi > 0$, after some algebra, it reads

$$\begin{pmatrix} \bar{p}_\mathfrak{e} - \bar{p}_\mathfrak{e}^R \\ \bar{T}_\mathfrak{e} - \bar{T}_\mathfrak{e}^R \end{pmatrix}' = \eta^R \begin{pmatrix} 1 & -\bar{\rho}_\mathfrak{e}^R \\ -r^R\frac{\gamma-1}{\gamma\bar{\rho}_\mathfrak{e}^R} & r^R \end{pmatrix} \begin{pmatrix} \bar{p}_\mathfrak{e} - \bar{p}_\mathfrak{e}^R \\ \bar{T}_\mathfrak{e} - \bar{T}_\mathfrak{e}^R \end{pmatrix}, \tag{7.2.3}$$

where the thermal diffusivity κ^R at the right state and the coefficients η^R and r^R are defined as $\kappa^R = (\gamma-1)\lambda/(\gamma\bar{\rho}_\mathfrak{e}^R)$, $\eta^R = -c^R M_R/D$, and $r^R = D/\kappa^R$. The matrix of (7.2.3) has two negative eigenvalues $\delta^\pm$

$$\delta^\pm = \tfrac{1}{2}\eta^R\Big(1 + r^R \pm \sqrt{(1+r^R)^2 - \tfrac{4}{\gamma}r^R}\Big). \tag{7.2.4}$$

Finally, for $\xi > 0$ one gets an analytical expression of the solution that combines decreasing exponential functions

$$\begin{aligned} \bar{p}_\mathfrak{e}(\xi) &= \bar{p}_\mathfrak{e}^R + \bar{\rho}_\mathfrak{e}^R(K^{R+}\,\mathrm{e}^{\delta^+\xi} + K^{R-}\,\mathrm{e}^{\delta^-\xi}), && \xi > 0, \\ \bar{T}_\mathfrak{e}(\xi) &= \bar{T}_\mathfrak{e}^R + (1 - \tfrac{\delta^+}{\eta^R})K^{R+}\,\mathrm{e}^{\delta^+\xi} + (1 - \tfrac{\delta^-}{\eta^R})K^{R-}\,\mathrm{e}^{\delta^-\xi}, && \xi > 0, \end{aligned}$$

where $K^{R\pm}$ are two integration constants that need to be determined by using the continuity and the jump of the derivative gradients in $\xi = 0$. Moreover, for $\xi < 0$, similar algebraic relations as those found in (7.2.3) are obtained by replacing state R by state L. It leads to similar eigenvalues as those in (7.2.4) by replacing state R by state L. However, the only way for having a non diverging solution is to get constant functions equal to the left constant state L by setting the integration constants $K^{L\pm} = 0$. Indeed, the only bounded solutions when ξ goes to $-\infty$ are constant solutions.

At $\xi = 0$, since $\bar{p}_\mathfrak{e}$ and $\bar{\rho}_\mathfrak{e}$ (and $\bar{T}_\mathfrak{e}$) are continuous functions, the system (7.2.2) leads to

$$\bar{p}_\mathfrak{e}(0)[\bar{v}_\mathfrak{h}]_{(0)} = D[\bar{p}_\mathfrak{e}']_{(0)}, \qquad \tfrac{\gamma}{\gamma-1}\bar{p}_\mathfrak{e}(0)[\bar{v}_\mathfrak{h}]_{(0)} = \lambda[\bar{T}_\mathfrak{e}']_{(0)} + \tfrac{\gamma}{\gamma-1}D[\bar{p}_\mathfrak{e}']_{(0)}, \tag{7.2.5}$$

where $[\cdot]_{(0)}$ denotes for the value of the jump in $\xi = 0$. The term of the left hand side in the second equality of (7.2.5) is the contribution of two terms: a first one coming from the convective part and a second one coming from the nonconservative product. Actually, since $\bar{p}_\mathfrak{e}$ is continuous and the derivative $\bar{v}_\mathfrak{h}'$ has a jump at $\xi = 0$, the nonconservative product in the second equation of (7.2.2) is not ambiguous. Finally, the second relation of (7.2.5) can be simplified by using the first one. (7.2.5) then becomes

$$\bar{p}_\mathfrak{e}(0)[\bar{v}_\mathfrak{h}]_{(0)} = D[\bar{p}_\mathfrak{e}']_{(0)}, \qquad [\bar{T}_\mathfrak{e}']_{(0)} = 0. \tag{7.2.6}$$

The second relation of (7.2.6) provides the continuity of the derivative of T_e in the discontinuity (at $\xi = 0$). In other words, T_e is a C^1 function. This result is consistent with the work of Zel'dovich & Raizer (1967), showing that the temperature of electron is smooth in the shock wave of a nonequilibrium fully ionized plasma. Moreover, the first relation of (7.2.6) can be seen as a relation between the jump of the pressure gradient in the discontinuity, the jump of the velocity and the diffusion coefficient D. This result is also consistent with the work of Zel'dovich & Raizer (1967), showing that the discontinuity of the shock wave in a plasma depend on the dissipative process. Defining the two characteristic lengths of the diffusion L_D associated to the electron diffusion coefficient and L_λ associated to the thermal conductivity by

$$L_D = \frac{D}{[\bar{v}_h]_{(0)}}, \qquad L_\lambda = \frac{\gamma-1}{\gamma}\frac{\lambda}{\bar{\rho}_e^R}\frac{1}{[\bar{v}_h]_{(0)}} = \frac{\kappa^R}{[\bar{v}_h]_{(0)}}, \qquad [\bar{v}_h]_{(0)} > 0, \tag{7.2.7}$$

(7.2.6) can be rewritten as

$$[\bar{p}_e']_{(0)} = \tfrac{1}{L_D}\bar{p}_e(0), \qquad [\overline{T}_e']_{(0)} = 0. \tag{7.2.8}$$

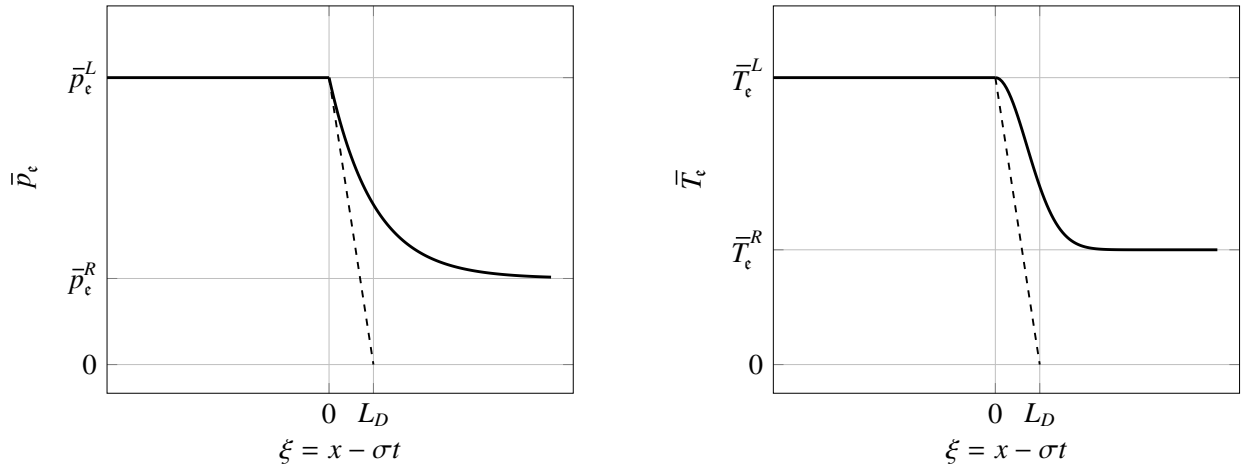

Figure 7-1: Scheme of the travelling wave with the characteristic diffusion length L_D

The jump compatibility relations for the pressure of electron $\bar{p}_e$ and for the electron temperature $\overline{T}_e$ link the states R and L at infinity. They are obtained by integrating (7.2.2) from 0^+ to ∞, then using (7.2.6) and the jump conditions for the heavy particle velocity $\bar{v}_h$. Finally, these relations can be combined to obtain the density jump conditions between the states R and L at infinity. One gets

$$\frac{\bar{p}_e^L}{\bar{p}_e^R} = \frac{(\gamma+1)M_R^2}{(1-\gamma)M_R^2+2\gamma}, \quad \frac{\overline{T}_e^L}{\overline{T}_e^R} = \frac{(\gamma-1)M_R^2+2}{(1-\gamma)M_R^2+2\gamma}, \quad \frac{\bar{\rho}_e^L}{\bar{\rho}_e^R} = \frac{(\gamma+1)M_R^2}{(\gamma-1)M_R^2+2}. \tag{7.2.9}$$

The state L at infinity does not depend on the diffusion coefficients D and λ. However, according to (7.2.6), the jump compatibility relations depend on the variables and their gradients in the discontinuity. This result is consistent with the work of Zel'dovich & Raizer (1967), and Shafranov (1957). Let us underline however that the relations of (7.2.9) are valid only for $M_R^2 < 2\gamma/(\gamma-1)$,

and a singularity is present when M_R goes to $\sqrt{2\gamma/(\gamma-1)}$. Thus, the obtained relations are valid for a Mach number range close to one. Notice that the jump condition $\bar{\rho}_{\mathfrak{e}}^L/\bar{\rho}_{\mathfrak{e}}^R$ is the same as for $\bar{\rho}_{\mathfrak{h}}^L/\bar{\rho}_{\mathfrak{h}}^R$ and is compatible with the Rankine-Hugoniot jump relations. In the case where the Mach number is equal to this value, it is not possible to solve the problem of the travelling wave and build a solution in the expected form. In addition, beyond this value, the solution is showing negative temperatures. Thus the decoupling of the system provides a reasonable solution only below this value.

7.2.2 Comparison with classical jump conditions

In this section, the jump conditions proposed in (7.2.9) are compared with other usual jump conditions from conservative system of equations.

First, one can consider a conservative system of equations where we replace the nonconservative equation of electron internal energy by an equation of conservation of electron entropy (see (M^{ent}) in Appendix D). The obtained model is called **Model** M^{ent}. In this case, one would get the following jump conditions:

$$\frac{\bar{p}_{\mathfrak{e}}^L}{\bar{p}_{\mathfrak{e}}^R} \underset{\mathcal{M}^{\text{ent}}}{:=} \left(\frac{(\gamma+1)M_R^2}{(\gamma-1)M_R^2+2}\right)^{\gamma}, \quad \frac{\bar{T}_{\mathfrak{e}}^L}{\bar{T}_{\mathfrak{e}}^R} \underset{\mathcal{M}^{\text{ent}}}{:=} \left(\frac{(\gamma+1)M_R^2}{(\gamma-1)M_R^2+2}\right)^{\gamma-1}. \tag{7.2.10}$$

Second, one can consider another conservative system of equations where the nonconservative product is considered as a source term: only the conservative part of the system is considered for getting the jump conditions (see (M^{src}) in Appendix D). The model obtained in that case is called **Model** M^{src} and the jump conditions read

$$\frac{\bar{p}_{\mathfrak{e}}^L}{\bar{p}_{\mathfrak{e}}^R} \underset{\mathcal{M}^{\text{src}}}{:=} \frac{(\gamma+1)M_R^2}{(\gamma-1)M_R^2+2}, \quad \frac{\bar{T}_{\mathfrak{e}}^L}{\bar{T}_{\mathfrak{e}}^R} \underset{\mathcal{M}^{\text{src}}}{:=} 1. \tag{7.2.11}$$

The jump conditions for the electron pressure and electron temperature obtained by the travelling wave method in (7.2.9) are then compared to those obtained by means of (7.2.10) and (7.2.11). In Figure 7-2, the three jump conditions are plotted as functions of the Mach number for Mach numbers between 1 and 1.5. We observe first that the isothermal jump conditions of **Model** M^{src} rapidly underestimates the post-jump temperature. Moreover, this model is not reasonable since the dynamics of smooth waves, such as rarefaction waves, is modified. Second, the jump conditions (7.2.11) of **Model** M^{ent} are similar to the ones of (7.2.9) for a Mach number regime close to 1. However, significant differences can be observed when the Mach number is increasing.

As a conclusion, by looking for piecewise smooth travelling wave solutions, we were able to get an analytical expression of the missing jump condition associated with the thermal energy of electrons, and the analytical travelling wave solution of the electron variables valid for a Mach number regime close to one. For that purpose, we had to decouple the problem: a discontinuity propagating at velocity σ where the jump conditions are prescribed by the usual Rankine-Hugoniot

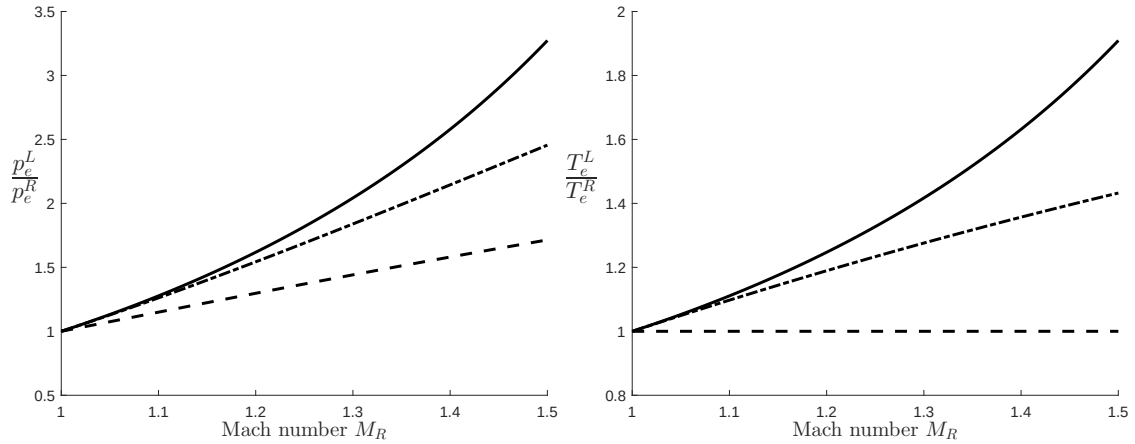

(a) $M_R \in [1, 1.5]$

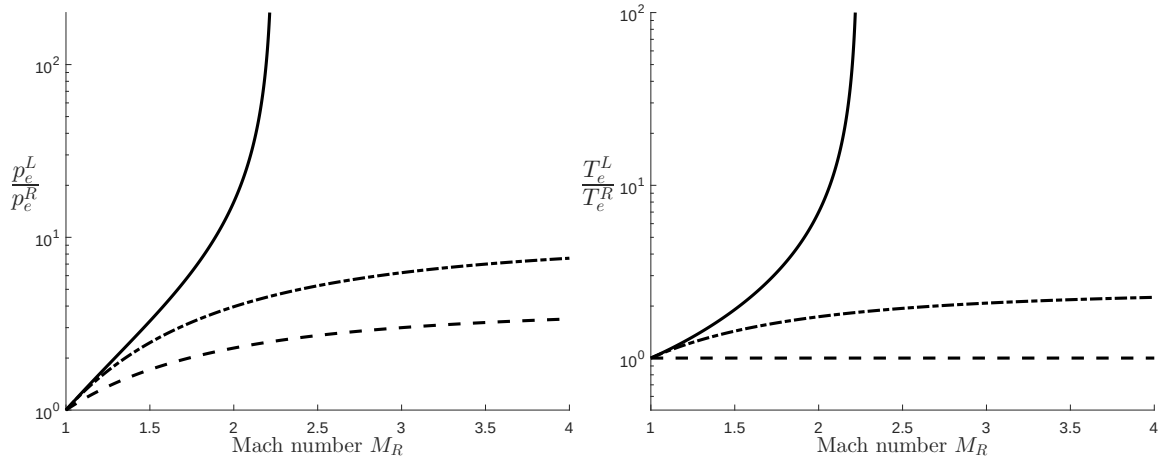

(b) $M_R \in [1, 4]$

Figure 7-2: Left: Ratio $\bar{p}_{\mathfrak{e}}^L / \bar{p}_{\mathfrak{e}}^R$ as a function of the Mach number M_R, from (7.2.9) in full line, from (7.2.10) in semi-dashed line and from (7.2.11) in dashed line. Right: Distribution of the ratio $\bar{T}_{\mathfrak{e}}^L / \bar{T}_{\mathfrak{e}}^R$. Top: Mach number range $M_R \in [1, 1.5]$. Bottom: Mach number range $M_R \in [1, 4]$.

relations solution to the sub-system ($M_{\bar{S}_1}$) and a continuous travelling wave propagating at the same velocity σ, solution to the sub-system ($M_{\bar{S}_2}$). The resulting jump conditions are valid in a neighborhood of Mach one and then lead to a singularity for larger Mach numbers. In the interval where they are valid, they exhibit rather important differences with the conditions found in the literature. At the end of this contribution, we will prove that the analytical expression obtained for the decoupled system is a very good approximation in a Mach range close to the one of the jump conditions for the fully coupled problem (M_S), which does not lead to any singular behavior. The jump condition for the fully coupled problem (M_S) will also be proved to be very different from the usual jump conditions of the literature. The next step is to verify numerically the jump conditions and if we can capture the analytical travelling waves.

7.3 Numerical scheme for the decoupled problem ($M_{\bar{S}_1}$)-($M_{\bar{S}_2}$)

In the previous section, we show the existence of a travelling wave for system ($M_{\bar{S}_2}$). The aim of this section is to develop numerical methods able to capture the dynamic of the travelling wave. First, we introduce a standard scheme based on a finite volume Godunov method with a standard discretization of the nonconservative product and then a specific treatment.

Note that the proposed method to treat the nonconservative term is independant of the chosen finite volume scheme. Numerical experiments for a Lax-Friedrichs scheme and an upwind scheme have been performed and led to the same conclusions.

7.3.1 Finite volume scheme with a consistent discretization of the nonconservative product

The electron variables $\bar{\rho}_{\mathfrak{e}}$ and $\bar{\rho}_{\mathfrak{e}}\bar{e}_{\mathfrak{e}}$ are initialized by using the analytical solution found in the previous section. The heavy variables $\bar{\rho}_{\mathfrak{h}}$, $\bar{v}_{\mathfrak{h}}$, and $\bar{\mathcal{E}}$ are discontinuities propagating at velocity σ, where the conditions are fixed by the Rankine-Hugoniot conditions.

A monodimensional finite volume Godunov method is used to discretize the electron sub-system ($M_{\bar{S}_2}$). We consider a finite domain of length L with N cells of length $\Delta x = L/N$. The position of each cell C_j, $1 \leq j \leq N$ is defined by its center x_j at the middle of the interfaces $x_{j+1/2}$ and $x_{j-1/2}$. The bounds of the domain are not taken into account as the simulations are stopped before any interaction occurs between the travelling wave and the boundary. Left and right Dirichlet conditions are then used. The time is also discretized with a timestep Δt. Figure 7-3 can be used to visualize these standard notations.

We denote by $\mathcal{U}_j^n$, $n \geq 0$, $1 \leq j \leq N$, the vector of the natural variables at time t^n in the cell C_j is

$$\mathcal{U}_j^n = \left(\mathcal{U}_{j,1}^n, \mathcal{U}_{j,2}^n\right), \quad \mathcal{U}_{j,1}^n = \bar{\rho}_{\mathfrak{e},j}^n \text{ and } \mathcal{U}_{j,2}^n = \bar{\rho}_{\mathfrak{e},j}^n \bar{e}_{\mathfrak{e},j}^n.$$

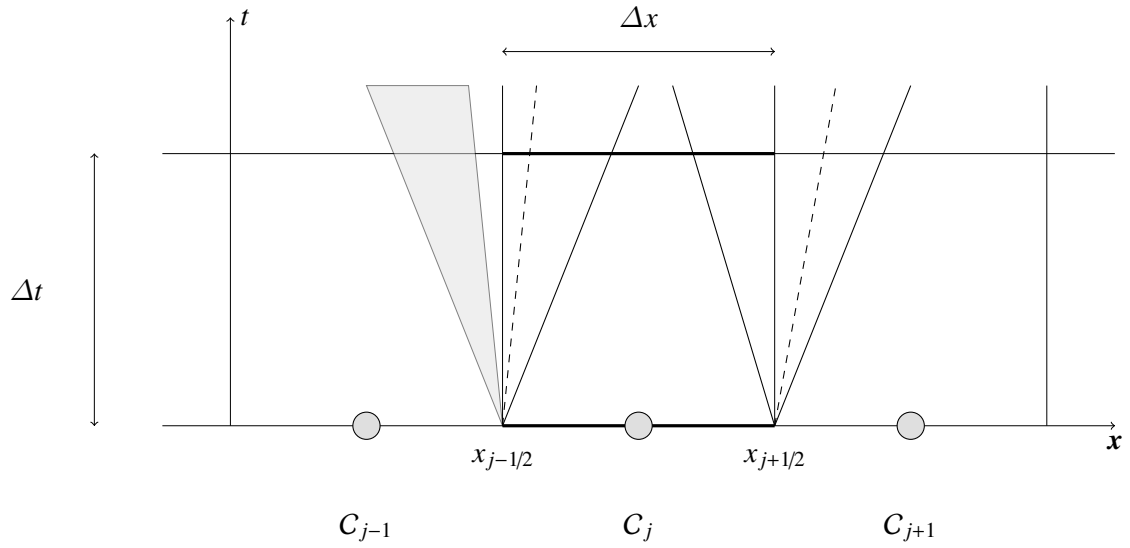

Figure 7-3: Notations for finite volume scheme.

The general scheme reads

$$\mathcal{U}_j^{n+1} = \mathcal{U}_j^n - \frac{\Delta t}{\Delta x}(F_{j+1/2}^n - F_{j-1/2}^n) + \frac{\Delta t}{\Delta x}(G_{j+1/2}^n - G_{j-1/2}^n) + N_j^n, \tag{7.3.1}$$

where $F_{j\pm1/2}^n$ are the convective fluxes at interfaces $j \pm 1/2$, $G_{j\pm1/2}^n$ the diffusive fluxes at interfaces $j \pm 1/2$, and N_j^n the value of the nonconservative term in the cell j.

The convective flux $F_{j+1/2}^n$ is computed by means of Godunov's scheme, by approximating the solution of the Riemann problem with the left and the right values given by the cells j and j+1 and by taking the value of the flux at the interface. Note that the solution of the Riemann problem used by this Godunov's solver is essentially the solution of the transport equation with a constant velocity but at the interfaces close to the discontinuity of the velocity $\bar{v}_{\mathfrak{h}}$ (in these cases, the travelling wave is used).

Then, the diffusive flux is calculated by using a second-order centered scheme

$$G_{j+1/2}^n = \frac{1}{\Delta x}\Big(D\frac{\gamma-1}{\overline{T}_{\mathfrak{e},j+1/2}^n}(\mathcal{U}_{j+1,2}^n - \mathcal{U}_{j,2}^n), \lambda(\overline{T}_{\mathfrak{e},j+1}^n - \overline{T}_{\mathfrak{e},j}^n) + D\gamma(\mathcal{U}_{j+1,2}^n - \mathcal{U}_{j,2}^n)\Big), \tag{7.3.2}$$

where $\overline{T}_{\mathfrak{e},j}^n = (\gamma-1)\bar{e}_{\mathfrak{e},j}^n = (\gamma-1)\mathcal{U}_{j,2}^n/\mathcal{U}_{j,1}^n$ and the interface temperature $\overline{T}_{\mathfrak{e},j+1/2}^n$ reads

$$\overline{T}_{\mathfrak{e},j+1/2}^n = \frac{\gamma-1}{2}\Big(\frac{\mathcal{U}_{j+1,2}^n}{\mathcal{U}_{j+1,1}^n} + \frac{\mathcal{U}_{j,2}^n}{\mathcal{U}_{j,1}^n}\Big) = \frac{1}{2}\Big(\overline{T}_{\mathfrak{e},j+1}^n + \overline{T}_{\mathfrak{e},j}^n\Big).$$

Note that the error of consistency of this second-order discretization can be bounded by a $O(\Delta x^2)$ term. This accuracy is sufficient for the proposed scheme, as the major error is done by the Go-

dunov's discretization of the hyperbolic part.

Finally, the second composant of the nonconservative term $N_j^n = (0, N_{j,2}^n)$ is computed as an approximation (as accurate as possible) of the integral over $[t^n, t^{n+1}] \times C_j$ of the nonconservative contribution

$$\int_{t^n}^{t^{n+1}} \int_{C_j} \bar{p}_{\mathfrak{e}} \partial_{\boldsymbol{x}} \bar{\boldsymbol{v}}_{\mathfrak{h}} \, \mathrm{d}\boldsymbol{x} \, \mathrm{d}t \simeq (\gamma - 1) \mathcal{U}_{j,2}^n \int_{t^n}^{t^{n+1}} \int_{C_j} \partial_{\boldsymbol{x}} \bar{\boldsymbol{v}}_{\mathfrak{h}} \, \mathrm{d}\boldsymbol{x} \, \mathrm{d}t,$$

where the integral of $\partial_{\boldsymbol{x}} \bar{\boldsymbol{v}}_{\mathfrak{h}}$ is exactly computed as the velocity $\bar{\boldsymbol{v}}_{\mathfrak{h}}$ is prescribed. The proposed scheme is then a consistent numerical scheme with a standard discretization of the nonconservative product that can be tested for capturing the travelling wave.

7.3.2 Results with the standard scheme

In this section, we present some numerical experiments, using the finite volume scheme with standard discretization for the non-conservative product proposed in the previous section. Different resolutions of the travelling wave are presented with a double objective: first, to capture the dynamic of the travelling wave with a fine enough mesh; second, to visualize the behaviour with a coarse mesh in order to understand how the scheme can capture a shock discontinuity. We focus on the 3-wave with respect to the wave structure of the Euler system ($M_{\bar{S}_1}$), so that the right state R is known. Besides, a supersonic regime is studied for a Mach number close to one in order to guarantee the existence of the travelling wave introduced in Section 7.2.

The number of nodes N and the length of the domain L are fixed: $N = 2000$ and $L = 10$. The initial position of the travelling wave (that is the position corresponding to $\xi = 0$ in the moving frame) is $0.2L$. The time discretization Δt is fixed by a Fourier condition $\Delta t \leq \frac{1}{2}\beta \Delta x^2$ where $\beta = \max(D, \kappa^R)$. All the simulations are stopped at $t = t_f = 1$, corresponding to a displacement of the travelling wave to $0.373L$. The electron thermal conductivity $\lambda = 0.001$ is fixed, so the associated characteristic length $L_\lambda = 7.6 \times 10^{-2}$ is fixed. This value has been chosen as a good compromise between the length of the domain, which is fixed, and the regularization of the profile of the electron temperature. However, the electron diffusion coefficient D is going to vary in our numerical experiments changing the resolution of the travelling wave. This diffusion length L_D is related to the diffusion coefficient D according to (7.2.7). It is an increasing function of D. Consequently, since the length of the domain and the number of nodes are fixed, we improve the resolution of the travelling wave in the characteristic length L_D by increasing the diffusion coefficient D. Simulations are conducted for diffusion coefficient D between 10^{-3} and 10^{-1} corresponding to different resolutions of the travelling wave and lengths L_D. The two extreme cases, denoted by case **OR** (over-resolved) and case **UR** (under-resolved), are reported in Table 7.1: in case **OR**, $L_D > L_\lambda$ whereas in case **UR**, $L_D \ll L_\lambda$. In Section 7.4, we will see that the physical test case in solar chromosphere conditions corresponds to cases where $L_D \ll L_\lambda$.

The right state and the left state have been initialized with the values given in Table 7.2. The left state of the travelling wave has been computed using Rankine-Hugoniot relations for the heavy particles variables and jump conditions given in (7.2.9) for the electronic variables.

Figure 7-4 show first that the travelling wave is well captured in the case **OR**: the dynamic of

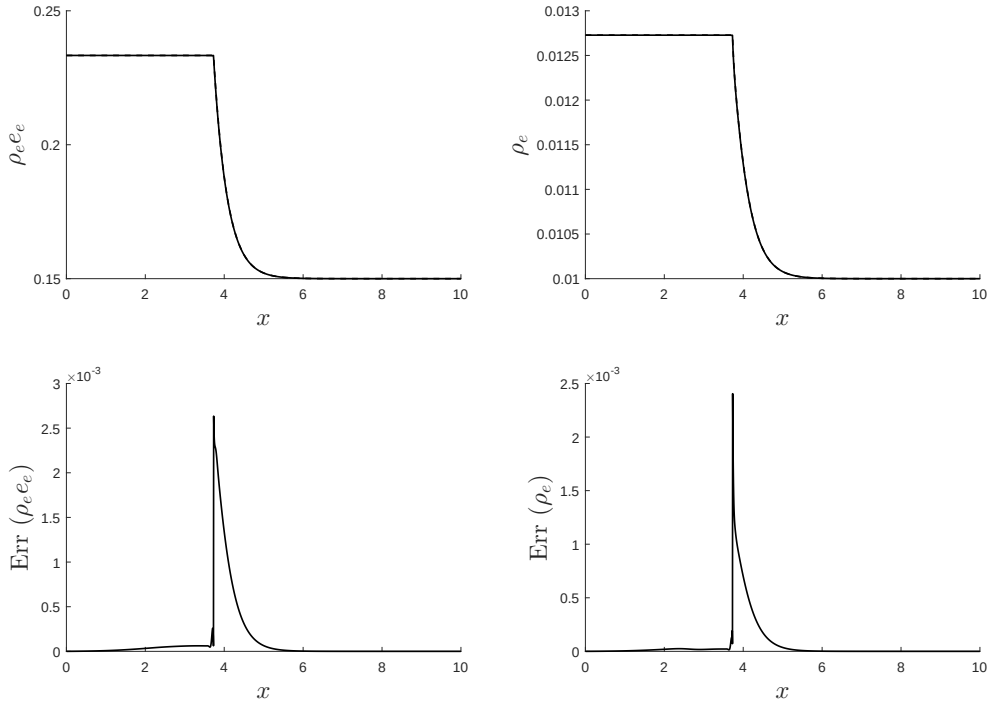

(a) Case **OR**

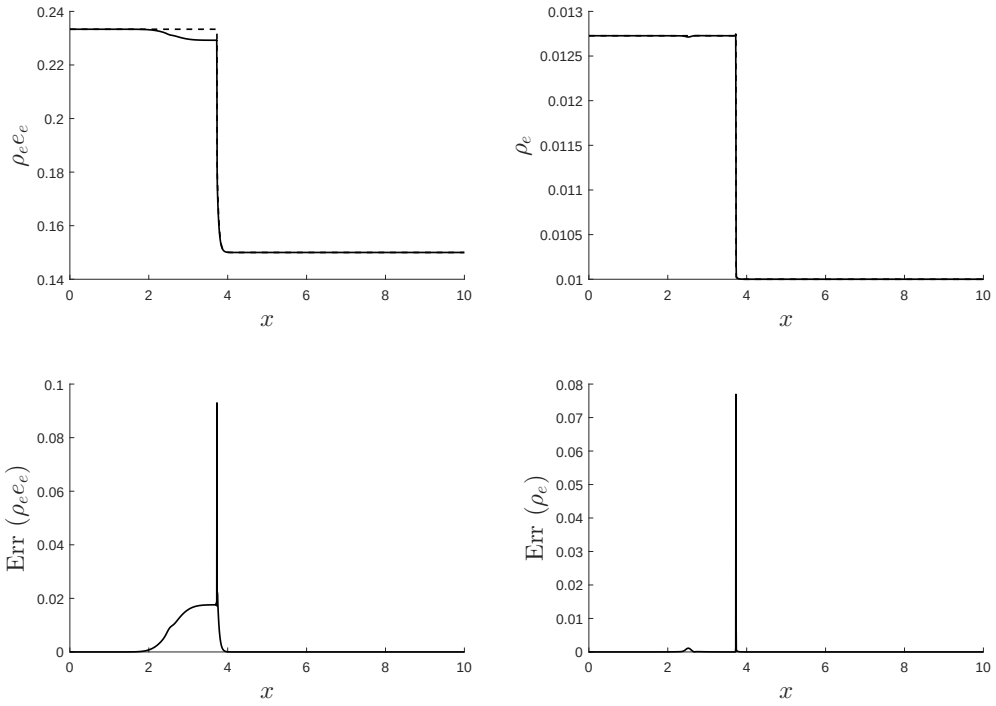

(b) Case **UR**

Figure 7-4: Top: analytical solution (dashed line), numerical solution (full line) for the travelling wave at $t = t_f = 1$. Bottom: relative error (Err). Left: internal energy of electrons $\bar{\rho}_{\mathfrak{e}}\bar{e}_{\mathfrak{e}}$. Right: density of electrons $\bar{\rho}_{\mathfrak{e}}$.

Table 7.1: Values of the diffusion coefficient D used in the numerical experiments

	case **OR**	case **UR**
D	10^{-1}	10^{-3}
L_D	3.055×10^{-1}	3.055×10^{-3}
Number of nodes in L_D	61.1	0.611

Table 7.2: Right and left states of the travelling wave

	$\bar{\rho}_{\mathfrak{h}}$	$\bar{\rho}_{\mathfrak{e}}$	$\bar{p}$	$\bar{p}_{\mathfrak{e}}$	$\bar{\boldsymbol{v}}_{\mathfrak{h}}$	Mach number
right state R	1	0.01	1	0.1	0.2	1.1832
left state L	1.274	0.01274	1.5	0.1556	0.527	0.8563

the travelling wave is preserved if the number of nodes in the length L_D is large enough; second, that a non-expected artificial numerical shock appears in the case **UR**. Two main contributions to the difference between the numerical and analytical solutions can be exhibited: a contribution upstream of the shock due to the numerical dissipation in the regular part of the travelling wave; a contribution downstream of the shock due to the error on the gradients in the discontinuity.

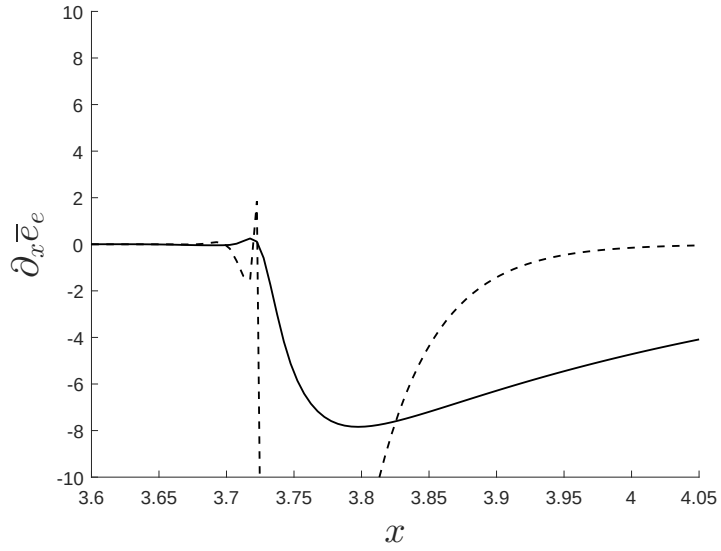

Figure 7-5: Gradient of $\bar{e}_{\mathfrak{e}}$ for case **OR** (full line) and case **UR** (dashed line) at $t = t_f = 1$.

Figure 7-5 represents the gradient of the electron energy $\boldsymbol{\partial}_{\boldsymbol{x}}\bar{e}_{\mathfrak{e}} = (\gamma-1)\boldsymbol{\partial}_{\boldsymbol{x}}\overline{T}_{\mathfrak{e}}$ close to the discontinuity for the cases **OR** and **UR** at $t = t_f = n_f\Delta t$, where n_f is the total number of iterations at the final time t_f. For each cell $1 \leq j \leq N$, the gradient is computed by means of a centered finite difference formula

$$(\boldsymbol{\partial}_{\boldsymbol{x}}\bar{e}_{\mathfrak{e}})_j^{n_f} = \frac{\bar{e}_{\mathfrak{e},j+1}^{n_f} - \bar{e}_{\mathfrak{e},j-1}^{n_f}}{2\Delta x}.$$

One can see that in the case **OR**, the gradient is small whereas in the case **UR**, a numerical artefact appears in the discontinuity. If the equality $\bar{T}_\mathfrak{e}'(0^+) = \bar{T}_\mathfrak{e}'(0^-)$ is verified numerically, one gets the proper travelling wave with the right jump condition. If not, an artefact is produced in the discontinuity, due to the poor resolution of the gradient in the discontinuity, resulting in an artificial numerical shock.

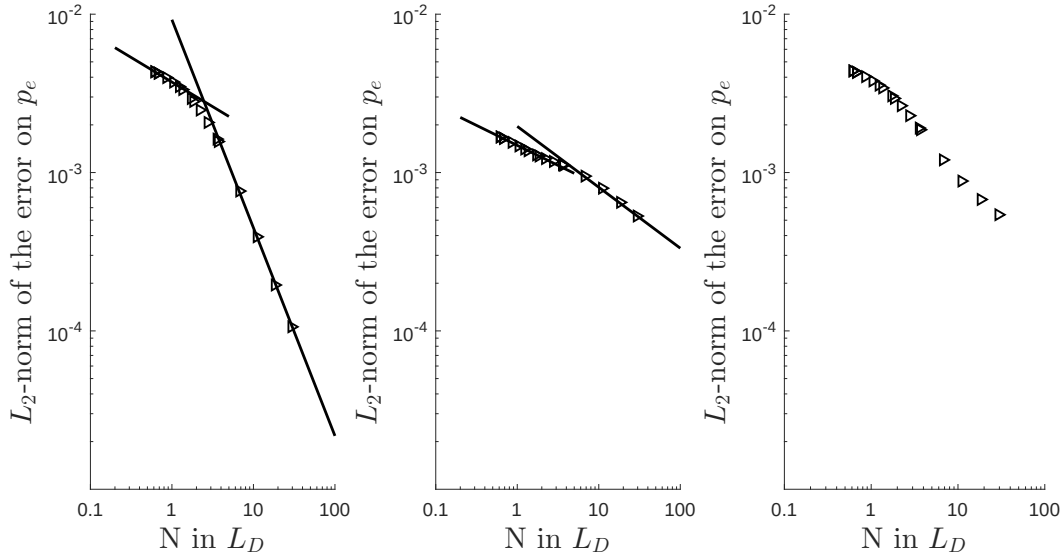

Figure 7-6: L_2-norm of the error on $\bar{p}_\mathfrak{e}$ with respect to the number of nodes in L_D. Left: downstream domain contribution (slopes of the lines: 0.3324 and 1.314); middle: upstream domain contribution (slopes of the lines: 0.2541 and 0.3846); right: full domain contribution.

Figure 7-6 shows the error in L_2-norm of $\bar{p}_\mathfrak{e}$ in function of the number of nodes in L_D, downstream and upstream of the shock. For the two areas studied, the dynamics of the L_2 norm of the error on $\bar{p}_\mathfrak{e}$ is the same: when the resolution of the wave is increasing, this norm is decreasing. Downstream of the shock, one can identify two dynamics for the L_2 norm. It can also be noted that the dynamic is changing when the error in L_2 norm downstream of the shock becomes greater than upstream of the shock. Moreover, it is exactly at these resolutions that we begin to observe the appearance of an artificial shock.

The conclusive remark of these numerical experiments is the following. If the gradients in the discontinuity are well resolved (that is the case when the spatial mesh is fine enough), then, the travelling wave is well captured; if not, an artificial numerical shock is produced and, in this case, the numerical dissipation is responsible of the dynamic of the travelling wave. While the wave is regularized, having a non-linear model with diffusion coming from physics implies that the conditions for solving the wave are identified. On the contrary, in systems based on general nonconservative hyperbolic equations, it is difficult to clearly identify how numerical dissipation impacts the resolution of the wave Abgrall & Karni (2010), Aregba-Driollet & Breil (2017).

Since the conditions for capturing the travelling wave have been identified, one wants to improve these results and build a new way for discretizing the nonconservative product allowing us to capture properly the travelling wave, even in weakly resolved cases. This is particularly relevant

in solar physics. Indeed, it will be seen in Section 7.4 that the structure of the travelling wave in the solar chromosphere conditions corresponds to a case where the characteristic length L_D is very small compared to the characteristic length L_λ. Consequently, using the presented standard scheme with the standard discretization of the nonconservative product, one would need a lot of nodes in order to capture properly the travelling wave.

7.3.3 Specific treatment of the nonconservative product

In this section, we develop an original method for discretizing the nonconservative term $N^n_{j,2}$. The idea is to express in a discretized sense the compatibility conditions (7.2.5) for the discontinuity, and deduce a new expression of the nonconservative term $N^n_{j,2}$ in order to satisfy these conditions. In that way, we aim at capturing the travelling wave even when the gradients are not fully resolved.

We consider the general scheme written in term of finite volumes (7.3.1) and specify the two vectorial coordinates by means of an index

$$\begin{cases} \mathcal{U}^{n+1}_{j,1} - \mathcal{U}^n_{j,1} + \dfrac{\Delta t}{\Delta x}(F^n_{j+1/2,1} - F^n_{j-1/2,1}) = 0 + \dfrac{\Delta t}{\Delta x}(G^n_{j+1/2,1} - G^n_{j-1/2,1}), \\ \mathcal{U}^{n+1}_{j,2} - \mathcal{U}^n_{j,2} + \dfrac{\Delta t}{\Delta x}(F^n_{j+1/2,2} - F^n_{j-1/2,2}) = N^n_{j,2} + \dfrac{\Delta t}{\Delta x}(G^n_{j+1/2,2} - G^n_{j-1/2,2}). \end{cases} \tag{7.3.3}$$

According to the relation found in (7.2.5), the jump of the gradient of $\bar{p}_\mathfrak{e}$ in the discontinuity is the same in the electron mass and electron thermal energy equations. In the discretized sense, one can simply link these two equations by multiplying the electron mass equation by a temperature $\overline{T}^n_{\mathfrak{e},j} = (\gamma - 1)\mathcal{U}^n_{j,2}/\mathcal{U}^n_{j,1}$:

$$\begin{cases} \overline{T}^n_{\mathfrak{e},j}(\mathcal{U}^{n+1}_{j,1} - \mathcal{U}^n_{j,1}) + \overline{T}^n_{\mathfrak{e},j}\dfrac{\Delta t}{\Delta x}(F^n_{j+1/2,1} - F^n_{j-1/2,1}) = \overline{T}^n_{\mathfrak{e},j}\dfrac{\Delta t}{\Delta x}(G^n_{j+1/2,1} - G^n_{j-1/2,1}), \\ \mathcal{U}^{n+1}_{j,2} - \mathcal{U}^n_{j,2} + \dfrac{\Delta t}{\Delta x}(F^n_{j+1/2,2} - F^n_{j-1/2,2}) = N^n_{j,2} + \dfrac{\Delta t}{\Delta x}(G^n_{j+1/2,2} - G^n_{j-1/2,2}). \end{cases} \tag{7.3.4}$$

According to (7.2.6), the derivative of the temperature $\overline{T}_\mathfrak{e}$ is continuous in the discontinuity so we have:

$$\overline{T}^n_{\mathfrak{e},j+1} - \overline{T}^n_{\mathfrak{e},j} = \overline{T}^n_{\mathfrak{e},j} - \overline{T}^n_{\mathfrak{e},j-1} \iff \overline{T}^n_{\mathfrak{e},j+1} - 2\overline{T}^n_{\mathfrak{e},j} + \overline{T}^n_{\mathfrak{e},j-1} = 0. \tag{7.3.5}$$

Consequently, the diffusive terms of the electron thermal energy equation (see (7.3.2)) can be simplified as

$$G^n_{j+1/2,2} - G^n_{j-1/2,2} = \frac{D\gamma}{\Delta x}\left(\mathcal{U}^n_{j+1,2} - 2\mathcal{U}^n_{j,2} + \mathcal{U}^n_{j-1,2}\right), \tag{7.3.6}$$

and coupled to second-order terms of the electron mass equation defined as

$$G^n_{j+1/2,1} - G^n_{j-1/2,1} = \frac{2D\,(\gamma - 1)}{\Delta x}\left[\frac{\left(\mathcal{U}^n_{j+1,2} - \mathcal{U}^n_{j,2}\right)}{\left(\overline{T}^n_{\mathfrak{e},j+1} + \overline{T}^n_{\mathfrak{e},j}\right)} - \frac{\left(\mathcal{U}^n_{j,2} - \mathcal{U}^n_{j-1,2}\right)}{\left(\overline{T}^n_{\mathfrak{e},j} + \overline{T}^n_{\mathfrak{e},j-1}\right)}\right], \tag{7.3.7}$$

Besides, the time derivative terms are not playing a role in the compatibility equation (7.2.5). We couple the electron mass equation with the electron thermal energy equation, providing a new expression for the nonconservative product:

$$N_{j,2}^n = \frac{\Delta_t}{\Delta_x}(F_{j+1/2,2}^n - F_{j-1/2,2}^n) - \frac{\gamma}{\gamma-1}\overline{T}_{\mathfrak{e},j}^n \frac{\Delta t}{\Delta x}(F_{j+1/2,1}^n - F_{j-1/2,1}^n) - \frac{\Delta t}{\Delta x}(H_{j+1/2}^n - H_{j-1/2}^n), \tag{7.3.8}$$

where the second-order terms of (7.3.8) are given by

$$H_{j\pm1/2}^n = \frac{\gamma}{2}(\overline{T}_{\mathfrak{e},j\pm1}^n - \overline{T}_{\mathfrak{e},j}^n)G_{j\pm1/2,1}^n. \tag{7.3.9}$$

This expression of the nonconservative product $N_{j,2}^n$ verifies (7.2.5) in the discretized sense, that is to say: 1- the continuity of $\overline{T}_{\mathfrak{e}}$ in the discontinuity of the travelling wave verifying (7.3.5), 2- the conditions on the jump of the gradient of $\bar{p}_{\mathfrak{e}}$ in the discontinuity.

However, the expression found in (7.3.8) for $N_{j,2}^n$ makes the global scheme not consistent with the system ($M_{\bar{S}_2}$): it is necessary to add correction terms. We have obtained a scheme able to catch the travelling wave only in the weakly discretized case. However, the scheme is no longer consistent with the initial system.

Thus, we want to build a numerical scheme in order to get proper compensations of the different terms in discontinuities in order to verify (7.2.5) in the discretized sense, and at the same time, to add correction terms for getting the consistency in order to capture properly the regular parts of the travelling wave. To obtain the correction terms, we focus only on the first order terms of the expression of the nonconservative terms in (7.3.8). Then, we add first order correction terms in (7.3.8) to be consistent with the initial system ($M_{\bar{S}_2}$). There are several possibilities to define the correction terms. In this work, we have focused on the correction terms which involve the gradients of $\bar{\rho}_{\mathfrak{e}}\bar{e}_{\mathfrak{e}}$ and $\bar{e}_{\mathfrak{e}}$ (or $\overline{T}_{\mathfrak{e}}$). By adding first order correction terms, the expression of the nonconservative product (7.3.8) reads:

$$N_{j,2}^{n\,*} = N_{j,2}^n - \Delta t(\gamma-1)\bar{v}_{\mathfrak{h},j}^n \frac{\mathcal{U}_{j,2}^n - \mathcal{U}_{j-1,2}^n}{\Delta x} + \Delta t \frac{\gamma}{\gamma-1}\bar{v}_{\mathfrak{h},j}^n \mathcal{U}_{j,1}^n \frac{\overline{T}_{\mathfrak{e},j}^n - \overline{T}_{\mathfrak{e},j+1}^n}{\Delta x}. \tag{7.3.10}$$

It is important to make sure that these additional correction terms are not playing any role in discontinuities, which could violate (7.2.5) in the discretized sense. We limit the impact of these additional terms in the discontinuities and one can show that the dynamic of the wave is not depending on the choice of the cut-off.

Figure 7-7 represent the L^2 norm of $\bar{p}_{\mathfrak{e}}$ in function of the number of nodes in L_D for three different way of discretizing the nonconservative product $N_{j,2}^n$. Results are presented for three methods: the standard way of discretizing $N_{j,2}^n$ described in 7.2, without correction terms of (7.3.8), and with correction terms $N_{j,2}^{n\,*}$ of (7.3.10). The formulation of the nonconservative product $N_{j,2}^n$ without correction terms is working well in the weakly discretized case for the travelling wave test cases. However, in the regularized case, an additional numerical shock is appearing and the L_2 norm is increasing with the number of nodes in L_D, because the scheme is not consistent. By adding correction terms and using the formulation of the nonconservative term $N_{j,2}^{n\,*}$ from (7.3.10),

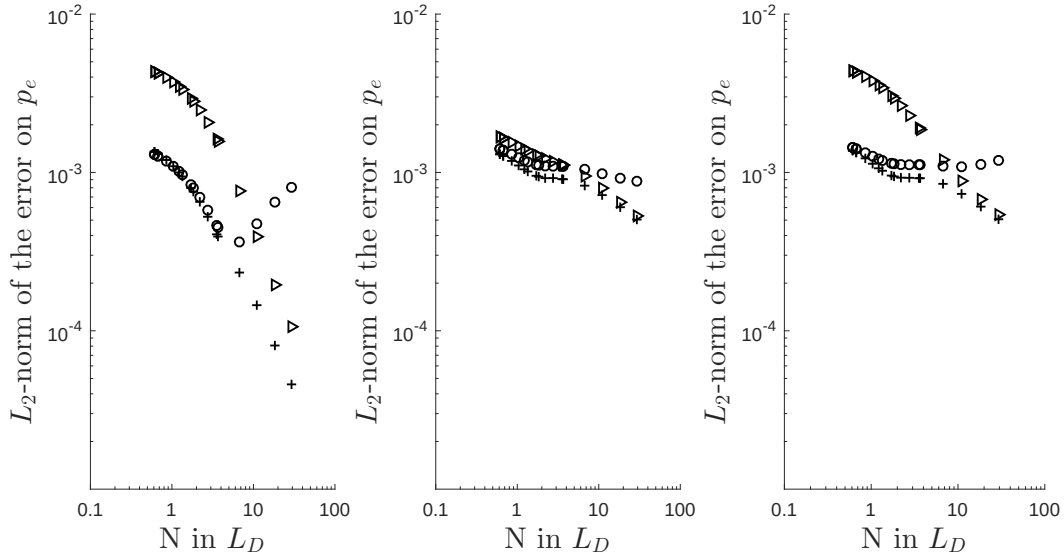

Figure 7-7: L^2-norm of the error on $\bar{p}_{\mathfrak{e}}$ with respect to the number of nodes in L_D, ▷ standard discretization, ∘ discretization without correction terms from (7.3.8), and + discretization with correction terms from (7.3.10). Left: downstream domain contribution; middle: upstream domain contribution; right: full domain contribution.

we have built a scheme which is able to capture the travelling wave in both the highly- and coarsely-resolved cases.

We could have built this numerical scheme because of the thorough understanding of the travelling wave linked to a good structure of the diffusion, as well as system allowing us to derive compatibility equations in the discontinuity.

7.4 Application in solar physics

In this section, we apply the previous development to a test case chosen so as to reproduce typical scales from solar chromosphere conditions. We study the ability of our scheme to resolve shock solutions in such conditions and design a specific numerical strategy based on the new scheme in order to cope with the nonconservative term. A 3-wave is considered by using the system ($M_{\bar{S}_2}$) with non-dimensional quantities for building the travelling wave in the solar chromosphere conditions.

First, we use atmospheric parameters from the model C of Vernazza et al. (1981) where the values of these parameters are given at 52 depth in the atmosphere from the low corona to the photosphere. For the purpose of the work, we have focused on the photospheric level at the heigth $h = 0\,km$. We consider $\bar{p}_{\mathfrak{e}}^R = \bar{p}_{\mathfrak{h}}{}^R$ at the right state, with only two species: electrons and protons H^+ as heavy particles. The transport coefficients D and λ are computed using third-order Sonine polynomials approximation based on a spectral Galerkin method used by Magin & Degrez (2004); Wargnier et al. (2019) considering local thermodynamic equilibrium for the fully ionized gas.

Then, we non-dimensionalize these quantities with reference quantities. The characteristic length of diffusion $L_0 = L_D$ is chosen as the reference length. The density of heavy particle is chosen as the reference density ρ_0. The reference velocity v_0 is the Alfvén velocity defined as $v_0 = B_0/\sqrt{\mu_0\rho_0}$ where B_0 is the reference magnetic field, chosen as $B_0 = 100$ G, and μ_0 the vacuum permeability.

Table 7.3: Reference quantities at the photospheric level

$\rho_0\ (kg.m^{-3})$	$L_0\ (m)$	$v_0\ (m.s^{-1})$	$T_0\ (K)$	$P_0\ (Pa)$	$n_0\ (m^{-3})$
1.873×10^{-4}	1.747×10^{-6}	6.518×10^{2}	6420	9927.42	1.12×10^{23}

Finally, after non-dimensionalizing the governing equations with reference quantities from Table 7.3, the travelling wave is investigated using values from Table 7.4 and Table 9.1. We have chosen a number of nodes of either $N = 1000$ or $N = 5000$ and a length of the domain $L/L_0 = 2\times10^5$.

Table 7.4: Right and left states at infinity of the travelling wave

	$\bar{\rho}_\mathfrak{h}$	$\bar{\rho}_\mathfrak{e}$	$\bar{p}$	$\bar{p}_\mathfrak{e}$	$\bar{\boldsymbol{v}}_\mathfrak{h}$
right state R	1	5.44×10^{-4}	0.5974	0.2987	0.07
left state L	1.6962	9.23×10^{-4}	1.5	0.9454	0.6787

Table 7.5: Diffusion coefficients and related typical lengths

D	κ^R	L_D/L_0	L_λ/L_0	L/L_0
10.7853	121 970.96	1	11309	200 000

After initializing the travelling wave, three numerical schemes are compared. The first scheme, denoted **scheme A**, is the standard scheme based on a standard discretization of the nonconservative product introduced in Section 7.3, where the timestep, denoted Δt_F, is limited by a Fourier stability condition, thus involving the largest diffusion coefficient, that is the electron thermal diffusivity κ^R. The second scheme, denoted **scheme B**, is based on the formulation of the nonconservative product described in (7.3.10), where the timestep is also limited by the same Fourier stability condition. The third scheme, denoted **scheme C**, is based on the formulation of the nonconservative product defined in (7.3.10), using an operator splitting approach based on a second-order Strang formalism in order to separate the convection and diffusion operators (see Strang (1968); Duarte et al. (2012); Descombes et al. (2014a); Duarte (2011)). The idea is to not be limited by the small timesteps Δt_F imposed by the Fourier stability condition, due to the electron thermal diffusivity. Concerning the **scheme C**, there are two possibilities for the operators : one can 1- gather diffusive terms and the nonconservative product, or 2- gather convective terms and the nonconservative product. In this work, we have focused on the second case. Indeed, according to (7.3.10), the expression of the nonconservative product depends on the thermal energy and density convective fluxes, which makes the second case a rather more natural choice. Besides, the computational time is drastically shorter in this case, since the nonconservative product is integrated only

one time during the convective timestep, whereas in the other case, the nonconservative product is integrated several times during the dissipative timestep.

The operators are splitted: one operator X corresponds to convective terms and the nonconservative product defined by (7.3.10), where the convective timestep, called Δt, is simply limited by a CFL condition; an other operator Y regroups diffusion terms, where the timestep Δt_F is computed based on the Fourier condition and integrated over several sub-timesteps in order to reach the convective timestep. The general scheme is summarized as follows:

$$U^{n+1} = Y^{\frac{\Delta t}{2}} X^{\Delta t} Y^{\frac{\Delta t}{2}} U^n. \tag{7.4.1}$$

In the proposed schemes, the values used for the convective timestep Δt and the diffusive timestep Δt_F are presented in Table 7.6. In order to perform the comparison between the timesteps used, we have compared them to the convective timestep $\Delta t = C \times \Delta x / \max(\bar{v}_{\mathfrak{h}}^R + c^R, \bar{v}_{\mathfrak{h}}^L + c^L)$ for $N = 1000$ and $N = 5000$, where the Courant number is $C = 0.2$.

Table 7.6: Timesteps used for the three schemes for $N = 1000$ and $N = 5000$

N	Δt	Δt_F
1000	2.233×10^1	4.095×10^{-1}
5000	4.466	1.64×10^{-2}

Results are presented in Figure 7-8a and Figure 7-8b for the electron energy $\bar{e}_{\mathfrak{e}}$, comparing the three schemes, at the final time $t = t_f = 30000$, for $N = 1000$ and $N = 5000$. In the solar chromosphere conditions, the characteristic scales are such that $L_\lambda \gg L_D$, because the electron diffusivity is much higher than the electron diffusion coefficient in such conditions. In the test case, the smallest spatial scale to be resolved is the length L_D, which is the characteristic scale related to the resolution of the travelling wave. By fixing the number of nodes N and the length of the domain L based on Table 9.1, the test case can be identified as a very weakly-resolved travelling wave test case.

In Figure 7-8a and Figure 7-8b, the standard scheme exhibits artificial numerical shock since the smallest scale is not properly resolved and small timesteps Δt_F have to be used, as expected. Switching to a proper treatment of the nonconservative term allows to reduce by a factor of 9, for $N = 5000$, the amplitude of the error on the electron temperature and to reduce drastically the artificial numerical shock, thus leading to a satisfactory level of resolution. However, using the new scheme based on Strang splitting operator techniques combined to the new formulation of the nonconservative product (**scheme C**) leads to an additional improvement of the resolution of all the scales of the travelling wave. The travelling wave can be well captured, while using splitting timesteps of the order of the convective CFL stability limitation, thus leading to a minimal amount of numerical dissipation in the convective step. In fact, based on the results obtained in the previous section, a good approximation of the travelling wave obtained with the **scheme A** would require several nodes in the characteristic length L_D thus leading to about a million nodes. In this context, the corresponding convective timestep and the diffusive timestep would be respectively $\Delta t = 8.94 \times 10^{-2}$ and $\Delta t_F = 4.01 \times 10^{-7}$ and the original scheme would become useless.

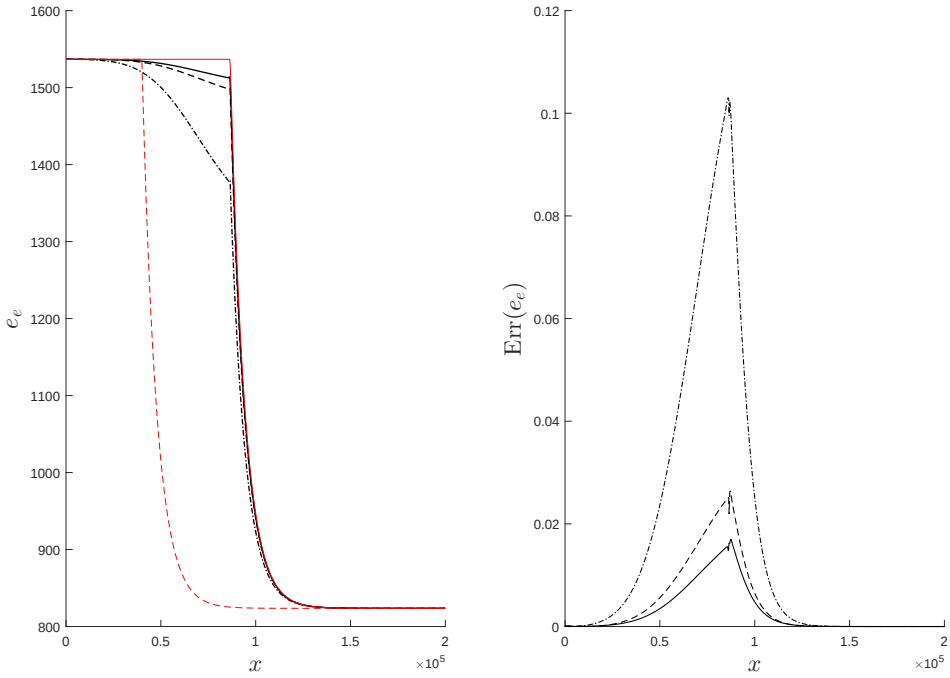

(a) $N = 1000$

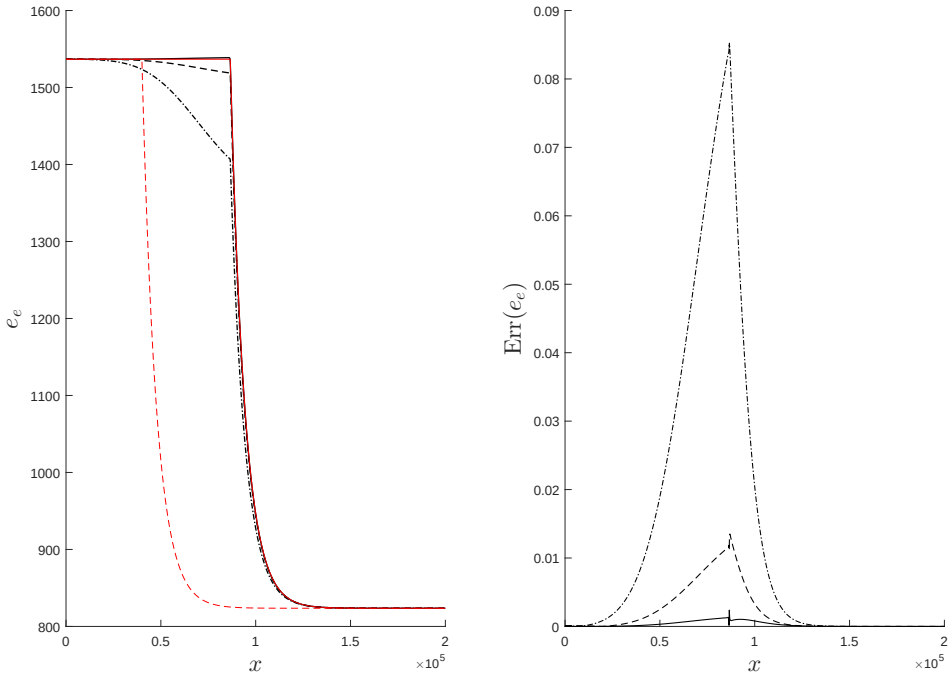

(b) $N = 5000$

Figure 7-8: Electron energy ($\bar{e}_e$) and relative error (Err) for the solar test case based on the values from Table 7.4 and Table 9.1. Exact solution at $t = 0$ (red dashed line) and $t = 30000$ (red full line). Numerical solution for **scheme A** (semi-dashed line), **scheme B** (dashed line), and **scheme C** (full line), at the final time $t = 30000$.

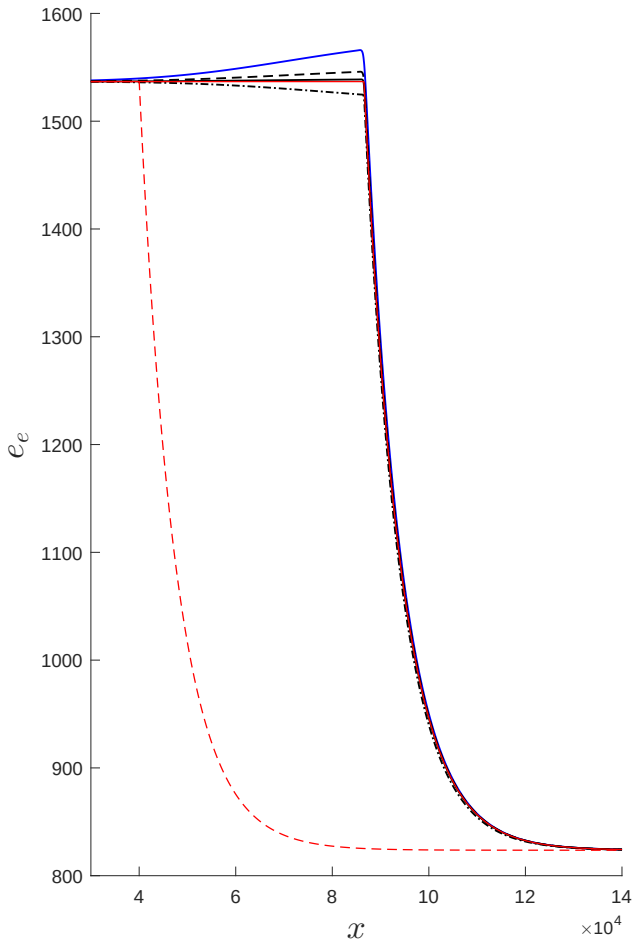

Figure 7-9: Electron energy ($\bar{e}_\epsilon$) for the solar test case based on the values from Table 7.4 and Table 9.1. Exact solution at $t = 0$ (red dashed line) and $t = 30000$ (red full line). Numerical solution for **scheme C** at the final time $t = 30000$, for $N = 5000$ in the domain $[30000, 140000]$ for several Courant number $C = 5 \times 10^{-2}$ (semi-dashed line), $C = 0.2$ (full black line), $C = 0.3$ (dashed line), $C = 0.4$ (full blue line).

In order to perform the analysis of the error generated by the splitting operation, several splitting timestep Δt have been tested for the presented test case, used in the **scheme C**. Results for several Courant number $C \in \{0.05, 0.2, 0.3, 0.4\}$ are shown in Figure 7-9, for $N = 5000$, at $t = 30000$. These results show that when the splitting timestep becomes too important (for Courant numbers $C = 0.3$ or $C = 0.4$), the travelling wave is no longer captured with a high level of accuracy, and an additional numerical artefact is obtained. However, for a splitting timestep where the Courant number is $C = 0.2$, we notice that the numerical solution is shown to be optimal.

7.5 Results for the fully coupled problem (M_S)

In this chapter, we have focused so far on the decoupled problem ($M_{\bar{S}_1}$) and ($M_{\bar{S}_2}$). In the case of the fully coupled problem (M_S), the problem is in fact very similar to the decoupled problem and one can solve for travelling wave solutions as well. However, we get a numerical solution instead of a complete analytical solution. In this study, we also consider a 3-wave.

7.5.1 Travelling wave solution and compatibility equations

In the fully coupled system (M_S), we solve for a travelling wave where the structure corresponds to 1- a constant state L, a weak discontinuity (smooth function with jump of derivative) and a regularization up to a constant state R for the electron variables $(p_\mathfrak{e}, \rho_\mathfrak{e})$ and 2- a constant state L, a discontinuity connecting state L to an intermediary state 0 and a regularization from state 0 to a constant R for the heavy variables $(\mathcal{E}, \boldsymbol{v}_\mathfrak{h}, \rho_\mathfrak{h})$. The structure of the wave is represented in Figure 7-10. The jump conditions are the Rankine-Hugoniot conditions, the thermal energy of electrons requires a numerical integration and the velocity jump is coupled to the weak jump of the electron variables. Actually, the structure of the wave for the heavy particles is very similar to the one identified by Zel'dovich & Raizer (1967) in §3, where the role of the heat conduction on the structure of the shock wave in gases has been studied.

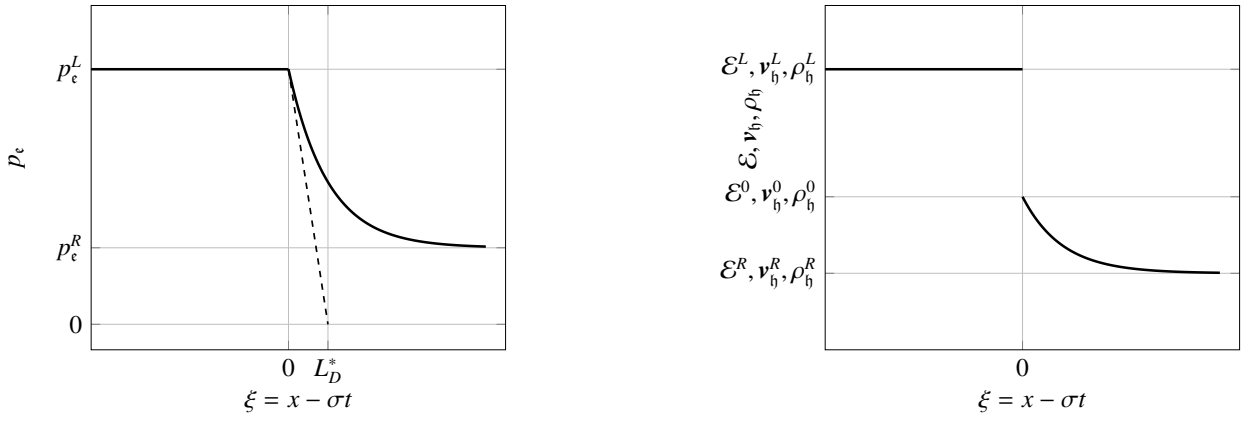

Figure 7-10: Structure of the travelling wave for the fully coupled problem (M_S)

Thus, the system (M_S) of partial differential equations becomes a system of ordinary differential equations:

$$\begin{cases} -\sigma\rho_{\mathfrak{h}}' + (\rho_{\mathfrak{h}}\boldsymbol{v}_{\mathfrak{h}})' = 0, \\ -\sigma(\rho_{\mathfrak{h}}\boldsymbol{v}_{\mathfrak{h}})' + (\rho_{\mathfrak{h}}\boldsymbol{v}_{\mathfrak{h}}^2 + p)' = 0, \\ -\sigma(\mathcal{E})' + (\mathcal{E}\boldsymbol{v}_{\mathfrak{h}} + p\boldsymbol{v}_{\mathfrak{h}})' = \lambda\, T_{\mathfrak{e}}'' + \frac{\gamma}{\gamma-1} D\, p_{\mathfrak{e}}'', \\ -\sigma\rho_{\mathfrak{e}}' + (\rho_{\mathfrak{e}}\boldsymbol{v}_{\mathfrak{h}})' = D(\frac{1}{T_{\mathfrak{e}}}p_{\mathfrak{e}}')', \\ -\frac{1}{\gamma-1}\sigma\, p_{\mathfrak{e}}' + \frac{1}{\gamma-1}(p_{\mathfrak{e}}\boldsymbol{v}_{\mathfrak{h}})' = -p_{\mathfrak{e}}\boldsymbol{v}_{\mathfrak{h}}' + \lambda\, T_{\mathfrak{e}}'' + \frac{\gamma}{\gamma-1} D\, p_{\mathfrak{e}}'', \end{cases} \tag{7.5.1}$$

As performed in the Section 7.2.1, we investigate the ordinary differential equations (7.5.1) at $\xi = 0$ in order to obtain the compatibility equations. Since $p_{\mathfrak{e}}$ and $\rho_{\mathfrak{e}}$ (and $T_{\mathfrak{e}}$) are continuous functions, the system (7.5.1) leads to

$$\begin{cases} [\rho_{\mathfrak{h}}\,(\boldsymbol{v}_{\mathfrak{h}} - \sigma)]_{(0)} = 0, \\ [m_{\mathfrak{h}}\boldsymbol{v}_{\mathfrak{h}} + p]_{(0)} = 0, \\ [\mathcal{E}\,(\boldsymbol{v}_{\mathfrak{h}} - \sigma) + p\boldsymbol{v}_{\mathfrak{h}}]_{(0)} = \lambda[T_{\mathfrak{e}}']_{(0)} + \frac{\gamma}{\gamma-1} D[p_{\mathfrak{e}}']_{(0)},, \\ p_{\mathfrak{e}}(0)[\boldsymbol{v}_{\mathfrak{h}}]_{(0)} = D[p_{\mathfrak{e}}']_{(0)}, \\ \frac{\gamma}{\gamma-1} p_{\mathfrak{e}}(0)[\boldsymbol{v}_{\mathfrak{h}}]_{(0)} = \lambda[T_{\mathfrak{e}}']_{(0)} + \frac{\gamma}{\gamma-1} D[p_{\mathfrak{e}}']_{(0)}, \end{cases} \tag{7.5.2}$$

where $m_{\mathfrak{h}} = \rho_{\mathfrak{h}}^0(\boldsymbol{v}_{\mathfrak{h}}^0 - \sigma) = \rho_{\mathfrak{h}}^L(\boldsymbol{v}_{\mathfrak{h}}^L - \sigma)$, and σ is defined by the Rankine-Hugoniot condition. Then, combining the equation of internal energy and density of electrons in (7.5.2), we obtain the compatibility equations for the full system

$$\begin{cases} [\rho_{\mathfrak{h}}\,(\boldsymbol{v}_{\mathfrak{h}} - \sigma)]_{(0)} = 0, \\ [m_{\mathfrak{h}}\boldsymbol{v}_{\mathfrak{h}} + p]_{(0)} = 0, \\ [\mathcal{E}\,(\boldsymbol{v}_{\mathfrak{h}} - \sigma) + p\boldsymbol{v}_{\mathfrak{h}}]_{(0)} = \frac{\gamma}{\gamma-1} D[p_{\mathfrak{e}}']_{(0)}, \\ p_{\mathfrak{e}}(0)[\boldsymbol{v}_{\mathfrak{h}}]_{(0)} = D[p_{\mathfrak{e}}']_{(0)}, \\ [T_{\mathfrak{e}}']_{(0)} = 0 \end{cases} \tag{7.5.3}$$

In (7.5.3), the compatibility equations at $\xi = 0$ for the internal energy and density of electrons are identical to those obtained in the previous sections. Except that, the jump of velocity is coupled with the compatibility equation for the total energy $\mathcal{E}$. We retrieve the fact that 1- the derivative of $T_{\mathfrak{e}}$ in the discontinuity is continuous and 2- the jump of the gradient $p_{\mathfrak{e}}$ is coupled with the jump of the velocity and the value of the electron pressure at the discontinuity. Here again the right hand side term of the fourth relation is the sum of the convective term of the internal energy of electron and nonconservative product. In addition, the first two compatibility equations remain independent from the last three equations, and give the jump of the total pressure and density of heavy-particle.

In this subsection, we have exhibit the structure of the travelling wave, the jump conditions for all the variables except the internal energy of electron which require a numerical integration. In addition, similarly as the decoupled problem, we have shown the compatibility equations which are identical except that an additional compatibility equation related the total energy is considered. In

order to obtain the missing jump relation and the travelling wave solution for $\xi > 0$, it is necessary to integrate (7.5.1). The latter is investigated in the next subsection.

7.5.2 Numerical integration and jump relations

In order to get an accurate estimation of the missing jump condition for the electron thermal energy of as a function of the Mach number M_R as well as the structure of the travelling wave, we integrate the ordinary differential equations of (7.5.1) using a Dormand-Prince (RKDP) method or DOPRI853 method (see Dormand & Prince (1980)). In the case of a 3-wave, we initialize the travelling wave from state L and, by numerical integration, compute the corresponding state R. In order to get an accurate estimation of the missing jump condition, a shooting method is used. The steps of the shooting method are the following: 1- we start the numerical integration of the travelling wave using the state L of the **case OR** in Section 7.3.2 of the decoupled problem, then 2- a state R associated to the initial state L is computed, finally 3- a dichotomy is used by initializing different state L until a good approximation of the expected state R is found. The missing jump condition of the fully coupled problem as a function of the Mach number can thus be obtained.

The results of the numerical integration are presented in Figure 7-11. The estimated jump condition for the fully coupled problem is compared with the jump conditions from the decoupled problem (7.2.9), (7.2.10) from the model M^{ent}, and (7.2.11) from the model M^{src}. The jump conditions of the decoupled problem (7.2.9) give a very good approximation of the jump conditions of the fully coupled problem in a reasonable Mach number range M_R close to one. Besides, in the fully coupled case, no singularities have been observed for the jump condition of $p_{\mathfrak{e}}$ and $T_{\mathfrak{e}}$ for the whole range of Mach number. The results show that the jump conditions from the conservative models M^{ent} and M^{src} clearly underestimated the post-shock temperature.

Finally, if having an analytical expression of the travelling wave for the fully coupled problem is not possible, relying on the same strategy designed in the study of the decoupled problem, we are able to analyze the fully coupled case. By integrating the ordinary differential equations of the fully coupled problem (7.5.1), we get the structure of the travelling wave as well as an evaluation of the missing jump condition of the internal energy of electron.

From this study, two conclusions can be drawn: 1- Relying on the missing jump condition proposed in the literature through various approximation yields a very poor approximation of the effective jump conditions, even in a Mach number range close to one and the present study allows to derive the physically sound jump conditions, 2- Focusing on the decoupled problem, at least in a reasonable Mach number range around one, is fully justified since it provides a very good approximation of the effective jump conditions.

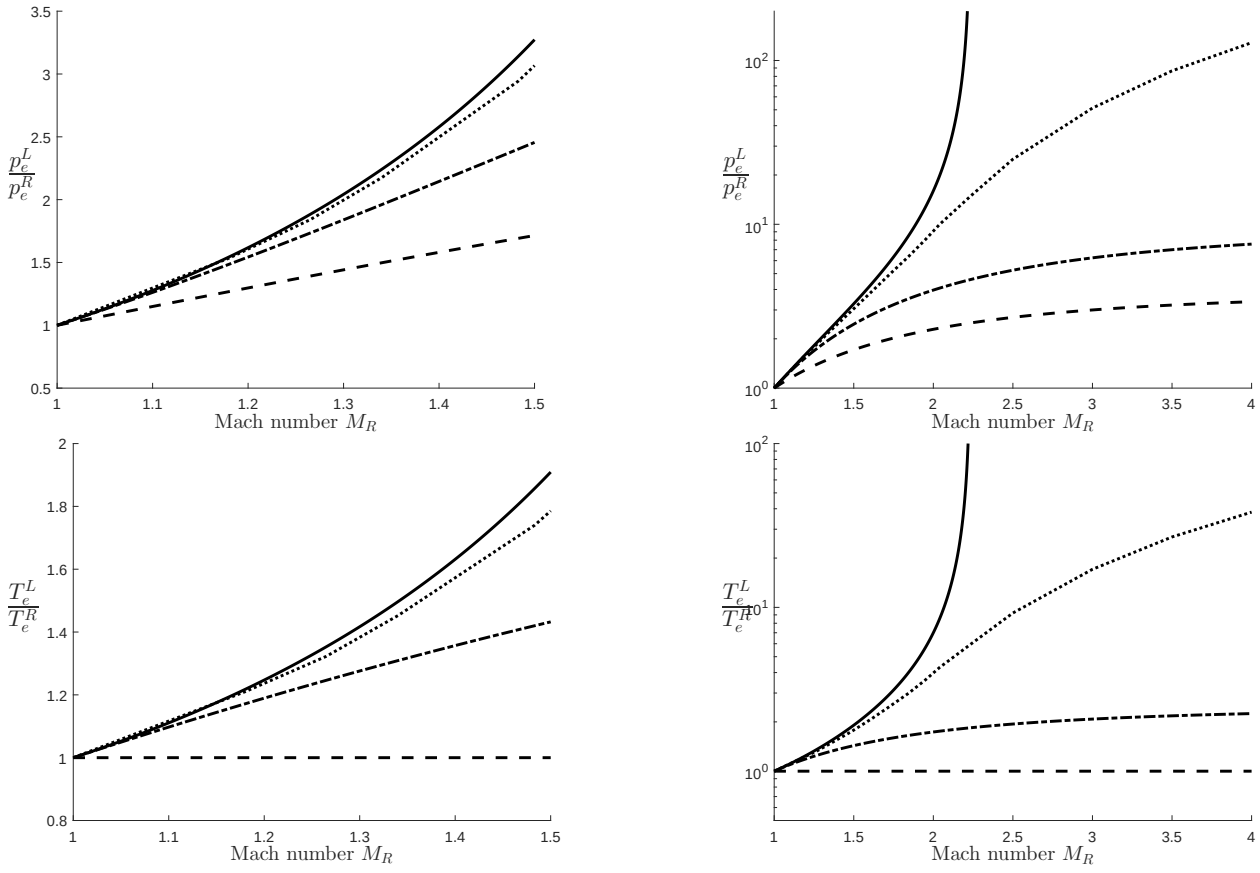

Figure 7-11: Jump of $p_{\mathfrak{e}}$ and $T_{\mathfrak{e}}$ as a function of the Mach number M_R. **In full line**: the jump from the decoupled system ($M_{\bar{S}_2}$), in **semi dashed-line**: model M^{ent} from the system (M^{ent}), in **dashed line**: model M^{src} from the system (M^{src}), in **dotted line**: jump from the fully coupled system from (M_S)

7.6 Particular case with an electric field

In this section, we focus on a particular case where we extend the ideas investigated in the previous Section 7.2 by considering the electric field in the subsystem of electrons. We exhibit the structure of the travelling wave and the corresponding jump relations. In this particular case, we will see that the strategy and development performed in the previous section are identical.

In this framework, if the electric field is considered, the system ($M_{\overline{S}_2}$) is modified to

$$\begin{cases} \partial_t \bar{\rho}_e + \boldsymbol{\partial_x}\cdot(\bar{\rho}_e \bar{\boldsymbol{v}}_h) = \boldsymbol{\partial_x}\cdot(\frac{1}{\overline{T}_e} D\left[\boldsymbol{\partial_x}\bar{p}_e - \bar{\rho}_e q_e \overline{\boldsymbol{E}}\right]), \\ \partial_t(\bar{\rho}_e \bar{e}_e) + \boldsymbol{\partial_x}\cdot(\bar{\rho}_e \bar{e}_e \bar{\boldsymbol{v}}_h) = -\bar{p}_e \boldsymbol{\partial_x}\cdot\bar{\boldsymbol{v}}_h + \boldsymbol{\partial_x}\cdot(\lambda \boldsymbol{\partial_x}\overline{T}_e + \frac{\gamma}{\gamma-1} D\left[\boldsymbol{\partial_x}\bar{p}_e - \bar{\rho}_e q_e \overline{\boldsymbol{E}}\right]), \\ \boldsymbol{\partial_x}\cdot\overline{\boldsymbol{E}} = q_e \dfrac{\bar{\rho}_h - \bar{\rho}_e}{\varepsilon_0} \end{cases} \tag{7.6.1}$$

As shown in (7.6.1), the dynamic of the electric field $\overline{\boldsymbol{E}}$ is defined by the Gauss's law. Here, for the sake of simplicity, we assume that $\varepsilon = 1$, thus $m_e = m_h = 1$. we look for piecewise smooth travelling wave for both the electron variables and electric field that propagate at the velocity σ. More precisely, $\overline{\boldsymbol{E}}$ is assumed to satisfy

- $\overline{\boldsymbol{E}} : \xi \mapsto \overline{\boldsymbol{E}}(\xi) \in C^0(\mathbb{R})$,
- $\overline{\boldsymbol{E}}$ is C^∞ on $(-\infty, 0)$ and $(0, +\infty)$,
- $\overline{\boldsymbol{E}}$ admits limits in $\pm\infty$ denoted by

$$\lim_{\xi\to-\infty} \overline{\boldsymbol{E}}(\xi) = \lim_{\xi\to+\infty} \overline{\boldsymbol{E}}(\xi) = 0,$$

In this framework, the electroneutrality is assumed at infinite states, but an induced electric field is allowed in the small diffusion region of the electrons. Here, the induced electric field is due to the decoupling between heavy particles and electrons.

Similarly as the previous subsection, we look for piecewise smooth travelling wave for both the electron variables and the electric field that propagate at the velocity σ. We consider that the heavy-particle variables read as piecewise constant functions. We assume that the right state R is known, and we look for state L connected to the state R. We investigate the system in three domains: $\xi > 0$, $\xi < 0$ and the interface at $\xi = 0$. System (7.6.1) of partial differential equations becomes a system of ordinary differential equations:

$$\begin{cases} -\sigma\bar{\rho}_e' + (\bar{\rho}_e \bar{\boldsymbol{v}}_h)' = \left(\dfrac{D}{T_e}\left[\bar{p}_e'' - (\bar{\rho}_e q_e \overline{\boldsymbol{E}})\right]\right)', \\ -\frac{1}{\gamma-1}\sigma\,\bar{p}_e' + \frac{1}{\gamma-1}(\bar{p}_e \bar{\boldsymbol{v}}_h)' = -\bar{p}_e \bar{\boldsymbol{v}}_h' + \lambda\,\overline{T}_e'' + \frac{\gamma}{\gamma-1}\left(D\left[\bar{p}_e'' - (\bar{\rho}_e q_e \overline{\boldsymbol{E}})\right]\right)', \\ \overline{\boldsymbol{E}}' = q_e \dfrac{\bar{\rho}_h - \bar{\rho}_e}{\varepsilon_0} \end{cases} \tag{7.6.2}$$

As shown in Section 7.2.1, at $\xi = 0$, since $\bar{p}_\mathfrak{e}$ and $\bar{\rho}_\mathfrak{e}$ (and $\overline{T}_\mathfrak{e}$) are continuous functions, the system (7.6.2) leads to the following compatibility equations

$$\begin{cases} \bar{p}_\mathfrak{e}(0)[\bar{v}_\mathfrak{h}]_{(0)} = D[\bar{p}'_\mathfrak{e}]_{(0)},, \\ \frac{\gamma}{\gamma-1}\bar{p}_\mathfrak{e}(0)[\bar{v}_\mathfrak{h}]_{(0)} = \lambda[\overline{T}'_\mathfrak{e}]_{(0)} + \frac{\gamma}{\gamma-1}D[\bar{p}'_\mathfrak{e}]_{(0)}, \\ [\overline{\boldsymbol{E}}']_{(0)} = 0 \end{cases} \tag{7.6.3}$$

or, equivalently,

$$\begin{cases} \bar{p}_\mathfrak{e}(0)[\bar{v}_\mathfrak{h}]_{(0)} = D[\bar{p}'_\mathfrak{e}]_{(0)},, \\ [\overline{T}'_\mathfrak{e}]_{(0)} = 0, \\ [\overline{\boldsymbol{E}}']_{(0)} = 0, \end{cases} \tag{7.6.4}$$

In summary, the compatibility equations for the electronic variables are identical to those obtained in Section 7.2. An additional compatibility equation for the electric field has been obtained, showing that the derivative of the electric field is continuous in the discontinuity at $\xi = 0$.

Then, we investigate the system (7.6.2) for $\xi > 0$. We obtain

$$\begin{cases} \bar{\rho}'_\mathfrak{e}(\bar{v}^R_\mathfrak{h} - \sigma) = \left(\dfrac{D}{\overline{T}_\mathfrak{e}}\left[\bar{p}''_\mathfrak{e} - (\bar{\rho}_\mathfrak{e} q_\mathfrak{e}\overline{\boldsymbol{E}})\right]\right)', \\ \frac{1}{\gamma-1}\bar{p}'_\mathfrak{e}(\bar{v}^R_\mathfrak{h} - \sigma) = \lambda\, \overline{T}''_\mathfrak{e} + \frac{\gamma}{\gamma-1}\left(D\left[\bar{p}''_\mathfrak{e} - (\bar{\rho}_\mathfrak{e} q_\mathfrak{e}\overline{\boldsymbol{E}})\right]\right)', \\ \overline{\boldsymbol{E}}' = q_\mathfrak{e}\dfrac{\bar{\rho}^R_\mathfrak{h} - \bar{\rho}_\mathfrak{e}}{\varepsilon_0} \end{cases} \tag{7.6.5}$$

After some algebra (integration of the first two systems as performed in the section), we obtain a linear system with source terms

$$\begin{pmatrix} \bar{p}_\mathfrak{e} - \bar{p}^R_\mathfrak{e} \\ \overline{T}_\mathfrak{e} - \overline{T}^R_\mathfrak{e} \\ \overline{\boldsymbol{E}} \end{pmatrix}' = \eta^R \begin{pmatrix} 1 & -\bar{\rho}^R_\mathfrak{e} & 0 \\ -r^R\frac{\gamma-1}{\gamma\bar{\rho}^R_\mathfrak{e}} & r^R & 0 \\ 0 & 0 & 0 \end{pmatrix} \begin{pmatrix} \bar{p}_\mathfrak{e} - \bar{p}^R_\mathfrak{e} \\ \overline{T}_\mathfrak{e} - \overline{T}^R_\mathfrak{e} \\ \overline{\boldsymbol{E}} \end{pmatrix} + \begin{pmatrix} \frac{\bar{p}_\mathfrak{e}}{\overline{T}_\mathfrak{e}} q_\mathfrak{e}\overline{\boldsymbol{E}} \\ -\gamma r^R \overline{T}^R_\mathfrak{e} \\ q_\mathfrak{e}\frac{\bar{\rho}^R_\mathfrak{h} - \bar{\rho}_\mathfrak{e}}{\varepsilon_0} \end{pmatrix} \tag{7.6.6}$$

Similarly, the case $\xi < 0$ can be obtained simply by replacing R by L in (7.6.6) and (7.6.5). Unlike the Section 7.2.1, it is not possible to easily obtain an analytical solution for the system (7.6.6) for $\xi > 0$ and $\xi < 0$. Thus, a numerical integration is required.

In this framework, it is necessary to define a numerical strategy in order to obtain the structure of the travelling wave. In order to perform this analysis, we have focused on the case **OR** where the structure and the jump conditions are well identified. Using an explicit Runge-Kutta method, we have integrated the system from $\xi = 0$ to $\xi = +\infty$. Thus, the initialization is based on the left state L of Table 7.2 and Table 7.1, and, in addition, we set $\overline{\boldsymbol{E}}(\xi = 0) = 0$. Besides, we have used $q_\mathfrak{e} = 10^{-2}$ and $\varepsilon_0 = 10^{-2}$. For the numerical integration, the values of the constants $T^R_\mathfrak{e}$, $\bar{p}^R_\mathfrak{e}$ and $\rho^R_\mathfrak{h}$ have been chosen from Table 7.2 and Table 7.1. By such a choice, we want to make use of our

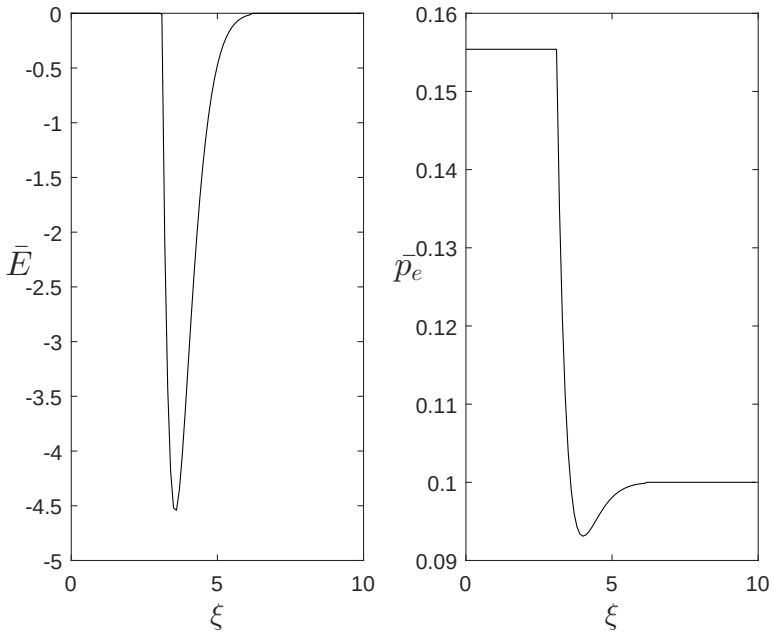

Figure 7-12: Distribution of the electric field $\overline{\boldsymbol{E}}$ and pressure of electrons $\bar{p}_{\mathfrak{e}}$

analysis based the decoupled problem without the electric field, where the left and right state have been found analytically. In addition, 10000 points have been used for the integration. The results have been obtained in Figure 7-12.

The integration shows that an induced electric field is created in the diffusion/decoupling region between the electrons and the heavy particles. But the field remains electrically neutral at the infinity states. In addition, we found numerically that, the right state for the electronic pressure is identical to the case where there is no electric field Table 7.2. On the other hand, the electric field disturbs the electronic pressure in the diffusion region.

Finally, the structure of the travelling wave remains similar to the case without electric field, and we note by this study that the jump conditions are identical. In the diffusion region, where we have a decoupling between the electrons and the heavy particles, an induced electric field is formed and disturbs the structure of the electronic pressure field. After identifying the compatibility equations in (7.6.4), we can easily extend the ideas of the Section 7.3.3, in order to develop a numerical method with specific treatment of the non-conservative term to capture this travelling wave even in cases where the discontinuity is under-resolved.

Conclusion

The general plasma model derived by Graille et al. (2009) has been presented in a simplified framework, without considering the electro-magnetic forces and under several assumptions, which inherits the difficulties of the general case in terms of evaluating jump conditions and simulating shock solutions. We have proposed a decoupling of the governing equations in order to derive an

analytic expression of the missing jump condition on the electron temperature. Even if valid for shock solutions in a range of Mach number close to one, we observe that this analytic jump condition is rather different from the jump conditions obtained in the literature and the discrepancies get worse as the Mach number increases. In order to reproduce numerically the structure of the travelling wave solution with the proper jump conditions, we have used a finite volume method of Godunov type. A naive consistant treatment of the nonconservative product proves that, for a fine resolution, the expected wave is well reproduced. We have verified the jump condition as well as the structure of the travelling wave obtained analytically and identified the required level of resolution in order to prevent the appearance of an additional artificial jump due to the numerical dissipation of the numerical scheme.

In this context, we have developed a numerical scheme with a specific treatment of the nonconservative product. The idea is to express the compatibility equations at the discontinuity of the travelling wave in a discretized sense. It gives the ability to predict the proper travelling wave even when the gradients are not fully resolved. We have thus built a scheme, which is able to capture the travelling wave in the highly- or weakly-resolved cases. Such a scheme is important since the weakly-discretized case is particularly relevant in the solar chromosphere conditions. We have also applied a Strang operator splitting technique in order to prevent the use of small time-steps limited by the presence of large diffusion terms and a Fourier stability condition. Eventually, a 1D travelling wave test case has been presented based on conditions found in the solar chromosphere, which allowed us to assess the numerical scheme and numerical strategy based on operator splitting. Such a strategy should prove very useful for applications in solar physics in order to gain computational cost, as well as obtain physically accurate simulations.

This scheme has then be validated numerically with a specific choice for the initial conditions. Indeed, we focused on particular solutions of the systems (M_S), ($M_{\bar{S}_1}$), and ($M_{\bar{S}_2}$) as travelling waves. We provide a numerical treatment of the nonconservative product that can be used in both cases **OR** and **UR**, that is even if the length L_D is much smaller than L_λ. However, the behaviour of this scheme was not investigated for more complicated initial conditions and in particular in the case where several travelling waves interact.

Furthermore, jump conditions based on our knowledge of the decoupled problem have been derived numerically for the fully coupled system and we were able to justify that studying the decoupled problem provides a good approximation of the original system in a range of Mach number close to one, as well as a good insight on the resolution of the problem for the general system of equations. The contributions proposed in this paper should also be extended to the case where electro-magnetic forces are present and the system is coupled with Maxwell's equations. This is the subject of our current research.

Part IV

High performance computing and results

CHAPTER 8

IMPLEMENTING INTO A MASSIVELY PARALLEL AMR CODE

Introduction and structure of the code

In the previous Chapters, we have focused on the development of numerical methods for the multicomponent systems coupled with Maxwell's equations. These methods have been developed for cases of non-uniform AMR cartesian grids. The goal of this numerical strategy was to guarantee that all relevant scales associated with the model and its applications, are correctly captured. In this chapter, we have focused on the implementation of this numerical strategy.

In many plasma applications, the spatial representation of a phenomena is localized in thin region. For instance, in the magnetic reconnection process, the phenomena is localized in the diffusion region, where the magnetic field lines are reconnecting. Therefore, fine meshes are needed in this region of the computational domain to catch correctly the dynamics of the reconnection. However, a uniform mesh would impose to use very fine meshes in the whole domain to obtain an accurate resolution of the region of interest. Therefore, the simulation would require high computation ressources. If the small scales are localized in certain static region of the computational domain, one possibility is to use unstructured grids. In this case, the mesh is defined by the user and fixed during the simulation. However, for complex multicomponent plasma flows, such as magnetic reconnection process, fixed unstructured grids would not provide accurate numerical resolution with low computational cost. In addition, fixed grids are not appropriate to catch the whole dynamic of the reconnection without a fine resolution. Another alternative to reduce these computing requirements and to catch such dynamics is to rather consider Adaptive Mesh Refinement (AMR) grids.

In AMR grids, the meshes are refined or coarsened dynamically during the simulation. AMR methods can reduce computational costs and memory while ensuring an accurate numerical resolution. The refining or coarsening process, should depend on a criterion fixed by the user. This

criterion can be based on error estimation methods or heuristic criterions. Such criterions have to be chosen in such a way that fine mesh are used only in the regions of interests. In this context, high resolution is used in regions of interest, to limit numerical diffusions of the proposed numerical scheme and to capture some stiff plasma flow structures. At the same time, a coarser mesh is used elsewhere.

Developing an efficient AMR code can be a very complex task that needs to take into account several issues related to the management of adaptive meshes and parallel computations. Indeed, managing AMR grids is not free in terms of Central Process Unit (CPU) and leads to an extra computational time compared to a uniform Cartesian mesh. In order to have an interesting performance compared with standard uniform grids code, the computation cost required for the AMR should be lower than the CPU time spent in the numerical resolution. The second issue is the scalability of the AMR code in parallel computations. Refining and coarsening the meshes has to be combined with a load balancing algorithm to ensure the partition of the load between the different computational resources after each operation on the meshes.

In addition, the implementation of the proposed multicomponent model requires an accurate calculation of the transport properties defined in the Chapter 4. This ensures that the dynamics of all species are correctly captured. Although the method has been identified and validated in the previous Chapters, it is still necessary to have a tool available where these properties are calculated with a high level of accuracy. In addition, this tool has to be coupled with an AMR code.

In this Chapter, the multicomponent models have been implemented with the numerical strategy established in the Chapter 6, in a massively parallel code called `CanoP`, which is an abstraction layer of the `p4est` library (see Drui (2017)), coupled to the "MUlticomponent Thermodynamic And Transport Properties for IONized gases, written in C++" `MUTATION++` developped by Scoggins (2017). The `p4est` library is a tree-based/cell-based parallel AMR library written in C language used for managing the mesh in parallel computation. It provides a high compression ratio of the data, is scalable on highly parallel architecture and is equation independent. The library is using a z-order space filling curve to manage the meshes, and, is defined in a such a way that there is a decoupling between the management of the mesh and numerical methods. Sufficient flexibility are given to the user to implement numerical schemes and models for several applications. In this context, the numerical schemes have been implemented into the `CanoP` code which is coupled to the `p4est` library. This code is mainly use to implement systems of equations with finite volume schemes on 2D and 3D adaptive grids. It has been used to integrate several type of applications, without modifying the structure of the code. The multicomponent models are solved using a Kurganov & Tadmor (2000) scheme. Then, several refinement criterions have been implemented into `CanoP` to be used for our numerical simulations. Finally, the `MUTATION++` library has been coupled to `CanoP` and is used for computing the transport properties. It has been designed for providing thermodynamic and transport properties for multicomponent partially ionized plasma in thermal nonequilibrium.

In Section 8.1, we present several structured AMR methods such as the block-based and cell-based methods. Among the possibilities used for managing AMR meshes, we justify the choice of the `p4est` library used in this thesis. Then, in Section 8.2, we exhibit the structure of the library and its main functionalities. In Section 8.3, we describe the `CanoP` code and the refinement

criterions used. Finally, in Section 8.4, the `MUTATION++` library and the coupling with `CanoP` are presented.

8.1 Structured Adaptive Mesh Refinement (SAMR) methods

In this work, we focus on structured AMR (SAMR) methods. They are characterized by a resolution of the solution over rectangular grids where the connectivity between cells is regular. The possible geometry of the mesh are quadrilateral in 2D and hexahedra in 3D. Such methods allow to develop an efficient mapping of the meshes, that can be encoded cheaply compared to Unstructured AMR (UAMR). On the other hand, the UAMR methods offer superior geometrical flexibility. However, the memory access during computation is highly irregular and the performance on vector or computers rather poor.

In this thesis, the geometric flexibility is only of secondary interest. The presented numerical methods are formulated on a cartesian mesh. Rectangular meshes allow optimizations that moderate some of the technical complexities of unstructured refinement techniques. Figure 8-1a and Figure 8-1b show an example of the differences between structured and unstructured mesh.

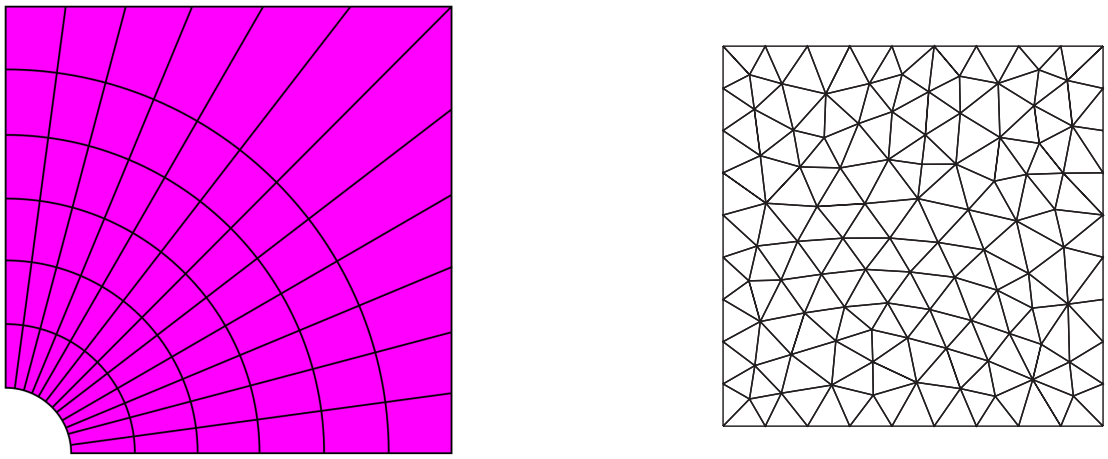

(a) Structured mesh

(b) Unstructured triangular mesh

Figure 8-1: Example of a structured triangular mesh and an unstructured triangular mesh in a unit box from Hiester et al. (2014)

Before going to the details of AMR methods, some relevant definitions related to AMR are introduced

- **Cell**: a spatial discretization element on which the numerical solution is computed,
- **Block**: a rectangular set of cells of same size.

- **Octree/quadtree**: The octree/quadtree denote the recursive tree structure, where the nodes correspond to an octant (3D) or a quadrant (2D). An octree (respectively quadtree) can be associated with 3D (respectively 2D) domains.

- **Meta-data**: The meta-data is a set of data used to manage the mesh. It can be associated to each cell and can contain the level of refinement of the cell, the associated block, the coordinate of the cell *etc*...

- **Level of refinement**: The level of refinement characterize the size of a cell or the dimension of a block. It is related to how much times the refinement operations have been performed from the coarsest grid.

- **Conforming/non-conforming mesh**: The mesh is said non-conforming if at a face separating two cells which are not at the same level of refinement, the corners defining the neighboring cells do not coincide.

- **The compression rate**: The compression rate is defined by the ratio

$$\eta_{\text{comp}} = \frac{N_{\text{unif}} - N_{\text{AMR}}}{N_{\text{unif}}}, \tag{8.1.1}$$

  where N_{unif} is the number of cells in a uniform grid configuration with a spatial discretization as fine as the finest cells of the AMR grid, and N_{AMR} is the total number of elements in a AMR grid configuration. This ratio may be used to characterize the gain in memory that AMR methods involve comparing with standard resolution with cartesian grids.

- **2:1 balance framework**: the size ratio between two neighbouring cells does not exceed two. This approach is used to to get better smooth transitions from coarse to fine cells.

In the literature, two main AMR approaches can be found: the **Block-based** AMR methods and the **tree-based** or **cell-based methods**. In the following, we exhibit the differences between the two approaches and the consequences of their implementation on the codes performances. Finally, we choose the most appropriate AMR method.

8.1.1 Block-based methods

The Block-based or Patch-based methods (see Berger & Oliger (1984); Dubey et al. (2016)) are based on pre-defined blocks called macro-meshes. It involves several grids on top of each other in regions where more accuracy is needed. The additional grids are finer than the original one that they replace. Once the grids are constructed, the equations are solved on the finer grids and then interpolated to the coarser ones.

An example of such grids can be found in Figure 8-2. An illustration of the parent-child grids relationships is shown. In Berger & Oliger (1984), the finer grids are not necessarily aligned with their parents grids. However, in Berger & Colella (1989), the numerical block-based methods are

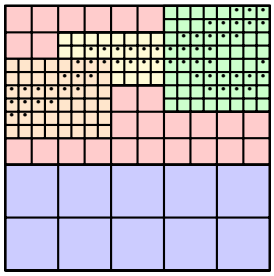

(a) Patches applied to flagged cells (cells marked with a dot).

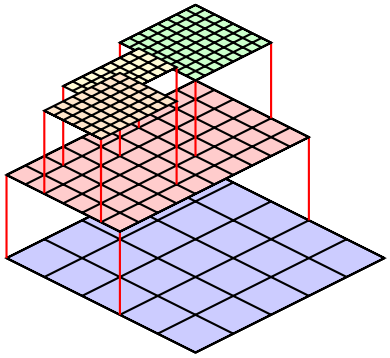

(b) Grid hierarchy structure

Figure 8-2: Example of overlapped grids illustrating patch-based AMR. Reprinted from Drui (2017).

shown to be accurate and more efficient if the fine grid starts and ends at the corner of a cell from the coarser grid and two overlapping cells have to be separated by at most one level.

For generating a block-based or patch-based grid, as shown in Figure 8-2, it is necessary to 1- define an initial uniform grid, 2- cluster the cells that have been flagged for a refinement process, and 3- create a grid with finer cells from this cluster. A widely used clustering algorithm can be found in the work of Berger & Rigoutsos (1991). However, it shows poor parallel performance with distributed computations as shown by Wissink et al. (2003). In this framework, a balance between the compression rate and the number of grids must be investigated. Indeed, when a high number of fine grids are involved, it is more difficult to manage them, and the treatment of boundaries is computationally expensive since the solution there requires interpolation procedure. Likewise, to avoid the regridding and clustering operations at each time step, a safety layer of fine cells are generated. Therefore, the compression rates of patch-based grids are often not as good as those of cell-based grids, which are presented in the next subsection.

In the following, a list of block-based AMR codes is given. This list of freely available codes is not exhaustive and is inspired from D. Calhoun (2014)'s website

- `BoxLib` is a widespread block-structured AMR framework, that is used for solving PDE's system. Several applications are based on `BoxLib` such as `CASTRO` (see Almgren et al. (2010)), `MAESTRO` (see Nonaka et al. (2010)) and `Nyx` (see Almgren et al. (2013)) codes.

- `SAMRAI` (see Hornung & Kohn (2002); Gunney & Anderson (2016)) is used for solving PDE's for several physical domains.

- `AMRClaw` (see Berger & J. Leveque (1997)) is an AMR version of finite volume code `ClawPack`. It is based on the works and algorithms of Berger & Colella (1989).

- `MPI-AMRVAC 2.0` (see Xia et al. (2018)), which is an open-source framework for the purpose of simulating astrophysical plasmas.

- `AMROC` (see Deiterding (2005)) is an MPI-parallel and C++ object oriented code based on the algorithmes from Berger & Colella (1989) for solving hyperbolic systems of conservation laws.

8.1.2 Cell-based methods

Unlike the block-based methods, the cell-based or tree-based AMR methods are more flexible for refining and coarsening the meshes. In addition, a higher compression rate can be reached. In this framework, the tree-based/cell-based methods involve modifications of an initial coarse mesh by means of recursively dividing its elements into multiple sub-elements with a fixed ratio, as shown in Figure 8-3. These elements may be blocks or individual cells: with individual cell, the method is called cell-based. There is no need for clustering algorithms, since each element can be refined or coarsened independently of the other elements of the grid.

The recursive refinement stages of the mesh can be represented by a tree structure, as shown in Figure 8-3. The tree consists of nodes related by edges. Each node of the tree can be a parent of four (respectively eight) children in the case of 2D (respectively 3D) space domain or/and a child of another parent node. The nodes of the tree are called octant in 3D or quadrant in 2D. We call leaves, the nodes that do not have children. The computational cells of the physical domain correspond to the leaves of the octree (in 3D) or quadtree (in 2D). The coarsening operation consists in replacing some leaves by their parent, while refining consists in creating new children from a leaf.

The tree structure approach allows to store linearly the mesh, modify it and go through all its cells. However, the use of such structure implies new difficulties in implementing numerical methods and defining storage strategies. One could store the whole tree structure, since it contains all the connectivities between the cells. However, this approach stores unnecessary tree-data and consumes memory. Furthermore, the iteration among the cells, like finding neighbors of a given cell, can lead in the worst cases to the whole tree traversal. An efficient meta-data management would then necessitate as little computation as possible. For this reason, it is more convenient to consider a linear storage of the leaves using minimal possible mesh-data. It allows to encode cheaply the cell positions and connectivities in a linear array.

Recent libraries developped by Sundar et al. (2007); Sundar et al. (2008); Ji et al. (2010), based on a tree linear storage, have been preferred. Such implementations are shown to use less memory and are easier to parallelize. These libraries are showing advantages in the context of High Performance Computing (HPC) simulations. In the following, a list of cell-based or tree-based AMR codes are provided

- `PARAMESH` (see MacNeice et al. (2000)) is a fully-linked tree-based framework. This AMR framework is equation-independent, as it only provides routines for the management of the meta-data.

- `p4est` (see Burstedde et al. (2011)) is a C cell-based library, based on the index of Morton for storing the leaves of trees in a linear array. The library is able to perform simulations over complex geometries. it is described in the next section

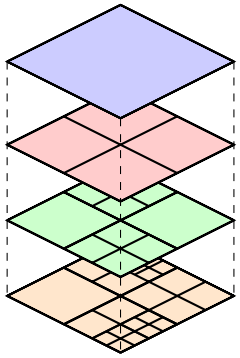

(a) Example of cell refinement process illustrating cell-based AMR.

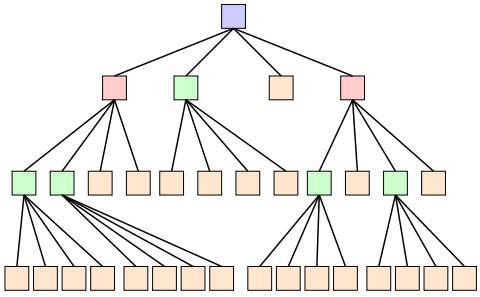

(b) Corresponding representation of the domain using a quadtree structure.

Figure 8-3: Example of a cell-based grid.

- `RAMSES` (see Teyssier (2002)) is a N-body solver and finite volume cell-based code for astrophysical applications.

In summary, we have exhibited the different aspects and issues of the AMR techniques. For the proposed numerical strategy, we define a list a criteria regarding the choice of an AMR library. The library should

- provide a high compression ratio of the data,
- scalable on highly parallel architectures
- be equation independent, and appropriate to several applications (including plasma application)

The first point show that a tree-based/cell-based AMR with a linear storage of the data would be more appropriate. The third point show that an AMR library which manage meta-data is required. These criteria are verified by the `p4est` library. In addition, as shown by Isaac et al. (2015) the scalability of `p4est` has been verified up to 458 000 cores. A presentation of the library and its functionalities is provided in the next section.

8.2 The `p4est` library

As described in the previous section, the `p4est` library is a tree-based and parallel AMR library written in C language. The library has been designed to be agnostic on the numerical methods and applications. As shown by Burstedde et al. (2011); Isaac et al. (2015), this library has shown a good parallel scalability up to 10^5 CPU cores. The p4est library is using a z-order space filling curve (and associated Morton's index) to manage the meshes. The meta-data are stored linearly and partitionned between the MPI processes. All the algorithms related to the mesh management

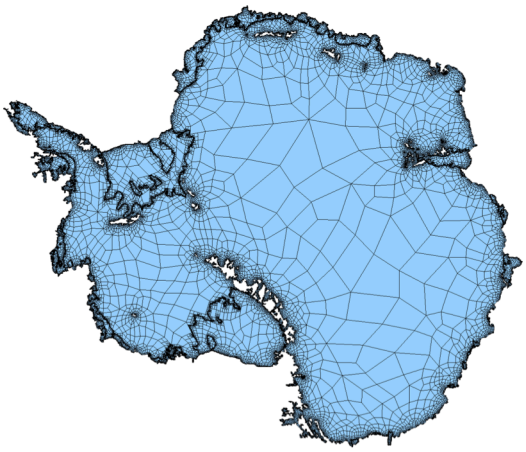

Figure 8-4: Top-view of the 3D gridding of Antarctica, made of 28000 octrees, reprinted from Isaac et al. (2015).

(such as refining or coarsening) are MPI parallelized. It can map domains of complex geometry by using a set of octrees (or forest). It provides the user with different functionalities to manage the meshes in a parallel computation with sufficient flexibility to implement several numerical schemes and several models for several applications. In the following, we present the outlines of the p4est library: how the meshes are stored and managed and the main functionalities provided by this library to develop new applications.

8.2.1 Macro-mesh and forest of trees

`p4est` enables to use an initial coarsened mesh of a physical space that can be defined manually by the user, or generated by some meshing software, such as `CUBIT` or `Gmsh`. The initial discretization, also called macro-mesh, allows to map complex domain geometry. This macro-mesh needs to be made of four-angled cells in 2D and hexahedral cells in 3D, and conforming. The library allows to map non-trivial datas such as disks or spheres. As an example, Figure 8-4 represents a 3D gridding of Antarctica.

In this representation, each macro cell covers a subdomain of the global domain that can be refined recursively into a tree structure (octree), where the collection of octrees that maps the whole domain is called here a forest of octrees. Each macro cell is mapped by a one-to-one correspondence to a reference cube. These macro-cubes represent the octant-root of the octrees. Their topological elements are: 6 faces in 3D and 4 in 2D; 12 edges in 3D (there is no edges in 2D); and 8 corners in 3D and 4 in 2D.

For more details about the representation of these topological elements, indexing, and connectivity encoding, we refer the reader to the work of Burstedde et al. (2011); Essadki (2018).

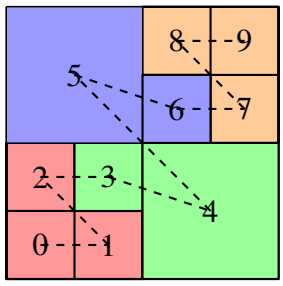

(a) Adaptively refined square domain. Mesh and z-order curve.

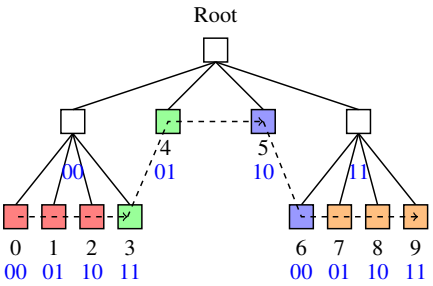

(b) The corresponding representation of the domain using a quadtree.

Figure 8-5: z-order traversal of the quadrants in one tree of the forest and load partition into four processes. Dashed line: z-order curve. Quadrant label: z-order index. Color: MPI processes.

8.2.2 Morton index and storage

In the `p4est` library, the z-order curve and Morton's index is used to store the leaves of each octrees. This method is used to index all the cells of a grid and store their data in a linear array, which can be partitioned and distributed over the MPI processes. In addition, the Morton's index allow to find easily a neighbor, a parent and a child for a given cell. An illustration can be found in Figure 8-5.

The linear storage allows to simplify the iteration among the octant and the search of the neighbors. In forest of trees, an octant is uniquely defined by its corresponding octree number, the coordinate position of its front lower left corner and the level of refinement. First, `p4est` groups the octants per-octree array. Therefore, it does not require to store the octree number associated to each octant. For each octree, `p4est` stores the position $x, y, z \in \{0, ..., 2^b - 1\}$ of the lower left corner of an octant with respect to the coordinate system of the octree and the level of refinement $0 \leq l \leq b$, where b is the maximum level of refinement fixed by the user in the `p4est` library. The relative coordinates of an octant in an octree are stored with $d \times b$ bits. The integer-based representation of the octant coordinate positions avoids topological errors due to roundoff of floating-point errors. Finally, to store an octant position in a linear array, `p4est` encodes the position (x, y, z) in an integer m using $d \times b$ bits as follows:

$$\bar{m}^2_{3i+2} = \bar{z}^2_i, \quad \bar{m}^2_{3i+1} = \bar{y}^2_i, \quad \bar{m}^2_{3i} = \bar{x}^2_i \tag{8.2.1}$$

where $0 \leq i \leq b - 1$. The notation $\bar{\bullet}^2$ indicates numbers written in base 2 and $\bar{\bullet}^2_i$ is the i-th bit of the binary representation. We underline that the physical coordinates are computed through the transformation mapping function between the macro-mesh and its cube $\left[0, 2^b - 1\right]^d$ octree-representation.

8.2.3 Main functionalities

Here, we summarize the main functionalities of the library. We remind that the library `p4est` has been developed to manage for an increasingly large spectrum of physical applications, since there is a decoupling between the mesh management, and, the numerical methods implemented.

Indeed, while `p4est` is managing the meta-data of the mesh structure, the user is free to define application data per cells. For example, the conservative variables, gradients, *etc*, as well as the functions that can be used in the numerical computation such as: updating the data, compute the reconstructed variables (slopes, gradients, interpolations, *etc*.) used mainly for high order numerical schemes such as Kurganov & Tadmor (2000), mark the cells to be refined or coarsened, *etc*. The functions defined by the user is used as callback functions of `p4est` functions.

Here, a summary of the main functionalities of `p4est` is given

- Definition of a new refined forest and repartition of the load between MPI processes,
- Iteration on the quadrants and mark the quadrants to be refined or coarsened,
- Ensure 2:1 balance through faces and corners. An example can be found in Figure 8-6,
- Partition the linearly stored mesh between the processes,
- Communicate the data of the quadrants located at the boudaries of each "processor-decomposition" domain to the other neighboring process.

In summary, the library is managing only the mesh structure and is independent of the considered application. Only the application data (called user-data in this work) needs to be specified by the user. Then, the user implements the functions that will perform tasks on the user-data.

In this thesis, we have focused on the `p4est` library for managing the mesh in the AMR framework. This library appears to be appropriate to the numerical strategy established in the previous Chapters. Indeed, the library is well adapted to manage AMR nonuniform cartesian mesh in a 2:1 balance framework. However, it is necessary to implement these numerical methods into a massively parallel code coupled to this library such as `CanoP`.

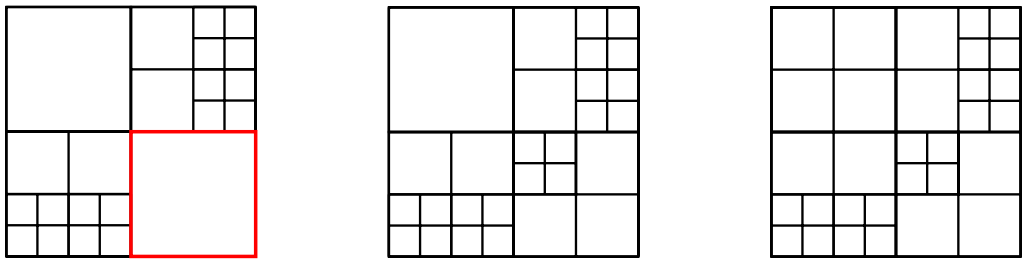

Figure 8-6: Cell based meshes that do and do not satisfy the 2:1 balance constraint. **Left:** Mesh not satisfying the 2:1 balance: the red cell is neighboring four times smaller cells. **Middle:** mesh satisfying the 2:1 balance through faces, but not through corners. **Right:** Mesh satisfying the 2:1 balance through faces and corners.

8.3 The `CanoP` code

`CanoP` is a C/C++ code which is used to solve systems of equations with Finite Volume (FV schemes) schemes on 2D and 3D adaptive grids. It is coupled with the `p4est` library. `CanoP` is an applicative layer on top of the `p4est` library, where several numerical schemes and applications are implemented. The framework of the code aims at facilitating the integration of new finite volume applications, or new finite volume features, such as high-order schemes, low-Mach number solvers, *etc*. This code is developed in collaboration between **Maison de la Simulation**, Energétique Moléculaire Macroscopique et Combustion (**EM2C**) laboratory, **CMAP** laboratory and IFP Energies nouvelles (**IFPEN**). In this context, several physical applications have been implemented using different FV schemes:

- a scalar advection upwind solver which has been implemented to test the parallel performance of `p4est` library Drui, Fikl, et al. (2016),
- Euler's equations with gravity source terms are solved using a HLLC scheme for the convective part and an elliptic solver for the gravity source term. This model is used mainly for astrophysics applications,
- 3-equation system to model two-phase flows is solved using a Suliciu's solver Drui, Larat, et al. (2016)
- Spray models based on moment methods implemented and tested in `CanoP` code Essadki, Mohamed et al. (2016)
- The multicomponent model (Mc) and (Mf) are solved using a Kurganov & Tadmor (2000) scheme for application to magnetic reconnection in solar physics. This application is coupled to `MUTATION++` library which is described in the next section.

The main goal of this code is the possibility to easily integrate several type of application, without modifying the structure of the code. The code is divided into two main parts: 1- a solver part

and 2- an application part. The solver part is the core of `CanoP` common to all the implemented applications. It is used to call `p4est` functions to manage the mesh and data storage, and define common functions between all `CanoP` applications. Then, we have the application part where the user is defining the data models (user data) and functions to be used as callback `p4est` functions or other functions defined in the solver part. In this thesis, we have implemented the multicomponent models (Mc) and (Mf) based on a numerical strategy which has been widely described in the Chapter 6.

8.3.1 The architecture

In this section, we present the main features and structure of the code. In Figure 8-7 the main code architecture and the link with the different libraries is shown. This scheme shows the organization of the code. We have

- **The application part**, where specific functions are implemented and defined, such as the user data model, for example, the conservative variables, gradients at interfaces (for the diffusive terms), transport coefficients (computed from `MUTATION++` library). In this part, it is left to the user to implement initial and boundary conditions and indicators for refinement and coarsening.
- **The solver part**, where common functionalities are implemented. For example, we have the main steps of the simulation: initialization, loop over time steps, finalization, functions to compute the timestep, the gradients for the diffusive fluxes and the convective fluxes. In addition we also have the functions to manage the mesh adaptation and the work load between the MPI processes. The solver part is linked with three libraries: the HDF5 library for the parallel output, the LUA library to read input data, and `p4est` library. In this thesis, the HDF5 files have been read with `Paraview`, which is an open-source, multi-platform data analysis and visualization application.

The three main steps of the code are illustrated in Figure 8-8. We have

1. **The initialization**: The MPI processes are initialized, the LUA input file is read and C++ class files are created from the setting parameters of the input files.
2. **The time step loop**: The solution is updated, the meshes is adapted during each iteration, and the solution is written in HDF5 files.
3. **The finalization**: All created objects and pointers are destroyed.

First, we have the initialization step. It is illustrated in Figure 8-9. At this step, it is possible to load a previous simulation from `p4est` library. Then, a macro-mesh (also called connectivity) and its corresponding forest structure is created, the initial uniform mesh is generated. We underline that in `CanoP`, the initial mesh is defined as the finest grid level, and then coarsened recursively according to a refinement criterion defined by the user.

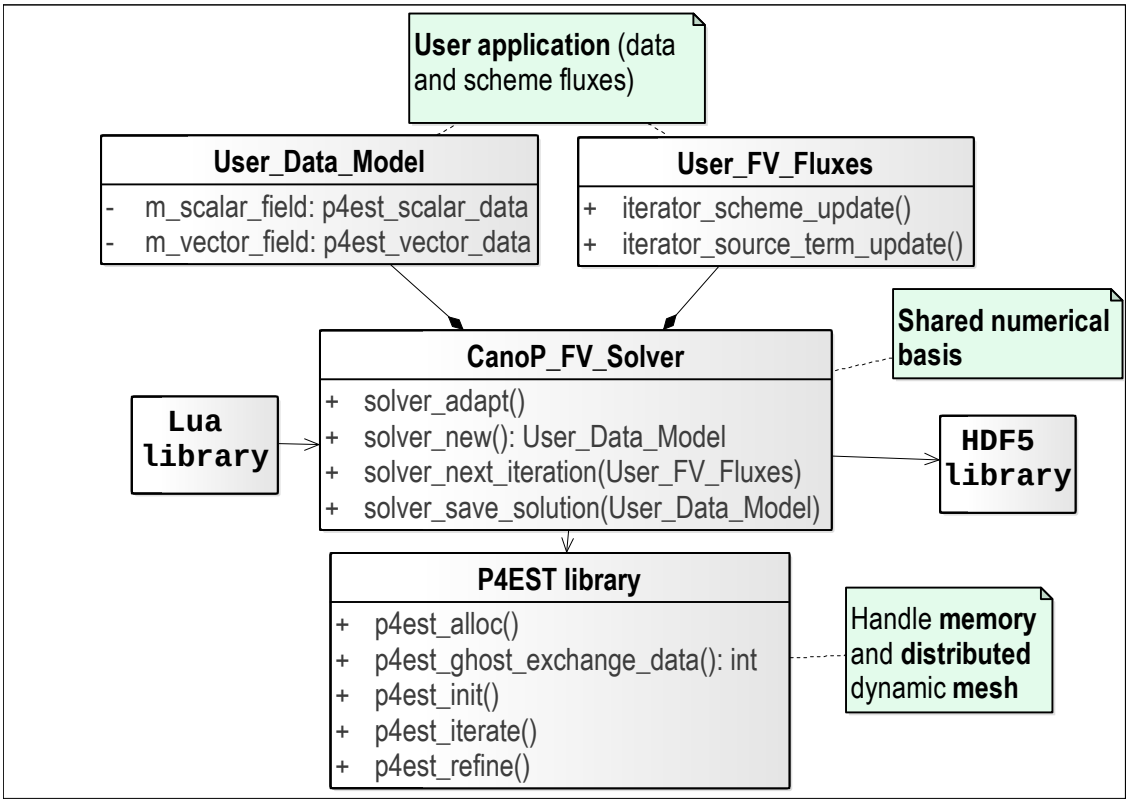

Figure 8-7: General CanoP architecture reprinted from Essadki (2018).

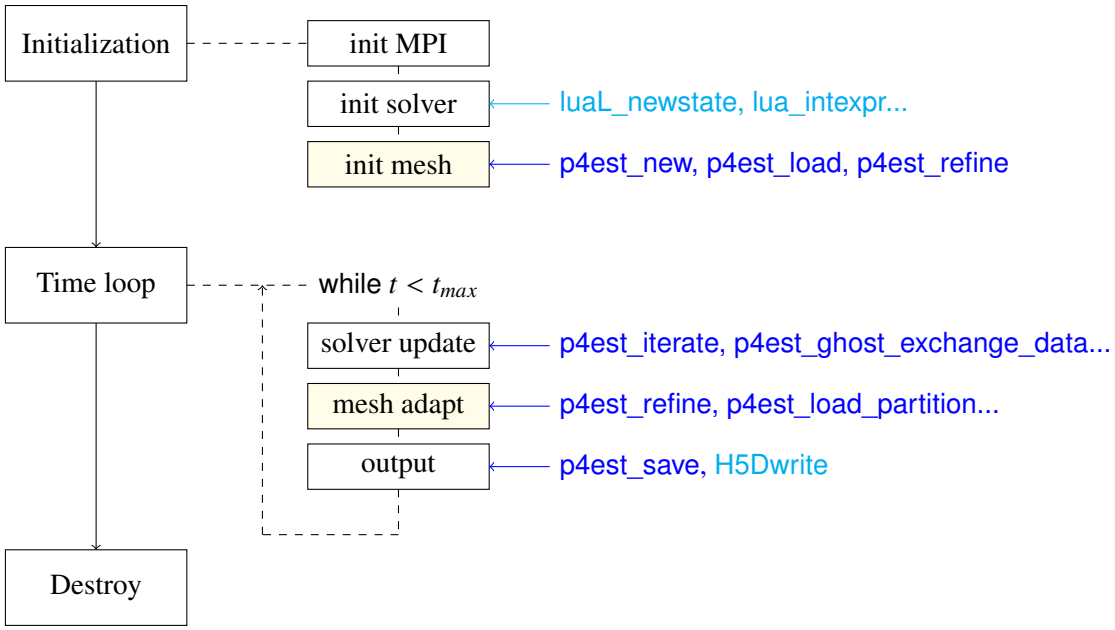

Figure 8-8: Sketch of the CanoP code structure and calls for p4est functions, reprinted from Drui (2017).

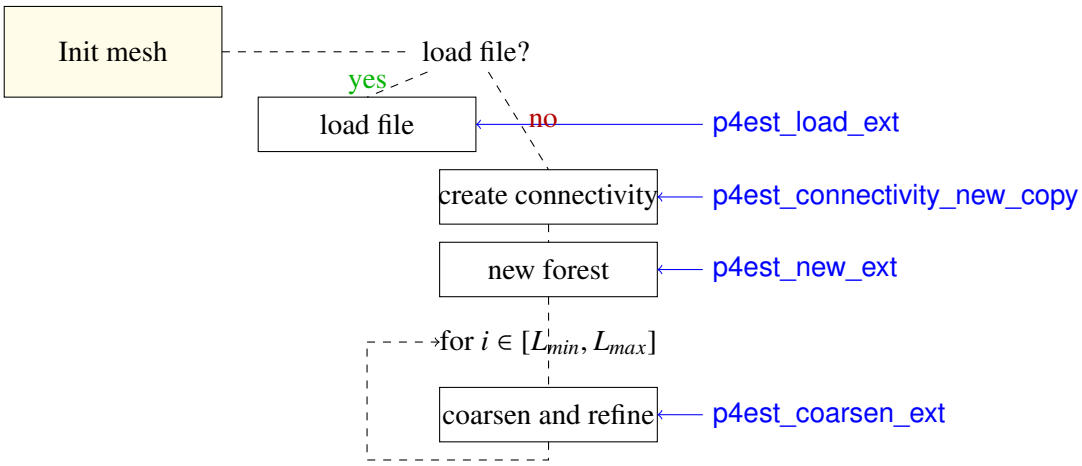

Figure 8-9: Zoom in the *init* part structure and calls for `p4est` functions, reprinted from Drui (2017).

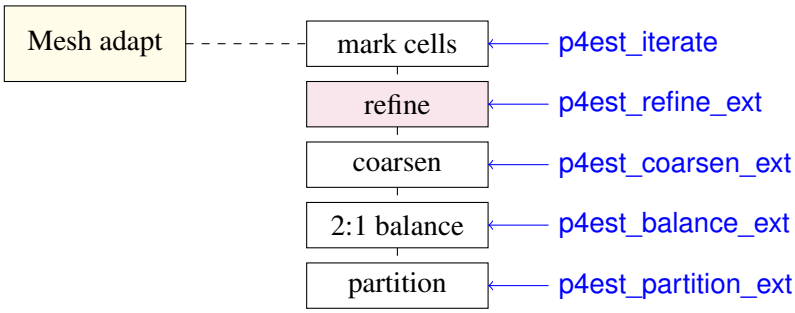

Figure 8-10: Zoom in the *mesh adapt* part structure and calls for `p4est` functions, reprinted from Drui (2017).

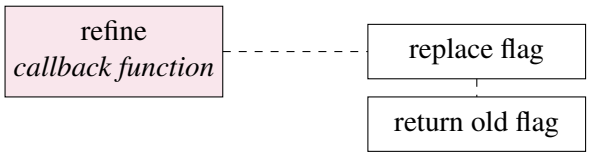

Figure 8-11: Zoom in the *refine* callback function, that informs `p4est` if the cell should be refined. Reprinted from Drui (2017).

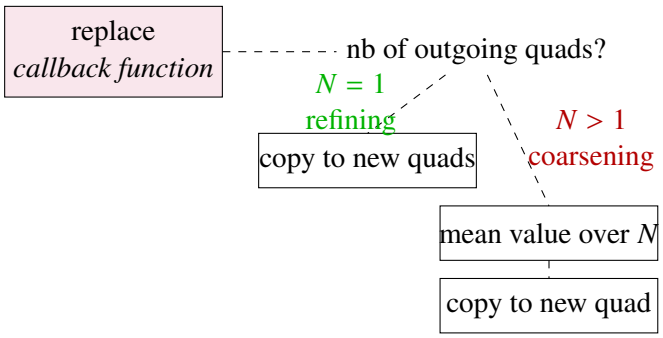

Figure 8-12: Zoom in the *replace* callback function, that computes the value of the newly created quadrants. Reprinted from Drui (2017).

Then, we have the mesh adaptation step. This step is summarized in Figure 8-10. This step is subdivived into five main steps, as follows

1. **Marking cells**: The cells are visited and marked in order to be refined or coarsed, according to the refinement criterion provided by the user.

2. **Refinement of the cells**: At this step, the size of the cells are modified. Two callback functions are used: the first function is replacing the flag of the cell (see Figure 8-11), the second one set the values in the new children cells (see Figure 8-12).

3. **Coarsening of the cells**: This step is identical to the previous refinement step. Similarly, two callback functions are used for coarsening the cells.

4. **2:1 balance**: The replace callback function is used by `p4est` to set the values in the new mesh.

5. **Partitioning**: The work load is re-partitioning on all the MPI processes.

As shown in Figure 8-12, it is necessary to defined a way for setting the values in the newly coarsened or refined cells. This will be investigated with further details in Section 8.3.2.

In this section, the architecture and callback functions of the `CanoP` code have been identified. The multicomponent models have been implemented in this code according to the numerical methods described in the previous Chapter 6. It is still necessary for the user to define refinement criterions for coarsening/refining the cells.

8.3.2 Refinement criterion

The definition of efficient refinement criteria is a complex task that depends on the physical phenomena involved in the simulation, as shown by Drui, Florence et al. (2016). In this thesis, we have considered only two heuristic criteria in order to test the mesh adaptation functionality of `p4est`.

Each time the adaptive mesh algorithm is called, a given criterion $C(\mathcal{U})$ is computed in each cell and compared to a given threshold θ. If $C(\mathcal{U}) > \theta_1$, then the current cell has to be refined. If all the siblings of a given octant verify $C(\mathcal{U}) \leq \theta_2$, then the octant is coarsened. Finally, the configuration of the mesh is in a 2:1 balance constraint. During coarsening, the new cell are computed as the mean value of the siblings cells. During refining, the new cells are computed as the mean value of their parent cell. In the following, two criterions are used: 1- a criterion on the density of heavy particles $\rho_{\mathfrak{h}}$ which is mainly used to capture all the small variations in the solution, and is considered as the most sensible criterion and 2- a criterion on the magnitude of the magnetic field. The chosen criterions are called the $\rho_{\mathfrak{h}}$-gradient and the $\boldsymbol{B}$-gradient, and are defined as

$$C(\mathcal{U})_i = D(\rho_{\mathfrak{h}})_i = \max\left(\frac{|\rho_{\mathfrak{h},i} - \rho_{\mathfrak{h},j}|}{\max(\rho_{\mathfrak{h},i}, \rho_{\mathfrak{h},j})} \;/\; j \in \mathcal{N}_q(i), \quad q = x, y, z\right), \tag{8.3.1}$$

$$C(\mathcal{U})_i = D(\boldsymbol{B})_i = \max\left(\frac{||\boldsymbol{B}|_i - |\boldsymbol{B}|_j|}{\max(|\boldsymbol{B}|_i, |\boldsymbol{B}|_j)} \;/\; j \in \mathcal{N}_q(i), \quad q = x, y, z\right), \tag{8.3.2}$$

In addition, we also introduce a mixed $\boldsymbol{B}$-$\rho_{\mathfrak{h}}$ criterion

$$C(\mathcal{U})_i = \max(D(\boldsymbol{B})_i, D(\rho_{\mathfrak{h}})_i) \tag{8.3.3}$$

In summary, we have presented the structure of the `CanoP` code combined with the `p4est` library. The multicomponent model (Mc) and (Mf) have been implemented into `CanoP`, based on the numerical methods defined in the Chapter 6. At this stage, it is possible to use such implementation to perform computation of multicomponent plasmas with `CanoP`. However, the question remains as to compute the transport coefficients of the diffusive terms introduced in the Chapter 4 with a high level of accuracy. Therefore, the `CanoP` code has been coupled with another library which is used for computing the transport coefficients defined in Chapter 4.

8.4 The Multicomponent Thermodynamic And Transport Properties for Ionized gases in C++ library

In order to compute the presented transport properties defined in Chapter 4, we have combined the `CanoP` code with a new software library called "MUlticomponent Thermodynamic And Transport properties for IONized gases, written in C++ (`MUTATION++`)" Scoggins & Magin (2014). The library has been designed for

- providing thermodynamic, transport, and chemical kinetic properties for multicomponent partially ionized plasma,
- computing the transport properties with a high level of accuracy,
- extending easily new data and algorithms if necessary,

- interfacing easily with CFD codes such as `CanoP`,
- being open source to promote code and data sharing among different research groups.

The `MUTATION++` library has been first developped at the von Karman Institute by Magin (2004) in Fortran language, and then by Scoggins & Magin (2014); Scoggins (2017) in C++ language and advanced Object-Oriented Programming (OOP) techniques. In this library, the collision integral database related to the Helium-Hydrogen mixture introduced in Chapter 5 and Chapter 4 have been implemented. All the transport properties related to the multicomponent models have been computed with this library.

In the literature, other libraries combined to CFD codes have been used for computing the thermodynamic or transport properties. For example, we have `cantera` (see Goodwin et al. (2016)) or `EGlib` (see Ern & Giovangigli (1996)). However, such libraries are mainly used for thermal equilibrium context and are mainly focus on combustion problems. On the contrary, the presented `MUTATION++` library can be used for higher temperature plasmas problem including thermal and chemical nonequilibrium effects. This library can be used for solar physics application.

In this thesis, `MUTATION++` library has been coupled to the numerical tool `CanoP` . In the following, an overview of the design of the library and how it interfaces with `CanoP` is presented. Finally, we show some details about the transport and thermodynamic properties implemented in the library. Further discussions on `MUTATION++` library can be found in the thesis of Scoggins (2017).

8.4.1 Coupling with `CanoP` code

This section is devoted to the coupling between the `CanoP` code and the library `MUTATION++`. An illustration of the coupling between the two codes is given in Figure 8-13. On the one hand, we have the `CanoP` code which is solving the multicomponent governing equations at each time step. On the other hand, for a given mixture, the transport coefficients are computed through the `MUTATION++` library at the same time, for each timestep. In order to compute the transport properties, it is necessary to link the two codes.

In this framework, an information has to be sent from the `CanoP` code to the library to provide the transport properties. This information is a vector of variable called "state-vector" $\widetilde{\mathcal{U}}$ computed in `CanoP`. The state-vector is linked with a state-model predefined in `MUTATION++` which represents a specific thermochemical model, which is interpreting the state vector and provides state-dependent properties back. For example, the equilibrium state model would interpret the state vector to compute the heavy thermal conductivity $\lambda_{\mathfrak{h}}$ as a function of the element densities and temperature. In this thesis, two state-model have been used: 1- a thermal equilibrium state-model with $T_{\mathfrak{e}} = T_{\mathfrak{h}}$ and 2- thermal nonequilibrium state-model with $T_{\mathfrak{e}} \neq T_{\mathfrak{h}}$. Therefore,

1. **In the thermal equilibrium state-model**: the state-vector associated to the multicomponent models are defined as $\widetilde{\mathcal{U}_{\mathrm{Mf}}} = (\rho_\alpha, T)\,,\ \alpha \in \mathrm{I}$ and $\widetilde{\mathcal{U}_{\mathrm{Mc}}} = (\rho_\alpha, T)\,,\ \alpha \in \mathrm{H}$.

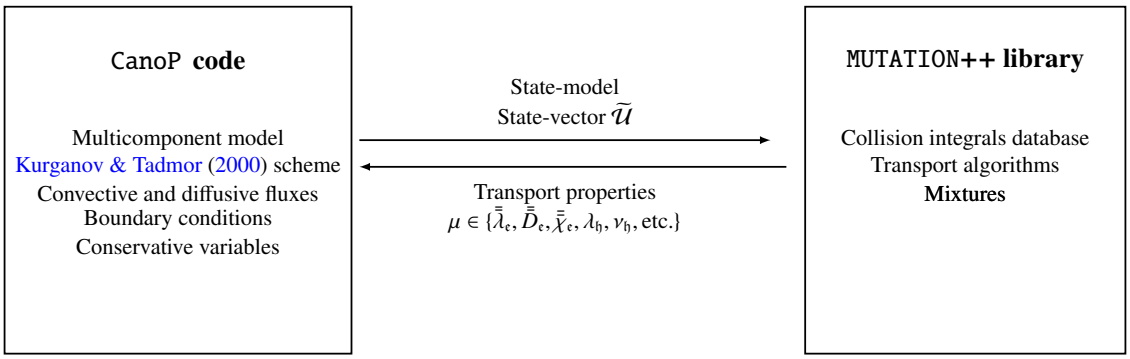

Figure 8-13: Coupling between MUTATION++ library and CanoP code

2. **In the thermal nonequilibrium state-model**: the state-vector is defined as $\widetilde{\mathcal{U}_{\text{Mf}}} = (\rho_\alpha, T_e, T_h)$, $\alpha \in \text{I}$ and $\widetilde{\mathcal{U}_{\text{Mc}}} = (\rho_\alpha, T_e, T_h)$, $\alpha \in \text{H}$.

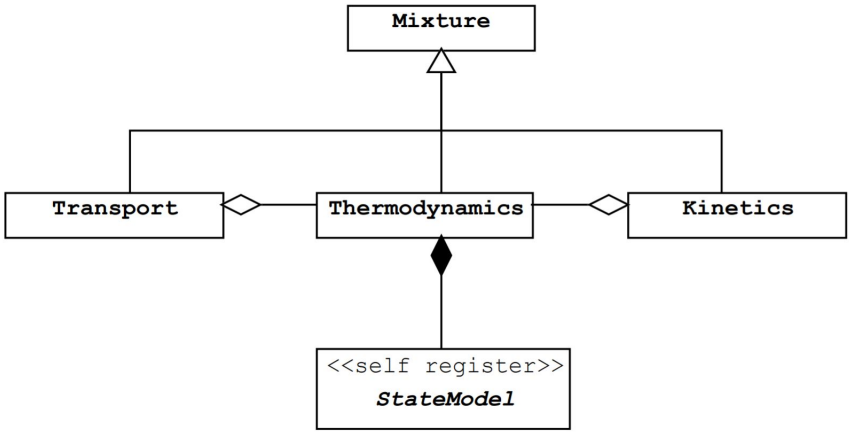

Figure 8-14: Overview of the MUTATION++ library, reprinted from Scoggins (2017).

Figure 8-14 is showing an overview of the MUTATION++ library. This library is composed of three main models: thermodynamics, transport and kinetics which are implemented as classes. First, we have a `mixture` which inherits the methods of each module, prodiving all the functionality in a single class. In this class, the transport coefficients of Chapters 5 and 4 are computed. Then, we have the `Thermodynamics` which owns a `StateModel` , where the state model concept is defined. It is self registering, which gives the possibility to the user to change the state-model at any time by using a string. In the next section, we focus on each of the main modules of MUTATION++, except the `Kinetics` class, since it has not been used in this thesis.

8.4.2 `Thermodynamics` module

This section is devoted to the `Thermodynamics` module. We provide a brief summary of this module. Further details of this module can be found in the work of Scoggins (2017).

In order to compute some of the properties of MUTATION++, it is necessary to have explicit knowledge of the mixture energy and enthalpy. In equilibrium flows, the composition of the mixure can be computed by a minimization of the Gibbs free energy with suitable mass constraints, as performed in Chapter 4 with the Helium-Hydrogen mixture. The mixture thermodynamic properties of a perfect gas can be described by a summation of pure species properties weighted by the species mass fractions, as done by Scoggins & Magin (2014); Scoggins (2017); Magin & Degrez (2004). As an example, we have the mixture enthalpy which is defined as $h = \sum_{i \in S} h_i y_i$, where h_i and y_i are the species specific enthalpy and mass fraction of species i.

In a mixture composed of several species, a thermodynamic library capable of producing individual species energy, enthalpy and entropy is required to obtain the thermodynamic functions. In this context, MUTATION++ includes two possibilities of computing such functions: 1- explicit determination of thermodynamics properties from a set of polynomials or 2- a direct evaluation of species partition functions. In the next subsection, a brief summary of the two approaches is presented. Then, an overview of the object-oriented design of the `Thermodynamics` module is provided.

NASA Polynomial Database

This thermodynamic database from J. McBride et al. (1993, 2002) is providing 7- and 9-coefficient polynomials for heat capacity, enthalpy and entropy as function of temperature. Further details about this database are given by Scoggins (2017). The species thermodynamic properties are given by

$$c_{pi} = R_i \sum_{j=0}^{4+q} a_{ij} T^{j-q}, \quad h_i = \int c_{pi} dT + b_{i1} R_i T, \quad s_i = \int \frac{c_{pi}}{T} dT + b_{i2} R_i, \tag{8.4.1}$$

where $q = 0$ for the 7-coefficient format or $q = 2$ for the 9-coefficient format, R_i and c_{pi} are the ideal gas constant and heat capacity of species i, a and b are coefficients provided by the database for several temperature ranges. The database is curve-fit for temperature up to 20000 K. For most species, the accuracy of these fits deteriorate beyond this temperature. However, the database is widely used for the high degree of accuracy in this temperature range.

The Rigid-Rotor and Harmonic Oscillator Model (RRHO) approximation

Another alternative used by MUTATION++ library, is to compute the species thermodynamic properties from the statistical mechanics through the internal partition function Q_i. It may be split into separate energy types:

$$Q_i = Q_i^T Q_i^{\text{int}}, \quad \text{and} \quad Q_i^{\text{int}} = Q_i^{\text{r}}(T_r) Q_i^{\text{v}}(T_v) Q_i^{\text{el}}(T_{el}), \tag{8.4.2}$$

where Q_i^T is the contribution of the translational energy of the partition function, and $Q_i^{\text{r}}(T_r)$, $Q_i^{\text{v}}(T_v)$ and $Q_i^{\text{el}}(T_{el})$ are the contribution of the rotational, vibrationnal and electronic energy mode, at temperature T_r, T_v and T_{el} respectively. Indeed, atoms and molecules can have discrete, quantized

energy levels. For the atoms, the contributions are only due to the translational and electronic energies, while molecules may have also rotational and vibrational energy contributions. In this thesis, the rigid rotator and harmonic oscillator approximations for molecules have been used. Under these assumptions, the rotational, vibrational and electronic partition functions are defined as

$$Q_i^{\mathrm{r}}(T_r) = \frac{1}{\sigma_i}\left(\frac{T_r}{\theta_i^r}\right)^{\frac{L_i}{2}}, \tag{8.4.3}$$

$$Q_i^{\mathrm{v}}(T_v) = \Pi_k \left[1 - \exp\left(-\frac{\theta_{ki}^v}{T_v}\right)\right]^{-1}, \tag{8.4.4}$$

$$Q_i^{\mathrm{el}}(T_{el}) = \sum_k a_{ki}^{el} \exp\left(-\frac{\theta_{ki}^{el}}{T_{el}}\right), \tag{8.4.5}$$

where $\theta_i^r = h^2/(8\pi^2 I_i k_B)$ is a characteristic temperature for rotation, $\theta_{ki}^v = h\nu_{ki}/k_B$ are characteristic temperatures for each vibrational mode k and ν_{ki} is the frequency of the harmonic-oscillator of the molecule i, $\theta_{ki}^{el} = E_{ki}^{el}/k_B$ are characteristic temperatures associated with the electronic level k, with energy E_{ki}^{el} and degeneracy a_{ki}^{el}. The constants σ_i and L_i are describing the symmetry and linearity of the molecule. Finally, the specific energy and entropy (see Vincenti & Kruger (1965)) of a species i, normalized by a gas constant R_u, are related to the partition function by

$$\widetilde{e_i} = T^2 \frac{\partial}{\partial T}(\ln Q_i) \tag{8.4.6}$$

$$\widetilde{s_i} = \ln \frac{Q_i}{N_i} + 1 + T\frac{\partial}{\partial T}(\ln Q_i) \tag{8.4.7}$$

where N_i is the number of particles in the volume considered. In the work of Scoggins (2017), a comparison of the NASA-9 and RRHO approach has been performed for an equilibrium air. In general, good agreement have been obtained between the two databases. However, large differences have been obtained for temperature above 12500 K. Therefore, for high-temperature applications+, such as heliophysical modeling, the RRHO method has been used.

Object-oriented design

Figure 8-15 is showing a simplified class diagram of the `Thermodynamics` module. This module is providing pure species and mixture thermodynamic functions to the `Mixture` class. `Thermodynamics` module is containing the `StateModel` (described in the previous subsection), `ThermoDB` and `MultiPhaseEquilSolver` objects.

The `MultiPhaseEquilSolver` is computing the equilibrium composition at fixed temperature, pressure and element fractions.

Then, the `StateModel` is an object to describe the state of the mixture described in the previous section. We have the `EquilStateModel`, which represents a mixture in thermochemical equilibrium including the effect of elemental demixing. Then, we have the `ChemNonEqStateModel` and

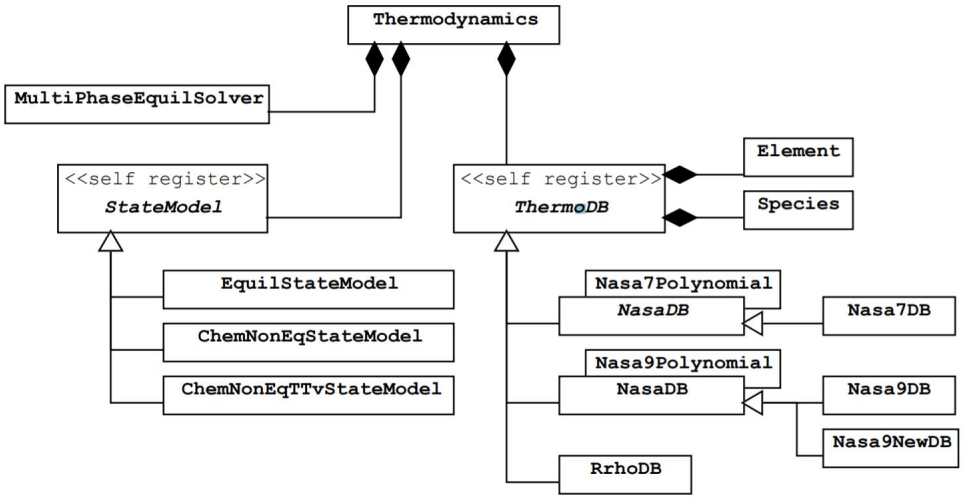

Figure 8-15: Overview of the `Thermodynamics` module, reprinted from Scoggins (2017).

`ChemNonEqTTvStateModel` which represent mixtures in chemical and thermochemical nonequilibrium. In this thesis, only the `ChemNonEqStateModel` and `ChemNonEqTTvStateModel` have been used for representing the thermal equilibrium ($T_e = T_h$) and nonequilibrium state-model ($T_e \neq T_h$).

Finally, we have the `ThermoDB` which is an interface for computing pure species thermodynamic properties. This module is also managing the loaded `Species` and `Elements` for the mixture considered. The type of thermodynamic database can be selected by the user through the self registration of the `ThermoDB` type. The three databases NASA-7, NASA-9 and RRHO have been implemented through the `NasaDB` and `RrhoDB` type respectively, in the `ThermoDB` class.

8.4.3 `Transport` module

Unlike the previous subsection, we focus here on the structure of the `Transport` module in the `MUTATION++` library. Only the design of the module is discussed here. The details of the transport coefficients, methods and algorithms have been widely described in Chapter 5 and Chapter 4.

Figure 8-16 is showing an overview of the `Transport` module implemented in `MUTATION++` library. This module is computing all the required transport coefficients. Four main abstract classes belong to the `Transport` module: 1- the self registering `ThermalConductivityAlgorithm` 2- `ViscosityAlgorithm`, 3- `DiffusionMatrix` and `ElectronSubSystem` class. In each of this class, all the algorithms are implemented to compute the thermal conductivity, viscosity, diffusion matrix and electron transport coefficients respectively. For example, in the `ThermalConducvity Algorithm` class, the Wilke and Gupta Yos mixture rules and the solution of the Chapman-linear transport system, can be solved either with the LDL^T decomposition or with iterative Conjugate-Gradient (CG) method. The `ViscosityAlgorithm` and `DiffusionMatrix` classes have been implemented in a similar way.

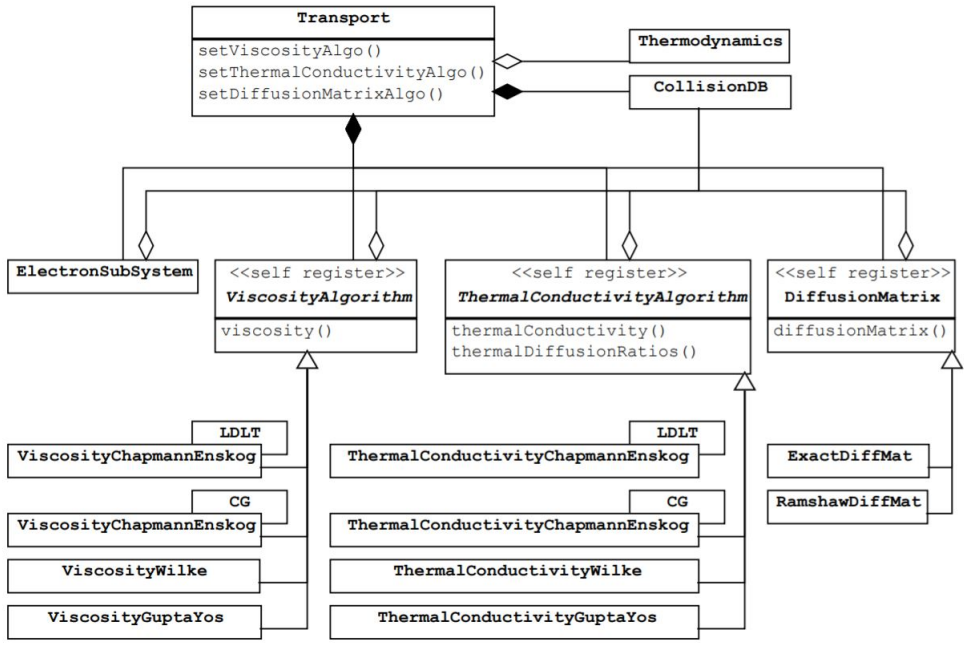

Figure 8-16: Overview of the `Transport` module, reprinted from Scoggins (2017).

As shown in Chapter 4, the transport coefficients require collision integrals data. In `MUTATION++`, the collision integrals data are managed in the `CollisionDB` class. This database is shown in Figure 8-17. The `CollisionDB` is divided into two categories:

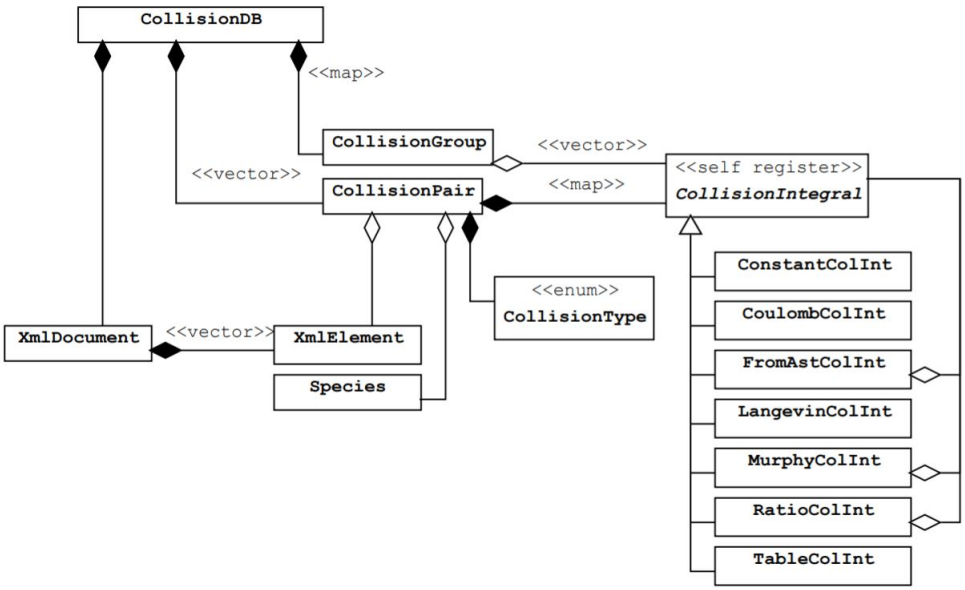

Figure 8-17: Overview of the `CollisionDB` class, reprinted from Scoggins (2017).

- The `CollisionGroup` object: This object is holding a collection of groups of collision integrals from a given name. For instance, the name "Q11ij" is the reduced collision integrals of order (1,1) for all pairs of heavy species.
- A vector of `CollisionPairs`: It represents 1-each of possible pair of species in the mixture, 2- determine the type of collision, and 3-load the collision integrals from an XML database if necessary (`XmlDocument` and `XmlElement`).

Finally, all the collision integrals are implemented in the `CollisionIntegral` self registering class. In this class, some of the `CollisionIntegral` types are functions of other collision integrals. For example, the `FromAstColInt` is computing $\bar{Q}_{ij}^{(1,1)}$ and $\bar{Q}_{ij}^{(2,2)}$, or A_{ij}^{*}, as function of the first two collision integrals.

Conclusion

The multicomponent systems have been implemented into the massively parallel code `CanoP`, based on the numerical strategy established in Chapter 6 for nonuniform AMR cartesian grids. The code is coupled to the library `p4est`, which is managing the mesh independently of the model and numerical methods implemented. This library provides a high compression ratio of the data and is scalable on highly parallel architectures. It is a tree-based/cell-based library which is using a z-order space filling curve to manage the meshes. In this chapter, the main functionalities of the library has been highlighted.

Then, we have presented the architecture of the `CanoP` code. It is an applicative layer built on top of the `p4est` library. The main goal of this code is the possibility to integrate several type of applications and numerical schemes. In this thesis, we have implemented the multicomponent systems into `CanoP` and coupled this code with the `MUTATION++` library. This library allows to compute the transport coefficients and algorithms presented in Chapter 4, with a high level of accuracy in thermal equilibrium ($T_e = T_h$) or nonequilibrium ($T_e \neq T_h$). The architecture of `MUTATION++` and its functionalities have been summarized in this Chapter.

The structure of the code has been presented and identified. However, it is still necessary to verify this implementation through several test cases. This step allows to verify the scalability of the code, the order of the scheme, the AMR capability of `p4est`, the incompressibility constraint of the magnetic field, *etc*. Finally, this step of verification will allow to perform AMR simulations of magnetic reconnection with multicomponent plasmas.

CHAPTER 9

VERIFICATION AND RESULTS

Introduction

Previous chapters have been dedicated to the description of the numerical strategy and the implementation of the multicomponent model into the massively parallel code `CanoP`. This chapter is devoted to the numerical results obtained with the `CanoP` code. The robustness and the accuracy of the numerical strategy presented in the previous chapter, are verified in sets of one, two and three dimensional test cases. We aim at proving that 1- the AMR solver is reaching a high level of accuracy once we have chosen a proper refinement criterion, 2- the proposed strategy is able to tackle the problem of magnetic reconnection under solar atmosphere conditions and 3- a high level scalability and efficiency of the parallel implementation of the numerical strategy is obtained.

In Section 9.1, the numerical strategy is verified on uniform grids. The implementation of the convective fluxes, the accuracy of the numerical scheme as well as the ability of the scheme to tackle the incompressibility constraint are verified. In Section 9.2, the AMR capability of `p4est` is verified. We show that, choosing an appropriate refinement criterion, the AMR is reaching a high level of accuracy combined with a high mesh compression rate, in both two and three dimensions. In Section 9.3, two and three dimensional simulations of magnetic reconnection in conditions representative of the solar atmosphere are performed, with the multicomponent model for both fully and partially ionized plasma. The results are compared with a classical single-fluid MHD model. The single-fluid MHD model has been implemented with the same numerical strategy used for the multicomponent model. In Section 9.4, the performance of the code is tested by studying the weak and strong scalability of `CanoP`.

Some of the results obtained in this Chapter are based on studies performed in Wargnier, Alvarez Laguna, et al. (2018). This Chapter constitutes the basis for Wargnier et al. (2019).

9.1 Verification on uniform grids

In order to verify the implementation, we have run test cases that are used as benchmarks in ideal MHD simulations. In the following, we verify 1-the implementation of the convective fluxes, 2- the accuracy of the numerical scheme and 3- the ability of our numerical strategy to tackle the solenoïdal constraint on the magnetic field. We do not solve for the full system defined by (*Mc*). Alternatively, only the convective part of the full system, without diffusive and source terms, is considered (except the component that is used for the divergence free constraint). For the purpose of the work, only verification results on uniform grids are shown for two dimensional configurations. In this section, only one species is considered, thus, only one mass conservation is considered.

9.1.1 Scheme verification

In order to assess and verify the accuracy of the presented scheme, the convection of an isentropic vortex in inviscid flow is studied, without considering the magnetic field, in both x and y directions, with a uniform mesh. It is used to show the ability of our scheme to accurately capture vortical flows. The exact solution of the test case is known (see H. Yee et al. (2000)).

The isentropic vortex is carried out in a two dimensional domain of $[0, 10] \times [0, 10]$ size with periodic boundary conditions. The vortex is in dynamical balance where the total pressure is balanced by the kinetic energy. At $t = 0$, the vortex is located at the middle of the domain. Then, the vortex will propagate and, at $t = 1$, it returns to the initial position. In the proposed test case, an isentropic vortex propagating only in the x direction has been considered. Similar results have been obtained for the other directions. The initial conditions are

$$\begin{aligned}\mathcal{U}(x, y, t = 0) = \Bigg(& \left[1 - \frac{(\gamma - 1)\varepsilon^2}{8\gamma\pi^2} e^{(1-r^2)}\right]^{\frac{1}{\gamma-1}}, \quad \rho_{\mathfrak{h}} \left[1 - \frac{\varepsilon}{2\pi\,(y - y_c)} e^{\frac{(1-r^2)}{2}}\right], \\ & \rho_{\mathfrak{h}} \frac{\varepsilon}{2\pi\,(x - x_c)} e^{\frac{(1-r^2)}{2}}, \quad \frac{p}{\gamma - 1} + \frac{1}{2}\rho_{\mathfrak{h}} |\boldsymbol{v}_{\mathfrak{h}}|^2, \quad \frac{1}{2}\frac{p}{\gamma - 1}, \quad 0, \quad 0, \quad 0\Bigg) \end{aligned} \tag{9.1.1}$$

where $\varepsilon = 5$, $x_c = y_c = 5$, the adiabatic constant $\gamma = 5/3$, $r = \sqrt{(x - x_c)^2 + (y - y_c)^2}$, and the total pressure p is defined as $p = \rho_{\mathfrak{h}}^{\gamma}$. Finally, the two numerical solutions are compared, at $t = 1$, with the analytical solution given in (9.1.3). The test case has been tested with several discretization $\Delta x = 10 \times 2^{-k}$ where $k \in \{4, 5, 6, 7\}$. A $CFL = 0.7$ is chosen. The L_1 norms of $\rho_{\mathfrak{h}}$, $\mathcal{E}$ and $\rho_{\mathfrak{h}} u_{\mathfrak{h}}$ are computed. Results are shown in Figure 9-1.

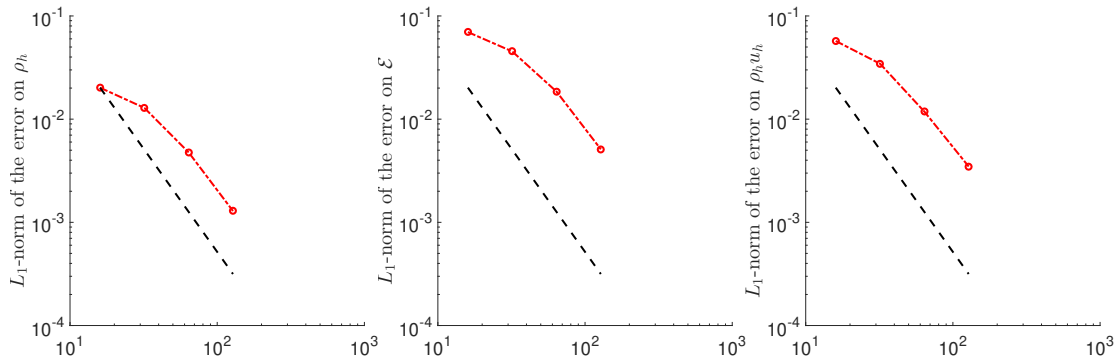

Figure 9-1: From left to right: L_1-norm of the error on $\rho_\mathfrak{h}$, $\mathcal{E}$ and $\rho_\mathfrak{h} u_\mathfrak{h}$ with respect to the number of mesh points. Reference second order slope (black dashed line). L_1-norm computed from the numerical solution (red line).

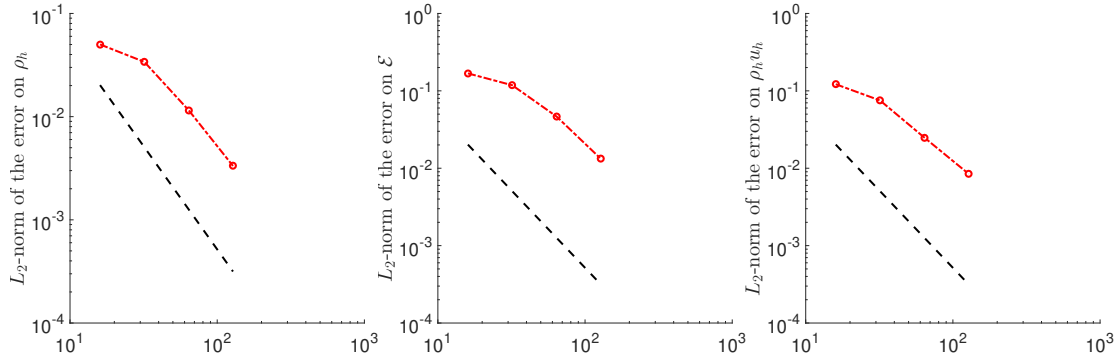

Figure 9-2: From left to right: L_2-norm of the error on $\rho_\mathfrak{h}$, $\mathcal{E}$ and $\rho_\mathfrak{h} u_\mathfrak{h}$ with respect to the number of mesh points. Reference second order slope (black dashed line). L_2-norm computed from the numerical solution (red line).

As expected, Figure 9-1 shows that the implementation is achieving a second order accuracy in all variables from the mesh tested with 128×128, without AMR. Similar results have been obtained with the L_2-norm of the error, as shown in Figure 9-2.

9.1.2 Rotor MHD and Orszag-Tang problem

In this section, the ability of the proposed numerical solver to tackle MHD shocks, shock-shock interactions, and the divergence-free constraint are verified. In order to perform the validation, we focus on two classical test cases: the Orszag & Tang (1979) (OT) configuration , and the rotor MHD problem. On the one hand, the OT configuration is based on a transition to 2D supersonic MHD turbulence and is used to validate MHD solvers. On the other hand, the rotor MHD problem is based on the evolution of a 2D strong torsional Alfvén wave, described by Balsara & Spicer (1999). The rotor MHD problem is a high-density disk that is rotating at large velocity inside a

constant pressure and constant magnetic field in the x direction. In both cases, a domain where $(x, y) \in [0, 1] \times [0, 1]$ with periodic boundary conditions in both directions, with a uniform mesh 256×256 is considered. The initial conditions for the Orszag-Tang test case $\mathcal{U}_{\text{OT}}(t = 0)$ and the rotor MHD test case $\mathcal{U}_{\text{r}}(t = 0)$ are

$$\mathcal{U}_{\text{OT}}(t = 0) = \left(\gamma \frac{5}{12\pi},\ -\rho_{\mathfrak{h}} sin(2\pi y),\ \rho_{\mathfrak{h}} sin(2\pi x),\ \mathcal{E}_{\text{OT}},\ \frac{5}{24\pi(\gamma - 1)},\ -sin(2\pi y),\ sin(4\pi x),\ 0\right)^T, \tag{9.1.2}$$

and

$$\begin{cases} r \geq r_0, & \mathcal{U}_{\text{r}}(t = 0) = \left(10,\ -\frac{2\rho_{\mathfrak{h}}(y-y_c)}{r_0},\ \frac{2\rho_{\mathfrak{h}}(x-x_c)}{r_0},\ \mathcal{E}_{\text{r}},\ \frac{1}{2(\gamma-1)},\ 5,\ 0,\ 0\right)^T, \\ r < r_0, & \mathcal{U}_{\text{r}}(t = 0) = \left(1 + 9f(r),\ -\frac{2\rho_{\mathfrak{h}}(y-y_c)f(r)}{r},\ \frac{2\rho_{\mathfrak{h}}(x-x_c)f(r)}{r},\ \mathcal{E}_{\text{r}},\ \frac{1}{2(\gamma-1)},\ 5,\ 0,\ 0\right)^T, \\ r < r_1, & \mathcal{U}_{\text{r}}(t = 0) = \left(1,\ 0,\ 0,\ \mathcal{E}_{\text{r}},\ \frac{1}{2(\gamma-1)},\ 5,\ 0,\ 0\right)^T. \end{cases} \tag{9.1.3}$$

Here, $\mathcal{E}_{\text{OT}} = 5/12\pi(\gamma - 1) + 1/2\rho_{\mathfrak{h}}|\boldsymbol{v}_{\mathfrak{h}}|^2 + |B|^2/8\pi$ and $\mathcal{E}_{\text{r}} = 1/(\gamma - 1) + 1/2\rho_{\mathfrak{h}}|\boldsymbol{v}_{\mathfrak{h}}|^2 + 25/8\pi$, the adiabatic constant is $\gamma = 5/3$, the radius is $r = \sqrt{(x - x_c)^2 + (y - y_c)^2}$, $r_0 = 0.115$ and $r_1 = 0.1$, the center of the disk is located at $y_c = x_c = 0.5$. A $CFL = 0.7$ is chosen. In order to maintain the divergence free constraint, $c_p = \sqrt{0.18 c_h}$ is considered, as chosen by Gomes et al. (2015a). The two test cases are run until $t = 0.5$ for the Orszag-Tang test case and until $t = 0.2$ for the rotor MHD problem.

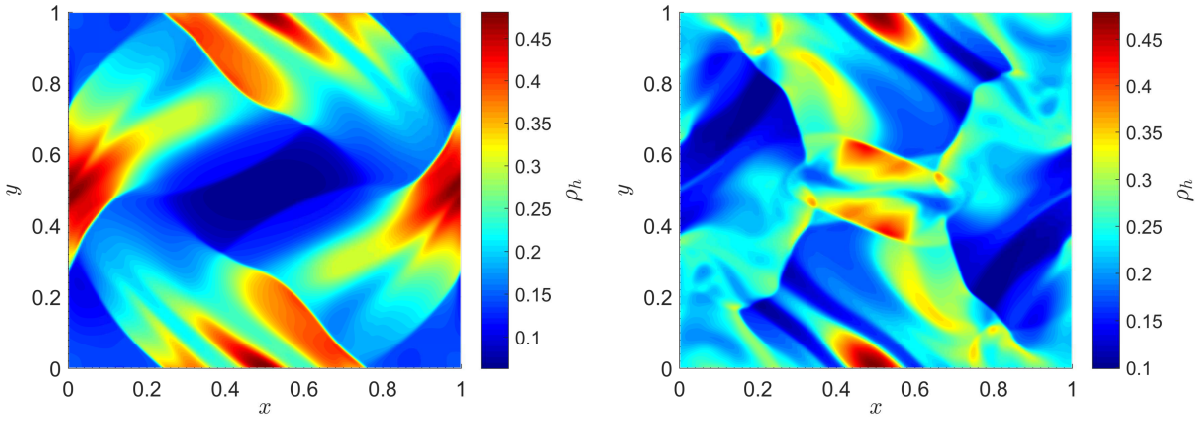

(a) Density distribution $\rho_{\mathfrak{h}}$ at $t = 0.25$.

(b) Density distribution $\rho_{\mathfrak{h}}$ at $t = 0.5$.

Figure 9-3: Density $\rho_{\mathfrak{h}}$ distribution for the OT test case at $t = 0.25$ and $t = 0.5$ on a uniform mesh 256×256.

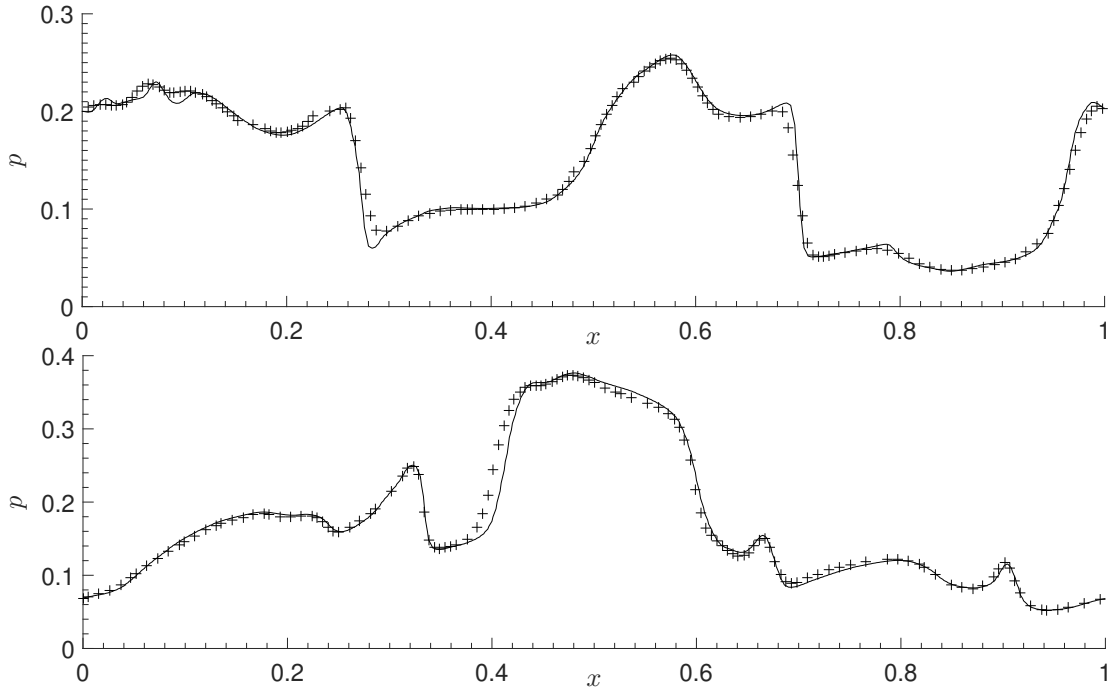

Figure 9-4: Total pressure p distribution at $y = 0.3125$ (top) and $y = 0.4277$ (bottom), at $t = 0.5$. Results from our simulation in full line on a uniform mesh 256×256, and + results from Londrillo & Zanna (2000) on a uniform mesh 192×192.

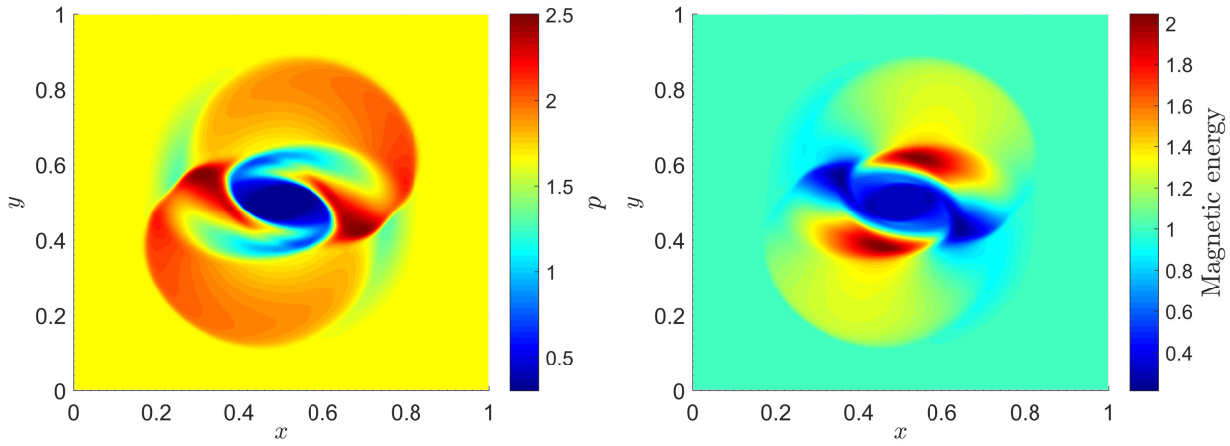

(a) Total pressure distribution p at $t = 0.15$.

(b) Magnetic energy distribution at $t = 0.15$.

Figure 9-5: Total pressure p and magnetic energy distribution in the Rotor MHD test case at $t = 0.15$ and on a mesh 256×256.

Figure 9-3 shows the distribution of the density $\rho_{\mathfrak{h}}$ at $t = 0.25$ and $t = 0.5$ for the OT test case. The results obtained show agreement with MHD solutions (see Christlieb et al. (2014); Tóth (2000)). Good agreements have been obtained with the other conservative variables. Besides, in

Figure 9-4, the total pressure p distribution along the lines $y = 0.4277$ and $y = 0.3125$ at $t = 0.5$ are in good agreement with the solution obtained by Londrillo & Zanna (2000) where a uniform mesh 192×192 has been used, and the divergence free constraint is discretized using a reconstruction method for high order upwind schemes based on the magnetic field potential.

In Figure 9-5, the results obtained for the total pressure p and magnetic energy, at $t = 0.15$, for the rotor MHD problem, are presented. The results are showing good agreement with the common solution, presented by Tóth (2000). Similar results have been obtained for the other conservative variables.

In the presented test cases, the level of accuracy and ability to capture discontinuities of the presented scheme, the implementation of the convective fluxes, and the ability to maintain the divergence free constraint have been verified.

9.1.3 Brio-Wu shock tube

In this section, we focus on the monodimensional Brio-Wu shock tube, described by Brio & Wu (1988). This test is a MHD shock tube, where the right and left states are initialized to different values. Generally, the Brio-Wu shock tube is mainly used to test if the code can accurately represent shocks, rarefactions, contact discontinuities, and the compound structures of ideal MHD. Therefore, we solve only for the convective part of the multicomponent model, and we underline that the nonconservative terms are not considered: the equation of internal energy of electrons is conservative. A monodimensional domain where $x \in [0, 1]$ is considered, with a uniform mesh $N = 2000$, thus, $\Delta x = 5 \times 10^{-4}$. The left state $x \leq 0.5$ is defined as

$$\mathcal{U}_{\mathrm{BW,L}}(t = 0) = \left(1, \quad 0, \quad 0, \quad \mathcal{E}_{\mathrm{Left}}, \quad \frac{p_{\mathrm{Left}}}{2(\gamma-1)}, \quad 0.75, \quad 0, \quad 0\right)^T, \tag{9.1.4}$$

and the right state $x > 0.5$ is defined as

$$\mathcal{U}_{\mathrm{BW,R}}(t = 0) = \left(0.125, \quad 0, \quad 0, \quad \mathcal{E}_{\mathrm{Right}}, \quad \frac{p_{\mathrm{Right}}}{2(\gamma-1)}, \quad 0.75, \quad -1, \quad 0\right)^T, \tag{9.1.5}$$

where $\mathcal{E}_{\mathrm{Left}} = p_{\mathrm{Left}}/(\gamma - 1) + 0.75^2/2$ and $\mathcal{E}_{\mathrm{Right}} = p_{\mathrm{Right}}/(\gamma - 1) + (0.75^2 + 1^2)/2$, $p_{\mathrm{Left}} = 1$ and $p_{\mathrm{Right}} = 0.1$, the adiabatic constant is $\gamma = 2$. A $CFL = 0.9$ is chosen. The test case is run until $t = 0.1$. The timestep is $\Delta t = 3.8 \times 10^{-5}$.

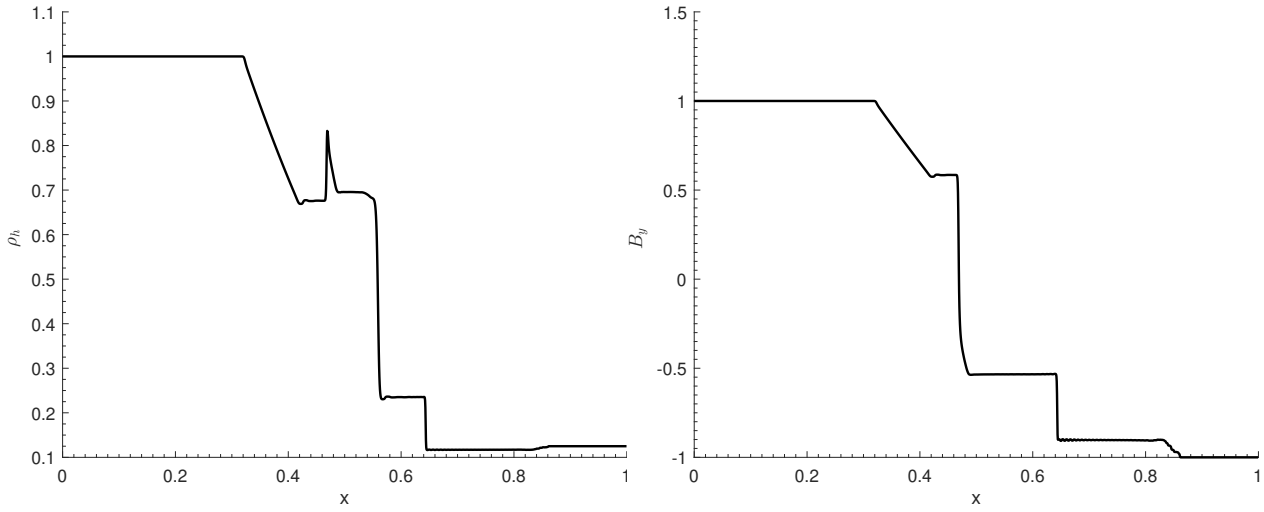

(a) Density distribution $t = 0.1$.

(b) B_y distribution at $t = 0.1$.

Figure 9-6: Distribution of the density and B_y in the Brio-Wu MHD test case at $t = 0.1$ and on a uniform mesh $N = 2000$.

Figure 9-6 represents the distribution of the density and component B_y at $t = 0.1$ for the Brio-Wu test case. The results obtained are showing good agreement with classical MHD solutions (see Brio & Wu (1988)). Good agreement have been obtained with all the conservative variables, except for the internal energy equation for electrons. Indeed, the latter equation is not conservative and is not considered by the classical ideal single fluid MHD equation. In the distribution of the density, we can notice the classical waves obtained from left to right: a fast rarefaction, a slow compound wave, a contact discontinuity, a slow shock, and a fast rarefaction wave.

Impact of the nonconservative term on the Brio-Wu solution

In the previous section, in order to perform the Brio Wu test case, the nonconservative term $p_e \cdot \partial_x \boldsymbol{v}_h$ has been considered as a source term. Therefore, the equation of internal energy of electrons is solved as a conservative equation. In this section, the distribution of the internal energy of electrons is compared for two cases: 1- a case where the nonconservative term is considered as a source term (as described previously), and 2- a case where the nonconservative term is considered as part of the hyperbolic system and discretized with a standard second order centered scheme as presented in Section 6.3.3.

Results are shown in Figure 9-7. In the case where the nonconservative is considered as a source term (left of Figure 9-7), we notice that the distribution of the internal energy of electrons is similar to the distribution of the density obtained in Figure 9-6a. All the classical waves have been retrieved. However, when the nonconservative term is considered (right of Figure 9-7), the structure of the waves are modified. The jump condition of the slow shock wave is different from the case where the nonconservative term is considered as a source term. Similarly, the jump condition of the contact discontinuity is modified. This result is consistent with our results obtained in Chap-

ter 7 and Chapter E. However, a deeper investigation is required to understand the impact of the nonconservative terms on the structure of the Brio-Wu solution, in particular the jump conditions, as performed in Chapter 7, considering the electromagnetic field.

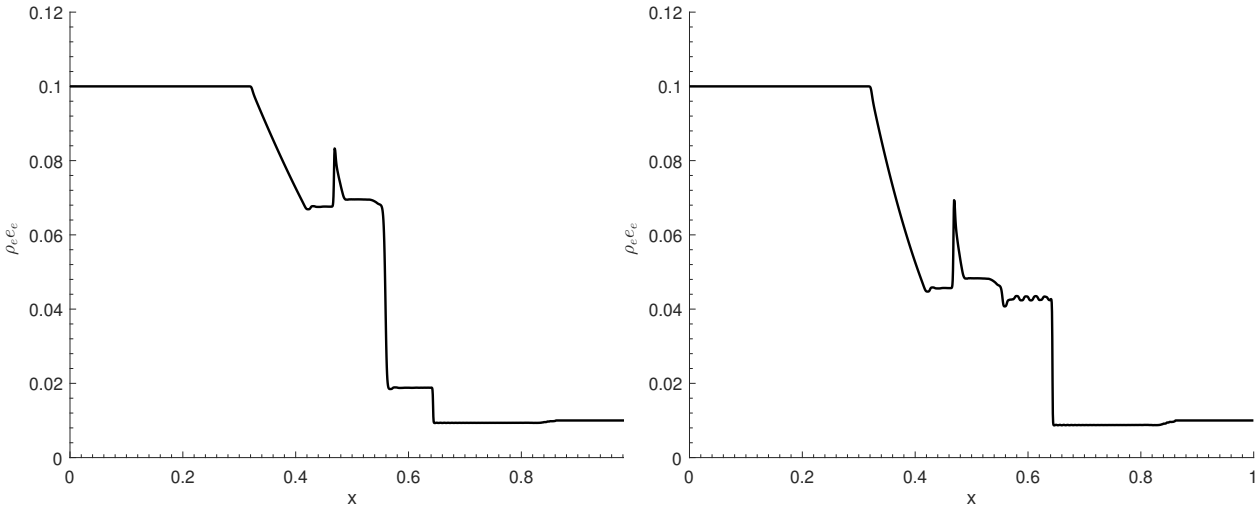

Figure 9-7: Distribution of the internal energy of electrons $\rho_e e_e$ at $t = 0.1$ with $N = 2000$. Left: case where the nonconservative term is considered as a source term. Right: case where the nonconservative term is taking into account, with a second order centered discretization of the gradient.

9.2 Verification of the AMR framework

In the following, several classical test cases are considered in order to verify 1- the AMR capability of `p4est` 2- the ability of the proposed numerical scheme to be combined with AMR and 3- the refinement criterions. Results with AMR grids are compared with results on uniform grids. For the sake of clarity, no diffusive or source terms are considered here. Thus, only one continuity equation is considered.

First, the Kelvin-Helmoltz instabilities test case is considered in order to verify that the dynamics captured by non-uniform AMR grid cases are similar to uniform grid cases. Then, as presented in the previous section, the ideal Orszag-Tang test case is considered. We focus on both two and three dimensional cases.

9.2.1 Two and three dimensional Kelvin-Helmotz instabilities

Kelvin-Helmholtz instability (KHI) (see Howard (1962)) is the name given to the primary instability that occurs when velocity shear is present within a continuous fluid or across fluid boundaries. The shear is converted into vorticity that, subject to secondary instabilities, cascades generating turbulence. The KHI is one of the most important hydrodynamical instabilities and plays a significant role in various parts of astrophysics. It plays a role in the interactions of the magnetopause and

solar wind (see Miura & Pritchett (1982)) and has been observed in the solar corona (see Ofman & Thompson (2011)). In this test case, a KHI with magnetic field has been considered.

Two dimensional case

The test case is set in a two dimensional domain of $[0,1] \times [0,1]$ size with periodic boundary conditions. We set two oppositely directed smooth streams, that is a slip surface. The initial conditions are

$$\mathcal{U}(x,y,t=0) = \left(\alpha_{\rho_\mathfrak{h}}\left[1+f_{\rho_\mathfrak{h}}(y)\right],\ \alpha_{\rho_\mathfrak{h}u_\mathfrak{h}}\left[1+f_{\rho_\mathfrak{h}u_\mathfrak{h}}(y)\right],\ \rho_\mathfrak{h}\xi(x),\ \mathcal{E}_{\text{tot}},\ \tfrac{2.5}{2(\gamma-1)},\ 0.5,\ 0,\ 0\right)^T, \tag{9.2.1}$$

where

$$\alpha_k = \frac{(k_{\text{in}}+k_{\text{out}})}{2}, \quad \begin{cases} f_k(y) = (k_{\text{in}}-k_{\text{out}})\,/\,(k_{\text{in}}+k_{\text{out}})\tanh\left(\frac{y-0.25}{\lambda}\right), & y<0.5 \\ f_k(y) = (k_{\text{out}}-k_{\text{in}})\,/\,(k_{\text{in}}+k_{\text{out}})\tanh\left(\frac{y-0.75}{\lambda}\right), & y\geq 0.5 \end{cases}, \ k\in\{\rho_\mathfrak{h},\rho_\mathfrak{h}u_\mathfrak{h}\} \tag{9.2.2}$$

where $\rho_{\mathfrak{h},\text{in}} = 1$ and $\rho_{\mathfrak{h},\text{out}} = 2$, $u_{\mathfrak{h},\text{in}} = -0.5$ and $u_{\mathfrak{h},\text{out}} = 0.5$, the thickness of the slip surface is $\lambda = 0.01$, ξ corresponds to a modal perturbation defined by $\xi(x) = 0.01 * \sin(2\pi x)$, the total energy is $\mathcal{E}_{\text{tot}} = 1/2\rho_\mathfrak{h}|\boldsymbol{v}_\mathfrak{h}|^2 + 2.5/(\gamma-1) + |\boldsymbol{B}|^2/8\pi$, and $\gamma = 1.4$. A $CFL = 0.5$ is considered and the simulation is run until $t = 2$. In order to maintain the divergence free constraint, $c_p = \sqrt{0.18 c_h}$ has been considered, as used by Gomes et al. (2015a). In order to test the AMR capability of `p4est`, a comparison between results from AMR and uniform grids has been performed.

The uniform grid is such as $\Delta x = 2^{-10}$ ($N = 1024$). The AMR grid is defined such as the minimum level of refinement is $\Delta x_{min} = 2^{-8}$ ($N = 256$) and $\Delta x_{max} = 2^{-10}$ ($N = 1024$). 160 MPI processes have been used for each simulations. In order to study the AMR capability of `p4est`, two cases are considered. Two cases based on a $\rho_\mathfrak{h}$-gradient criterion (see Section 8.3.2) have been considered, : $\theta_1 = \theta_2 = \theta = 0.001$ called **Case HPR** (high compression rate), and $\theta = 0.008$ called **Case WPR** (weak compression rate). Following this strategy, the optimal compression rate, required to ensure a good quality of the solution of the test case, can be determined.

Figure 9-8 and Figure 9-9 represent the distribution of the density and level of refinement for the three cases (uniform, **Case HPR** and **Case WPR**) at $t = 0.8$ and $t = 1.6$, respectively. At $t = 0.8$, the compression rate is 88% and 67% in the **Case HPR** and **Case WPR**, respectively. At $t = 1.6$, the compression rate is 84% and 46% in the **Case HPR** and **Case WPR**, respectively.

In Figure 9-8 and Figure 9-9, the formation of vortices, at the two interfaces between the two plasma fluids of density $\rho_\mathfrak{h} = 2$ and $\rho_\mathfrak{h} = 1$, has been obtained. Besides, the AMR method seems to refine in the regions of interest, *i.e*, at the interface between the two plasma fluids, where the vortices are created. The results show that the global dynamics of the vortices is similar in both uniform and AMR grid cases. However, differences have been observed at the scales of the vortices between the **Case HPR** and **Case WPR**, due to the lack of refinement of the **Case HPR** at these scales, due to the choice of the criterion used. Therefore in the **Case HPR**, the dynamics of small scales is lost, whereas in the **Case WPR** the dynamics of the instabilities is retrieved. The uniform

grid and **WPR** cases are showing very good agreement. Therefore, an optimal compression rate of 46%-67% has been reached for this test case. In Wargnier, Alvarez Laguna, et al. (2018); Wargnier et al. (2019), we underline that this test case has been compared with the `RAMSES` code (Teyssier (2002)) and shows good agreement.

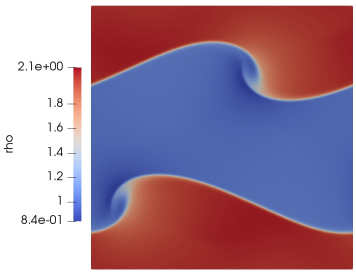

(a) Density on uniform grid

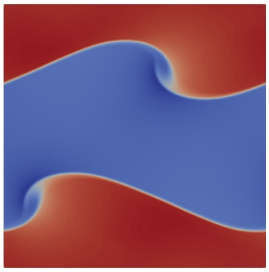

(b) Density, **Case WPR**

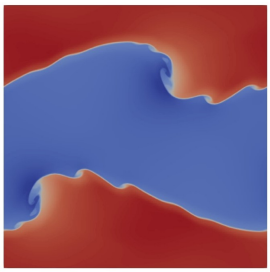

(c) Density, **Case HPR**

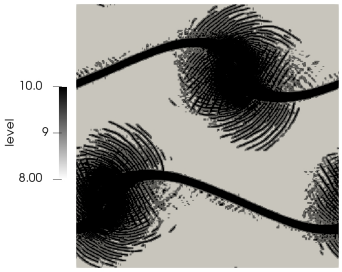

(d) Level of refinement, **Case WPR** (e) Level of refinement, **Case HPR**

Figure 9-8: KHI: Distribution of the density (top) and level of refiment (bottom) at $t = 0.8$

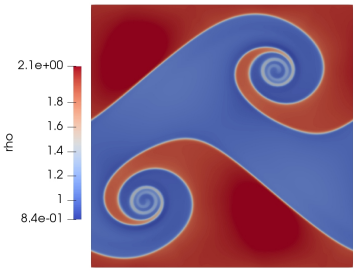

(a) Density on uniform grid

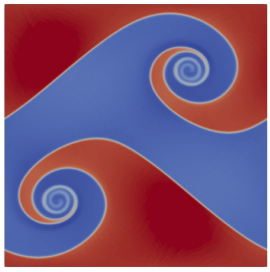

(b) Density, **Case WPR**

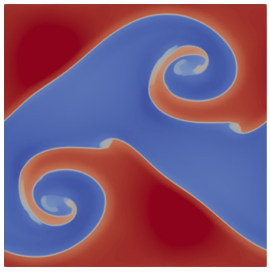

(c) Density, **Case HPR**

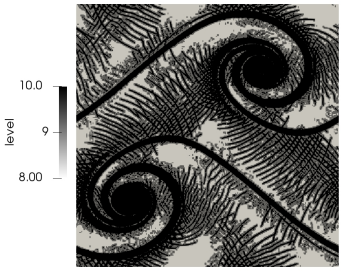

(d) Level of refinement, **Case WPR** (e) Level of refinement, **Case HPR**

Figure 9-9: KHI: Distribution of the density (top) and level of refiment (bottom) at $t = 1.6$

Three dimensional case

In order to verify the AMR ability of the code to handle 3D problem, we have set the corresponding 3D MHD Kelvin-Helmoltz instabilities case in a $[0,1] \times [0,1] \times [0,1]$ periodic box. Similar conditions as the two dimensional problem have been used. The CFL number and parameters used for the divergence free constraint are identical to those used in the two dimensional problem. Here, a discretization such as the minimum level of refinement is $\Delta x_{min} = 2^{-6}$ ($N = 64$) and $\Delta x_{max} = 2^{-8}$ ($N = 256$) has been chosen. A ρ-gradient criterion has been chosen. Similarly as the two dimensional case, two cases have been considered : $\theta = 0.005$ called **Case HPR** (high compression rate), and $\theta = 0.03$ called **Case WPR** (weak compression rate).

Figure 9-10 and Figure 9-11 represent the three dimensional distribution of the density and level of refinement for the three cases (uniform, **Case HPR** and **Case WPR**) at $t = 0.8$ and $t = 1.2$, respectively. At $t = 0.8$, the compression rate is 89.94% and 75% in the **Case HPR** and **Case WPR** respectively. At $t = 1.2$, the compression rate is 86.22% and 64% in the **Case HPR** and **Case WPR** respectively.

The results are similar to those obtained in the two dimensional case. The global evolution of the vortices have been obtained, and the refinement has been performed at the interface between the two plasma fluids. However, small scales structures have not been captured in the **Case HPR**. Similarly as the two dimensional case, good agreements have been obtained between the uniform case and the **Case WPR**. An optimal compression rate of 75%-64% has been obtained for the 3D test case. Additionally, the computational time required for the three dimensional AMR case was about less than an hour. In the uniform grid case, about four hours were required to perform the test case.

Finally, all these results have shown that the proposed numerical scheme combined with AMR has been validated and verified in both 2D and 3D cases. At the same time, the AMR capability of `p4est` has been evaluated. The results have shown that a high compression rate can be reached. Additionally, the results are in good agreement with the literature. Indeed, the results have been compared with the `RAMSES` code with uniform grids and show good agreement, as described in Wargnier, Alvarez Laguna, et al. (2018).

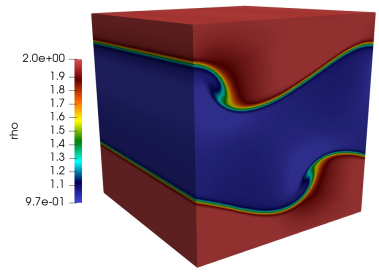

(a) Density on uniform grid

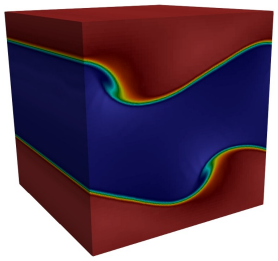

(b) Density, **Case WPR**

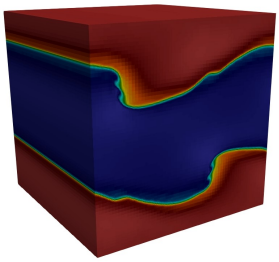

(c) Density, **Case HPR**

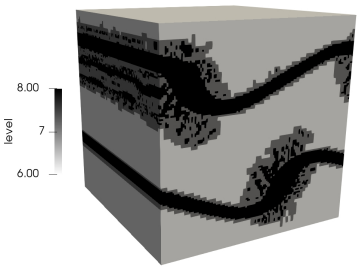

(d) Level of refinement, **Case WPR**

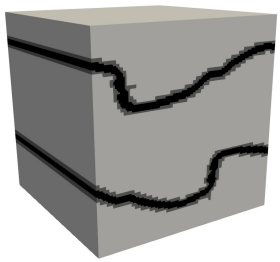

(e) Level of refinement, **Case HPR**

Figure 9-10: KHI: 3D Distribution of the density (top) and level of refinement (bottom) at $t = 0.8$.

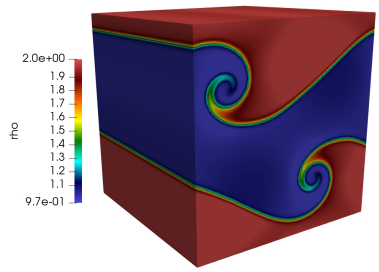

(a) Density on uniform grid

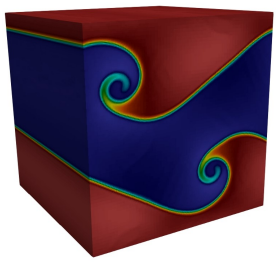

(b) Density, **Case WPR**

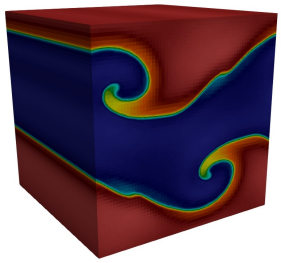

(c) Density, **Case HPR**

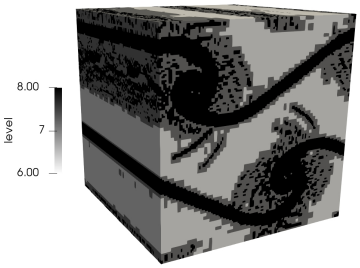

(d) Level of refinement, **Case WPR**

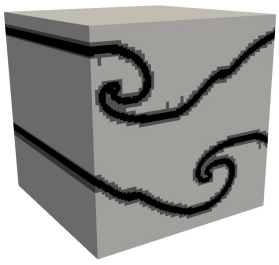

(e) Level of refinement, **Case HPR**

Figure 9-11: KHI: 3D Distribution of the density (top) and level of refinement (bottom) at $t = 1.2$

9.2.2 Two and three dimensional Orszag-Tang test case

In this section, we verify the ability of the proposed numerical combined with AMR to perform the Orszag-Tang (OT) configuration (see Orszag & Tang (1979)), as presented in Section 9.1.2. In addition, the 3D OT test case is investigated.

Two dimensional case

In this case, a domain where $(x, y) \in [0, 1] \times [0, 1]$, with periodic boundary conditions in both directions, is considered. The initial conditions of the OT test case have been given in (9.1.2). Identical initial conditions and parameters of the simulation, as those presented in Section 9.1.2, have been used.

As presented in the previous section, the AMR capability of `p4est` is tested and a comparison between results from AMR and uniform grid is performed. The uniform grid is such as $\Delta x = 2^{-10}$ ($N = 1024$). The AMR grid is defined such as the minimum level of refinement is $\Delta x_{min} = 2^{-8}$ ($N = 256$) and $\Delta x_{max} = 2^{-10}$ ($N = 1024$). A $\rho_{\mathfrak{h}}$-gradient has been chosen as the refinement criterion. We consider two cases on AMR grids: $\theta_1 = \theta_2 = \theta = 0.001$ called **Case HPR** (high compression rate), and $\theta = 0.008$ called **Case WPR** (weak compression rate).

Figure 9-12 and Figure 9-13 represent the distribution of the density and level of refinement for the three cases (uniform, **Case HPR** and **Case WPR**), for the OT test case, at $t = 0.25$ and $t = 0.5$, respectively. At these timesteps, the compression rate is around 84% and 62% in the **Case HPR** and **Case WPR**, respectively.

These results show that very good agreement have been obtained between the three cases. However, some of the shocks involved in the uniform grid case have not been captured in the **Case HPR**, because of the numerical diffusion induced by the high mesh compression rate. The **Case WPR** appears to show better agreement with the uniform grid case.

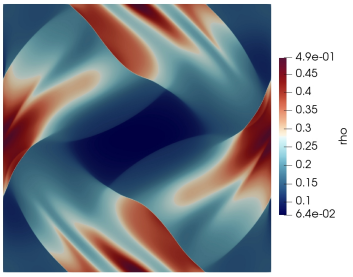

(a) Density on uniform grid

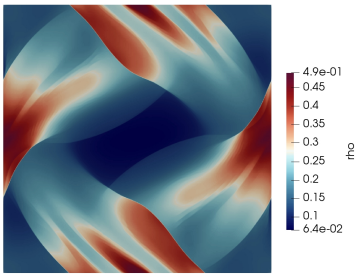

(b) Density, **Case WPR**

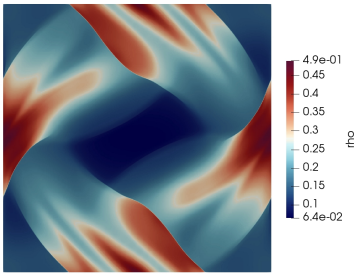

(c) Density, **Case HPR**

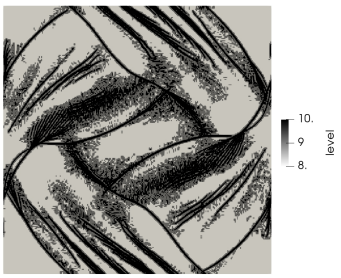

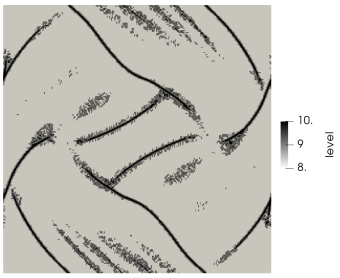

(d) Level of refinement, **Case WPR** (e) Level of refinement, **Case HPR**

Figure 9-12: OT: Distribution of the density (top) and level of refinement (bottom) at $t = 0.25$

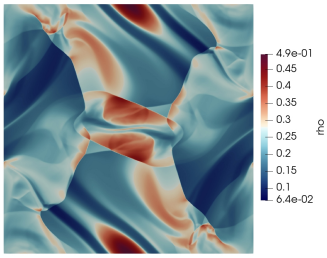

(a) Density on uniform grid

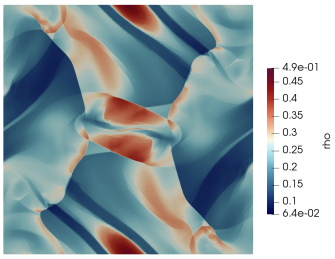

(b) Density, **Case WPR**

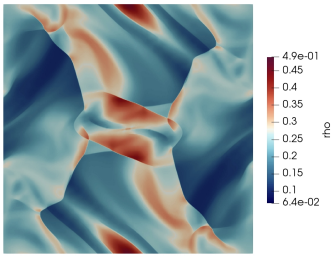

(c) Density, **Case HPR**

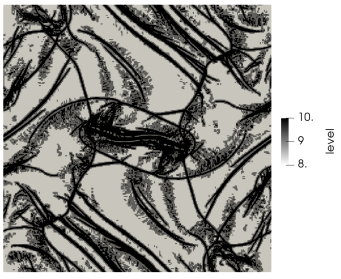

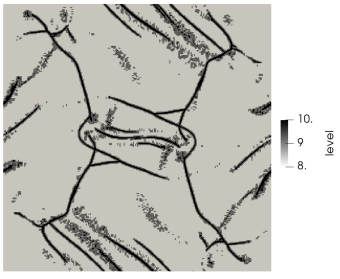

(d) Level of refinement, **Case WPR** (e) Level of refinement, **Case HPR**

Figure 9-13: OT: Distribution of the density (top) and level of refinement (bottom) at $t = 0.5$

Three dimensional case

In this section, the OT problem in a three dimensional configuration is studied. In this case, a domain where $(x, y, z) \in [0, 1]\times[0, 1]\times[0, 1]$, with periodic boundary conditions in both directions, is considered. The initial conditions of the 3D OT test case are identical to (9.1.2), except that

$$\rho_\mathfrak{h} w_\mathfrak{h} = 0, \tag{9.2.3}$$
$$B_x = \sin(2\pi y)\cos(2\pi z), \tag{9.2.4}$$
$$B_y = \sin(4\pi x)\cos(2\pi z), \tag{9.2.5}$$
$$B_z = 0. \tag{9.2.6}$$

Here, a discretization such as the minimum level of refinement is $\Delta x_{min} = 2^{-6}$ ($N = 64$) and $\Delta x_{max} = 2^{-8}$ ($N = 256$) has been chosen. The uniform grid is such as $\Delta x = \Delta x_{max} = 2^{-8}$ ($N = 256$). A ρ-gradient criterion has been chosen. Here, two cases are considered: $\theta_1 = \theta_2 = \theta = 0.01$ (case **WPR**) and $\theta = 0.03$ (case **HPR**). As performed in the previous section, the AMR capability of `p4est` on a 3D OT test case is investigated.

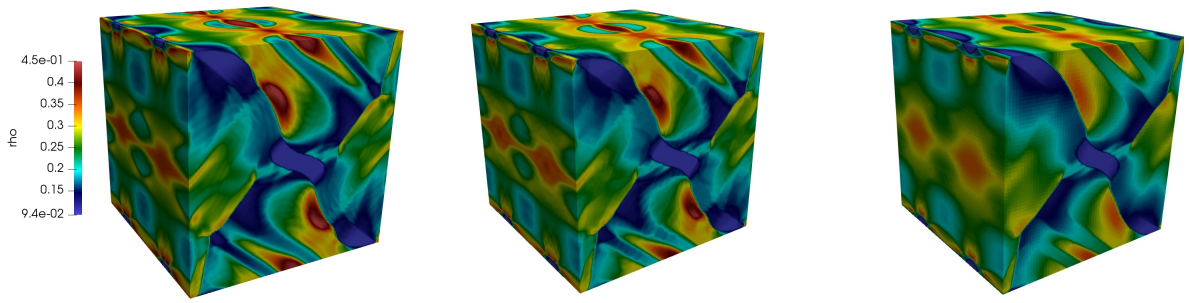

(a) Density on uniform grid (b) Density, **Case WPR** (c) Density, **Case HPR**

Figure 9-14: OT: 3D Distribution of the density at $t = 0.4$ for several compression rates. Middle: $\theta = 0.01$. Right: $\theta = 0.03$

Figure 9-14 shows the distribution of the density for three cases (from left to right: uniform, **Case HPR** and **Case WPR**), for the 3D OT test case, at $t = 0.4$. The compression rate is around 73% and 20% in the **Case HPR** and **Case WPR**, respectively.

Results show that, very good agreement have been obtained between the uniform grid case and the **Case WPR**, *i.e*, with a compression rate of 20%. However, strong differences have been obtained with the **Case HPR**. Here, the optimal mesh compression rate in the OT test case appears to be smaller than the one obtained in the KHI test case, since a lot of shock waves are involved, thus, the mesh is refined in a lot of regions of the domain.

9.3 Results

9.3.1 Results for a fully ionized plasma and comparison with the single-fluid approach on a uniform grid in a highly collisional regime

In this section, the results are presented using two models for a fully ionized plasma $S = \{\mathfrak{e}, H^+\}$: (1) the multicomponent plasma model for fully ionized plasma from (Mf), which includes diffusion fluxes and source terms and (2) a reference single-fluid MHD model with isotropic diffusive fluxes (see Wray et al. (2015)). Both models have been discretized following the numerical strategy established in Chapter 6, based on a KT scheme. First, the comparison is performed in a two dimensional magnetic reconnection configuration under photosphere conditions. In a second study, in order to analyze the influence of the thermal non-equilibrium process on the dynamic of this magnetic reconnection, we will study the same test case where we will artificially change the value of the parameter τ (mean collision time between electron and H^+) in the multicomponent model, in order to be in a weakly collisional regime. Finally, the idea is to see for this case of magnetic reconnection, the difference between the two models in various collisional regimes. A summary of the differences between the two models compared in this section is given in Figure 3-1.

We choose a reference length of $L^* = 100$ km and characteristic properties of the photosphere such as a reference temperature $T^* = 8000$ K, a total pressure $P^* = 10^4$ Pa, a reference density of heavy particles H^+ such as $\rho^* = 7.573\times 10^{-5}\, kg.m^{-3}$, and a strong magnitude of magnetic field such as $B^* = 1000$ G (conditions that can be found in a sunspot at the photosphere). Using `MUTATION++` library (further details about the library are given in Section 8.4), the mean collision time between electron and H^+ is found to be $\tau^* = 4.81 \times 10^{-12}$ s. The reference timescale t^* is also defined as $t^* = L^*/v^*$, where v^* is the characteristic speed computed as the reference speed of sound. Under these conditions, we have $\tau^*/t^* \approx 10^{-9}$, which implies that we are in a highly collisional regime. Then, all the quantities are normalized with these reference values. The transport properties are computed using the `MUTATION++` library and are presented in the following Table 9.1; where the transport coefficients of the single-fluid MHD model are shown as well as the parallel and perpendicular components of the tensor of each electron transport coefficients.

Table 9.1: Transport coefficients used both in the multicomponent and single fluid MHD model

$\eta^{\parallel}\ [\Omega.m]$	$\nu_{\mathfrak{h}}\ [Pa.s]$	$\lambda_{\mathfrak{h}}\left[W.m^{-1}.K^{-1}\right]$	$\lambda_{\mathfrak{e}}^{\parallel}\left[W.m^{-1}.K^{-1}\right]$	$\chi_{\mathfrak{e}}^{\parallel}[-]$	
3.378×10^{-4}	4.45×10^{-7}	0.0138	0.3514	0.644	
$\eta^{\perp}\ [\Omega.m]$	$\eta^{\odot}\ [\Omega.m]$	$\lambda_{\mathfrak{e}}^{\perp}\left[W.m^{-1}.K^{-1}\right]$	$\lambda_{\mathfrak{e}}^{\odot}\left[W.m^{-1}.K^{-1}\right]$	$\chi_{\mathfrak{e}}^{\perp}[-]$	$\chi_{\mathfrak{e}}^{\odot}[-]$
3.338×10^{-4}	-2.85×10^{-6}	0.3506	-0.0153	0.6429	-0.02

Initially, a magnetic field configuration consisting of a double 2D Harris current sheet is considered (see Mignone et al. (2012); Alvarez Laguna et al. (2016, 2018)). The configuration contains a

small perturbation for the magnetic field in the center of each current sheet in order to initiate the reconnection. The total pressure is balanced by the magnetic pressure, and the initial velocity field is set to zero. A domain where $(x, y) \in [0, 1] \times [0, 1]$ with periodic boundary conditions in all the directions, with a uniform mesh 256×256, is considered, where the current sheets are located at $y = 1/4$ and $y = 3/4$. Thus, in the subdomain $x \in [0, 1]$ and $y \in [0, 1/2]$, the initial conditions for the multicomponent model are $\mathcal{U}(t = 0) = \mathcal{U}_0$

$$\mathcal{U}_0 = \left(\left(1 + \frac{\psi_0}{\cosh^2\left(\frac{y-1/4}{\delta}\right)}\right),\ 0,\ 0,\ \frac{p}{\gamma - 1} + \frac{|B|^2}{8\pi},\ \frac{p}{2(\gamma - 1)},\ B_0 \tanh\left(\frac{y - 1/4}{\delta}\right) - B'_x,\ B'_y,\ 0\right), \tag{9.3.1}$$

where the width of the sheet is $\delta/L^* = 0.01$, the amplitude of the perturbation is $\psi_0 = 0.1$, the magnetic field is $B_0 = 1$, the perturbed magnetic field are

$$B'_x = \psi_0 \pi \cos\left(2\pi\left[x - x_c\right]\right) \sin\left(\pi\left[y - y_c\right]\right), \quad \text{and} \quad B'_y = 2\psi_0 \pi \sin\left(2\pi\left[x - x_c\right]\right) \cos\left(\pi\left[y - y_c\right]\right)^T.$$

Where $x_c = 1/2$ and $y_c = 1/4$. A $CFL = 0.5$ is considered. In order to maintain the divergence free constraint, similarly as in the previous section, we choose $c_p = \sqrt{0.18 c_h}$ and c_h is computed as the fastest magnetosonic wave. The two test cases are run until $t = 0.5$.

Figure 9-15 shows the evolution of the transverse current density and the density for the single fluid MHD model (left and middle), and the evolution of the total density for the multicomponent model (right), at time $t = 0.05, 0.1$ and $t = 0.4$. Figure 9-16, at the top, shows the distribution of the internal energy of electron at time $t = 0.1$ for the single fluid MHD model and multicomponent model in the highly collisional regime. Figure 9-16, at the bottom, shows the distribution of the internal energy of electron and the ratio between the internal energy of electron and heavy particle, for the multicomponent model, in the weakly collisional regime, at time $t = 0.1$.

In Figure 9-15 and Figure 9-16, we clearly see the dynamics of the magnetic reconnection. In Figure 9-15, if we focus on the evolution of the transverse current, we see that the magnetic lines are changing their topology forming a current sheet in the center of the domain and two separatrices. The results show that the density is decreasing in the middle of the reconnection but is increasing after the reconnection process. This is due to the mechanism of the magnetic reconnection where the particles are outflowing the reconnection region in the y direction. We retrieve this dynamics of the reconnection, which can be found in the literature involving different initial conditions (see Alvarez Laguna et al. (2016)). Finally, in Figure 9-15, if we focus on the evolution of the density and compare the results from the multicomponent and single fluid MHD model (middle and right figures), we see that the dynamics of the reconnection is similar for both models, in the highly collisional regime. Besides, in Figure 9-16, at the top, we see that the distribution of the electron internal energy at $t = 0.1$ is similar for the two models (left and right snapshots). In addition, we highlight the low additional computing cost required to solve the multicomponent system compared to the resolution of the single-fluid MHD model.

Under the same conditions, we have tested a configuration where the multicomponent model is in a weakly collisional regime. In order to force the system to be in this regime, we take an artificial

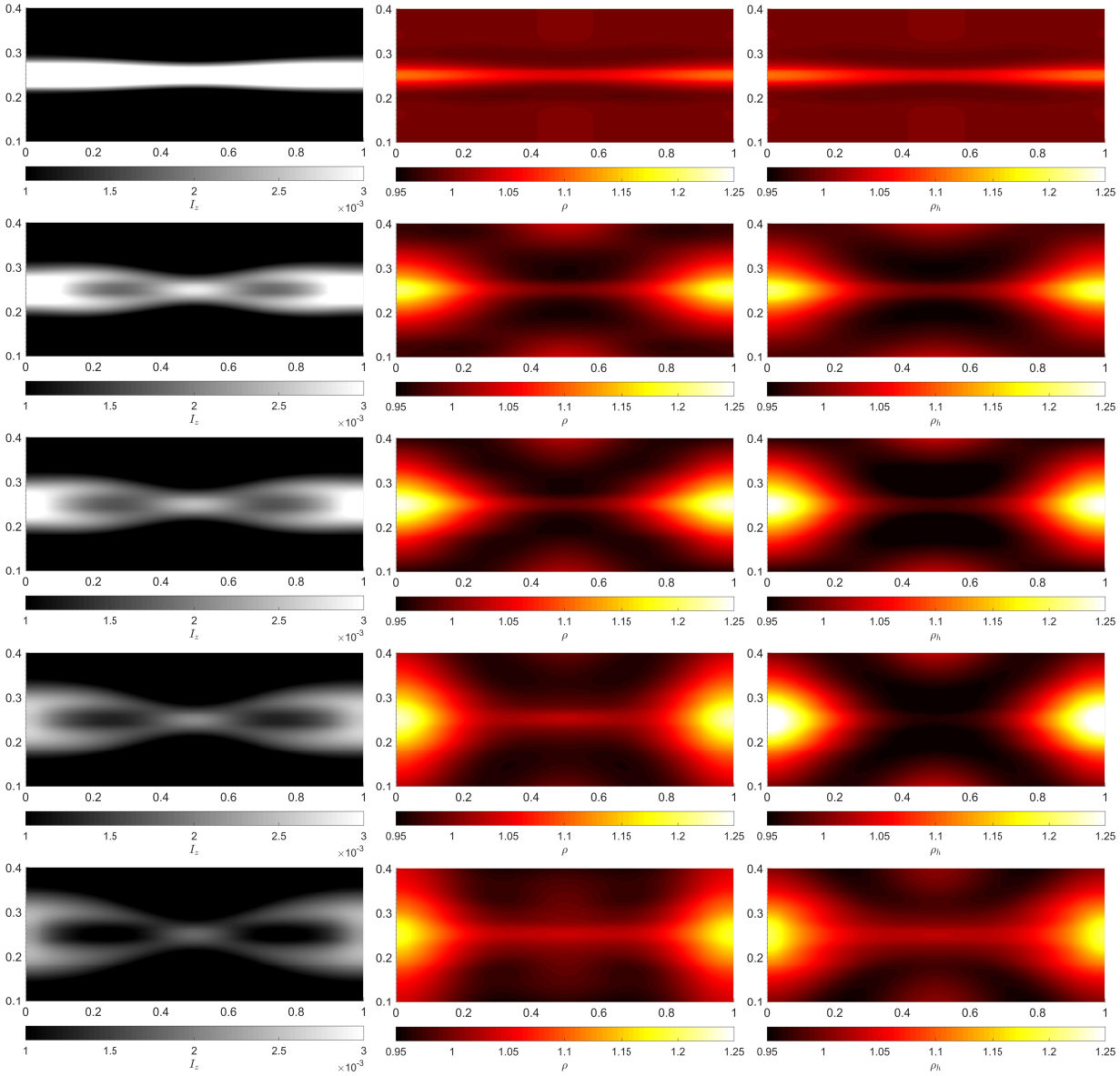

Figure 9-15: Left and middle: Distribution of the transverse current density and density ρ distribution from the single-fluid MHD model, right: distribution of the total density $\rho = \rho_{\mathfrak{e}} + \rho_{\mathfrak{h}}$ from the multicomponent model. From top to bottom: $t = 0.05,\ 0.1,\ 0.2,\ 0.3$ and $t = 0.4$ respectively.

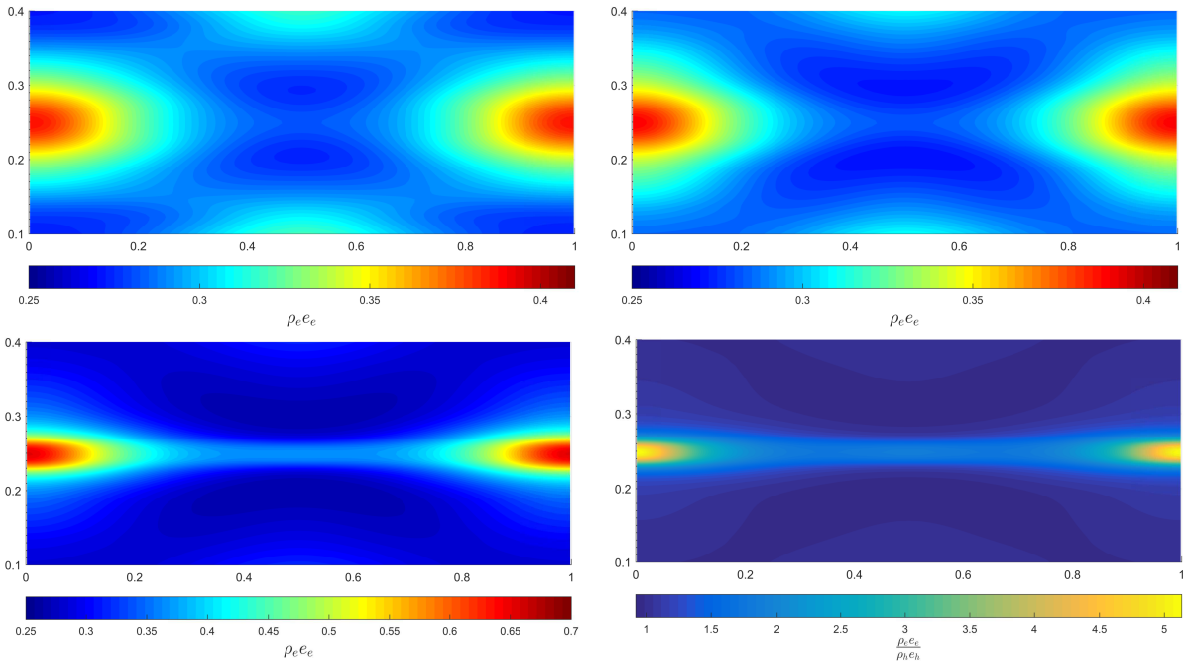

Figure 9-16: Top: Distribution of the internal energy of electrons for the single fluid-MHD model (left), the multicomponent model (right) in the highly collisional regime, at $t = 0.1$. Bottom: Distribution of the internal energy of electron in the weakly collisional regime (left), distribution of the ratio between internal energy of electrons and heavy particles in the weakly collisional regime (right), at $t = 0.1$.

high mean collision time τ^* such as $\tau^*/t^* \approx 10^3$, which can be representative of a weakly collisional regime. Physically, these regimes can be found in the solar corona. Figure 9-16, on the bottom left, represents the distribution of the internal energy of electrons, and Figure 9-16, on the right, represents the ratio between the internal energy of electrons and heavy particles, at the time $t = 0.1$. We see that the dynamic of the reconnection is different for the strongly collisional regime. The internal energy of electrons becomes higher in the reconnection region as well as in the magnetic islands. From Figure 9-16, we estimate that in the reconnection region $\rho_e e_e \approx 1.85\rho_h e_h$ and in the magnetic islands we have $\rho_e e_e \approx 5\rho_h e_h$. In this configuration, the internal energy distribution between the electrons and heavy particles becomes different, due to the power developped by the electromagnetic field present in the equation of internal energy of electrons. We have an imbalance between the temperature of electrons and the temperature of heavy particles. The impact of the thermal non-equilibrium process on the dynamics transfer is still a work in progress.

Finally, the two models have been compared in a two dimensional magnetic reconnection configuration under solar photosphere conditions. The chosen conditions are in a highly collisional regime, where both models are valid. The results have shown that the dynamics of the reconnection are very similar in both models. Thus, the presented multicomponent model has been validated in the highly collisional regime. Then, we have artificially decreased the collisional time in order to mimic a magnetic reconnection configuration in a weakly collisional regime under the same initial conditions. In this configuration, the thermal non-equilibrium between electrons and heavy particles induces a change of dynamics of the magnetic reconnection since the internal energy of electrons is increasing in the reconnection region as well as in the formed magnetic islands, because of the power developed by the electromagnetic field (Joule effect). These results illustrate the potential of the proposed model and assesses the proposed numerical strategy.

9.3.2 Two and three dimensional magnetic reconnection of a fully ionized plasma on AMR grids

In the previous section, a magnetic reconnection configuration test case has been identified to verify the implementation of the multicomponent model for a fully ionized plasma. In this section, we have focused on the identical test case described in Section 9.3.1. We perform the same test case, except that we use AMR grids in a two and three dimensional configuration. As presented in the previous section, a double 2D and 3D Harris current sheet has been considered. In the 3D configuration, a perturbation of the density in th z direction has been considered.

In order to maintain the divergence free constraint, similarly as the previous section, we choose $c_p = \sqrt{0.18 c_h}$. The two test cases are run until $t = 0.5$. In the 2D case, we choose a discretization such as the minimum level of refinement is $\Delta x_{min} = 2^{-9}$ ($N = 512$) and $\Delta x_{max} = 2^{-12}$ ($N = 4096$). A $\boldsymbol{B}$-gradient criterion has been chosen with $\theta = 10^{-3}$. In this case, 160 MPI processes have been used.

In the 3D magnetic reconnection test case, a box of size $(x, y, z) \in [0, 1] \times [0, 1] \times [0, 1]$ has been considered with periodic boundary conditions. The same CFL number and the parameters for maintaining the divergence free constraint are similar as those used in the 2D test case. In the

3D case, $\Delta x_{min} = 2^{-6}$ ($N = 64$) and $\Delta x_{max} = 2^{-8}$ ($N = 256$). In this case, 640 MPI processes have been used.

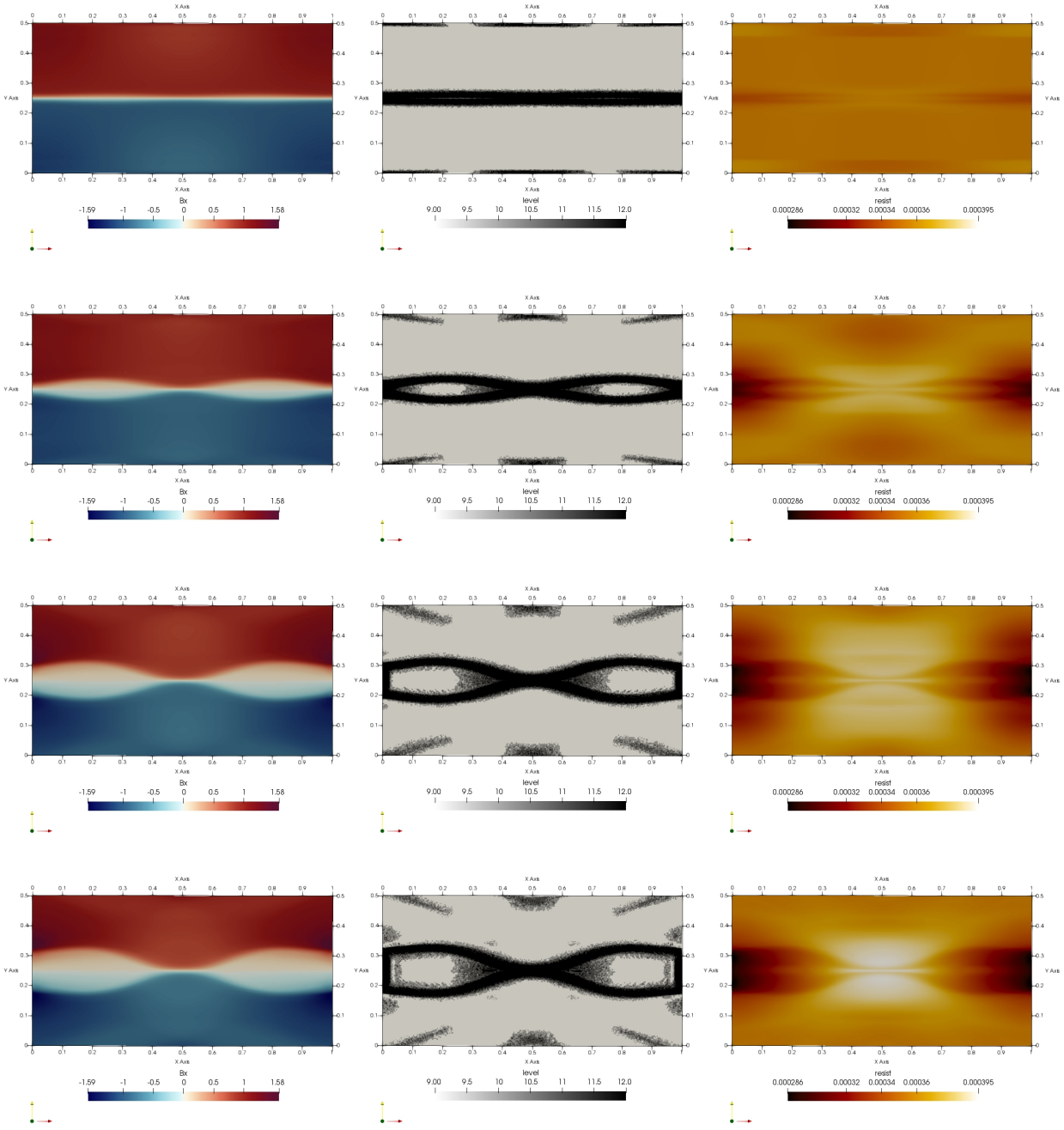

Figure 9-17: Left: Distribution of the x-component of the $\boldsymbol{B}$ field, middle: distribution of the level of refinement, right: distribution of the parallel component of the non-dimensional resistivity. From top to bottom: $t = 0.05,\ 0.2,\ 0.4,\ 0.5$.

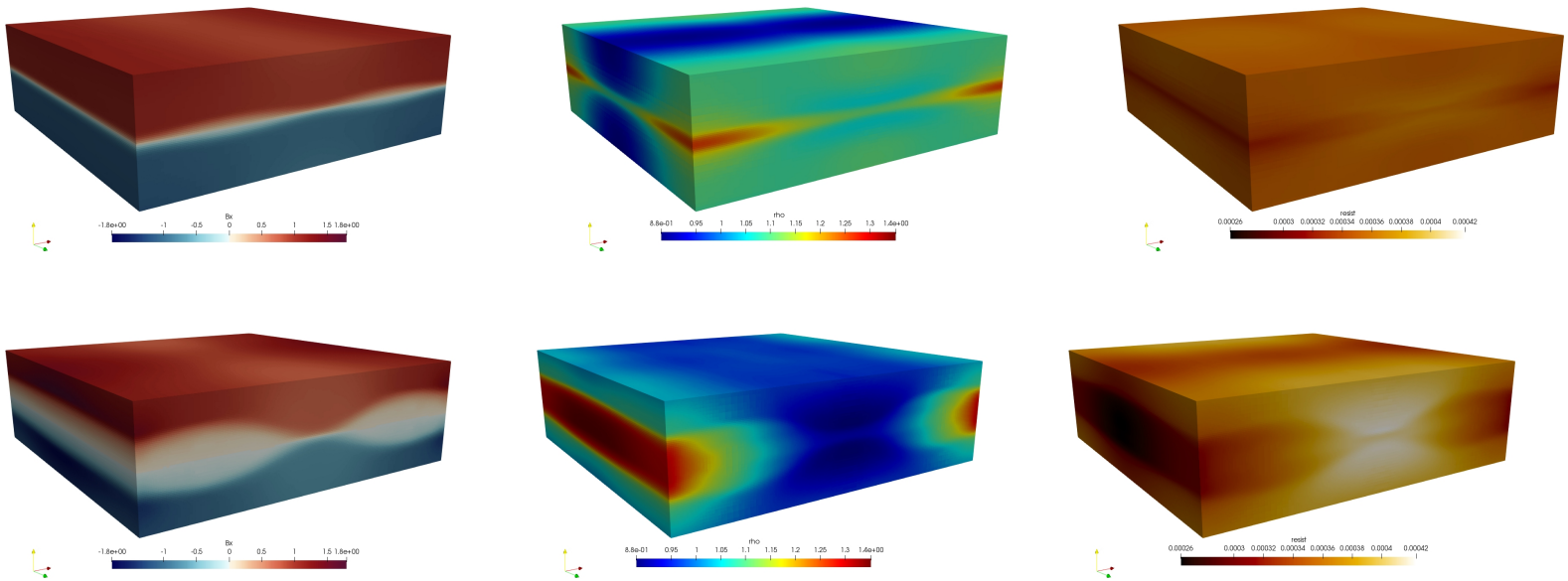

Figure 9-18: Left: Distribution of the x-component of the $\boldsymbol{B}$ field, middle: distribution of the total density $\rho = \rho_{\mathfrak{h}} + \rho_{\mathfrak{e}}$, right: distribution of the parallel component of the non-dimensional resistivity, for a cross section between $y = 0.1$ and $y = 0.4$. From top to bottom: $t = 0.1,\ 0.5$.

Figure 9-17 shows the evolution of the x-component of the $\boldsymbol{B}$ field, the level of refinement and the non-dimensional parallel component of the resistivity computed with `MUTATION++` at time $t = 0.05,\ 0.2,\ 0.4,\ 0.5$. Figure 9-18 shows the evolution of the x-component of the $\boldsymbol{B}$ field, the total density and the non-dimensional parallel component of the resistivity computed with `MUTATION++` at time $t = 0.1,\ 0.5$, for a cross section between $y = 0.1$ and $y = 0.4$.

For the chosen case, the distribution of the x-component of the magnetic field shows the formation of two separatrices as well as a current sheet in the diffusion region. Here, we underline that the current sheet is more numerically resolved thanks to AMR. Besides, we clearly see the adaptive mesh refinement capability of the `p4est` library in 2D and 3D, where the mesh is refined in the regions of interest. Indeed, the finest mesh is located at the current sheet, where the energy exchanges are taking place. It is especially at this region where the magnetic energy is converted into thermal and kinetic energy. The mesh compression rate is about 30%. Then, by coupling the `CanoP` code with the `MUTATION ++` library, we have been able to compute, for example, the distribution of the parallel component of the resistivity with a high level of accuracy. We see that the resistivity is maximum at the reconnection region and minimum at the outlet region. Finally, the presented tool has the ability to perform a high performance massively parallel computation of both 2D and 3D magnetic reconnection configuration, with adaptive mesh refinement capability, combined to the possibility to compute the transport properties with a high level of accuracy. The 3D magnetic reconnection simulation is assessing the potential of the proposed approach.

9.3.3 Two dimensional magnetic reconnection for a partially ionized plasma under solar chromosphere conditions

We focus on a physical test case of magnetic reconnection with partially ionized plasma whose conditions are representative of the solar chromosphere. The goal is to reproduce a case of chromospheric jet, such as spicules, with the multicomponent model. At first, we will identify the conditions where we perform this physical case.

As described in Chapter 1, the magnetic reconnection is observed to take place in partially ionized plasmas in the solar chromosphere. Under these conditions, a variety of interactions, such as collisions between particles are present during the magnetic reconnection. When the width of the current sheet is comparable to the collisional mean-free-path the dynamics of each species may differ. These effects are not captured by the single-fluid MHD approach.

The parameters of the simulation are inspired from the work of Alvarez Laguna et al. (2016); Leake et al. (2013). In the following, we consider the multicomponent model (*Mc*). Three different species are considered: H, H^+ and electrons. We choose a reference length of $L^* = 1000$ km and characteristic properties of the solar chromosphere, such as number densities $n^*_H = n^* = 6 \times 10^{18}\, m^{-3}$ and $n^*_{H^+} = 6 \times 10^{15}\, m^{-3}$, for H and H^+ respectively, and a total pressure $p^* = 7.95$ Pa. We obtain the following reference values: the reference magnetic field is $B^* = \sqrt{p^* \mu_0} = 3.2 \times 10^{-3}$ T, the Alfven speed is $v^* = B^* / \sqrt{\mu_0 \rho^*_{H^+}} = 9.02 \times 10^5\ m.s^{-1}$, a reference temperature such as $T^* = p^* / (n^*_H + n^*_{H^+}) k_B = 7.94 \times 10^8$ K and the characteristic time is $t^* = 1.1$ s. The mean collision time between electron and heavy-particles is found to be $\tau^* = 1.37 \times 10^{-3}$ s. Therefore, in these

conditions, the plasma is in a highly collisional regime, almost at thermal equilibrium between electrons and heavy-particles. We normalize all the quantities with these reference values. The transport properties are computed using the `MUTATION++` library. We have considered isotropic transport properties for the electrons.

Initially, a magnetic field configuration forming a Harris current sheet is considered. A small perturbation in the magnetic field is considered in the center in order to force the reconnection to occur at the center of the domain. The total pressure is balanced by the magnetic pressure, and the initial velocity field is set to zero. The initial ionization level is set to 0.1%. We consider a domain where $(x, y) \in [0, 1] \times [0, 1]$ with open boundary conditions in all the directions. The values of the perturbation are defined as $\xi = 0.01\delta^2$ (amplitude of the perturbation), $\delta = 0.1$ (characteristic length of the perturbation) and $\psi_0 = 0.1$ (perturbation on the densities). The initial conditions read $\mathcal{U}(t = 0) = \mathcal{U}_0^{\text{part}}$

$$\mathcal{U}_0^{\text{part}} = \left(\rho_H,\ 0.001\rho_H,\ 0,\ 0,\ \frac{p}{\gamma - 1} + \frac{|B|^2}{8\pi},\ \frac{p_e}{(\gamma - 1)},\ B_0 \tanh\left(\frac{y - 1/2}{\delta}\right) - B'_x,\ B'_y,\ 0\right)^T, \quad (9.3.2)$$

where the initial density ρ_H of neutrals H reads

$$\rho_H = \left(1 + \frac{\psi_0}{\cosh^2\left(\frac{y-1/2}{\delta}\right)}\right). \quad (9.3.3)$$

The total pressure and pressure of neutrals are defined by

$$p = \frac{|B|^2}{8\pi}, \quad p_H = 0.001\rho_H T_0, \quad (9.3.4)$$

where $T_0 = 1.1964 \times 10^{-5}$ and $B_0 = 0.025$. The perturbed magnetic field reads

$$B'_x = B_0 \frac{\xi}{\delta^2}(y - 1/2)\, e^{-\left[(x-1/2)/\delta\right]^2 - \left[(y-1/2)/\delta\right]^2}, \quad \text{and} \quad B'_y = B_0 \frac{\xi}{\delta^2}(x - 1/2)\, e^{-\left[(x-1/2)/\delta\right]^2 - \left[(y-1/2)/\delta\right]^2}.$$

The physical properties used in this simulation are described as follows. The specific heat ratio for all the species is $\gamma = 5/3$. The initial temperature is $T = 9500$ K. The transport properties are presented in the following Table 9.2.

A $CFL = 0.5$ is considered. In order to maintain the divergence free constraint, similarly as in the previous section, we choose $c_p = \sqrt{0.18 c_h}$ and c_h is computed as the fastest magnetosonic wave. The two test cases are run until $t = 200$. We choose a discretization such as the minimum level of refinement is $\Delta x_{min} = 2^{-6}$ ($N = 64$) and $\Delta x_{max} = 2^8$ ($N = 256$). A a mixed $\boldsymbol{B}$-$\rho_{\mathfrak{h}}$ gradient criterion has been chosen with $\theta = 10^{-3}$. In this case, 160 MPI processes have been used.

Figure 9-19 and Figure 9-20 represent the distribution of the transverse component of the current density $\mathbf{I}_z$, the temperature of heavy-particles, the x-component of the heavy-particle velocity $u_{\mathfrak{h}}$ and the diffusion velocity of the ions H^+ respectively. The distribution of the current density shows the formation of the current sheet and the separatrices. The distribution of the tempera-

Table 9.2: Transport coefficients used in the multicomponent MHD model for partially ionized plasma

$\eta\ [\Omega.m]$	$\nu_{\mathfrak{h}}\ [Pa.s]$	$\lambda_{\mathfrak{h}}\left[W.m^{-1}.K^{-1}\right]$	$\lambda_{\mathfrak{e}}\left[W.m^{-1}.K^{-1}\right]$	$\chi_{\mathfrak{e}}[-]$
1.04	8×10^{-5}	2.37	0.02	0.22
$D_{H,H}\left[m.s^{-2}\right]$	$D_{H^+,H}$	D_{H^+,H^+}	$\alpha_{\mathfrak{e},H}[-]$	$\alpha_{\mathfrak{e},H^+}[-]$
1.17	1188	1.18×10^{6}	0.81	0.19
$\chi_{\mathfrak{e}H}\ [-]$	$\chi_{\mathfrak{e}H^+}\ [-]$	$\chi_{\mathfrak{h},H}\ [-]$	$\chi_{\mathfrak{h},H^+}\ [-]$	
2×10^{-4}	-2×10^{-4}	1×10^{-3}	-1×10^{-3}	

ture shows that the temperature is increasing at the outflow, reaching 1.9×10^{-5} (corresponding to 15086 K). In Figure 9-20, a small decoupling between ions and neutrals can be observed. This decoupling can be noticed in the distribution of the x-component of the diffusion velocity of the ions $\boldsymbol{V}_{x,H^+}$. The velocity $u_{\mathfrak{h}}$ is increasing until $|u_{\mathfrak{h}}| = 0.001$ (corresponding to 902 $m.s^{-2}$). Note that, the diffusion velocity of the neutrals is negligible compared with the hydrodynamic velocity $u_{\mathfrak{h}}$ (we found $\boldsymbol{V}_{x,H} = 10^{-10}$). The distribution of $\boldsymbol{V}_{x,H^+}$, shows that the ions are moving faster than the neutrals with a difference of velocities about 6×10^{-7} (corresponding to 0.5 $m.s^{-1}$). The decoupling between ions and neutrals is small in the x-direction. Indeed, during the reconnection, the ions are accelerated by the Lorentz force and, in their motion, they drag the neutrals by collisions, as described by Alvarez Laguna et al. (2016).

The presented results are preliminary and required a deeper study. The complete study of the numerical simulation of magnetic reconnection process with the multicomponent model will constitue the basis of a future work in Wargnier et al. (2019).

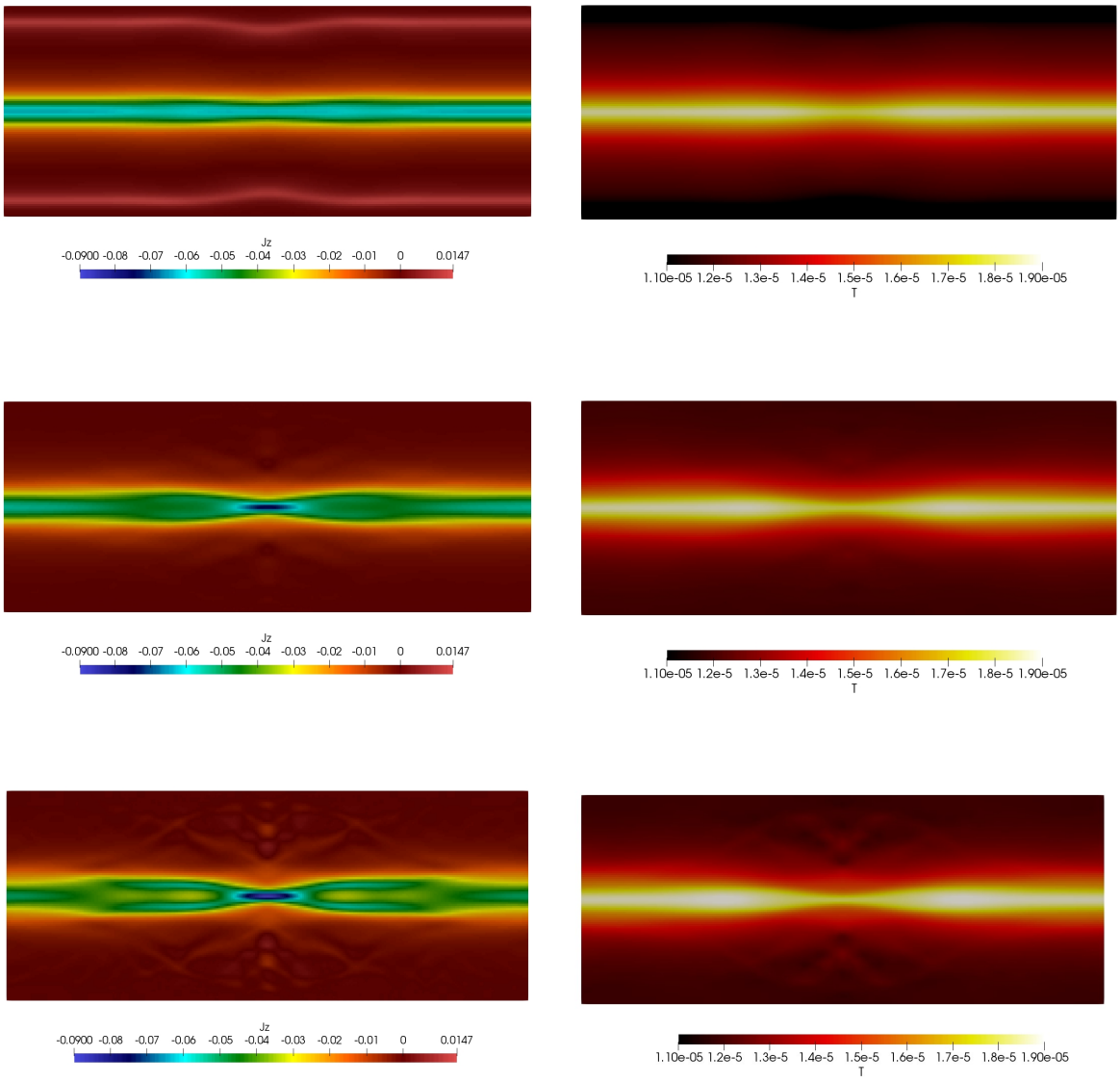

Figure 9-19: Left: Distribution of the transverse component of the total current $\mathbf{I}_z$, right: temperature of heavy-particles, for $y \in [0.3,\ 0.7]$. From top to bottom: at $t = 40,\ 80$ and 120.

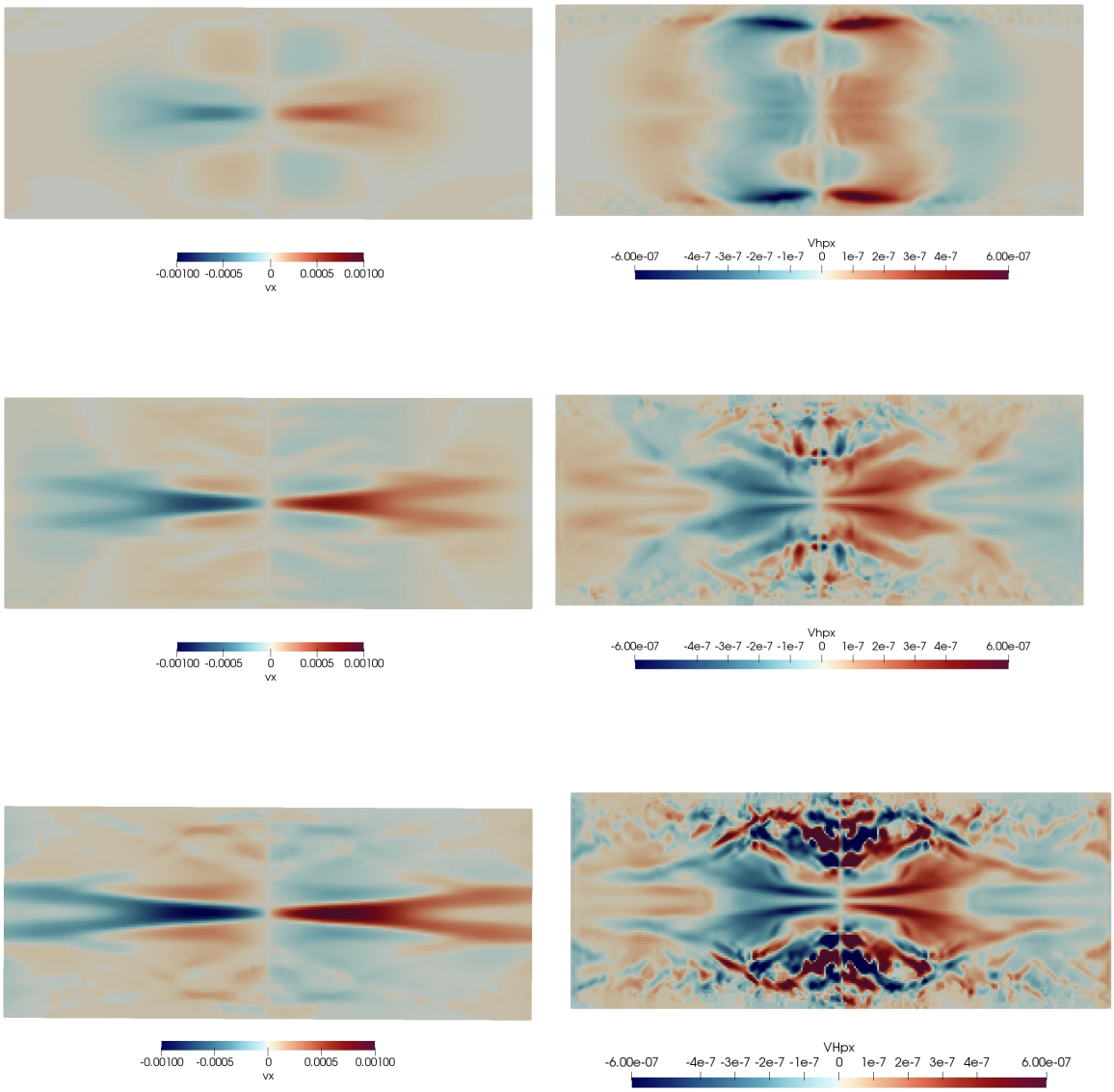

Figure 9-20: Left: Distribution of the velocity in the x direction $u_{\mathfrak{h}}$, right: distribution of the diffusion velocity of the ions $\boldsymbol{V}_{x,H^+}$, for $y \in [0.3,\ 0.7]$. From top to bottom: at $t = 40,\ 80$ and 120.

9.4 Performance: weak and strong capability of CanoP

In this section, we present the results of a weak and strong scalabity study of CanoP performed on the PRACE supercomputer TGCC/IRENE, in order to assess its ability at using efficiently large scale computing ressources. TGCC IRENE supercomputer is made of 1 656 nodes, dual socket equipped with the Intel Skylake 8168 processor which has 24 computing cores per chip.

In order to obtain representative results, as well as to limit the amount of computing time required by this study, we chose to use the spherical blast wave test case, or the so-called Sedov expansion from Stone et al. (2008), using the Euler hydrodynamics system, without magnetic field. For the weak scaling study, we follow the methodology of D. A. Calhoun & Burstedde (2017), and use the replicated domain technique in order to ensure each MPI task has the same amount of work, as well as periodic border conditions.

Figure 9-21 illustrates CanoP weak scaling using the blast wave initial condition for both 2D and 3D problems, ranging the study from 48 to 24576 MPI processes, that is from a single node up to 512 nodes. The tests are made in a stressfull AMR load, indeed the full AMR cycle (refine, coarsen, 2-to-1 balance, repartion) is done after each time time. Let us also mention that by design, during the blast wave evolution the total number of mesh-cells increase by more than an order of magnitude. The 2D problem uses 7 levels of refinement (minimal level is 5, max level is 12), while the 3D problem uses 5 levels of refinement (from level 4 to 9). At the end of simulation, the 2D problem is made of 11 000 cells per MPI process, and respectively 47 000 cells per MPI process for the 3D blast wave problem. For this particular choice of test cases, Figure 9-21 shows that

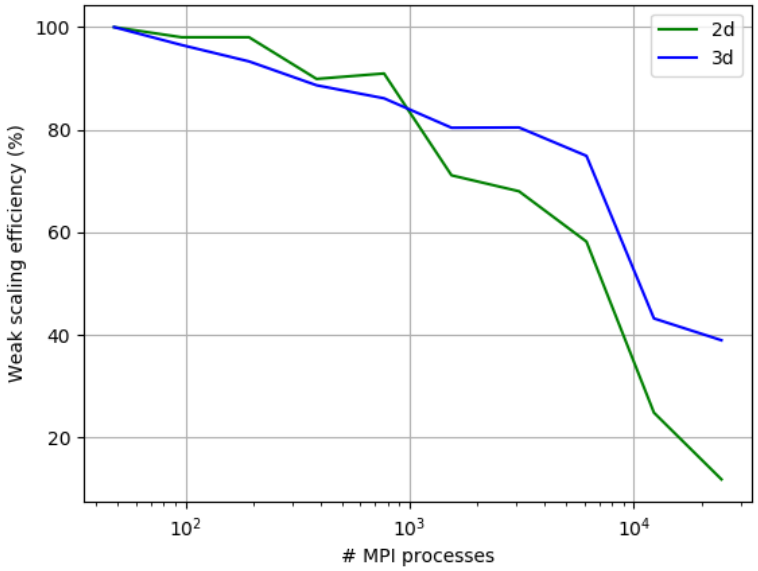

Figure 9-21: CanoP weak scaling study efficiency for a 2D (green) and 3D (blue) blast wave problem from 1 node (48 MPI processes) up to 512 nodes (24576 MPI processes).

weak scaling is rather good (efficiency $\geq 70\%$) when the number of MPI processes is below 4000 in the 2D case, and below 8000 in the 3D case. Going beyong these numbers, the important point here is that more cells per MPI process makes better MPI weak scaling efficiency. This is why here, the 3D case displays better results.

We present the result of a strong scaling study of CanoP using as before a large blast wave problem. We performed three series of simulations corresponding to a different number of mesh cells in the initial condition. We define respectively a small 3D problem (2.5 millions of cells), a medium one (18 millions of cells) and a large one (590 millions of cells). The medium and large problem initial condition is obtained by replicating the small problem, i.e. performing multiple sedov expansion in the simulation domain. As for the weak scaling study, in Figure 9-22 we

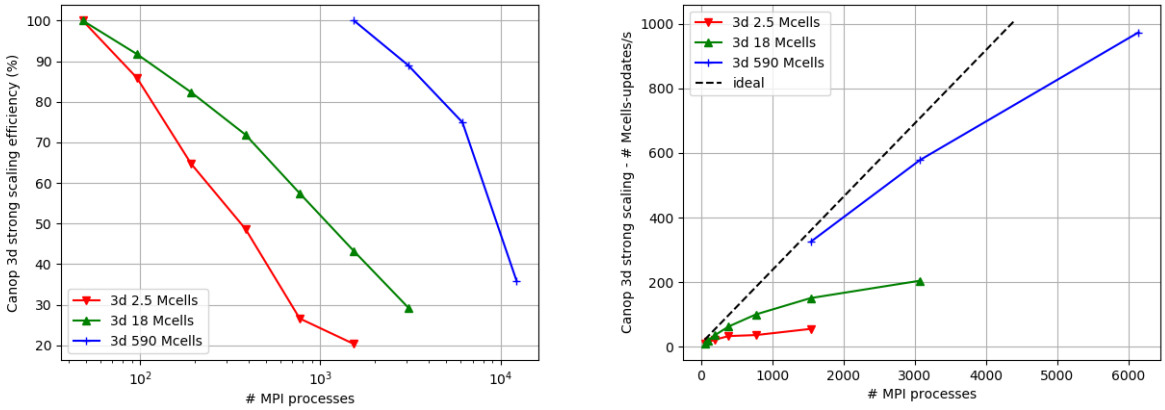

Figure 9-22: CanoP 3D strong scaling study using blast wave problem. Three types of simulation runs are performed using different initial conditions with increasing total number of cells form 2.5 millions to 590 millions of cells. The red curve correspond to the strong scaling study from 1 node (48 MPI process) up to 32 nodes (1536 MPI processes). Green and blue curves correspond respectively to the medium and large scale problems with 18 and 590 millions of cells. Figure on the left display strong scaling results as a percentage compared to ideal scaling. On the right the same results are displayed using the absolute metric : total number of cells updated per second.

observe that the small problem (red curve) cannot scale above 200 MPI process; indeed in that case, the number of cells per MPI process is to low to compensate the cost of the AMR cycle. The medium range problem (green curve) displays much better results. Finally, as shown on the blue curve of Figure 9-22, using a large scale problem (590 millions of cells), one obtains very good strong scaling results, that is an efficiency above 70 % up to $\sim$ 6000 MPI processes (around 100 000 cells per MPI processes). Finally, this kind of study strongly depends on the given problem, but we chose on purpose test cases where the number of cells per MPI processes is low, overall CanoP performance significantly improves for large problems.

Conclusion

The accuracy of the numerical scheme has been verified. Results have shown that the implementation is achieving a second order of accuracy in space and time without AMR. Then, we have shown the ability of the proposed numerical solver to 1- capture discontinuities and 2- maintain the incompressibility constraint on the magnetic field. We have shown that the code is robust at handling the formation of MHD shocks and shock-shock interaction.

In addition, we have tested the AMR capability of `p4est`, the refinement criterion and the ability of the proposed numerical scheme to be combined with AMR, by performing the OT and KHI test cases in both two and three dimensional configurations. These results have been compared with uniform grid cases. In both cases, we have seen that a high mesh compression rate has been reached. Finally, the proposed tool allows to 1- catch the same dynamics as the uniform grid cases while reducing the number of cells and the time computational costs, and 2- refine only in regions of our interest.

Simulations of magnetic reconnection on uniform and AMR grids have been performed. First, we have focused on a simulation of magnetic reconnection with a fully ionized plasma on uniform grids. The results have been compared with a classical single-fluid model. The latter model has been implemented with the same numerical strategy. The transport coefficients have been computed with the same method introduced in Chapter 4, except that in the single-fluid approach, the transport coefficients are isotropic. In the highly collisional regime, the two models are giving the same dynamics, as predicted in Chapter 3 (see Figure 3-1). Therefore, the presented multi-component model has been validated in the highly collisional regime, for a fully ionized plasma. Under the same conditions, a weakly collisional regime has been investigated, in order to assess the impact of the thermal nonequilibrium on the magnetic reconnection process. In particular, the dynamics of the magnetic reconnection is modified since the internal energy of electrons is increasing in the reconnection region.

Under identical conditions, we have performed a two and three dimensional magnetic reconnection of fully ionized plasmas, on AMR grids, using a $\boldsymbol{B}$-gradient refinement criterion. We have seen that the presented tool can perform a high performance massively parallel computation for both 2D and 3D magnetic reconnection, while the mesh is adapted and refined in the region of our interest (reconnection region). The tool is combined with the possibility to compute the transport properties with a high level of accuracy, *i.e.*, with `MUTATION++` library.

Additionally, we have performed a 2D magnetic reconnection with a partially ionized plasma, under solar chromosphere conditions. We have highlighted the different dynamics of neutrals and ions in a magnetic reconnection process. As a final result, this work has lead to the development of a tool which is able to tackle partially ionized plasmas problems, including the effect of collisions. The tool is able to tackle anisotropy and non-equilibrium effects that are completely neglected by standard MHD approximations. However, as performed by Alvarez Laguna et al. (2016), the inclusion of chemistry (ionization and recombination) appears to be essential to fully describe the process. Therefore, this final step is required to consider additional relevant effects in the magnetic reconnection.

CHAPTER 10

GENERAL CONCLUSION

The general framework of this thesis was settled by the development of a model for magnetized multicomponent plasmas, with a detailed description of the dissipative effects and the development of an efficient numerical strategy, guaranteeing robustness and high accuracy, in order to simulate a magnetic reconnection process under Sun chromosphere conditions. Four main aspects have been investigated. First, we have developed a unified fluid model, derived from kinetic theory, for plasmas valid in the whole solar atmosphere, inheriting a rigorous mathematical structure combined with proper asymptotic limits. This development is based on the work performed by Graille et al. (2009). The model is derived from a generalized Chapman-Enskog expansion based on a dimensional analysis. Then, the transport properties have been studied and computed with a high level of accuracy, for conditions representative of our application. An efficient numerical strategy associated with the model has been established. This strategy has been implemented in a massively parallel code to perform AMR numerical simulations of magnetic reconnections, with a high level of accuracy.

10.1 Conclusion

The main contributions of this work, are summarized in the following

- In terms of mathematical modeling, in Chapter 2 and Chapter 3
  - We have extended the work of Graille et al. (2009) by coupling the model with nondimensional Maxwell's equations. A scaling consistent with the one proposed by Graille et al. (2009) has been proposed.
  - The Chapman-Enskog expansion leads to a unified fluid model, established in the heavy-particle reference frame, where all the species diffuse in this reference frame.

The approach has an extended range of validity for partially and fully ionized plasmas, non and weakly magnetized plasmas and general multicomponent mixtures. It is valid in the solar atmosphere, including conditions where the electroneutrality is not assumed. It allows thermal nonequilibrium processes between electrons and heavy-particles. At the last order investigated, the Navier-Stokes equations for heavy-particles and first order drift diffusion equations for electrons have been obtained. Additionally, the transport fluxes for electrons and heavy-particles have been presented. Similarities have been obtained with the model of Kolesnikov (2003).

  - A comparison with the approach of Braginskii (1965) has been performed. Unlike Graille et al. (2009), Braginskii (1965) has not considered a multiscale analysis at the kinetic level, *i.e.*, from the Boltzmann equations.
  - In the context of our application, we have taken the asymptotic limit of the general model for which the Debye length is considered as small. This limit leads to a simplified framework, where the electroneutrality is assumed. We have obtained the multicomponent model. This approach has been compared with the classical multi-fluid and single-fluid MHD models. In this context, the advantages and disadvantages of the multicomponent approach have been highlighted.
  - The model of Graille et al. (2009) coupled with the set of Maxwell's equation allows to derive a generalized Ohm's law. The electric field can be expressed in terms of multicomponent electromagnetic matrices, taking into account all the possible interactions in a multicomponent mixture. Therefore, a new general expression of the resistivity has been defined, in terms of transport coefficients of the multicomponent model.
  - The eigenstructure of the multicomponent model have been studied. The eigenvalues of the model are identical to the classical single-fluid MHD model. However, since thermal nonequilibrium processes have been considered in the multicomponent model, the equation of internal energy of electrons is found to be nonconservative. In this thesis, the nonconservative terms have been considered as a source term. However, an alternative would be to consider these terms as part of the hyperbolic problem. This alternative allows to obtain the exact solution of the corresponding Riemann problem. However, this case has not been fully investigated in this thesis. Only a simplified case, where no electromagnetic field has been considered, has been studied. Further details are given in Wargnier, Faure, et al. (2018) and in Chapter 7.

- In terms of transport properties, in Chapter 4 and Chapter 5

  - The transport coefficients have been computed from a spectral Galerkin method expanded in Laguerre-Sonine polynomials. The transport systems of electrons and heavy-particles have been expressed up to the third order in Laguerre-Sonine polynomials approximation. The transport coefficients depend on the collision integrals. They link the macroscopic transport fluxes to microscopic dynamics of binary particles collisions.
  - In this thesis, we have focused on a Helium-Hydrogen mixture in order to be representative of the solar atmosphere. The kinetic data, which allows to compute the collision

integrals, have been taken from Bruno et al. (2011). In order to solve the heavy-particle transport systems, we have focused on efficient algorithms developed by Magin & Degrez (2004).

  - In order to validate the presented method, a comparison with the model of Braginskii (1965) has been performed in terms of transport coefficients, for a fully ionized plasma. Good agreement have been obtained between the two approaches.
  - The transport coefficients of the multicomponent model have been computed for a Helium-Hydrogen mixture under conditions representative of the solar atmosphere. Additionally, we have computed all the components of the generalized Ohm's law. Finally, postprocessing calculations have been performed based on the results of a pore simulation (see Kitiashvili et al. (2010)) with the Helium-Hydrogen mixture in thermochemical equilibrium, in the highly turbulent upper layer of the solar convective zone. The transport properties have also been computed in the whole solar atmosphere by postprocessing a simulation performed by Carlsson et al. (2016); Gudiksen et al. (2011).

- In terms of numerical strategy, in Chapter 6 and Chapter 7
  - In order to guarantee that all the scales of the multicomponent systems are captured, a numerical strategy combined with a cell-based AMR approach has been established. One of the main difficulties encountered with the multicomponent systems is the presence of diffusive and source terms. In the context of solar physics, the timesteps are limited by Fourier conditions, which are smaller than the classical convective timestep.
  - After investigating the state-of-the-art, we have discretized the multicomponent systems following the path of Kurganov & Tadmor (2000) (KT). This approach allows to be extended to multidimensional problem and be combined with operator splitting techniques to integrate diffusive, convective and source terms separately. Therefore, the problems encountered with small timesteps can be tackled. As shown in Chapter 9, this numerical strategy is second order of accuracy in space and time.
  - Starting from a monodimensional case, we have extended the KT approach to AMR nonuniform grids in a 2:1 balance framework, in multidimensional cases. In this strategy, the nonconservative terms have been standardly discretized by taking the value of the current cell and a second order centered gradient. The relaxation terms have been decoupled from the convective-diffusive system using a Strang operator splitting approach and integrated in time with a second order implicit scheme. A GLM mixed parabolic-hyperbolic correction method has been used for verifying the incompressibility constraint of the magnetic field.
  - In this thesis, the nonconservative terms of the multicomponent system have been standardly discretized. However, when discontinuities or shock waves are involved, nonphysical shocks may appear if the numerical diffusion is higher than the physical diffusion. In this context, it is required first to perform a deeper study of the multicomponent system when discontinuities or shock waves are involved. This study allows to identify

the characteristic scales of the system which have to be numerically resolved to capture the discontinuities. In this work, we have guaranteed that in our numerical simulations a sufficient number of cells has been considered to resolve these characteristic scales. We have guaranteed that the physical dissipation is dominating the numerical diffusion, thus, non physical shocks appearing at discontinuities are avoided.

- A study of the nonconservative terms has been performed, based on a simplified framework where no electromagnetic field has been considered. A decoupling of the governing equations has been proposed. By looking for smooth travelling wave solutions, an analytic expression of the missing jump condition on the electron temperature has been obtained. In order to reproduce numerically the structure of the travelling wave solution with the proper jump conditions, a finite volume Godunov method has been used. A naive consistent treatment of the nonconservative product has been used to show that, for a sufficient level of discretization, the travelling wave is captured. This first study allows to identify the characteristic scales and the required level of resolution to prevent the appearance of a non physical shock due to the numerical dissipation of the numerical scheme.
- Based on the previous analysis, we have developed a numerical scheme with a specific treatment of the nonconservative product to capture the travelling wave for any discretization.

- In terms of scientific computing, in Chapter 8 and Chapter 9

  - The multicomponent model has been implemented in the massively parallel code `CanoP`. The code is coupled with the `p4est` library, which is managing the mesh independently of the model and numerical methods implemented.
  - We have coupled the `CanoP` code with `MUTATION++` library, to compute the transport coefficients presented in Chapter 4 and Chapter 5, with a high level of accuracy, in thermal equilibrium and nonequilibrium.
  - The implementation has been verified. Results have shown that the implementation is achieving a second order of accuracy in space and time. We have verified the proposed numerical solver to capture discontinuities and maintain the incompressibility constraint on the magnetic field. We have also tested the AMR capability of `p4est`. We have shown that we can capture the same dynamics as uniform grid cases while reducing the number of cells and the time computational costs, and, refine only in regions of our interest.
  - Preliminary but promising numerical simulations of magnetic reconnections have been performed for fully and partially ionized plasmas under solar atmosphere conditions. Therefore, we have developed a tool which can perform a high performance massively parallel computation of multicomponent plasmas combined with the possibility of computing the transport properties with a high level of accuracy.

10.2 Perspectives

Finally, let us mention some perspectives of the present work:

- In terms of mathematical modeling
  - In depth study and comparison between the multicomponent and multi-fluid approach. In this context, the domain of validity of both models, in terms of temporal and spatial scales, may be studied. Additionally, the differences in terms of scaling and dimensional analysis used to derive both models from non dimensional Boltzmann equations can be highlighted.
  - Including the radiative effects and chemistry reactions. These effects are relevant to fully describe the magnetic reconnection process in solar chromosphere conditions, as shown by Alvarez Laguna et al. (2016). These effects can be considered in the multicomponent model and are consistent with its domain of validity and hypotheses.
  - Extension of the work performed in Chapter 7. Study of the jump conditions and travelling wave solutions for an extended system where the Maxwell's equations are considered. Additionally, a study of the nonconservative terms in a simplified multicomponent system where no electromagnetic field is considered, considering cases where $\gamma_e \neq \gamma_h$, following the work performed by Chalons & Coquel (2007), can be first envisioned.
- In terms of transport properties
  - Extension of the collision integrals data by including more interactions involving metals and additional heavy species (for example {O, C, Fe, Si}). This strategy allows to consider a more realistic approach to describe the collisions involved in the solar atmosphere.
- In terms of numerical strategy
  - Switching from second order in space and time to higher order schemes combined with a cell based AMR strategy. As performed by Essadki (2018) in `CanoP`, where a model for two phase flow applications has been used, a Discontinuous Galerkin (DG) method can be envisioned to discretize the multicomponent model.
  - The numerical strategy described in this thesis can be combined with proper time integration methods to discretize source terms related to chemistry reactions (see Duarte (2011)). Therefore, the numerical stifness associated with these terms can be tackled.
  - Development of a specific numerical strategy associated with the general model (without considering the asymptotic limit) valid at Debye length scales. Development of an asymptotic preserving scheme to resolve Debye length scales, as described by Alvarez Laguna et al. (2019) for low-temperature plasma applications.

  - Extension of the work performed in Chapter 7 to the fully coupled system and multicomponent model combined with Maxwell's equations. Identification of the travelling wave solution and scales which have to be numerically resolved to develop a specific numerical treatment of the nonconservative terms.

- In terms of scientific computing

  - Implementation of `CanoP` into Pleiades Supercomputer [1]. This implementation will be performed during the NASA Summer Program 2019. Numerical simulations of magnetic reconnection process, with a multicomponent model, with a high level of details, will be performed.
  - Comparison between the multi-fluid, single-fluid MHD with ambipolar resistivity and multicomponent model based on a similar numerical strategy as the one described in Chapter 6. Therefore, the impact of modeling on the magnetic reconnection process under solar atmosphere conditions will be highlighted.

[1] Pleiades is a petascale supercomputer housed at the NASA Advanced Supercomputing (NAS) facility at NASA Ames Research Center. As of November 2016 it is ranked the world's thirteenth-fastest computer on the TOP500 list with a LINPACK rating of 5.95 petaflops (5.95 quadrillion floating point operations per second) and a peak performance of 7.25 petaflops from its most recent hardware upgrade.

APPENDIX A

NONDIMENSIONAL COLLISION AND STREAMING OPERATORS AT SUCCESSIVE ORDERS

As presented in Graille et al. (2009), we write the nondimensional collision and streaming operators at successive orders, for electrons and heavy particles from ($\mathrm{B}^{\varepsilon}_{\mathfrak{e}}$) and ($\mathrm{B}^{\varepsilon}_{i\in\mathrm{H}}$).

A.1 Electrons

In ($\mathrm{B}^{\varepsilon}_{\mathfrak{e}}$), at successive orders, the electron streaming operators reads

$$\mathcal{D}^{-2}_{\mathfrak{e}}\left(f^0_{\mathfrak{e}}\right) = \delta_{b1} q_{\mathfrak{e}} \left(\boldsymbol{C}_{\mathfrak{e}} \wedge \boldsymbol{B}\right) \cdot \boldsymbol{\partial}_{\boldsymbol{C}_{\mathfrak{e}}} f^0_{\mathfrak{e}},$$

$$\mathcal{D}^{-1}_{\mathfrak{e}}\left(f^0_{\mathfrak{e}}, \phi_{\mathfrak{e}}\right) = \mathcal{D}^{-1}_{\mathfrak{e}}\left(f^0_{\mathfrak{e}}\right) + q_{\mathfrak{e}} \left(\delta_{b1} \boldsymbol{C}_{\mathfrak{e}} \wedge \boldsymbol{B}\right) \cdot \boldsymbol{\partial}_{\boldsymbol{C}_{\mathfrak{e}}} \left(f^0_{\mathfrak{e}} \phi_{\mathfrak{e}}\right),$$

$$\mathcal{D}^{-1}_{\mathfrak{e}}\left(f^0_{\mathfrak{e}}\right) = \frac{1}{M_{\mathfrak{h}}} \boldsymbol{C}_{\mathfrak{e}} \cdot \boldsymbol{\partial}_{\boldsymbol{C}_{\mathfrak{e}}} f^0_{\mathfrak{e}} + q_{\mathfrak{e}} \left(\frac{1}{M_{\mathfrak{h}}} \boldsymbol{E}' + \delta_{b0} \boldsymbol{C}_{\mathfrak{e}} \wedge \boldsymbol{B}\right) \cdot \boldsymbol{\partial}_{\boldsymbol{C}_{\mathfrak{e}}} \left(f^0_{\mathfrak{e}}\right),$$

$$\mathcal{D}^{0}_{\mathfrak{e}}\left(f^0_{\mathfrak{e}}, \phi_{\mathfrak{e}}, \phi^2_{\mathfrak{e}}\right) = \mathcal{D}^{0}_{\mathfrak{e}}\left(f^0_{\mathfrak{e}}, \phi_{\mathfrak{e}}\right) + q_{\mathfrak{e}} \left(\delta_{b1} \boldsymbol{C}_{\mathfrak{e}} \wedge \boldsymbol{B}\right) \cdot \boldsymbol{\partial}_{\boldsymbol{C}_{\mathfrak{e}}} \left(f^0_{\mathfrak{e}} \phi^2_{\mathfrak{e}}\right),$$

$$\begin{aligned}\mathcal{D}^{0}_{\mathfrak{e}}\left(f^0_{\mathfrak{e}}, \phi_{\mathfrak{e}}\right) =& \partial_t f^0_{\mathfrak{e}} + \frac{1}{M_{\mathfrak{h}}} \boldsymbol{C}_{\mathfrak{e}} \cdot \boldsymbol{\partial}_{\boldsymbol{x}} \left(f^0_{\mathfrak{e}} \phi_{\mathfrak{e}}\right) + \boldsymbol{v}_{\mathfrak{h}} \cdot \boldsymbol{\partial}_{\boldsymbol{x}} f^0_{\mathfrak{e}} - \left(\boldsymbol{\partial}_{\boldsymbol{C}_{\mathfrak{e}}} f^0_{\mathfrak{e}} \otimes \boldsymbol{C}_{\mathfrak{e}}\right) : \boldsymbol{\partial}_{\boldsymbol{x}} \boldsymbol{v}_{\mathfrak{h}} \\ &+ q_{\mathfrak{e}} \left(\delta_{b0} M_{\mathfrak{h}} \boldsymbol{v}_{\mathfrak{h}} \wedge \boldsymbol{B} + \delta_{b(-1)} \boldsymbol{C}_{\mathfrak{e}} \wedge \boldsymbol{B}\right) \cdot \boldsymbol{\partial}_{\boldsymbol{C}_{\mathfrak{e}}} f^0_{\mathfrak{e}} \\ &+ q_{\mathfrak{e}} \left(\frac{1}{M_{\mathfrak{h}}} \boldsymbol{E}' + \delta_{b0} \boldsymbol{C}_{\mathfrak{e}} \wedge \boldsymbol{B}\right) \cdot \boldsymbol{\partial}_{\boldsymbol{C}_{\mathfrak{e}}} \left(f^0_{\mathfrak{e}} \phi_{\mathfrak{e}}\right),\end{aligned}$$

$$\mathcal{D}^{1}_{\mathfrak{e}}\left(f^0_{\mathfrak{e}}, \phi_{\mathfrak{e}}, \phi^2_{\mathfrak{e}}, \phi^3_{\mathfrak{e}}\right) = \mathcal{D}^{1}_{\mathfrak{e}}\left(f^0_{\mathfrak{e}}, \phi_{\mathfrak{e}}, \phi^2_{\mathfrak{e}}\right) + q_{\mathfrak{e}} \left(\delta_{b1} \boldsymbol{C}_{\mathfrak{e}} \wedge \boldsymbol{B}\right) \cdot \boldsymbol{\partial}_{\boldsymbol{C}_{\mathfrak{e}}} \left(f^0_{\mathfrak{e}} \phi^3_{\mathfrak{e}}\right),$$

$$
\begin{aligned}
\mathcal{D}_{\mathfrak{e}}^{1}\left(f_{\mathfrak{e}}^{0},\phi_{\mathfrak{e}},\phi_{\mathfrak{e}}^{2}\right) =& \partial_{t}\left(f_{\mathfrak{e}}^{0}\phi_{\mathfrak{e}}\right)+\frac{1}{M_{\mathfrak{h}}}\boldsymbol{C}_{\mathfrak{e}}\cdot\boldsymbol{\partial}_{\boldsymbol{x}}\left(f_{\mathfrak{e}}^{0}\phi_{\mathfrak{e}}^{2}\right)+\boldsymbol{v}_{\mathfrak{h}}\cdot\boldsymbol{\partial}_{\boldsymbol{x}}\left(f_{\mathfrak{e}}^{0}\phi_{\mathfrak{e}}\right)\\
&-M_{\mathfrak{h}}\frac{D\boldsymbol{v}_{\mathfrak{h}}}{Dt}\cdot\boldsymbol{\partial}_{\boldsymbol{C}_{\mathfrak{e}}}f_{\mathfrak{e}}^{0}-\left(\boldsymbol{\partial}_{\boldsymbol{C}_{\mathfrak{e}}}\left(f_{\mathfrak{e}}^{0}\phi_{\mathfrak{e}}\right)\otimes\boldsymbol{C}_{\mathfrak{e}}\right):\boldsymbol{\partial}_{\boldsymbol{x}}\boldsymbol{v}_{\mathfrak{h}}\\
&+q_{\mathfrak{e}}\left(\delta_{b(-1)}M_{\mathfrak{h}}\boldsymbol{v}_{\mathfrak{h}}\wedge\boldsymbol{B}+\delta_{b(-2)}\boldsymbol{C}_{\mathfrak{e}}\wedge\boldsymbol{B}\right)\cdot\boldsymbol{\partial}_{\boldsymbol{C}_{\mathfrak{e}}}f_{\mathfrak{e}}^{0}\\
&+q_{\mathfrak{e}}\left(\delta_{b0}M_{\mathfrak{h}}\boldsymbol{v}_{\mathfrak{h}}\wedge\boldsymbol{B}+\delta_{b(-1)}\boldsymbol{C}_{\mathfrak{e}}\wedge\boldsymbol{B}\right)\cdot\boldsymbol{\partial}_{\boldsymbol{C}_{\mathfrak{e}}}\left(f_{\mathfrak{e}}^{0}\phi_{\mathfrak{e}}\right)\\
&+q_{\mathfrak{e}}\left(\frac{1}{M_{\mathfrak{h}}}\boldsymbol{E}'+\delta_{b0}\boldsymbol{C}_{\mathfrak{e}}\wedge\boldsymbol{B}\right)\cdot\boldsymbol{\partial}_{\boldsymbol{C}_{\mathfrak{e}}}\left(f_{\mathfrak{e}}^{0}\phi_{\mathfrak{e}}^{2}\right),
\end{aligned}
$$

where $\boldsymbol{E}'=\boldsymbol{E}+\delta_{b1}M_{\mathfrak{h}}^{2}\boldsymbol{v}_{\mathfrak{h}}\wedge\boldsymbol{B}$.

At successive orders, the electron collision operators reads

$$
\mathcal{J}_{\mathfrak{e}}^{-2}=0,
$$

$$
\mathcal{J}_{\mathfrak{e}}^{-1}=\mathcal{J}_{\mathfrak{e}\mathfrak{e}}\left(f_{\mathfrak{e}}^{0}\phi_{\mathfrak{e}},f_{\mathfrak{e}}^{0}\right)+\mathcal{J}_{\mathfrak{e}\mathfrak{e}}\left(f_{\mathfrak{e}}^{0},f_{\mathfrak{e}}^{0}\phi_{\mathfrak{e}}\right)+\sum_{j\in\mathrm{H}}\mathcal{J}_{\mathfrak{e}j}^{0}\left(f_{\mathfrak{e}}^{0}\phi_{\mathfrak{e}},f_{j}{}^{0}\right),
$$

$$
\begin{aligned}
\mathcal{J}_{\mathfrak{e}}^{0} =&\mathcal{J}_{\mathfrak{e}\mathfrak{e}}\left(f_{\mathfrak{e}}^{0}\phi_{\mathfrak{e}}^{2},f_{\mathfrak{e}}^{0}\right)+\mathcal{J}_{\mathfrak{e}\mathfrak{e}}\left(f_{\mathfrak{e}}^{0}\phi_{\mathfrak{e}},f_{\mathfrak{e}}^{0}\phi_{\mathfrak{e}}\right)+\mathcal{J}_{\mathfrak{e}\mathfrak{e}}\left(f_{\mathfrak{e}}^{0},f_{\mathfrak{e}}^{0}\phi_{\mathfrak{e}}^{2}\right)+\sum_{j\in\mathrm{H}}\mathcal{J}_{\mathfrak{e}j}^{0}\left(f_{\mathfrak{e}}^{0}\phi_{\mathfrak{e}},f_{j}{}^{0}\right)\\
&+\sum_{j\in\mathrm{H}}\left[\mathcal{J}_{\mathfrak{e}j}^{0}\left(f_{\mathfrak{e}}^{0}\phi_{\mathfrak{e}},f_{j}{}^{0}\phi_{j}\right)+\mathcal{J}_{\mathfrak{e}j}^{1}\left(f_{\mathfrak{e}}^{0},f_{j}{}^{0}\phi_{j}\right)+\mathcal{J}_{\mathfrak{e}j}^{2}\left(f_{\mathfrak{e}}^{0},f_{j}{}^{0}\right)\right]
\end{aligned}
$$

$$
\begin{aligned}
\mathcal{J}_{\mathfrak{e}}^{1} =&\mathcal{J}_{\mathfrak{e}\mathfrak{e}}\left(f_{\mathfrak{e}}^{0}\phi_{\mathfrak{e}}^{3},f_{\mathfrak{e}}^{0}\right)+\mathcal{J}_{\mathfrak{e}\mathfrak{e}}\left(f_{\mathfrak{e}}^{0}\phi_{\mathfrak{e}}^{2},f_{\mathfrak{e}}^{0}\phi_{\mathfrak{e}}\right)+\mathcal{J}_{\mathfrak{e}\mathfrak{e}}\left(f_{\mathfrak{e}}^{0}\phi_{\mathfrak{e}},f_{\mathfrak{e}}^{0}\phi_{\mathfrak{e}}^{2}\right)+\mathcal{J}_{\mathfrak{e}\mathfrak{e}}\left(f_{\mathfrak{e}}^{0},f_{\mathfrak{e}}^{0}\phi_{\mathfrak{e}}^{3}\right)\\
&+\sum_{j\in\mathrm{H}}\left[\mathcal{J}_{\mathfrak{e}j}^{0}\left(f_{\mathfrak{e}}^{0}\phi_{\mathfrak{e}}^{2},f_{j}{}^{0}\phi_{j}\right)+\mathcal{J}_{\mathfrak{e}j}^{0}\left(f_{\mathfrak{e}}^{0}\phi_{\mathfrak{e}},f_{j}{}^{0}\phi_{j}^{2}\right)+\mathcal{J}_{\mathfrak{e}j}^{1}\left(f_{\mathfrak{e}}^{0}\phi_{\mathfrak{e}},f_{j}{}^{0}\phi_{j}\right)\right]\\
&+\sum_{j\in\mathrm{H}}\left[\mathcal{J}_{\mathfrak{e}j}^{1}\left(f_{\mathfrak{e}}^{0},f_{j}{}^{0}\phi_{j}^{2}\right)+\mathcal{J}_{\mathfrak{e}j}^{2}\left(f_{\mathfrak{e}}^{0}\phi_{\mathfrak{e}},f_{j}{}^{0}\right)+\mathcal{J}_{\mathfrak{e}j}^{2}\left(f_{\mathfrak{e}}^{0},f_{j}{}^{0}\phi_{j}\right)+\mathcal{J}_{\mathfrak{e}j}^{3}\left(f_{\mathfrak{e}}^{0},f_{j}{}^{0}\right)\right].
\end{aligned}
$$

A.2 Heavy particles

In ($\mathrm{B}_{i\in\mathrm{H}}^{\varepsilon}$), at successive orders, the heavy-particle streaming operators reads

$$
\begin{aligned}
\mathcal{D}_{i}^{0}\left(f_{i}^{0}\right) =&\partial_{t}f_{i}^{0}+\left(\frac{1}{M_{\mathfrak{h}}}\boldsymbol{C}_{i}+\boldsymbol{v}_{\mathfrak{h}}\right)\cdot\boldsymbol{\partial}_{\boldsymbol{x}}f_{i}^{0}+\frac{q_{i}}{m_{i}}\left(\frac{1}{M_{\mathfrak{h}}}\boldsymbol{E}'+\delta_{b1}\boldsymbol{C}_{i}\wedge\boldsymbol{B}\right)\cdot\boldsymbol{\partial}_{\boldsymbol{C}_{i}}f_{i}^{0}\\
&-M_{\mathfrak{h}}\frac{D\boldsymbol{v}_{\mathfrak{h}}}{Dt}\cdot\boldsymbol{\partial}_{\boldsymbol{C}_{i}}f_{i}^{0}-\left(\boldsymbol{\partial}_{\boldsymbol{C}_{i}}f_{i}^{0}\otimes\boldsymbol{C}_{i}\right):\boldsymbol{\partial}_{\boldsymbol{x}}\boldsymbol{v}_{\mathfrak{h}},
\end{aligned}
$$

$$\begin{aligned}\mathcal{D}_i^1\left(f_i^0,\phi_i\right)=&\partial_t\left(f_i^0\phi_i\right)+\left(\frac{1}{M_\mathfrak{h}}\boldsymbol{C}_i+\boldsymbol{v}_\mathfrak{h}\right)\cdot\boldsymbol{\partial}_{\boldsymbol{x}}\left(f_i^0\phi_i\right)+\frac{q_i}{m_i}\delta_{b0}\left[\left(\boldsymbol{C}_i+M_\mathfrak{h}\boldsymbol{v}_\mathfrak{h}\right)\wedge\boldsymbol{B}\right]\cdot\boldsymbol{\partial}_{\boldsymbol{C}_i}f_i^0\\&+\frac{q_i}{m_i}\left(\frac{1}{M_\mathfrak{h}}\boldsymbol{E}'+\delta_{b0}\boldsymbol{C}_i\wedge\boldsymbol{B}\right)\cdot\boldsymbol{\partial}_{\boldsymbol{C}_i}\left(f_i^0\phi_i\right)\\&-M_\mathfrak{h}\frac{D\boldsymbol{v}_\mathfrak{h}}{Dt}\cdot\boldsymbol{\partial}_{\boldsymbol{C}_i}\left(f_i^0\phi_i\right)-\left(\boldsymbol{\partial}_{\boldsymbol{C}_i}\left(f_i^0\phi_i\right)\otimes\boldsymbol{C}_i\right)\wedge\boldsymbol{\partial}_{\boldsymbol{x}}\boldsymbol{v}_\mathfrak{h}.\end{aligned}$$

The heavy-particle collision operators are given by

$$\mathcal{J}_i^{-1}=0,$$

$$\begin{aligned}\mathcal{J}_i^0=&\sum_{j\in\mathrm{H}}\mathcal{J}_{ij}\left(f_i^0\phi_i,f_j{}^0\right)+\mathcal{J}_{ij}\left(f_i^0,f_j{}^0\phi_j\right)\\&+\mathcal{J}_{i\mathfrak{e}}^1\left(f_i^0,f_\mathfrak{e}^0\phi_\mathfrak{e}\right)+\mathcal{J}_{i\mathfrak{e}}^2\left(f_i^0,f_\mathfrak{e}^0\right)\\\mathcal{J}_i^1=&\sum_{j\in\mathrm{H}}\mathcal{J}_{ij}\left(f_i^0\phi_i^2,f_j{}^0\right)+\mathcal{J}_{ij}\left(f_i^0\phi_i,f_j{}^0\phi_j\right)+\mathcal{J}_{ij}\left(f_i^0,f_j{}^0\phi_j^2\right)\\&+\mathcal{J}_{i\mathfrak{e}}^1\left(f_i^0\phi_i,f_\mathfrak{e}^0\phi_\mathfrak{e}\right)+\mathcal{J}_{i\mathfrak{e}}^1\left(f_i^0,f_\mathfrak{e}^0\phi_\mathfrak{e}^2\right)+\mathcal{J}_{i\mathfrak{e}}^2\left(f_i^0\phi_i,f_\mathfrak{e}^0\right)\\&+\mathcal{J}_{i\mathfrak{e}}^2\left(f_i^0,f_\mathfrak{e}^0\phi_\mathfrak{e}\right).\end{aligned}$$

APPENDIX B

TRANSPORT SYSTEMS

In this appendix, we exhibit the matrices of the transport systems involved in the model. The latter are given up to the third of order of Laguerre-Sonine polynomials approximation.

B.1 Electrons

The transport system considered are defined in (4.2.6) and (4.2.7). The corresponding transport matrices are defined as

$$L_{\mathfrak{e}\mathfrak{e}}^{pq} = \frac{16}{3}\frac{p}{k_B T_{\mathfrak{e}}}\sqrt{\frac{m_{\mathfrak{e}}}{2\pi k_B T_{\mathfrak{e}}}}\tilde{L}_{\mathfrak{e}\mathfrak{e}}^{pq}, \tag{B.1.1}$$

$$\tilde{L}_{\mathfrak{e}\mathfrak{e}}^{00} = \sum_{j\in \mathrm{H}} x_j \bar{Q}_{\mathfrak{e}j}^{(1,1)}, \tag{B.1.2}$$

$$\tilde{L}_{\mathfrak{e}\mathfrak{e}}^{01} = \tilde{L}_{\mathfrak{e}\mathfrak{e}}^{10} = \sum_{j\in \mathrm{H}} x_j \left(\frac{5}{2}\bar{Q}_{\mathfrak{e}j}^{(1,1)} - 3\bar{Q}_{\mathfrak{e}j}^{(1,2)}\right), \tag{B.1.3}$$

$$\tilde{L}_{\mathfrak{e}\mathfrak{e}}^{02} = \tilde{L}_{\mathfrak{e}\mathfrak{e}}^{20} = \sum_{j\in \mathrm{H}} x_j \left(\frac{35}{8}\bar{Q}_{\mathfrak{e}j}^{(1,1)} - \frac{21}{2}\bar{Q}_{\mathfrak{e}j}^{(1,2)} + 6\bar{Q}_{\mathfrak{e}j}^{(1,3)}\right), \tag{B.1.4}$$

$$\tilde{L}_{\mathfrak{e}\mathfrak{e}}^{11} = \sum_{j\in \mathrm{H}} x_j \left(\frac{25}{4}\bar{Q}_{\mathfrak{e}j}^{(1,1)} - 15\bar{Q}_{\mathfrak{e}j}^{(1,2)} + 12\bar{Q}_{\mathfrak{e}j}^{(1,3)}\right) + x_{\mathfrak{e}}\sqrt{2}\bar{Q}_{\mathfrak{e}\mathfrak{e}}^{(2,2)}, \tag{B.1.5}$$

$$\tilde{L}_{\mathfrak{e}\mathfrak{e}}^{12} = \tilde{L}_{\mathfrak{e}\mathfrak{e}}^{21} = \sum_{j\in \mathrm{H}} x_j \left(\frac{175}{16}\bar{Q}_{\mathfrak{e}j}^{(1,1)} - \frac{315}{8}\bar{Q}_{\mathfrak{e}j}^{(1,2)} + 57\bar{Q}_{\mathfrak{e}j}^{(1,3)} - 30\bar{Q}_{\mathfrak{e}j}^{(1,4)}\right) + x_{\mathfrak{e}}\sqrt{2}\left(\frac{7}{4}\bar{Q}_{\mathfrak{e}\mathfrak{e}}^{(2,2)} - 2\bar{Q}_{\mathfrak{e}\mathfrak{e}}^{(2,3)}\right), \tag{B.1.6}$$

$$\tilde{L}^{22}_{\mathfrak{e}\mathfrak{e}} = \sum_{j\in\mathrm{H}} x_j\Big(\frac{1225}{64}\bar{Q}^{(1,1)}_{\mathfrak{e}j} - \frac{735}{8}\bar{Q}^{(1,2)}_{\mathfrak{e}j} + \frac{399}{2}\bar{Q}^{(1,3)}_{\mathfrak{e}j} - 210\bar{Q}^{(1,4)}_{\mathfrak{e}j} + 90\bar{Q}^{(1,5)}_{\mathfrak{e}j}\Big) + x_{\mathfrak{e}}\sqrt{2}\Big(\frac{77}{16}\bar{Q}^{(2,2)}_{\mathfrak{e}\mathfrak{e}} - 7\bar{Q}^{(2,3)}_{\mathfrak{e}\mathfrak{e}} + 5\bar{Q}^{(2,4)}_{\mathfrak{e}\mathfrak{e}}\Big), \quad \text{(B.1.7)}$$

$$L^{Bpq}_{\mathfrak{e}\mathfrak{e}} = 0, \quad p \neq q, \quad \text{(B.1.8)}$$

$$L^{B00}_{\mathfrak{e}\mathfrak{e}} = \frac{q_{\mathfrak{e}}}{k_B T_{\mathfrak{e}}}|\boldsymbol{B}|, \quad \text{(B.1.9)}$$

$$L^{B11}_{\mathfrak{e}\mathfrak{e}} = \frac{5}{2}\frac{q_{\mathfrak{e}}}{k_B T_{\mathfrak{e}}}|\boldsymbol{B}|, \quad \text{(B.1.10)}$$

$$L^{B22}_{\mathfrak{e}\mathfrak{e}} = \frac{35}{8}\frac{q_{\mathfrak{e}}}{k_B T_{\mathfrak{e}}}|\boldsymbol{B}|, \quad \text{(B.1.11)}$$

and the right-hand sides are given as

$$\beta^{pD_{\mathfrak{e}}}_{\mathfrak{e}} = \delta_{p0}, \quad \text{(B.1.12)}$$

$$\beta^{p\lambda'_{\mathfrak{e}}}_{\mathfrak{e}} = \frac{5}{2}\delta_{p1}, \quad \text{(B.1.13)}$$

$$\beta^{0D_i}_{\mathfrak{e}} = \frac{8}{3}n_i\sqrt{\frac{2m_{\mathfrak{e}}}{\pi k_B T_{\mathfrak{e}}}}\bar{Q}^{(1,1)}_{\mathfrak{e}i}, \quad \text{(B.1.14)}$$

$$\beta^{1D_i}_{\mathfrak{e}} = \frac{8}{3}n_i\sqrt{\frac{2m_{\mathfrak{e}}}{\pi k_B T_{\mathfrak{e}}}}\Big(\frac{5}{2}\bar{Q}^{(1,1)}_{\mathfrak{e}i} - 3\bar{Q}^{(1,2)}_{\mathfrak{e}i}\Big), \quad \text{(B.1.15)}$$

$$\beta^{2D_i}_{\mathfrak{e}} = \frac{8}{3}n_i\sqrt{\frac{2m_{\mathfrak{e}}}{\pi k_B T_{\mathfrak{e}}}}\Big(\frac{35}{8}\bar{Q}^{(1,1)}_{\mathfrak{e}i} - \frac{21}{2}\bar{Q}^{(1,2)}_{\mathfrak{e}i} + 6\bar{Q}^{(1,3)}_{\mathfrak{e}i}\Big), \quad \text{(B.1.16)}$$

where $\bar{Q}^{(l,s)}_{ij}$ are the so-called reduced collision integrals between specie i and j, x_j is the mole fraction of specie j.

B.2 Heavy-particles

The usual collision integral ratios are defined as

$$A^*_{ij} = \bar{Q}^{(2,2)}_{ij}/\bar{Q}^{(1,1)}_{ij}, \quad \text{(B.2.1)}$$

$$B^*_{ij} = (5\bar{Q}^{(1,2)}_{ij} - 4\bar{Q}^{(1,3)}_{ij})/\bar{Q}^{(1,1)}_{ij}, \quad \text{(B.2.2)}$$

$$C^*_{ij} = \bar{Q}^{(1,2)}_{ij}/\bar{Q}^{(1,1)}_{ij}. \quad \text{(B.2.3)}$$

In addition, we define binary diffusion coefficients and pure species viscosities for heavy species as

$$n\mathcal{D}_{ij} = \frac{3}{16}\sqrt{\frac{2\pi k_B T_\mathfrak{h}(m_i+m_j)}{m_i m_j}}\frac{1}{\bar{Q}_{ij}^{(1,1)}}, \quad i,j \in \mathrm{H}, \tag{B.2.4}$$

$$\eta_i = \frac{5}{16}\frac{\sqrt{\pi k_B T_\mathfrak{h} m_i}}{\bar{Q}_{ii}^{(2,2)}}, \quad i \in \mathrm{H}. \tag{B.2.5}$$

The matrix Λ_{ij}^{00} is given as

$$\Lambda_{ij}^{00} = \Lambda_{ji}^{00} = -\frac{\hat{x}_i\hat{x}_j}{\mathcal{D}_{ij}}, \quad i \neq j, \tag{B.2.6}$$

$$\Lambda_{ii}^{00} = -\sum_{j\neq i}\Lambda_{ij}^{00}, \tag{B.2.7}$$

The matrices $G_{ij}^{\nu_\mathfrak{h}}$ and $G_{ij}^{\lambda_\mathfrak{h}}$ are given as

$$G_{ij}^{\nu_\mathfrak{h}} = \frac{\hat{x}_i\hat{x}_j}{n_\mathfrak{h}\mathcal{D}_{ij}}\frac{1}{m_i+m_j}\left(\frac{6}{5}A_{ij}^* - 2\right), \quad i \neq j, \tag{B.2.8}$$

$$G_{ii}^{\nu_\mathfrak{h}} = \sum_{\substack{j\in\mathrm{H}\\ j\neq i}}\frac{\hat{x}_i\hat{x}_j}{n_\mathfrak{h}\mathcal{D}_{ij}}\frac{1}{m_i+m_j}\left(\frac{6}{5}\frac{m_j}{m_i}A_{ij}^* + 2\right) + \frac{\hat{x}_i^2}{\eta_i}. \tag{B.2.9}$$

and

$$G_{ij}^{\lambda_\mathfrak{h}} = \frac{1}{25k_B}\frac{\hat{x}_i\hat{x}_j}{n_\mathfrak{h}\mathcal{D}_{ij}}\frac{m_i m_j}{(m_i+m_j)^2}\left(16A_{ij}^* + 12B_{ij}^* - 55\right), \quad i \neq j, \tag{B.2.10}$$

$$G_{ii}^{\lambda_\mathfrak{h}} = \frac{1}{25k_B}\sum_{\substack{j\in\mathrm{H}\\ j\neq i}}\frac{\hat{x}_i\hat{x}_j}{n_\mathfrak{h}\mathcal{D}_{ij}}\frac{m_i m_j}{(m_i+m_j)^2}\left(16A_{ij}^* - 12\frac{m_j}{m_i}B_{ij}^* + 25\frac{m_j}{m_i} + 30\frac{m_i}{m_j}\right) + \frac{4m_i}{15k_B}\frac{\hat{x}_i^2}{\eta_i}. \tag{B.2.11}$$

The matrices Λ_{ij}^{01} and Λ_{ii}^{01} are defined as

$$\Lambda_{ij}^{01} = \frac{1}{25k_B}\frac{\hat{x}_i\hat{x}_j}{n_\mathfrak{h}\mathcal{D}_{ij}}\frac{m_i}{m_i+m_j}\left(12C_{ij}^* - 10\right), \quad i \neq j, \tag{B.2.12}$$

$$\Lambda_{ii}^{01} = -\frac{1}{25k_B}\sum_{\substack{j\in\mathrm{H}\\ j\neq i}}\frac{\hat{x}_i\hat{x}_j}{n_\mathfrak{h}\mathcal{D}_{ij}}\frac{m_j}{m_i+m_j}\left(12C_{ij}^* - 10\right). \tag{B.2.13}$$

APPENDIX C

COLLISION INTEGRALS FOR HELIUM-HYDROGEN MIXTURE

Table C.1: Collision integrals for the Helium-Hydrogen mixture

Pair	Integral	A	B	C	D
e - He	$\Omega^{(1,1)}$	-0.014733	0.31368	-2.1119	6.27103
	$\Omega^{(1,2)}$	-0.018123	0.37964	-2.5286	7.14163
	$\Omega^{(1,3)}$	-0.020812	0.42975	-2.8313	7.74623
	$\Omega^{(1,4)}$	-0.022943	0.46758	-3.0475	8.15423
	$\Omega^{(1,5)}$	-0.024634	0.49595	-3.1987	8.41723
	$\Omega^{(2,2)}$	-0.0095221	0.18765	-1.1781	4.09863
	$\Omega^{(2,3)}$	-0.011237	0.22092	-1.3941	4.57213
	$\Omega^{(2,4)}$	-0.012949	0.25423	-1.6104	5.04293
	$\Omega^{(3,3)}$	-0.017302	0.35291	-2.2985	6.55863
	B^*	-0.001847	0.068457	-0.65597	1.7848
e - H	$\Omega^{(1,1)}$	-0.011572	0.18473	-1.0182	5.64803
	$\Omega^{(1,2)}$	-0.015026	0.24683	-1.4094	6.47703
	$\Omega^{(1,3)}$	-0.018271	0.30472	-1.7683	7.21983
	$\Omega^{(1,4)}$	-0.0211	0.3539	-2.0651	7.81623
	$\Omega^{(1,5)}$	-0.023753	0.39899	-2.3297	8.33163
	$\Omega^{(2,2)}$	-0.0090666	0.12187	-0.57859	4.66363
	$\Omega^{(2,3)}$	-0.011848	0.17381	-0.92237	5.42313
	$\Omega^{(2,4)}$	-0.014536	0.22352	-1.2448	6.11663
	$\Omega^{(3,3)}$	-0.015494	0.25065	-1.4315	6.52193
	B^*	-0.004669	0.11576	-0.84972	1.9748

Pair	Integral	A	B	C	D
e - H_2	$\Omega^{(1,1)}$	-0.028362	0.58924	-3.8003	9.97153
	$\Omega^{(1,2)}$	-0.031181	0.62883	-3.9466	10.1218
	$\Omega^{(1,3)}$	-0.03472	0.68488	-4.2153	10.5166
	$\Omega^{(1,4)}$	-0.03669	0.70874	-4.2754	10.4934
	$\Omega^{(1,5)}$	-0.038109	0.72212	-4.2733	10.3505
	$\Omega^{(2,2)}$	-0.026429	0.54934	-3.5035	8.85983
	$\Omega^{(2,3)}$	-0.030398	0.62401	-3.9635	9.84043
	$\Omega^{(2,4)}$	-0.033838	0.68698	-4.3404	10.6207
	$\Omega^{(3,3)}$	-0.031315	0.62568	-3.8851	9.83433
	B^*	-0.011368	0.30012	-2.4241	6.0123
H - H	$\Omega^{(1,1)}$	-0.013454	0.2317	-1.5045	6.73953
	$\Omega^{(1,2)}$	-0.01485	0.2466	-1.5422	6.66603
	$\Omega^{(1,3)}$	-0.015287	0.24393	-1.477	6.41773
	$\Omega^{(1,4)}$	-0.015344	0.23548	-1.3851	6.14383
	$\Omega^{(1,5)}$	-0.015163	0.22364	-1.2789	5.85833
	$\Omega^{(2,2)}$	-0.013855	0.25897	-1.8112	7.72343
	$\Omega^{(2,3)}$	-0.015936	0.29417	-2.008	8.02893
	$\Omega^{(2,4)}$	-0.017438	0.3178	-2.1314	8.19923
	$\Omega^{(3,3)}$	-0.011861	0.19419	-1.2495	6.22753
	B^*	-0.0044276	0.10321	-0.71988	1.662
H - H_2	$\Omega^{(1,1)}$	-0.0058204	0.06777	-0.46381	4.34483
	$\Omega^{(1,2)}$	-0.0067084	0.078802	-0.52534	4.40953
	$\Omega^{(1,3)}$	-0.0073782	0.087268	-0.57657	4.47633
	$\Omega^{(1,4)}$	-0.007783	0.092251	-0.61282	4.53203
	$\Omega^{(1,5)}$	-0.0087293	0.1046	-0.67069	4.58043
	$\Omega^{(2,2)}$	-0.0067272	0.086157	-0.54979	4.58543
	$\Omega^{(2,3)}$	-0.0074796	0.09627	-0.6076	4.66553
	$\Omega^{(2,4)}$	-0.0078467	0.099329	-0.62131	4.66213
	$\Omega^{(3,3)}$	-0.0068846	0.086956	-0.5771	4.58263
	B^*	-0.0012832	0.028955	-0.17133	0.42888
H_2 - H_2	$\Omega^{(1,1)}$	-0.0013857	0.0075796	-0.17097	3.98863
	$\Omega^{(1,2)}$	-0.0009285	-0.0049958	-0.076543	3.69543
	$\Omega^{(1,3)}$	-0.0011767	-0.0026811	-0.084871	3.65463
	$\Omega^{(1,4)}$	-0.0011854	-0.0048476	-0.065782	3.57153
	$\Omega^{(1,5)}$	-0.0011601	-0.0074251	-0.044945	3.49233
	$\Omega^{(2,2)}$	-0.001275	0.0065953	-0.14522	3.99443
	$\Omega^{(2,3)}$	-0.001153	0.0014902	-0.10174	3.83823
	$\Omega^{(2,4)}$	-0.0011963	-3.11E-05	-0.083559	3.75193
	$\Omega^{(3,3)}$	-0.0010494	-0.00068583	-0.098286	3.78903
	B^*	0.00044797	-0.0048013	0.024633	0.058708

Pair	Integral	A	B	C	D
He - H	$\Omega^{(1,1)}$	-0.0044957	0.059373	-0.4869	4.40523
	$\Omega^{(1,2)}$	-0.0051453	0.06766	-0.53136	4.42153
	$\Omega^{(1,3)}$	-0.0057162	0.075485	-0.57704	4.46413
	$\Omega^{(1,4)}$	-0.0062045	0.082162	-0.61625	4.50343
	$\Omega^{(1,5)}$	-0.0066414	0.088141	-0.65131	4.54033
	$\Omega^{(2,2)}$	-0.0047947	0.066343	-0.51085	4.54233
	$\Omega^{(2,3)}$	-0.0053748	0.074722	-0.55923	4.59453
	$\Omega^{(2,4)}$	-0.0058691	0.081967	-0.60237	4.64773
	$\Omega^{(3,3)}$	-0.0049766	0.066742	-0.51853	4.45463
	B^*	-0.00064003	0.017335	-0.1148	0.35513
H - He^+	$\Omega^{(1,1)}$	-0.017678	0.27836	-1.6232	6.79613
	$\Omega^{(1,2)}$	-0.018099	0.26623	-1.4651	6.31103
	$\Omega^{(1,3)}$	-0.017118	0.23024	-1.1751	5.60043
	$\Omega^{(1,4)}$	-0.015809	0.1908	-0.87863	4.90923
	$\Omega^{(1,5)}$	-0.014443	0.15249	-0.60048	4.27783
	$\Omega^{(2,2)}$	-0.022105	0.40151	-2.6296	9.17743
	$\Omega^{(2,3)}$	-0.02308	0.40652	-2.5909	8.92373
	$\Omega^{(2,4)}$	-0.022675	0.38594	-2.3995	8.38833
	$\Omega^{(3,3)}$	-0.013448	0.18829	-1.0594	5.68323
	B^*	-0.0047455	0.09588	-0.556	1.0548
He - He^+	$\Omega^{(1,1)}$	0.006721899	0.08524224	-0.51744862	7.113622712
	$\Omega^{(1,2)}$	-0.0046728	0.032817	-0.14117	4.22423
	$\Omega^{(1,3)}$	-0.0024618	-0.018612	0.20806	3.44373
	$\Omega^{(1,4)}$	-0.0005112	-0.062743	0.50002	2.80683
	$\Omega^{(1,5)}$	0.0012171	-0.10096	0.74733	2.27783
	$\Omega^{(2,2)}$	-0.0099987	0.17302	-1.223	6.85623
	$\Omega^{(2,3)}$	-0.0091033	0.14744	-1.0232	6.33183
	$\Omega^{(2,4)}$	-0.0078482	0.11577	-0.79042	5.76113
	$\Omega^{(3,3)}$	-0.0038512	0.023685	-0.12429	4.32583
	B^*	-0.0021252	0.040908	-0.20397	0.36213
He - H_2	$\Omega^{(1,1)}$	-0.0049427	0.118	-1.0874	6.3348
	$\Omega^{(1,2)}$	-0.0025006	0.058232	-0.60334	4.9858
	$\Omega^{(1,3)}$	-0.0013749	0.031065	-0.38717	4.3885
	$\Omega^{(1,4)}$	-0.00084773	0.018421	-0.28748	4.0832
	$\Omega^{(1,5)}$	-0.00056447	0.011661	-0.23462	3.8849
	$\Omega^{(2,2)}$	-0.0052141	0.12242	-1.0978	6.3956
	$\Omega^{(2,3)}$	-0.0030459	0.069825	-0.67677	5.2543
	$\Omega^{(2,4)}$	-0.00192	0.042756	-0.46248	4.6504
	$\Omega^{(3,3)}$	-0.0031194	0.071984	-0.69861	5.2668
	B^*	-0.0011069	0.026368	-0.20512	0.58179

Pair	Integral	A	B	C	D
H^+ - H	$\Omega^{(1,1)}$	-0.016757968	0.303256239	-2.118266815	11.31736434
	$\Omega^{(1,2)}$	-0.01634	0.27935	-1.8718	8.81803
	$\Omega^{(1,3)}$	-0.015136	0.24217	-1.5718	8.02423
	$\Omega^{(1,4)}$	-0.013595	0.20051	-1.2553	7.23413
	$\Omega^{(1,5)}$	-0.011967	0.1592	-0.95267	6.50413
	$\Omega^{(2,2)}$	-0.01966	0.37756	-2.6459	10.6618
	$\Omega^{(2,3)}$	-0.020057	0.37523	-2.5756	10.3422
	$\Omega^{(2,4)}$	-0.019825	0.36032	-2.4252	9.87333
	$\Omega^{(3,3)}$	-0.013939	0.23967	-1.6551	8.46143
	B^*	-0.0036323	0.082192	-0.55691	1.3265
H^+ - H_2	$\Omega^{(1,1)}$	-0.022201	0.40038	-2.6252	10.0915
	$\Omega^{(1,2)}$	-0.028092	0.50051	-3.1936	11.0794
	$\Omega^{(1,3)}$	-0.032868	0.57751	-3.606	11.7452
	$\Omega^{(1,4)}$	-0.037076	0.64316	-3.9444	12.2668
	$\Omega^{(1,5)}$	-0.04086	0.70066	-4.2322	12.6953
	$\Omega^{(2,2)}$	-0.024738	0.47817	-3.2958	11.627
	$\Omega^{(2,3)}$	-0.031264	0.59941	-4.0315	13.0039
	$\Omega^{(2,4)}$	-0.034729	0.65776	-4.3526	13.5212
	$\Omega^{(3,3)}$	-0.019124	0.34409	-2.3298	9.55173
	B^*	-0.011798	0.27196	-1.9614	4.612
H^+ - He	$\Omega^{(1,1)}$	-0.01808	0.33378	-2.4849	10.2082
	$\Omega^{(1,2)}$	-0.020575	0.36683	-2.6103	10.1454
	$\Omega^{(1,3)}$	-0.022327	0.38573	-2.6505	9.96833
	$\Omega^{(1,4)}$	-0.023514	0.39445	-2.6332	9.71653
	$\Omega^{(1,5)}$	-0.024103	0.3927	-2.5583	9.38213
	$\Omega^{(2,2)}$	-0.022023	0.43627	-3.2493	11.7829
	$\Omega^{(2,3)}$	-0.024843	0.48125	-3.4692	11.9784
	$\Omega^{(2,4)}$	-0.026645	0.50563	-3.558	11.9378
	$\Omega^{(3,3)}$	-0.01808	0.33378	-2.4849	10.2082
	B^*	-0.005992	0.14012	-1.0183	2.5408
He - He	$\Omega^{(1,1)}$	-0.0034229	0.05176	-0.46608	4.14693
	$\Omega^{(1,2)}$	-0.0035904	0.05201	-0.45855	4.05273
	$\Omega^{(1,3)}$	-0.0039133	0.056402	-0.48375	4.05673
	$\Omega^{(1,4)}$	-0.0042671	0.061801	-0.51684	4.08873
	$\Omega^{(1,5)}$	-0.0046175	0.067331	-0.55113	4.12943
	$\Omega^{(2,2)}$	-0.0031211	0.046183	-0.41094	4.10603
	$\Omega^{(2,3)}$	-0.0032703	0.047262	-0.41343	4.06303
	$\Omega^{(2,4)}$	-0.0035118	0.050733	-0.43443	4.07403
	$\Omega^{(3,3)}$	-0.0032544	0.046435	-0.41406	4.00943
	B^*	9.93E-05	0.0010243	-0.0079574	0.1174

APPENDIX D

CONSERVATIVE MODELS

We introduce two additional models.

Model M^{ent} with a conservation equation of entropy:

$$\begin{cases} \partial_t(\rho_{\mathfrak{h}}) + \boldsymbol{\partial_x}(\rho_{\mathfrak{h}}\boldsymbol{v}_{\mathfrak{h}}) = 0, \\ \partial_t(\rho_{\mathfrak{h}}\boldsymbol{v}_{\mathfrak{h}}) + \boldsymbol{\partial_x}(\rho_{\mathfrak{h}}\boldsymbol{v}_{\mathfrak{h}}^2 + p) = 0, \\ \partial_t(\mathcal{E}) + \boldsymbol{\partial_x}(\mathcal{E}\boldsymbol{v}_{\mathfrak{h}} + p\boldsymbol{v}_{\mathfrak{h}}) = 0, \\ \partial_t(\rho_{\mathfrak{e}}) + \boldsymbol{\partial_x}(\rho_{\mathfrak{e}}\boldsymbol{v}_{\mathfrak{h}}) = 0, \\ \partial_t(\rho_{\mathfrak{e}} s_{\mathfrak{e}}) + \boldsymbol{\partial_x}(\rho_{\mathfrak{e}} s_{\mathfrak{e}}\boldsymbol{v}_{\mathfrak{h}}) = 0, \end{cases} \tag{M^{ent}}$$

where the electron entropy $s_{\mathfrak{e}}$ is defined by the relation $p_{\mathfrak{e}} = (\gamma - 1)\rho_{\mathfrak{e}}^{\gamma} \exp(s_{\mathfrak{e}}/c_v)$, where c_v is the electron specific heat at constant volume.

Model M^{src}, with the nonconservative product as a source term:

$$\begin{cases} \partial_t(\rho_{\mathfrak{h}}) + \boldsymbol{\partial_x}(\rho_{\mathfrak{h}}\boldsymbol{v}_{\mathfrak{h}}) = 0, \\ \partial_t(\rho_{\mathfrak{h}}\boldsymbol{v}_{\mathfrak{h}}) + \boldsymbol{\partial_x}(\rho_{\mathfrak{h}}\boldsymbol{v}_{\mathfrak{h}}^2 + p) = 0, \\ \partial_t(\mathcal{E}) + \boldsymbol{\partial_x}(\mathcal{E}\boldsymbol{v}_{\mathfrak{h}} + p\boldsymbol{v}_{\mathfrak{h}}) = 0, \\ \partial_t(\rho_{\mathfrak{e}}) + \boldsymbol{\partial_x}(\rho_{\mathfrak{e}}\boldsymbol{v}_{\mathfrak{h}}) = 0, \\ \partial_t(\rho_{\mathfrak{e}} e_{\mathfrak{e}}) + \boldsymbol{\partial_x}(\rho_{\mathfrak{e}} e_{\mathfrak{e}}\boldsymbol{v}_{\mathfrak{h}}) = 0. \end{cases} \tag{M^{src}}$$

APPENDIX E

HYPERBOLIC STRUCTURE OF THE SIMPLIFIED SYSTEMS AND IMPACT OF THE NONCONSERVATIVE TERM

In this appendix, we study the hyperbolic structure of the simplified system (M_S) and exhibit the impact of the nonconservative term $p_\mathfrak{e}\boldsymbol{\partial_x}\cdot\boldsymbol{v}_\mathfrak{h}$. Therefore, two systems are considered: a system called (M_S^{hyp}) where the nonconservative term is considered as part of the hyperbolic structure, and (M^{src}) where the nonconservative term is considered as a source term, defined in the previous appendix.

From the system (M_S), we identify the corresponding nonconservative hyperbolic system (removing the diffusive terms) which reads

$$\begin{cases} \partial_t\rho_\mathfrak{h} + \boldsymbol{\partial_x}\cdot(\rho_\mathfrak{h}\boldsymbol{v}_\mathfrak{h}) = 0, \\ \partial_t(\rho_\mathfrak{h}\boldsymbol{v}_\mathfrak{h}) + \boldsymbol{\partial_x}\cdot(\rho_\mathfrak{h}\boldsymbol{v}_\mathfrak{h}\otimes\boldsymbol{v}_\mathfrak{h} + p\mathbb{I}) = 0, \\ \partial_t\mathcal{E} + \boldsymbol{\partial_x}\cdot(\mathcal{E}\boldsymbol{v}_\mathfrak{h} + p\boldsymbol{v}_\mathfrak{h}) = 0, \\ \partial_t\rho_\mathfrak{e} + \boldsymbol{\partial_x}\cdot(\rho_\mathfrak{e}\boldsymbol{v}_\mathfrak{h}) = 0, \\ \partial_t(\rho_\mathfrak{e}e_\mathfrak{e}) + \boldsymbol{\partial_x}\cdot(\rho_\mathfrak{e}e_\mathfrak{e}\boldsymbol{v}_\mathfrak{h}) + p_\mathfrak{e}\boldsymbol{\partial_x}\cdot\boldsymbol{v}_\mathfrak{h} = 0, \end{cases} \tag{M_S^{hyp}}$$

Then, we recall the following system (M^{src}), where the nonconservative term is considered as a source term

$$\begin{cases} \partial_t(\rho_\mathfrak{h}) + \boldsymbol{\partial_x}(\rho_\mathfrak{h}\boldsymbol{v}_\mathfrak{h}) = 0, \\ \partial_t(\rho_\mathfrak{h}\boldsymbol{v}_\mathfrak{h}) + \boldsymbol{\partial_x}(\rho_\mathfrak{h}\boldsymbol{v}_\mathfrak{h}^2 + p) = 0, \\ \partial_t(\mathcal{E}) + \boldsymbol{\partial_x}(\mathcal{E}\boldsymbol{v}_\mathfrak{h} + p\boldsymbol{v}_\mathfrak{h}) = 0, \\ \partial_t(\rho_\mathfrak{e}) + \boldsymbol{\partial_x}(\rho_\mathfrak{e}\boldsymbol{v}_\mathfrak{h}) = 0, \\ \partial_t(\rho_\mathfrak{e}e_\mathfrak{e}) + \boldsymbol{\partial_x}(\rho_\mathfrak{e}e_\mathfrak{e}\boldsymbol{v}_\mathfrak{h}) = 0. \end{cases} \tag{M^{src}}$$

In the following, we consider a monodimensional case. First, we focus on the study of (M_S^{hyp}) . Then, we intend to compare with the study of (M^{src}). The differences will be highlighted in red.

E.1 Case with (M_S^{hyp})

First, we rewrite the system (M_S^{hyp}) as follow

$$\partial_t \mathcal{U} + \mathcal{A}(\mathcal{U})\partial_x \mathcal{U} = 0, \tag{E.1.1}$$

where

$$\mathcal{U} = \left(\rho_{\mathfrak{h}},\, \rho_{\mathfrak{h}} \boldsymbol{v}_{\mathfrak{h}},\, \mathcal{E},\, \rho_{\mathfrak{e}},\, \rho_{\mathfrak{e}} e_{\mathfrak{e}}\right)^T, \tag{E.1.2}$$

$$\mathcal{A}(\mathcal{U}) = \begin{pmatrix} 0 & 1 & 0 & 0 & 0 \\ (\frac{\alpha}{2}-1)\boldsymbol{v}_{\mathfrak{h}}^2 & (2-\alpha)\boldsymbol{v}_{\mathfrak{h}} & \alpha & 0 & 0 \\ (\frac{\alpha}{2}\boldsymbol{v}_{\mathfrak{h}}^2 - \frac{\mathcal{H}}{\rho_{\mathfrak{h}}})\boldsymbol{v}_{\mathfrak{h}} & \frac{\mathcal{H}}{\rho_{\mathfrak{h}}} - \alpha \boldsymbol{v}_{\mathfrak{h}}^2 & (1+\alpha)\boldsymbol{v}_{\mathfrak{h}} & 0 & 0 \\ -\frac{\rho_{\mathfrak{e}}}{\rho_{\mathfrak{h}}}\boldsymbol{v}_{\mathfrak{h}} & \frac{\rho_{\mathfrak{e}}}{\rho_{\mathfrak{h}}} & 0 & \boldsymbol{v}_{\mathfrak{h}} & 0 \\ -\frac{\rho_{\mathfrak{e}} e_{\mathfrak{e}}}{\rho_{\mathfrak{h}}}(1+\alpha)\boldsymbol{v}_{\mathfrak{h}} & \frac{\rho_{\mathfrak{e}} e_{\mathfrak{e}}}{\rho_{\mathfrak{h}}}(1+\alpha) & 0 & 0 & \boldsymbol{v}_{\mathfrak{h}} \end{pmatrix}, \tag{E.1.3}$$

where $\alpha = \gamma - 1$ and $\mathcal{H} = \mathcal{E} + p$. Then, we can compute the eigenvalues and eigenvectors of $\mathcal{A}$ as follow:

$$\lambda_1 = \boldsymbol{v}_{\mathfrak{h}} - c, \qquad r_1 = \left(1,\, \boldsymbol{v}_{\mathfrak{h}} - c,\, \tfrac{\mathcal{H}}{\rho_{\mathfrak{h}}} - \boldsymbol{v}_{\mathfrak{h}} c,\, \tfrac{\rho_{\mathfrak{e}}}{\rho_{\mathfrak{h}}},\, (1+\alpha)\tfrac{\rho_{\mathfrak{e}} e_{\mathfrak{e}}}{\rho_{\mathfrak{h}}}\right)^T, \tag{E.1.4}$$

$$\lambda_2 = \boldsymbol{v}_{\mathfrak{h}}, \qquad r_2 = \left(1,\, \boldsymbol{v}_{\mathfrak{h}},\, \tfrac{1}{2}\boldsymbol{v}_{\mathfrak{h}}^2,\, 0,\, 0\right)^T, \tag{E.1.5}$$

$$\lambda_3 = \boldsymbol{v}_{\mathfrak{h}} + c, \qquad r_3 = \left(1,\, \boldsymbol{v}_{\mathfrak{h}} + c,\, \tfrac{\mathcal{H}}{\rho_{\mathfrak{h}}} + \boldsymbol{v}_{\mathfrak{h}} c,\, \tfrac{\rho_{\mathfrak{e}}}{\rho_{\mathfrak{h}}},\, (1+\alpha)\tfrac{\rho_{\mathfrak{e}} e_{\mathfrak{e}}}{\rho_{\mathfrak{h}}}\right)^T, \tag{E.1.6}$$

$$\lambda_4 = \boldsymbol{v}_{\mathfrak{h}}, \qquad r_4 = \left(0,\, 0,\, 0,\, 1,\, 0\right)^T, \tag{E.1.7}$$

$$\lambda_5 = \boldsymbol{v}_{\mathfrak{h}}, \qquad r_5 = \left(0,\, 0,\, 0,\, 0,\, 1\right)^T, \tag{E.1.8}$$

where $c = \sqrt{\gamma p/\rho_{\mathfrak{h}}}$. Then, we define the entropy $s_{\mathfrak{e}}$ and $s_{\mathfrak{h}}$ as

$$p_{\mathfrak{h}} = \alpha \rho_{\mathfrak{h}}^{\gamma} \mathrm{e}^{\left(\frac{s_{\mathfrak{h}}}{\gamma-1}\right)}, \quad p_{\mathfrak{e}} = \alpha \rho_{\mathfrak{e}}^{\gamma} \mathrm{e}^{\left(\frac{s_{\mathfrak{e}}}{\gamma-1}\right)}. \tag{E.1.9}$$

Finally, we can also compute the Riemann invariants associated with the eigenvectors:

$$\beta_1^1 = s_{\mathfrak{h}}, \quad \beta_1^2 = \boldsymbol{v}_{\mathfrak{h}} + \tfrac{2c}{\alpha}, \quad \beta_1^3 = \tfrac{\rho_{\mathfrak{h}}}{\rho_{\mathfrak{e}}}, \quad \beta_1^4 = \tfrac{\rho_{\mathfrak{h}}^{\gamma}}{\rho_{\mathfrak{e}} e_{\mathfrak{e}}}, \tag{E.1.10}$$

$$\beta_2^1 = \boldsymbol{v}_{\mathfrak{h}}, \quad \beta_2^2 = p, \quad \beta_2^3 = \rho_{\mathfrak{e}}, \quad \beta_2^4 = \rho_{\mathfrak{e}} e_{\mathfrak{e}}, \tag{E.1.11}$$

$$\beta_3^1 = s_\mathfrak{h}, \quad \beta_3^2 = \boldsymbol{v}_\mathfrak{h} - \tfrac{2c}{\alpha}, \quad \beta_3^3 = \tfrac{\rho_\mathfrak{h}}{\rho_\mathfrak{e}}, \quad \beta_3^4 = \tfrac{\rho_\mathfrak{h}^\gamma}{\rho_\mathfrak{e} e_\mathfrak{e}}, \tag{E.1.12}$$

$$\beta_4^1 = \rho_\mathfrak{h}, \quad \beta_4^2 = \rho_\mathfrak{h}\boldsymbol{v}_\mathfrak{h}, \quad \beta_4^3 = \mathcal{E}, \quad \beta_4^4 = \rho_\mathfrak{e} e_\mathfrak{e}, \tag{E.1.13}$$

$$\beta_5^1 = \rho_\mathfrak{h}, \quad \beta_5^2 = \rho_\mathfrak{h}\boldsymbol{v}_\mathfrak{h}, \quad \beta_5^3 = \mathcal{E}, \quad \beta_5^4 = \rho_\mathfrak{e}. \tag{E.1.14}$$

Finally, based on the Riemann invariants, we look for all the connected states $\mathcal{U}^*$ to the state $\mathcal{U}^0$ by shock and rarefaction waves.

E.1.1 1-rarefaction wave

We look for the states $\mathcal{U}^*$ connected to the state $\mathcal{U}^0$ by a 1-rarefaction wave. These states are configured by $p^* < p^0$, as follow

$$\boldsymbol{v}_\mathfrak{h}^* = \boldsymbol{v}_\mathfrak{h}^0 - \frac{2}{\alpha}\sqrt{\frac{\gamma}{\rho_\mathfrak{h}^0}}(p^0)^{\frac{1}{2\gamma}}\left[(p^*)^{\frac{\gamma-1}{2\gamma}} - (p^0)^{\frac{\gamma-1}{2\gamma}}\right], \tag{E.1.15}$$

$$\rho_\mathfrak{h}^* = \rho_\mathfrak{h}^0\left(\frac{p^*}{p^0}\right)^{\frac{1}{\gamma}}, \quad \rho_\mathfrak{e}^* = \rho_\mathfrak{e}^0\left(\frac{p^*}{p^0}\right)^{\frac{1}{\gamma}}, \quad p_\mathfrak{e}^* = p_\mathfrak{e}^0\frac{p^*}{p^0}. \tag{E.1.16}$$

In addition, a complete computation of the rarefaction wave can be performed. We introduce a parameter ζ which configures the rarefaction wave. Thus, after some algebra, we have

$$\boldsymbol{v}_\mathfrak{h}(\zeta) = \boldsymbol{v}_\mathfrak{h}^0 + \frac{2}{\gamma+1}(\zeta - \zeta^0), \tag{E.1.17}$$

$$\rho_\mathfrak{h}(\zeta) = \left[(\rho_\mathfrak{h}^0)^{\frac{\alpha}{2}} - \frac{\gamma-1}{\gamma+1}\frac{1}{\sqrt{\gamma}}\frac{(\rho_\mathfrak{h}^0)^{\frac{\gamma}{2}}}{\sqrt{p^0}}(\zeta - \zeta^0)\right]^{\frac{2}{\alpha}}, \tag{E.1.18}$$

$$\rho_\mathfrak{e}(\zeta) = \rho_\mathfrak{e}^0\frac{\rho_\mathfrak{h}(\zeta)}{\rho_\mathfrak{h}^0}, \quad p_\mathfrak{e}(\zeta) = p_\mathfrak{e}^0\left(\frac{\rho_\mathfrak{h}(\zeta)}{\rho_\mathfrak{h}^0}\right)^\gamma, \quad p(\zeta) = p^0\left(\frac{\rho_\mathfrak{h}(\zeta)}{\rho_\mathfrak{h}^0}\right)^\gamma. \tag{E.1.19}$$

E.1.2 1-shock wave

We look for the states $\mathcal{U}^*$ connected to the state $\mathcal{U}^0$ by a 1-shock wave using the Rankine-Hugoniot condition. These states are configured by $p^* > p^0$ (for an entropic shock wave), as follow

$$m_\mathfrak{h} = \sqrt{\frac{\rho_\mathfrak{h}^0(p^* + p^0\mu^2)}{1-\mu^2}}, \quad \sigma = \boldsymbol{v}_\mathfrak{h}^0 - \frac{m_\mathfrak{h}}{\rho_\mathfrak{h}^0}, \tag{E.1.20}$$

$$v_{\mathfrak{h}}^* = v_{\mathfrak{h}}^0 - \frac{p^* - p^0}{m_{\mathfrak{h}}}, \quad \rho_{\mathfrak{h}}^* = \frac{m_{\mathfrak{h}}}{v_{\mathfrak{h}}^* - \sigma}, \quad \rho_{\mathfrak{e}}^* = \rho_{\mathfrak{e}}^0 \frac{\rho_{\mathfrak{h}}^*}{\rho_{\mathfrak{h}}^0}, \tag{E.1.21}$$

where $\mu^2 = (\gamma - 1)/(\gamma + 1)$. We do not have a jump relation for $p_{\mathfrak{e}}$ since the last equation of (M_S^{hyp}) is not conservative.

E.1.3 3-rarefaction wave

As presented in Section E.2.1, we look for the states $\mathcal{U}^*$ connected to the state $\mathcal{U}^0$ by a 3-rarefaction wave, as follow

$$v_{\mathfrak{h}}^* = v_{\mathfrak{h}}^0 + \frac{2}{\alpha}\sqrt{\frac{\gamma}{\rho_{\mathfrak{h}}^0}}(p^0)^{\frac{1}{2\gamma}}\left[(p^*)^{\frac{\gamma-1}{2\gamma}} - (p^0)^{\frac{\gamma-1}{2\gamma}}\right], \tag{E.1.22}$$

$$\rho_{\mathfrak{h}}^* = \rho_{\mathfrak{h}}^0\left(\frac{p^*}{p^0}\right)^{\frac{1}{\gamma}}, \quad \rho_{\mathfrak{e}}^* = \rho_{\mathfrak{e}}^0\left(\frac{p^*}{p^0}\right)^{\frac{1}{\gamma}}, \quad p_{\mathfrak{e}}^* = p_{\mathfrak{e}}^0\frac{p^*}{p^0}. \tag{E.1.23}$$

A complete computation of the rarefaction wave can be performed by introducing a parameter ζ. Thus, after some algebra, we have

$$v_{\mathfrak{h}}(\zeta) = v_{\mathfrak{h}}^0 + \frac{2}{\gamma + 1}(\zeta - \zeta^0), \tag{E.1.24}$$

$$\rho_{\mathfrak{h}}(\zeta) = \left[(\rho_{\mathfrak{h}}^0)^{\frac{\alpha}{2}} + \frac{\gamma - 1}{\gamma + 1}\frac{1}{\sqrt{\gamma}}\frac{(\rho_{\mathfrak{h}}^0)^{\frac{\gamma}{2}}}{\sqrt{p^0}}(\zeta - \zeta^0)\right]^{\frac{2}{\alpha}}, \tag{E.1.25}$$

$$\rho_{\mathfrak{e}}(\zeta) = \rho_{\mathfrak{e}}^0\frac{\rho_{\mathfrak{h}}(\zeta)}{\rho_{\mathfrak{h}}^0}, \quad p_{\mathfrak{e}}(\zeta) = p_{\mathfrak{e}}^0\left(\frac{\rho_{\mathfrak{h}}(\zeta)}{\rho_{\mathfrak{h}}^0}\right)^{\gamma}, \quad p(\zeta) = p^0\left(\frac{\rho_{\mathfrak{h}}(\zeta)}{\rho_{\mathfrak{h}}^0}\right)^{\gamma}. \tag{E.1.26}$$

E.1.4 3-shock wave

As presented in Section E.2.2, we look for the states $\mathcal{U}^*$ connected to the state $\mathcal{U}^0$ by a 3-shock wave using the Rankine-Hugoniot condition. These states are configured by $p^* > p^0$ (for an entropic shock wave), as follow

$$m_{\mathfrak{h}} = -\sqrt{\frac{\rho_{\mathfrak{h}}^0(p^* + p^0\mu^2)}{1 - \mu^2}}, \quad \sigma = v_{\mathfrak{h}}^0 - \frac{m_{\mathfrak{h}}}{\rho_{\mathfrak{h}}^0}, \tag{E.1.27}$$

$$v_{\mathfrak{h}}^* = v_{\mathfrak{h}}^0 - \frac{p^* - p^0}{m_{\mathfrak{h}}}, \quad \rho_{\mathfrak{h}}^* = \frac{m_{\mathfrak{h}}}{v_{\mathfrak{h}}^* - \sigma}, \quad \rho_{\mathfrak{e}}^* = \rho_{\mathfrak{e}}^0\frac{\rho_{\mathfrak{h}}^*}{\rho_{\mathfrak{h}}^0}. \tag{E.1.28}$$

We do not have a jump relation for $p_\mathfrak{e}$ since the last equation of (M_S^{hyp}) is not conservative.

E.2 Case with (M^{src})

We rewrite the system M^{src} as follow

$$\partial_t \mathcal{U} + \mathcal{A}(\mathcal{U})\partial_x \mathcal{U} = 0, \tag{E.2.1}$$

where

$$\mathcal{U} = \left(\rho_\mathfrak{h},\, \rho_\mathfrak{h} \boldsymbol{v}_\mathfrak{h},\, \mathcal{E},\, \rho_\mathfrak{e},\, \rho_\mathfrak{e} e_\mathfrak{e}\right)^T, \tag{E.2.2}$$

$$\mathcal{A}(\mathcal{U}) = \begin{pmatrix} 0 & 1 & 0 & 0 & 0 \\ (\frac{\alpha}{2}-1)\boldsymbol{v}_\mathfrak{h}^2 & (2-\alpha)\boldsymbol{v}_\mathfrak{h} & \alpha & 0 & 0 \\ (\frac{\alpha}{2}\boldsymbol{v}_\mathfrak{h}^2 - \frac{\mathcal{H}}{\rho_\mathfrak{h}})\boldsymbol{v}_\mathfrak{h} & \frac{\mathcal{H}}{\rho_\mathfrak{h}} - \alpha \boldsymbol{v}_\mathfrak{h}^2 & (1+\alpha)\boldsymbol{v}_\mathfrak{h} & 0 & 0 \\ -\frac{\rho_\mathfrak{e}}{\rho_\mathfrak{h}}\boldsymbol{v}_\mathfrak{h} & \frac{\rho_\mathfrak{e}}{\rho_\mathfrak{h}} & 0 & \boldsymbol{v}_\mathfrak{h} & 0 \\ -\frac{\rho_\mathfrak{e} e_\mathfrak{e}}{\rho_\mathfrak{h}}\boldsymbol{v}_\mathfrak{h} & \frac{\rho_\mathfrak{e} e_\mathfrak{e}}{\rho_\mathfrak{h}} & 0 & 0 & \boldsymbol{v}_\mathfrak{h} \end{pmatrix}, \tag{E.2.3}$$

where $\alpha = \gamma - 1$ and $\mathcal{H} = \mathcal{E} + p$. Then, we can compute the eigenvalues and eigenvectors of $\mathcal{A}$ as follow:

$$\lambda_1 = \boldsymbol{v}_\mathfrak{h} - c, \qquad r_1 = \left(1,\, \boldsymbol{v}_\mathfrak{h} - c,\, \frac{\mathcal{H}}{\rho_\mathfrak{h}} - \boldsymbol{v}_\mathfrak{h} c,\, \frac{\rho_\mathfrak{e}}{\rho_\mathfrak{h}},\, \frac{\rho_\mathfrak{e} e_\mathfrak{e}}{\rho_\mathfrak{h}}\right)^T, \tag{E.2.4}$$

$$\lambda_2 = \boldsymbol{v}_\mathfrak{h}, \qquad r_2 = \left(1,\, \boldsymbol{v}_\mathfrak{h},\, \tfrac{1}{2}\boldsymbol{v}_\mathfrak{h}^2,\, 0,\, 0\right)^T, \tag{E.2.5}$$

$$\lambda_3 = \boldsymbol{v}_\mathfrak{h} + c, \qquad r_3 = \left(1,\, \boldsymbol{v}_\mathfrak{h} + c,\, \frac{\mathcal{H}}{\rho_\mathfrak{h}} + \boldsymbol{v}_\mathfrak{h} c,\, \frac{\rho_\mathfrak{e}}{\rho_\mathfrak{h}},\, \frac{\rho_\mathfrak{e} e_\mathfrak{e}}{\rho_\mathfrak{h}}\right)^T, \tag{E.2.6}$$

$$\lambda_4 = \boldsymbol{v}_\mathfrak{h}, \qquad r_4 = \left(0,\, 0,\, 0,\, 1,\, 0\right)^T, \tag{E.2.7}$$

$$\lambda_5 = \boldsymbol{v}_\mathfrak{h}, \qquad r_5 = \left(0,\, 0,\, 0,\, 0,\, 1\right)^T, \tag{E.2.8}$$

where $c = \sqrt{\gamma p/\rho_\mathfrak{h}}$. Then, we define the entropy $s_\mathfrak{e}$ as $s_\mathfrak{h}$ as

$$p_\mathfrak{h} = \alpha \rho_\mathfrak{h}^\gamma \mathrm{e}^{\left(\frac{s_\mathfrak{h}}{\gamma-1}\right)}, \quad p_\mathfrak{e} = \alpha \rho_\mathfrak{e}^\gamma \mathrm{e}^{\left(\frac{s_\mathfrak{e}}{\gamma-1}\right)}. \tag{E.2.9}$$

Finally, we can also computed the Riemann invariants associated with the eigenvectors:

$$\beta_1^1 = s_\mathfrak{h}, \quad \beta_1^2 = \boldsymbol{v}_\mathfrak{h} + \tfrac{2c}{\alpha}, \quad \beta_1^3 = \tfrac{\rho_\mathfrak{h}}{\rho_\mathfrak{e}}, \quad \beta_1^4 = \tfrac{\rho_\mathfrak{h}}{\rho_\mathfrak{e} e_\mathfrak{e}}, \tag{E.2.10}$$

$$\beta_2^1 = \boldsymbol{v}_\mathfrak{h}, \quad \beta_2^2 = p, \quad \beta_2^3 = \rho_\mathfrak{e}, \quad \beta_2^4 = \rho_\mathfrak{e} e_\mathfrak{e}, \tag{E.2.11}$$

$$\beta_3^1 = s_\mathfrak{h}, \quad \beta_3^2 = \boldsymbol{v}_\mathfrak{h} - \tfrac{2c}{\alpha}, \quad \beta_3^3 = \tfrac{\rho_\mathfrak{h}}{\rho_\mathfrak{e}}, \quad \beta_3^4 = \tfrac{\rho_\mathfrak{h}}{\rho_\mathfrak{e} e_\mathfrak{e}}, \tag{E.2.12}$$

$$\beta_4^1 = \rho_\mathfrak{h}, \quad \beta_4^2 = \rho_\mathfrak{h}\boldsymbol{v}_\mathfrak{h}, \quad \beta_4^3 = \mathcal{E}, \quad \beta_4^4 = \rho_\mathfrak{e} e_\mathfrak{e}, \tag{E.2.13}$$

$$\beta_5^1 = \rho_\mathfrak{h}, \quad \beta_5^2 = \rho_\mathfrak{h}\boldsymbol{v}_\mathfrak{h}, \quad \beta_5^3 = \mathcal{E}, \quad \beta_5^4 = \rho_\mathfrak{e}. \tag{E.2.14}$$

In the following, we look for all the connected states $\mathcal{U}^*$ to the state $\mathcal{U}^0$ by shock and rarefaction waves.

E.2.1 1-rarefaction wave

We look for the states $\mathcal{U}^*$ connected to the state $\mathcal{U}^0$ by a 1-rarefaction wave. These states are configured by $p^* < p^0$, as follow

$$\boldsymbol{v}_\mathfrak{h}^* = \boldsymbol{v}_\mathfrak{h}^0 - \frac{2}{\alpha}\sqrt{\frac{\gamma}{\rho_\mathfrak{h}^0}}(p^0)^{\frac{1}{2\gamma}}\left[(p^*)^{\frac{\gamma-1}{2\gamma}} - (p^0)^{\frac{\gamma-1}{2\gamma}}\right], \tag{E.2.15}$$

$$\rho_\mathfrak{h}^* = \rho_\mathfrak{h}^0\left(\frac{p^*}{p^0}\right)^{\frac{1}{\gamma}}, \quad \rho_\mathfrak{e}^* = \rho_\mathfrak{e}^0\left(\frac{p^*}{p^0}\right)^{\frac{1}{\gamma}}, \quad p_\mathfrak{e}^* = p_\mathfrak{e}^0\left(\frac{p^*}{p^0}\right)^{\frac{1}{\gamma}}. \tag{E.2.16}$$

In addition, a complete computation of the rarefaction wave can be performed. We introduce a parameter ζ which configures the rarefaction wave. Thus, after some algebra, we have

$$\boldsymbol{v}_\mathfrak{h}(\zeta) = \boldsymbol{v}_\mathfrak{h}^0 + \frac{2}{\gamma+1}(\zeta - \zeta^0), \tag{E.2.17}$$

$$\rho_\mathfrak{h}(\zeta) = \left[(\rho_\mathfrak{h}^0)^{\frac{\alpha}{2}} - \frac{\gamma-1}{\gamma+1}\frac{1}{\sqrt{\gamma}}\frac{(\rho_\mathfrak{h}^0)^{\frac{\gamma}{2}}}{\sqrt{p^0}}(\zeta - \zeta^0)\right]^{\frac{2}{\alpha}}, \tag{E.2.18}$$

$$\rho_\mathfrak{e}(\zeta) = \rho_\mathfrak{e}^0\frac{\rho_\mathfrak{h}(\zeta)}{\rho_\mathfrak{h}^0}, \quad p_\mathfrak{e}(\zeta) = p_\mathfrak{e}^0\frac{\rho_\mathfrak{h}(\zeta)}{\rho_\mathfrak{h}^0}, \quad p(\zeta) = p^0\left(\frac{\rho_\mathfrak{h}(\zeta)}{\rho_\mathfrak{h}^0}\right)^\gamma. \tag{E.2.19}$$

E.2.2 1-shock wave

We look for the states $\mathcal{U}^*$ connected to the state $\mathcal{U}^0$ by a 1-shock wave using the Rankine-Hugoniot condition. These states are configured by $p^* > p^0$ (for an entropic shock wave) as follow

$$m_\mathfrak{h} = \sqrt{\frac{\rho_\mathfrak{h}^0(p^* + p^0\mu^2)}{1-\mu^2}}, \quad \sigma = \boldsymbol{v}_\mathfrak{h}^0 - \frac{m_\mathfrak{h}}{\rho_\mathfrak{h}^0}, \tag{E.2.20}$$

$$v_{\mathfrak{h}}^* = v_{\mathfrak{h}}^0 - \frac{p^* - p^0}{m_{\mathfrak{h}}}, \quad \rho_{\mathfrak{h}}^* = \frac{m_{\mathfrak{h}}}{v_{\mathfrak{h}}^* - \sigma}, \quad \rho_{\mathfrak{e}}^* = \rho_{\mathfrak{e}}^0 \frac{\rho_{\mathfrak{h}}^*}{\rho_{\mathfrak{h}}^0}, \quad p_{\mathfrak{e}}^* = p_{\mathfrak{e}}^0 \frac{\rho_{\mathfrak{h}}^*}{\rho_{\mathfrak{h}}^0}, \tag{E.2.21}$$

where $\mu^2 = (\gamma - 1)/(\gamma + 1)$. We have a jump relation for $p_{\mathfrak{e}}$ since the last equation of (M^{src}) is conservative.

E.2.3 3-rarefaction wave

As presented in Section E.2.1, we look for the states $\mathcal{U}^*$ connected to the state $\mathcal{U}^0$ by a 3-rarefaction wave, as follow

$$v_{\mathfrak{h}}^* = v_{\mathfrak{h}}^0 + \frac{2}{\alpha}\sqrt{\frac{\gamma}{\rho_{\mathfrak{h}}^0}}(p^0)^{\frac{1}{2\gamma}}\left[(p^*)^{\frac{\gamma-1}{2\gamma}} - (p^0)^{\frac{\gamma-1}{2\gamma}}\right], \tag{E.2.22}$$

$$\rho_{\mathfrak{h}}^* = \rho_{\mathfrak{h}}^0\left(\frac{p^*}{p^0}\right)^{\frac{1}{\gamma}}, \quad \rho_{\mathfrak{e}}^* = \rho_{\mathfrak{e}}^0\left(\frac{p^*}{p^0}\right)^{\frac{1}{\gamma}}, \quad p_{\mathfrak{e}}^* = p_{\mathfrak{e}}^0\left(\frac{p^*}{p^0}\right)^{\frac{1}{\gamma}}. \tag{E.2.23}$$

A complete computation of the rarefaction wave can be performed by introducing a parameter ζ. Thus, after some algebra, we have

$$v_{\mathfrak{h}}(\zeta) = v_{\mathfrak{h}}^0 + \frac{2}{\gamma + 1}(\zeta - \zeta^0), \tag{E.2.24}$$

$$\rho_{\mathfrak{h}}(\zeta) = \left[(\rho_{\mathfrak{h}}^0)^{\frac{\alpha}{2}} + \frac{\gamma - 1}{\gamma + 1}\frac{1}{\sqrt{\gamma}}\frac{(\rho_{\mathfrak{h}}^0)^{\frac{\gamma}{2}}}{\sqrt{p^0}}(\zeta - \zeta^0)\right]^{\frac{2}{\alpha}}, \tag{E.2.25}$$

$$\rho_{\mathfrak{e}}(\zeta) = \rho_{\mathfrak{e}}^0\frac{\rho_{\mathfrak{h}}(\zeta)}{\rho_{\mathfrak{h}}^0}, \quad p_{\mathfrak{e}}(\zeta) = p_{\mathfrak{e}}^0\frac{\rho_{\mathfrak{h}}(\zeta)}{\rho_{\mathfrak{h}}^0}, \quad p(\zeta) = p^0\left(\frac{\rho_{\mathfrak{h}}(\zeta)}{\rho_{\mathfrak{h}}^0}\right)^{\gamma}. \tag{E.2.26}$$

E.2.4 3-shock wave

As presented in Section E.2.2, we look for the states $\mathcal{U}^*$ connected to the state $\mathcal{U}^0$ by a 3-shock wave using the Rankine-Hugoniot condition. These states are configured by $p^* > p^0$ (for an entropic shock wave), as follow

$$m_{\mathfrak{h}} = -\sqrt{\frac{\rho_{\mathfrak{h}}^0(p^* + p^0\mu^2)}{1 - \mu^2}}, \quad \sigma = v_{\mathfrak{h}}^0 - \frac{m_{\mathfrak{h}}}{\rho_{\mathfrak{h}}^0}, \tag{E.2.27}$$

$$\boldsymbol{v}_{\mathfrak{h}}^{*} = \boldsymbol{v}_{\mathfrak{h}}^{0} - \frac{p^{*} - p^{0}}{m_{\mathfrak{h}}}, \quad \rho_{\mathfrak{h}}^{*} = \frac{m_{\mathfrak{h}}}{\boldsymbol{v}_{\mathfrak{h}}^{*} - \sigma}, \quad \rho_{\mathfrak{e}}^{*} = \rho_{\mathfrak{e}}^{0}\frac{\rho_{\mathfrak{h}}^{*}}{\rho_{\mathfrak{h}}^{0}}, \quad p_{\mathfrak{e}}^{*} = p_{\mathfrak{e}}^{0}\frac{\rho_{\mathfrak{h}}^{*}}{\rho_{\mathfrak{h}}^{0}}. \tag{E.2.28}$$

Finally, we have a jump relation for $p_{\mathfrak{e}}$ since the last equation of (M^{src}) is conservative.

In summary, the eigenvalues of the two systems are identical but the eigenvectors are modified. Therefore, the corresponding Riemann invariants are different. Additionally, concerning the jump conditions for the rarefaction waves, no differences have been observed for all the fields except the internal energy of electrons (only in the case where the adiabatic constant for heavy-particles and electrons are equal $\gamma = \gamma_{\mathfrak{e}} = \gamma_{\mathfrak{h}}$). Finally, concerning the shock waves, no jump conditions have been obtained for the internal energy of electron in the case of (M_S^{hyp}), since the equation is nonconservative. However, the jump conditions of the other variables are identical in both systems.

APPENDIX F

RÉSUMÉ DE LA THÈSE

F.1 Problématique et objectif

Les reconnexions magnétiques (RM) sont un problème fondamental de physique des plasmas et un défi scientifique majeur. Ce mécanisme très instationnaire, et qui peut faire intervenir des dynamiques rapides, permet de convertir l'énergie magnétique en énergie cinétique et thermique lors d'une réorganisation de la topologie des lignes de champ. Il concerne un large spectre d'applications allant de la physique solaire à la fusion nucléaire et intervient dans une très large variét é és de plasmas rencontrés en astrophysique. Il est en particulier à l'origine de phénomènes tels que les éruptions solaires ou les éjections de masses coronales (EMC).

Ces éruptions solaires sont à l'origine du vent solaire et de potentielles tempêtes magnétiques qui peuvent avoir un impact crucial sur la magnétosphère et la terre. L'étude de ces évènements solaire fait partie de la météorologie spatiale ou Space Weather. Il s'agit d'un domaine qui englobe l'activité de l'atmosphère solaire et son interaction avec l'environnement spatial terrestre qui peuvent influencer la performance, la fiabilité et le fonctionnement de technologies comme les satellites de télécommunications, et, dans des cas plus graves, impacter l'être humain. Notre société moderne basée sur les nouvelles technologies s'avère très vulnérable à la météorologie spatiale. Par conséquent, nous pouvons nous attendre à avoir de plus en plus de problèmes de sécurité liés à l'activité solaire qu'il s'agit de prévoir à travers une compréhension scientifique de processus physiques comme les reconnexions magnétiques.

Des travaux théoriques, et plus récemment numériques et expérimentaux, ont été menés par plusieurs groupes scientifiques; cependant, certains aspects fondamentaux des reconnexions magnétiques restent aujourd'hui mal compris et l'on observe des grandes différences entre modèles numériques et observations expérimentales. Par ailleurs, la simulation de ces modèles pose un certain nombre de difficultés lorsque l'on cherche à complexifier le modèle pour reproduire la physique. En particulier, certaines questions restent ouvertes : qu'est ce qui détermine le taux

de conversion de l'énergie magnétique vers l'énergie cinétique/thermique ? Quel phénomène physique initialise ces reconnexions ? Quelles sont les échelles spatiales et temporelles associées au processus de ces reconnexions dans l'atmosphère solaire ?

Actuellement, les modèles numériques utilisés pour représenter ces reconnexions sont focalisés essentiellement sur des modèles résistifs mono-fluide ou des modèles multi-fluides pour des plasmas partiellement ou totalement ionisés. Dans le premier cas, le plasma est considéré comme un fluide unique interagissant avec le champ électromagnétique. Ainsi le système d'équation associé est couplé aux équations de Maxwell. Dans le deuxième cas, le plasma est considéré comme un gaz multi-espèce où chaque particule (neutres, ions, électrons ou molécules) interagit avec d'autres particules en échangeant de l'énergie ou de la quantité de mouvement, par exemple. Cette dernière approche, bien que complexe, considère un large spectre d'échelles qui permet de représenter le processus des reconnexions magnétiques avec plus de précision que dans l'approche mono-fluide. Ces modèles fournissent des repreésentations correctes de plasmas dans un régime fortement collisionnel, comme dans la photosphère par exemple. Cependant très peu d'études ont été réalisées dans des conditions où le plasma est réactif et peut atteindre des régimes fortement ou faiblement collisionel comme c'est le cas dans la chromosphère solaire où les reconnexions magnétiques jouent un rôle important, notamment dans la météorologie spatiale. Au dessus de la chromosphère se trouve la zone de transition, une région où le plasma est peu dense et faiblement collisionnel. Par ailleurs, c'est une région critique où la température augmente de façon importante, de quelques dizaines de milliers de Kelvin à des millions de Kelvin. Cette observation reste aujourd'hui inexpliquée et hors de portée de nos modèles actuels. Cependant le processus des reconnexions magnétiques reste un des phénomènes fondamentaux qui permettrait d'expliquer cette augmentation de température.

La thèse propose donc de contribuer grâce à une approche transdisciplinaire à : 1- établir à partir de la théorie cinétique un modèle détaillé pour plasma multicomposant et partiellement ionisé réactif, cohérent et bien structuré mathématiquement, pour simuler les reconnexions magnétiques dans des conditions relatives à la chromosphère solaire sur la base des travaux de B. Graille, T. Magin et M. Massot. La formulation du modèle est générale, 2D et 3D, incluant l'effet de toutes les espèces (comme les ions, les neutres, les électrons ou molécules), des propriétés détaillées de transports et de résistivités afin de décrire les collisions entre les particules avec un haut niveau de précision; 2- proposer une stratégie numérique capable de résoudre le large spectre d'échelles spatiales et temporelles sur la base d'une approche volume finis couplé à une adaptation de maillage dynamique basé sur un code de calcul nommé CanoP basé sur la bibliothèque p4est développé en interaction avec la Maison de la Simulation, ainsi que dans un autre code nommé StellarBox de la NASA; 3- proposer une vérification de l'approche sur un ensemble de cas classiques dans le domaine en utilisant CanoP, puis une validation de la stratégie numérique proposée afin de réaliser une simulation numérique directe de reconnexion magnétique.

Ce projet permettra des avancées scientifiques de base, technologiques et socio-économiques :

- Dans les domaines des mathématiques, de la physique des plasmas, de la physique solaire et de la simulation numérique intensive aboutissant à une meilleure compréhension et une analyse détaillé de phénomènes physiques fondamentaux

- Par la réalisation d'outils numériques efficaces et précis ayant un impact bien au delà de la physique solaire, pour la fusion nucléaire (ITER) ou pour la propulsion électrique
- Par la contribution à une meilleure prédiction de la météorologie spatiale et à la réduction de l'impact sur les systèmes de communications

F.2 Modèles pour plasma partiellement ionisés magnétisés hors équilibre

La plupart des simulations de plasmas ionisés sont basés sur des modèles mono-fluide aussi bien idéaux que résistifs, dans un contexte non-, faiblement ou fortement collisionel. Dans ce cas, le plasma est supposé être constitué d'un seul fluide affecté par la présence d'un champ magnétique. Malheureusement, les modèles mono-fluide idéaux ne peuvent pas capturer les reconnexions magnétiques et les modèles mono-fluide résistif présentent des taux de reconnexions (ou des échelles temporelles) beaucoup plus bas que ceux observés expérimentalement. La description des phénomènes à l'échelle microscopique utilisant la théorie cinétique des gaz (ou modèle cinétique) est intéressante mais elle présente des coûts en calculs bien trop importants. Enfin, nous avons la catégorie des modèles multi-fluides. Ces modèles sont utilisés pour simuler les reconnexions magnétiques dans différents régimes collisionnels. Braginskii était le premier à formuler un modèle résistif « two-fluid » où les systèmes de transport dépendent de la direction du champ magnétique, mais les réactions chimiques ne sont pas considérées et il n'est adapté que pour des plasmas totalement ionisés à haute température. On notera également le modèle de Kolesnikov, avec des propriétés de transport qui dépendent du champ magnétique, mais sans réaction chimique et qui n'a jamais été dans le cadre de simulation numérique. Enfin nous avons les modèles « three-fluid », considérant séparément les ions, les électrons et les neutres, pour des plasmas partiellement ionisés. On notera le modèle Meier et Shumlak qui propose un modèle prenant en compte les réactions chimiques avec les mêmes propriétés de transport que Braginskii. Ce modèle n'a cependant pas été utilisé pour des simulations numériques. Le modèle « three-fluid » le plus utilisé reste cependant le modèle établit par Ofman qui s'était intéressé aux reconnexions dans la couronne solaire. Cependant, les calculs réalisés à partir de ce modèle n'ont été que partiellement validé par rapport aux observations expérimentales. Plus récemment, un nouveau modèle a été introduit par Khomenko. Ces multiples approches posent plusieurs problèmes, notamment au niveau de la raideur numérique, outre le fait qu'elles ne permettent pas de reproduire correctement le phénomène de RM dans sa généralité par manque de généralité du modèle. La structure mathématique de ces modèles, en particulier les modèles « multi-fluid » conduit à des incohérences mathématiques et physiques et le calcul des coefficients de transport est trop approximatif.

Dans cette thèse, nous développons un modèle basé sur la théorie cinétique des gaz dans la lignée de travaux de Magin, Massot et Graille, où les coefficients de transport sont développés à l'échelle microscopique et basés sur des données expérimentales en calculant des intégrales de collisions développées à l'aide de la méthode spectrale de Galerkin. C'est un nouveau modèle « single-fluid » pour plasma multicomposant, où les espèces diffusent dans un même référentiel

(celui des particules lourdes), développé sur une structure mathématique solide. C'est un modèle mathématique général adapté pour des plasmas totalement ou partiellement ionisés pour différentes gammes de champ magnétique (champ magnétique fort et faible) et différents régimes collisionnels. Mais ce modèle n'a été développé que pour un plasma non réactif pour des applications hypersoniques. Dans ce contexte, nous avons développé un modèle basé sur cette théorie pour caractériser un plasma réactif (partiellement et complètement ionisé) dans un contexte où on considère des reconnexions magnétiques dans la chromosphère solaire. Ce développement s'est réalisé en plusieurs étapes, en commençant par considérer un cas simple de plasma totalement ionisé constitué d'électrons et de H+, puis en généralisant dans le cas partiellement ionisé multicomposant à l'équilibre chimique et thermique, puis finalement en obtenant le modèle final hors équilibre thermique et chimique dans un context où les échelles caractéristiques sont plus grandes devant les échelles de l'ordre de la longueur de Debye. L'étape finale du développement a consisté à coupler avec les équations de Maxwell et à obtenir une loi d'Ohm généralisé ainsi qu'une nouvelle définition de la résistivité au sens des coefficients de transport pour des plasmas multicomposants. Plusieurs détails concernant le dévelopement du modèle sont donnés dans la section suivante. Par ailleurs, le département Aérospatial et Aéronautique de l'institut von Karman (VKI) a développé un outil numérique pour des plasmas réactifs à haute enthalpie hors équilibre dans des écoulements hypersoniques. Cet outil numérique est MUTATION++. Il est utilisé pour calculer les propriétés thermodynamiques et cinétiques d'un plasma quelconque, composé de plusieurs espèces. Les coefficients de transport qui ont permis la fermeture de nos équations ont été calculés via cette librairie. Les propriétés anisotropiques des systèmes de transport ont été implémentées et comparées avec la littérature, notamment avec le modèle de Braginskii pour toutes les étapes du développement.

La structure mathématique complète du modèle a été étudiée. Nous avons étudié l'hyperbolicité de la partie convective, la cohérence thermodynamique au sens d'une production d'entropie signée et un ensemble de relations de réciprocité de Onsager de la partie transport issue d'un scaling mixte hyperbolique (espèces lourdes) – parabolique (électrons) permettant la symétrisation entropique complète ou partielle de l'ensemble du système d'EDP couplé au système de Maxwell, en particulier dans le contexte de la nouvelle loi d'Ohm généralisée dans le cadre fortement magnétisé. Le fait d'aboutir à un modèle possédant à la fois une complexité et une validité permettant d'embrasser les problématiques physiques posées par la reconnexion magnétique dans l'atmosphère solaire et ayant une bonne structure mathématique permet finalement de développer une stratégie numérique de premier plan. L'ensemble de cette stratégie a reposé sur une approche transdisciplinaire déjà éprouvée entre les partenaires du projet de thèse.

F.3 Étape de développement du modèle

Nous détaillons ici les étapes de développement du modèle complet.

Dans un premier temps, nous avons développé entièrement le modèle dans un cas de plasma totalement ionisé constitué d'électrons et de H+. Nous avons étudié les propriétés de transport et inclus dans la librairie les propriétés anisotropiques des systèmes de transport. L'anisotropie des

propriétés de transport est primordiale car il a été prouvé que cela avait un impact important sur la précision du taux de reconnexion magnétiques. Nous avons comparé ce modèle avec le modèle « multi-fluid » de Braginskii/Woods, pour un cas de plasma totalement ionisé dans des conditions relatives à l'atmosphère solaire.

Le modèle précédent a été généralisé, en développant ce dernier dans un cas de plasma partiellement ionisé en considérant plusieurs espèces. Le modèle a ensuite été généralisé pour des plasmas hors équilibre thermique et chimique pour des échelles considéré plus grandes que les échelles associés à la longueur de Debye. Dans cette nouvelle approche, la cinétique chimique peut être considéré, cela n'impacte pas la validité du modèle. Cette extension du modèle est importante car les plasmas dans la photosphère et la basse chromosphère du soleil sont partiellement ionisés et réactifs. En effet, dans cette partie du soleil, on peut observer des réactions comme ionisation, recombinaison des espèces et échange de charge. Enfin, étant donné la nouveauté du modèle, de nouveaux effets microscopiques comme l'effet Kolesnikov ont été étudiés.

Enfin, l'étape finale du développement a été l'obtention de la fermeture des équations pour le champ magnétique. Notre nouveau système d'équation de Navier Stokes est naturellement couplé avec les équations de Maxwell. Par conséquent, nous avons pu développer une nouvelle loi d'Ohm basé sur ces propriétés de transport, et avons défini une nouvelle résistivité. Cette loi d'Ohm a ensuite comparée avec la littérature, notamment avec celle de Braginskii, dans le contexte d'un plasma totalement ionisé. Ce résultat important a permis notamment de caractériser tous les phénomènes dissipatifs qui peuvent engendrer une reconnexion magnétique dans le cadre du modèle que nous avons proposé.

F.4 Nouvelle stratégie numérique

Sur la base d'un modèle physiquement pertinent et mathématiquement rigoureux, l'objectif de la thèse a été d'établir un outil numérique qui va permettre de réaliser des simulations 2D/3D de reconnexions magnétiques. Cette stratégie numérique a reposé sur une étape importante: étudier la résolution du problème de Riemann et développer un solveur de Riemann pour la partie convective du système d'équations décrivant le plasma hors équilibre thermique qui contient des termes non-conservatifs issus naturellement de la modélisation pour les variables électroniques. Il s'agit d'une étude d'analyse numérique fine en collaboration avec Benjamin Graille et Sylvain Faure du LMO. Notons que cette étude a constituée une avancée importante dans le domaine des mathématiques appliquées.

Cette base a permis ensuite de développer un solveur volumes finis avec adaptation de maillage avec une approche de type reconstruction d'ordre deux standard sur la base du code CanoP développé en collaboration avec la Maison de la Simulation utilisant la bibliothèque de programme p4est. Cette approche permet de faire de l'AMR tout en garantissant un équilibrage de charge d'excellente qualité jusqu'à plusieurs dizaines de milliers de cœurs. La stratégie numérique proposée a été couplée à la librairie MUTATION++ afin de réaliser des simulations numériques tout en garantissant que les propriétés de transport sont calculés avec un haut niveau de précision. L'adaptation de maillage dans ce cadre très multi-échelle où la dynamique de la reconnexion mag-

nétique dépend dans certaines études du niveau de résolution que l'on utilise et le lien avec un modèle multi-échelle rigoureux, a permis une avancée marquante dans le domaine. Cette stratégie nous dispose d'un outil de calcul permettant d'effectuer des vérifications, de comparer des modèles ou de réaliser des simulations numériques de plasmas multicomposants.

F.5 Vérification, validation et simulation de reconnexion magnétique

Cette partie repose sur les outils de parties précédentes et se décompose en plusieurs étapes. La première partie de vérification concerne la simulation d'un ensemble de configuration tests comme Orzag-Tang ou Brio-Wu, communs dans le domaine pour la vérification des codes et une comparaison détaillée des divers niveaux de modèle développés en lien avec les modèle classique du domaine. Par ailleurs, la capabilité de p4est à réaliser de l'adaptation de maillage a été testé. L'ordre du schéma proposé, la capacité du schéma numérique à maintenir la contrainte d'incrompressibilité du champ magnétique a été testé.

Ensuite, nous avons détaillé l'impact de la modélisation single-fluid/multicomposant dans un contexte de reconnexion magnétique. Ce type de comparaison est très utile à la communauté et a permis une avancée importante dans la compréhension de l'impact de la modélisation sur le phénomène de reconnexion. Là encore, ce type d'avancée a reposé sur un ensemble d'outils existants et sur une interaction transdisciplinaire déjà éprouvée et sur laquelle la thèse s'est appuyé. Enfin, similairement aux publications de Leake et de Alvarez-Laguna, une simulation de reconnexion magnétique pour plasma partiellement ionisé avec le nouveau modèle a été proposé.

F.6 Moyen du projet et structure de collaboration transdisciplinaire

Les problèmes astrophysiques 3D comme celui que nous avons étudié dans le cadre de notre projet représentent un vrai challenge pour le calcul haute performance. C'est la raison pour laquelle nous avons eu accès au superordinateur Pléiades de la Supercomputing Division - classé dans le top500 des calculateurs les plus puissants au monde – afin de réaliser des simulations 3D. L'accès au mésocentre de calcul de CentraleSupélec ainsi qu'un lien effectif avec la Maison de la Simulation à Saclay dans le cadre du code CanoP, a permis d'avoir les meilleurs outils pour mener à bien les simulations.

Le sujet de thèse a représente un défi important et a proposé une véritable percée dans le domaine en associant des institutions partenaires couvrant l'ensemble des disciplines impliquées pour lever les verrous dans le domaine (mathématiques, physique des plasmas, physique solaire, ingénierie, HPC) et ayant l'expérience de projet à l'interface des disciplines.

REFERENCES

Abdulle, A. (2001, June). Fourth order chebyshev methods with recurrence relation. *SIAM J. Sci. Comput.*, *23*(6), 2041–2054. Retrieved from https://doi.org/10.1137/S1064827500379549 doi: 10.1137/S1064827500379549

Abeele, D. V. (2000). *An efficient computational model for inductively coupled air plasma flows under thermal and chemical non-equilibrium* (Unpublished doctoral dissertation). von Karman Institute for Fluid dynamics, Rhode-Saint-Genese, Belgium.

Abgrall, R., & Karni, S. (2010). A comment on the computation of non-conservative products. *Journal of Computational Physics*, *229*, 2759–2763.

Adams, N., & Shariff, K. (1996). A high-resolution hybrid compact-eno scheme for shock-turbulence interaction problems. *Journal of Computational Physics*, *127*(1), 27 - 51. Retrieved from http://www.sciencedirect.com/science/article/pii/S0021999196901564 doi: https://doi.org/10.1006/jcph.1996.0156

Almgren, A. S., Beckner, V. E., Bell, J. B., Day, M. S., Howell, L. H., Joggerst, C. C., ... Zingale, M. (2010, Jun). CASTRO: A New Compressible Astrophysical Solver. I. Hydrodynamics and Self-gravity. *The Astrophysical Journal*, *715*(2), 1221-1238. doi: 10.1088/0004-637X/715/2/1221

Almgren, A. S., Bell, J. B., Lijewski, M. J., Lukić, Z., & Van Andel, E. (2013, Mar). Nyx: A Massively Parallel AMR Code for Computational Cosmology. *The Astrophysical Journal*, *765*(1), 39. doi: 10.1088/0004-637X/765/1/39

Alonso Asensio, I., Alvarez Laguna, A., Aissa, M. H., Poedts, S., Ozak, N., & Lani, A. (2019, Jun). A GPU-enabled implicit Finite Volume solver for the ideal two-fluid plasma model on unstructured grids. *Computer Physics Communications*, *239*, 16-32. doi: 10.1016/j.cpc.2019.01.019

Alvarez Laguna, A., Pichard, T., Magin, T., Chabert, P., Bourdon, A., & Massot, M. (2019, Apr). An asymptotic preserving well-balanced scheme for the isothermal fluid equations in low-temperature plasma applications. *arXiv e-prints*, arXiv:1904.13092.

Alvarez Laguna, A., Lani, A., Deconinck, H., Mansour, N. N., & Poedts, S. (2016, August). A fully-implicit finite-volume method for multi-fluid reactive and collisional magnetized plasmas on unstructured meshes. *Journal of Computational Physics*, *318*, 252-276. doi: 10.1016/j.jcp .2016.04.058

Alvarez Laguna, A., Ozak, N., Lani, A., Mansour, N., Deconinck, H., & Poedts, S. (2018, 05). A versatile numerical method for the multi-fluid plasma model in partially- and fully-ionized plasmas. *Journal of Physics: Conference Series*, *1031*, 012015.

Alvarez-Laguna, A., Ozak, N., Lani, A., Mansour, N. N., Deconinck, H., & Poedts, S. (2018, may). A versatile numerical method for the multi-fluid plasma model in partially- and fully-ionized plasmas. *Journal of Physics: Conference Series*, *1031*, 012015. Retrieved from https://doi.org/10.1088%2F1742-6596%2F1031%2F1%2F012015 doi: 10.1088/1742-6596/1031/1/012015

Amano, T. (2015). Divergence-free approximate riemann solver for the quasi-neutral two-fluid plasma model. *Journal of Computational Physics*, *299*, 863 - 886. Retrieved from http://www.sciencedirect.com/science/article/pii/S0021999115004805 doi: https://doi.org/10.1016/j.jcp.2015.07.035

Amari, T., Canou, A., & Aly, J.-J. (2014, October). Characterizing and predicting the magnetic environment leading to solar eruptions. *Nature*, *514*, 465-469. doi: 10.1038/nature13815

Amari, T., Canou, A., Aly, j.-j., Delyon, F., & Alauzet, F. (2018, 02). Magnetic cage and rope as the key for solar eruptions. *Nature*, *554*, 211-215. doi: 10.1038/nature24671

Andre, P., Bussiere, W., & Rochette, D. (2007). Transport coefficients of ag–sio2 plasmas. *Plasma Chem Plasma Process*, *27*, 381-403. doi: 10.1007/s11090-007-9086-y

Aregba-Driollet, D., & Breil, J. (2017). Modelling and numerical approximation for the nonconservative bitemperature euler model. *Mathematical modelling and numerical analysis*.

Arminjon, P., & Touma, R. (2008). Finite volume central schemes for three-dimensional ideal mhd. In S. Benzoni-Gavage & D. Serre (Eds.), *Hyperbolic problems: Theory, numerics, applications* (pp. 323–330). Berlin, Heidelberg: Springer Berlin Heidelberg.

Artebrant, R., & Torrilhon, M. (2008, 03). Increasing the accuracy in locally divergence-preserving finite volume schemes for mhd. *Journal of Computational Physics*, *227*, 3405-3427. doi: 10 .1016/j.jcp.2007.12.003

Asplund, M., Grevesse, N., Sauval, A. J., & Scott, P. (2009, September). The Chemical Composition of the Sun. *Annual Review of Astronomy and Astrophysics*, *47*, 481-522. doi: 10.1146/annurev.astro.46.060407.145222

Aubreton, J., Elchinger, M. E., Rat, V., & Fauchais, P. (2003, 01). Two-temperature transport coefficients in argon–helium thermal plasmas. *Journal of Physics D Applied Physics*, *37*, 34-41. doi: 10.1088/0022-3727/37/1/007

Aubreton, J., Elchinger, M. F., Fauchais, P., Rat, V., & André, P. (2004, jul). Thermodynamic and transport properties of a ternary ar–h2–he mixture out of equilibrium up to 30 000 k at atmospheric pressure. *Journal of Physics D: Applied Physics*, *37*(16), 2232–2246. Retrieved from https://doi.org/10.1088%2F0022-3727%2F37%2F16%2F004 doi: 10.1088/0022-3727/37/16/004

Aunai, N., Hesse, M., Zenitani, S., Kuznetsova, M., Black, C., Evans, R., & Smets, R. (2013). Comparison between hybrid and fully kinetic models of asymmetric magnetic reconnection: Coplanar and guide field configurations. *Physics of Plasmas*, *20*(2), 022902. Retrieved from https://doi.org/10.1063/1.4792250 doi: 10.1063/1.4792250

Baboolal, S. (2001, 03). Finite-difference modeling of solitons induced by a density hump in a plasma multi-fluid. *Mathematics and Computers in Simulation*, *55*, 309–316. doi: 10.1016/S0378-4754(00)00310-4

Balbás, J., & Tadmor, E. (2006, 01). Nonoscillatory central schemes for one- and two-dimensional magnetohydrodynamics equations. ii: High-order semidiscrete schemes. *SIAM J. Scientific Computing*, *28*, 533-560. doi: 10.1137/040610246

Balsara, D. S. (1998a, may). Linearized formulation of the riemann problem for adiabatic and isothermal magnetohydrodynamics. *The Astrophysical Journal Supplement Series*, *116*(1), 119–131. Retrieved from https://doi.org/10.1086%2F313092 doi: 10.1086/313092

Balsara, D. S. (1998b, may). Total variation diminishing scheme for adiabatic and isothermal magnetohydrodynamics. *The Astrophysical Journal Supplement Series*, *116*(1), 133–153. Retrieved from https://doi.org/10.1086%2F313093 doi: 10.1086/313093

Balsara, D. S. (2004, mar). Second-order–accurate schemes for magnetohydrodynamics with divergence-free reconstruction. *The Astrophysical Journal Supplement Series*, *151*(1), 149–184. Retrieved from https://doi.org/10.1086%2F381377 doi: 10.1086/381377

Balsara, D. S., Amano, T., Garain, S., & Kim, J. (2016). A high-order relativistic two-fluid electrodynamic scheme with consistent reconstruction of electromagnetic fields and a multi-dimensional riemann solver for electromagnetism. *Journal of Computational Physics*, *318*, 169 - 200. Retrieved from http://www.sciencedirect.com/science/article/pii/S0021999116301334 doi: https://doi.org/10.1016/j.jcp.2016.05.006

Balsara, D. S., & Käppeli, R. (2017). Von neumann stability analysis of globally divergence-free rkdg schemes for the induction equation using multidimensional riemann solvers. *Journal of Computational Physics*, *336*, 104 - 127. Retrieved from http://www.sciencedirect.com/science/article/pii/S0021999117300724 doi: https://doi.org/10.1016/j.jcp.2017.01.056

Balsara, D. S., & Shu, C.-W. (2000). Monotonicity preserving weighted essentially non-oscillatory schemes with increasingly high order of accuracy. *Journal of Computational Physics*, *160*(2), 405 - 452. Retrieved from http://www.sciencedirect.com/science/article/pii/S002199910096443X doi: https://doi.org/10.1006/jcph.2000.6443

Balsara, D. S., & Spicer, D. S. (1999). A staggered mesh algorithm using high order godunov fluxes to ensure solenoidal magnetic fields in magnetohydrodynamic simulations. *Journal of Computational Physics*, *149*(2), 270 - 292. Retrieved from http://www.sciencedirect.com/science/article/pii/S0021999198961538 doi: https://doi.org/10.1006/jcph.1998.6153

Bardos, C., Golse, F., & Levermore, D. (1991, 04). Fluid dynamic limits of kinetic equations. i. formal derivations. *Journal of Statistical Physics*, *63*, 323-344.

Baty, H. (2019, Apr). FINMHD: an adaptive finite element code for magnetic reconnection and plasmoid chains formation in Magnetohydrodynamics. *arXiv e-prints*, arXiv:1904.11173.

Baty, H., Forbes, T. G., & Priest, E. R. (2014). The formation and stability of petschek reconnection. *Physics of Plasmas*, *21*(11), 112111. Retrieved from https://doi.org/10.1063/1.4901918 doi: 10.1063/1.4901918

Bauer, A., Pakmor, R., Springel, V., Schaal, K., Chandrashekar, P., & Klingenberg, C. (2015, 09). Astrophysical hydrodynamics with a high-order discontinuous Galerkin scheme and adaptive mesh refinement. *Monthly Notices of the Royal Astronomical Society*, *453*(4), 4278-4300. Retrieved from https://doi.org/10.1093/mnras/stv1859 doi: 10.1093/mnras/stv1859

Bauer, A., & Springel, V. (2012, 06). Subsonic turbulence in smoothed particle hydrodynamics and moving-mesh simulations. *Monthly Notices of the Royal Astronomical Society*, *423*(3), 2558-2578. Retrieved from https://doi.org/10.1111/j.1365-2966.2012.21058.x doi: 10.1111/j.1365-2966.2012.21058.x

Bellot Rubio, L., & Orozco Suárez, D. (2019, Feb 18). Quiet sun magnetic fields: an observational view. *Living Reviews in Solar Physics*, *16*(1), 1. Retrieved from https://doi.org/10.1007/s41116-018-0017-1 doi: 10.1007/s41116-018-0017-1

Berger, M., & Colella, P. (1989). Local adaptive mesh refinement for shock hydrodynamics. *Journal of Computational Physics*, *82*(1), 64 - 84. Retrieved from http://www.sciencedirect.com/science/article/pii/0021999189900351 doi: https://doi.org/10.1016/0021-9991(89)90035-1

Berger, M., & J. Leveque, A. (1997, 12). Adaptive mesh refinement using wave-propagation algorithms for hyperbolic systems. *SIAM Journal on Numerical Analysis*, *35*. doi: 10.1137/S0036142997315974

Berger, M., & Oliger, J. (1984). Adaptive mesh refinement for hyperbolic partial differential equations. *Journal of Computational Physics*, *53*(3), 484–512. doi: 10.1016/0021-9991(84)90073-1

Berger, M., & Rigoutsos, I. (1991, 9). An algorithm for point clustering and grid generation. *IEEE Transactions on Systems, Man and Cybernetics*, *21*(5), 1278–1286. doi: 10.1109/21.120081

Bharti, L., Hirzberger, J., & Solanki, S. K. (2013, Apr). Fine structures in the atmosphere above a sunspot umbra. *Astronomy and Astrophysics*, *552*, L1. doi: 10.1051/0004-6361/201220777

Bhowmik, P., & Nandy, D. (2018, 12). Prediction of the strength and timing of sunspot cycle 25 reveal decadal-scale space environmental conditions. *Nature Communications*, *9*. doi: 10.1038/s41467-018-07690-0

Biagi, S. (2012). *Transport of electrons in gas mixtures.* http://rjd.web.cern.ch/rjd/cgi-bin/cross?update. ([Online])

Biskamp, D. (2000). *Magnetic Reconnection in Plasmas*.

Boris, J. P., & Book, D. L. (1973). Flux-corrected transport. i. shasta, a fluid transport algorithm that works. *Journal of Computational Physics*, *11*(1), 38 - 69. Retrieved from http://www.sciencedirect.com/science/article/pii/0021999173901472 doi: https://doi.org/10.1016/0021-9991(73)90147-2

Bourdon, A., Darny, T., Pechereau, F., Pouvesle, J.-M., Viegas, P., Iséni, S., & Robert, E. (2016, mar). Numerical and experimental study of the dynamics of a mus helium plasma gun discharge with various amounts of n2 admixture. *Plasma Sources Science and Technology*, *25*(3), 035002. Retrieved from https://doi.org/10.1088%2F0963-0252%2F25%2F3%2F035002 doi: 10.1088/0963-0252/25/3/035002

Brackbill, J. (1985). Fluid modeling of magnetized plasmas. *Space Sci. Rev.*, *42*, 153. doi: https://doi.org/10.1007/BF00218230

Brackbill, J., & Barnes, D. (1980). The effect of nonzero div(b) on the numerical solution of the magnetohydrodynamic equations. *Journal of Computational Physics*, *35*(3), 426 - 430. Retrieved from http://www.sciencedirect.com/science/article/pii/0021999180900790 doi: https://doi.org/10.1016/0021-9991(80)90079-0

Braginskii, S. I. (1965). Transport Processes in a Plasma. *Reviews of Plasma Physics*, *1*, 205.

Brandenburg, A., & Zweibel, E. G. (1994, June). The formation of sharp structures by ambipolar diffusion. *The astrophysical journal*, *427*, L91-L94. doi: 10.1086/187372

Bray, I., Konovalov, D., & McCarthy, I. (1991, 07). Coupled-channel optical calculation of electron-hydrogen scattering: Elastic scattering from 0.5 to 30 ev. *Physical review. A*, *43*, 5878-5885. doi: 10.1103/PhysRevA.43.5878

Brecht, S. H., Lyon, J., Fedder, J. A., & Hain, K. (1981). A simulation study of east-west imf effects on the magnetosphere. *Geophysical Research Letters*, *8*(4), 397-400. Retrieved from https://agupubs.onlinelibrary.wiley.com/doi/abs/10.1029/GL008i004p00397 doi: 10.1029/GL008i004p00397

Brio, M., & Wu, C. (1988). An upwind differencing scheme for the equations of ideal magnetohydrodynamics. *Journal of Computational Physics*, *75*(2), 400 - 422. Retrieved from http://www.sciencedirect.com/science/article/pii/0021999188901209 doi: https://doi.org/10.1016/0021-9991(88)90120-9

Brull, S., Breil, J., Aregba-Driollet, D., Dubroca, B., & Estibals, E. (2018). Modelling and numerical approximation for the nonconservative bitemperature euler model. *ESAIM: Math. Model. Numer. Anal.*. (Forthcoming article)

Brunger, M. J., & Buckman, S. J. (2002). Electron–molecule scattering cross-sections. i. experimental techniques and data for diatomic molecules. *Physics Reports*, *357*(3), 215 - 458. Retrieved from http://www.sciencedirect.com/science/article/pii/S0370157301000321 doi: https://doi.org/10.1016/S0370-1573(01)00032-1

Bruno, D., Capitelli, M., Catalfamo, C., & Giordano, D. (2011). Transport properties of high-temperature air in a magnetic field. *Physics of Plasmas*, *18*(1), 012308. Retrieved from https://doi.org/10.1063/1.3533430 doi: 10.1063/1.3533430

Burnett, D. (1935). The distribution of velocities in a slightly non-uniform gas. *Proceedings of the London Mathematical Society*, *s2-39*(1), 385-430. doi: 10.1112/plms/s2-39.1.385

Burstedde, C., Wilcox, L., & Ghattas, O. (2011). p4est: Scalable algorithms for parallel adaptive mesh refinement on forests of octrees. *SIAM Journal on Scientific Computing*, *33*(3), 1103-1133. Retrieved from https://doi.org/10.1137/100791634 doi: 10.1137/100791634

Calhoun, D. (2014). Adaptive mesh refinement resources.. Retrieved from https://math.boisestate.edu/~calhoun/www_personal/research/amr_software/

Calhoun, D. A., & Burstedde, C. (2017). Forestclaw: A parallel algorithm for patch-based adaptive mesh refinement on a forest of quadtrees. *CoRR*, *abs/1703.03116*. Retrieved from http://arxiv.org/abs/1703.03116

Candler, G. V., & Maccormack, R. W. (1991). Computation of weakly ionized hypersonic flows in thermochemical nonequilibrium. *Journal of Thermophysics and Heat Transfer*, 266–273.

Capitelli, M., Bruno, D., & Laricchiuta, A. (2013). *In fundamental aspects of plasma chemical physics i*. Springer.

Capitelli, M., Gorse, C., Longo, S., & Giordano, D. (2000). Collision integrals of high-temperature air species. *Journal of Thermophysics and Heat Transfer*, *14*(2), 259-268. Retrieved from https://doi.org/10.2514/2.6517 doi: 10.2514/2.6517

Cargill, P. (2013, 06). From flares to nanoflares: magnetic reconnection on the SunJames Dungey Lecture. *Astronomy and Geophysics*, *54*(3), 3.16-3.20. Retrieved from https://doi.org/10.1093/astrogeo/att078 doi: 10.1093/astrogeo/att078

Cargill, P. J., De Moortel, I., & Kiddie, G. (2016, May). Coronal Density Structure and its Role in Wave Damping in Loops. *The astrophysical journal*, *823*, 31. doi: 10.3847/0004-637X/823/1/31

Carlsson, M., Hansteen, V. H., Gudiksen, B. V., Leenaarts, J., & De Pontieu, B. (2016, January). A publicly available simulation of an enhanced network region of the Sun. *Astronomy and astrophysics*, *585*.

Carlsson, M., & Stein, R. F. (1995, February). Does a nonmagnetic solar chromosphere exist? *The Astrophysical Journal*, *440*, L29-L32. doi: 10.1086/187753

Cercignani, C. (1987). *The boltzmann equation and its applications*. Springer-Verlag, New York.

Chakravarthy, S. R., & Osher, S. (1983). Numerical experiments with the osher upwind scheme for the euler equations. *AIAA Journal*, *21*(9), 1241-1248. Retrieved from https://doi.org/10.2514/3.60143 doi: 10.2514/3.60143

Chalons, C., & Coquel, F. (2007). Numerical capture of shock solutions of nonconservative hyperbolic systems via kinetic functions. In C. Calgaro, J.-F. Coulombel, & T. Goudon (Eds.), *Analysis and simulation of fluid dynamics* (pp. 45–68). Basel: Birkhäuser Basel.

Chalons, C., & Coquel, F. (2017). A new comment on the computation of non-conservative products using roe-type path conservative schemes. *Journal of Computational Physics*, *335*, 592–604.

Chapman, S., & T.G., C. (1939, second edition, 1960). *The mathematical theory of non-uniform gases*. University Press, Cambridge.

Chhabra, R., Uhlherr, P., Richardson, J., R. Stallcop, J., Partridge, H., & Levin, E. (1996, 05). H-h2 collision integrals and transport coefficients. *Chemical Physics Letters*, *254*. doi: 10.1016/0009-2614(96)00285-0

Chmieleski, R. M., & Ferziger, J. H. (1967). Transport properties of a nonequilibrium partially ionized gas in a magnetic field. *The Physics of Fluids*, *10*(12), 2520-2530. Retrieved from https://aip.scitation.org/doi/abs/10.1063/1.1762071 doi: 10.1063/1.1762071

Christlieb, A. J., Rossmanith, J. A., & Tang, Q. (2014). Finite difference weighted essentially non-oscillatory schemes with constrained transport for ideal magnetohydrodynamics. *J. Comput. Phys.*, *268*, 302 - 325.

Cockburn, B., Karniadakis, G., & Shu, C.-W. (2000). *Discontinuous galerkin methods: Theory, computation and applications* (1st ed.). Springer-Verlag Berlin Heidelberg. doi: 10.1007/978-3-642-59721-3

Colella, P. (1985). A direct eulerian muscl scheme for gas dynamics. *SIAM Journal on Scientific and Statistical Computing*, *6*(1), 104-117. Retrieved from https://doi.org/10.1137/0906009 doi: 10.1137/0906009

Coquel, F., & Marmignon, C. (1995). A roe-type linearization for the euler equations for weakly ionized multi-component and multi-temperature gas. *12th Computational Fluid Dynamics Conference, Fluid Dynamics and Co-located Conferences*.

Crockett, R. K., Colella, P., Fisher, R. T., Klein, R. I., & McKee, C. F. (2005, Mar). An unsplit, cell-centered Godunov method for ideal MHD. *Journal of Computational Physics*, *203*(2), 422-448. doi: 10.1016/j.jcp.2004.08.021

Croes, V., Tavant, A., Lucken, R., Martorelli, R., Lafleur, T., Bourdon, A., & Chabert, P. (2018). The effect of alternative propellants on the electron drift instability in hall-effect thrusters: Insight from 2d particle-in-cell simulations. *Physics of Plasmas*, *25*(6), 063522. Retrieved from https://doi.org/10.1063/1.5033492 doi: 10.1063/1.5033492

Dai, W., & Woodward, P. (1994). Extension of the piecewise parabolic method to multidimensional ideal magnetohydrodynamics. *Journal of Computational Physics*, *115*(2), 485 - 514. Retrieved from http://www.sciencedirect.com/science/article/pii/S0021999184712125 doi: https://doi.org/10.1006/jcph.1994.1212

Dai, W., & Woodward, P. (1997, 07). A high-order godunov-type scheme for shock interactions in ideal magnetohydrodynamics. *SIAM Journal on Scientific Computing*, *18*, 957-981. doi: 10.1137/S1064827593257729

Dal Maso, G., Le Floch, P., & Murat, F. (1995). Definition and weak stability of nonconservative products. *J. Math. Pures et Appl*, *74*, 483–548.

Daru, V., & Tenaud, C. (2000). Evaluation of tvd high resolution schemes for unsteady viscous shocked flows. *Computers and Fluids*, *30*(1), 89 - 113. Retrieved from http://www.sciencedirect.com/science/article/pii/S0045793000000062 doi: https://doi.org/10.1016/S0045-7930(00)00006-2

Daru, V., & Tenaud, C. (2004). High order one-step monotonicity-preserving schemes for unsteady compressible flow calculations. *Journal of Computational Physics*, *193*(2), 563 - 594. Retrieved from http://www.sciencedirect.com/science/article/pii/S0021999103004327 doi: https://doi.org/10.1016/j.jcp.2003.08.023

Davis, S. F. (1988, May). Simplified second-order godunov-type methods. *SIAM J. Sci. Stat. Comput.*, *9*(3), 445–473. Retrieved from https://doi.org/10.1137/0909030 doi: 10.1137/0909030

Dawson, J. M. (1983, Apr). Particle simulation of plasmas. *Rev. Mod. Phys.*, *55*, 403–447. Retrieved from https://link.aps.org/doi/10.1103/RevModPhys.55.403 doi: 10.1103/RevModPhys.55.403

Daybelge, U. (1970). Unified transport theory of partially ionized nonisothermal plasmas. *Journal of Applied Physics*, *41*(5), 2130-2139. Retrieved from https://doi.org/10.1063/1.1659178 doi: 10.1063/1.1659178

De Pontieu, B., McIntosh, S. W., Carlsson, M., Hansteen, V. H., Tarbell, T. D., Boerner, P., ... Title, A. M. (2011, January). The Origins of Hot Plasma in the Solar Corona. *Science*, *331*, 55. doi: 10.1126/science.1197738

De Pontieu, B., McIntosh, S. W., Hansteen, V. H., & Schrijver, C. J. (2009, Aug). Observing the Roots of Solar Coronal Heating—in the Chromosphere. *The astrophysical journal*, *701*(1), L1-L6. doi: 10.1088/0004-637X/701/1/L1

De Pontieu, B., Rouppe van der Voort, L., McIntosh, S. W., Pereira, T. M. D., Carlsson, M., Hansteen, V., ... Boerner, P. (2014, Oct). On the prevalence of small-scale twist in the solar chromosphere and transition region. *Science*, *346*(6207), 1255732. doi: 10.1126/science.1255732

Dedner, A., Kemm, F., Kröner, D., Munz, C.-D., Schnitzer, T., & Wesenberg, M. (2002, January). Hyperbolic Divergence Cleaning for the MHD Equations. *Journal of Computational Physics*, *175*, 645-673. doi: 10.1006/jcph.2001.6961

Dedner, A., Rohde, C., & Wesenberg, M. (2003, 01). A new approach to divergence cleaning in magnetohydrodynamic simulations. *Hyperbolic Problems: Theory, Numerics, Applications*. doi: 10.1007/978-3-642-55711-8_47

Degond, P., & B., L. (1996). Transport coefficients of plasmas and disparate mass binary gases. *Transport Theory and Statistical Physics*, *25*(6), 595-633. Retrieved from https://doi.org/10.1080/00411459608222915 doi: 10.1080/00411459608222915

Degond, P., & Lucquin-Desreux, B. (1996a). The asymptotics of collision operators for two species of particles of disparate masses. *Mathematical Models and Methods in Applied Sciences*, *06*(03), 405-436.

Degond, P., & Lucquin-Desreux, B. (1996b). Transport coefficients of plasmas and disparate mass binary gases. *Transport Theory and Statistical Physics*, *25*(6), 595-633.

Degond, P., & Lucquin-Desreux, B. (1996c, 10). Transport coefficients of plasmas and disparate mass binary gases. *Transport Theory and Statistical Physics*, *25*, 595-633. doi: 10.1080/00411459608222915

Deiterding, R. (2005). Detonation structure simulation with amroc. In L. T. Yang, O. F. Rana, B. Di Martino, & J. Dongarra (Eds.), *High performance computing and communications* (pp. 916–927). Berlin, Heidelberg: Springer Berlin Heidelberg.

Deiterding, Ralf. (2011). Block-structured adaptive mesh refinement - theory, implementation and application. *ESAIM: Proc.*, *34*, 97-150. Retrieved from https://doi.org/10.1051/proc/201134002 doi: 10.1051/proc/201134002

Descombes, S., Duarte, M., Dumont, T., Laurent, F., Louvet, V., & Massot, M. (2014a). Analysis of operator splitting in the nonasymptotic regime for nonlinear reaction-diffusion equations.

Application to the dynamics of premixed flames. *SIAM Journal on Numerical Analysis*, *52*(3), 1311–1334.

Descombes, S., Duarte, M., Dumont, T., Laurent, F., Louvet, V., & Massot, M. (2014b). Analysis of operator splitting in the nonasymptotic regime for nonlinear reaction-diffusion equations. application to the dynamics of premixed flames. *SIAM Journal on Numerical Analysis*, *52*(3), 1311-1334. Retrieved from https://doi.org/10.1137/130926006 doi: 10.1137/130926006

DeVore, C. (1991). Flux-corrected transport techniques for multidimensional compressible magnetohydrodynamics. *Journal of Computational Physics*, *92*(1), 142 - 160. Retrieved from http://www.sciencedirect.com/science/article/pii/002199919190295V doi: https://doi.org/10.1016/0021-9991(91)90295-V

Devoto, R. S. (1966, June). Transport Properties of Ionized Monatomic Gases. *Physics of Fluids*, *9*, 1230-1240. doi: 10.1063/1.1761825

Devoto, R. S. (1967). Transport coefficients of partially ionized argon. *The Physics of Fluids*, *10*(2), 354-364. doi: 10.1063/1.1762115

Devoto, R. S. (1973). Transport coefficients of ionized argon. *The Physics of Fluids*, *16*(5), 616-623. doi: 10.1063/1.1694396

Devoto, S. R. (1969, 01). Transport coefficients of partially ionized hydrogen. *Journal of Plasma Physics*, *2(4)*.

De Pontieu, B., Title, A. M., Lemen, J. R., Kushner, G. D., Akin, D. J., Allard, B., ... Waltham, N. (2014, Jul 01). The interface region imaging spectrograph (iris). *Solar Physics*, *289*(7), 2733–2779. Retrieved from https://doi.org/10.1007/s11207-014-0485-y doi: 10.1007/s11207-014-0485-y

Dormand, J., & Prince, P. (1980). A family of embedded runge-kutta formulae. *Journal of Computational and Applied Mathematics*, *6*(1), 19–26.

Drui, F. (2017). *Eulerian modeling and simulations of separated and disperse two-phase flows : development of a unified modeling approach and associated numerical methods for highly parallel computations* (Theses, Université Paris-Saclay). Retrieved from https://tel.archives-ouvertes.fr/tel-01618320

Drui, F., Fikl, A., Kestener, P., Kokh, S., Larat, A., Le Chenadec, V., & Massot, M. (2016). Experimenting with the p4est library for amr simulations of two-phase flows. *ESAIM: Proc.*, *53*, 232-247. Retrieved from https://doi.org/10.1051/proc/201653014 doi: 10.1051/proc/201653014

Drui, F., Larat, A., Kokh, S., & Massot, M. (2016, July). *A hierarchy of simple hyperbolic two-fluid models for bubbly flows.* Retrieved from https://hal.archives-ouvertes.fr/hal-01349441 (working paper or preprint)

Drui, Florence, Fikl, Alexandru, Kestener, Pierre, Kokh, Samuel, Larat, Adam, Le Chenadec, Vincent, & Massot, Marc. (2016). Experimenting with the p4est library for amr simulations of two-phase flows. *ESAIM: Proc.*, *53*, 232-247. Retrieved from https://doi.org/10.1051/proc/201653014 doi: 10.1051/proc/201653014

Duarte, M. (2011). *Adaptive time-space numerical methods for the simulations of multi-scale reaction waves* (Unpublished doctoral dissertation). Ecole Centrale Paris, France. (https://tel.archives-ouvertes.fr/tel-00667857)

Duarte, M., Massot, M., Descombes, S., Tenaud, C., Dumont, T., Louvet, V., & Laurent, F. (2012). New resolution strategy for multiscale reaction waves using time operator splitting, space adaptive multiresolution, and dedicated high order implicit/explicit time integrators. *SIAM Journal on Scientific Computing*, *34*(1), A76-A104.

Dubey, A., Almgren, A., Bell, J., Berzins, M., Brandt, S., Bryan, G., ... Weide, K. (2016, Oct). A Survey of High Level Frameworks in Block-Structured Adaptive Mesh Refinement Packages. *arXiv e-prints*, arXiv:1610.08833.

Ern, A., & Giovangigli, V. (1994). *Multicomponent transport algorithms*. Springer-Verlag, Berlin,.

Ern, A., & Giovangigli, V. (1995). Fast and accurate multicomponent transport property evaluation. *Journal of Computational Physics*, *10*, 105-116.

Ern, A., & Giovangigli, V. (1996). *Eglib: A general-purpose fortran library for multicomponent transport property evaluation* (Tech. Rep.). Technical report, CERMICS.

Ern, A., & Giovangigli, V. (2010). Multicomponent transport algorithms for partially ionized mixtures. *Journal of Computational Physics*, *11*, 4117-4142.

Essadki, M. (2018). *Contribution to a unified Eulerian modeling of fuel injection : from dense liquid to polydisperse spray* (Theses, Université Paris-Saclay). Retrieved from https://tel.archives-ouvertes.fr/tel-01928584

Essadki, Mohamed, de Chaisemartin, Stéphane, Massot, Marc, Laurent, Frédérique, Larat, Adam, & Jay, Stéphane. (2016). Adaptive mesh refinement and high order geometrical moment method for the simulation of polydisperse evaporating sprays. *Oil Gas Sci. Technol. - Rev. IFP Energies nouvelles*, *71*(5), 61. Retrieved from https://doi.org/10.2516/ogst/2016012 doi: 10.2516/ogst/2016012

Evans, C. R., & Hawley, J. F. (1988, September). Simulation of magnetohydrodynamic flows - A constrained transport method. *The Astrophysical Journal*, *332*, 659-677. doi: 10.1086/166684

Ferraro, N., & Jardin, S. (2009, 11). Calculations of two-fluid magnetohydrodynamic axisymmetric steady-states. *Journal of Computational Physics*, *228*, 7742-7770. doi: 10.1016/j.jcp.2009.07.015

Ferziger, J. H., & Kaper, H. G. (1973). Mathematical theory of transport processes in gases. *American Journal of Physics*, *41*(4), 601-603. doi: 10.1119/1.1987312

Fröhlich, C., & Lean, J. (2004, 12). Solar radiative output and its variability: Evidence and mechanisms. *Astronomy and Astrophysics Review*, *12*, 273-320. doi: 10.1007/s00159-004-0024-1

Giovangigli, V. (1990). Mass conservation and singular multicomponent diffusion algorithms. *Impact of Computing in Science and Engineering*, *2*(1), 73 - 97. Retrieved from http://www.sciencedirect.com/science/article/pii/089982489090004T doi: https://doi.org/10.1016/0899-8248(90)90004-T

Giovangigli, V. (1997). Projected iterative algorithms with applications to multicomponent transport. *Linear Algebra Appl.*, *250*, 289-315.

Giovangigli, V., & Graille, B. (2009, 02). Projected iterative algorithms for complex symmetric systems arising in magnetized multicomponent transport. *Linear Algebra and its Applications*, *430*, 1404-1422. doi: 10.1016/j.laa.2008.11.001

Godunov, S. K. (1959). A difference method for numerical calculation of discontinuous solutions of the equations of hydrodynamics. *Mat. Sb. (N.S.)*, *47*(3), 271-306.

Godunov, S. K. (1999). Reminiscences about difference schemes. *Journal of Computational Physics*, *153*(1), 6 - 25. Retrieved from http://www.sciencedirect.com/science/article/pii/S002199919996271X doi: https://doi.org/10.1006/jcph.1999.6271

Goedbloed, J., Keppens, R., & Poedts, S. (2010). *Advanced magnetohydrodynamics: With applications to laboratory and astrophysical plasmas*. Cambridge University Press. Retrieved from https://books.google.fr/books?id=wHDyYpsqp04C

Goedbloed, J., & Poedts, S. (2004). *Principles of magnetohydrodynamics with applications to laboratory and astrophysical plasmas*. Cambridge University Press.

Gomes, A. K. F., Domingues, M. O., Schneider, K., Mendes, O., & Deiterding, R. (2015a). An adaptive multiresolution method for ideal magnetohydrodynamics using divergence cleaning with parabolic–hyperbolic correction. *Applied Numerical Mathematics*, *95*, 199 - 213.

Gomes, A. K. F., Domingues, M. O., Schneider, K., Mendes, O., & Deiterding, R. (2015b). An adaptive multiresolution method for ideal magnetohydrodynamics using divergence cleaning with parabolic–hyperbolic correction. *Applied Numerical Mathematics*, *95*, 199 - 213. Retrieved from http://www.sciencedirect.com/science/article/pii/S0168927415000173 (Fourth Chilean Workshop on Numerical Analysis of Partial Differential Equations (WONAPDE 2013)) doi: https://doi.org/10.1016/j.apnum.2015.01.007

Gontikakis, C., Winebarger, A. R., & Patsourakos, S. (2013). Spectral diagnostic of a microflare. evidences of resonant scattering in c iv 1548 å, 1550 å lines. *A&A*, *550*, A16. Retrieved from https://doi.org/10.1051/0004-6361/200913423 doi: 10.1051/0004-6361/200913423

Goodwin, D. G., Moffat, H. K., & Speth, R. L. (2016, January). *Cantera: An Object-oriented Software Toolkit for Chemical Kinetics, Thermodynamics, and Transport Processes. Version 2.2.1.* Retrieved from https://doi.org/10.5281/zenodo.45206 doi: 10.5281/zenodo.45206

Goossens, M. (1991). Magnetohydrodynamic waves and wave heating in non-uniform plasmas. In E. R. Priest & A. W. Hood (Eds.), *Geophysical and astrophysical mhd* (p. 137-172).

Grad, H. (1949). On the kinetic theory of rarefied gases. *Communications on Pure and Applied Mathematics*, *2*(4), 331-407. doi: 10.1002/cpa.3160020403

Grad, H. (1963). Asymptotic theory of the boltzmann equation. *The Physics of Fluids*, *6*(2), 147-181. doi: 10.1063/1.1706716

Graille, B., Magin, T. E., & Massot, M. (2009). Kinetic theory of plasmas: translational energy. *Mathematical Models and Methods in Applied Sciences*, *19*(04), 527-599.

Greenshields, C. J., Weller, H. G., Gasparini, L., & Reese, J. M. (2010). Implementation of semi-discrete, non-staggered central schemes in a colocated, polyhedral, finite volume framework, for high-speed viscous flows. *International Journal for Numerical Methods in Fluids*, *63*(1), 1-21. Retrieved from https://onlinelibrary.wiley.com/doi/abs/10.1002/fld.2069 doi: 10.1002/fld.2069

Grossmann, W., & Tataronis, J. (1973, Jun 01). Decay of mhd waves by phase mixing. *Zeitschrift fur Physik A Hadrons and nuclei*, *261*(3), 217–236. Retrieved from https://doi.org/10.1007/BF01391914 doi: 10.1007/BF01391914

Guang-Shan, J., & Cheng-Chin, W. (1999). A high-order weno finite difference scheme for the equations of ideal magnetohydrodynamics. *Journal of Computational Physics*, *150*(2), 561 - 594. Retrieved from http://www.sciencedirect.com/science/article/pii/S0021999199962071 doi: https://doi.org/10.1006/jcph.1999.6207

Gudiksen, B. V., Carlsson, M., Hansteen, V. H., Hayek, W., Leenaarts, J., & Martínez-Sykora, J. (2011, July). The stellar atmosphere simulation code Bifrost. Code description and validation. *Astronomy and astrophysics*, *531*, A154.

Gunney, B. T., & Anderson, R. W. (2016). Advances in patch-based adaptive mesh refinement scalability. *Journal of Parallel and Distributed Computing*, *89*, 65 - 84. Retrieved from http://www.sciencedirect.com/science/article/pii/S0743731515002129 doi: https://doi.org/10.1016/j.jpdc.2015.11.005

Gupta, G. P., & Mathur, K. C. (1978, oct). Differential cross sections for the elastic scattering of electrons by hydrogen atoms at intermediate energies. *Journal of Physics B: Atomic and Molecular Physics*, *11*(19), 3401–3409. Retrieved from https://doi.org/10.1088%2F0022-3700%2F11%2F19%2F015 doi: 10.1088/0022-3700/11/19/015

Gupta, N. R., M. Yos, J., Thompson, R., & Lee, K.-P. (1990, 09). A review of reaction rates and thermodynamic and transport properties for an 11-species air model for chemical and thermal nonequilibrium calculations to 30000 k. *NASA RP-1232*.

Haines, M. G. (1990). 'transport processes in plasmas' vol. 1: Classical transport; vol. 2: Neoclassical transport, r. balescu, north-holland press, 1988. *Journal of Plasma Physics*, *43*(3), 483–485. doi: 10.1017/S0022377800014938

Hairer, E., Nørsett, S. P., & Wanner, G. (1993). *Solving ordinary differential equations I: Nonstiff problems*. Berlin: Springer-Verlag, Second Edition.

Harten, A., D. Lax, P., & van Leer, B. (1983, 01). On upstream differencing and godunov-type schemes for hyperbolic conservation laws. *SIAM Rev*, *25*, 35-61.

Hartlep, T., Busse, F. H., Hurlburt, N. E., & Kosovichev, A. G. (2012, Jan). Magnetohydrodynamic simulations of flows around rotating and non-rotating axisymmetric magnetic flux concentrations. *Monthly Notices of the Royal Astronomical Society*, *419*(3), 2325-2328.

Hassanzadeh, H., Abedi, J., & Pooladi-Darvish, M. (2009). A comparative study of flux-limiting methods for numerical simulation of gas-solid reactions with arrhenius type reaction kinetics. *Computers and Chemical Engineering*, *33*, 133-143.

Heitsch, F., & Zweibel, E. G. (2003, Jan). Fast Reconnection in a Two-Stage Process. *The astrophysical journal*, *583*(1), 229-244. doi: 10.1086/345082

Hesthaven, J., & Warburton, T. (2007). *Nodal discontinuous galerkin methods: Algorithms, analysis, and applications* (Vol. 54). Springer Science and Business Media.

Heyvaerts, J., & Priest, E. (1982, 12). Coronal heating by phase-mixed shear alfven waves. *Astronomy and Astrophysics*, *117*, 220-234.

Hiester, H., Piggott, M., Farrell, P., & Allison, P. (2014, 01). Assessment of spurious mixing in adaptive mesh simulations of the two-dimensional lock-exchange. *Ocean Modelling*, *73*, 30–44. doi: 10.1016/j.ocemod.2013.10.003

Hill, D., & Pullin, D. (2004). Hybrid tuned center-difference-weno method for large eddy simulations in the presence of strong shocks. *Journal of Computational Physics*, *194*(2), 435 - 450. Retrieved from http://www.sciencedirect.com/science/article/pii/S002199910300490X doi: https://doi.org/10.1016/j.jcp.2003.07.032

Hirschfelder, J., Bird, R. B., & Curtiss, C. F. (1964). *Molecular theory of gases and liquids; rev. version*. New York, NY: Wiley. Retrieved from https://cds.cern.ch/record/108119

Horiuchi, R. (2018). The role of magnetic islands in collisionless driven reconnection: A kinetic approach to multi-scale phenomena. *Plasma*, *1*(1), 68–77. Retrieved from https://www.mdpi.com/2571-6182/1/1/7 doi: 10.3390/plasma1010007

Hornung, R. D., & Kohn, S. R. (2002). Managing application complexity in the samrai object-oriented framework. *Concurrency and Computation: Practice and Experience*, *14*(5), 347-368. Retrieved from https://onlinelibrary.wiley.com/doi/abs/10.1002/cpe.652 doi: 10.1002/cpe.652

Howard, L. N. (1962). Hydrodynamic and hydromagnetic stability. by s. chandrasekhar. clarendon press: Oxford university press, 1961. 652 pp. £5. 5s. *Journal of Fluid Mechanics*, *13*(1), 158–160.

Isaac, T., Burstedde, C., Wilcox, L., & Ghattas, O. (2015). Recursive algorithms for distributed forests of octrees. *SIAM Journal on Scientific Computing*, *37*(5), C497-C531. Retrieved from https://doi.org/10.1137/140970963 doi: 10.1137/140970963

Jancel, R., & Kahan, T. (1966). *Electrodynamics of plasmas*. London: New York Wiley.

Ji, H., Lien, F.-S., & Yee, E. (2010, 11). A new adaptive mesh refinement data structure with an application to detonation. *Journal of Computational Physics*, *229*, 8981-8993. doi: 10.1016/j.jcp.2010.08.023

J. McBride, B., Gordon, S., & A. Reno, M. (1993, 11). Coefficients for calculating thermodynamic and transport properties of individual species. *NASA Technical Memorandum 4513*.

J. McBride, B., J. Zehe, M., & Gordon, S. (2002, 10). Nasa glenn coefficients for calculating thermodynamic properties of individual species. *Technical Report 211556, NASA*.

Kaneko, S. (1960). Kinetic Theory in a Uniform Magnetic Field. *J. Phys. Soc. Japan*, *1*, 1685-1690.

Khomenko, E. (2017, January). On the effects of ion-neutral interactions in solar plasmas. *Plasma Physics and Controlled Fusion*, *59*(1), 014038.

Khomenko, E., Collados, M., Díaz, A., & Vitas, N. (2014). Fluid description of multi-component solar partially ionized plasma. *Physics of Plasmas*, *21*(9), 092901. Retrieved from https://doi.org/10.1063/1.4894106 doi: 10.1063/1.4894106

Khomenko, E., & Collados Vera, M. (2012, December). Simulations of Chromospheric Heating by Ambipolar Diffusion. In *Second atst-east meeting: Magnetic fields from the photosphere to the corona.* (Vol. 463, p. 281).

Kihara, T., Taylor, M. H., & Hirschfelder, J. O. (1960). Transport properties for gases assuming inverse power intermolecular potentials. *The Physics of Fluids*, *3*(5), 715-720. doi: 10.1063/1.1706115

Kitiashvili, I. N., Couvidat, S., & Lagg, A. (2015, July). Using Realistic MHD Simulations for Modeling and Interpretation of Quiet-Sun Observations with the Solar Dynamics Observatory Helioseismic and Magnetic Imager. *The astrophysical journal*, *808*, 59.

Kitiashvili, I. N., Kosovichev, A. G., Wray, A. A., & Mansour, N. N. (2010, August). Mechanism of Spontaneous Formation of Stable Magnetic Structures on the Sun. *The astrophysical journal*, *719*, 307-312. doi: 10.1088/0004-637X/719/1/307

Klimchuk, J. A. (2015, Apr). Key aspects of coronal heating. *Philosophical Transactions of the Royal Society of London Series A*, *373*(2042), 20140256-20140256. doi: 10.1098/rsta.2014.0256

Kolesnikov, A. F. (1974). The equations of motion of a multicomponent partially ionized two-temperature mixture of gases in an electromagnetic field with transport coefficients in higher approximations. *Technical Report 1556*.

Kolesnikov, A. F. (2003, 01). General formulation of multicomponent plasmas transport with ambipolar approach for weakly ionized gases. *41st Aerospace Sciences Meeting and Exhibit*.

Kosugi, T., Matsuzaki, K., Sakao, T., Shimizu, T., Sone, Y., Tachikawa, S., ... Golub, L. (2007, Jun 01). The hinode (solar-b) mission: An overview. *Solar Physics*, *243*(1), 3–17. Retrieved from https://doi.org/10.1007/s11207-007-9014-6 doi: 10.1007/s11207-007-9014-6

Kowalski, A. F., Butler, E., Daw, A. N., Fletcher, L., Allred, J. C., De Pontieu, B., ... Cauzzi, G. (2019, Jun). Spectral Evidence for Heating at Large Column Mass in Umbral Solar Flare Kernels. I. IRIS Near-UV Spectra of the X1 Solar Flare of 2014 October 25. *The Astrophysical Journal*, *878*(2), 135. doi: 10.3847/1538-4357/ab1f8b

Krstic, P. S. (2002, Oct). Inelastic processes from vibrationally excited states in slow $h^+ + h_2$ and $h + h_2^+$ collisions: Excitations and charge transfer. *Phys. Rev. A*, *66*, 042717. Retrieved from https://link.aps.org/doi/10.1103/PhysRevA.66.042717 doi: 10.1103/PhysRevA.66.042717

Krstic, P. S., & Schultz, D. R. (1999, jul). Elastic scattering and charge transfer in slow collisions: isotopes of h and h+colliding with isotopes of h and with he. *Journal of Physics B: Atomic, Molecular and Optical Physics*, *32*(14), 3485–3509. Retrieved from https://doi.org/10.1088%2F0953-4075%2F32%2F14%2F317 doi: 10.1088/0953-4075/32/14/317

Krstic, P. S., & Schultz, D. R. (2003, jan). Elastic processes involving vibrationally excited molecules in cold hydrogen plasmas. *Journal of Physics B: Atomic, Molecular and Optical Physics*, *36*(2), 385–398. Retrieved from https://doi.org/10.1088%2F0953-4075%2F36%2F2%2F318 doi: 10.1088/0953-4075/36/2/318

Kruger, C., Mitchner, M., & Daybelge, U. (1968, 09). Transport properties of mhd-generator plasmas. *AIAA Journal*, *6*, 1712-1723. doi: 10.2514/3.4849

Kruger, C. H., & Mitchner, M. (1967). Kinetic theory of two-temperature plasmas. *The Physics of Fluids*, *10*(9), 1953-1961. Retrieved from https://aip.scitation.org/doi/abs/10.1063/1.1762391 doi: 10.1063/1.1762391

Kumar, K. (1966). Polynomial expansions in kinetic theory of gases. *Annals of Physics*, *37*(1), 113 - 141. Retrieved from http://www.sciencedirect.com/science/article/pii/0003491666902806 doi: https://doi.org/10.1016/0003-4916(66)90280-6

Kurganov, A., & Lin, C.-T. (2007, 03). On the reduction of numerical dissipation in central-upwind schemes. *COMMUNICATIONS IN COMPUTATIONAL PHYSICS Commun. Comput. Phys*, *2*, 141-163.

Kurganov, A., & Petrova, G. (2000). Central schemes and contact discontinuities. *ESAIM: Mathematical Modelling and Numerical Analysis - Modélisation Mathématique et Analyse Numérique*, *34*(6), 1259-1275. Retrieved from http://www.numdam.org/item/M2AN_2000__34_6_1259_0

Kurganov, A., Petrova, G., & Popov, B. (2007). Adaptive semidiscrete central-upwind schemes for nonconvex hyperbolic conservation laws. *SIAM Journal on Scientific Computing*, *29*(6), 2381-2401. doi: 10.1137/040614189

Kurganov, A., & Tadmor, E. (2000). New high-resolution central schemes for nonlinear conservation laws and convection–diffusion equations. *Journal of Computational Physics*, *160*(1), 241 - 282. Retrieved from http://www.sciencedirect.com/science/article/pii/S0021999100964593 doi: https://doi.org/10.1006/jcph.2000.6459

Lankalapalli, S., Flaherty, J. E., Shephard, M. S., & Strauss, H. (2007, July). An adaptive finite element method for magnetohydrodynamics. *Journal of Computational Physics*, *225*, 363-381. doi: 10.1016/j.jcp.2006.12.010

Lapenta, G. (2008, 06). Self-feeding turbulent magnetic reconnection on macroscopic scales. *Physical review letters*, *100*, 235001. doi: 10.1103/PHYSREVLETT.100.235001

Lapenta, G. (2012, February). Particle simulations of space weather. *Journal of Computational Physics*, *231*, 795-821. doi: 10.1016/j.jcp.2011.03.035

Lapenta, G., Pierrard, Viviane, Keppens, Rony, Markidis, Stefano, Poedts, Stefaan, Sebek, Ondrej, ... Borremans, Kris (2013). Swiff: Space weather integrated forecasting framework. *J. Space Weather Space Clim.*, *3*, A05. Retrieved from https://doi.org/10.1051/swsc/2013027 doi: 10.1051/swsc/2013027

Lax, P., & Wendroff, B. (1960). Systems of conservation laws. *Communications on Pure and Applied Mathematics*, *13*(2), 217-237. Retrieved from https://onlinelibrary.wiley.com/doi/abs/10.1002/cpa.3160130205 doi: 10.1002/cpa.3160130205

Leake, J. E., Lukin, V. S., & Linton, M. G. (2013). Magnetic reconnection in a weakly ionized plasma. *Physics of Plasmas*, *20*(6), 061202. doi: 10.1063/1.4811140

Leake, J. E., Lukin, V. S., Linton, M. G., & Meier, E. T. (2012, December). Multi-fluid Simulations of Chromospheric Magnetic Reconnection in a Weakly Ionized Reacting Plasma. *The Astrophysical Journal*, *760*, 109. doi: 10.1088/0004-637X/760/2/109

Li, F., & Shu, C.-W. (2005, Jun 01). Locally divergence-free discontinuous galerkin methods for mhd equations. *Journal of Scientific Computing*, *22*(1), 413–442. Retrieved from https://doi.org/10.1007/s10915-004-4146-4 doi: 10.1007/s10915-004-4146-4

Li, Y., Ding, M. D., Hong, J., Li, H., & Gan, W. Q. (2019, Jul). Different Signatures of Chromospheric Evaporation in Two Solar Flares Observed with IRIS. *The Astrophysical journal*, *879*(1), 30. doi: 10.3847/1538-4357/ab245a

Li, Y., & Lin, C. D. (1999, Sep). Calculations of some weakly bound diatomic molecular negative ions. *Phys. Rev. A*, *60*, 2009–2014.

Londrillo, P., & del Zanna, L. (2004, Mar). On the divergence-free condition in Godunov-type schemes for ideal magnetohydrodynamics: the upwind constrained transport method. *Journal of Computational Physics*, *195*(1), 17-48. doi: 10.1016/j.jcp.2003.09.016

Londrillo, P., & Zanna, L. D. (2000). High-order upwind schemes for multidimensional magnetohydrodynamics. *The Astrophysical Journal*, *530*(1), 508. Retrieved from http://stacks.iop.org/0004-637X/530/i=1/a=508

Lowrie, R. B., & Edwards, J. (2008). Radiative shock solutons with grey nonequilibrium diffusion. *Shock waves*, *18*, 129–143.

Lowrie, R. B., & Rauenzahn, R. M. (2007). Radiative shock solutons in the equilibrium diffusion limit. *Shock waves*, *16*, 445–453.

Lucquin-Desreux, B. (1998). Fluid limit for magnetized plasma. *Transport Theory and Statistical Physics*, *27*, 99.

Luo, H., Baum, J. D., & Löhner, R. (2008, October). A discontinuous galerkin method based on a taylor basis for the compressible flows on arbitrary grids. *J. Comput. Phys.*, *227*(20), 8875–8893. Retrieved from http://dx.doi.org/10.1016/j.jcp.2008.06.035 doi: 10.1016/j.jcp.2008.06.035

MacNeice, P., Olson, K. M., Mobarry, C., de Fainchtein, R., & Packer, C. (2000). Paramesh: A parallel adaptive mesh refinement community toolkit. *Computer Physics Communications*, *126*(3), 330 - 354. Retrieved from http://www.sciencedirect.com/science/article/pii/S0010465599005019 doi: https://doi.org/10.1016/S0010-4655(99)00501-9

Magin, T., & Degrez, G. (2004, Oct). Transport properties of partially ionized and unmagnetized plasmas. *Phys. Rev. E*, *70*, 046412. Retrieved from https://link.aps.org/doi/10.1103/PhysRevE.70.046412 doi: 10.1103/PhysRevE.70.046412

Magin, T. E. (2004). *A model for inductive plasma wind tunnels*. Université Libre de Bruxelles, Faculté des sciences appliquées.

Magin, T. E., & Degrez, G. (2004, August). Transport algorithms for partially ionized and unmagnetized plasmas. *J. Comput. Phys.*, *198*(2), 424–449. Retrieved from http://dx.doi.org/10.1016/j.jcp.2004.01.012 doi: 10.1016/j.jcp.2004.01.012

Markidis, S., Lapenta, G., & Uddin, R. (2010, 3 1). Multi-scale simulations of plasma with ipic3d. *Mathematics and Computers in Simulation*, *80*(7), 1509–1519. doi: 10.1016/j.matcom.2009.08.038

Martínez-Sykora, J., De Pontieu, B., Hansteen, V. H., & Carlsson, M. (2015, December). Impact of the Ion-Neutral Interaction Effects in the Solar Chromosphere. *AGU Fall Meeting Abstracts*, SH31B-2411.

Martínez-Sykora, J., Pontieu, B. D., Hansteen, V., & Carlsson, M. (2015). The role of partial ionization effects in the chromosphere. *Philosophical Transactions of the Royal Society A: Mathematical, Physical and Engineering Sciences*, *373*(2042), 20140268. Retrieved from https://royalsocietypublishing.org/doi/abs/10.1098/rsta.2014.0268 doi: 10.1098/rsta.2014.0268

Mason, E. A., Munn, R. J., & Smith, F. J. (1967). Transport coefficients of ionized gases. *The Physics of Fluids*, *10*(8), 1827-1832. doi: 10.1063/1.1762365

Masser, T. O., Wohlbier, J. G., & Lowrie, R. B. (2011). Shock wave structure for a fully ionized plasma. *Shock waves*, *21*, 367–381.

Mcintosh, S., De Pontieu, B., Carlsson, M., Hansteen, V., Boerner, P., & Goossens, M. (2011, 07). Alfvenic waves with sufficient energy to power the quiet solar corona and fast solar wind. *Nature*, *475*, 477-80. doi: 10.1038/nature10235

Meyer, W., & Frommhold, L. (1994, 05). Long-range interactions in h-he:ab initio potential, hyperfine pressure shift and collision-induced absorption in the infrared. *Theoretica Chimica Acta*, *88*, 201-216. doi: 10.1007/BF01113614

Mignone, A. (2007, 02). A simple and accurate riemann solver for isothermal mhd. *Journal of Computational Physics*, *225*. doi: 10.1016/j.jcp.2007.01.033

Mignone, A., & Tzeferacos, P. (2010, Mar). A second-order unsplit Godunov scheme for cell-centered MHD: The CTU-GLM scheme. *Journal of Computational Physics*, *229*(6), 2117-2138. doi: 10.1016/j.jcp.2009.11.026

Mignone, A., Tzeferacos, P., & Bodo, G. (2010, Aug). High-order conservative finite difference GLM-MHD schemes for cell-centered MHD. *Journal of Computational Physics*, *229*(17), 5896-5920. doi: 10.1016/j.jcp.2010.04.013

Mignone, A., Zanni, C., Tzeferacos, P., van Straalen, B., Colella, P., & Bodo, G. (2012). The pluto code for adaptive mesh computations in astrophysical fluid dynamics. *The Astrophysical Journal*, *198*(1), 7.

Mihalas, D., & Mihalas, B. W. (1984). *Foundations of radiation hydrodynamics*. New York: Oxford University Press.

Miura, A., & Pritchett, P. L. (1982, September). Nonlocal stability analysis of the MHD Kelvin-Helmholtz instability in a compressible plasma. *Journal of Geophysical Research*, *87*, 7431-7444. doi: 10.1029/JA087iA09p07431

Munz, C.-D., Omnes, P., Schneider, R., Sonnendrücker, E., & Voß, U. (2000). Divergence correction techniques for maxwell solvers based on a hyperbolic model. *Journal of Computational Physics*, *161*(2), 484 - 511. Retrieved from http://www.sciencedirect.com/science/article/pii/S0021999100965070 doi: https://doi.org/10.1006/jcph.2000.6507

Nessyahu, H., & Tadmor, E. (1990, 04). Non-oscillatory central differencing for hyperbolic conservation laws. *Journal of Computational Physics*, *87*, 408-463. doi: 10.1016/0021-9991(90)90260-8

Ni, L., Kliem, B., Lin, J., & Wu, N. (2015, Jan). Fast Magnetic Reconnection in the Solar Chromosphere Mediated by the Plasmoid Instability. *The Astrophysical Journal*, *799*(1), 79. doi: 10.1088/0004-637X/799/1/79

Ni, L., Lukin, V. S., Murphy, N. A., & Lin, J. (2018, April). Magnetic reconnection in the low solar chromosphere with a more realistic radiative cooling model. *Physics of Plasmas*, *25*(4), 042903. doi: 10.1063/1.5018351

Nonaka, A., Almgren, A. S., Bell, J. B., Lijewski, M. J., Malone, C. M., & Zingale, M. (2010, Jun). MAESTRO: An Adaptive Low Mach Number Hydrodynamics Algorithm for Stellar Flows. *Astrophysical Journal Suppliment*, *188*(2), 358-383. doi: 10.1088/0067-0049/188/2/358

N. Parker, E. (1972, 07). Topological dissipation and the small-scale fields in turbulent gases. *Astrophys. J.*, *174*. doi: 10.1086/151512

Ofman, L., & Thompson, B. J. (2011, June). SDO/AIA Observation of Kelvin-Helmholtz Instability in the Solar Corona. *The Astrophysical Journal Letters*, *734*, L11.

Olson, R. E., & Liu, B. (1980, Oct). Interactions of h and h^- with he and ne. *Phys. Rev. A*, *22*, 1389–1394. Retrieved from https://link.aps.org/doi/10.1103/PhysRevA.22.1389 doi: 10.1103/PhysRevA.22.1389

Orszag, S. A., & Tang, C.-M. (1979). Small-scale structure of two-dimensional magnetohydrodynamic turbulence. *Journal of Fluid Mechanics*, *90*(1), 129–143.

Pamela, S., Huijsmans, G., Thornton, A., Kirk, A., Smith, S., Hoelzl, M., & Eich, T. (2019). A wall-aligned grid generator for non-linear simulations of mhd instabilities in tokamak plasmas. *Computer Physics Communications*, *243*, 41 - 50. Retrieved from http://www.sciencedirect.com/science/article/pii/S0010465519301560 doi: https://doi.org/10.1016/j.cpc.2019.05.007

Papini, E., Landi, S., & Del Zanna, L. (2018, May). Fast magnetic reconnection: The ideal tearing instability in classic, Hall, and relativistic plasmas. In *Journal of physics conference series* (Vol. 1031, p. 012020). doi: 10.1088/1742-6596/1031/1/012020

Pares, C. (2006). Numerical methods for nonconservative hyperbolic systems: a theoretical framework. *SIAM J. Numer. Anal.*, *44*, 300–321.

Park, C., Jaffe, R. L., & Partridge, H. (2001). Chemical-kinetic parameters of hyperbolic earth entry. *Journal of Thermophysics and Heat Transfer*, *15*(1), 76-90. Retrieved from https://doi.org/10.2514/2.6582 doi: 10.2514/2.6582

Parker, E. N. (1957). Sweet's mechanism for merging magnetic fields in conducting fluids. *Journal of Geophysical Research (1896-1977)*, *62*(4), 509-520. Retrieved from https://agupubs.onlinelibrary.wiley.com/doi/abs/10.1029/JZ062i004p00509 doi: 10.1029/JZ062i004p00509

Parker, E. N. (1988, July). Nanoflares and the solar X-ray corona. *The astrophysical journal*, *330*, 474-479. doi: 10.1086/166485

Pelanti, M., & Shyue, K. (2014). A mixture-energy-consistent six-equation two-phase numerical model for fluids with interfaces cavitation and evaporation waves. *J. Comput. Phys.*, *259*, 331–357.

Petit, J.-P., & Darrozes, J.-S. (1975). New formulation of the equations of motion of an ionized gas in collision dominated regime. *Journal de Mecanique*, *14*, 745-759.

Petschek, H. E. (1964). Magnetic Field Annihilation. *NASA Special Publication*, *50*, 425.

Poedts, S., Goossens, M., & Kerner, W. (1989, Mar 01). Numerical simulation of coronal heating by resonant absorption of alfvén waves. *Solar Physics*, *123*(1), 83–115. Retrieved from https://doi.org/10.1007/BF00150014 doi: 10.1007/BF00150014

Powell, K. G., Roe, P. L., Linde, T. J., Gombosi, T. I., & Zeeuw, D. L. D. (1999). A solution-adaptive upwind scheme for ideal magnetohydrodynamics. *Journal of Computational Physics*, *154*(2), 284 - 309. Retrieved from http://www.sciencedirect.com/science/article/pii/S002199919996299X doi: https://doi.org/10.1006/jcph.1999.6299

Priest, E., Heyvaerts, J., & Title, A. (2002, 9 1). A flux-tube tectonics model for solar coronal heating driven by the magnetic carpet. *Astrophysical Journal*, *576*(1), 533–551. doi: 10.1086/341539

P. T. Groth, C., & Northrup, S. (2005, 06). Parallel implicit adaptive mesh refinement scheme for body-fitted multi-block mesh. *17th AIAA Computational Fluid Dynamics Conference*. doi: 10.2514/6.2005-5333

Qiu, J., & Shu, C.-W. (2004). Hermite weno schemes and their application as limiters for runge–kutta discontinuous galerkin method: one-dimensional case. *Journal of Computational Physics*, *193*(1), 115 - 135. Retrieved from http://www.sciencedirect.com/science/article/pii/S0021999103004212 doi: https://doi.org/10.1016/j.jcp.2003.07.026

Raviart, P.-A., & Sainsaulieu, L. (1995). A nonconservative hyperbolic system modeling spray dynamics. part I: solution of the riemann problem. *Mathematical Models and Methods in Applied Sciences*, *05*(03), 297-333.

Raviart, P. A., & Thomas, J. M. (1977). A mixed finite element method for 2-nd order elliptic problems. In I. Galligani & E. Magenes (Eds.), *Mathematical aspects of finite element methods* (pp. 292–315). Berlin, Heidelberg: Springer Berlin Heidelberg.

Riabov, V. V. (1996). Approximate calculation of transport coefficients of earth and mars atmospheric dissociating gases. *Journal of Thermophysics and Heat Transfer*, *10*(2), 209-216. Retrieved from https://doi.org/10.2514/3.777 doi: 10.2514/3.777

Roe, P. (2003, 11). Characteristic-based schemes for the euler equations. *Annual Review of Fluid Mechanics*, *18*, 337-365. doi: 10.1146/annurev.fl.18.010186.002005

Rogava, A., Osmanov, Z., & Poedts, S. (2010, May). Self-heating and its possible relationship to chromospheric heating in slowly rotating stars. *Monthly Notices of the Royal Astronomical Society*, *404*(1), 224-231. doi: 10.1111/j.1365-2966.2009.16159.x

R. Stallcop, J., Levin, E., & Partridge, H. (1998, 10). Transport properties of hydrogen. *Journal of Thermophysics and Heat Transfer - J THERMOPHYS HEAT TRANSFER*, *12*, 514-519. doi: 10.2514/2.6370

Russell, H. N. (1929, July). On the Composition of the Sun's Atmosphere. *The Astrophysical Journal*, *70*, 11. doi: 10.1086/143197

S. Benilov, M. (1996, 07). Momentum and energy exchange between species of a multicomponent gas mixture due to inelastic and reactive collisions. *Physics of Plasmas*, *3*. doi: 10.1063/1.871714

S. Benilov, M. (1997, 03). A kinetic derivation of multifluid equations for multispecies nonequilibrium mixtures of reacting gases. *Physics of Plasmas*, *4*. doi: 10.1063/1.872151

Schindler, K., Hesse, M., & Birn, J. (1988). General magnetic reconnection, parallel electric fields, and helicity. *Journal of Geophysical Research: Space Physics*, *93*(A6), 5547-5557. Retrieved from https://agupubs.onlinelibrary.wiley.com/doi/abs/10.1029/JA093iA06p05547 doi: 10.1029/JA093iA06p05547

Schmidt, M. (1989). Elementary processes in hydrogen-helium plasmas cross sections and reaction rate coefficients. by r. k. janev, w. d. langer, k. evans, jr., d. e. post, jr. springer-verlag heidelberg, new york, london, paris, tokyo (springer series on atoms and plasmas vol. 4) 326 p. 107

fig. *Contributions to Plasma Physics*, *29*(1), 10-10. Retrieved from https://onlinelibrary.wiley.com/doi/abs/10.1002/ctpp.2150290103 doi: 10.1002/ctpp.2150290103

Scholer, M. (1989). Undriven magnetic reconnection in an isolated current sheet. *Journal of Geophysical Research: Space Physics*, *94*(A7), 8805-8812. Retrieved from https://agupubs.onlinelibrary.wiley.com/doi/abs/10.1029/JA094iA07p08805 doi: 10.1029/JA094iA07p08805

Scoggins, J. B. (2017). *Development of numerical methods and study of coupled flow, radiation, and ablation phenomena for atmospheric entry* (Theses, Université Paris-Saclay). Retrieved from https://tel.archives-ouvertes.fr/tel-01639797

Scoggins, J. B., Knisely, C. P., & Magin, T. E. (2016). Crossed contributions to electron and heavy-particle transport fluxes for magnetized plasmas in the continuum regime. *AIP Conference Proceedings*, *1786*(1), 130002. Retrieved from https://aip.scitation.org/doi/abs/10.1063/1.4967628 doi: 10.1063/1.4967628

Scoggins, J. B., & Magin, T. E. (2014, jun). Development of mutation++: Multicomponent thermodynamic and transport properties for ionized plasmas written in c++. *11th AIAA/ASME Joint Thermophysics and Heat Transfer Conference*.

Scoggins, J. B., & Magin, T. E. (2015). Gibbs function continuation for linearly constrained multiphase equilibria. *Combustion and Flame*, *162*(12), 4514 - 4522.

Shafranov, V. (1957). The structure of shock waves in a plasma. *Soviet Phys. JETP*, *5*.

Sharp, T. (1970). Potential-energy curves for molecular hydrogen and its ions. *Atomic Data and Nuclear Data Tables*, *2*, 119 - 169. Retrieved from http://www.sciencedirect.com/science/article/pii/S0092640X70800079 doi: https://doi.org/10.1016/S0092-640X(70)80007-9

Shay, M. A., Haggerty, C. C., Matthaeus, W. H., Parashar, T. N., Wan, M., & Wu, P. (2018). Turbulent heating due to magnetic reconnection. *Physics of Plasmas*, *25*(1), 012304. Retrieved from https://doi.org/10.1063/1.4993423 doi: 10.1063/1.4993423

Shelyag, S., Khomenko, E., de Vicente, A., & Przybylski, D. (2016, March). Heating of the Partially Ionized Solar Chromosphere by Waves in Magnetic Structures. *The Astrophysical Journal*, *819*, L11. doi: 10.3847/2041-8205/819/1/L11

Shu, C.-W. (1998). Essentially non-oscillatory and weighted essentially non-oscillatory schemes for hyperbolic conservation laws. In *Advanced numerical approximation of nonlinear hyperbolic equations: Lectures given at the 2nd session of the centro internazionale matematico estivo (c.i.m.e.) held in cetraro, italy, june 23–28, 1997* (pp. 325–432). Berlin, Heidelberg: Springer Berlin Heidelberg. Retrieved from https://doi.org/10.1007/BFb0096355 doi: 10.1007/BFb0096355

Shu, C.-W., & Osher, S. (1988). Efficient implementation of essentially non-oscillatory shock-capturing schemes. *Journal of Computational Physics*, *77*(2), 439 - 471. Retrieved from http://www.sciencedirect.com/science/article/pii/0021999188901775 doi: https://doi.org/10.1016/0021-9991(88)90177-5

Shumlak, U., & Loverich, J. (2003). Approximate riemann solver for the two-fluid plasma model. *Journal of Computational Physics*, *187*(2), 620 - 638. Retrieved from http://www.sciencedirect.com/science/article/pii/S0021999103001517 doi: https://doi.org/10.1016/S0021-9991(03)00151-7

Shyn, T., & Grafe, A. (1992, 10). Angular distribution of electrons elastically scattered from hydrogen atoms. ii. *Physical review. A*, *46*, 2949-2951. doi: 10.1103/PhysRevA.46.2949

Sijacki, D., Hernquist, L., Vogelsberger, M., Genel, S., Nelson, D., Kereš, D., & Springel, V. (2013, 01). Moving mesh cosmology: tracing cosmological gas accretion. *Monthly Notices of the Royal Astronomical Society*, *429*(4), 3353-3370. Retrieved from https://doi.org/10.1093/mnras/sts595 doi: 10.1093/mnras/sts595

Sijacki, D., Hernquist, L., Vogelsberger, M., Pakmor, R., & Mocz, P. (2013, 10). A discontinuous Galerkin method for solving the fluid and magnetohydrodynamic equations in astrophysical simulations. *Monthly Notices of the Royal Astronomical Society*, *437*(1), 397-414. Retrieved from https://doi.org/10.1093/mnras/stt1890 doi: 10.1093/mnras/stt1890

Siscoe, G. (2000). The space-weather enterprise: past, present, and future. *Journal of Atmospheric and Solar-Terrestrial Physics*, *62*(14), 1223 - 1232. Retrieved from http://www.sciencedirect.com/science/article/pii/S1364682600000742 (Space Weather Week) doi: https://doi.org/10.1016/S1364-6826(00)00074-2

Smith, P. D., & Sakai, J. I. (2008, August). Chromospheric magnetic reconnection: two-fluid simulations of coalescing current loops. *Astronomy and Astrophysics*, *486*, 569-575. doi: 10.1051/0004-6361:200809624

Solanki, S. (2003, 04). Sunspots: An overview. *Astronomy and Astrophysics Review*, *11*, 153-286. doi: 10.1007/s00159-003-0018-4

Sourd, B., Aubreton, J., Elchinger, M.-F., Labrot, M., & Michon, U. (2006, March). High temperature transport coefficients in e/C/H/N/O mixtures. *Journal of Physics D Applied Physics*, *39*, 1105-1119. doi: 10.1088/0022-3727/39/6/016

Sovinec, C., Glasser, A., Gianakon, T., Barnes, D., Nebel, R., Kruger, S., ... Chu, M. (2004). Nonlinear magnetohydrodynamics simulation using high-order finite elements. *Journal of Computational Physics*, *195*(1), 355 - 386. Retrieved from http://www.sciencedirect.com/science/article/pii/S0021999103005369 doi: https://doi.org/10.1016/j.jcp.2003.10.004

Spitzer, L. (1963). Physics of fully ionized gases. *American Journal of Physics*, *31*(11), 890-891. Retrieved from https://doi.org/10.1119/1.1969155 doi: 10.1119/1.1969155

Stone, J. M., Gardiner, T. A., Teuben, P., Hawley, J. F., & Simon, J. B. (2008, September). Athena: A New Code for Astrophysical MHD. *The Astrophysical Journal Supplement Series*, *178*, 137-177.

Strang, G. (1968). On the construction and comparison of difference schemes. *SIAM Journal on Numerical Analysis*, *5*(3), 506–517.

Strauss, H., & Longcope, D. (1998). An adaptive finite element method for magnetohydrodynamics. *Journal of Computational Physics*, *147*(2), 318 - 336. Retrieved from http://www.sciencedirect.com/science/article/pii/S0021999198960910 doi: https://doi.org/10.1006/jcph.1998.6091

Sundar, H., Sampath, R. S., Adavani, S. S., Davatzikos, C., & Biros, G. (2007, Nov). Low-constant parallel algorithms for finite element simulations using linear octrees. In *Sc '07: Proceedings of the 2007 acm/ieee conference on supercomputing* (p. 1-12). doi: 10.1145/1362622.1362656

Sundar, H., Sampath, R. S., & Biros, G. (2008, August). Bottom-up construction and 2:1 balance refinement of linear octrees in parallel. *SIAM J. Sci. Comput.*, *30*(5), 2675–2708. Retrieved from http://dx.doi.org/10.1137/070681727 doi: 10.1137/070681727

Suresh, A., & Huynh, H. (1997). Accurate monotonicity-preserving schemes with runge–kutta time stepping. *Journal of Computational Physics*, *136*(1), 83 - 99. Retrieved from http://www.sciencedirect.com/science/article/pii/S0021999197957454 doi: https://doi.org/10.1006/jcph.1997.5745

Susanto, A., Ivan, L., De Sterck, H., & Groth, C. (2013, October). High-order central eno finite-volume scheme for ideal mhd. *J. Comput. Phys.*, *250*(C), 141–164. Retrieved from http://dx.doi.org/10.1016/j.jcp.2013.04.040 doi: 10.1016/j.jcp.2013.04.040

Sutton, G., & Sherman, H. (1965). *Engineering magnetohydrodynamics*. McGraw-Hill.

Sweby, P. (1984). High resolution schemes using flux limiters for hyperbolic conservation laws. *SIAM Journal on Numerical Analysis*, *21*(5), 995-1011. doi: 10.1137/0721062

Takahashi, K., Yamada, S., & Yamada. (2014, Apr). Exact Riemann solver for ideal magnetohydrodynamics that can handle all types of intermediate shocks and switch-on/off waves. *Journal of Plasma Physics*, *80*(2), 255-287. doi: 10.1017/S0022377813001268

Tang, K. T., & Toennies, J. P. (2003). The van der waals potentials between all the rare gas atoms from he to rn. *The Journal of Chemical Physics*, *118*(11), 4976-4983. doi: 10.1063/1.1543944

Tang, K. T., Toennies, J. P., & Yiu, C. L. (1995, Feb). Accurate analytical he-he van der waals potential based on perturbation theory. *Phys. Rev. Lett.*, *74*, 1546–1549. Retrieved from https://link.aps.org/doi/10.1103/PhysRevLett.74.1546 doi: 10.1103/PhysRevLett.74.1546

Teyssier, R. (2002, Apr). Cosmological hydrodynamics with adaptive mesh refinement. A new high resolution code called RAMSES. *Astronomy and Astrophysics*, *385*, 337-364. doi: 10.1051/0004-6361:20011817

Tirsky, G. A. (1993). Up-to-date gasdynamic models of hypersonic aerodynamics and heat transfer with real gas properties. *Annual Review of Fluid Mechanics*, *25*(1), 151-181. doi: 10.1146/annurev.fl.25.010193.001055

Tolman, E. A., Loureiro, N. F., & Uzdensky, D. A. (2018, Feb). Development of tearing instability in a current sheet forming by sheared incompressible flow. *Journal of Plasma Physics*, *84*(1), 905840115. doi: 10.1017/S002237781800017X

Toro, E. (2009). *Riemann solvers and numerical methods for fluid dynamics* (3rd ed.). Springer-Verlag Berlin Heidelberg. doi: 10.1007/b79761

Toro, E., Spruce, M., & Speares, W. (1994, 07). Restoration of the contact surface in the hll-riemann solver. *Shock Waves*, *4*, 25-34. doi: 10.1007/BF01414629

Torrilhon, M. (2003, 04). Uniqueness conditions for riemann problems of ideal magnetohydrodynamics. *Journal of Plasma Physics*, *69*, 253 - 276. doi: 10.1017/S0022377803002186

Tsap, Y., & Stepanov, A. (2011, 09). Ambipolar diffusion and magnetic reconnection. *Proceedings of The International Astronomical Union*, *274*, 302-305. doi: 10.1017/S1743921311007174

Tóth, G. (2000). The div(b)=0 constraint in shock-capturing magnetohydrodynamics codes. *Journal of Computational Physics*, *161*(2), 605 - 652. Retrieved from http://www.sciencedirect.com/science/article/pii/S0021999100965197 doi: https://doi.org/10.1006/jcph.2000.6519

Ugai, M. (1999). Computer studies on the spontaneous fast reconnection model as a nonlinear instability. *Physics of Plasmas*, *6*(5), 1522-1531. Retrieved from https://doi.org/10.1063/1.873405 doi: 10.1063/1.873405

van der Holst, B., & Keppens, R. (2007, September). Hybrid block-AMR in cartesian and curvilinear coordinates: MHD applications. *Journal of Computational Physics*, *226*, 925-946. doi: 10.1016/j.jcp.2007.05.007

van Albada, G. D., van Leer, B., & Roberts, W. W. (1997). A comparative study of computational methods in cosmic gas dynamics. In *Upwind and high-resolution schemes* (pp. 95–103). Berlin, Heidelberg: Springer Berlin Heidelberg. Retrieved from https://doi.org/10.1007/978-3-642-60543-7_6 doi: 10.1007/978-3-642-60543-7_6

Van Leer, B. (1997). On the relation between the upwind-differencing schemes of godunov, engquist—osher and roe. In *Upwind and high-resolution schemes* (pp. 33–52). Berlin, Heidelberg: Springer Berlin Heidelberg. Retrieved from https://doi.org/10.1007/978-3-642-60543-7_3 doi: 10.1007/978-3-642-60543-7_3

van Leer, B. (1997). Towards the ultimate conservative difference scheme. *Journal of Computational Physics*, *135*(2), 229 - 248. Retrieved from http://www.sciencedirect.com/science/article/pii/S0021999197957041 doi: https://doi.org/10.1006/jcph.1997.5704

Vernazza, J. E., Avrett, E. H., & Loeser, R. (1981, April). Structure of the solar chromosphere. III - Models of the EUV brightness components of the quiet-sun. *The Astrophysical Journal Supplement series*, *45*, 635-725. doi: 10.1086/190731

Vincenti, W. G., & Kruger, C. H. (1965). *Introduction to physical gas dynamics*. New York, Wiley.

Vranjes, J., Petrovic, D., Poedts, S., Kono, M., & Čadež, V. (2006). Unstable kinetic alfvén wave in partially ionized plasma. *Planetary and Space Science*, *54*(6), 641 - 644. Retrieved from http://www.sciencedirect.com/science/article/pii/S0032063306000067 doi: https://doi.org/10.1016/j.pss.2005.12.015

Vranjes, J., & Poedts, S. (2009, 06). The universally growing mode in the solar atmosphere: Coronal heating by drift waves. *MNRAS*, *398*. doi: 10.1111/j.1365-2966.2009.15180.x

Vranjes, J., & Poedts, S. (2010, 10). Drift waves in the corona: heating and acceleration of ions at frequencies far below the gyrofrequency. *Monthly Notices of the Royal Astronomical Society*, *408*(3), 1835-1839. Retrieved from https://doi.org/10.1111/j.1365-2966.2010.17249.x doi: 10.1111/j.1365-2966.2010.17249.x

Wargnier, Q., Alvarez Laguna, A., Kestener, P., Graille, B., Mansour, N. N., Massot, M., & Magin, T. (2018). Mathematical modeling and high fidelity adaptive simulations of astrophysical plasmas with accurate transport: application in solar physics. In *Nasa technical memorandum, proveedings of the 2018 summer program* (p. 1-16).

Wargnier, Q., Alvarez Laguna, A., Magin, T., Massot, M., Graille, B., & Kestener, P. (2018). Multicomponent fluid model for two-temperature plasmas derived from kinetic theory : application to magnetic reconnection. *Theory of Fusion Plasmas, JPCS*.

Wargnier, Q., Alvarez Laguna, A., Massot, M., Kestener, P., & Mansour, N. N. (2019). Mathematical modeling and high fidelity adaptive simulations of partially ionized plasmas with accurate multicomponent transport: application to magnetic reconnection in solar physics. *In preparation for Journal of Computational Physics*.

Wargnier, Q., Faure, S., Graille, B., Magin, T., & Massot, M. (2018). Numerical treatment of the nonconservative product in a multiscale fluid model for plasmas in thermal nonequilibrium: application to solar physics. *ArXiv e-prints*. (https://arxiv.org/abs/1806.10436)

Wargnier, Q., Laguna, A. A., Scoggins, J. B., Mansour, N. N., Massot, M., & Magin, T. (2019). Consistent transport properties in a two temperature multicomponent plasma model: Application to the magnetized sun chromosphere. *Astronomy and Astrophysics*. (submitted)

Waterson, N. P., & Deconinck, H. (2007, May). Design principles for bounded higher-order convection schemes - a unified approach. *J. Comput. Phys.*, *224*(1), 182–207. Retrieved from http://dx.doi.org/10.1016/j.jcp.2007.01.021 doi: 10.1016/j.jcp.2007.01.021

Wiegelmann, T., Thalmann, J. K., & Solanki, S. K. (2014, November). The magnetic field in the solar atmosphere. *The Astronomy and Astrophysics review*, *22*, 78. doi: 10.1007/s00159-014-0078-7

Wilke, C. R. (1950). A viscosity equation for gas mixtures. *The Journal of Chemical Physics*, *18*(4), 517-519. doi: 10.1063/1.1747673

Williams, J. F. (1975a, sep). Electron scattering from atomic hydrogen. III. absolute differential cross sections for elastic scattering of electrons of energies from 20 to 680 eV. *Journal of Physics B: Atomic and Molecular Physics*, *8*(13), 2191–2199. Retrieved from https://doi.org/10.1088%2F0022-3700%2F8%2F13%2F011 doi: 10.1088/0022-3700/8/13/011

Williams, J. F. (1975b, jul). Electron scattering from hydrogen atoms. II. elastic scattering at low energies from 0.5 to 8.7 eV. *Journal of Physics B: Atomic and Molecular Physics*, *8*(10), 1683–1692. Retrieved from https://doi.org/10.1088%2F0022-3700%2F8%2F10%2F018 doi: 10.1088/0022-3700/8/10/018

Wissink, A., Hysom, D., & Hornung, R. (2003, 01). Enhancing scalability of parallel structured amr calculations. *Proceedings of the International Conference on Supercomputing*, 336-347. doi: 10.1145/782814.782861

Wójcik, D., Murawski, K., & Musielak, Z. E. (2019, aug). Partially ionized solar atmosphere: Two-fluid waves and their cutoffs. *The Astrophysical Journal*, *882*(1), 32. Retrieved from https://doi.org/10.3847%2F1538-4357%2Fab3224 doi: 10.3847/1538-4357/ab3224

Woods, L. C. (1995). *An introduction to the kinetic theory of gases and magnetoplasmas.* (Vol. 286). Cambridge University Press.

Wray, A. A., Bensassi, K., Kitiashvili, I. N., Mansour, N. N., & Kosovichev, A. G. (2015, July). Simulations of Stellar Magnetoconvection using the Radiative MHD Code 'StellarBox'. *ArXiv e-prints*. (https://arxiv.org/abs/1507.07999)

Wright, M., Bose, D., Palmer, G., & Levin, E. (2005, 12). Recommended collision integrals for transport property computations part 1: Air species. *Aiaa Journal - AIAA J*, *43*. doi: 10.2514/1.16713

Wright, M., Hwang, H., & Schwenke, D. (2007, 01). Recommended collision integrals for transport property computations part ii: Mars and venus entries. *Aiaa Journal - AIAA J*, *45*, 281-288. doi: 10.2514/1.24523

Xia, C., Teunissen, J., El Mellah, I., Chané, E., & Keppens, R. (2018, Feb). MPI-AMRVAC 2.0 for Solar and Astrophysical Applications. *The astrophysical journal supplement series*, *234*(2), 30. doi: 10.3847/1538-4365/aaa6c8

Yee, H., Vinokur, M., & Djomehri, M. (2000). Entropy splitting and numerical dissipation. *J. Comput. Phys.*, *162*(1), 33 - 81.

Yee, K. S. (1966). Numerical solution of initial boundary value problems involving maxwell's equations in isotropic media. *IEEE Trans. Antennas and Propagation*, 302–307.

Zel'dovich, Y. B., & Raizer, Y. P. (1967). *Physics of shock waves and high-temperature hydrodynamic phenomena* (Vol. 2). New York and London: Academic Press. (W.D. Hayes and R.F. Probstein Editors)

Zhdanov, V. (2002). *Transport processes in multicomponent plasma* (Vol. 44). Taylor & Francis Group.

Zhou, G. (1885). *Numerical simulations of physical discontinuities in single and multi-fluid flows for arbitrary mach numbers.* Ph.D. Thesis, Chalmers University of Technology.

Zhu, W., long Feng, L., Xia, Y., Shu, C.-W., Gu, Q., & Fang, L.-Z. (2013, oct). Turbulence in the intergalactic medium: solenoidal and dilatational motions and the impact of numerical viscosity. *The Astrophysical Journal*, *777*(1), 48. Retrieved from https://doi.org/10.1088%2F0004-637x%2F777%2F1%2F48 doi: 10.1088/0004-637x/777/1/48

Zweibel, E. G. (1989, May). Magnetic reconnection in partially ionized gases. *The astrophysical journal*, *340*, 550-557. doi: 10.1086/167416

université PARIS-SACLAY | École doctorale de mathématiques Hadamard (EDMH)

Titre : Modélisation mathématique et simulation des plasmas hors équilibres pour la prédiction de la reconnexion magnétique : application à l'atmosphère solaire

Mots Clefs : Magnétohydrodynamique, physique solaire, plasmas hors équilibre, théorie cinétique des gaz, coefficients de transport, calcul massivement parallèle, Reconnexion magnétique

Résumé :

La capacité de modéliser, simuler et prédire le phénomène de reconnexion magnétique est un enjeu crucial pour de nombreuses applications (ITER, plasmas astrophysiques) et impacte la prédiction du « temps solaire » et des « orages magnétiques » pouvant perturber de manière nocive les satellites. L'enjeu scientifique fondamental est la description du transfert instationnaire d'énergie magnétique en énergie cinétique et thermique, encore hors d'atteinte des modèles magnéto-hydrodynamique (MHD) actuels. L'objectif premier de la thèse est le développement d'un modèle fluide cohérent de plasma magnétisé hors équilibre thermique et chimique avec une description détaillée des effets dissipatifs basée sur la théorie cinétique des gaz et une bonne structure mathématique. Le deuxième objectif est focalisé sur la fermeture du modèle fluide et la dérivation de ses propriétés transports calculés au niveau cinétique. Le troisième repose sur le développement d'une stratégie numérique innovante, précise et robuste, dans un code de calcul massivement parallèle avec adaptation de maillage permettant de capturer tout le spectre d'échelle en jeu et la raideur numérique en résultant. L'ensemble des coefficients de transport, la thermodynamique et la chimie correspondante seront étudiés et comparés aux données préalablement utilisées dans le domaine. Puis on montrera que le modèle et sa simulation, issus d'un travail transdisciplinaire impliquant ingénierie, physique des plasmas, physique solaire, mathématique, et calcul scientifique et parallèle, est capable d'aborder la physique du phénomène. La validation de l'approche à travers une série de cas test issus de l'application à la dynamique de l'atmosphère solaire en collaboration avec la NASA et le VKI permettra de disposer d'un outil, le code `CanoP`, ouvert à la communauté, capable de lever plusieurs verrous scientifiques et technologiques.

Title : Mathematical modeling and simulation of non-equilibrium plasmas for the prediction of magnetic reconnection: application to the solar atmosphere

Keys words : Magnetohydrodynamics, solar physics, magnetized plasmas out of equilibrium, kinetic theory of gases, transport coefficients, massively parallel computing, Magnetic reconnection

Abstract : The ability to model, simulate and predict magnetic reconnection (MR) is a stumbling block in order to predict space weather and geomagnetic storms, which can lead to harmful perturbation of satellites. Some fundamental aspects of MR are not yet well understood. The scientific issue at stake is the proper description of the unsteady energy transfer from magnetic energy to kinetic and thermal energy, which is still out of reach for the standard Magneto-hydrodynamics (MHD) models. The first objective of the present thesis is to develop a coherent fluid model for magnetized plasmas out of thermal and chemical equilibrium with a detailed description of the dissipative effects based on kinetic theory of gases, which thus inherits a proper mathematical structure. The second objective of the thesis is to focus on the closure of the fluid model and derive its transport properties computed at the kinetic level. The third goal is the development of a new numerical strategy, with high accuracy and robustness, based on a massively parallel code with adaptive mesh refinement able to cope with the full spectrum of scales of the model and related stiffness. The whole set of transport coefficients, thermodynamics relations and chemical rates in this magnetized two-temperature setting will be studied and compared to the one in the literature used in the field. Then, we will show that the model and related numerical strategy, obtained from this transdisciplinary work involving engineering, plasma physics, solar physics, mathematics, scientific computing and High-Performance Computing (HPC), is able to tackle the problem of MR. The validation of the approach through a series of test-cases relevant for the application to the dynamics of solar atmosphere in collaboration with VKI and NASA will provide a tool, the CanoP code, open to the community, capable of resolving several critical scientific and technological issues.